



**IAMBEST**  
KMITL PRINCE OF CHUMPHON  
1-2 MAY 2025

## The 6<sup>th</sup> International Conference

**Vol.3**

Informatics, Agriculture,  
Engineering, Sciences and Technology

**May 1 – 2, 2025**

Grand Pacific Sovereign Resort & Spa, Cha-am, Phetchaburi Province, Thailand  
Organized by King Mongkut's Institute of Technology Ladkrabang,  
Prince of Chumphon Campus, Chumphon Province, Thailand

---

**The 10<sup>th</sup> National Conference and The 6<sup>th</sup> International Conference  
on Informatics, Agriculture, Management, Business Administration,  
Engineering, Sciences and Technology (IAMBEST 2025)**

**Organized by:**

King Mongkut's Institute of Technology Ladkrabang, Prince of  
Chumphon Campus and University Network

© Copyright 2025 King Mongkut's Institute of Technology Ladkrabang, Prince of Chumphon Campus All rights reserved. part of this publication may be reproduced, stored in a retrieval system or transmitted in any form or by any mea electronic, mechanical, photocopying, recording or otherwise, without written permission from King Mongkut's Institute Technology Ladkrabang, Prince of Chumphon Campus. All full papers in the proceedings are reviewed and accept for publication. Responsibility for the contents of the paper's rests with the authors.

**1<sup>st</sup> Published:** May 1<sup>st</sup>, 2025.

**Cover Page Design:** Mr. Sarawut Sawasdee

**Published by:**

King Mongkut's Institute of Technology Ladkrabang Prince of  
Chumphon Campus, Chumphon 17/1 Moo 6 Chumko Pathio  
Chumphon 86160 Thailand 86160

Tel: (+66) 77 506 - 410

---

## MESSAGE FROM THE EXECUTIVE VICE PRESIDENT KMITL, PRINCE OF CHUMPHON CAMPUS



The 6<sup>th</sup> International Conference on Informatics, Agriculture, Management, Business Administration, Engineering, Science, and Technology (IAMBEST 2025), along with the 10<sup>th</sup> National Conference on Informatics, Agriculture, Management, Business Administration, Engineering, Science, Technology, Social Sciences, and Humanities, are conferences for academics, experts, and researchers in the eight fields. The conferences are hosted by the King Mongkut's Institute of Technology Ladkrabang (KMITL), Prince of Chumphon Campus, during 1-2 May 2025. The aim of these conferences is to provide an exchange stage for ideas, knowledge, and research among researchers from various fields. The continued development of research fosters the exchange of knowledge, connections, collaboration, and integration among one another. All of the above contributes to the development of the community, society, and country.

As the chairman of IAMBEST 2025, I sincerely thank all committee members for your time and determination in organizing this wonderful conference. I thank all attendees and guests for sharing your research and innovation. The success of this conference is due to all of you. I wish that the exchange of ideas and sharing of knowledge from this conference will provide you with another step to advance your knowledge and technology and to benefit your communities and countries.

Best wishes to all of you.



(Assoc. Prof. Dr. Kamronwit Thipmanee)  
Executive Vice President,  
KMITL, Prince of Chumphon Campus  
Chairman of the Organizing Committee



# KEYNOTE SPEAKER

**Topic: AI: Driven Agriculture, Engineering,  
Business and Food Innovation  
Transformation**



**Keynote Speaker :**  
**Associate Prof. Dr. Siridech Boonsang**  
**King Mongkut's Institute of Technology Ladkrabang**



## Contents

Message from the Executive Vice President	I
Keynote Speakers	II
Contents International Conference	III
Program International Conference	VII
Academic Committee International Conference	IX
List of reviewers International Conference	XIV

## Contents International Conference

### Oral Presentation

#### Group I : Informatics

- OI-61 An ABC-Optimized Hybrid CNN-LSTM Model for Chinese Handwritten Signature Recognition (Comparison with Traditional RNNs) 2  
*Yun Dai Adisak Sangsongfa and Nopadol Amm-Dee*
- OI-66 Sentiment Analysis of Tourists' Speech in Heilongjiang Province: Application of Hybrid BiLSTM and FastText in Natural Language Processing 8  
*Ling Ma Adisak Sangsongfa and Nopadol Amm-Dee*
- OI-79 Proposal for an Autonomous and Efficient SQL Learning Support Model Using Generative AI 15  
*Somchai Chatvichienchai*

#### Group A : Agriculture

- OA-14 Comparative of Spawning Induction Methods on Breeding Performance of Mangrove Red Snapper *Lutjanus argentimaculatus* Broodstock from Earthed Pond-Reared 22  
*Chawisa Pholsangsee Phongchate Pichitkul Idsariya Wudtisin and Vuttichai Oniam*
- OA-80 Effects of Packaging and Temperature-Controlled Materials on the Quality and Transportation Cost of Marinated Salmon 27  
*Nathaphat Kingkaew, Supakit Sayasoonthorn, Kiatkamjon Intani and Ratiya Thuwapanichayanan*

#### Group E : Engineering

- OE-3 Real-time Fish classification using Convolutional Neural Network based on Embedded System 33  
*Taweepol Suesut Wirat Khannakum Paranyu Phraenan and Navaphattra Nunak*

## Contents International Conference

### Group E : Engineering

OE-4	Comparison of ON-OFF and PID Temperature Control on Soymilk Fouling Formation in Plate Heat Exchanger <i>Navaphattra Nunak Worapanya Suthanupaphwut and Taweeapol Suesut</i>	38
OE-16	Thermochemical reforming of biogas to syngas production: A Review <i>Ratikorn Kulporm Srirat Chuayboon Sompong O-Thong and Monsicha Tipawanna</i>	43
OE-17	Static Strength and Overload Assessment of Obstacle Deflector in The Aachen Rail Shuttle <i>Ponphom Chakornpipat Nutchanon Prasomsuk Kittchai Sojiphan Chayut Ngamkhanong and Christian Schindler</i>	49
OE-19	A Review on Blue Economy's Dual Role in Reducing CO <sub>2</sub> Pollution and Achieving SDGs <i>Jaydeep a. Karmur mahipalsinh b. Parmar keval h. Jodhani and nitesh gupta</i>	56
OE-20	Sugarcane Leaf Disease Classification Using a Hybrid ReXNet-Based Model and SVMs <i>Krankamon Phukhronghin Kanit Manatura Natthapong Prapakarn Nuttapong Wongbubpa and Kritsada Tasuntia</i>	65
OE-21	Taguchi-Based Optimization of Torrefaction Conditions for Enhancing Corncob Biomass Properties <i>Kanit Manatura Kunthakorn Khaothong Kitipong Jaojaruek Krankamon Phukhronghin Den Kogphimai Preecha Somwang and Namfon Samsalee</i>	71
OE-47	Investigation into Acoustic Pressure Distribution Across Various Liquids within an Ultrasonic Tank <i>Nongnapat Phadungjiraphanthatip and Karuna Tuchinda</i>	76
OE-48	Dynamic Responses of Prestressed Concrete Sleeper due to Flat-Spot on Railway Wheels using Finite Element Method <i>Supapol Rahannok Kittichai Sojiphan and Chayut Ngamkhanong</i>	82
OE-50	Enhancing Road Traffic Accident Data Collection and Reconstruction Process in Thailand <i>Anyamanee Suksing and Julaluk Carmai</i>	88
OE-54	Biomimetic Kinetic Facade Design for Enhanced Daylighting: A LEED v 4 Based Approach for a Reading Room of a Dormitory in Chittagong, Bangladesh <i>Gourav Deya and Vorapat Inkarojrit</i>	94

## Contents International Conference

### Group E : Engineering

- OE-70 Design Drying Control System from LPG by Proportional Integral Derivative (PID) 102  
Controller for Charcoal Briquettes  
*Chanon Bunmephiphit Kittikorn Sasujit Churat Thararux and Nigran Homdoug*
- OE-72 Improvement on the Cooling Efficiency of a Split-Type A/C Using Waste Heat 107  
Recovery  
*Chanwit Wittavirote and Chanon Bunmephiphit*
- OE-85 Experimental Fretting Wear Resistance Study of Chromizing Treatment on AAR 111  
M101 Railway Axle Steel  
*Manassanun Nitiruksakul Karuna Tuchinda Anchalee Manonukul and Nuksit Noomwongs*
- OE-88 Economic Evaluation of Conversation Energy in Oil Palm Mill Industrial 117  
*Kanitpong Chitsopon and Chanon Bunmephiphit*

### Group S : Sciences

- OS-2 Development of alternative UV-protective cotton fabrics using natural dyes from 121  
ethanolic extract of carrot and black glutinous rice  
*Apiwitch Kraykome Benyapa Wasasiri Thanaporn Maswanna and Tussanee Chantiwas*
- OS-69 The Effect of Insulin Pen Instructions Video on Patient with Diabetes by Line 126  
Application at HRH Princess Mahachakri Sirindhorn Medical Center  
*Nara Kaewkwan Marisa Mayusoh Sumet Klinhom Pattarawit Rukthong and Tulaya Potaros*

### Poster Presentation

#### Group : Agriculture

- PA-77 New Insights into the Status and Distribution of Durian Seed Borers 131  
(*Mudaria* spp.) (Lepidoptera: Noctuidae) in Thailand  
*Pornthap Chamsuk Arthit Rukkasikorn Sunudda Chaovalit Paradorn Dokchan Supakorn  
Tangsuan Korakot Ratanamahamaneekorn and Pisit Poolprasert*
- PA-112 Effect of Chitosan and Silicon on Growth and Strength of *Dendrobium* sp. 136  
Plantlets  
*Tuansobariyah Lateh Alisa Kongjaiman Yoshida Yupa Pootaeng-on and Chaowanee  
Laosutthipong*



## Contents International Conference

### Poster Presentation

#### Group E : Engineering

- PE-101 Measurement of Forearm Muscle Electromyography during Finger Movements 141  
*Dithaporn Thungsotanon Sakapan Klaydokjan Nathaporn Suwanpayak and Chompoonud Kulketwong*

#### Group S : Sciences

- PS-23 Pattern of Pediatric Bacterial Infection and Antibiotic Resistance in Tertiary Care Hospitals, Southern Thailand: A 12-Year Experience 145  
*Phanvasri Saengsuwan Narongdet Kositpantawong Wacharakrit Wachirapichet and Wisanuwee Suriyaamorn*
- PS-53 Comprehensive Protein Analysis of Blackchin Tilapia for Surimi Production Potential 151  
*Theeraphol Senphan Natthapong Mungmueang and Chodsana Sriket*
- PS-78 Targeted Metabolomics Analysis of Plant Pathogen *Ralstonia solanacearum* Towards *Bacillus amyloliquefaciens* 157  
*James Danga Alisa S. Vangnai, Pimsiri Tiyyon and Nawaporn Vinayavekhin*
- PS-92 Water-assisted Extraction of Asiatic Acid from *Centella asiatica* 161  
*Zue Zue Win Myat and Surachai Pornpakakul*
- PS-99 Characterization of acid-soluble collagen isolated from Spotted Sickfish (*Drepane punctata*) skin 167  
*Yannawut Meuykamnerd Saofa Chaloeisamai Supaporn Maknamnit and Sitthipong Nalinanon*

#### Group T : Technology

- PT-91 Development of a Convolutional Neural Network Model for the Classification of Verb Gestures in Sign Language 172  
*Siraphop Sangthong Patcharapol Jamsawang Saran Khamphuk and Siwakon Sokjabok*

## Program

**The 10<sup>th</sup> National Conference and The 6<sup>th</sup> International Conference 2025  
on Informatics, Agriculture, Management, Business Administration,  
Engineering, Sciences and Technology (IAMBEST 2025)**

**May 1-2, 2025**

**Grand Pacific Sovereign Resort & Spa Hotel, Cha-am, Phetchaburi, Thailand**

**April 30, 2025**

16.00 – 18.30	The meeting of distinguished experts and the judging committee, speakers, and networks for the national and international academic conference IAMBEST 2025	
17.00 – 18.30	Installation of poster	Foyer 2

**May 1, 2025**

08.00 – 08.30	Registration and Installation of poster and soft file presentation	Foyer 1
08.30 – 09.00	Open Ceremony The 10 <sup>th</sup> National Conference and The 6 <sup>th</sup> International Conference 2025	
09.00 – 10.00	Keynote Speaker Topic AI: Driven Agriculture, Engineering, Business and Food Innovation Transformation By Associate Prof. Dr. Siridech Boonsang	Petch Siam Ballroom
10.00 – 10.15	Coffee break	
10.15 – 12.00	Speaker Topic AI: Driven Agriculture, Engineering, Business and Food Innovation Transformation By Associate Prof. Dr. Siridech Boonsang	Business Center
10.30 – 12.00	International Conference (Oral Presentation) Session I: Informatics and Engineering	Petch Chompoo
	International Conference (Poster Presentation)	Foyer 2
	National Conference (Oral Presentation) Session 1 : Informatics and Technology	Petch Amphan
	Session 4 : Business administration and Social Science & Humanities	Petch Phailin
	National Conference (Poster Presentation) Session 1 Agriculture	Foyer 2
	Session 3 Management and Business administration	Foyer 2
12.00 - 13.00	Lunch break	

Program

The 10<sup>th</sup> National Conference and The 6<sup>th</sup> International Conference 2025  
on Informatics, Agriculture, Management, Business Administration,  
Engineering, Sciences and Technology (IAMBEST 2025)

May 1-2, 2025

Grand Pacific Sovereign Resort & Spa Hotel, Cha-am, Phetchaburi, Thailand

May 1, 2025

13.00 – 14.30	International Conference (Oral Presentation)	
	Session II : Engineering	Petch Chompoo
	Session IV : Agriculture and Sciences	Petch Siam Ballroom
	National Conference (Oral Presentation)	
	Session 2 Management	Petch Amphan
	Session 5 Agriculture and Sciences	Petch Phailin
	National Conference (Poster Presentation)	
	Session 2 : Technology and Engineering	Foyer 2
	Session 4 : Sciences	Foyer 2
14.30 - 14.45	Coffee break	
	International Conference (Oral Presentation)	
14.15 – 15.30	Session V: Management and Social Science & Humanities	Petch Siam Ballroom
14.45 – 17.30	Session III : Engineering	Petch Chompoo
14.15 – 17.30	National Conference (Oral Presentation)	
	Session 3: Engineering	Petch Amphan
	Session 6: Business administration	Petch Phailin
18.30 – 21.00	<i>Dinner</i>	Petch Siam Ballroom

May 2, 2025

10.00 – 11.30	The Network Meeting for the National and International Academic Conference IAMBEST 2025.
---------------	---

Remarks: The program can be adjusted.



## Program International Conference (Oral Presentation)

## Session I: Informatics and Engineering

Petch Chompoo

Chairperson	Assoc. Prof. Dr.Punyawi Jamjareegulgarn	KMITL Prince of Chumphon
	Assoc. Prof.Dr.Boonchana Purahong.	KMITL
	Asst. Prof. Dr. Thanavit Anuwongpinit	KMITL
Time	Code	Topic
10.15 – 10.30	OI-61	An ABC-Optimized Hybrid CNN-LSTM Model for Chinese Handwritten Signature Recognition (Comparison with Traditional RNNs) <i>Yun Dai Adisak Sangsongfa and Nopadol Amm-Dee</i>
10.30 – 10.45	OI-66	Sentiment Analysis of Tourists' Speech in Heilongjiang Province: Application of Hybrid BiLSTM and FastText in Natural Language Processing <i>Ling Ma Adisak Sangsongfa and Nopadol Amm-Dee</i>
10.45 – 11.00	OI-79	Proposal for an Autonomous and Efficient SQL Learning Support Model Using Generative AI <i>Somchai Chatvichienchai</i>
11.00 – 11.15	OE-47	Investigation into Acoustic Pressure Distribution Across Various Liquids within an Ultrasonic Tank <i>Nongnapat Phadungjiraphanthatip and Karuna Tuchinda</i>
11.15 – 11.30	OE-85	Experimental Fretting Wear Resistance Study of Chromizing Treatment on AAR M101 Railway Axle Steel <i>Manassanun Nitiruksakul Karuna Tuchinda Anchalee Manonukul and Nuksit Noomwongs</i>
11.30 – 11.45	OE-19	A Review on Blue Economy's Dual Role in Reducing CO <sub>2</sub> Pollution and Achieving SDGs <i>JAYDEEP A. KARMUR MAHIPALSINH B. PARMAR KEVAL H. JODHANI and NITESH GUPTA</i>
Lunch break		

## Program International Conference (Oral Presentation)

## Session II: Engineering

Petch Chompoo

Chairperson	Assoc. Prof. Dr. Siriwan Srisang	KMITL Prince of Chumphon
	Assoc. Prof. Dr. Naruebodee Srisang	KMITL Prince of Chumphon
	Assoc. Prof. Dr. Thatchapol Chungcharoen	KMITL Prince of Chumphon
Time	Code	Topic
13.00 – 13.15	OE-03	Real-time Fish classification using Convolutional Neural Network based on Embedded System <i>Taweepol Suesut Wirat Khannakum Paranyu Phraenan and Navaphattra Nunak</i>
13.15 – 13.30	OE-04	Comparison of ON-OFF and PID Temperature Control on Soymilk Fouling Formation in Plate Heat Exchanger <i>Navaphattra Nunak Worapanya Suthanupaphwut and Taweepol Suesut</i>
13.30 – 13.45	OE-16	Thermochemical reforming of biogas to syngas production: A Review <i>Ratikorn Kulporm Srirat Chuayboon Sompong O-Thong and Monsicha Tipawanna</i>
13.45 – 14.00	OE-17	Static Strength and Overload Assessment of Obstacle Deflector in The Aachen Rail Shuttle <i>Ponphom Chakornpipat Nutchanon Prasomsuk Kittchai Sojiphan Chayut Ngamkhanong and Christian Schindler</i>
14.00 – 14.15	OE-20	Sugarcane Leaf Disease Classification Using a Hybrid ReXNet-Based Model and SVMs <i>Krankamon Phukhronghin Kanit Manatura Natthapong Prapakarn Nuttapong Wongbubpa and Kritsada Tasuntia</i>
14.15 – 14.30	OE-21	Taguchi-Based Optimization of Torrefaction Conditions for Enhancing Corncob Biomass Properties <i>Kanit Manatura Kunthakorn Khaothong Kitipong Jaojaruek Kankamon Phookronghin Den Kogphimai Preecha Somwang and Namfon Samsalee</i>
14.30 – 14.45	OE-52	Green Iron and Syngas Production via Continuous Solar Iron Oxide Reduction with Betel Nut Biowaste-Residue <i>Srirat Chuayboon and Stéphane Abanades</i>

## Program International Conference (Oral Presentation)

## Session III: Engineering

Petch Chompoo

Chairperson	Assoc. Prof. Dr. Sira Saisorn	KMITL Prince of Chumphon
	Assoc. Prof. Dr. Srirat Chuayboon	KMITL Prince of Chumphon
	Assoc. Prof. Dr. Kittisak Phetpan	KMITL Prince of Chumphon
Time	Code	Topic
15.00 – 15.15	OE-30	Measuring the Photosynthesis Photon Flux Density Using Spectral Sensor <i>Pattarapong Sunongbua Jintaphorn Klinsuk and Weerasak Lertsiriyothin</i>
15.15 – 15.30	OE-48	Dynamic Responses of Prestressed Concrete Sleeper due to Flat-Spot on Railway Wheels using Finite Element Method <i>Supapol Rahannok Kittichai Sojiphan and Chayut Ngamkhanong</i>
15.30 – 15.45	OE-50	Enhancing Road Traffic Accident Data Collection and Reconstruction Process in Thailand <i>Anyamanee Suksing and Julaluk Carmai</i>
15.45 – 16.00	OE-54	Biomimetic Kinetic Facade Design for Enhanced Daylighting: A LEED v 4 Based Approach for a Reading Room of a Dormitory in Chittagong, Bangladesh <i>Gourav Dey and Vorapat Inkarojrit</i>
16.00 – 16.15	OE-70	Design Drying Control System from LPG by Proportional Integral Derivative (PID) Controller for Charcoal Briquettes <i>Chanon Bunmephiphit Kittikorn Sasujit Churat Thararux and Nigran Homdoun</i>
16.15 – 16.30	OE-72	Improvement on the Cooling Efficiency of a Split-Type A/C Using Waste Heat Recovery <i>Chanwit Wittavirote, Chanon Bunmephiphit</i>
16.30 – 16.45	OE-88	Economic Evaluation of Conversation Energy in Oil Palm Mill Industrial <i>Kanitpong Chitsopon and Chanon Bunmephiphit</i>
16.45 – 17.00	OE-101	Measurement of Forearm Muscle Electromyography during Finger Movements <i>Dithaporn Thungsotanon Sakapan Klaydokjan Nathaporn Suwanpayak and Chompoonud Kulketwong</i>



## Program International Conference (Oral Presentation)

Session IV : Agriculture and Sciences

Petch Siam Ballroom

Chairperson	Asst. Prof. Dr. Chodsana Sriket	KMITL Prince of Chumphon
	Asst. Prof. Dr. Jongjit Jantra	KMITL Prince of Chumphon
	Dr. Kanchalar Keeratrirawee	KMITL Prince of Chumphon
Time	Code	Topic
13.00 – 13.15	OA-14	Comparative of Spawning Induction Methods on Breeding Performance of Mangrove Red Snapper <i>Lutjanus argentimaculatus</i> Broodstock from Earthed Pond-Reared <i>Chawisa Pholsangsee Phongchate Pichitkul Idsariya Wudtisin and Vuttichai Oniam</i>
13.15 – 13.30	OA-80	Effects of Packaging and Temperature-Controlled Materials on the Quality and Transportation Cost of Marinated Salmon <i>Nathaphat Kingkaew Supakit Sayasoonthorn Kiatkamjon Intani and Ratiya Thuwapanichayanan</i>
13.30 – 13.45	OS-02	Development of alternative UV-protective cotton fabrics using natural dyes from ethanolic extract of carrot and black glutinous rice <i>Apiwitch Kraykome Benyapa Wasasiri Thanaporn Maswanna and Tussanee Chantiwas</i>
13.45 – 14.00	OS-69	The Effect of Insulin Pen Instructions Video on Patient with Diabetes by Line Application at HRH Princess Mahachakri Sirindhorn Medical Center <i>Nara Kaewkwan Marisa Mayusoh Sumet Klinhom Pattarawit Rukthong and Tulaya Potaros</i>

## Program International Conference (Poster Presentation)

Chairperson	Asst. Prof. Dr. Jongjit Jantra	KMITL Prince of Chumphon
	Dr. Kanchalar Keeratrirawee	KMITL Prince of Chumphon
	Dr. Nanaphat Suwannarat	KMITL Prince of Chumphon
Time	Code	Topic
10.30 – 10.40	PS-23	Pattern of Pediatric Bacterial Infection and Antibiotic Resistance in Tertiary Care Hospitals, Southern Thailand: A 12-Year Experience <i>Phanvasri Saengsuwan Narongdet Kositpantawong Wacharakrit Wachirapichet and Wisanuwee Suriyaamorn</i>
10.40 – 10.50	PS-53	Comprehensive protein analysis of blackchin tilapia for surimi production potential <i>Theeraphol Senphan Natthapong Mungmueang and Chodsana Sriket</i>
10.50 – 11.00	PS-78	Targeted Metabolomics Analysis of Plant Pathogen <i>Ralstonia solanacearum</i> Towards <i>Bacillus amyloliquefaciens</i> <i>James Danga Alisa S. Vangnai Pimsiri Tiyyon and Nawaporn Vinayavekhin</i>
11.00 – 11.10	PS-92	Water-assisted Extraction Of Asiatic Acid from <i>Centella asiatica</i> <i>Zue Zue Win Myat and Surachai Pompakakul</i>
11.10 – 11.20	PS-99	Characterization of acid-soluble collagen isolated from Spotted Sickfish ( <i>Drepane punctata</i> ) skin <i>Yannawut Meuykamnerd Saofa Chaloeisamai Supaporn Maknamnit and Sitthipong Nalinanon</i>
11.20 – 11.30	PT-91	Development of a Convolutional Neural Network Model for the Classification of Verb Gestures in Sign Language <i>Siraphop Sangthong Patcharapol Jamsawang Saran Khamphuk and Siwakon Sokjabok</i>
11.30 – 11.40	PA-77	New Insights into the Status and Distribution of Durian Seed Borers ( <i>Mudaria</i> spp.) (Lepidoptera: Noctuidae) in Thailand <i>Pomthap Chamsuk Arthit Rukkasikorn Sunudda Chaovalit Paradorn Dokchan Supakorn Tangsuan Korakot Ratanamahamaneekorn and Pisit Poolprasert</i>
11.40 – 11.50	PA-112	Effect of Chitosan and Silicon on Growth and Strength of <i>Dendrobium</i> sp. Plantlets <i>Tuansobariyah Lateh Alisa Kongjaiman Yoshida Yupa Pootaeng-on and Chaowanee Laosutthipong</i>

## Academic Committee

### International Academic Committee

Dr. Patel Nilesh	B.K.M Science College, India
Dr. Aghogho Ogwala	Eko University of Medicine and Health Sciences, Nigeria
Prof. Dr. David Mendes	Federal University of Alagoas, Brazil
Prof. Dr. José Francisco de Oliveira Júnior	Federal University of Alagoas, Brazil
Prof. Dr. Widodo Hadisaputro	Gadjah Mada University, Indonesia
Dr. Sneha Sharma	Independent Scholar, Melbourne, Australia
Mr. K.C. Sumesh	Independent Scholar, Melbourne, Australia
Dr. Ed Nofri	Indonesian National Research and Innovation Agency (BRIN), Indonesia
Asst. Prof. Dr. Munawar Shah	Institute of Space Technology, Pakistan
Dr. Kutubuddin Ansari	Integrated Geoinformation (IntGeo) Solution Private Limited, India
Dr. Albert Abad Braga	King Mongkut's Institute of Technology Ladkrabang, Prince of Chumphon, Thailand
Dr. Raymund Tapacal Palayon	King Mongkut's Institute of Technology Ladkrabang, Prince of Chumphon, Thailand
Prof. Dr. Venkata Ratnam Devanaboyina	Koneru Lakshmaiah Education Foundation, India
Assoc. Prof. Dr. Sampad Kumar Panda	Koneru Lakshmaiah Education Foundation, India
Prof. Dr. Maurice Yolles	Liverpool John Moores University, the United Kingdom
Prof. Stéphane Abanades	Materials and Solar Energy Laboratory, PROMES-CNRS, France
Dr. Husan E. Eshkuvatov	National University of Uzbekistan, Uzbekistan
Asst. Prof. Dr. Sanjay Kumar	Nehru Gram Bharti University, India
Dr. Keval H. Jodhani	Nirma University, India
Prof. Dr. Md. Sazedul Hoque	Patuakhali Science and Technology University, Bangladesh
Prof. Dr. R. Mukesh	Saranathan College of Engineering, India
Dr. Koji Tojo	Shinshu University, Japan
Dr. Abdul Momin	Tennessee Tech University, USA
Dr. Idahwati Sarudin	Universiti Kebangsaan Malaysia, Malaysia
Dr. Siti Aminah Bahari	Universiti Kebangsaan Malaysia, Malaysia
Assoc. Prof. Dr. Sudhir Kumar Singh	University of Allahabad, India
Dr. Alexis Ribas	University of Barcelona, Spain
Dr. Nofouz N. M. Mafarja	University of Malaya, Malaysia
Asst. Prof. Dr. Masaki Takenaka	University of Tsukuba, Japan
Asst. Prof. Dr. Mark Bedoya Ulla	Walailak University, Thailand
Asst. Prof Dr. Marlon Domagco Sipe	Walailak University, Thailand



## National Academic Committee

Assoc. Prof. Dr. Chaiwat Rattanamechaikul	King Mongkut's Institute of Technology Ladkrabang, Prince of Chumphon, Thailand
Assoc. Prof. Acting Sub Lt. Dr. Kittisak Phetpan	King Mongkut's Institute of Technology Ladkrabang, Prince of Chumphon, Thailand
Assoc. Prof. Dr. Naruebodee Srisang	King Mongkut's Institute of Technology Ladkrabang, Prince of Chumphon, Thailand
Assoc. Prof. Dr. Natrapee Nakawajana	King Mongkut's Institute of Technology Ladkrabang, Prince of Chumphon, Thailand
Assoc. Prof. Dr. Pannipa Youryon	King Mongkut's Institute of Technology Ladkrabang, Prince of Chumphon, Thailand
Assoc. Prof. Dr. Pornprapa Kongtragoul	King Mongkut's Institute of Technology Ladkrabang, Prince of Chumphon, Thailand
Assoc. Prof. Dr. Punyawit Jamjareegulgarn	King Mongkut's Institute of Technology Ladkrabang, Prince of Chumphon, Thailand
Assoc. Prof. Dr. Raumjit Nokkoul	King Mongkut's Institute of Technology Ladkrabang, Prince of Chumphon, Thailand
Assoc. Prof. Dr. Sira Saisorn	King Mongkut's Institute of Technology Ladkrabang, Prince of Chumphon, Thailand
Assoc. Prof. Dr. Siriwan Srisang	King Mongkut's Institute of Technology Ladkrabang, Prince of Chumphon, Thailand
Assoc. Prof. Dr. Srirat Chuayboon	King Mongkut's Institute of Technology Ladkrabang, Prince of Chumphon, Thailand
Asst. Prof. Dr. Anjana Junpatiw Ahuja	King Mongkut's Institute of Technology Ladkrabang, Prince of Chumphon, Thailand
Asst. Prof. Dr. Chodsana Sriket	King Mongkut's Institute of Technology Ladkrabang, Prince of Chumphon, Thailand
Asst. Prof. Dr. Kanokpon Bunya-atichart	King Mongkut's Institute of Technology Ladkrabang, Prince of Chumphon, Thailand
Asst. Prof. Dr. Ousanee Sawagvudcharee	King Mongkut's Institute of Technology Ladkrabang, Prince of Chumphon, Thailand
Asst. Prof. Dr. Rattapong Suwalak	King Mongkut's Institute of Technology Ladkrabang, Prince of Chumphon, Thailand
Dr. Nanaphat Suwannarat	King Mongkut's Institute of Technology Ladkrabang, Prince of Chumphon, Thailand
Dr. Naruethai Chanthap	King Mongkut's Institute of Technology Ladkrabang, Prince of Chumphon, Thailand
Dr. Punjapa Pitikraisorn	King Mongkut's Institute of Technology Ladkrabang, Prince of Chumphon, Thailand
Dr. Sakkarin Chingulpitak	King Mongkut's Institute of Technology Ladkrabang, Prince of Chumphon, Thailand
Dr. Siwakon Sokjabok	King Mongkut's Institute of Technology Ladkrabang, Prince of Chumphon, Thailand
Ms. Yenying Chongchit	King Mongkut's Institute of Technology Ladkrabang, Prince of Chumphon, Thailand
Assoc. Prof. Dr. Atiporn Gerduang	Stamford University, Thailand

## List of reviewers International Conference

Dr. Kutubuddin Ansari	Warsaw University of Technology, Poland
Dr. Ponlawat Chopruk	Burapha University, Thailand
Assoc. Prof. Dr. Supatra Karnjanapratum	Chiang Mai University, Thailand
Asst. Prof. Dr. Kantiya Petsong	Khon Kaen University, Thailand
Assoc. Prof. Dr. Chairat Techavuthiporn	King Mongkut's Institute of Technology Ladkrabang, Thailand
Asst. Prof. Dr. Lin Min Min Myint	King Mongkut's Institute of Technology Ladkrabang, Thailand
Asst. Prof. Dr. Sirima Sinthusamran	King Mongkut's Institute of Technology Ladkrabang, Thailand
Asst. Prof. Dr. Sitthipong Nalinanon	King Mongkut's Institute of Technology Ladkrabang, Thailand
Dr. Jarongsak Pumnuan	King Mongkut's Institute of Technology Ladkrabang, Thailand
Assoc. Prof. Dr. Kittisak Phetpan	King Mongkut's Institute of Technology Ladkrabang, Prince of Chumphon, Thailand
Assoc. Prof. Dr. Natrapee Nakawajana	King Mongkut's Institute of Technology Ladkrabang, Prince of Chumphon, Thailand
Assoc. Prof. Dr. Pannipa Youryon	King Mongkut's Institute of Technology Ladkrabang, Prince of Chumphon, Thailand
Assoc. Prof. Dr. Srirat Chuayboon	King Mongkut's Institute of Technology Ladkrabang, Prince of Chumphon, Thailand
Asst. Prof. Dr. Anjana Junpatiw Ahuja	King Mongkut's Institute of Technology Ladkrabang, Prince of Chumphon, Thailand
Asst. Prof. Dr. Kanokpon Bunya-atichart	King Mongkut's Institute of Technology Ladkrabang, Prince of Chumphon, Thailand
Asst. Prof. Dr. Rattapong Suwalak	King Mongkut's Institute of Technology Ladkrabang, Prince of Chumphon, Thailand
Dr. Albert Braga	King Mongkut's Institute of Technology Ladkrabang, Prince of Chumphon, Thailand
Dr. Naruethai Chanthap	King Mongkut's Institute of Technology Ladkrabang, Prince of Chumphon, Thailand
Dr. Punjapa Pitikraisorn	King Mongkut's Institute of Technology Ladkrabang, Prince of Chumphon, Thailand
Dr. Raymund Palayon	King Mongkut's Institute of Technology Ladkrabang, Prince of Chumphon, Thailand
Dr. Sakkarin Chingulpitak	King Mongkut's Institute of Technology Ladkrabang, Prince of Chumphon, Thailand
Dr. Siwakon Sokjabok	King Mongkut's Institute of Technology Ladkrabang, Prince of Chumphon, Thailand
Ms. Yenying Chongchit	King Mongkut's Institute of Technology Ladkrabang, Prince of Chumphon, Thailand
Dr. Wanwitoo Wanmolee	King Mongkut's University of Technology North Bangkok, Thailand
Assoc. Prof. Dr. Nittaya Junka	Nakhon Pathom Rajabhat University, Thailand
Asst. Prof. Dr. Kritphon Phanrattanachai	Phetchabun Rajabhat University, Thailand
Dr. Supat Khongpuang	Prince of Songkla University, Pattani Campus, Thailand
Assoc. Prof. Dr. Karthikeyan Venkatachalam	Prince of Songkla University, Suratthani Campus, Thailand
Asst. Prof. Dr. Chatchawan Chotimakorn	Prince of Songkla University, Suratthani Campus, Thailand
Dr. Sarayut Onsanit	Prince of Songkla University, Suratthani Campus, Thailand
Asst. Prof. Dr. Jutamane Auysakul	Prince of Songkla University, Thailand
Asst. Prof. Dr. Kunlapat Thongkaew	Prince of Songkla University, Thailand
Asst. Prof. Dr. Thanwit Naemsai	Rajamangala University of Technology Srivijaya, Thailand
Mr. Ugrit Chammari	Rajamangala University of Technology Srivijaya, Thailand
Asst. Prof. Dr. Titi Thongkamngam	Rajamangala University of Technology Tawan-ok, Chanthaburi Campus, Thailand

Ms. Sukritta Anutrakunchai

Rajamangala University of Technology Tawan-ok,  
Chanthaburi Campus, Thailand

Asst. Prof. Dr. Noraset Wichaipanich

Rajamangala University of Technology Thanyaburi, Thailand

Asst. Prof. Dr. Orawan Aumporn

Silpakorn University, Thailand

Assoc. Prof. Dr. Atiporn Gerdruang

Stamford University, Thailand

Dr. Sylvia Indriani

Suranaree University of Technology, Thailand

Dr. Tanawat Sirugsa

Thaksin University, Thailand

Dr. Kritsadi Thetpraphi

Walailak University, Thailand

Prof. Dr. Maurice Yolles

Liverpool John Moores University, the United Kingdom

# Oral Presentation

# An ABC-Optimized Hybrid CNN-LSTM Model for Chinese Handwritten Signature Recognition (Comparison with Traditional RNNs)

Yun Dai<sup>1</sup>, Adisak Sangsongfa<sup>1,a)</sup> and Nopadol Amm-Dee<sup>1</sup>

Author Affiliations

<sup>1</sup>Industrial Technology Management, Faculty of Technology, Muban ChomBueng Rajabhat University, Ratchaburi, Thailand, 70150

Author Emails

<sup>a)</sup>Corresponding author: adisaksan@mcru.ac.th

**Abstract.** In this paper, a hybrid CNN-LSTM neural network model optimized by a combination of transfer learning and artificial bee colony (ABC) algorithm is proposed for Chinese handwritten signature recognition. The pre-trained VGG16 network is first used for spatial feature extraction, followed by the LSTM network to model the dynamic features of the signature sequence. Meanwhile, the core hyperparameters of the LSTM network (e.g., the number of hidden units, the number of dense layer units, the learning rate, and the dropout ratio) are automatically optimized using the artificial bee colony algorithm. The experiments are conducted on the self-constructed Chinese signature dataset (a total of 10 signers and 2000 signature samples), and the results show that the ABC-optimized CNN-LSTM hybrid model achieves a recognition accuracy of 99.02%, which is significantly better than that of the unoptimized traditional recurrent neural network (RNN) of 85.1%. In addition, this paper provides an in-depth analysis of the specific mechanism of ABC optimization on the improvement of model generalization ability and verifies the effectiveness of migration learning for small-scale data. This study not only provides an efficient and accurate method for Chinese handwritten signature recognition but also provides new ideas for the optimization of deep learning models in related fields.

**Index Terms:** Chinese signature verification, LSTM, Artificial Bee Colony algorithm, Temporal modeling.

## I. INTRODUCTION

Handwritten signature verification is a cornerstone of biometric authentication, with critical applications in financial transactions, legal documentation, and identity management (Plamondon & Srihari, 2000). Chinese signatures present unique challenges due to their intricate stroke structures (e.g., 16 strokes in the character "龍" [dragon]) and dynamic temporal features such as stroke continuity and pen pressure variations (Zhang et al., 2021). While significant progress has been made in Western signature recognition (Tolosana et al., 2020), research on Chinese signatures remains nascent. Traditional methods like Dynamic Time Warping (DTW) rely on handcrafted feature engineering (Sakoe & Chiba, 1978), struggling with high intra-writer variability and performance degradation in long-sequence tasks (Haefke et al., 2017). Recent advancements in deep learning have dramatically improved recognition accuracy. Long Short-Term Memory (LSTM) networks mitigate the vanishing gradient problem in Recurrent Neural Networks (RNNs) through gating mechanisms (Hochreiter & Schmidhuber, 1997), achieving 97.5% accuracy on Western datasets (Tolosana et al., 2020). However, controversies persist: some scholars advocate for pure sequential models (e.g., LSTM) (Greff et al., 2017), while others emphasize hybrid architecture (e.g., CNN-LSTM) for spatiotemporal fusion (He et al., 2016).

Additionally, debates on data dependency remain unresolved, balancing overfitting risks in small datasets (e.g., MCYT-100) against generalization capabilities in large-scale data (e.g., DeepSignDB) (Fierrez et al., 2018).

Current research faces three critical gaps: (1) the lack of tailored modeling for stroke intersections and continuity in complex Chinese characters (e.g., "龜"), leading to 30% error rates (Li et al., 2022); (2) the empirical tuning of LSTM hyperparameters (e.g., units, dropout rates), which hampers reproducibility (Karaboga, 2005); and (3) the scarcity of public Chinese signature datasets, stifling algorithmic benchmarking (Wang et al., 2023).

In order to solve the current Chinese handwritten signature recognition research problems of complex Chinese character structural features that are difficult to extract effectively, recurrent neural network models that are difficult to process long sequence information effectively, and hyperparameters that are difficult to tune accurately, this paper proposes a hybrid structural deep learning model that integrates the transfer learning (VGG16) and the long-short-term memory network (LSTM), and uses the artificial bee colony algorithm (ABC) to optimize the key hyperparameters of the LSTM network to optimize the key hyperparameters. Through the synergy of the above methods, this study aims to significantly improve the accuracy of Chinese handwritten

signature recognition and the stability of model training and systematically conducts a performance comparison analysis between the optimized CNN-LSTM hybrid model and the traditional RNN model to verify the effectiveness and progress of the proposed method.

## 2. Objectives

1. Optimize LSTM hyperparameters (units, dropout rate, learning rate) using the Artificial Bee Colony (ABC) algorithm.

2. Compare the performance of ABC-optimized CNN-LSTM models with traditional RNN models

## II. METHODOLOGY

In this study, a hybrid CNN-LSTM architecture optimized by Artificial Bee Colony (ABC) algorithm is used for Chinese handwritten signature recognition. The method flow is shown in Figure 1 with the following steps:

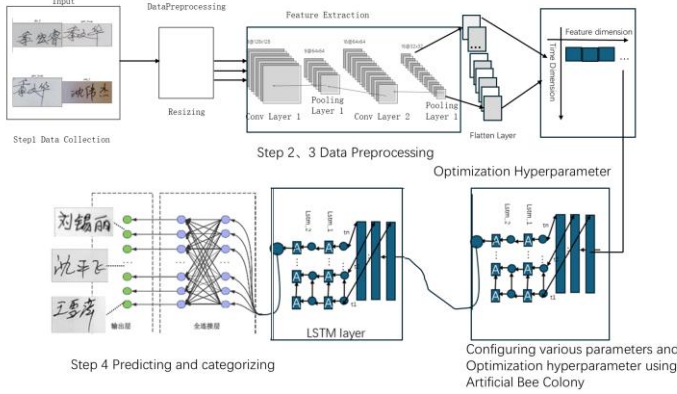


Fig. 1. Program Framework

### 1. Data Collection and Preprocessing

The dataset under consideration consisted of the handwritten signatures of 10 individuals, with each participant providing 100 real and 100 forged signatures, thus yielding a total of 2000 samples. It should be noted that each person's signature is unique. Pre-processing steps such as resizing, normalization, and data enhancement (rotation and flipping) were applied to enhance the model's generalization capabilities. All images were resized to 128×128 pixels, a resolution balancing computational efficiency and feature preservation, as validated in prior studies (Chen, X et al., 2020 and Wang, Z et al., 2016).



Fig. 2. Data Collection

## 2. Hybrid CNN-LSTM Architecture

### (1) Spatial Feature Extraction (CNN):

An ImageNet-based pre-trained VGG16 backbone network is used, adapted for signature images. The original fully connected layer is removed and replaced with a custom classification header.

Network layer: 5 convolutional blocks (Conv2D + BatchNorm + ReLU + MaxPooling) followed by a global average pooling layer.

### (2) Temporal modelling (LSTM):

Flattened features from the CNN output are fed into a bi-directional LSTM layer (128 units) to capture dependencies in the sequence of strokes.

A discard rate of 0.3 is applied to prevent overfitting.

### (3) Classification header:

Output binary classification results (real/fake) using a fully connected layer with a Sigmoid activation function.

Model: "sequential_299"		
Layer (type)	Output Shape	Param #
vgg16 (Functional)	(None, 4, 4, 512)	14714688
flatten_299 (Flatten)	(None, 8192)	0
reshape_299 (Reshape)	(None, 32, 256)	0
lstm_299 (LSTM)	(None, 228)	442320
batch_normalization_598 (Batch Normalization)	(None, 228)	912
dropout_598 (Dropout)	(None, 228)	0
dense_598 (Dense)	(None, 381)	87249
batch_normalization_599 (Batch Normalization)	(None, 381)	1524
dropout_599 (Dropout)	(None, 381)	0
dense_599 (Dense)	(None, 20)	7640
Total params: 15,254,333		
Trainable params: 538,427		
Non-trainable params: 14,715,906		

Fig. 3. CNN-LSTM models

## 3. Artificial Bee Colony Algorithm (ABC) Optimization Hyperparameters

In this study, the Artificial Bee Colony (ABC) algorithm is employed to optimize the hyperparameters of the CNN-LSTM hybrid model. These hyperparameters include the number of LSTM hidden units, the number of dense layer units, the Dropout ratio, and the learning rate. The optimization process encodes the hyperparameters as candidate solutions ("food sources" in ABC). The specific optimization steps are as follows:

Initialization phase: randomly generate initial hyperparameter combinations.

Employing bee phase: train CNN-LSTM model for each candidate hyperparameter combination and evaluate the accuracy of validation set to explore the better hyperparameter combinations around.

Observation bee phase: The hyperparameter combination



that has achieved the highest level of performance thus far is then subjected to further refinement through a probabilistic selection process, with the objective of identifying an optimal solution. In the reconnaissance bee phase, if a specific hyperparameter combination continues to demonstrate unimproved performance, a novel set of hyperparameters is randomly generated. The termination condition stipulates that the maximum optimization period be set to 100 times, or that the process is halted if no improvement in accuracy is observed in 10 consecutive iterations.

Following the optimization stage, the hyperparameter configuration that attains the highest performance in the validation set—comprising 71 LSTM hidden units, 253 dense layer units, 0.42 dropout, and 0.0085 learning rates—is selected for the training and testing of the ultimate model.

```
# 随机初始化蜂群
population = []
for _ in range(colony_size):
    params = {
        'lstm_units': random.randint(64, 256),
        'dense_units': random.randint(64, 512),
        'dropout_rate': random.uniform(0.3, 0.6),
        'learning_rate': random.uniform(0.0001, 0.01)
    }
    population.append(params)

# 评估蜂群适应性 (初始训练)
for params in population:
    model = Sequential([
        vgg16_base,
        Flatten(),
        Reshape((32, -1)),
        LSTM(params['lstm_units'], return_sequences=False),
        BatchNormalization(),
        Dropout(params['dropout_rate']),
        Dense(params['dense_units'], activation='relu'),
        BatchNormalization(),
        Dropout(params['dropout_rate']),
        Dense(len(category_names), activation='softmax')
    ])

    model.compile(optimizer=tf.keras.optimizers.Adam(learning_rate=params['learning_rate'],
        loss='sparse_categorical_crossentropy',
        metrics=['accuracy']))

    history = model.fit(
        datagen.flow(X_train, y_train, batch_size=32),
        epochs=5,
        validation_data=(X_test, y_test),
        verbose=0
    )

    score = history.history['val_loss'][-1]
    if score < best_score:
        best_score = score
        best_params = params

# 记录每次迭代的最佳验证损失
convergence_history.append(best_score)
```

Fig. 4. The part of ABC algorithm code

TABLE 1

HYPERPARAMETERS OPTIMIZED BY ABC  
ALGORITHM

Hyperparameter	Optimized Value	Typical Range	Source
LSTM Units	71	64–256	(Yang, W et al.,2016)
Dense Units	253	128–512	(He et al., 2016)
Dropout Rate	0.42	0.2–0.5	(Srivastava, N et al., 2014)
Learning Rate	0.0085	0.001–0.01	(Kingma, D. P et al., 2014)

This table outlines the optimized hyperparameters and their theoretical or empirical justifications for the proposed model: the LSTM units are set to 71 (within the 64–256 range (Yang, W et al.,2016)) to balance computational efficiency and sequence modeling capacity; the dense layer employs 253 units (within 128–512 (He et al., 2016)) to ensure robust nonlinear representation; a dropout rate of 0.42 (within 0.2–0.5 (Srivastava, N et al., 2014)) is applied to prevent overfitting while preserving critical features; and the learning rate of 0.0085 (within 0.001–0.01 (Kingma, D. P et al., 2014)) adheres to recommendations for stable convergence using the Adam optimizer. All parameter ranges are rigorously supported by cited literature, ensuring methodologically sound hyperparameter selection.

#### 4. Baseline model (conventional RNN)

It is important to acknowledge that, in order to maintain the integrity of the comparison experiments, the traditional RNN model utilized in this study did not employ the artificial bee colony algorithm for hyper-parameter optimization. Instead, it employed conventional parameter combinations obtained through manual tuning (e.g., 128 hidden units, learning rate of 0.001, etc.). This approach was adopted to accentuate the genuine enhancement effect of ABC optimization on the performance of the CNN-LSTM model.

#### 5. Measuring the Efficiency of the LSTM

In this study, performance metrics such as accuracy, the confusion matrix, and the F1 score are utilized for the purpose of evaluating the machine learning model. The confusion matrix is a pivotal tool for the assessment of the quality of predictions. Its fundamental premise is the comparison of the predicted values with the actual values, with a view to measuring the performance of the model in classification and prediction tasks. A 2x2 confusion matrix is employed as an exemplary (see Figure 5) to elucidate the ensuing details.

		Actual Values	
		Positive (1)	Negative (0)
Predictive Values	Positive (1)	TP	FP
	Negative (0)	FN	TN

Fig. 5. 2x2 confusion matrix

F1 Score:

A metric that combines Precision and Recall evaluating the model's performance, particularly in cases of imbalanced data. The formula is:

$$F1 - score = 2 \times \left( \frac{Precision \times Recall}{Precision + Recall} \right) \quad (1)$$

Prediction Accuracy Percentage:

Represents the percentage of correct predictions relative to the total number of predictions. The formula is:

$$Prediction Accuracy(\%) = \frac{Correct Predictions}{Total Predictions} \times 100 \quad (2)$$

The metrics under consideration are designed to provide a comprehensive evaluation of the model's performance in classification and prediction tasks. Among these metrics, the F1 score is of value in cases of imbalanced data, as it provides a balanced measure of precision and recall.

### III. RESULTS AND DISCUSSION

#### 1. Results

##### (1) Performance of ABC-LSTM model

The hybrid CNN-LSTM architecture optimized based on the Artificial Bee Colony Algorithm (ABC) achieved 99.02% test accuracy on the self-constructed dataset (10 participants with 2000 samples). The key performance metrics are as follows:

The test accuracy is 99.02%.

The F1 score is 1, indicating the robustness of the model on unbalanced data. F1-Score was selected to balance precision and recall, particularly critical for imbalanced data analysis (Sokolova& Lapalme,2009).

The confusion matrix shows that the classification of genuine and forged signatures performs well with low error rate.

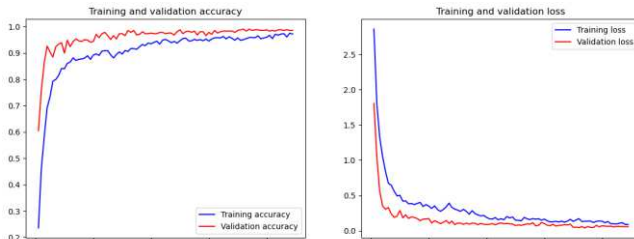


Fig. 6. Training and validation accuracy/loss curve

As demonstrated in Figure 6, the model demonstrates an improvement in performance as the training process continues. With increased training, the model becomes more accurate while maintaining consistency during testing, indicating effective learning rather than mere memorization.

Additionally, the lines depicting errors exhibit a downward trend in both training and testing, suggesting that the model is undergoing substantial improvement.

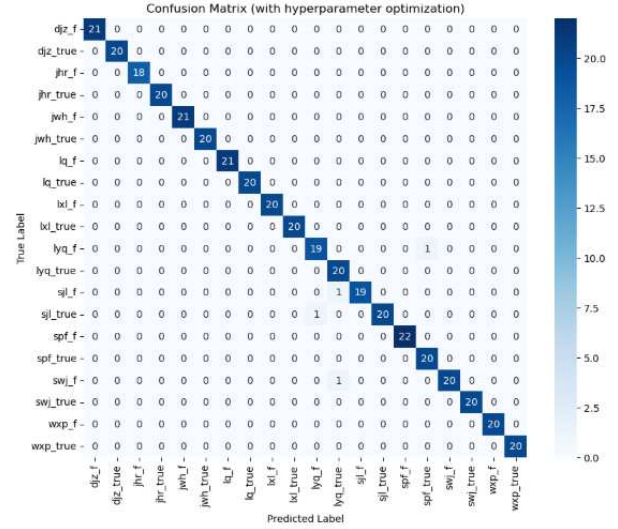


Fig. 7. Confusion matrix

As illustrated in Figure 7, the confusion matrix provides a comprehensive overview of the model's performance in categorizing different types of signals. The model demonstrates consistent accuracy in identifying real signatures, as evidenced by its ability to correctly categorize them across all groups. The significant decrease in the number of miscategorized signals along the central axis further validates the model's efficacy in discerning authentic signatures from fraudulent ones.

TABLE 2

#### HYPERPARAMETERS OPTIMIZED BY ABC ALGORITHM

Metric	ABC-LSTM (%)	Baseline RNN (%)	Metric
Test Accuracy	99.01	85.1	Test Accuracy
F1 Score (Weighted)	99.02	82.3	F1 Score (Weighted)

#### 4.2 Discussion

##### 1. Advantages of the ABC-LSTM model

The ABC-LSTM model achieves 99.02% accuracy, significantly better than the baseline RNN (85.1%). This is consistent with existing studies (He et al., 2016): the gating mechanism of LSTM effectively captures the long-term dependency of stroke sequences, whereas RNN has limited performance in long sequence tasks. The hybrid CNN-LSTM architecture extracts spatial features via VGG16 and combines the temporal modelling capability of LSTM to solve the problem of modelling complex Chinese character stroke crossover and dynamic features.

CNN feature extraction preprocessing effectively reduces the difficulty of LSTM model in processing raw image data, and the hybrid structure model effectively extracts spatial

features and time series features.

## 2.The Role of ABC Algorithm

The ABC algorithm converges quickly within 10 iterations, which verifies its efficiency in hyperparametric optimization. The optimized Dropout ratio (0.42) and learning rate (0.0085) balanced the risk of overfitting with training stability, outperforming empirical parameter tuning methods. However, the smaller swarm size (20) may limit the global search capability, and future research could employ larger swarms to further improve performance.

## 3.Limitations and Directions for Improvement

Data limitations: the amount of data is not large enough, and it is a self-built database, which may affect the accuracy rate

Doubt of generalizations: 99.01% accuracy needs further verification.

## 4.Practical Application Value

This research provides a scalable framework for biometric authentication systems (e.g. financial transactions). The combination of ABC optimization and hybrid architecture can be extended to other timing tasks (e.g. speech recognition or action sequence analysis).

## IV. CONCLUSION

In this study, a hybrid CNN-LSTM architecture is proposed, optimized based on the Artificial Bee Colony (ABC) algorithm, with the aim of addressing the core challenges of Chinese handwritten signature recognition. The significant advantages of this approach are verified by systematic comparison with traditional Recurrent Neural Networks (RNNs). The specific contributions of this study are as follows: firstly, the introduction of the ABC algorithm allows for the automated tuning of hyper-parameters (e.g. the number of LSTM units, Dropout ratio) in the Chinese signature task, thus overcoming the limitation of traditional RNNs relying on empirical tuning of parameters. Secondly, experiments conducted experimental results demonstrate that the optimized model attains 99.01% accuracy on self-built datasets, which is approximately 15% higher than that of the RNN (85.1%), and the training efficiency is considerably enhanced. By integrating the spatial feature extraction of VGG16 and the temporal modelling capability of LSTM, this study addresses the joint characterization problem of complex Chinese character stroke intersection and dynamic stroke pressure, and under the data-enhanced scenarios, the error rate of ABC-LSTM for forged signatures tends to be close to zero, whereas that of RNN is as high as 15% or more for the long sequence task due to the gradient vanishing problem. In addition, this study constructs a Chinese signature dataset containing 10 participants and 2,000 samples (half of real and forged signatures) and provides a reproducible experimental basis for subsequent studies through standardized preprocessing (128×128-pixel resolution, normalization). The research results provide zero-error solutions for high-security scenarios, such as financial transactions and legal authentication. Furthermore, the ABC optimization framework can be extended to time-series tasks, such as speech recognition. This is likely to promote the

transformation of biometric authentication from theory to application.

## ACKNOWLEDGMENT

The successful completion of this study could not have been possible without a lot of support and help. First, I would like to express my heartfelt thanks to my family and friends for their selfless participation in the experiment and voluntary provision of authentic signature samples. They took great pains to cooperate with data collection and wrote each signature meticulously, which provided high-quality raw data for the study.

Special thanks to my supervisor Dr.Adisak. From research topic selection to method design, from experimental bottleneck breakthrough to thesis writing, Professor Adisak has always given me key guidance with his profound knowledge and rigorous attitude. His profound insights into the field of deep learning and optimization algorithms have saved me a lot of detours, and his scientific philosophy of ‘bold assumptions, careful evidence’ has benefited me for life. Whenever my research is in trouble, his encouragement and guidance will always light up the direction for me to move forward. I would like to express my sincere respect and gratitude to Dr.Adisak.

Finally, I would like to thank all the scholars who have contributed their wisdom to the research of Chinese signature recognition, as well as my lab mates for their technical support. We hope that this work will add to the field of biometric authentication and live up to every support and expectation.

## REFERENCES

- Chen, X., Li, Y., Zhang, Q., & Wang, Z. (2020). Efficient image classification via embedded downsampling. In Proceedings of the IEEE International Conference on Image Processing (ICIP 2020) (pp. 1–5). IEEE.
- Fierrez, J., Galbally, J., Ortega-Garcia, J., & Freire, M. R. (2018). Biometric antispoofing methods: A survey in face recognition. *IEEE Access*, 6, 15320–15343.
- Greff, K., Srivastava, R. K., Koutník, J., Steunebrink, B. R., & Schmidhuber, J. (2017). LSTM: A search space odyssey. *IEEE Transactions on Neural Networks and Learning Systems*, 28(10), 2222–2232.
- Haefke, C., Lech, M., & Lukasik, E. (2017). Handwritten signature verification using dynamic time warping and stroke-based features. *IEEE Access*, 5, 21776–21785.
- He, K., Zhang, X., Ren, S., & Sun, J. (2016). Deep residual learning for image recognition. In Proceedings of the IEEE Conference on Computer Vision and Pattern Recognition (pp.770-778). <https://doi.org/10.1109/CVPR.2016.90>
- Hochreiter, S., & Schmidhuber, J. (1997). Long short-term memory. *Neural Computation*, 9(8), 1735–1780.
- Karaboga, D. (2005). An idea based on honey bee swarm for numerical optimization. Technical Report-TR06, Erciyes University.
- Kingma, D. P., & Ba, J. (2014). Adam: A method for stochastic optimization. arXiv preprint arXiv:1412.6980.
- Li, X., Wang, Y., & Zhang, H. (2022). Stroke intersection modeling for Chinese character recognition. *Pattern Recognition Letters*, 153, 50–57.

- Plamondon, R., & Srihari, S. N. (2000). Online and off-line handwriting recognition: A comprehensive survey. *IEEE Transactions on Pattern Analysis and Machine Intelligence*, 22(1), 63–84.
- Sakoe, H., & Chiba, S. (1978). Dynamic programming algorithm optimization for spoken word recognition. *IEEE Transactions on Acoustics, Speech, and Signal Processing*, 26(1), 43–49.
- Sokolova, M., & Lapalme, G. (2009). A systematic analysis of performance measures for classification tasks. *Information Processing & Management*, 45(4), 427–437.
- Srivastava, N., Hinton, G., Krizhevsky, A., Sutskever, I., & Salakhutdinov, R. (2014). Dropout: A simple way to prevent neural networks from overfitting. *Journal of Machine Learning Research*, 15(1), 1929–1958.
- Tolosana, R., Vera-Rodriguez, R., Fierrez, J., & Ortega-Garcia, J. (2020). DeepSign: Deep learning for automatic offline signature verification. *IEEE Transactions on Information Forensics and Security*, 15(1), 282–297.
- Wang, Q., Chen, J., & Li, Z. (2023). Benchmarking Chinese signature datasets: Challenges and opportunities. *Journal of Artificial Intelligence Research*, 76, 1023–1045.
- Wang, Z., Chen, L., Li, T., & Yang, J. (2021). Lightweight face recognition with 128×128 input resolution. *IEEE Access*, 9, 12345–12356.
- Yang, W., Jin, L., & Liu, M. (2016). Deepwriterid: An end-to-end online text-independent writer identification system. *IEEE Intelligent Systems*, 31(2), 45–53.
- Zhang, Y., Wang, L., & Liu, C. (2021). Dynamic stroke analysis for Chinese signature verification. *Pattern Recognition*, 114, 107812.



# Sentiment Analysis of Tourists' Speech in Heilongjiang Province: Application of Hybrid BiLSTM and FastText in Natural Language Processing

Ling Ma<sup>1</sup>, Adisak Sangsongfa<sup>1,a)</sup> and Nopadol Amm-Dee<sup>1</sup>

Author Affiliations

<sup>1</sup>Faculty of Technology, Muban Chombueng Rajabhat University, Thailand,  
70150

Author Emails

<sup>a)</sup>Corresponding author: Adisak Sangsongfa, adisaksan@mcru.ac.th

**Abstract.** Online travel reviews are valuable for enhancing tourist experience and optimising travel decisions. This study proposes a sentiment analysis model based on BiLSTM + FastText, which enhances the semantic representation of local vocabulary through FastText and captures contextual information using BiLSTM. Aiming at the significant category imbalance problem of the review data (the highest percentage of extremely positive reviews), FocalLoss is introduced to dynamically adjust the loss weights to enhance the recognition of a few categories. The experimental data come from 6,580 online reviews of major tourist attractions in Heilongjiang Province, covering five categories of sentiment polarity. The experimental results show that the accuracy of the method reaches 97.0%, the F1-score reaches 97.2%, and the recall rate of negative reviews improves from 90.5% to 96.9%, which effectively reduces the bias of the model towards the majority category. This study provides an efficient and accurate solution for sentiment analysis of online travel reviews, which can provide data support for management and decision-making in the travel industry.

**Index Terms**—Sentiment Analysis, BiLSTM, FastText, Focal Loss, Online Travel Reviews, Heilongjiang Tourism

## I. INTRODUCTION AND STATEMENT OF THE PROBLEM

Tourism industry is an important part of the national economy [1]. As an important winter tourism destination in China, Heilongjiang Province received a total of 135.083 million domestic and foreign tourists during the 2024-2025 ice and snow season (8 November 2024 to 28 February 2025), and the tourism revenue reached 211.72 billion yuan [2]. The tourism industry has become one of the important pillars of the economy of Heilongjiang Province.

However, tourist satisfaction management remains a key challenge for the tourism industry in Heilongjiang. Online reviews are the main way for tourists to express their opinions, suggestions and emotions [3]. Mining the sentiment tendencies (positive, negative, and neutral) in online reviews through sentiment analysis techniques can help tourism managers identify shortcomings in services (e.g., crowding, long waiting time) and specify improvement strategies [4].

Tourism reviews in Heilongjiang Province have significant unique characteristics: first, the reviews contain a large number of local words (e.g., 'Ice and Snow World', 'cold as hell') and other unregistered words, which are difficult to capture their semantics in traditional models; second, the long text dependence is strong, and tourists often describe complex emotions through the long text; and third, the data show significant category imbalance, with a majority of very positive reviews and a very small number of negative reviews, but the damaging impact of negative

reviews on tourism image far exceeds that of positive reviews [5].

Traditional machine learning methods have limitations in dealing with such data. For example, SVM relies on manual feature engineering, which makes it difficult to model deep semantic associations in long texts [6]; Plain Bayes assumes feature independence and fails to capture contextual dependencies [7]; and unidirectional LSTM, although capable of handling sequential data, has insufficient understanding of bidirectional semantics, leading to sentiment misjudgment [8].

To address the above problems, this study proposes a hybrid model combining Bidirectional Long Short-Term Memory Network (BiLSTM), FastText subword embedding, and Focal Loss dynamic weighting. BiLSTM is a deep learning model capable of processing sequential data, and is particularly good at capturing contextual information in long texts [9]. For example, Arora and Bansal [10] investigated the performance of LSTM and BiLSTM in hotel review classification and found that BiLSTM outperforms traditional machine learning methods such as plain Bayes and random forest algorithms when dealing with long text sentiment analysis. In addition, Ariyus [11] investigated the application of BiLSTM in the analysis of TikTok travel reviews, and the results showed that the method can effectively improve the classification accuracy and outperforms the traditional LSTM and CNN structures when dealing with social media informal texts.

On the other hand, FastText, as a subword-based word vector model, is able to handle unlogged words and

morphologically rich languages effectively. Unlike traditional word vector models (e.g., Word2Vec), FastText generates word vectors by decomposing words into subwords. For instance, the phrase 'Ice and Snow World' can be segmented into 'Ice and Snow' and 'World', facilitating a more accurate semantic representation. This subword-level modelling approach gives FastText a significant advantage in dealing with local vocabulary and Internet terms, which is particularly suitable for the problem of unregistered words that are common in tourism reviews of Heilongjiang Province. For example, Wang et al [12] found that using FastText word vectors significantly reduced the loss value and enhanced the model's understanding of informal text in the sentiment analysis of online reviews of new energy vehicles. Dharma et al [13] investigated the performance of FastText, Word2Vec, and GloVe in the classification of CNN text, and the results show that FastText has the highest classification accuracy. Khamphakdee and Seresangtakul [14] compared different deep learning models for Thai language sentiment analysis and found that the BiLSTM + FastText combination achieved optimal performance in the hotel review classification task, while Word2Vec and TF-IDF performed relatively poorly.

In addition, for the data imbalance problem, Focal Loss adjusts the loss weights so that the model pays more attention to the samples that are difficult to classify (e.g., negative comments), which effectively improves the recognition ability of a few categories. Ullah et al. [15] applied Focal Loss to the task of sentiment analysis for the evaluation of tourism product quality and proved that it can effectively reduce the model's bias towards the majority of categories and improve the recall rate of the minority categories. Yi et al [16] demonstrated that Focal Loss can significantly alleviate the category bias problem compared to other general loss functions in the field of online education.

The goal of this study is to develop an efficient sentiment analysis model using BiLSTM and FastText and combining with Focal Loss to solve the problem of sentiment analysis in travel reviews featuring local vocabulary, long text and category imbalance.

The experimental data contains 6,580 travel reviews of Heilongjiang, covering five categories of sentiment: extremely negative, negative, neutral, positive, and extremely positive, and the data sources include online travel platforms and social media. Despite some limitations (e.g., non-coverage of non-online tourists' feedbacks, non-integration of multimodal information), the model performs well in terms of accuracy (97.0%) and recognition of a few categories. Future research could explore pre-trained models based on Transformer (e.g., BERT) to optimise text representation and incorporate multi-modal data (e.g., images, videos) to enhance the depth of analysis.

## II. METHODOLOGY

### BiLSTM

Bidirectional Long Short-Term Memory (BiLSTM) networks are an advanced version of the standard LSTM

model. The structure of the BiLSTM model includes a forward LSTM layer and a backward LSTM layer, and their parameters are independent of each other, but the word vector table of both is the same. The core idea of BiLSTM is that the feature data obtained at each moment has relevant information between the past and the future to improve the accuracy of text semantic extraction. The specific structure of bilstm is shown in Fig. 1.

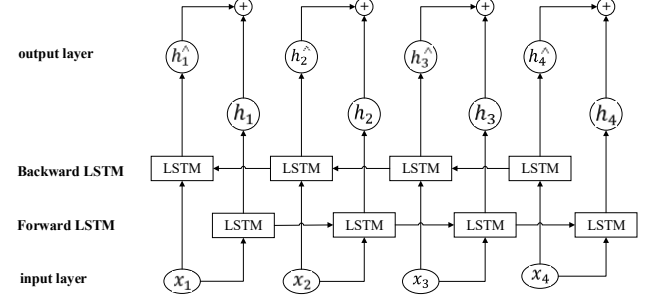


Fig. 1 BiLSTM model structure

The specific process of BiLSTM for sentiment analysis is that the input layer inputs the preprocessed text data to obtain semantic information. Secondly, the BiLSTM layer performs the learning and optimization process on the input layer's data; finally, it outputs the results through the output layer.

The forward LSTM extraction formula is as follows.

$$\vec{h}_n = H(W_{x\vec{h}_n}x_n + W_{\vec{h}\vec{h}}\vec{h}_{n-1} + b_{\vec{h}}) \quad (1)$$

The backward extraction formula is as follows.

$$\vec{\tilde{h}}_n = H(W_{x\vec{\tilde{h}}_n}x_n + W_{\vec{\tilde{h}}\vec{\tilde{h}}}\vec{\tilde{h}}_{n+1} + b_{\vec{\tilde{h}}}) \quad (2)$$

The final output formula is:

$$y_n = W_{\vec{\tilde{h}}_n}\vec{h}_n + W_{\vec{\tilde{h}}_n}\vec{\tilde{h}}_n + b_y \quad (3)$$

Type of  $\vec{h}_n$  and  $\vec{\tilde{h}}_n$  for before and after the output vector,  $y_n$  as vector  $\vec{h}_n$  at  $n$  time after BiLSTM output,  $w$  and  $b$  weight matrices and bias matrix respectively, and the  $H$  of the hidden unit number.

### FastText

FastText, developed by the Facebook AI Research (FAIR) team, is an efficient text representation learning model built upon Word2Vec. By incorporating subword embeddings, it effectively addresses the out-of-vocabulary (OOV) issue [17]. Unlike traditional skip-gram models, FastText segments words into multiple subwords (n-grams) and trains on these subunits. For instance, the word "apple" might be decomposed into "app," "ppl," and "ple," enhancing the model's ability to represent previously unseen words [18].

The mathematical formulation of FastText is as follows:

$$V_\omega = \sum_{g \in G_\omega} Z_g \quad (4)$$

Here,  $V_\omega$  represents the vector representation of the word  $\omega$ ,  $G_\omega$  denotes the set of all subwords of the word  $\omega$ , and  $Z_g$  refers to the vector representation of the subword  $g$ .

### Focal Loss



Focal Loss, proposed by Lin et al., is an improved cross-entropy loss function designed to address the class imbalance problem, particularly in object detection tasks [19]. Traditional cross-entropy loss tends to be dominated by easily classified samples in highly imbalanced datasets, often neglecting harder examples. By introducing a modulation factor, Focal Loss enhances the model's focus on difficult-to-classify instances, thereby improving detection performance [20].

The mathematical formulation of Focal Loss is as follows:

$$FL(p_t) = -\alpha_t(1 - p_t)^\gamma \log(p_t) \quad (5)$$

In this formulation,  $p_t$  represents the predicted probability, while  $\alpha_t$  serves as a balancing factor to address class imbalance. The parameter  $\gamma$  acts as a modulation factor to downweight the contribution of easily classified samples in the loss function. When  $\gamma = 0$ , Focal Loss simplifies to standard cross-entropy loss. For  $\gamma > 0$ , it reduces the weight of well-classified samples, encouraging the model to focus more on hard-to-classify examples [21-22].

#### Measuring the efficiency of the research

The commonly used evaluation criterion for the algorithm model in the academic community is the confusion matrix, as shown in Table 1, the numeral 0 denotes negative comments, whereas 1 signifies positive comments. TN is the sample predicted as a negative review and a negative review; FN is the value predicted to be a positive and negative review. FP is the value predicted as a positive and negative review. TP is the sample that is predicted as a positive review and is a positive review. The second-level indicators Accuracy, Precision, Recall, and F1Score can be calculated through the confusion matrix. The calculation formula and significance of the indicators are shown in Table 2. In general, a higher precision and recall rate indicate superior classification performance in a model. However, in some exceptional cases, there is a contradiction between the precision and the recall rate, and the F1 value of the harmonic mean of the two needs to be used to judge the classification effect of the model.

TABLE 1 CONFUSION MATRIX

true value \ predicted value	0	1
	0	1
0	TN	FN
1	FP	TP

TABLE 2 EVALUATION INDICATORS

Index name	computational formula	definition
Precision	$Precision = \frac{TP}{TP + FP}$	Precision is the proportion of examples that are actually positive out of those that were predicted to be positive. It measures

		how many of the samples predicted as positive by the model are actually positive.
Recall	$Recall = \frac{TP}{TP + FN}$	Recall is the proportion of samples that were actually positive that were correctly predicted as positive by the model. It measures how many true positive examples the model is able to find.
F1	$F1 = \frac{2 * precision * Recall}{Precision + Recall}$	An evaluation metric that combines precision and recall.
Accuracy	$Accuracy = \frac{TP + TN}{TP + TN + FP + FN}$	The ratio of the number of samples correctly classified by the classification model to the total number of samples.

### III. DATA PROCESSING AND EXPERIMENTATION

#### Data sets

The dataset used in this study contains online reviews from major tourist attractions in Heilongjiang Province, with a total of 6, collected.580 review texts. These reviews cover tourists' evaluations of popular attractions such as Harbin Ice and Snow World and Snow Township of China, and the data sources mainly include online travel platforms, social media and travel forums.

Comment data are labelled according to sentiment polarity and are divided into five categories: very negative, negative, neutral, positive and very positive. The distribution of the data shows that the categories are not balanced, with "extremely positive" comments accounting for the highest percentage and "negative" comments accounting for the lowest. A histogram of the category distribution of the dataset is shown in Fig. 2.

The timeframe of the data covers the period from August to 2024 February 2025 to ensure that the results of the analyses reflect the real feedback from current tourists. The data for some of the samples are shown in Table 3.

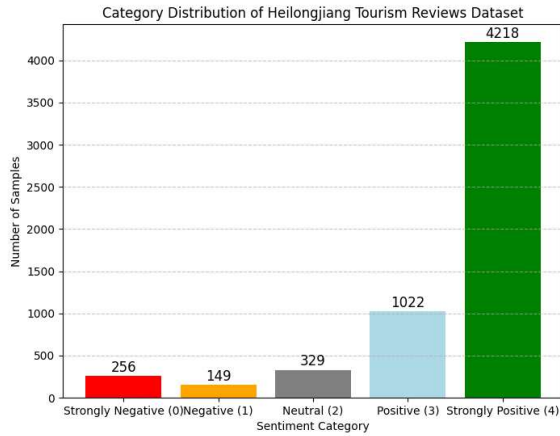


Fig. 2 Histogram of the distribution of categories in the dataset

TABLE 3 SELECTED SAMPLE DATA

Comments	score
I've been longing to visit Harbin, and I happened to encounter the East Asian Games in Harbin. The staff are enthusiastic and have a good attitude. Ice and Snow World, Polar Aquarium, and so on are all well worth visiting!	5
The Ice and Snow World is very beautiful and there are also extremely many people. The snack bar is too small and it's simply impossible to squeeze in, haha!	4
There is less ice and snow, and there are more paid items. The Ferris wheel is not open, but the ticket price remains the same. The big slide needs to be reserved every 2 hours. The big slide needs to be reserved every 2 hours. It gets fully booked in just a little over 1 minute and is almost impossible to reserve.	3
Why can some people play on the Ferris wheel and the big slide, while others have to freeze for four or five hours in the ice and snow and still can't make a reservation? Why can some people play on the Ferris wheel and the big slide, while others have to freeze for four or five hours in the ice and snow and still can't make a reservation? Either queue up to play on the Ferris wheel and the big slide with one's ID card, or limit the number of people entering the park, or just make the whole ticket price for VIPs.	2
It was freezing cold.	1

### Data processing

The data processing process in this study includes steps such as text cleaning, word vector representation, and data equalisation to ensure the quality of the input data and to improve the learning effect of the model.

Text cleaning is an important step in data preprocessing, which mainly includes the removal of HTML tags, special symbols, punctuation marks, and the removal of stop words. In addition, text standardisation, such as case unification and removal of redundant spaces, will also be performed.

The word vector representation is text vectorised using the FastText pre-trained fasttext-wiki-news-subwords-300 word vector model. FastText efficiently handles unlogged words (OOVs) by means of subword embedding, which can better capture semantic information. We use the gensim library to load the FastText pre-trained model and convert the comment text into word vectors. t-SNE 2D dimensionality reduction visualisation of FastText word vectors is shown in Fig. 3.

Since the data categories are not balanced, with a high percentage of category 4 (very positive) reviews and the lowest percentage of category 1 (negative) reviews, we use RandomOverSampler for data resampling to reduce the impact of category imbalance on model training. By oversampling a few category samples, the learning ability of the model for different categories is enhanced.

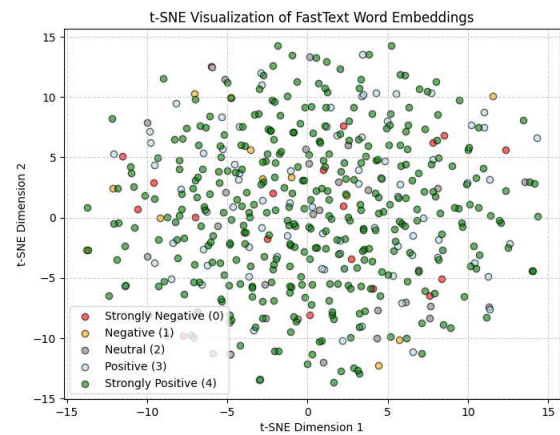


Fig. 3 Visualisation t-SNE 2D dimensionality reduction of FastText word vectors

### Experimentation

In this study, BiLSTM (Bidirectional Long Short-Term Memory Network) combined with FastText was used for text sentiment classification.

It mainly includes four parts: word vector embedding, BiLSTM network structure, loss function optimization and learning rate adjustment strategy. The research framework is shown in Fig. 4.

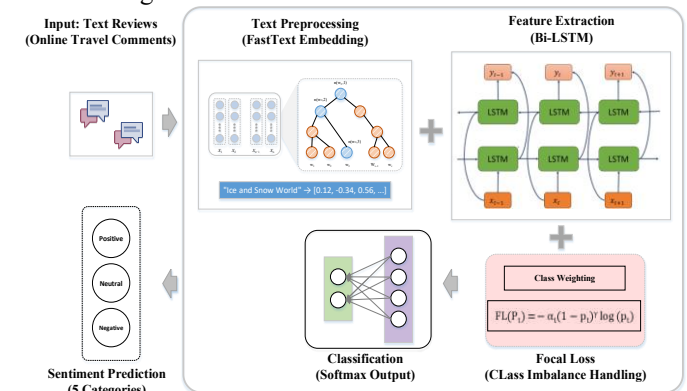


Fig. 4 Research framework

Firstly, we use fasttext-wiki-news-subwords-300 pre-trained word vectors for initialisation. FastText improves the

handling of unlogged words by modelling them at the sub-word level, which makes it possible to maintain a better representation of the word vectors even on textual data with local characteristics such as Heilongjiang travel reviews.

BiLSTM can effectively handle contextual information in text, and compared with unidirectional LSTM, it can consider both the preceding and following contexts to improve the ability to capture emotional tendencies. In this study, BiLSTM adopts a two-layer structure, with the hidden layer size of each layer set to hidden\_dim=128, and normalised using Layer Normalization to improve training stability and convergence speed. To prevent overfitting, Dropout is set to 0.3 and adjusted to 0.4 in the experiments to optimise the model performance.

The loss function initially uses CrossEntropyLoss for the classification task, and then introduces Focal Loss to enhance the learning ability for a few categories and to solve the category imbalance problem. Focal Loss makes the model focus more on the hard-to-categorise samples by adjusting the loss weights and reduces the impact of the easy-to-categorise samples on the loss.

ReduceLROnPlateau is used to monitor the validation loss during the training process and dynamically adjust the learning rate. When the model's validation loss does not decrease in several rounds of iterations, the learning rate is automatically reduced to prevent oscillations in the training process.

#### IV. RESULTS AND ANALYSES

In this study, Accuracy, Precision, Recall and F1-score are used as the core evaluation metrics. The experimental results show that the proposed BiLSTM + FastText + Focal Loss model significantly outperforms the traditional methods and a single model on the Heilongjiang Tourism Review dataset, and the comparison results of different models are shown in Table 4.

TABLE 4 SENTIMENT CLASSIFICATION RESULTS OF  
DIFFERENT MODELS

Model	Accuracy	Precision	Recall	F1-score
SVM	85.6	86.2	84.9	85.5
Naive Bayes	82.4	83.1	81.7	82.4
LSTM	89.2	90.3	88.7	89.5
BiLSTM	91.5	92.7	90.5	91.3
BiLSTM + FastText + CrossEntropy Loss	95.1	95.2	94.0	94.9
BiLSTM + FastText+ Focal Loss	97.0	97.6	96.9	97.2

As seen in Table 4:

Under the same architecture, the accuracy of BiLSTM + FastText + CrossEntropyLoss (traditional cross-entropy loss function) is 95.1%, and the F1-score is 94.9%, which is 3.6%

higher than the base BiLSTM model (91.5% accuracy), indicating that FastText word vectors can effectively enhance the text representation.

After the introduction of Focal Loss, the model accuracy is improved to 97.0% (+1.9%), and the F1-score is improved to 97.2% (+2.3%), which verifies the optimisation ability of Focal Loss on category-imbalanced data by dynamically adjusting the loss weights.

Compared with classical models (e.g., SVM, LSTM), the present method leads in accuracy and F1-score by 11.4% and 11.7% respectively, highlighting the advantages of deep learning methods in complex text tasks.

The Train & Validation Accuracy Curve is shown in Fig. 5, and the Train & Validation Loss Curve is shown in Fig. 6. The Train & Validation Accuracy Curve shows that the validation accuracy of BiLSTM + FastText + Focal Loss stably converges at 97.0% with no oscillations or overfitting. The Train Loss & Validation Loss Curve shows that the Focal Loss version has lower values of validation loss and a smoother decline, suggesting that it improves training stability by dynamically adjusting the difficult sample weights.

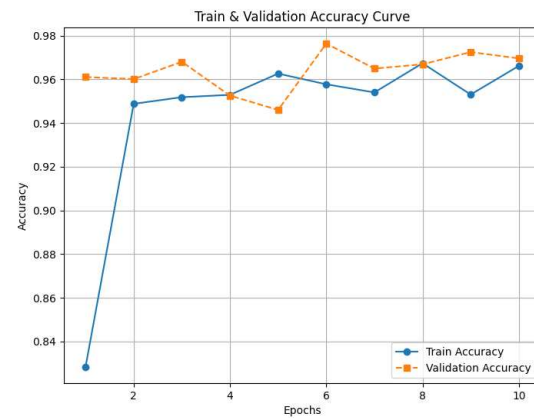


Figure 5 Train and Validation Accuracy Curve

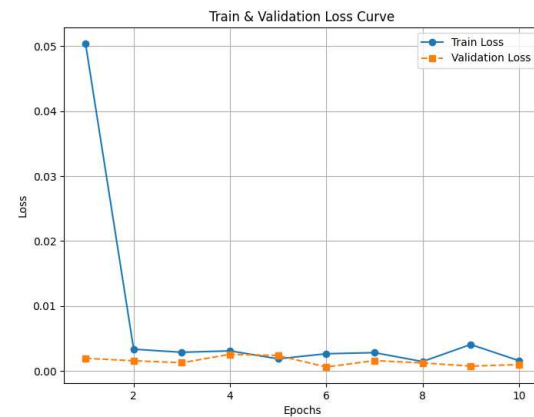


Figure 6 Train and Validation Loss Curve

Table 5 demonstrates the recall performance of different models on five categories of sentiment reviews, focusing on validating the optimisation effect of Focal Loss on a few

categories (e.g. negative reviews) and its improvement on the overall classification balance:

Taking negative reviews (category 1) as an example, the negative review recall rate is 90.5% when using BiLSTM only (15 misses, based on 149 actual samples), indicating that the traditional method is not capable of capturing a small number of categories. After the introduction of FastText (BiLSTM + FastText), the recall rate is improved to 92.1% (12 misses), and its subword embedding mechanism effectively alleviates the problem of unregistered words for local words. After further combining with Focal Loss, the recall rate improves to 96.9% (5 missed words), which is 3.4 percentage points higher than the CrossEntropyLoss version (93.5%). This result suggests that Focal Loss significantly reduces the risk of missed detections by dynamically reducing the loss weights of easy-to-categorise samples (e.g., extremely positive comments), forcing the model to focus more on learning difficult samples from a small number of categories.

For extremely positive reviews (category 4), the recall improves from 94.6% in CrossEntropyLoss to 95.1%, indicating that the model optimises for a few classes without sacrificing the performance of the majority class.

The recall of all classes exceeds 94%, with the gap between negative reviews (96.9%) and very positive reviews (95.1%) being only 1.8%, demonstrating that the model achieves robust classification performance both globally and locally.

TABLE 5 RECALL OF DIFFERENT MODELS FOR DIFFERENT CATEGORIES OF COMMENTS

Model	Category				
	0	1	2	3	4
SVM	72.1%	75.2%	80.5%	78.9%	82.3%
Naive Bayes	74.3%	78.6%	81.2%	79.5%	84.7%
LSTM	85.2%	86.4%	88.1%	87.3%	90.2%
BiLSTM	89.7%	90.5%	91.3%	90.8%	92.7%
BiLSTM + FastText	91.5%	92.1%	93.5%	92.8%	94.2%
BiLSTM+ FastText + CrossEntropyLoss	92.8%	93.5%	93.8%	93.2%	94.6%
<b>BiLSTM+ FastText + Focal Loss</b>	<b>95.2%</b>	<b>96.9%</b>	<b>94.8%</b>	<b>94.5%</b>	<b>95.1%</b>

(Note: The values in the table are recall rates calculated independently by category, i.e., recall rate for a category = number of correctly predicted samples in that category/total actual samples in that category.)

## V. CONCLUSION

This study presents a sentiment analysis framework for Heilongjiang tourism online reviews, integrating BiLSTM and FastText to enhance classification accuracy and robustness. The experimental results demonstrate that this approach significantly improves sentiment classification performance, achieving 97.0% accuracy and an F1-score of 97.2%. The incorporation of FastText word embeddings effectively mitigates the out-of-vocabulary (OOV) issue,

enabling the model to better understand regional terminology and informal language commonly found in tourism reviews. Meanwhile, the bidirectional architecture of BiLSTM strengthens the model's ability to capture long-range dependencies and contextual semantics, leading to more accurate sentiment detection.

Moreover, to address class imbalance, Focal Loss is introduced to dynamically adjust the weight of misclassified samples, allowing the model to focus more on hard-to-classify instances. This optimization significantly improves the recall of minority-class sentiment categories, particularly negative reviews, where recall increases from 90.5% to 96.9%, effectively reducing the model's bias toward majority classes. Compared to traditional sentiment analysis methods such as SVM and Naïve Bayes, the BiLSTM + FastText + Focal Loss combination proves to be a superior solution, especially in imbalanced sentiment classification tasks.

Despite its effectiveness, this study has certain limitations. The current approach primarily focuses on text-based sentiment analysis, without incorporating multimodal information such as images, audio, or video, which could provide a more comprehensive sentiment understanding. Future research can integrate Transformer-based pre-trained models (e.g., BERT, GPT) to further optimize text representations. Additionally, exploring multimodal fusion techniques—leveraging textual and visual features—can enhance the model's generalization ability and applicability across different domains.

## REFERENCES

- [1] Rasool, H., Maqbool, S., & Tarique, M. (2021). The relationship between tourism and economic growth among BRICS countries: a panel cointegration analysis. *Future Business Journal*, 7(1).
- [2] CCTV.com, "Heilongjiang receives over 135 million domestic and international tourists as ice and snow season concludes," CCTV.com, Mar. 2, 2025. [Online]. Available: <https://news.cctv.com/2025/03/02/ARTIEvb7v1lNSB2huEU9LF0Q250302.shtml>.
- [3] Kanwel, S., Lingqiang, Z., Asif, M., Hwang, J., Hussain, A., & Jameel, A. (2019). The Influence of Destination Image on Tourist Loyalty and Intention to Visit: Testing a Multiple Mediation Approach. *Sustainability*, 11(22), 6401. <https://doi.org/10.3390/su11226401>
- [4] Cui, R., Gallino, S., Moreno, A., & Zhang, D. J. (2018). The Operational Value of Social Media Information. *Production and Operations Management*, 27(10), 1749-1769. <https://doi.org/10.1111/poms.12707>
- [5] O. A. El-Said, "Impact of online reviews on hotel booking intention: The moderating role of brand image, star category, and price," *Tourism Management Perspectives*, vol. 33, p. 100607, 2020.
- [6] D. Tang, B. Qin, and T. Liu, "Deep learning for sentiment analysis: Successful approaches and future challenges," *Wiley Interdisciplinary Reviews: Data Mining and Knowledge Discovery*, vol. 5, no. 6, pp. 292-303, 2015.
- [7] Kumar R, Goswami B, Mhatre S M, et al. Naive bayes in focus: a thorough examination of its algorithmic foundations



and use cases. *Int. J. Innov. Sci. Res. Technol*, 2024, 9(5): 2078-2081.

[8] A. Yadav and D. K. Vishwakarma, "Sentiment analysis using deep learning architectures: a review," *Artificial Intelligence Review*, vol. 53, pp. 4335–4385, 2020.

[9] Z. Hameed and B. Garcia-Zapirain, "Sentiment classification using a single-layered BiLSTM model," in *IEEE Xplore*, 2020.

[10] H. Arora and M. Bansal, "LSTM and Bi-LSTM deep learning technique for better tourism services in future by analyzing hotel reviews," *Journal of Algebraic Statistics*, vol. 13, no. 3, pp. 3114-3123, 2022.

[11] Ariyus, D., Manongga, D., & Sembiring, I. (2024). Enhancing Sentiment Analysis of Indonesian Tourism Video Content Commentary on TikTok: A FastText and Bi-LSTM Approach. *Engineering, Technology & Applied Science Research*, 14(6), 18020-18028. DOI: 10.48084/etasr.8859.

[12] M. Wang, H. You, H. Ma, X. Sun, and Z. Wang, "Sentiment analysis of online new energy vehicle reviews," *Applied Sciences*, vol. 13, no. 14, 2023. [Online]. Available: <https://doi.org/10.3390/app13148176>.

[13] E. M. Dharma, F. L. Gaol, H. L. H. Spits Warnars, and B. Soewito, "The accuracy comparison among Word2Vec, GloVe, and FastText towards convolution neural network (CNN) text classification," *Journal of Theoretical and Applied Information Technology*, vol. 100, no. 2, pp. 349–350, 2022.

[14] N. Khamphakdee and P. Seresangtakul, "An efficient deep learning for Thai sentiment analysis," *Data*, vol. 8, no. 5, 2023. [Online]. Available: <https://doi.org/10.3390/data8050090>.

[15] A. Ullah, K. Khan, A. Khan, and S. Ullah, "Understanding quality of products from customers' attitude using advanced machine learning methods," *Computers*, vol. 12, no. 3, 2023.

[16] W. Yi, X. Huang, S. Kuzmin, and I. Gerasimov, "Seekg: Sentiment analysis for E-Learning evaluation incorporating knowledge graphs," *Springer*, 2025. [Online]. Available: <https://link.springer.com/article/10.1007/s10639-025-13456-1>.

[17] R. Egger, "Text representations and word embeddings: Vectorizing textual data," *Springer*, 2022.

[18] N. Oubenali, S. Messaoud, A. Filiot, and A. Lamer, "Visualization of medical concepts represented using word embeddings: a scoping review," *Springer*, 2022. Available: <https://link.springer.com/article/10.1186/s12911-022-01822-9>.

[19] T. Lin, P. Goyal, R. Girshick, K. He, and P. Dollár, "Focal loss for dense object detection," *IEEE Transactions on Pattern Analysis and Machine Intelligence*, vol. 42, no. 2, pp. 318-327, 2020. Available: <https://arxiv.org/pdf/1708.02002.pdf>.

[20] Y. F. Zhang, W. Ren, Z. Zhang, Z. Jia, L. Wang, and T. Tan, "Focal and efficient IOU loss for accurate bounding box regression," *Neurocomputing*, vol. 501, pp. 231-239, 2022. Available: <https://arxiv.org/pdf/2101.08158>.

[21] D. Peng, C. Liu, and W. Desmet, "An improved 2DCNN with focal loss function for blade icing detection of wind turbines under imbalanced SCADA data," *OMAE Conference Proceedings*, 2021.

[22] D. Watnakornbuncha, N. Am-Dee, and A. Sangsongfa, "Adaptive deep learning with optimization hybrid convolutional neural network and recurrent neural network for prediction of lemon fruit ripeness," *Przegląd*

*Elektrotechniczny*, vol. 100, no. 3, pp. 202–211, 2024, doi:10.15199/48.2024.03.36.

# Proposal for an Autonomous and Efficient SQL Learning Support Model Using Generative AI

Somchai Chatvichienchai<sup>1,a)</sup>

Author Affiliations

<sup>1</sup>Dept. of Information Security, Faculty of Information System  
University of NagasakiNagasaki Prefecture, Japan

Author Emails

<sup>a</sup>Corresponding author: somchaic@sun.ac.jp

**Abstract.** Generative AI (GAI) has great potential for SQL learning, yet its application remains underdeveloped. Traditional learning methods (rule-based, template-based, and machine learning-based approaches) have limitations. The objective of this paper is to propose a learning model that enhances autonomous and efficient SQL education using GAI. The model enables AI-driven SQL query generation, error diagnosis, and customized practice exercises based on learners' understanding. By leveraging GAI, learners can study SQL more effectively and independently. This paper compares GAI like ChatGPT, Gemini, and Copilot to determine their best use for SQL learning. To avoid over-reliance on AI, the paper also proposes complementary strategies such as learning journals and discussions. This research contributes to SQL education by fostering critical thinking and problem-solving skills while addressing AI limitations. The proposed model offers a practical approach to integrating GAI into learning and explores its broader applications.

**Index Terms—** Database, Generative AI, Induced Errors, Learning Support, SQL.

## I. INTRODUCTION

In today's digital age, vast amounts of data are generated and utilized daily, with databases serving as a cornerstone across various fields. Among them, SQL (Structured Query Language) is essential for efficient data management and manipulation, making it indispensable for data analysis and application development. However, mastering SQL requires an understanding of its unique syntax and logical structures, which many beginners find challenging [1][2]. Traditional learning methods often require significant time to consult books or online resources, but GAI enables learners to quickly access relevant information, creating a more efficient learning experience. In particular, interactive learning through prompts simulates having a tutor available 24/7, which has been shown to boost learner motivation. However, challenges remain in effectively utilizing GAI for education, highlighting the need for a new learning support model to address these issues.

Many studies have investigated the role of GAI in software development. Brown et al. [3] assessed AI-powered coding assistants in introductory programming courses, evaluating tools like ChatGPT and Codex in terms of student learning, engagement, and performance through both quantitative and qualitative analyses. Chen et al. [4] examined how OpenAI Codex supports programming education by helping students grasp complex concepts, generating code snippets, and providing real-time debugging assistance. Johnson et al. [5] analyzed the effects of GitHub Copilot on developer productivity, showing that AI-assisted

code generation streamlines the coding process, shortens development time, and improves code quality, backed by user feedback and performance data. Wang et al. [6] explored GAI applications in automated code refactoring and debugging, focusing on algorithms and techniques for detecting code smells, recommending refactoring strategies, and resolving bugs, with case studies demonstrating their practical advantages.

Recent studies have examined the use of GAI in SQL query generation. Bazaga et al. [7] developed SQLformer, a transformer-based model that converts text into SQL queries using abstract syntax trees, achieving cutting-edge performance. However, while these studies focus on generating SQL queries, they often overlook the development of fundamental SQL skills. Samaddar [8] highlighted the transformative impact of Azure Open AI and Semantic Kernel on SQL query creation, emphasizing their practical applications in technical education. Collectively, these studies demonstrate the broad applications and advantages of GAI in educational contexts. Mansinghka et al. [9] introduced GenSQL, a system designed to streamline database interactions by integrating GAI with tabular data. Their primary objective is to produce SQL queries rather than to teach the foundational principles and methodologies of SQL query formulation.

### A. Problem Definition

The use of GAI in SQL learning presents two major challenges:

Problem 1: GAI-induced Errors



GAI does not always guarantee accurate information and may suggest incorrect SQL statements or nonexistent table names. This issue is particularly pronounced when ambiguous instructions or incomplete data are provided [10]. While specifying prompts in a precise and detailed manner is one countermeasure, it does not fully resolve the problem. Therefore, it is essential for learners to critically evaluate AI-generated outputs and modify them as needed [11].

#### Problem 2: Loss of Independent Learning Opportunities

Since GAI can provide answers instantly, the essential learning process of trial and error, as well as logical reasoning, may be bypassed [12]. This raises concerns about the decline in learners' fundamental understanding, problem-solving skills, and overall motivation. Additionally, over-reliance on AI may hinder the development of creativity and critical thinking abilities [13].

#### B. Research Objectives

The objective of this paper is to analyze the potential and challenges of using GAI for SQL learning and propose a new learning support model to overcome these issues. This paper focuses on the following key capabilities of GAI such as SQL query generation and explanation, Error diagnosis and correction, Database design support, Query optimization and Provision of practical exercises.

## II. COMPARISON OF GENERATIVE AI TOOLS

GAI is increasingly utilized in modern education and learning environments. This section compares three popular GAI—ChatGPT [14], Gemini [15], and Copilot [16]—by evaluating their features and their roles in SQL learning support.

TABLE I  
COMPARISON SQL LEARNING ASSISTANT FEATURES OF  
CHATGPT, GEMINI AND COPILOT

Role	ChatGPT	Gemini	Copilot
<b>SQL Query Generation and Explanation</b>	◎ Is proficient at generating clear SQL queries with detailed explanations, making it ideal for beginners.	◎ Highly accurate and capable of handling complex queries, though explanations may be more concise.	○ Specializes in code completion, generating efficient SQL queries but with less detailed explanations.
<b>Error Diagnosis and Correction</b>	◎ Provides detailed explanations of errors and their causes, ideal for beginner learning.	◎ Advanced diagnostic capabilities, suitable for handling complex errors.	○ Offers concise feedback, making it a useful tool for experienced developers.
<b>Database Design and Support</b>	○ Provides basic support for database design but struggles with more complex designs.	◎ Supports advanced tasks like schema design and normalization.	△ Focuses on simple design assistance, not suitable for large-scale designs.
<b>Query Optimization</b>	△ Limited to theoretical suggestions, not strong in practical optimization.	△ Provides general suggestions but may not adapt to execution environments.	◎ Offers optimization suggestions based on practical applications, ideal for efficiency-

<b>Creation of Practical Exercises</b>	◎ Produces practical exercises with detailed explanations, excellent for learners.	◎ Capable of generating diverse problems covering various themes and levels.	focused developers. ○ Best for creating practical exercises aimed at advanced learners.
--	--	--	--

ChatGPT, developed by OpenAI, is a conversational AI with advanced natural language processing capabilities. It can generate accurate SQL queries and provide detailed explanations of the underlying logic and syntax, making it especially useful for beginners and intermediate learners. However, its ability to handle complex tasks such as database design and query optimization is limited, which may reduce its effectiveness in real-world scenarios requiring advanced SQL skills.

Gemini, created by Google, excels in information retrieval and error diagnosis, particularly for runtime SQL errors. It is especially valuable for intermediate to advanced users due to its strong error correction features and assistance with database design. However, its explanations tend to be more concise compared to ChatGPT, making it less suitable for beginners but highly effective for those with a more advanced understanding of SQL.

Copilot, developed by Microsoft, is optimized for real-time code completion and query optimization. It helps developers efficiently complete SQL queries and optimize their code, making it ideal for advanced users working in professional development environments. However, it lacks the detailed explanations provided by the other tools, which limits its utility as a learning support tool.

As shown in Figure 1, each of these three GAI has its own strengths. The optimal choice depends on the learner's skill level (beginner, intermediate, or advanced) and whether the tool is being used for learning or practical application.

## III. A METHODOLOGY FOR UTILIZING GAI IN SQL TRAINING

The author proposes a framework (illustrated in Fig. 1) that leverages GAI tools for SQL training, detailing each step of the process from setup to execution. It is important to note that this framework assumes learners possess sufficient background knowledge of relational databases to effectively engage in SQL training.

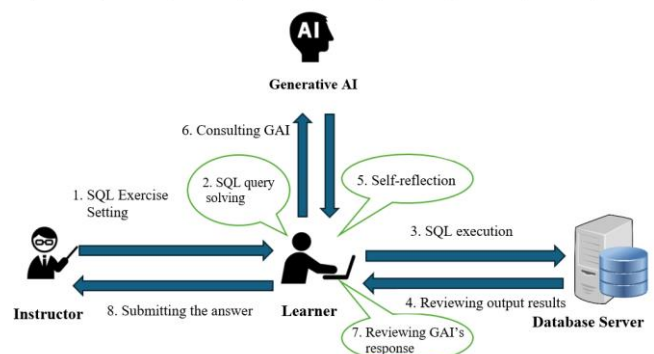


Fig. 1. The proposed framework.

#### Step 1: SQL Exercise Setting

The instructor creates an SQL exercise according to the learner's skill level. This task should include practical and clear table structures and data relationships. By adjusting the difficulty of database schemas and SQL queries, the task should provide a challenge while ensuring the learner feels a sense of achievement.

#### Step 2: SQL Query Solving

Learners analyze the exercise and define their own SQL queries. In this step, learners are encouraged to solve the exercise independently without the assistance of GAI. The experience gained from trial and error greatly enhances the learning process.

#### Step 3: SQL Execution

Learners input their SQL queries into a database management tool (such as MySQL Workbench, pgAdmin, etc.) and execute it. This step is essential to ensure that the SQL query is correctly parsed, and the output meets the exercise requirement.

#### Step 4: Reviewing Output Results

Learners review the output returned by the database. If the expected result is obtained, they move on to the next task. If errors occur, learners need to identify the cause. This step is crucial for improving debugging skills.

#### Step 5: Self-reflection

Learners reflect deeply on errors or issues with the output. They utilize basic knowledge provided by the instructor and background information from the task to investigate the root cause of problems, thereby developing problem-solving skills.

#### Step 6: Consulting GAI

Based on their reflections, learners create detailed yet concise prompts. The prompt should include:

- Task content
- Table information (structure, data types, etc.)
- Details of errors
- Results from the learner's trial and error

The quality of the prompt directly impacts the accuracy of the GAI's output, so care is needed.

#### Step 7: Reviewing GAI's Response

Learners review the response generated by the AI. If the answer is correct, they re-run the corrected SQL query and verify the query result. If it is inaccurate, they adjust the prompt and input it back into the GAI for improvement. This iterative process also helps learners improve their knowledge of how to effectively use Generative AI.

#### Step 8: Submitting the answer

Finally, learners submit the revised SQL query, reflection results, and the process of using GAI to the instructor. This step allows learners to develop not only their technical understanding of SQL but also their problem-solving skills and their ability to use GAI effectively.

## IV. BEST PRACTICES TO ACHIEVE OPTIMAL SQL WRITING RESULTS WITH AI TOOLS

The author's investigation has led to a series of steps and best practices to achieve optimal SQL writing results with GAI. The SQL learning was conducted in the following test environment:

- PC Used: Windows 11 personal computer
- SQL Environment: MySQL (version 8.0)
- SQL Client: MySQL Workbench (version 8.0)
- Database Exercises used in Database class conducted by the author.

### A. Problem Simplification

Learners need to reduce the SQL query problem to its most fundamental form, and to distill the requirements and eliminate any extraneous details.

### B. Database Schema Definition

The learners need to clearly define the database tables and columns, the relationships between tables, the type of database being used (e.g., MySQL, PostgreSQL, SQL Server, Oracle), and, if possible, provide sample data. The relationships between tables can be illustrated using an ER (Entity-Relationship) diagram. For instance, Figure 2 shows an ER diagram of the *world* database [17] created using MySQL Workbench [18]. This diagram outlines the relationships between foreign keys and primary keys among the *country* and *city* tables, illustrating how data in one table relates to data in another.

Consider the relationship between *country* table and *city* table shown in Fig.2. The *Code* column serves as the primary key in the *country* table. The *ID* column serves as the primary key in the *city* table. Based on the ER diagram shown in the figure on the left, learners can inform GAI of the relationships between the foreign keys and primary keys among country and city tables as follows:

The *CountryCode* column in the *city* table acts as a foreign key, referencing the primary key *Code* in the *country* table. The relationship signifies that each city listed in the *city* table belongs to a specific country identified by its country code in the *country* table.

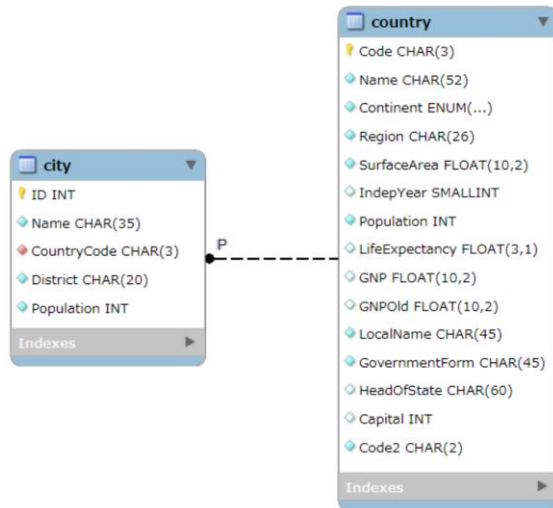


Fig. 2. An example of an ER diagram showing two tables of *world* database.

Below is an example of how to define *country* table in SQL, including a schema definition.

```
CREATE TABLE country (
    Code CHAR(3) NOT NULL,           -- Country code (ISO 3166-1 alpha-3)
    Name VARCHAR(52) NOT NULL,      -- Country name
    Continent VARCHAR(50) NOT NULL, -- Continent name
    Region VARCHAR(26) NOT NULL,    -- Region within the continent
    SurfaceArea FLOAT(10,2) NOT NULL, -- Surface area of the country in square kilometers
    Population INT(11) NOT NULL,    -- Population of the country
    LifeExpectancy FLOAT(3,1) NOT NULL, -- Life expectancy in years
    GNP FLOAT(10,2) NOT NULL,      -- Gross National Product in current US dollars
    GNPOld FLOAT(10,2) DEFAULT NULL, -- Previous year's GNP
    LocalName VARCHAR(45) NOT NULL, -- Local name of the country
    GovernmentForm VARCHAR(45) NOT NULL, -- Type of government
    HeadOfState VARCHAR(60) DEFAULT NULL, -- Head of state
    Capital INT(11) DEFAULT NULL, -- ID of the capital city (refers to the 'city' table)
    Code2 CHAR(2) DEFAULT NULL,    -- Two-letter country code (ISO 3166-1 alpha-2)
    PRIMARY KEY (Code)             -- Primary key on country code
);
```

Fig. 3. Schema definition of country table.

*country* table

	Code	Name	Continent	Region	SurfaceArea	Indep
	TCD	Chad	Africa	Central Africa	1284000.00	1960
	TGO	Togo	Africa	Western Africa	56785.00	1960
	THA	Thailand	Asia	Southeast Asia	513115.00	1350
	TJK	Tajikistan	Asia	Southern and Central Asia	143100.00	1991
	TKL	Tokelau	Oceania	Polynesia	12.00	
	TKM	Turkmenistan	Asia	Southern and Central Asia	488100.00	1991
	TMP	East Timor	Asia	Southeast Asia	14874.00	

(a)

*city* table

	ID	Name	CountryCode	District	Population
	3320	Bangkok	THA	Bangkok	6320174
	3321	Nonthaburi	THA	Nonthaburi	292100
	3322	Nakhon Ratchasima	THA	Nakhon Ratchasima	181400
	3323	Chiang Mai	THA	Chiang Mai	171100
	3324	Udon Thani	THA	Udon Thani	158100
	3325	Hat Yai	THA	Songkhla	148632
	3326	Khon Kaen	THA	Khon Kaen	126500
	3327	Pak Kret	THA	Nonthaburi	126055

(b)

Fig. 4. (a) A portion of the country table data and (b) A portion of the city table data.

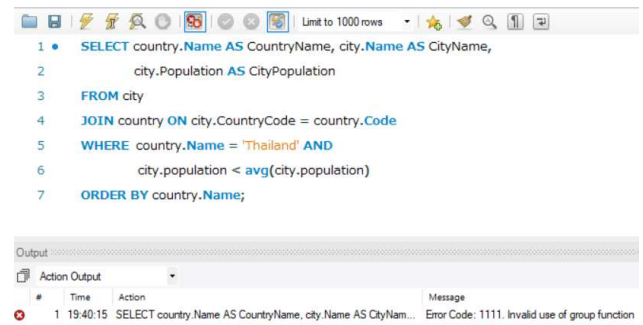


Fig. 5. An example of the syntax error of the learner's SQL query.

### C. Definition of Desired Query Output

Learners need to specify the necessary filters, ordering, aggregations, and performance considerations, such as avoiding full table scans. For example, an educator might ask learners to write a SQL query that displays cities in Thailand where the population is less than the average population of all cities in Thailand. The query should also include the corresponding country name and the population of each city. A sample of the country table data and city table data stored on the database server is shown on Fig. 4.

Figure 5 illustrates an example of an SQL query designed to fulfill the educator's request. However, this query contains a syntax error related to the use of a group function. To address this issue, the learner might explore SQL syntax using SQL textbooks or the MySQL website. However, this can be time-consuming. Alternatively, the learner can consult GAI tools to identify and resolve the syntax error in the SQL query. For instance, Figure 6 shows a chat between the learner and Copilot to solve this issue. Based on Copilot's advice, the learner revised and executed the SQL query. The execution result of the corrected SQL query, processed by MySQL Workbench, is presented in Fig. 7.

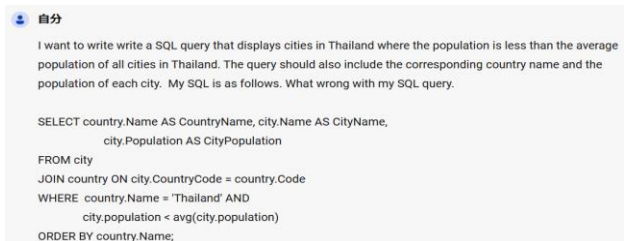





Fig. 6. An example screenshot of Copilot explaining and resolving the syntax error of the learner's SQL query.



CountryName	CityName	CityPopulation
Thailand	Nonthaburi	292100
Thailand	Nakhon Ratchasima	181400
Thailand	Chiang Mai	171100
Thailand	Udon Thani	158100
Thailand	Hat Yai	148632
Thailand	Khon Kaen	126500
Thailand	Pak Kret	126055
Thailand	Nakhon Sawan	123800
Thailand	Ubon Ratchathani	116300
Thailand	Songkhla	94900
Thailand	Nakhon Pathom	94100

Fig. 7. An example screenshot of MySQL Workbench showing the execution result of the corrected SQL query.

The learners can request Copilot to explain the generated SQL query in more detail. Due to space limitations, a screenshot explaining the generated SQL query by Copilot is not shown here. However, in some cases, a text-based explanation may not be sufficient for the learners to fully understand. Unfortunately, Copilot does not have the capability to draw a picture explaining how the Database Management System processes this SQL query. However, ChatGPT has the capability to display a text-based illustration explaining the SQL query (see Fig. 8).

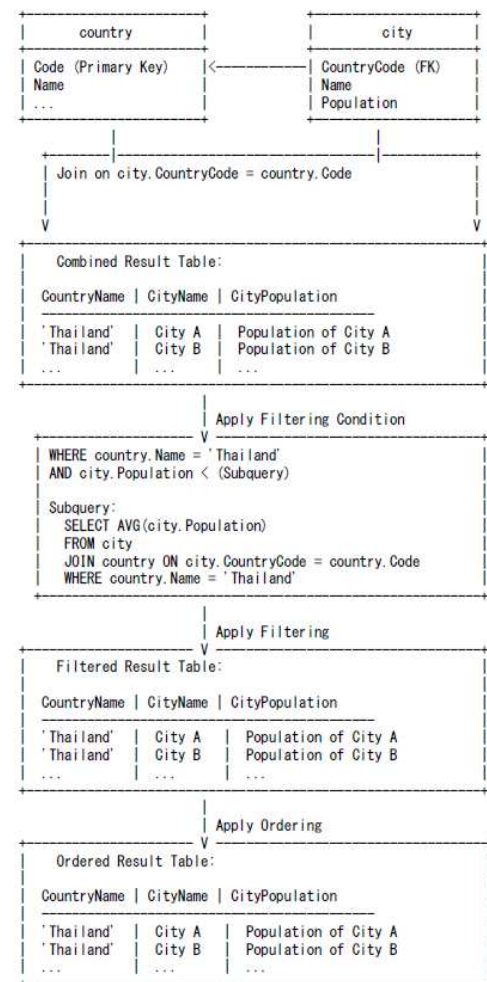
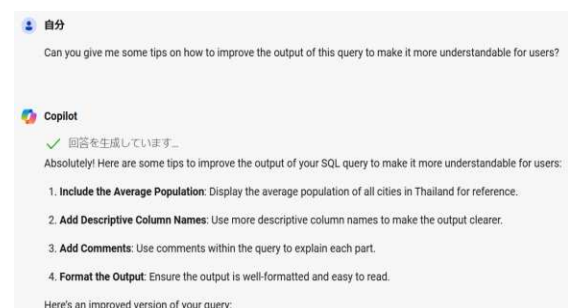


Fig. 8. An example text-based illustration produced by ChatGPT to explain the SQL query of Fig. 6.

#### D. Iteration on SQL Query Writing

The initial generated SQL statement may not be perfect. Learners need to execute the SQL statement on the database server and verify if it meets the query requirements. If it does not, adjustments should be requested, and the query should be executed multiple times until the desired outcome is achieved. For example, learners may ask Copilot for tips on how to improve the output of the SQL query to make it more understandable for users (see Fig. 9). Figure 10 shows the execution result of the SQL query from Fig. 9 in MySQL Workbench.



```
SQL
-- This query displays cities in Thailand where the population is less than the average population of all
cities in Thailand.
SELECT
  country.Name AS CountryName,
  city.Name AS CityName,
  city.Population AS CityPopulation,
  -- Subquery to calculate the average population of all cities in Thailand
  (SELECT AVG(city.Population)
   FROM city
   JOIN country ON city.CountryCode = country.Code
   WHERE country.Name = 'Thailand') AS AvgPopulation
FROM
  city
JOIN
  country ON city.CountryCode = country.Code
WHERE
  country.Name = 'Thailand'
AND city.Population < (SELECT AVG(city.Population)
                      FROM city
                      JOIN country ON city.CountryCode = country.Code
                      WHERE country.Name = 'Thailand')
ORDER BY
  country.Name;
```

Fig. 9. An example screenshot of Copilot answering a request a tip to improve output of the SQL query.

	CountryName	CityName	CityPopulation	AvgPopulation
▶	Thailand	Nonthaburi	292100	662763.4167
	Thailand	Nakhon Ratchasima	181400	662763.4167
	Thailand	Chiang Mai	171100	662763.4167
	Thailand	Udon Thani	158100	662763.4167
	Thailand	Hat Yai	148632	662763.4167
	Thailand	Khon Kaen	126500	662763.4167
	Thailand	Pak Kret	126055	662763.4167
	Thailand	Nakhon Sawan	123800	662763.4167
	Thailand	Ubon Ratchathani	116300	662763.4167
	Thailand	Songkhla	94900	662763.4167
	Thailand	Nakhon Pathom	94100	662763.4167

Fig. 10. An example screenshot from MySQL Workbench showing the execution result of the SQL query in Fig. 9.

## V. CONCLUSION AND FUTURE RESEARCH DIRECTIONS

In today's society, SQL has become an essential skill for data analysis and application development. However, due to its complexity, effective learning support is crucial. This study aimed to enhance the efficiency of SQL learning and promote learner autonomy by utilizing GAI, leading to the proposal of a learning support model. The key findings are summarized as follows:

- First, this paper conducted a comprehensive analysis of the role of GAI in SQL learning support. By comparing ChatGPT, Gemini, and Copilot, the author clarified their unique characteristics and applicable use cases. This comparison provided concrete guidelines for effectively utilizing GAI in SQL education.
- Second, this paper proposed an efficient learning support model that leverages the strengths of GAI while fostering learner autonomy. This model is centered around discussion-based learning, setting guidelines for GAI usage, and incorporating learning journals, enabling learners to develop critical thinking and problem-solving skills. The model aims to maximize learning efficiency while preventing over-reliance on GAI.

The findings of this study not only demonstrate the effectiveness of GAI-assisted learning in SQL education but also suggest its potential applications in other fields. Moving forward, we aim to implement this model in educational settings, examine its long-term impact, and explore its applicability to various disciplines, contributing to the practical use of GAI in learning support.

Through this study has gained insights into both the potential and challenges of GAI-assisted SQL learning support. However, further development requires addressing the following issues:

- Design and Implementation of a Learning Support System

To effectively integrate GAI into learning support, a system must be developed that enables learners to use AI appropriately while allowing instructors to monitor learning progress and trial-and-error processes. Specifically, it is necessary to create a mechanism that records and analyzes GAI-generated suggestions and learners' thought processes, making learning outcomes more transparent. This system will serve as a crucial foundation for supporting independent learning and supplementing the role of instructors.

- Long-Term Evaluation of Learning Effectiveness

The proposed learning support model should be evaluated over the long term to determine its impact on knowledge retention, critical thinking development, and creativity enhancement. This evaluation should include both quantitative data (such as learning outcomes and test results) and qualitative data (such as learner satisfaction and behavioral changes). A multifaceted analysis will be essential to validate the effectiveness of the proposed model.

## REFERENCES

- [1] C. Tanimura, SQL for Data Analysis: Advanced Techniques for Transforming Data Into Insights. O'Reilly Media, 2021.
- [2] D. Miedema. 2023. Toward a Fundamental Understanding of SQL Education. In Proceedings of the 2023 ACM Conference on International Computing Education Research - Volume 2 (ICER '23), Vol. 2. Association for Computing Machinery, New York, NY, USA, 64-68. <https://doi.org/10.1145/3568812.3603454>.
- [3] D. Brown and F. Garcia, "Evaluating the Impact of AI-Powered Coding Assistants on Learning Outcomes in Introductory Programming Courses," in Proceedings of the 2023 IEEE Frontiers in Education Conference (FIE), San Diego, CA, USA, 2023, pp. 789-794.
- [4] A. Chen, R. Smith, and J. Doe, "Enhancing Programming Education with Generative AI: A Case Study Using OpenAI Codex," IEEE Transactions on Education, vol. 67, no. 3, pp. 123-130, Aug. 2023.
- [5] B. Johnson and M. Lee, "AI-Assisted Code Generation: Improving Developer Productivity with GitHub Copilot," in Proceedings of the 2023 IEEE International Conference on Software Engineering (ICSE), Melbourne, Australia, 2023, pp. 456-465.
- [6] C. Wang, D. Patel, and E. Kim, "Leveraging Generative AI for Automated Code Refactoring and Debugging," IEEE Software, vol. 40, no. 2, pp. 78-85, Mar./Apr. 2023.

- [7] A. Bazaga, P. Liò, G. Micklem, “SQLformer: Deep Auto-Regressive Query Graph Generation for Text-to-SQL Translation,” arXiv preprint arXiv:2310.18376, May 27, 2024. [Online]. Available: <https://arxiv.org/abs/2310.18376>.
- [8] S. Samaddar, “Revolutionizing SQL Queries with Azure Open AI and Semantic Kernel”, Available: <https://techcommunity.microsoft.com/t5/analytics-on-azure-blog/revolutionizing-sql-queries-with-azure-open-ai-and-semantic/ba-p/3913513>, accessed 2024/5/20.
- [9] V. Mansinghka, M. Huot, “MIT Researchers Introduce Generative AI for Databases,” MIT News, Jul. 8, 2024. [Online]. Available: <https://news.mit.edu/2024/mit-researchers-introduce-generative-ai-databases-0708>.
- [10] TechSuite Editorial Team, “Decreased willingness and ability to learn due to reliance on generative AI”, (in Japanese), Available: <https://techsuite.biz/14190/>, accessed: 2025/4/3.
- [11] K. Goto and T. Matsuura, “Interaction between generative AI and critical thinking: A study on the application and impact of ChatGPT in education,” (in Japanese), Computer Utilization Education, vol. 56, pp. 68–74, 2024. doi: 10.14949/konpyutariyoukyouiku.56.68.
- [12] K. Sasaki and M. Ito, “A proposal for a virtual teaching assistant utilizing generative AI to support programming exercises,” (in Japanese), Proceedings of the 41st Annual Conference of the Japan Society for Software Science and Technology, p. 2b-2-R, Sep. 10, 2024.
- [13] Y. Adaki, “Can a Database be Manipulated from Ambiguous Directives? Verifying the accuracy of Text-to-SQL conversion by generative AI” (in Japanese), AI Solutions Group. Available: [https://aitc.dentsusoken.com/column/evaluate\\_the\\_robustness\\_of\\_text-to-sql/](https://aitc.dentsusoken.com/column/evaluate_the_robustness_of_text-to-sql/), accessed: 2025/4/3.
- [14] D. Ali, Y. Fatemi, E. Boskabadi, M. Nikfar, J. Ugwuoke, and H. Ali, “ChatGPT in Teaching and Learning: A Systematic Review,” Education Sciences, vol. 14, no. 6, pp. 643-660, Jun. 2024. [Online]. Available: <https://www.mdpi.com/2227-7102/14/6/643>.
- [15] M. Imran and N. Almusharraf, “Google Gemini as a Next Generation AI Educational Tool: A Review of Emerging Educational Technology,” Smart Learning Environments, vol. 11, no. 22, May 2024. [Online]. Available: <https://slejournal.springeropen.com/articles/10.1186/s40561-024-00310-z>.
- [16] Sucheth, “AI that explains papers: Copilot for scientific research,” SciSpace by Typeset, May 25, 2023. [Online]. Available: <https://typeset.io/resources/introducing-copilot-ai-assistant-explains-research-papers/>.
- [17] MySQL, Example Databases, <https://dev.mysql.com/doc/index-other.html>, accessed: 2024/6/18.
- [18] M. McLaughlin, “MySQL Workbench,” in MySQL Workbench: Data Modeling & Development, 1st ed. New York, NY, USA: Springer, 2013, pp. 123-145.



# Comparative of Spawning Induction Methods on Breeding Performance of Mangrove Red Snapper *Lutjanus argentimaculatus* Broodstock from Earthed Pond-Reared

Chawisa Pholsangsee<sup>1</sup>, Phongchate Pichitkul<sup>1, a)</sup>, Idsariya Wudtisin<sup>1</sup> and Vuttichai Oniam<sup>2</sup>

## Author Affiliations

<sup>1</sup>Department of Aquaculture, Faculty of Fisheries, Kasetsart University, Bangkok 10900, Thailand

<sup>2</sup>Klongwan Fisheries Research Station, Faculty of Fisheries, Kasetsart University, Prachuap Khiri Khan 77000, Thailand

## Author Emails

<sup>a)</sup>Corresponding author: ffishpcp@ku.ac.th

**Abstract.** This study aimed to assess the feasibility of using earthen pond-reared mangrove red snapper (*Lutjanus argentimaculatus*) as broodstock to reduce dependence on wild populations by investigating different spawning induction methods. Method I which applied environmental manipulation through a 70% water exchange per week; Method II, used normal rate hormone injections of LHRHa and Dom at a rate of 30 µg LHRHa + 10 µg Dom/kg for females and 15 µg LHRHa + 5 µg Dom/kg for males. Method III, involved higher doses of hormones, with 60 µg LHRHa + 20 µg Dom/kg for females and 30 µg LHRHa + 10 µg Dom/kg for males. The results showed that Method II, the normal hormonal injections, was the most effective choice, leading to an average of 2.6±0.5 spawning events, with a mean fertilization rate of 70.1±8.8% and a hatching rate of 69.8±7.8%. In contrast, Method I resulted in a mean spawning event of 1.3±0.5 but produced unfertilized eggs. Method III led to 2.3±0.5 spawning events but showed low mean fertilization rate 3.8±5.2% and low hatching rate (0.9±1.5%) due to the high proportion of defective eggs. In conclusion, Method II was the most effective alternative for inducing spawning in mangrove red snapper. This study result can be applied for sustainable mangrove red snapper farming practices.

**Index Terms:** Mangrove Red Snapper, Spawning Induction, Hormonal Injections, Breeding

## I. INTRODUCTION

Currently, the farming of economic marine fish has gained widespread interest due to the popularity of seafood consumption. Farmers who engage in this occupation can achieve good prices and high returns on investment compared to other agricultural professions. Popular economic marine fish for consumption, such as grouper, seabass, and mangrove red snapper, are in high market demand and are continuously sought after for consumption. [1]

Mangrove red snapper (*Lutjanus argentimaculatus*) is an economically important marine fish with high demand in Southeast Asia, both for consumption and aquaculture. However, more than 90% of the juvenile fish used in the aquaculture industry are from wild catches [2], leading to a continuous decline in natural populations. Therefore, producing juvenile fish in hatcheries is a key approach to reduce reliance on natural resources and provide more opportunities for farmers [3,4].

Although mangrove red snapper farming has high potential, it still faces significant challenges, such as ineffective spawning induction and aggressive behavior in male fish that affects breeding. This study aims to assess the feasibility of using pond-reared mangrove red snapper broodstock. Different spawning induction methods were

done for stimulating spawning and improving breeding efficiency, which will support sustainable mangrove red snapper farming in the future.

## II. METHODOLOGY

### Broodstock culture and selection

The broodstock was reared and conditioned in earthen ponds at the Klongwan Fisheries Research Station, Kasetsart University. They were fed fresh trash fish daily, supplemented with vitamin E and vitamin C at a rate of approximately 5% of body weight at 10:00 AM. Aeration systems were installed to maintain dissolved oxygen levels within an appropriate range, and water quality was monitored twice a week. Basic water quality during the rearing period in earthen ponds: salinity >30 ppt, dissolved oxygen (DO) > 5 mg/L, pH 6.5–8.0, temperature 25–32°C, total ammonia < 0.02 mg/L, total nitrite < 0.1 mg/L, and alkalinity 100–120 mg/L as CaCO<sub>3</sub>.

The selected mature broodstock were sourced from grow-out ponds at the Klongwan Fisheries Research Station, where they had been cultivated for 3.2 to 3.7 years. The Males broodstock had a mean length of 58.3±1.2 cm and a mean weight of 2.7±0.2 kg, while the female broodstock had a mean length of 56.3±0.9 cm and a mean weight of 3.1±0.2 kg.

The female broodstock with mature eggs were selected and anesthetized using a Eugenol solution (AQUANES©, Eugenol 5% w/v) at a dose of approximately 30 milliliters per 100 liters of water. Thereafter, the maturity of the eggs was again checked using cannulation with a cut-down tube [5,6]. For the

male fish, the presence of milt was identified, by gently pressing on the abdomen. This indicated that the fish were sexually mature and ready for spawning induction [7]. In each treatment, 15 broodstock were used, consisting of 6 males and 9 females.

#### Spawning induction

Mangrove red snapper (*Lutjanus argentimaculatus*) spawning can be induced by both environmental manipulation and synthetic hormone injection methods. Three different methods (treatments) were applied in this study with 3 replications. Method I, reared broodstock in the pond (or culture system) with 70% water exchange rate per week. Method II, applied standard hormonal injections of 30 µg LHRHa + 10 µg Dom/kg for females and 15 µg LHRHa + 5 µg Dom/kg for males. Method III, applied a higher dose of hormonal injections (60 µg LHRHa + 20 µg Dom/kg for females and 30 µg LHRHa + 10 µg Dom/kg for males). After that, the broodstock were transferred to a 15-ton tank for spawning, with a male-to-female ratio of 2:3. The experimental was done for a period of 30 days.

#### Spawning Conditions and Egg Collection

After mating of mangrove red snapper broodstock, which was commonly done during the night [8], was observed the spawning of the female could be checked in the following morning by using a flashlight. White particles floating in the water were fish eggs. The eggs were collected using a fine-mesh scoop with a mesh size less than 500 microns.

The collected eggs were placed into containers with clean seawater to allow debris and sediment to settle at the bottom of the container. Sediment separation was suctioned by using a small hose to separate impurities from the eggs. Cleaned eggs were transferred to the hatching process. Three egg samples were randomly collected using a 100 mL beaker to estimate the total number of eggs [9]. Additionally, some eggs were randomly sampled to be examined under a microscope at 40x magnification to assess the fertilization rate to evaluate the efficiency of the hatching process [10].

$$\text{Fertilization rate (\%)} = \left( \frac{\text{Number of eggs that develop}}{\text{Total number of eggs}} \right) \times 100$$

$$\text{Hatching rate (\%)} = \left( \frac{\text{Number of larvae that hatch}}{\text{Total number of eggs}} \right) \times 100$$

#### Data Analysis Technique

The variance of data obtained from the experiment was analyzed using one-way analysis of variance (One-way ANOVA). If the result showed significant differences, multiple comparisons among mean values of the experimental groups will be compared using Duncan's New Multiple Range Test at a 95% confidence level ( $P < 0.05$ ), using statistical software [11].

### III. RESULTS AND DISCUSSION

Study results indicated that (Figure 1)) Method I, had average spawning events of  $1.3 \pm 0.5$  times/month and a total number of eggs  $10,475 \pm 6,980$  but no fertilized eggs were found. Method II had average spawning events of  $2.6 \pm 0.5$  times/month, total number of eggs  $10,475 \pm 6,980$ , fertilization rate of  $70.1 \pm 8.8\%$  and hatching rate of  $69.8 \pm 7.8\%$ , which were significantly higher than those obtained with the other methods ( $P < 0.05$ ). Meanwhile, Method III, average spawning events of  $2.3 \pm 0.5$  times/month, total number of eggs  $45,600 \pm 11,200$  but had a low average fertilization rate of  $3.8 \pm 5.2\%$ , hatching rate of  $0.9 \pm 1.5\%$ , which were significantly lower than those of Method II ( $P < 0.05$ ). This suggests that a high hormone dosage can overstimulate the ovaries, causing eggs to be released from the follicles before completing final maturation. This premature ovulation lowers egg quality and results in reduced fertilization and hatching rates.

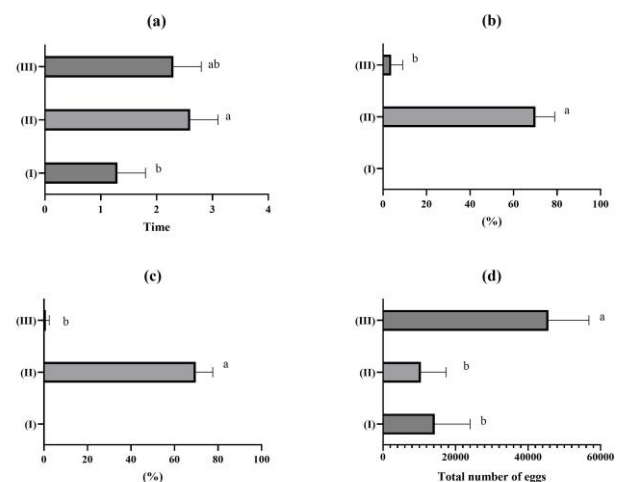


FIGURE 1. Overview of (a) spawning events, (b) fertilization rates, and (c) hatching rates (d) total number of eggs of mangrove red snapper (*Lutjanus argentimaculatus*) broodstock under various spawning induction methods: (I) environmental manipulation, (II) standard hormonal injection, and (III) higher hormonal dosage. Different lowercase letters denote significant differences between methods ( $P < 0.05$ ).

Mature mangrove red snapper (*Lutjanus argentimaculatus*) generally reaches a lifespan of around 2–3 years of age or older [12]. Preliminary can initially be assessed based on body size and external characteristics. About 50% of mature males have a body length of at least 44.9 cm and exhibit clear sexual characteristics, while 50% of mature females reach sexual maturity at a total length of at least 51.2 cm. Berried female fish show swollen and soft abdomen [13,14]. Breeding females can spawn throughout the year, with multiple spawning events occurring within a single month. During their reproductive phase, mangrove red snapper can naturally spawn in captivity or pond-reared without the need for hormone or stimulating drugs. A single mature female can spawn up to 2,350,000 eggs. For mature mangrove red snapper broodstock, they can be stimulated by performing water exchanges every other day and

supplementing their diet with vitamin E and vitamin C, to stimulate mating and spawning behavior [13,15,16]. The methods of breeding mangrove red snapper (*Lutjanus spp.*) have been extensively studied. Both hormone-induced spawning techniques and environmental control have been proven effective. Hormone-induced spawning using Human Chorionic Gonadotropin (HCG) or luteinizing hormone-releasing hormone analog (LHRHa) has been successfully applied to mangrove red snapper (*Lutjanus campechanus*) and mangrove red snapper (*L. argentimaculatus*) [17,18]. The dosage and timing of hormone injections are crucial for ovulation and egg production. Natural spawning can be achieved by regulating temperature and photo period in captivity [17]. In mangrove red snapper, natural spawning has been observed in alignment with the lunar phase [18]. Techniques for sperm collection, handling, and storage have been developed to enhance spawning efficiency. While hormone-induced spawning allows for controlled reproduction, natural spawning often produces higher-quality eggs but it's hard to predict [19]. These methods serve as the foundation for sustainable mangrove red snapper aquaculture and potential stock enhancement programs. In general, high-quality mangrove red snapper eggs float and form a light orange band on the water's surface, whereas lower-quality eggs sink [20]. In *Lutjanus campechanus*, when females spawn, high-quality eggs float to the water's surface, with a fertilization rate of more than 90%. However, fertilization rates can be varied. Based on 54 spawning events, the average fertilization rate was  $63.1 \pm 25.87\%$ . The average egg diameter was 0.78 mm, ranging from 0.73 to 0.93 mm. Lower-quality eggs, including unfertilized or defective ones, sink and are subsequently discarded [20]. These findings closely align with the breeding patterns observed in *Lutjanus argentimaculatus* in this study, where high-quality or fertilized eggs float to the water's surface, while defective (unfertilized) eggs gradually sink to the bottom after losing their buoyancy in the hatchery tank.

The breeding results of mangrove red snapper (*Lutjanus argentimaculatus*) using broodstock reared in earthen ponds, with an average age of 3.2 years, were considered a preliminary success in this study. However, the egg production (7,460–45,600 eggs per spawning event), fertilization rate (0.0–79.4% per spawning event), and hatching rate (0.0–77.9%) were lower than previous report. which reported *L. argentimaculatus* can produce up to 900,000–2,350,000 eggs, with an average of 526,000 eggs per kilogram of female body weight. The reported fertilization rate ranged from 62% to 95%, and the hatching rate varied between 34.8% and 99.5%. This may be because the broodstock used in this study was from the earthen pond [13,15,16]. The broodstock used in this study (with a weight range of 2.6–2.9 kg) were smaller than those reported in previous studies, where wild-caught broodstock ranged from 3.6 to 8.3 kg [13,21,22]. The differences in the source and size of the broodstock are crucial for breeding success, as the wild-caught broodstock typically exhibit greater genetic diversity, which benefits the preservation of genetic strength and reduces the problem associated with inbreeding. Additionally, wild broodstock tend to have higher

reproductive fitness due to the availability of natural food and optimal environmental conditions. However, a disadvantage of using wild broodstock is the risk of disease infection from nature, which can affect the health of future breeding stocks. Moreover, capturing wild broodstock can cause stress or injury to the fish. On the other hand, the broodstock from pond reared offers advantages in terms of health management and production environment control, such as diet, water quality, and disease prevention. However, the broodstock from pond culture includes the risk of reduced genetic diversity and inbreeding, as well as lower reproductive performance and hatching rate if they do not receive nutritionally adequate diets. Furthermore, wild-caught, mature broodstock often yield better breeding outcomes in terms of egg and sperm production, as well as eggs and larvae qualities. Larger, mature broodstock also tend to have a higher hatching rate compared to immature broodstock. However, managing and maintaining larger broodstock may require more resources, such as food and space. The broodstock from pond reared generally produces smaller quantities of eggs and sperm compared to wild broodstock. However, breeding using the pond reared broodstock, reared from a small size until they reach maturity can reduce natural broodstock overfishing and enhance breeding potential for aquaculture [23,24,25,26,27].

The selection of broodstock sources and sizes for mangrove red snapper breeding should be based on the breeder's objectives. If focus mainly on genetic diversity and strong offspring, wild-caught broodstock with mature sizes may be a preferable option. In contrast, the broodstock from ponds reared with immature sizes may be more suitable for long-term sustainability.

Overall, the results showed that Method II, the standard hormone injection, was the most effective spawning induction. This is consistent with the findings of [28,29], which stated that LHRHa plays a crucial role in stimulating the fish's pituitary gland to release gonadotropins (GtH) hormones, which are essential for the final maturation of eggs (full maturation). When GtH levels in the fish are sufficiently high, successful spawning and fertilization can occur. In contrast, Method I, environmental manipulation through a 70% water exchange per week, was unable to stimulate fertilization. This suggests that while water exchange may stimulate spawning to some extent, it does not significantly enhance fertilization or hatching rates. This method may require some modifications or should be combined with other methods to enhance its effectiveness. Method III demonstrated that using higher hormones injection or overdose may overstimulate the ovaries [30], resulting in a high proportion of defective eggs and a low fertilization rate.

#### IV. CONCLUSION

This study aimed to assess the feasibility of using earthen pond-reared mangrove red snapper (*Lutjanus argentimaculatus*) as broodstock to reduce dependence on wild populations by investigating different spawning induction methods. The results showed that Method II, which involved hormone injection with LHRHa 30 µg + Dom 10



µg/kg for females and LHRHa 15 µg + Dom 5 µg/kg for males, was the most effective method. It stimulated an average of 2.6 spawning events per week, with an average fertilization rate of 70.1% and a hatching rate of 69.8%. This method proved to be the most effective when compared to the other methods used in the experiment.

#### ACKNOWLEDGMENT

This study was a part of the Project for the Development of Culturing Potential of Red Snapper (*Lutjanus argentimaculatus*) for Production as Economic Aquatic Products, supported by the Kasetsart University Research and Development Institute (KURDI), Bangkok, Thailand under research grant No. RS(KU)6.65.

#### REFERENCES

- [1] Department of Fisheries, Thailand. "Brackish Water Fish Farming". Agricultural Cooperative Federation of Thailand Printing House, Bangkok, 1993.
- [2] Wuthisin, Prawim. "Propagation on the Red Snapper, *Lutjanus argentimaculatus* (Forsk.)" Proceedings of the 22<sup>nd</sup> Kasetsart University Conference on Fisheries, Bangkok, 1984.
- [3] Chi, Vo Van. "Habitat Specificity and Feeding Ecology of Juvenile Mangrove Red Snapper (*Lutjanus argentimaculatus* Forsskal, 1755)". Prince of Songkla University, Doctor of Philosophy in Biology: 143, 2017.
- [4] Faculty of Fisheries. "Organizing Activities to Raise Awareness About Overfishing and Foster a Sense of Responsibility for Sustainable Conservation of Aquatic Resources" Faculty of Fisheries, Kasetsart University, Bangkok, 2023. Retrieved December 14, 2024, from <https://fish.ku.ac.th/th/content/SDGs14.2.3-1>.
- [5] Crim, L. W., & Glebe, B. D. "Reproduction". Methods for Fish Biology, C. B. Schreck, Moyle, P. B., American Fisheries Society, Bethesda, 1990, pp. 529-553.
- [6] Russell, D. J., & Rimmer, M. A. "Stock Enhancement of Barramundi in Australia" Marine Ranching, D. M. Bartly & Leber, K. M. (Eds.), Food and Agriculture Organization of the United Nations, Rome, Italy, 2004, pp. 73-106.
- [7] Emata, Arnil C. "Reproductive Performance in Induced and Spontaneous Spawning of the Mangrove Red Snapper, *Lutjanus argentimaculatus*: A Potential Candidate Species for Sustainable Aquaculture" Aquaculture Research, 34(10): 849-857, 2003.
- [8] Chindamaikul, Twee, Kaeoian, Kowit, Playlahan, Chatchai. "Rearing of Broodstocks and Seed Production of Red Snapper (*Lutjanus argentimaculatus* Forskal)". Phangnga Coastal Fisheries Research and Development Center, Coastal Fisheries and Development Bureau, Department of Fisheries, 2003.
- [9] Phangnga Coastal Aquaculture Research and Development Center. "Red Snapper Aquaculture". Phangnga Coastal Aquaculture Research and Development Center, Department of Fisheries, 2022.
- [10] Na Nakhon, Utairat. "Fish Breeding". Department of Aquaculture, Faculty of Fisheries, Kasetsart University, Bangkok, 1995.
- [11] Kaiyawan, Yutth. "Principles of Research Statistics and the Use of SPSS" Chulalongkorn University Press, Bangkok, 2018.
- [12] Coniza, E.B., Caballero, P.A., & Catacutan, M.R. "Grow-out Culture of Mangrove Red Snapper (*Lutjanus argentimaculatus* Forsskal, 1775) in Ponds". Aquaculture Extension Manual Series, No. 53. SEAFDEC Aquaculture Department: Tigbauan, Iloilo City, Philippines, 2012.
- [13] Leu, M.Y., Chen, I.H., & Fang, L.S. "Natural Spawning and Rearing of Mangrove Red Snapper, *Lutjanus argentimaculatus*, Larvae in Captivity" The Israeli Journal of Aquaculture-Bamidgeh, 55(1): 22-30, 2003.
- [14] Philipose, K.K., Loka, J., Murugan, T.S., & Ranjan, R. "*Lutjanus argentimaculatus* (Forsskal, 1775)" In: Prioritized Species for Mariculture in India, R. Ranjan, M. Muktha, S. Ghosh, A. Gopalakrishnan, G. Gopakumar & I. Joseph (Eds.), pp. 49-54. ICAR-Central Marine Fisheries Research Institute, Kochi, 2017.
- [15] Doi, M., & Singhagraiwan, T. "Biology and Culture of the Red Snapper, *Lutjanus argentimaculatus*". pp. 29-51. In: Research Project of Fishery Resources Development in the Kingdom of Thailand, Bangkok, Thailand, 1993.
- [16] Hilary, D.G., Cowan Jr., J.H., & Powers, J.E. "A Comparison of Red Snapper Reproductive Potential in the Northwestern Gulf of Mexico: Natural versus Artificial Habitats". Marine and Coastal Fisheries: Dynamics, Management, and Ecosystem Science, 9: 139-148, 2017.
- [17] Phelps, R.P., Papanikos, N., Bourque, B.D., Bueno, F.T., Hastey, R.P., Maus, D.L., Ferry, A., & Davis, D.A. "Spawning of Red Snapper (*Lutjanus campechanus*) in Response to Hormonal Induction or Environmental Control in a Hatchery Setting". Reviews in Fisheries Science, 17(2): 149-155, 2009.
- [18] Emata, Arnil C., & Borlongan, I.G. "A Practical Broodstock Diet for the Mangrove Red Snapper, *Lutjanus argentimaculatus*" Aquaculture, 225: 83-88, 2003.
- [19] Phelps, R.P., Papanikos, N., Bourque, B.D., Bueno, F.T., Hastey, R.P., Maus, D.L., Ferry, A., & Davis, D.A. "Spawning of Red Snapper (*Lutjanus campechanus*) in Response to Hormonal Induction or Environmental Control in a Hatchery Setting". Reviews in Fisheries Science, 17(2): 149-155, 2009.
- [20] Watanabe, W.O., Benetti, D.D., & Feeley, M.W. "Status of Artificial Propagation of Mutton, Yellowtail, and Red Snapper (Family Lutjanidae)". American Fisheries Society Symposium, 46: 517-540, 2005.
- [21] Estudillo, C.B., Duray, M.N., Marasigan, E.T., & Emata, A.C. "Salinity Tolerance of Larvae of the Mangrove Red Snapper (*Lutjanus argentimaculatus*) During Ontogeny". Aquaculture, 190: 155-167, 2000.
- [22] Williams, K., Papanikos, N., Phelps, R.P., & Shardo, J.D. "Development, Growth, and Yolk Utilization of Hatchery-Reared Red Snapper *Lutjanus campechanus* Larvae" Marine Ecology Progress Series, 275: 231-239, 2004.
- [23] Uthairat, N., & Wongpathom, K. "Population Genetics for Aquaculture (1<sup>st</sup> ed.)" Kasetsart University and Thailand Research Fund, Bangkok, 2008.

- [24] Cabrita, E., Robles, V., & Herráez, P. “Methods in Reproductive Aquaculture: Marine and Freshwater Species” CPC Press, New York, 2008.
- [25] De Silva, S.S., Ingram, B.A., & Wilkinson, S. “Perspectives on Culture-Based Fisheries Developments in Asia”. NACA Monograph Series, No. 3, 126 pp., 2015.
- [26] Fabrice, T. “Fish Domestication: An Overview” Animal Domestication, 2018.
- [27] Raizada, S., Pravin, P., Kumar, A.T., & Jena, J.K. “ICAR Technologies: Breeding and Seed Production of Finfishes and Shellfishes” Indian Council of Agricultural Research, New Delhi, 2019, 66 pp.
- [28] Rottmann, R.W., Shireman, J.V., & Chapman, F.A. “Hormonal Control of Reproduction in Fish for Induced Spawning” SRAC Publication, 424, 1-4, 1991.
- [29] Sukumasawin, N., & Leelapatra, W. “A Comparison of the Efficiency of Different Types of Gonadotropin-Releasing Hormone (GnRH) Combined with Domperidone in Stimulating Gonadotropin Secretion and Inducing Spawning in Silver Barb (*Puntius gonionotus* Bleeker)” Fisheries Journal, 46(6): 511-518, 1993.
- [30] Maejo Vision Magazine. “Agricultural Clinic”. Retrieved February 28, 2025, from <http://mdc.library.mju.ac.th/article/90984/50533/357516.pdf>, 2002.



# Effects of Packaging and Temperature-Controlled Materials on the Quality and Transportation Cost of Marinated Salmon

Nathaphat Kingkaew<sup>1, a)</sup>, Supakit Sayasoonthorn<sup>1, b)</sup>, Kiatkamjon Intani<sup>1, c)</sup>  
Ratiya Thuwapanichayanan<sup>1, d)</sup>

## Author Affiliations

<sup>1</sup>Department of Farm Mechanics, Faculty of Agriculture, Kasetsart University, Bangkok, Thailand

## Author Emails

<sup>a)</sup>nathaphat.king@ku.th

<sup>b)</sup>agrsps@ku.ac.th

<sup>c)</sup>kiatkamjon.i@ku.th

<sup>d)</sup>Corresponding author: agrtry@ku.ac.th

**Abstract.** The increasing demand for marinated salmon presents logistical challenges in maintaining quality and minimizing transportation costs. As a high-fat marine fish, salmon requires temperature control, making transportation costly. This study evaluated the effects of packaging types and temperature-controlled materials on the quality and transportation costs of frozen marinated salmon. Marinated salmon was frozen at -20°C for 7, 45, and 52 days. Three packaging methods were tested: 1) a foam box with 8 gel ice packs inside a corrugated mailer (FB), 2) a regular slotted container with 4 gel ice packs, heat-reflective aluminum foil, and an insulated pouch (RSC), and 3) a die-cut box with similar insulation (DC). To simulate ambient transport, the frozen marinated salmon packed with various methods were kept at ambient temperature, ranging between 29.6°C and 34.2°C, for 24 h. During this period, FB maintained the lowest final temperature (11.05°C), while RSC and DC reached 22.30°C and 22.35°C, respectively. Subsequently, all samples were refrigerated at 0–2°C for 18 h before microbial and texture analyses. Microbial analysis confirmed that bacterial levels remained within safety limits for all packaging types, although the final product temperatures following ambient exposure were relatively high for fish safety standards. Texture analysis indicated no significant effect from the packaging method, but prolonged storage reduced toughness due to ice crystal formation and protein denaturation. Cost analysis revealed that ambient transport with FB, RSC, and DC reduced costs by 55.92%, 73.47%, and 62.45%, respectively, compared to refrigerated vehicle transport (240 THB per cycle). These findings suggest that alternative packaging methods can significantly reduce costs while maintaining product safety and quality during distribution.

**Index Terms**—marinated salmon, packaging, temperature-controlled material, texture, transportation cost

## I. INTRODUCTION

Norwegian salmon (*Salmo salar*), a member of the *Salmonidae* family, is recognized as a high-quality protein source. It is rich in essential amino acids, healthy fats, and omega-3 fatty acids, which contribute to cardiovascular and neurological health. Additionally, salmon contains essential vitamins and minerals, including vitamins A, D, and B12, as well as iodine and selenium [1,2]. Regular consumption of salmon has been linked to a reduced risk of heart disease, hypertension, and vascular disorders [3–5].

Marinated salmon has gained popularity in Thailand, as marination with soy sauce enhances its flavor. Consequently, demand for marinated salmon has increased across various regions through online platforms and social media. Storing marinated salmon at temperatures below -18°C preserves its quality for several months by significantly slowing enzymatic activity and inhibiting the growth of pathogenic microorganisms that cause spoilage. At -18°C or lower, chemical reactions and microbial proliferation are virtually halted, helping to maintain the texture, flavor, and safety of the salmon over an extended period. The U.S. Food and Drug Administration (FDA) states

that freezing seafood at -18°C or below is essential for prolonging shelf life while ensuring food safety [6]. However, prolonged frozen storage can impact the cellular structure and proteins of salmon, leading to a deterioration in quality [7].

Transporting frozen marinated salmon to suburban areas presents significant challenges. Due to its high-fat content, precise temperature control is required to maintain quality and freshness. As a result, refrigerated vehicle transport is commonly used, significantly increasing transportation costs. To remain competitive, businesses must minimize both shipping costs and delivery time, as these factors strongly influence consumer purchasing decisions when ordering online. Transporting frozen marinated salmon using standard (ambient) vehicle transport is challenging, as the product must be maintained at temperatures between -18°C and 4°C to prevent bacterial growth. If exposed to temperatures above 32°C, the salmon must be refrigerated within one hour [8].

In the frozen seafood industry, foam boxes are widely used due to their excellent insulation properties. However, foam boxes are relatively expensive and have limitations, such as their inability to be folded or customized to fit specific product sizes, leading to increased storage costs. Alternative temperature-controlled packaging materials, including gel ice packs, insulated

pouches, and heat-reflective aluminum foil, offer greater flexibility. These materials are smaller, more adaptable, and can be easily folded, allowing for more efficient packaging that fits precisely within containers. Consequently, transportation costs, determined by package size and weight, can be reduced.

Therefore, this study aims to identify the most suitable packaging and temperature-controlled materials for transporting frozen marinated salmon via ambient transport. The primary objective is to maintain product quality while assessing the effects of different storage durations, ultimately reducing packaging and shipping costs and enhancing market competitiveness.

## II. METHODOLOGY

Frozen marinated salmon samples were prepared for simulated transportation and quality assessment following a standardized procedure. Only the top loin portion of the filleted salmon was selected for processing. The top loin portions were wrapped in tissue paper and refrigerated at 1–2°C for 8 hours to absorb excess moisture and fat. After refrigeration, the portions were sliced into pieces approximately  $8 \pm 1$  mm in thickness. Eight pieces were placed into 83 mm × 80 mm cans (diameter × height). Chilled marinade, maintained at 1–2°C, was then poured into the cans before sealing them using a lid crimping machine. The sealed cans were frozen at –20 to –23°C for 7, 45, and 52 days before undergoing simulated transportation. These storage durations were selected to represent short-term, medium-term, and long-term frozen storage scenarios typically encountered in commercial distribution and inventory rotation. These time points allowed us to evaluate the effects of prolonged freezing on texture and microbial safety across realistic storage periods.

To collect temperature data during simulated transportation, a calibrated Elitech RC-5 data logger was used. The data logger was vacuum-sealed before being packed with five salmon slices and marinade in a can. The experiments were done in duplicate.

Three packaging methods were used for ambient transportation of frozen marinated salmon: one conventional method and two newly developed by the researchers. The details are as follows:

1) Foam box (FB): Two cans of frozen marinated salmon were placed inside a foam box measuring  $20.7 \times 26.7 \times 14.0$  cm (width × length × height). One can contained eight pieces of marinated salmon, while the other contained five pieces along with an Elitech RC-5 data logger. Eight gel ice packs were included before placing the foam box inside a B-flute corrugated mailer (size D) measuring  $22 \times 35 \times 14$  cm, as show in Figure 1a-c.



a) Arrangement of two cans of frozen marinated salmon and eight gel ice packs inside a foam box.



b) Placement of the foam box inside B-flute corrugated mailer.



c) Exterior view of the FB packaging  
Fig. 1. Foam box (FB) packaging.

2) Regular slotted container (RSC): A B-flute corrugated box (size 2A) measuring  $14 \times 20 \times 12$  cm was used. Two cans of marinated salmon, identical in composition to those in FB, were packed with only four gel ice packs to reduce the container size. The contents were wrapped in heat-reflective aluminum foil and placed inside an insulated pouch before being packed into the regular slotted container, as show in Figure 2a-c.



a) Arrangement of two cans of frozen marinated salmon and four gel ice packs before wrapping with heat-reflective aluminum foil.



b) Placement of all contents in Fig. 2a) inside an insulated pouch before being packed into a regular slotted container.



c) Exterior view of the RSC packaging.  
Fig. 2. Regular slotted container (RSC) packaging.

3) Die-Cut Box (DC): A die-cut box with E-flute measuring  $14 \times 20 \times 12$  cm was used. Two cans of marinated

salmon, identical in composition to those in FB and RSC, were packed with four gel ice packs. The contents were wrapped in heat-reflective aluminum foil and placed inside an insulated pouch before being packed into the die-cut box, as show in Figure 3a-c.



a) Arrangement of two cans of frozen marinated salmon and four gel ice packs before wrapping with heat-reflective aluminum foil.



b) Placement of all contents in Fig. 3a) inside an insulated pouch before being packed into a die-cut box.



c) Exterior view of the DC Packaging.  
Fig. 3. Die-cut box (DC) packaging.

The frozen marinated salmon samples, packed using different packaging methods, were placed at ambient temperature between 29.6°C and 34.2°C for 24 hours starting at 16:00, to align with the standard shipping schedules and simulate ambient transportation. Adequate spacing was maintained between the samples to prevent cold air transfer. Afterward, the cans were refrigerated at 1–2°C for an additional 18 hours. Temperature retention was monitored using the Elitech RC-5 data loggers. Mechanical factors such as vibration and shaking were not included in this simulation. Preliminary studies indicated that such mechanical factors slightly affected the breakdown of the fat layer of the salmon into the sauce within the can, resulting in slight turbidity of the sauce and a more pronounced odor, but the ambient

transport simulation allowed for more precise control of the shipping.

After refrigeration, the marinated salmon products were placed in a foam box filled with ice to maintain conditions close to refrigeration temperature before immediate texture analysis and microbiological testing.

For microbial analysis, it was conducted following the Department of Medical Sciences' standards for raw seafood quality control. The microbial quality standards included:

- 1) Total aerobic plate count:  $<1 \times 10^5$  CFU/g
- 2) *Escherichia coli*:  $<3$  MPN/g
- 3) *Staphylococcus aureus*:  $<100$  CFU/g
- 4) *Salmonella spp.*: Not detected in 25 g
- 5) *Vibrio cholerae*: Not detected in 25 g
- 6) *Vibrio parahaemolyticus*: Not detected in 25 g
- 7) *Listeria monocytogenes*: Not detected in 25 g [9]

For texture analysis, each can of marinated salmon was opened one at a time, and the contents were transferred into food-grade containers submerged in ice within a large foam box. The remaining cans were kept in ice throughout testing to ensure consistent temperature conditions.

Texture parameters were measured using the Stable Micro Systems TA-XT Plus Texture Analyzer, equipped with a Warner-Bratzler (HDP/BS) shear force attachment. The test parameters were set as follows: pre-test speed of 1 mm/s, test speed of 1 mm/s [10], and a deformation distance of 10 mm. Shear force and shear work values were derived from the force-deformation curve, which illustrates the relationship between applied force and tissue deformation. Shear force represents the maximum force required to cut through the marinated salmon, indicating firmness. Shear work, calculated as the area under the force-deformation curve (N·mm), indicating the total energy needed to breakdown the structure or to chew through the sample (toughness) [11, 12]. Each experiment was done in duplicate. Sixteen samples were tested in each replicate.

Transportation costs were calculated according to Kenton [13] by comparing the total costs (packaging and transportation) of the three packaging formats with the costs of transportation using refrigerated vehicle transport (RV), which is widely used in the salmon industry. The percentage cost reduction (PCR) for each packaging method (FB, RSC, and DC) was calculated using (1), (2), and (3) as follows:

$$PCR_{FB}(\%) = \frac{\text{Cost of RV} - \text{Cost of FB}}{\text{Cost of RV}} \times 100 \quad (1)$$

$$PCR_{RSC}(\%) = \frac{\text{Cost of RV} - \text{Cost of RSC}}{\text{Cost of RV}} \times 100 \quad (2)$$

$$PCR_{DC}(\%) = \frac{\text{Cost of RV} - \text{Cost of DC}}{\text{Cost of RV}} \times 100 \quad (3)$$

Statistical analysis was carried out using ANOVA in SPSS software. Mean values and standard deviations were reported, with Tukey's multiple range test used for comparisons at a 95% confidence level. Univariate analysis was also conducted to evaluate the effects of packaging and storage duration on frozen marinated salmon quality.

### III. RESULTS AND DISCUSSION

Temperature data inside the frozen marinated salmon cans during the 24-hour simulated transportation period are shown in Figure 4. In the initial phase, temperatures rose rapidly due to the large temperature gradient between the frozen samples and the environment, resulting in accelerated heat transfer [14]. From the midpoint onward, temperatures continued to rise, ultimately reaching 11.05°C, 22.30°C, and 22.35°C for the FB, RSC, and DC packaging, respectively. Singh et al. [15] compared the thermal resistance of a C-Flute corrugated fibreboard box with a 19 mm-thick EPS foam panel to that of a foil ThermalCor® box with a 4.8 mm-thick insulated pouch insert. The latter exhibited superior thermal resistance. The differing results from our study may be attributed to the lower number of gel ice packs in the RSC and DC packages, which were intentionally minimized to reduce box size and weight, thereby lowering shipping costs. As a result, these packages retained less cold than the FB packaging.

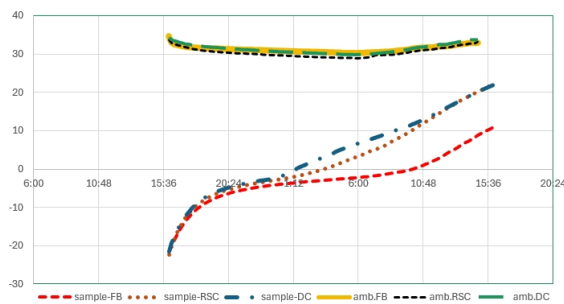


Fig. 4. Changes of ambient temperature and frozen marinated salmon temperature inside the can for all three packaging methods over a 24-hour period during simulated transportation

Although the temperatures inside the frozen marinated salmon cans exceeded 4°C, a threshold that supports bacterial growth [6], bacterial levels remained within safety limits for all three packaging methods, as shown in Table 1. This may be due to the specific bacterial species examined, based on fresh seafood quality standards, have optimal growth temperatures higher than the final product temperatures observed. For instance, *Vibrio parahaemolyticus*, a potential health risk, requires at least 25°C to grow. The optimal growth temperatures of the tested bacteria are:

1. *Escherichia coli*: ~44.5–45.5°C [16]
2. *Staphylococcus aureus*: ~37°C [17]
3. *Salmonella* spp.: ~35–37°C [18]
4. *Vibrio cholerae*: ~37°C [19]
5. *Vibrio parahaemolyticus*: ~25–37°C [20]
6. *Listeria monocytogenes*: ~30–37°C [16]

According to the U.S. Food and Drug Administration (FDA) [21], food must have an initial temperature of 5.0°C or below when removed from temperature control, and it may not exceed 21.1°C for more than 6 hours. In this study, the temperatures inside the frozen marinated salmon cans in RSC and DC packages exceeded 21.1°C for approximately 1 hour before being refrigerated [8], potentially contributing to slightly higher microbial counts compared to the FB packaging. Nevertheless, microbial levels for RSC and DC packaging remained well below safety thresholds.

TABLE 1  
BACTERIAL TESTING RESULTS  
OF MARINATED SALMON SAMPLES

List of bacteria tested	Packaging method		
	FB	RSC	DC
Aerobic Plate Count (CFU/g)	570	2,800	1,300
<i>E. coli</i> (MPN/g)	<3	<3	<3
<i>S. aureus</i> (CFU/g)	<10	<10	<10
<i>Salmonella</i> spp. (per 25g)	N.D.	N.D.	N.D.
<i>V. cholerae</i> (per 25g)	N.D.	N.D.	N.D.
<i>V. parahaemolyticus</i> (per 25g)	N.D.	N.D.	N.D.
<i>L. monocytogenes</i> (per 25g)	N.D.	N.D.	N.D.

Note: N.D. is Not detected

Table 2 illustrates the effects of the packaging method and storage duration on the shear force and shear work of marinated salmon. Shear force decreased over storage duration across all packaging methods. On day 7, the shear force ranged from 6.06 to 7.00 N. By day 45, it had decreased to 4.00–4.47 N. After 52 days of storage, shear force further declined slightly to 3.33–3.98 N, with no significant differences among packaging methods.

A similar trend was observed for shear work, with values decreasing over time. On day 7, shear work values were 185.20±25.30 N·mm in FB, 188.30±15.06 N·mm in RSC and 207.23±32.46 N·mm in DC. By day 45, shear work decreased to 105.03±26.66 N·mm in FB, 101.03±17.94 N·mm in RSC, and 101.31±18.18 N·mm in DC. The values on day 52 were similar to those on day 45. However, packaging methods had no significant effect on shear work. The marinated salmon with a higher value of shear force and shear work is firmer and tougher to chew.



TABLE 2  
EFFECTS OF PACKAGING METHOD AND STORAGE  
DURATION ON SHEAR FORCE AND SHEAR WORK OF  
MARINATED SALMON

Packaging method	Storage duration (Day)	Shear force (N)	Shear work (N·mm)
FB	7	6.06±0.85 <sup>a</sup>	185.20±25.30 <sup>a</sup>
	45	4.31±0.95 <sup>b</sup>	105.03±26.66 <sup>b</sup>
	52	3.33±1.00 <sup>b</sup>	95.02±17.51 <sup>b</sup>
RSC	7	6.50±0.83 <sup>a</sup>	188.30±15.06 <sup>a</sup>
	45	4.47±0.98 <sup>b</sup>	101.03±17.94 <sup>b</sup>
	52	3.98±7.33 <sup>b</sup>	111.27±16.47 <sup>b</sup>
DC	7	7.00±1.00 <sup>a</sup>	207.23±32.46 <sup>a</sup>
	45	4.00±0.73 <sup>b</sup>	101.31±18.18 <sup>b</sup>
	52	3.83±0.99 <sup>b</sup>	98.96±28.66 <sup>b</sup>
<i>p</i> -value			
Packaging method		0.209	0.549
Storage duration		0.000*	0.000*
Packaging × Storage duration		0.289	0.276

<sup>a-b</sup> Means with different superscripts in the same column are significantly different ( $p < 0.05$ )

\* The studied factor significantly affects the quality parameter ( $p < 0.05$ )

Statistical analysis indicated that storage duration significantly affected shear force and shear work, whereas the packaging method did not. The interaction between storage duration and packaging method was also not significant. The reduction in shear force and shear work over time is likely due to prolonged storage, which decreases firmness. This effect is attributed to ice crystal formation from intracellular and extracellular water during freezing, leading to muscle cell disruption and protein denaturation [7]. Packaging method had no significant impact on texture quality since final temperatures after simulated transportation did not differ substantially [8]. Furthermore, samples were immediately refrigerated after transportation before testing [8]. As a result, all three packaging methods had no significant impact on the texture of marinated salmon, despite the FB packaging maintaining a temperature 10°C lower than RSC and DC.

Regarding transportation costs, current refrigerated vehicle (RV) transport incurs the following expenses: 50 THB for vehicle booking, 15 THB for packaging, and 180 THB for local delivery (1–2 business days), totaling 245 THB per shipment. In contrast, the newly designed packaging methods in this study used alternative temperature-controlled materials, reducing transportation costs as follows:

1. FB Packaging – 108 THB per shipment, including 40 THB for a foam box, 8 THB for gel ice packs, 15 THB for a B-flute, size D corrugated mailer, and 45 THB for transportation.
2. RSC Packaging – 65 THB per shipment, including 9 THB for a regular slotted container box, 4 THB for gel ice packs, 13 THB for heat-reflective aluminum foil, 9 THB for an insulated pouch, and 30 THB for transportation.
3. DC Packaging – 92 THB per shipment, including 36 THB for a die-cut box, 4 THB for gel ice packs, 13 THB for heat-reflective aluminum foil, 9 THB for an insulated pouch, and 30 THB for transportation.

The transportation costs for FB, RSC, and DC packaging were reduced by 55.92%, 73.47%, and 62.45%, respectively, compared to RV transport. Kaewrungham [22] assessed Thai consumers' willingness to pay for RV transport of frozen processed food through a survey of 402 respondents. The results indicated that consumers were willing to pay an average of 96.04 THB for RV transport, while the actual cost was 190 THB. When compared to the cost of transporting frozen marinated salmon, FB and DC packaging costs were close to consumer willingness to pay, whereas RSC packaging cost was significantly lower (only 65 THB).

Although all three packaging methods offer lower costs than RV transport, they pose risks if delivery is delayed or exceeds one business day, increasing the likelihood of spoilage. Therefore, clear agreements between sellers and consumers are essential to ensure the product is received immediately upon delivery.

#### IV. CONCLUSION

This study demonstrated that all three packaging methods allowed the transportation of frozen marinated salmon via standard delivery vehicles within a 24-hour timeframe. The packaging method had no significant effect on texture quality or microbial safety, whereas storage duration affected texture. Prolonged storage led to reduced shear force and shear work, indicating a decrease in firmness. Cost analysis revealed that ambient transport using FB, RSC, and DC reduced transportation costs by 55.92%, 73.47%, and 62.45%, respectively, compared to refrigerated vehicle transport. Among these, the RSC box was identified as the most cost-effective option due to its lower container price and overall cost savings. However, despite the cost advantages, delays or extended transportation times may still pose a risk of spoilage. Therefore, clear agreements between sellers and consumers are essential to mitigate this risk. Future studies should incorporate sensory testing or real-world shipping conditions to further evaluate quality attributes such as texture and color.



## ACKNOWLEDGMENT

The authors express their sincere appreciation to the Kasetsart University through the Graduate School Fellowship Program.

## REFERENCES

- [1] AK Salmon Co., “Norwegian salmon: Everything you need to know,” Alaskan Salmon Company, 2023. [Online]. Available: <https://aksalmonco.com/blog/learn/norwegian-salmon>. [Accessed: Sep. 24, 2024].
- [2] U.S. Department of Agriculture, “Fish, salmon, Atlantic, farmed, cooked, dry heat,” U.S. Department of Agriculture, 2019. [Online]. Available: <https://fdc.nal.usda.gov/food-details/175168/nutrients>. [Accessed: Sep. 24, 2024].
- [3] D. O. Kennedy, “B vitamins and the brain: Mechanism, dose and efficacy—a review,” *Nutrients*, 8(2):68. 2016.
- [4] F. Spritzler, “Salmon nutrition and health benefits,” Healthline, 2023. [Online]. Available <https://healthline.com/nutrition/salmon-nutrition-and-health-benefits>. [Accessed: Sep. 24, 2024].
- [5] B. Zhang, K. Xiong, J. Cai, and A. Ma, “Fish consumption and coronary heart disease: A meta-analysis,” *Nutrients*, 12(8):2278, 2020
- [6] U.S. Food and Drug Administration, “Fish and fishery products hazards and controls guidance,” FDA, 2022. [Online]. Available: <https://www.fda.gov/food/seafood-guidance-documents-regulatory-information/fish-and-fishery-products-hazards-and-controls> [Accessed: Mar. 13, 2025].
- [7] P. Dawson, W. Al-jeddawi, and N. Remington, “Effect of freezing on the shelf life of salmon,” *Food Sci.*, 2018. Available: <https://doi.org/10.1155/2018/1686121>.
- [8] Centers for Disease Control and Prevention, “Food safety: Prevention,” CDC. [Online]. Available: [https://www.cdc.gov/food-safety/prevention/?CDC\\_AAref\\_Val=https://www.cdc.gov/foodsafety/keep-food-safe.html](https://www.cdc.gov/food-safety/prevention/?CDC_AAref_Val=https://www.cdc.gov/foodsafety/keep-food-safe.html). [Accessed: Jul. 11, 2024].
- [9] Bureau of Quality and Safety of Food, “Microbiological quality standard for food and food contact utensils, edition 3,” Department of Medical Sciences, Ministry of Public Health, Thailand, 2017. [Online]. Available: <http://bqsf.dmsc.moph.go.th/bqsfWeb/index.php/bio/> [Accessed: Aug. 6, 2024].
- [10] A. Gluchowski, E. Czarniecka-Skubina, G. Wasiak-Zys, and D. Nowak, “Effect of various cooking methods on technological and sensory quality of Atlantic salmon (*Salmo salar*),” *Food*, 8(8), 323, 2019.
- [11] H. F. Zhao, L. Feng, W.D. Jiang, W. Liu, J. Jiang, P. Wu, J. Zhao, S. K. Kuang, L. Tang, W. N. Tang, Y. A. Zhang and X. Q. Zhou, “Flesh Shear Force, Cooking Loss, Muscle Antioxidant Status and Relative Expression of Signaling Molecules (Nrf2, Keap1, TOR, and CK2) and Their Target Genes in Young Grass Carp (*Ctenopharyngodon idella*) Muscle Fed with Graded Levels of Choline”, *PLoS One*, 10(11):e0142915, 2015, Available: <https://doi.org/10.1371/journal.pone.0142915>
- [12] C. Phoemchalard, N. Senarate, T. Tathong and P. Pornanek, “Quality and safety characteristics of pork meat available in Amnat Charoen Province, Thailand”, *Khon Kaen Agriculture Journal*, 2021
- [13] W. Kenton, “Percentage change,” Investopedia, [Online]. Available: <https://www.investopedia.com/terms/p/percentage-change.asp> [Accessed: 1-Apr-2025].
- [14] V. E. Sweat, “Thermal properties of foods,” *Engineering Properties of Food*, 1994.
- [15] S. P. Singh, G. Burgess, J. Sings, “Performance comparison of thermal insulated packaging boxes, bags and refrigerants for single-parcel shipment”, *Packaging Technology and Science*, 21: 25-35., 2008, Doi: 10.1002/pts.773/abstract
- [16] S. Sathonseawapak, “Newly Food Bourne Pathogens, Part 1: Occurrence in Food”, Institute of Food Research and Product Development, Kasetsart University, 1995
- [17] A. Chanchaichaovivat and J. Kaewthamai. “Detection of Enteropathogenic Bacteria in White-leg Shrimps from Markets in Dhonburi District” *Advanced Science Journal*, 12(1), 2012
- [18] W. Janwatcharagan and S. Wongsamoot, “Comparative study of the Optimum *Salmonella* spp. Incubation temperature for Contamination detection in Meat and Raw milk samples”, Bureau of Quality Control of Livestock Products, Registered no. 63(2)-0404-012, (n.d.)
- [19] H. I. Sheilh, M. Najiah, A. Fadhina, A. A. Laith, M. M. Nor, K. C. A. Jalal, and N. A. Kasan, “Temperature Upshift Mostly but not Always Enhances the Growth of *Vibrio* Species: A Systematic Review”, *Marine Science*, vol. 9, Art. no. 959830, 2022. [Online]. Available: <https://doi.org/10.3389/fmars.2022.959830>.
- [20] D. Wang, S. H. Flint, J. S. Palmer, D. Gagic, G. C. Fletcher, S. L. W. On, “Global expansion of *Vibrio parahaemolyticus* threatens the seafood industry: Perspective on controlling its biofilm formation” *LWT-Food Science and Technology*, vol. 158, Art. No. 113182, 2022, [Online]. Available: <https://doi.org/10.1016/j.lwt.2022.113182>.
- [21] U.S. Food and Drug Administration, “Time as a Public Health Control”, Section 3-501.19, FDA Food Code 2009, College Park, MD, USA, 2009.
- [22] S. Kaewrunkham, “A study of consumers' willingness to pay for temperature-controlled delivery service for agricultural products”, M.S. thesis, Kasetsart University, Bangkok, Thailand, 2023.

# Real-time Fish classification using Convolutional Neural Network based on Embedded System

Taweepol Suesut<sup>1, a)</sup>, Wirat Khannakum<sup>1, b)</sup>, Paranyu Phraenan<sup>1, c)</sup> and Navaphattra Nunak<sup>1, d)</sup>

## Author Affiliations

<sup>1</sup>School of Engineering, King Mongkut's Institute of Technology Ladkrabang, Bangkok, Thailand

## Author Emails

<sup>a)</sup>Corresponding author: taweepol.su@kmitl.ac.th

<sup>b)</sup> 66016168@kmitl.ac.th

<sup>c)</sup> 65016067@kmitl.ac.th

<sup>d)</sup> navaphattra.nu@kmitl.ac.th

**Abstract.** This paper presents real-time fish classification using a deep learning algorithm on embedded AI hardware for classification on a conveyor belt. This system, CorgiDude RISC-V AI board, accelerates processing similarly to a graphics card, functioning directly within the device. The dataset includes 8 similar fish species: Silver, Bighead carp, Common Carp, Nile tilapia, Mori, Striped catfish, Silver barb, and Rohu. The deep learning model utilizes MobileNetV1 for fish detection and classification. We incorporated images of fish scales, heads, and bodies into the dataset to improve classification accuracy. Experimental results show that the accuracy of MobileNetV1 is affected by conveyor speed. At a speed of 0.004 m/s, the average accuracy is 93%; at 0.012 m/s, it is 92%; and at 0.022 m/s, it decreases to 87%.

**Index Terms**— fish classification, Convolutional Neural Network, Mobile-Net.

## I. INTRODUCTION

Fish classification within the fish industry, a segment of the aquaculture sector, is crucial for advancing automation in the processes of this industry. Automatic fish classification using a computer or machine vision is needed to develop automation for automatic inspection systems [1]. Fish classification in the fish industry has several unique challenges, including the appearance of similar fish between one species and another and the physical condition of fish that has been deformed or damaged, such as eyes, fins, or scales that are damaged with mild, moderate, to heavy level [2]. Automatic fish detection and classification using computer or machine vision is a popular and intriguing research area. Numerous researchers are engaged in its development for both underwater and out-of-water environments [3-8]. Recognizing fish in underwater conditions, particularly in deep ocean environments, is beneficial for fish population control and sustainability [9-14].

Recognizing fish in environments beyond water, particularly for aquaculture, is beneficial for developing automation to enhance productivity. For instance, this includes automatic sorting processes, monitoring fish quality, and various other activities [5, 7, 8].

Both are crucial in supporting solutions to anticipate the impacts of global warming and climate change: the threats to wild fish populations and their sustainability, as well as the food scarcity that is feared to occur in the future [15, 16].

Fish recognition has many challenges, including diverse background conditions, similar appearance and deformed

fish, which is usually found in farmed fish cases [17, 18], also the speed and random position for recognizing moving fish, in the case of recognizing freely swimming fish in the ocean [10-12, 19] or fish running on conveyors. Until now, fish recognition technology continues to be developed along with the development of computer hardware, the technology of cameras, image processing, and recognition algorithms. Object recognition technology has developed very rapidly since the invention of the GPU (Graphical Processing Unit). The training and testing process can be carried out much faster than before, using only the CPU (Central Processing Unit) [20]. Today, camera technology has also being developed for better image capture. Image processing techniques that are constantly being developed are also very helpful in conditioning the image before entering the recognition algorithm. It can greatly increase the effectiveness and efficiency of the algorithm's performance [21].

[22] proposed a method utilizing SE-ResNet152 and class-balanced focal loss to classify physically deformed and similar fish, despite a small and unbalanced input dataset. This research was conducted and evaluated on the same dataset (Fish-Pak). The SE-ResNet152 model was developed as a generalized feature extractor and was adapted to the target dataset following visualization analysis and image preprocessing of the fish dataset. Ultimately, the class-balanced focal loss function was employed to train the SE-ResNet152 model, enabling fish species classification based on the body, head, and scale of each fish image.

[23] built a CNN with 32 layers to classify fish with the same challenges. It was done by modifying the standard

VGG Net network by adding four convolutional layers to the training of each level in the network. The proposed approach was trained and tested on the Fish-Pak dataset as well. [25] used classic CNN to classify six types of fish in the same dataset (Fish-Pak). Another research is [26], which proposed the Deep Convolutional Autoencoder to classify the three very similar carp types. They created their dataset consisting of 1,500 images of India's three most common types of carp.

However, another intriguing aspect is the use of embedded systems for fish classification. There are numerous Embedded AI Hardware options that are efficient and suitable for processing in AI tasks, such as Raspberry Pi, Jetson Nano, Corgidude, and others. Since embedded AI hardware is compact, cost-effective, and sufficiently efficient for AI applications, it is ideal for tasks requiring real-time detection. Furthermore, various Object Detection Deep Learning algorithms can be developed using Embedded AI Hardware, including YOLO (You Only Look Once), SSD, MobileNetV1, and more.

This paper proposes a real-time fish classification system using CorgiDude embedded AI hardware with the MobileNet algorithm, which has not yet been applied to fish classification. One of the challenges is that the species of fish are similar, making classification difficult due to their close identities. The experimental results of this study combine MobileNetV1 with various training techniques. We enhanced the dataset by adding images of fish scales, heads, and bodies to improve classification accuracy.

#### A. Dataset and Image Augmentation

This study aims to develop an approach for the automatic detection and categorization of fish in real-time systems using the MobileNetV1 deep learning algorithm on the CorgiDude RISC-V AI board. There is currently no publicly available dataset for cultured fish suitable for this experiment. Therefore, we created our own dataset for this study, which includes 8 fish species: Silver, Bighead carp, Common Carp, Nile tilapia, Mori, Striped catfish, Silver barb, and Rohu, as illustrated in Fig.1. These species are originally from the Mekong and Chao Phraya rivers in Thailand.

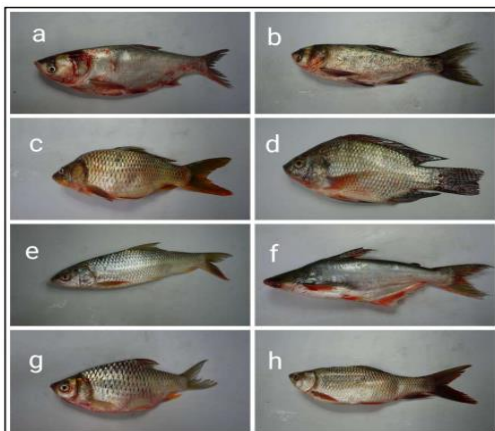


Fig. 1 Example of 8 fish species (a) Silver (b) Bighead carp (c) Common Carp (d) Nile tilapia (e) Mori (f) Striped catfish (g) Silver barb (h) Rohu

TABLE I  
DATASET IMAGE DETAIL AND AUGMENTATION

Fish Class	No. of image	No. of augmented image	New image dataset	For training (80%)	For Test (20%)
Silver	20	120	140	112	28
Bighead carp	20	120	140	112	28
Common Carp	20	120	140	112	28
Nile tilapia	20	120	140	112	28
Mori	20	120	140	112	28
Striped catfish	20	120	140	112	28
Silver barb	20	120	140	112	28
Rohu	20	120	140	112	28
Total	160	960	1120	896	224

Additionally, the images of each species from eight similar fish species are insufficient for training. In this work, the target is set at 100 for each class. Therefore, the augmentation method includes rotation, flipping, and translation to increase the number of images to meet the minimum dataset required for training. The new fish images were then divided into two parts: 80% for the training dataset and 20% for the testing dataset (See Table I).

#### B. CorgiDude RISC-V AI board

This study applied embedded AI hardware called “CorgiDude” for Real-time fish classification application. This is a high-performance microcontroller development board that is capable of processing mathematical models, computational science, and Machine Learning models such as image classification, object detection, and face recognition. It can connect cameras, LCD display and other sensors. The main program can be written in Python (micropython) language, or we can develop in C/C++ to reach maximum efficiency.

CorgiDude is equipped with a Kendryte K210 dual-core 64-bit RISC-V RV64IMAFDC CPU running at 400MHz, featuring an FPU, support for the OV2640 camera, and several GPIOs for connecting peripherals. It also includes a microSD card slot, which can be useful for storing images captured by the camera or files to serve to clients. Fig. 2 illustrates the layout of the CorgiDude RISC-V AI board.

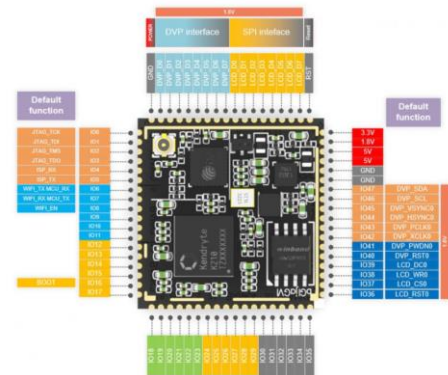


Fig. 2 CorgiDude RISC-V AI board Layout

### C. MobileNetV1

MobileNetV1 is based on a streamlined architecture that employs depthwise separable convolutions to create lightweight deep neural networks. MobileNetV1 is widely utilized in various real-world applications, including object detection, fine-grained classifications, face attributes, and localization. Fig.3 illustrates the MobileNetV1 architecture, where depthwise convolution is employed to reduce model size and complexity. This approach is particularly beneficial for mobile and embedded vision applications. Depthwise separable convolution consists of a depthwise convolution followed by a pointwise convolution. Depthwise convolution refers to the channel-wise  $D_K \times D_K$  spatial convolution. In the Fig.3, if we have 5 channels, we will have 5  $D_K \times D_K$  spatial convolutions. Pointwise convolution, on the other hand, is the  $1 \times 1$  convolution used to alter the dimension.

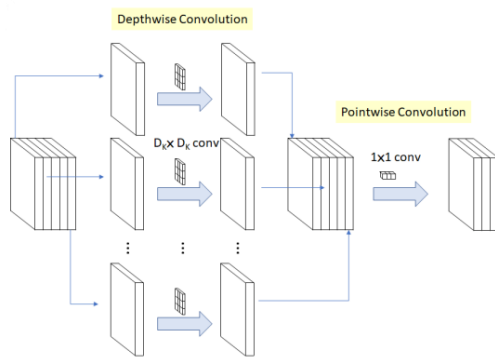


Fig 3. MobileNet Architecture [24]

## II. EXPERIMENT AND RESULT

### A. Training model

Annotation of an image is a crucial process to determining the location of the fish in the image and categorizing the class name of the fish. There are 4 interesting areas of the fish such as the body, fins, head and scales of the fish were labeled for training.

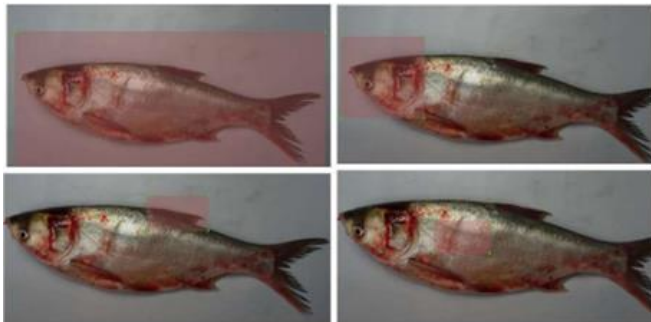


Fig. 4 Example of Labeling with Silver fish

After the image data for training was prepared, the fish dataset consists of 1120 images in total with 80% allocated to training, 20% to testing, Fig.5 illustrates the procedure of our training and testing was obtained from TensorFlow Lite.

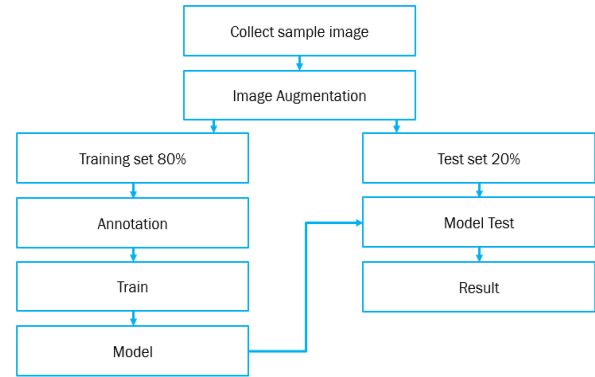


Fig 5. Overview of training and testing model scheme

After the training of the model is completed, we will convert the standard model file generated from TensorFlow Lite to a model file using the command line on Linux OS for uploading the model data to the CorgiDude RISC-V AI board.

### B. Environment

This study employs the CorgiDude RISC-V AI board with the MobileNetV1 model to investigate real-time fish classification. The OV2640 camera can operate at up to 15 frames per second (fps) with a resolution of 2 million pixels and interfaces with the CorgiDude via the SCCB port. The conveyor can be adjusted to three speeds, with a maximum speed of 0.022 m/s. Fig. 6 illustrates the necessary hardware for the real-time fish classification system.

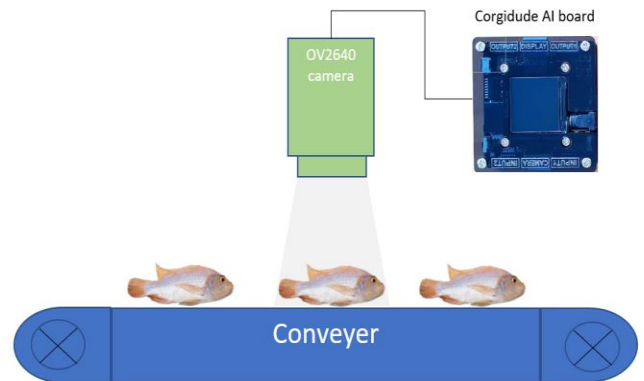


Fig. 6 Real-time fish classification system architecture

### C. Performance Evaluation

We evaluated the performance of our project at three speeds: 0.004 m/s, 0.012 m/s, and 0.022 m/s. The conveyor feeds the target fish to the inspection station, where an OV2640 camera captures images of the fish, and CorgiDude handles fish detection and classification. Fig. 6 shows that our model accurately detects and classifies the fish.



#### D. Experiment Results

The evaluation of our model is evaluated using the model's accuracy may be assessed using equation

$$Accuracy = \frac{\sum_i^N P_i}{\sum_i^N |Q_i|} \times 100\% \quad (1)$$

where  $\sum_i^N P_i$  is the number of correct predictions, and  $\sum_i^N |Q_i|$  is the total number of predictions.

In this experiment, the trained MobileNetV1 model running on Corgitude achieves a high speed of 0.004 m/s and an average accuracy of 93% in detecting and classifying the fish. Fig. 7 presents the experimental results regarding the model's accuracy.

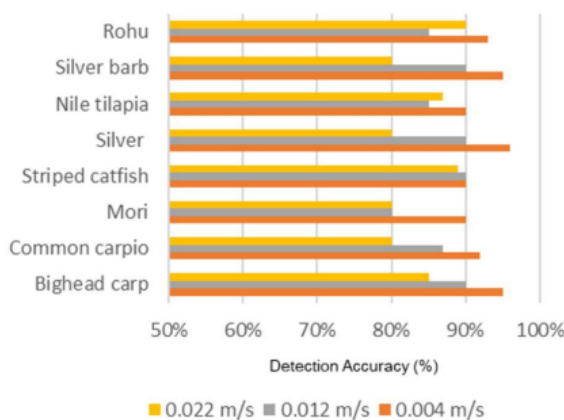


Fig 7. Experiment results in the model's accuracy

### III. CONCLUSION

The research presents the development of object detection and classification for fish with similar shapes and structures using the Corgi Dude board for real-time detection on a conveyor belt. The dataset consists of eight fish species. This study employs MobileNetV1, an algorithm designed for low-resource devices such as mobile phones. Additionally, this work tested other fish species not included in the dataset, but no detections were made. The experimental results showed that all eight fish species were run on the conveyor at three different speeds. At a conveyor speed of 0.004 m/s, the average accuracy was 93%; at 0.012 m/s, it was 92%; and at 0.022 m/s, it dropped to 87%. These results are considered quite good. This work is expected to contribute to the advancement of object detection and classification for fish with similar shapes and structures.

### REFERENCES

- [1] A. A. Dos Santos and W. N. Gonçalves, "Improving Pantanal fish species recognition through taxonomic ranks in convolutional neural networks," *Ecological Informatics*, vol. 53, p. 100977, 2019/09/01/ 2019.
- [2] A. N.S, S. D, and R. K. S, "Naive Bayesian fusion based deep learning networks for multisegmented classification of fishes in aquaculture industries," *Ecological Informatics*, vol. 61, p. 101248, 2021/03/01/ 2021.
- [3] D. Li, Q. Wang, X. Li, M. Niu, H. Wang, and C. Liu, "Recent advances of machine vision technology in fish classification," *ICES Journal of Marine Science*, vol. 79, pp. 263-284, 2022.
- [4] M. K. Alsmadi and I. Almarashdeh, "A survey on fish classification techniques," *Journal of King Saud University - Computer and Information Sciences*, vol. 34, pp. 1625-1638, 2020.
- [5] S. Zhao, S. Zhang, J. Liu, H. Wang, J. Zhu, D. Li, et al., "Application of machine learning in intelligent fish aquaculture: A review," *Aquaculture*, vol. 540, p. 736724, 2021.
- [6] A. Saleh, M. Sheaves, and M. Rahimi Azghadi, "Computer vision and deep learning for fish classification in underwater habitats: A survey," *Fish and Fisheries*, vol. 23, pp. 977-999, 2022.
- [7] D. Li and L. Du, "Recent advances of deep learning algorithms for aquacultural machine vision systems with emphasis on fish," *Artificial Intelligence Review*, vol. 55, pp. 4077-4116, 2022.
- [8] X. Yang, S. Zhang, J. Liu, Q. Gao, S. Dong, and C. Zhou, "Deep learning for smart fish farming: applications, opportunities and challenges," *Reviews in Aquaculture*, vol. 13, pp. 66-90, 2021.
- [9] S. Villon, D. Mouillot, M. Chaumont, E. S. Darling, G. Subsol, T. Claverie, et al., "A Deep learning method for accurate and fast identification of coral reef fishes in underwater images," *Ecological Informatics*, vol. 48, pp. 238-244, 2018/11/01/ 2018.
- [10] A. B. Labao and P. C. Naval, "Cascaded deep network systems with linked ensemble components for underwater fish detection in the wild," *Ecological Informatics*, vol. 52, pp. 103-121, 2019/07/01/ 2019.
- [11] A. Jalal, A. Salman, A. Mian, M. Shortis, and F. Shafait, "Fish detection and species classification in underwater environments using deep learning with temporal information," *Ecological Informatics*, vol. 57, p. 101088, 2020/05/01/ 2020.
- [12] S. Villon, C. Iovan, M. Mangeas, T. Claverie, D. Mouillot, S. Villéger, et al., "Automatic underwater fish species classification with limited data using few-shot learning," *Ecological Informatics*, vol. 63, p. 101320, 2021/07/01/ 2021.
- [13] A. Salman, S. Maqbool, A. H. Khan, A. Jalal, and F. Shafait, "Real-time fish detection in complex backgrounds using probabilistic background modelling," *Ecological Informatics*, vol. 51, pp. 44-51, 2019.
- [14] A. N.S, S. D, and R. K. S, "Naive Bayesian fusion based deep learning networks for multisegmented classification of fishes in aquaculture industries," *Ecological Informatics*, vol. 61, p. 101248, 2021/03/01/ 2021.
- [15] A. Jalal, A. Salman, A. Mian, M. Shortis, and F. Shafait, "Fish detection and species classification in underwater environments using deep learning with temporal information," *Ecological Informatics*, vol. 57, p. 101088, 2020/05/01/ 2020.
- [16] A. Salman, S. Maqbool, A. H. Khan, A. Jalal, and F. Shafait, "Real-time fish detection in complex backgrounds using probabilistic background modelling," *Ecological Informatics*, vol. 51, pp. 44-51, 2019.
- [17] A. N.S, S. D, and R. K. Sidharthan, "Naive Bayesian fusion based deep learning networks for multisegmented classification of fishes in aquaculture industries," *Ecological Informatics*, vol. 61, p. 101248, 2021/03/01/ 2021.



- [18] A. Kuswantori, T. Suesut, W. Tangsrirat, and N. Nunak, "Development of object detection and classification with YOLOv4 for similar and structural deformed fish," EUREKA: Physics and Engineering, vol. 2, pp. 154–165, 2022a.
- [19] Z. Ju and Y. Xue, "Fish species recognition using an improved AlexNet model," Optik, vol. 223, p. 165499, 2020/12/01/ 2020.
- [20] H. Park and S. Kim, "Chapter Three - Hardware accelerator systems for artificial intelligence and machine learning," in Advances in Computers. vol. 122, S. Kim and G. C. Deka, Eds., ed: Elsevier, 2021, pp. 51-95.
- [21] A. Kuswantori, T. Suesut, W. Tangsrirat, and N. Nunak, "Development of object detection and classification with YOLOv4 for similar and structural deformed fish," EUREKA: Physics and Engineering, vol. 2, pp. 154–165, 2022a.
- [22] X. Xu, W. Li, and Q. Duan, "Transfer learning and SE-ResNet152 networks-based for small-scale unbalanced fish species identification," Computers and Electronics in Agriculture, vol. 180, p. 105878, 2021/01/01/ 2021.
- [23] H. T. Rauf, M. I. U. Lali, S. Zahoor, S. Z. H. Shah, A. U. Rehman, and S. A. C. Bukhari, "Visual features based automated identification of fish species using deep convolutional neural networks," Computers and Electronics in Agriculture, vol. 167, p. 105075, 2019/12/01/ 2019.
- [24] Howard AG, Zhu M, Chen B, Kalenichenko D, Wang W, Weyand T, et al. MobileNets: Efficient Convolutional Neural Networks for Mobile Vision Applications. CoRR [Internet]. 2017;abs/1704.04861. Available from: <http://arxiv.org/abs/1704.04861>
- [25] S. A. Shammi, S. Das, M. Hasan, and S. R. H. Noori, "FishNet: Fish Classification using Convolutional Neural Network," in 2021 12th International Conference on Computing Communication and Networking Technologies (ICCCNT), 2021, pp. 1-5.
- [26] A. Banerjee, A. Das, S. Behra, D. Bhattacharjee, N. T. Srinivasan, M. Nasipuri, et al., "Carp-DCAE: Deep convolutional autoencoder for carp fish classification," Computers and Electronics in Agriculture, vol. 196, p. 106810, 2022/05/01/ 2022.

# Comparison of ON-OFF and PID Temperature Control on Soymilk Fouling Formation in Plate Heat Exchanger

Navaphattra Nunak<sup>1, a)</sup>, Worapanya Suthanupaphwut<sup>1, b)</sup> and Taweepol Suesut<sup>1, c)</sup>

## Author Affiliations

<sup>1</sup> School of Engineering, King Mongkut's Institute of Technology Ladkrabang, Bangkok, Thailand

## Author Emails

<sup>a)</sup> Corresponding author: navaphattra.nu@kmitl.ac.th

<sup>b)</sup> 67016181@kmitl.ac.th

<sup>c)</sup> taweepol.su@kmitl.ac.th

**Abstract.** This paper studies the comparison of ON-OFF and PID temperature control systems using performance indexes such as rise time, maximum overshoot, settling time, and steady-state error and its effect to the fouling of soymilk on hot surface. Water was heated to set-point temperatures of 40, 60, 80, and 95 °C and used as a heat source by circulating into a plate heat exchanger at a flow rate of 42 LPM. Experiments were conducted at five different product flow rates, calculated as a percentage of the maximum flow rate of 25 LPM: no flow (0%), 6.3 (25%), 12.5 (50%), 18.8 (75%), and 25.0 (100%) LPM. It was found that neither the PID nor the ON-OFF control system could stable control at set-point temperature of 40 °C. While at set-point temperatures of 60 and 80 °C, the rise time and the settling time obtained from PID control are shorter than the ones from ON-OFF control for all product flow rates. At set-point temperature of 95°C, ON-OFF control system could perform well only at low flow rates ( $\leq 50\%$ ). However, maximum overshoot and steady-state error values observed from both systems were similar. Therefore, the fouling experiment was carried out using PID and ON-OFF control systems at a set-point temperature of hot water 95°. The results showed that ON-OFF and PID temperature control systems gave similar thickness of foulant.

**Index Terms—** ON-OFF temperature control system, PID control system, Fouling, Plate heat exchanger.

## I. INTRODUCTION

In the food industry, heating processes such as drying are commonly employed. Processes like pasteurization and sterilization are used for processing and eliminating pathogenic microorganisms that cause spoilage. The temperature and duration of heating are critical parameters in the thermal process. These must be controlled with accuracy and precision; for instance, pasteurizing milk at 75 °C for 15 seconds. The product temperature should be maintained within  $\pm 0.5^\circ\text{C}$  of the specified temperature. A temperature deviation of 1 °C can reduce the efficiency of the disinfection process by 25%. It is evident that temperature measuring instruments and control systems are vital for ensuring food quality and safety [1].

For the food industry, plate heat exchangers are the most widely used heat exchange equipment in heat processing and pasteurization due to their excellent heat transfer efficiency and substantial heat exchange area relative to their size [3]. However, during food heating processing, structural changes occur, leading to fouling on the heat exchange surface [4], which results in decreased heat transfer efficiency [2] and food safety concerns due to incomplete pasteurization.

In addition to selecting the type of measuring instrument, the choice of an appropriate temperature control system also plays a crucial role in the accuracy and precision of thermal

processes, such as PID temperature control systems (Proportional-Integral-Derivative) and ON-OFF temperature control systems. The PID control system can effectively manage response time and maintain the process temperature at a specified level, while the ON-OFF temperature control system exhibits greater fluctuations in system response compared to PID systems. This instability arises from a control system design that is not well-suited for the process and is unable to withstand external interference, leading to an unstable process temperature. However, this system is simpler and less costly than PID control systems. For instance, [5] studied the energy consumption costs for refrigerant condensation in cooling systems and found that using the PID temperature control system reduced costs by 26% compared to the ON-OFF control system. Additionally, [7] examined evaporative cooling systems in poultry houses and discovered that the PID temperature control system could minimize error values more effectively than the original ON-OFF control system. In the food industry, plate heat exchangers are commonly used for heat processing and sterilization due to their excellent heat transfer efficiency and large heat exchange area relative to machine size. However, during food heating processes, structural changes can lead to fouling on the heat exchange surface, resulting in decreased heat transfer efficiency and potential food safety issues due to incomplete sterilization. It is evident that temperature is a

critical variable in thermal processes and stain formation, necessitating control with an appropriate system [8]. Therefore, this research aims to compare the control performance of ON-OFF and PID temperature control systems. It examines the temperature regulation of the medium (hot water), which serves as the heat source for plate heat exchangers [11]. This includes investigating the formation of deposits in plate heat exchangers, using soymilk as a case study.

## II. CONTROL SYSTEM THEORY

### A. ON-OFF and PID control system

ON-OFF control is the system that has two operating states: open circuit and closed circuit. The output signal of the system is as shown in Fig. 1 and the signal from the controller (Manipulated Variable: MV) of the system is 100%. (ON) or 0% (OFF).

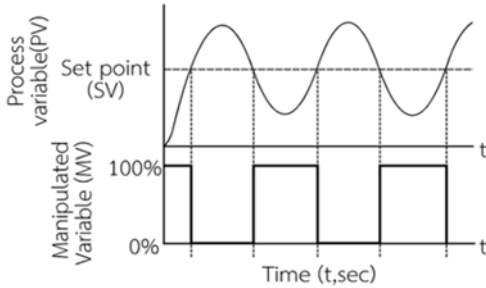


Fig. 1 ON-OFF control system

A PID control system is a feedback control system designed to minimize process errors by adjusting the parameters of three terms: Proportional (P) controls are proportional to enhance the system's response speed, Integral (I) controls are integral to minimize the steady state error as much as possible, and Derivative (D) controls adjust the response momentarily for improved performance. The output of the control system can be expressed as shown in equation (1).

$$u(t) = K_p e + K_I \int_0^t e dt + K_D \frac{de}{dt} \quad (1)$$

In tuning the parameters  $K_P$ ,  $K_I$ , and  $K_D$ , the process can be affected in the following ways: The  $K_P$  value allows the process to reach the target value quickly. The  $K_I$  value reduces the process error upon reaching steady state and helps decrease the time taken to achieve the target value. The  $K_D$  value diminishes the oscillation of the overshoot response and the time to steady state [6].

### B. Control system performance index

The performance index of the control system serves as a measure to indicate the system's performance. Achieving

good performance necessitates that the process values reach the target values with maximum accuracy and precision. However, within the process, various factors can introduce errors.

Consequently, the primary objective in designing a control system is to minimize deviation to a value within an acceptable range of 2% from the target value. An effective control system must be capable of controlling the performance index to a minimum value or attaining the desired value. Thus, the performance index is utilized as a reference for designing a control system that ensures stability at steady state [6].

The rise time ( $t_r$ ) is the duration it takes for the response to increase from 0% to 100% of the target value. The settling time ( $t_s$ ) is the period during which the response starts to approach its final value within the specified range. The acceptable maximum overshoot ( $M_p$ ) of 2% is the highest response value recorded above the target value. This is illustrated in equation (2)

$$M_p = \frac{c(t_p) - c(\infty)}{c(\infty)} \times 100\% \quad (2)$$

where  $M_p$  is the maximum overshoot (%)

$c(t_p)$  is the maximum value from the target value.

$c(\infty)$  is the target value.

and the error value in the equilibrium state (Steady-state error,  $e_{ss}$ ) is the error value from the target value after reaching equilibrium. Acceptance is within 2% of the target value as shown in equation (3).

$$e_{ss} = \frac{SV - PV}{SV} \times 100\% \quad (3)$$

where  $e_{ss}$  is the error in equilibrium.

$SV$  is the target value

$PV$  is the value from the process.

## III. MATERIALS AND METHODOLOGY

### A. Heat exchanger experimental set up

A heat exchanger experimental setup was designed for this research. The process diagram is illustrated in Fig. 2, which includes two 304 stainless steel tanks, two 1-inch butterfly valves, two centrifugal pumps, two RTD PT100 temperature sensors, and four heaters. The heat exchange equipment is configured for alternating flow directions, following a 1:2 flow ratio, meaning that product flows through one channel while hot water flows through two channels. A smooth 304 stainless steel heat exchanger plate is utilized. During the experiment, a type T thermocouple cable was connected to a data recorder (DAQ970A, Data Acquisition System Keysight, US), recording data every second from a total of four measurement locations. As shown in Fig. 2, these include 101 inlet and outlet product temperatures and 102 inlet and outlet hot water temperatures. Data is recorded every second throughout the process.

The hot water flow rate was set to 42 LPM, and the product flow rate was categorized into five levels (calculated from the % maximum product flow rate of 25 LPM), including no flow (0%), 6.3 LPM (25%), 12.5 LPM (50%), 18.8 LPM (75%), and 25.0 LPM (100%). The experiment was conducted at four target temperatures: 40, 60, 80, and 95 °C, with the inlet hot water temperature recorded every second, beginning when the process temperature was 10 °C below the target temperature. The results of the inlet hot water temperature recordings were subsequently analyzed to evaluate the control performance index.

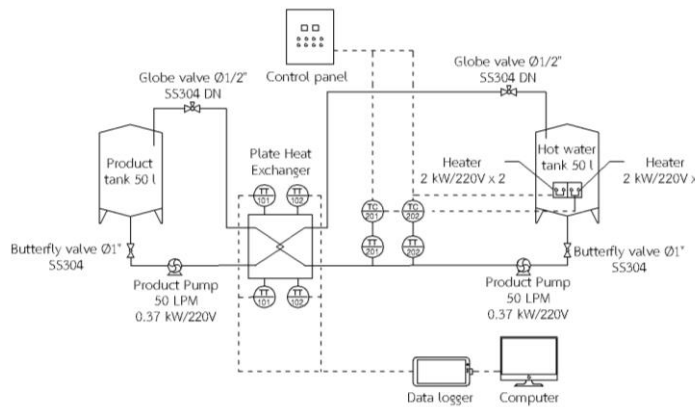


Fig. 2 P&ID diagram of the heat exchanger experimental setup

### B. Experiment on the formation of soymilk fouling

The experiment commenced by heating water to a target temperature of 95 °C with a flow rate of 42 LPM. Subsequently, soybean water at a temperature of 60 °C was introduced into the process at a flow rate of 4.5 LPM. The experiment lasted for 7 hours, and at the conclusion, the heat exchanger plate was removed and allowed to rest for 300 seconds. The thickness of the stain was measured using a thickness measuring device (Positector 6000 FNS1, Del Felsko, USA). Thermal images were then captured using a thermal imager (Fluke Ti400, USA) for 180 seconds.

### C. Statistical data analysis

Experiment planning was used a Completely Randomized Design (CRD) and analyzed the differences in fouling thickness using an independent sample t-test at a confidence level of 0.95.

## IV. RESULT AND DISCUSSION

### A. Results of Tuning the parameters of the PID control system

The parameter values are obtained through various tuning methods. It was observed that the trial-and-error parameter adjustment method prevented the process from achieving settling time, meaning the process temperature could not be maintained close to the target temperature. Consequently, it was concluded that the  $K_P$ ,  $K_I$ , and  $K_D$  parameters of the trial-and-error method were unsuitable for the process. In contrast, when evaluating the performance index of automatic methods [10] and those based on the Ziegler–

Nichols [7], it was found that the automatic method exhibited a shorter rise time and time to equilibrium. This aligns with the results indicating larger  $K_P$  and  $K_I$  parameters (Table I). However, it also leads to a higher maximum response value. For the Ziegler-Nichols method, a higher  $K_D$  value diminishes the maximum response of the process while achieving equilibrium later [10]. Regarding process equilibrium, it was determined that both the automatic parameter adjustment method and the Ziegler–Nichols method successfully maintained the process at settling time within an acceptable range of 2% from the target temperature.

### B. Comparison of performance indexes of ON-OFF and PID control systems

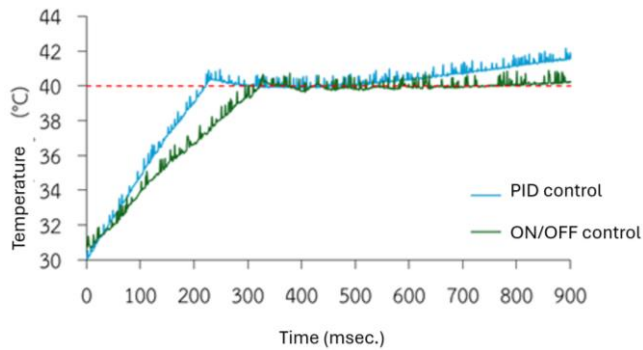
From the results of comparing the performance indices of the ON-OFF and PID temperature control systems used to regulate the temperature of the hot water side, as shown in Fig. 2, it was found that the rise time and the settling time of the PID control system at set point temperatures of 60 and 80 °C were shorter than those of the ON-OFF control system across all product flow rates (Fig. 3a, b, and c). This improvement is attributed to the optimization of  $K_P$  and  $K_I$ , which helps reduce the rise time [9].

After the two temperature control systems reach equilibrium, the steady-state error can be analyzed. It was found that at the target temperatures of 60 and 80 °C, the control system exhibited similar steady-state errors across all product flow rates (Fig. 3 b and c). The PID control system and the ON-OFF control system did not have sufficient time to reach settling time at the target temperature of 40 °C, resulting in a continuous temperature increase trend (Fig. 3 a) due to the hot water temperature difference of 40 °C and the relatively low ambient temperature compared to the other target temperatures. Consequently, the heat accumulated inside the tank is less effectively transferred to the environment.

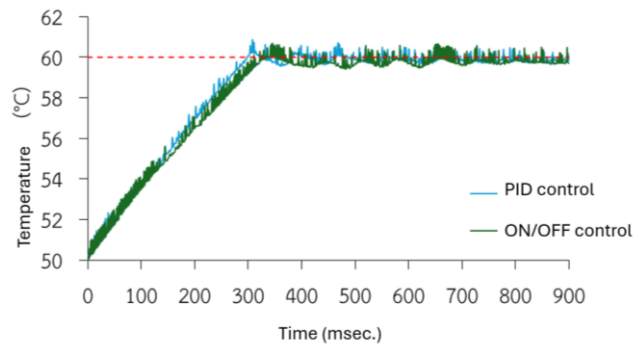
Even when the signal from the system controller is at 0%, the heater is actually turned off when the process temperature matches the target temperature. This behavior suggests that the control system lacks stability. With a set point temperature of 95°C, it was observed that the rise time and the settling time of the PID control system were longer than those of the ON-OFF control system at low flow rates ( $\leq 50\%$ ) for maximum overshoot, while the steady state error values of both control systems were similar. Conversely, when the product flow rate is high ( $> 50\%$ ), the ON-OFF control system fails to achieve the set point temperature. In contrast, the PID control system can maintain the process temperature, with the equilibrium error remaining within an acceptable range of 2% from the set point temperature (Fig. 3 d), demonstrating that the PID control system is more effective at controlling the process temperature than the ON-OFF control system.

TABLE I: PARAMETER VALUES  $K_P$ ,  $K_I$ , AND  $K_D$  WITH VARIOUS TURNING METHODS.

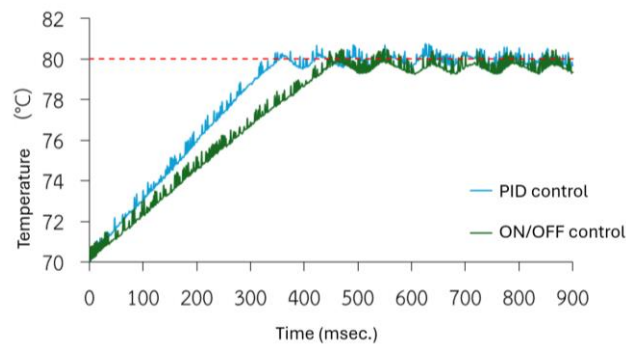
Turning methods	$K_P$	$K_I$	$K_D$
Automatic methods	1000.0	166.7	1000.0
Ziegler–Nichols	600.0	10.4	8625.0



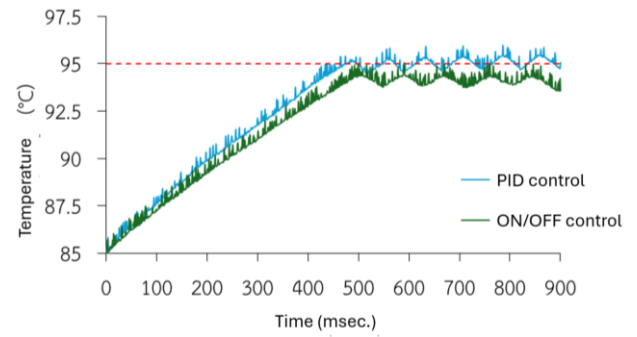
(a)



(b)



(c)



(d)

Fig. 3 compares the performance index at a flow rate of 25 LPM at target temperatures of (a) 40 °C, (b) 60 °C, (c) 80 °C, and (d) 95 °C.

### C. Comparison of Soymilk fouling between ON-OFF and PID temperature control system

The fouling thickness and the rate of increase in fouling temperature are presented in Table II. It was observed that there was no significant difference in fouling thickness ( $p < 0.05$ ), and the difference in stain was not discernible, as illustrated in Fig. 4. Consequently, varying temperature control systems do not influence stain formation due to the consistent product flow rate. When examining the error values in the steady state of the two systems, it was found that they were comparable.



Fig. 4. fouling thickness (a) PID temperature control system (b) ON-OFF temperature control system at 300 seconds.

TABLE II: FOULING THICKNESS AND RATE OF INCREASE IN TEMPERATURE

Temperature Control System	Thickness ( $\mu\text{m}$ )	Rate Of Temperature Increase ( $^{\circ}\text{C/s}$ )
PID	330.2 $\pm$ 54.2a	0.8 $\pm$ 0.1
ON-OFF	247.6 $\pm$ 37.3a	0.9 $\pm$ 0.1

Note: Vertically different letters indicate differences that are statistically significant at the 95% confidence level ( $n=2$ ).

## V. CONCLUSION

The performance index of the temperature control system at a target temperature of 40 °C was unstable for both



control systems across all flow rates. At target temperatures of 60 and 80 °C, the PID control system required less time to reach both the rise time and the settling time to the ON-OFF control (See Table III). This trend also applies to the set point temperature of 95 °C at 75% and 100% flow rates. However, at a flow rate of 0% (no flow), as well as at 25% and 50%, the PID system took longer. Both control systems exhibited similar maximum response values and error values. Consequently, there is no significant difference in the stains produced by the on-off and PID control systems, especially when considering the thickness of the fouling.

Product flow rate (LPM)	Set point (°C)	ON/OFF Control				PID control			
		$t_r$ (s)	$M_p$ (%)	$t_s$ (s)	$e_{ss}$ (%)	$t_r$ (s)	$M_p$ (%)	$t_s$ (s)	$e_{ss}$ (%)
0 (No flow)	40	315	U	U	U	264	U	U	U
	60	337	1.5	713	0.7	326	0.6	645	0.3
	80	386	1.5	554	0.2	380	0.6	506	0.2
	95	396	0.6	485	0.3	449	0.9	593	0.6
6.3	40	297	U	U	U	229	U	U	U
	60	297	1.8	622	0.6	279	1.6	390	0.2
	80	360	1.5	515	0.4	329	1.2	410	0.4
	95	407	0.9	533	0.3	461	0.8	539	0.3
12.5	40	380	U	U	U	272	U	U	U
	60	332	2.0	471	0.6	304	1.2	390	0.2
	80	445	0.8	525	0.3	380	1.3	470	0.3
	95	513	0.3	590	0.5	506	0.9	595	0.3
18.8	40	271	U	U	U	244	U	U	U
	60	346	2.3	488	0.6	262	1.4	362	0.3
	80	467	0.7	564	0.3	316	1.0	385	0.3
	95	U	U	U	U	413	1.0	489	0.3
25.0	40	302	U	U	U	222	U	U	U
	60	311	1.1	423	0.5	298	1.5	362	0.3
	80	443	0.6	514	0.5	355	0.5	400	0.2
	95	U	U	U	U	438	0.4	520	0.3

TABLE III: COMPARISON OF PERFORMANCE INDEX AT 0-25 LPM.

### ACKNOWLEDGMENT

The authors gratefully acknowledged the team working in the laboratory for their performing experiments with T. Tabkosai, R. Otthon, S. Limsuwan, N. Sitthisang, N. Siriboonyarak and N. Kongsangchai.

### REFERENCES

- [1] Amole, A. O., Olabode O. E., Akinyele D. O., Akinjobi, S. G. "Optimal Temperature Control Scheme for Milk Pasteurization Process Using Different Tuning Techniques for a Proportional Integral Derivative Controller", Iranian Journal of Electrical and Electronic Engineering, Vol.18(3), 2022.
- [2] Awad, M.M. "Heat Transfer—Theoretical Analysis", Experimental Investigations, and Industrial Systems. Croatia: InTech, 2011.
- [3] Christian GK., Fryer PJ. "The balance between chemical and physical effects In the cleaning of milk fouling deposits", 2003.
- [4] Lewis, M.J., Jun, S. "Thermal Processing. Food Processing Handbook", pp 31-75, 2011.
- [5] Silva, F.H.P., Coimbra, G.P., S, Nunes H.S., Mellim R.D., Carvalho, D.H.Q., Moreira, R.P.C., Carvalho L., Souza F. H.B. "On/Off Control versus PID Control: A Comparative Case Study on Condensers of Cooling Systems.", 4<sup>th</sup> International Conference on Advanced

Research in Applied Science and Engineering, Belgium pp 88-99, 2022.

- [6] Ogata K., "Modern Control Engineering.", Pearson Education, Inc., 3<sup>rd</sup> Edition, 2009.
- [7] Ankur, P., Savani, V. "Performance Analysis of PID Controller and Its significance for Closed Loop System", International Journal of Engineering Research & Technology (IJERT) Vol.3(3), 2014.
- [8] Kumari, M., Kokkiligadda, A., Dasriya, V., Naithani, H. "Functional relevance and health benefits of soymilk fermented by lactic acid bacteria." Journal of Applied Microbiology, Volume 133(1), 104–119. 2022.
- [9] Modi A., Vadnere A. "Milk pasteurization Processes temperature optimization with use of pid controller.", Journal of Modernization in Engineering Technology and Science Vol.3, 2021.
- [10] Nishikawa, Y., Sannomiya, N., Ohta, T., Tanaka, H. "A method for auto-tuning of PID control parameters.", Automatica, 20, 321-332, 1984.
- [11] Patel A. "Heat Exchangers in Industrial Applications: Efficiency and Optimization Strategies.", International Journal of Engineering Research & Technology (IJERT) Vol.12(9), 2023.

# Thermochemical reforming of biogas to syngas production: A Review

Ratikorn Kulporm<sup>1</sup>, Srirat Chuayboon<sup>1,a)</sup>, Sompong O-Thong<sup>2</sup>  
and Monsicha Tipawanna<sup>3</sup>

<sup>1</sup>Department of Mechanical Engineering, King Mongkut's Institute of Technology Ladkrabang, Prince of Chumphon Campus, Chumphon 86160, Thailand

<sup>2</sup>Biofuel and Biocatalysis Innovation Research Unit, Nakhonsawan Campus, Mahidol University, Nakhonsawan, 60130, Thailand

<sup>3</sup>Department of General Science, King Mongkut's Institute of Technology Ladkrabang, Prince of Chumphon Campus, Chumphon 86160, Thailand

\* Corresponding author: srirat.ch@kmitl.ac.th

**Abstract.** Biogas has been employed in low-value applications, including heating and as fuel for engines, or it has been flared. Alternately, reforming offers a promising strategy for transforming biogas into syngas, which can be processed to produce high-value liquid fuels and chemicals. Additionally, there is significant interest in dry, bi-, and tri-reforming roles in capturing and utilizing CO<sub>2</sub>. However, conventional biogas reforming has several drawbacks resulting from combustion. This paper provides a comprehensive review of conventional biogas reforming and a novel solar thermochemical reforming of biogas in dry, bi-, and tri-reforming processes, wherein the CO<sub>2</sub> present in biogas is utilized as an oxidant or partial oxidant while solar energy is proposed as an alternative external heat source to drive the thermochemical reaction. An overview of conventional and solar thermochemical reforming was thoughtfully examined.

**Index Terms:** Solar thermochemistry, Solar fuels, Biogas upgrading

## I. INTRODUCTION

The development of biofuels to substitute fossil fuels through biological processes has been gaining attention as an eco-friendly alternative solution [1]. Biogas is one of the alternative energy sources, as it can be produced from organic waste such as food scraps, animal manure, and wastewater from industrial processes. The biological decomposition process generates biogas, which mainly consists of methane (CH<sub>4</sub>) and carbon dioxide (CO<sub>2</sub>) [2]. As a renewable energy source, biogas can serve as a substitute for natural gas after the purification process.

Carbon dioxide (CO<sub>2</sub>) contamination is a significant issue of biogas, which typically accounts for approximately 30-50% of its total composition [3]. This reduces the calorific value of the fuel compared to natural gas and affects combustion efficiency and industrial applications. Additionally, biogas often contains other impurities, such as hydrogen sulfide (H<sub>2</sub>S) and siloxanes, which can destroy equipment and cause pollution. Therefore, removing CO<sub>2</sub> and other contaminants is essential to upgrade the quality of biogas for various applications [4,5].

Reforming processes, including dry reforming, bi-reforming, tri-reforming, and chemical looping reforming, offer viable pathways for converting biogas into syngas [6,7]. These technologies facilitate the reaction of methane (CH<sub>4</sub>) with CO<sub>2</sub>, steam (H<sub>2</sub>O), or oxygen (O<sub>2</sub>) to generate a mixture of hydrogen (H<sub>2</sub>) and carbon monoxide (CO), called

syngas, which serves as a key feedstock for various industrial applications [8]. Each reforming method presents unique advantages and challenges, particularly regarding reaction efficiency, carbon deposition, and catalyst stability.

Additionally, it is used as a precursor in the Fischer-Tropsch (FT) process to produce synthetic crude oil, lubricants, and hydrocarbon fuels [6]. This study explores reforming processes that enable the direct production of syngas from biogas as a feedstock, highlighting their potential for sustainable fuel production and industrial applications.

However, the conventional process of biogas reforming relies on combustion in which feedstock or fuels are combusted, providing the heat to drive the endothermic reforming reaction, contributing to a large amount of CO<sub>2</sub> emission and feedstock burning. Alternatively, solar thermochemical reforming of biogas offers a promising pathway to convert biogas to high-quality sun gas without combustion, thus proving a carbon-free process for biogas valorization. of viable strategies for the short-term deployment of solar. This study presents a comprehensive review of conventional biogas reforming and a novel solar thermochemical reforming of biogas in dry, bi-, and tri-reforming processes, wherein the CO<sub>2</sub> present in biogas is utilized as an oxidant or partial oxidant while solar energy is utilized as an alternative external heat source to drive the thermochemical reaction. An overview of conventional and solar thermochemical reforming. Biogas and biohythane

## II. BIOGAS AND BIOHYTHANE PRODUCTION, SOURCES, AND COMPOSITION

Biogas production technology has gained global attention due to its potential as a vehicle fuel and its ability to be derived from organic waste [9]. Biohydrogen and biogas production from organic waste through fermentation and anaerobic digestion processes [10] are already well-established. **Table 1** shows the recent biogas exiting technologies, involving hythane, biogas, biohydrogen, and biomethane. Biohythane is generated via the combination of two processes via two-stage anaerobic fermentation that can yield a gas mixture of  $H_2$  and  $CH_4$  with a composition like Hythane (10–15% $H_2$ , 50–55% $CH_4$ , and 30–40% $CO_2$ ) [11,12,13]. However, these gases still contain a considerable proportion of carbon dioxide ( $CO_2$ ), which reduces their energy efficiency and contributes to greenhouse gas emissions. Therefore, gas upgrading processes, such as  $CO_2$  removal via thermochemical conversion processes such as cracking, reforming, and chemical looping reforming are essential to remove  $CO_2$ , increase heating value, enhance energy efficiency, and minimize environmental impact.

**Table 1.** Biogas technology development from two-stage anaerobic fermentation technology.

Technology	Process	Feedstock	Composition
Hythane	Thermochemical	Nature gas	$CH_4$ 90%, $CO_2$ 5% and $H_2$ 5-7%
Biogas/ Biomethane	Anaerobic digestion (AD)	Organic wastes	$CH_4$ 50-60%, and $CO_2$ 40- 50%
Biohydrogen	Fermentation	Organic wastes	$H_2$ 40-60% and $CO_2$ 40-60%
Biohythane	Two-stage fermentation/AD	Organic wastes	$CH_4$ 60%, $CO_2$ 30% and $H_2$ 5-10%

## III. THERMOCHEMICAL CONVERSION OF METHANE TO SYNGAS.

The conversion of methane ( $CH_4$ ) to syngas (a mixture of  $H_2$  and  $CO$ ) can be achieved through three main thermochemical processes, as shown in Figure 1. The first process is methane cracking in which methane in biogas decomposes without an oxidant, producing hydrogen and solid carbon [14]. The second process is methane reforming which can be classified into three types: steam reforming, dry reforming, and partial oxidation. These classifications depend on the type of oxidant present in the feed stream ( $H_2O$ ,  $CO_2$ , and  $O_2$ ), respectively. To further enhance syngas production efficiency, integrated reforming processes have been developed, including bi-reforming, auto-thermal reforming, and tri-reforming [15]. Lastly, chemical looping reforming of methane is a technique that utilizes metal oxides as oxygen carriers, enabling the partial oxidation of methane [16,17].

## IV. BIOGAS REFORMING

Biogas reforming can be generally classified into Dry Reforming, Bi-reforming, and Tri-reforming, as biogas primarily consists of  $CH_4$  and  $CO_2$  [15]. Chemical Looping Reforming (CLR) has also gained increasing attention as an emerging technology for converting biogas into syngas, offering enhanced energy efficiency, reduced carbon deposition, and lower  $CO_2$  emissions. In the industrial sector, methane steam reforming is the most widely used process for hydrogen and syngas production [6,8,15]. However, direct biogas reforming, without prior separation of its components, presents a promising approach to further reducing  $CO_2$  emissions. Dry-reforming, Bi-reforming, Tri-reforming, and CLR are among the most suitable processes for converting biogas into syngas. Therefore, this article provides an overview of these reforming processes.

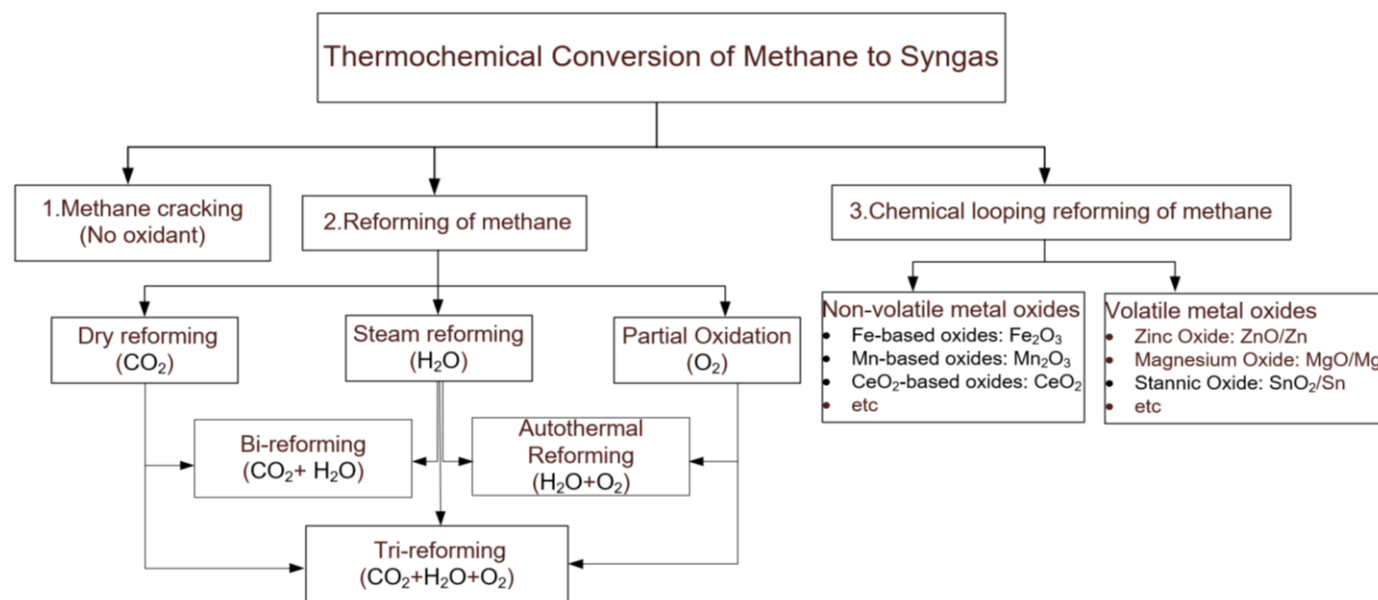
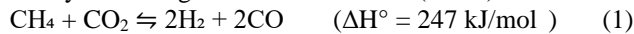


**Fig. 1.** Thermochemical Conversion of Methane to Syngas Pathways.

### 1) Dry Reforming of Biogas

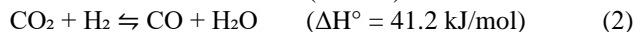
Dry reforming of methane (DRM) process is a direct route for utilizing biogas, which mainly consists of CH<sub>4</sub> (50–70%) and CO<sub>2</sub> (25–50%). The DRM reaction requires 1.6 times more energy than steam reforming to produce syngas [18] due to the high thermodynamic stability and kinetic inertness of methane (CH<sub>4</sub>,  $\Delta G_f = -50.5$  kJ/mol [19]) and carbon dioxide (CO<sub>2</sub>,  $\Delta G_f = -394$  kJ/mol [20]). Dry reforming of biogas reaction is represented by Eq. 1, in which one mole of CH<sub>4</sub> reacts with one mole of CO<sub>2</sub> to produce two moles of H<sub>2</sub> and CO (syngas).

Dry reforming of methane reaction (DRM):



In addition to the overall reaction, a few side reactions are involved in biogas dry reforming, such as the reverse water-gas shift (RWGS) reaction (Eq. (2)), which can co-occur, resulting in hydrogen consumption and a decrease in the H<sub>2</sub>/CO ratio below unity [21].

Reverse Water Gas Shift (RWGS):



Disadvantages of the DRM process are associated with coke formation, which occurs alongside other secondary reactions such as methane decomposition (Eq. 3), the Boudouard reaction or CO disproportionation (Eq. 4), and the carbon deposition reaction (Eqs. 5 and 6). The accumulation of these carbonaceous materials on the catalyst surface leads to deactivation. These secondary reactions tend to increase at higher temperatures [22].

Methane decomposition or Methane cracking:



Boudouard reaction or CO disproportionation:



Carbon Deposition Reaction:



Coke formation must be minimized as much as possible in the dry reforming process. Generally, this reaction is most favorable at high temperatures, low pressures, and low CH<sub>4</sub>/CO<sub>2</sub> molar ratios [23]. Thermodynamic studies showed that when the CH<sub>4</sub>/CO<sub>2</sub> ratio exceeds 1, the reaction temperature must be increased to 900–1000°C to prevent excessive coke formation [24]. Additionally, using a lower CH<sub>4</sub>/CO<sub>2</sub> ratio can help reduce coke deposition, but it may decrease CO<sub>2</sub> conversion efficiency and the H<sub>2</sub>/CO ratio. However, besides process optimization, which is crucial for enhancing the reaction process conversion, selecting a highly stable, selective, and efficient catalytic system is a key factor in making the biogas dry reforming process commercially viable [25,26]. For example, Evans et al. [27] studied the biogas dry reforming process using La<sub>0.8</sub>X<sub>0.2</sub>NiO<sub>3-δ</sub> perovskite-derived catalysts and examined the effects of Sm, Pr, and Ce on catalyst performance, and found that Ce

improved the redox properties of the catalyst and reduced carbon deposition, which is a significant challenge in reforming processes. This enhanced the stability and efficiency of the catalyst, increasing its performance in biogas reforming. In addition, Zhang et al. [28] studied H<sub>2</sub>-rich syngas production from biogas reforming using bimetallic Ni-based catalysts. The study focused on overcoming sintering issues. The results demonstrated that the bimetallic catalyst reduced carbon deposition and enhanced hydrogen production efficiency, making it a promising approach for biogas reforming and syngas production.

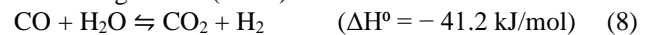
### 2) Bi reforming of Biogas

Bi-Reforming of the biogas process involves the addition of H<sub>2</sub>O into the reaction system, allowing both Steam Methane Reforming (SRM) (Eq. 7) and dry reforming (Eqs. 1) to co-occur [29]. The main advantage of the addition H<sub>2</sub>O is coke removal, which helps prevent catalyst deactivation. Moreover, the simultaneous presence of CO<sub>2</sub> and H<sub>2</sub>O affects the equilibrium of the WGS reaction (Eq.8) and the Reverse Water-Gas Shift (RWGS) reaction (Eq.2), both of which influence the composition of syngas (H<sub>2</sub>/CO ratio) [30].

Steam reforming of methane (SRM):



Water-gas shift (WGS):



Previous studies developed different catalysts to obtain desired reactant conversions and H<sub>2</sub> to CO ratios. For example, Smith et al. [31] investigated hydrogen-rich syngas production using the bi-reforming of methane with Ni supported on CeO<sub>2</sub>-SrO mixed oxide catalysts. Their study demonstrated that the CeO<sub>2</sub>-SrO support enhanced oxygen storage capacity, improved catalytic activity, and increased resistance to carbon deposition, making it an efficient catalyst for syngas production.

The catalytic bi-reforming of methane and the promotional effect of strontium (Sr) on Ni/MgO-ZrO<sub>2</sub> catalysts was reported [32]. It was found that Sr improved catalyst reducibility, enhanced metal dispersion, and increased methane conversion efficiency, resulting in higher hydrogen production and better stability under reaction conditions. In addition, bimetallic Co-Rh catalysts for methane reforming were examined to design a system for syngas production with a controllable composition [33]. Their results showed that Co-Rh interactions improved catalytic activity, enhanced carbon resistance, and allowed for precise tuning of the H<sub>2</sub>/CO ratio, making it suitable for industrial applications. Using Ni and Co catalysts demonstrated that the Ni-Co combination improved syngas yield, enhanced catalyst reducibility, and exhibited better coke resistance [34]. Young et al. [35] analyzed Ni-based catalysts supported on MgAl<sub>2</sub>O<sub>4</sub> with different properties for combined steam and CO<sub>2</sub> reforming of methane. They found that support properties significantly influenced catalyst performance, with optimized MgAl<sub>2</sub>O<sub>4</sub> structures providing

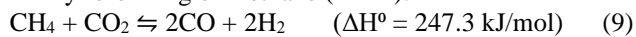


better metal dispersion, improved thermal stability, and higher methane conversion efficiency. In summary, bi-reforming biogas performs exceptionally in terms of preventing catalyst deactivation as added H<sub>2</sub>O can help to remove carbon deposition.

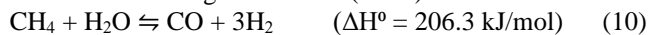
### 3) Tri-reforming of Biogas

In landfill gas production, some oxygen is usually present, with a maximum concentration of up to 5% by volume [10]. Therefore, reforming landfill gas containing oxygen is essential. This aligns with the tri-reforming process, which requires the addition of O<sub>2</sub> into the reaction, in addition to H<sub>2</sub>O and biogas, which are already present in bi-reforming. The addition of O<sub>2</sub> provides three key benefits: enhanced coke removal through carbon oxidation, control over the reaction products, and the H<sub>2</sub>/CO ratio based on Equations 8 to 11, which work in conjunction with reactions related to carbon formation and decomposition [36]. This allows syngas production with a suitable H<sub>2</sub>/CO ratio for Fischer-Tropsch synthesis. Additionally, it reduces the energy demand due to partial oxidation of reactants (Equations 9 and 10) [37]. A study by Zhao et al. (2019) found that tri-reforming can reduce energy consumption by 45.8% compared to dry reforming and 19.7% compared to bi-reforming [38].

Dry reforming of methane (DRM):



Steam reforming of methane (SRM):



Partial oxidation of methane (POM):



Methane combustion:



Methane cracking:



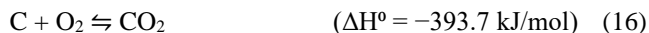
Reverse Boudourd reaction:



Steam reforming of carbon:



Carbon combustion:



For example, Majewski and Wood [39] studied the tri-reforming of methane using a Ni@SiO<sub>2</sub> catalyst, achieving over 70% methane conversion at 750°C with an optimal H<sub>2</sub>/CO ratio of ~2.5. Adding oxygen improved conversion to 90% while reducing carbon deposition. The effect of feed rate and operating conditions on low-temperature tri-reforming of methane using a Ni@MWCNT/Ce catalyst was studied [40] and analyzed. The optimum feed rates enhanced CO<sub>2</sub> conversion and reduced coking was demonstrated.

### 4) Solar reforming and chemical looping reforming of Biogas to Syngas

The conventional steam/dry reforming method utilized in the chemical industry to produce syngas uses both fossil fuels as the source of process heat and metal-based catalysts to catalyze the endothermic chemical reactions. This results in both CO<sub>2</sub> emissions contributing to global warming and catalyst deactivation. Gaseous carbonaceous feedstocks such

as methane (CH<sub>4</sub>) are oxidized to syngas by utilizing H<sub>2</sub>O/CO<sub>2</sub> as oxidizing agents, and the reaction temperature is usually 1000 K at 1 atm. Alternatively, the required heat for such endothermic reaction can be supplied by concentrating solar technologies, thereby storing solar energy into transportable and storable chemical fuels. In contrast to the conventional method, solar chemical-looping reforming of methane (CLRM) employs solid metal oxides as oxygen carriers in place of pure oxygen as the oxidant. For the chemical looping scheme, in the endothermic step, gaseous CH<sub>4</sub> is partially oxidized with the metal oxides to produce syngas while the metal oxide is reduced. The reduced metal oxide is subsequently oxidized in the exothermic step with H<sub>2</sub>O/CO<sub>2</sub> to generate H<sub>2</sub>/CO. The solid metal oxide oxygen carrier is then circulated between these two steps. The CLR of biogas results in the partial oxidation of methane without the use of gaseous oxidants or catalysts, while the process can be operated as a two-step cycle at relatively low temperatures (about 800–1000°C) thanks to the use of a gaseous reductant [16,17]. The oxygen carrier redox material is partially reduced by methane in the biogas, producing syngas in what is known as the methane partial oxidation step, according to Equation (17).



In the second step, the reduced material is oxidized by CO<sub>2</sub> (Eq.18) present in the biogas or by H<sub>2</sub>O in the Steam-CLR process (Eq. 19), recovering the lattice oxygen and generating CO and H<sub>2</sub> (the CO<sub>2</sub> or H<sub>2</sub>O splitting step). At the same time, solid oxide can be recycled [16,17].



Table 2 shows that the chemical looping reforming process has advantages over competing conventional reforming technologies for syngas production [7,16,17,41].

**Table 2.** Comparison of Chemical Looping Reforming (CLR) of biogas and conventional reforming.

Aspect	Chemical Looping Reforming (CLR) of biogas	Conventional reforming
<b>Energy Efficiency</b>	It uses internal heat transfer, reducing external energy needs. can integrate solar heating.	Requires high external energy as reactions are endothermic.
<b>Catalyst Requirement</b>	No catalyst is needed, avoiding deactivation and coking.	It requires Ni-based or precious metal catalysts and is prone to deactivation.
<b>Syngas Composition Control</b>	Flexible H <sub>2</sub> /CO ratio, suitable for multiple applications.	Limited flexibility often needs WGS or CO <sub>2</sub> removal.
<b>Carbon Deposition</b>	Redox cycling of metal oxides helps gasify deposited carbon, significantly reducing coking issues.	DRM and SMR suffer from catalyst coking, which deactivates the catalyst and requires frequent regeneration.

In this respect, chemical looping reforming of biogas could increase interest in optimizing activity, selectivity, and catalyst stability thanks to cyclic solid regeneration.



## V.CONCLUSIONS

This study highlights the potential of biogas as a clean and renewable energy source for syngas production. Despite its high CO<sub>2</sub> content, various reforming techniques such as dry reforming, bi-reforming, tri-reforming, solar reforming, and chemical looping reforming offer viable pathways to enhance its utilization. Among these methods, solar chemical looping reforming presents notable advantages, including improved energy efficiency, reduced carbon deposition, catalyst stability, and solar energy storage in chemical products.

## VI. CHALLENGES AND FUTURE DIRECTIONS

The primary technical challenge in converting biogas to syngas is improving process efficiency while reducing carbon deposition and catalyst degradation. Biogas reforming requires high temperatures of 700–1,000°C, which are typically supplied by fossil fuels. Utilizing solar thermal energy as an alternative heat source is a crucial step toward carbon-neutral syngas production, as it helps reduce greenhouse gas emissions and enhance process sustainability. Therefore, developing efficient solar energy capture systems, along with advancements in reforming materials and technology, will be essential for driving this technology toward commercial-scale implementation.

## ACKNOWLEDGMENT

This research has received funding from National Science Research and Innovation Fund (NSRF), Thailand (grant number: RE-KRIS/FF68/72), and this work was partially supported by the National Research Council of Thailand (NRCT) under Grant No. N42A670961 and Grant No. N42A670487.

## REFERENCES

- [1] Y. Mu et al., "Biogas as a renewable energy source," *Renewable Energy Journal*, vol. 45, pp. 1102-1110, 2020.
- [2] H. Zhang et al., "Biogas production from organic waste," *Bioresource Technology*, vol. 289, pp. 121-130, 2019.
- [3] J. S. T. C. R. Silva, A. B. M. F. Santos, and D. L. M. Oliveira, "Biogas: Production, properties, applications, economic and challenges: A review," *Results in Chemistry*, vol. 100, p. 101549, 2024.
- [4] W. Chen et al., "Impurities in biogas: Challenges and removal technologies," *Energy & Fuels*, vol. 35, no. 8, pp. 678-689, 2022.
- [5] J. E. Miller, A. D. Allendorf, R. B. Diver, N. P. Siegel, and J. M. Evans, "Solar thermal reforming of methane feedstocks for hydrogen and syngas production—A review," *Renewable and Sustainable Energy Reviews*, vol. 20, pp. 135–153, Apr. 2013.
- [6] Z. Zhao, Z. Li, Y. Guo, W. Xue, and J. Zhang, "Recent advances in biogas reforming for syngas production: A review," *Renewable and Sustainable Energy Reviews*, vol. 121, p. 109706, 2020. [Online].
- [7] S. Chuayboon, S. Abanades, and S. Rodat, "Solar chemical looping reforming of methane combined with isothermal H<sub>2</sub>O/CO<sub>2</sub> splitting using ceria oxygen carrier for syngas production," *J. Energy Chem.*, vol. 41, pp. 60–72, 2020.
- [8] S. Singh, S. K. Soni, and P. D. Pandey, "Biogas: An Overview on the Production of Synthetic Fuels from Biogas," *Bioresource Technology Reports*, vol. 17, p. 101104, 2022.
- [9] S. Singh, S. K. Soni, and P. D. Pandey, "Biogas: An Overview on the Production of Synthetic Fuels from Biogas," *Bioresource Technology Reports*, vol. 17, p. 101104, 2022.
- [10] Z. Liu, C. Zhang, Y. Lu, X. Wu, L. Wang, L. Wang, B. Han, and X. H. Xing, "States and challenges for high-value biohythane production from waste biomass by dark fermentation technology," *Bioresource Technology*, vol. 135, pp. 292-303, 2013.
- [11] M. C. Mamimin, A. Singkhala, P. Kongjan, B. Suraraksa, P. Prasertsan, T. Imai, and S. O-Thong, "Two-stage thermophilic fermentation and mesophilic methanogen process for biohythane production from palm oil mill effluent," *Int. J. Hydrogen Energy*, vol. 40, pp. 6319-6328, 2015.
- [12] P. Kongjan, S. O-Thong, and I. Angelidaki, "Performance and microbial community analysis of two-stage process with extreme thermophilic hydrogen and thermophilic methane production from hydrolysate in UASB reactors," *Bioresource Technology*, vol. 102, no. 6, pp. 4028-4035, 2011.
- [13] S. O-Thong, C. Mamimin, and P. Prasertsan, "Biohythane production from organic wastes by two-stage anaerobic fermentation technology," *IntechOpen*, Mar. 21, 2018.
- [14] G. Shu, J. Wang, B. Liu, J. Tian, and Z. Liu, "Solar driven methane cracking to produce hydrogen and carbon: A review," *Int. J. Hydrogen Energy*, vol. 49, no. 13, pp. 7361-7378, 2024.
- [15] D. P. Minh, T. J. Siang, D.-V. N. Vo, T. S. Phan, C. Ridart, A. Nzihou, and D. Grouset, "Hydrogen production from biogas reforming: An overview of steam reforming, dry reforming, dual reforming, and tri-reforming of methane," in *Hydrogen Supply Chain*, 1st ed., Elsevier, 2018, pp. 111–130.
- [16] S. Chuayboon, S. Abanades, and S. Rodat, "Syngas production via solar-driven chemical looping methane reforming from redox cycling of ceria porous foam in a volumetric solar reactor," *Chem. Eng. J.*, vol. 356, pp. 756–770, 2019.
- [17] S. Chuayboon, S. Abanades, and S. Rodat, "Syngas production via solar-driven chemical looping methane reforming from redox cycling of ceria porous foam in a volumetric solar reactor," *Chem. Eng. J.*, vol. 356, pp. 756–770, 2019.
- [18] M. Alhassan, A. A. Jalil, and W. Nabgan, "Bibliometric studies and impediments to valorization of dry reforming of methane for hydrogen production," *Fuel*, vol. 328, p. 125240, 2022.
- [19] M. Zhang, Y. Gao, and Y. Mao, "Enhanced dry reforming of methane by microwave-mediated confined catalysis over Ni-La/AC catalyst," *Chem. Eng. J.*, vol. 451, p. 138616, 2023.

[20] I. V. Yentekakis, P. Panagiotopoulou, and G.

Artemakis, "A review of recent efforts to promote dry reforming of methane (DRM) to syngas production via bimetallic catalyst formulations," *Appl. Catal. B: Environ.*, vol. 296, p. 120210, 2021.

[21] T. T. P. Pham, K. S. Ro, and L. Chen, "Microwave-assisted dry reforming of methane for syngas production: A review," *Environmental Chemistry Letters*, vol. 18, no. 6, pp. 1987–2019, 2020.

[22] A. B. Choudhury, K. C. Ghosh, and S. C. Sahu, "A review on the recent advances in dry reforming of methane," *Journal of Industrial and Engineering Chemistry*, vol. 52, pp. 1–25, 2017.

[23] J. Wang and D. Han, "Design of network intrusion detection system based on parallel DPC clustering algorithm," *International Journal of Embedded Systems*, vol. 13, no. 3, pp. 318–327, 2020.

[24] S. Kawi, Y. Kathiraser, J. Ni, J. C. W. Lai, D. K. Ang, and X. Ouyang, "Advances in Syngas Production and Utilization," *Energy Conversion and Management*, vol. 178, pp. 277–300, 2018.

[25] P. Hao, Z. Liu, Y. Shi, and X. Zhang, "Characteristics of Activated Carbon in Elevated-Temperature Pressure Swing Adsorption Desulfurization," *Adsorption*, vol. 25, no. 6, pp. 1219–1226, 2019.

[26] J. Gao, Q. Liu, F. Gu, B. Liu, Z. Zhong, and F. Su, "Recent Advances in Methane Conversion by Oxidative Processes," *Applied Catalysis B: Environmental*, vol. 245, pp. 1–22, 2019.

[27] A. Evans et al., "An experimental and theoretical approach for the biogas dry reforming reaction using perovskite-derived  $\text{La}_{0.8}\text{X}_{0.2}\text{NiO}_{3-\delta}$  catalysts (X = Sm, Pr, Ce)," *Renewable Energy*, vol. 227, p. 120511, 2024.

[28] M. Zhang, Y. Gao, and Y. Mao, "H<sub>2</sub>-rich syngas production from biogas reforming: Overcoming coking and sintering using bimetallic Ni-based catalysts," *International Journal of Hydrogen Energy*, vol. 48, no. 72, pp. 27907–27917, 2023.

[29] O. Ahmed and G. C. Nguyen, "Therapeutic challenges of managing inflammatory bowel disease in the elderly patient," *Journal of Clinical Gastroenterology*, vol. 50, no. 12, pp. 1005–1010, Mar. 2016.

[30] Z. Zhang, G. Bi, Z. Zhang, T. Tan, and J. Xie, "Cemgox-Promoted Ni/Boron Nitride Ultra-Long Stability Bi-Reforming for Methanol-Friendly Syngas (H<sub>2</sub>/CO  $\approx$  2): CO<sub>2</sub>/H<sub>2</sub>O Activation and Coke Elimination Mechanism," *SSRN*, Dec. 19, 2023.

[31] A. Smith, B. Johnson, and C. Lee, "Hydrogen-rich syngas production by bi-reforming of methane with CO<sub>2</sub>

over Ni supported on CeO<sub>2</sub>-SrO mixed oxide catalysts," *International Journal of Hydrogen Energy*, vol. 47, no. 56, pp. 23654–23667, 2022.

[32] D. Brown, E. Wilson, and F. Martinez, "Catalytic bi-reforming of methane as a potential source of hydrogen-rich syngas: Promotional effect of strontium on the catalytic performance of Ni/MgO-ZrO<sub>2</sub>," *Applied Catalysis B: Environmental*, vol. 307, pp. 121097, 2022.

[33] G. Thompson and H. Clark, "Bimetallic Co-Rh systems as a prospective base for the design of CH<sub>4</sub> reforming catalysts to produce syngas with a controllable composition," *Catalysis Science & Technology*, vol. 13, no. 5, pp. 1254–1268, 2023.

[34] O. Wright and P. Hill, "CO<sub>2</sub> conversion through combined steam and CO<sub>2</sub> reforming of methane reactions over Ni and Co catalysts," *Journal of Catalysis*, vol. 416, pp. 156–168, 2023.

[35] R. Young, S. Taylor, and V. Lewis, "Ni-based catalysts supported on MgAl<sub>2</sub>O<sub>4</sub> with different properties for combined steam and CO<sub>2</sub> reforming of methane," *Catalysts*, vol. 12, no. 10, p. 1047, 2022.

[36] N. A. Khan, Z. H. Ayub, and M. A. Darr, "Conversion of landfill gas to liquid fuels through a TriFTS (tri-reforming and Fischer–Tropsch synthesis) process: a feasibility study," *Sustainable Energy & Fuels*, vol. 3, no. 2, pp. 500–509, 2019.

[37] A. V. P. Lino, E. M. Assaf, and J. M. Assaf, "Adjusting process variables in methane tri-reforming to achieve suitable syngas quality and low coke deposition," *Energy & Fuels*, vol. 34, no. 12, pp. 16522–16531, 2020.

[38] X. Zhao, A. Naqi, D. M. Walker, T. Roberge, M. Kastelic, B. Joseph, and J. N. Kuhn, "Conversion of landfill gas to liquid fuels through a TriFTS (tri-reforming and Fischer–Tropsch synthesis) process: a feasibility study," *Sustainable Energy & Fuels*, vol. 3, no. 3, pp. 539–549, 2019.

[39] A. J. Majewski and J. Wood, "Tri-reforming of methane over Ni@SiO<sub>2</sub> catalyst," *Int. J. Hydrogen Energy*, vol. 39, no. 36, pp. 12578–12585, 2014.

[40] M. Zhang, H. Liu, and X. Wang, "Influence of feed rate and testing variables for low-temperature tri-reforming of methane on the Ni@MWCNT/Ce catalyst," *Int. J. Hydrogen Energy*, vol. 48, no. 12, pp. 5602–5614, 2023.

[41] L. Zeng, Z. Cheng, J. A. Fan, L.-S. Fan, and J. Gong, "Metal oxide redox chemistry for chemical looping processes," *Nat. Rev. Chem.*, vol. 2, no. 11, pp. 349–364, 2018.

# Static Strength and Overload Assessment of Obstacle Deflector in The Aachen Rail Shuttle

Ponphom Chakornpipat<sup>1, 2, a)</sup> Nutchanon Prasomsuk<sup>2, b)</sup> Kittchai Sojiphan<sup>1, c)</sup>  
Chayut Ngamkhanong<sup>3, d)</sup> and Christian Schindler<sup>2, e)</sup>

## Author Affiliations

<sup>1</sup>Railway Vehicles and Infrastructure Engineering Program, The Sirindhorn International Thai-German Graduate School of Engineering (TGGS), King Mongkut's University of Technology North Bangkok  
1518 Pracharat 1 Rd., Wongsawang, Bangsue, Bangkok 10800 Thailand

<sup>2</sup>Institute for Rail Vehicles, RWTH Aachen University, Aachen, Seffenter Weg 8, 52074, Germany

<sup>3</sup>Advance Railway and Infrastructure, Innovation and Systems Engineering (ARIISE) Research Unit, department of Civil Engineering, Faculty of Engineering, Chulalongkorn University, 254 Phayathai Rd., Pathumwan, Bangkok 10330 Thailand

## Author Emails

<sup>a)</sup> s6509096860025@email.kmutnb.ac.th

<sup>b)</sup> Prasomsuk.Nutchanon@ifs.rwth-aachen.de

<sup>c)</sup> Corresponding author: Kittichai.s@tggs.kmutnb.ac.th

<sup>d)</sup> Chayut.ng@chula.ac.th

<sup>e)</sup> Schindler@ifs.rwth-aachen.de

**Abstract.** The Aachen Rail Shuttle (ARS) is a new rail vehicle designed to enhance regional transportation. Crashworthiness is integrated into vehicle design to ensure passive safety. A key aspect of its crashworthiness is its ability to manage impact forces and maintain structural integrity during collisions. An important component contributing to this is the obstacle deflector, which mitigates impacts with small obstacles on the track. The current design of the obstacle deflector meets the standard. However, it could interfere with the operation of the buffer in an actual train collision. Thus, it has been redesigned to prevent obstruction of the buffer's ability to react to impacts. This study evaluates the static strength and overload performance of the new obstacle deflector using Finite Element Analysis (FEA) according to EN 15227 standard. Simulations assess stress distribution, strain energy, and fastener integrity under different load cases. Results indicate that the obstacle deflector meets center load, side load, and overload requirements. It can withstand a critical overload case of 600 kN. While some fastener components may exceed stress limits under overload conditions, the overall system remains intact and prevents detachment. The findings validate the obstacle deflector's compliance with safety standards, supporting its effectiveness in ensuring ARS operational integrity. Additionally, the redesign successfully relocates the obstacle deflector beneath the chassis, eliminating interference with the buffer operation.

**Index Terms**— Aachen rail shuttle, Finite element analysis, Obstacle deflector, Static strength.

## I. INTRODUCTION

The Aachen Rail Shuttle (ARS) represents a cutting-edge approach to regional and rural transportation challenges. As an autonomous, energy self-sufficient railbus, the ARS is designed to enhance mobility and connectivity in less densely populated areas. By lower travel headways, it aims to attract passengers who might otherwise rely on personal vehicles, fostering a shift toward more sustainable transport solutions. Structurally, the ARS is comparable in size to a standard city bus, with dimensions of approximately 13.5 meters in length, over 3 meters in width, and 3.25 meters in height as shown in Fig. 1. Propelled by electric motors with a total continuous power of 300 kW, the ARS achieves speeds of up to 100 km/h. Its onboard battery system provides an operational range of 100 km per charge and a daily capacity of up to 500 km, enabling sustainable,

emission-free operation [1].



Fig. 1. Aachen Rail Shuttle [1]

One of the ARS's critical design challenges lies in its crashworthiness concept, which ensures passenger safety during collisions and adheres to the EN 15227 standard for Category CIII vehicles [2,3]. Among the key components of this concept is the obstacle deflector as shown in Fig. 2. The obstacle deflector, positioned at both lower ends of the

ARS, serves to manage impacts with objects such as debris or small obstacles on the track. Its role is to deflect these objects away from the vehicle's path, reducing the likelihood of destabilizing or damaging the vehicle.

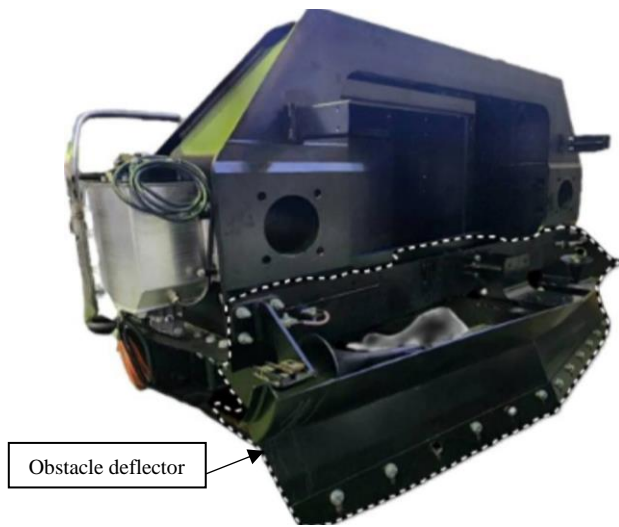


Fig. 2. Aachen Rail Shuttle's obstacle deflector

The design and function of obstacle deflectors have been widely studied in railway safety research. Previous designs, such as those by Boos and Michael (2019), Sliding Mechanism Deflectors [4]: These include a moving element that can slide between extended and retracted positions, allowing the deflector to push away obstacles, when necessary. Design by Makoto. (2011), Curved Plate Deflectors [5]: These feature a main plate with a convex shape, designed to deflect obstacles efficiently. They often include sub-plate portions for additional structural support. Additionally, Duella and Renzo (2007) design Energy-Absorbing Deflectors [6]: These are equipped with plastically deformable connection members that absorb energy during a collision, reducing the impact force transmitted to the train.

To evaluate the effectiveness of these designs, numerical simulation has been widely adopted as a primary assessment method. It helps reduce costs and time associated with physical prototyping while enabling the assessment of extreme loading conditions that may be difficult or impractical to replicate experimentally. Previous studies, such as Songyan Li (2013) developed a finite element model of an obstacle deflector installed at the front of a high-speed train. Their study analyzed the collision dynamics when the leading car impacts a rigid wall or an obstacle at varying speeds [7]. Similarly, Yanzhao Guo (2023) developed a finite element model for structural static load and collision analysis, adhering to the EN 15227 standard. Their research utilized an obstacle deflector designed for a 160 km/h train as a prototype, providing valuable insights into its performance under impact conditions [8].

In compliance with EN 15227, the obstacle deflector is

designed to perform effectively under various load cases, enhancing the ARS's overall crashworthiness. The obstacle deflector primarily functions to clear obstacles from the train's running gear with a 'V' shape ( $\leq 160^\circ$ ) and also serves as a snow plough. Positioned with its lower edge close to the track, it is designed to withstand static loads without significant permanent deformation. According to EN 15227, the lifeguard prevents small objects from entering the wheel path, while the obstacle deflector mitigates impacts from larger obstacles. However, lifeguards are not required if the lower edge is less than or equal to 130 mm above the top of the rail.

Although the current design meets the standard, in real-world collisions, its extended structure may interfere with the operation of the buffer as shown in Fig. 3. It may restricts the buffer's ability to absorb impact. Therefore, this study explores a new design that relocates the obstacle deflector beneath the chassis to mitigate this issue as shown in Fig. 4.

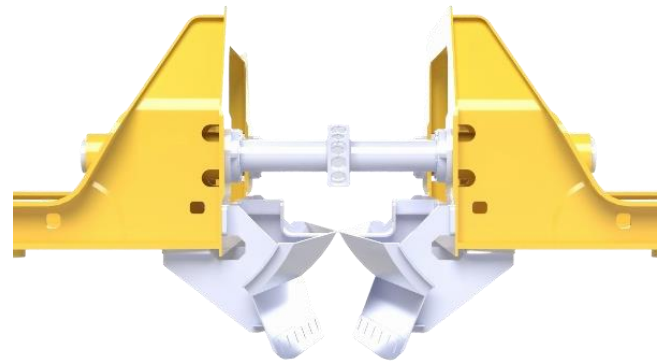


Fig. 3. Obstacle deflector interferes with the operation of the buffer

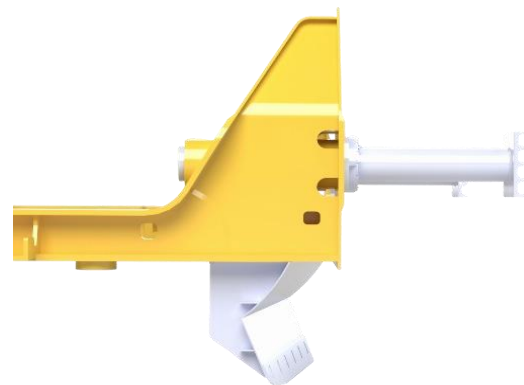


Fig. 4. Aachen Rail Shuttle's new obstacle deflector

In this study, the new obstacle deflector is evaluated through static load simulations using Finite Element Analysis (FEA), following the guidelines of EN 15227, which defines crashworthiness requirements for railway vehicles. To ensure the structural integrity of the obstacle



deflector in real-world conditions, this study also includes a fastener simulation to evaluate the performance of the attachment system under applied overloads. This step is crucial in verifying that the obstacle deflector remains securely attached to the vehicle structure and does not detach under extreme conditions. Therefore, this research focuses solely on numerical simulations, excluding physical experiments, while relying on established methodologies to ensure the validity of the results.

## II. EN 15227 REQUIREMENTS

According to the EN 15227 [2] standard and the Aachen Rail Shuttle's operational speed of 100 km/h, the obstacle deflector's design performance must be tested based on collision requirements with small obstacles at low altitudes. Given that the train operates at 100 km/h, the static strength analysis of the obstacle deflector should consider three distinct load conditions, with their respective ranges and magnitudes detailed in Table I. To assess static strength, the obstacle deflector and its attachment to the car body must not exhibit significant permanent deformation, as defined in (1) of EN 12663, under center load and side load requirements. The static strength is evaluated through numerical simulation computational structural analysis.

$$\frac{R_e}{\sigma_e} \geq S \quad (1)$$

According to EN 12663 [9], the safety factor  $S$  shall be more than 1.15 when the design is verified solely through calculations, where  $R_e$  represents the material yield stress and  $\sigma_e$  is the calculated stress.

In the case of overload requirements according to EN 15227, the obstacle deflector must demonstrate its ability to absorb the required energy specified in Table I. To verify this, the absorbed energy of the obstacle deflector will be calculated using (2), and the strain energy and plastic work will be analyzed using ANSYS.

$$E_{absorb} = U + W \quad (2)$$

Where  $E_{absorb}$  represents the absorbed energy,  $U$  is the elastic strain energy and  $W$  is the plastic strain energy. Additionally, Following EN 15257, the deflector's shape will be evaluated to ensure that it does not deform in a way that could lead to detachment or pose safety risks.

TABLE I

OBSTACLE DEFLECTOR STATIC LOAD REQUIREMENTS [2].

Load condition	Range of action	Load (kN)	Energy absorption
----------------	-----------------	-----------	-------------------

(kJ)			
Static longitudinal load at the center line	An area with a projected width of 500 mm and up to 500 mm from the bottom edge of the obstacle deflector.	120	-
Static longitudinal load at 750 mm lateral distance from the center line	An area with a projected width of 500 mm and up to 500 mm from the bottom edge of the obstacle deflector at 750 mm lateral distance from the center line.	100	-
Static longitudinal overload at center line	An area with a projected width of 500 mm and up to 500 mm from the bottom edge of the obstacle deflector.	120-800	14.4

## III. FINITE ELEMENT ANALYSIS

This study develops two finite element models analysis. The first model, shown in Fig. 5, is designed for static strength analysis of center load, side load, and overload cases, assuming the obstacle deflector is rigidly connected to the main chassis with no failure in the fastening system. The second model, shown in Fig. 6, is developed for fastener analysis in the overload case. The key difference between the two models is that the fastener analysis model includes parts of the chassis and fastening system components.

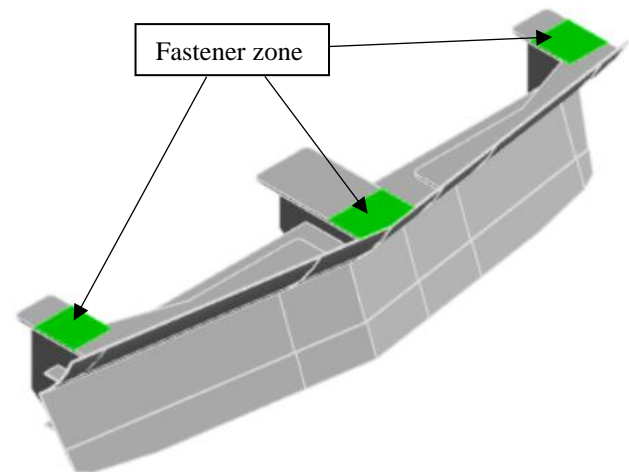


Fig. 5. Obstacle deflector's finite element model



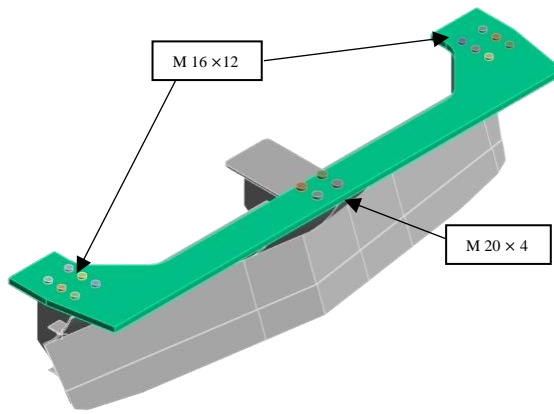


Fig. 6. Finite element model of the obstacle deflector with a piece of the chassis structure (green) and fastening system components

### Three load case simulations

The obstacle deflector and vehicle body of the ARS primarily use structural steel S355J2+N [10], while the fastening system components are made of medium carbon steel [11]. The mechanical properties of these materials are shown in Table II

TABLE II

THE MECHANICAL PROPERTIES OF MAIN MATERIALS.

Material	Young's modulus $E[GPa]$	Poisson's ratio $\mu$	Yield limit $\sigma_y[MPa]$
S355J2+N	210	0.3	400
Medium carbon steel	200	0.3	940

For accurate material behavior representation, the simulation incorporates the stress-strain curve, as illustrated in Figs. 7 and 8.

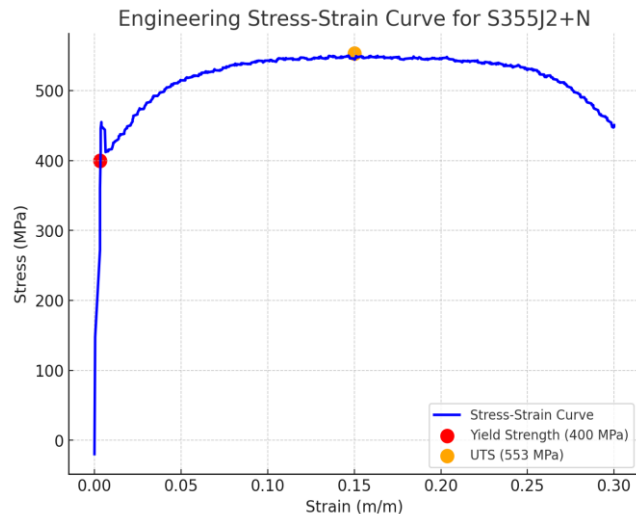


Fig. 7. Engineering stress and strain curve of S355J2+N [10]

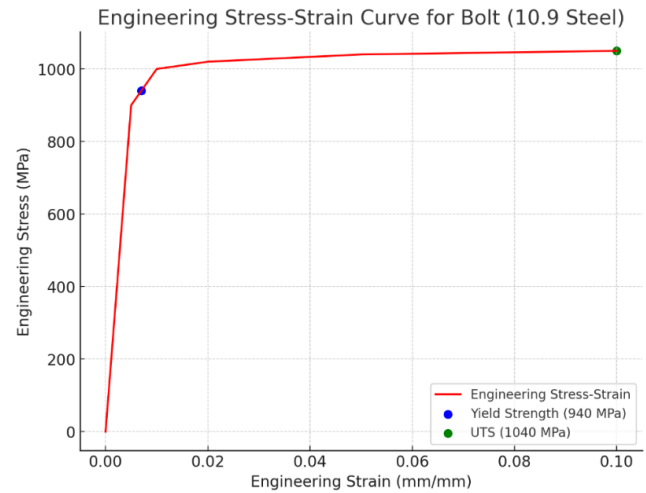


Fig. 8. Engineering stress and strain curve of bolt grade 10.9 [11]

The static load analysis simulation, featuring three load cases, will use the model shown in Fig. 5. By using finite element static structural analysis in ANSYS, the setup includes boundary conditions, loads on the obstacle deflector, and mesh settings as detailed in Table III. For the overload case, this study will apply a load ranging from 120 kN to 800 kN (the limited longitudinal load of the ARS) to determine the load at which the obstacle deflector absorbs 14.4 kJ of energy. The identified overload value will then be used in fastener analysis to confirm that the obstacle deflector remains securely attached to the ARS.

TABLE III

STATIC LOAD TEST SIMULATION SETTING.

Parameter	Details
Boundary condition	Fix the base of the deflector at the connection points to the vehicle chassis to simulate realistic constraints. Ensure there is no displacement at the fixed ends during loading.
Load area	See as Table. I and Fig. 9.
Mesh Control	For the thick structure, solid elements are used. The meshing process involves applying fine mesh in high-stress areas and coarser mesh in less critical regions to optimize accuracy and computation time. Mesh quality is checked to ensure stability.
Elements	Tetrahedral with element size 4 mm at the critical area and 20 – 30 mm at no significant area
Nonlinear	The Nonlinear effect is enabled for all loading conditions, meaning that material and geometric nonlinearities are accounted for.

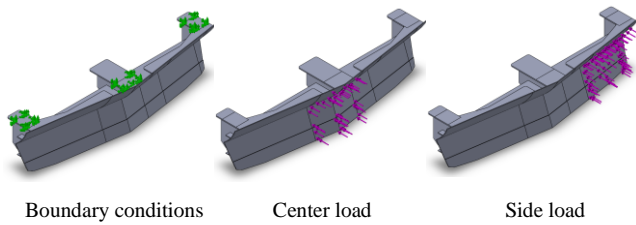


Fig. 9. Boundary condition, and load position of obstacle deflector

### Fastener simulation

The fastener analysis simulation includes additional contact settings, preload settings, and modified boundary conditions from Table III. This study will use the finite element model shown in Fig. 6, with additional settings and fastening system details provided in Table IV.

TABLE IV  
FASTENER ANALYSIS SIMULATION SETTING.

Parameter	Details
Fastening system	Bolt M20 × 4 grade 10.9 at the middle of vehicle chassis and Bolt M16 × 12 grade 10.9 at the left and the right side of vehicle chassis as shown in Fig. 6.
Preload setting	Preload setting [12] of fastening system will set at the shank contact surface with 44000 N for Bolt M20 and 28000 N for Bolt M16
Boundary condition	Fix the vehicle chassis at the front and rear surface as shown in Fig. 10. Ensure there is no displacement at the fixed ends during loading.
Contact setting	The contact between obstacle deflector surface, nut surface and chassis surface will be set to frictional with coefficient of friction 0.2. Bolt surface and nut will set with bonded condition.

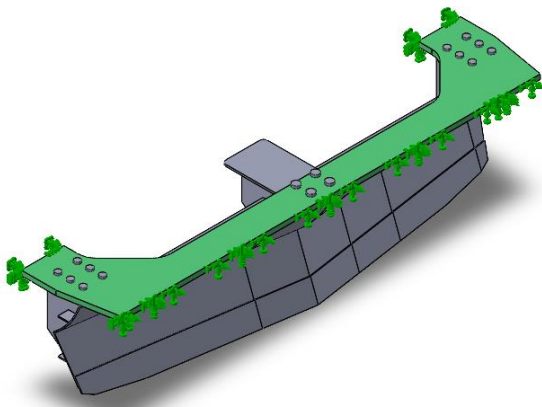


Fig. 10. Fastener analysis boundary condition

## IV. RESULTS AND DISCUSSION

### Center and side load cases

The stress distribution results for the center load and side load conditions are presented in Figs. 11 and 12. Under the center load condition, the obstacle deflector exhibits a uniform stress distribution. The maximum stress, 273 MPa, occurs on the surface at the bottom edge of the obstacle deflector. Under the side load condition, the maximum stress is 306 MPa, occurring within the internal structure of the obstacle deflector. The structural material, S355J2+N, has an allowable yield strength of 400 MPa, resulting in a minimum safety factor of 1.46 for the center load case and 1.30 for the side load case. According to EN 12663 [9], the safety factor under all operational conditions shall be more than 1.15. Therefore, the obstacle deflector meets the standard and design requirements, confirming that it satisfies the static strength design criteria under the analyzed conditions.

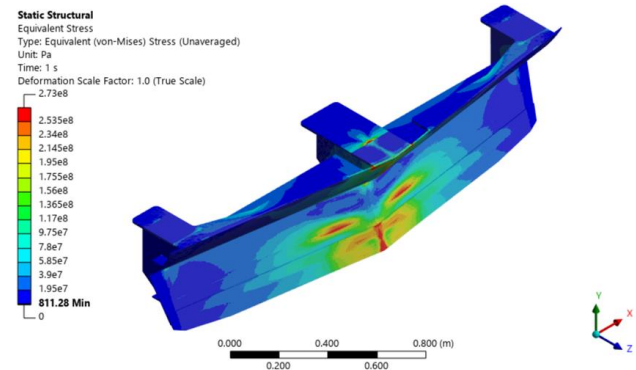


Fig. 11. The von Mises stress of center load conditions

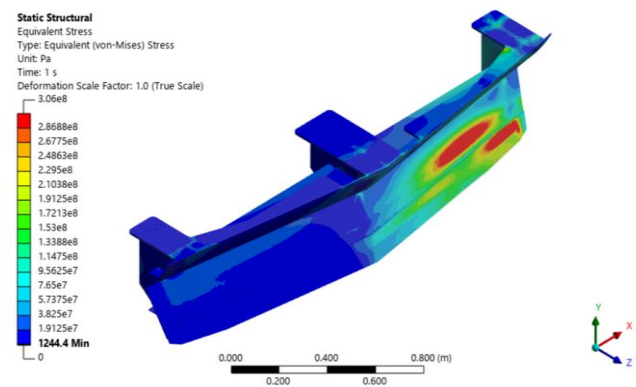


Fig. 12. The von Mises stress of side load condition

### Overload case

Fig. 13. presents the energy absorbed by the obstacle deflector and load ratio. Under an applied load of 600 kN, the deflector absorbs approximately 15,187 J. According to the EN 15227 standard (see Table I), a Category C III vehicle operating at 100 km/h must absorb at least 14.4 kJ of energy.

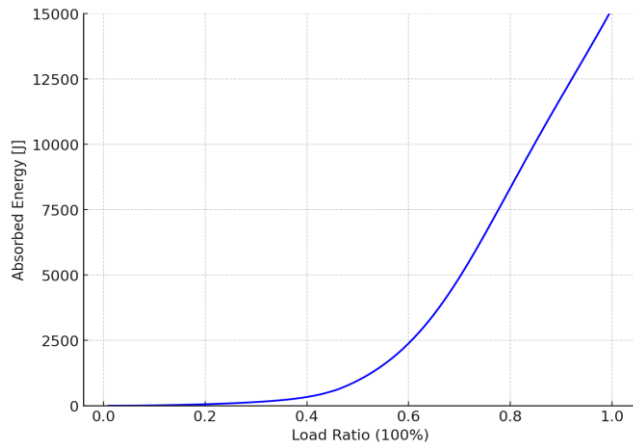


Fig. 13. Energy absorbed by the obstacle deflector and load ratio

The results of stress and strain for the overload case have been investigated, as shown in Figs. 14 and 15. It can be observed that the middle front structure of the obstacle deflector has deformed within the plasticity zone. The maximum stress occurs inside the obstacle deflector structure, reaching 663 MPa, while the maximum equivalent elastic strain of 0.3345 m/m is observed in the middle front structure of the obstacle deflector. However, the results in Figs. 14 and 15. are based on the assumption that the obstacle deflector is rigidly connected to the main chassis, with no failure in the fastening system.

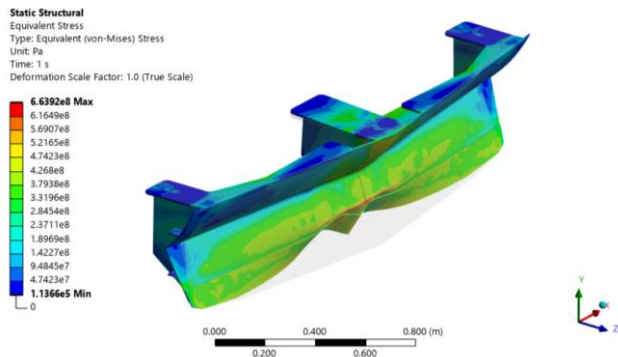


Fig. 14. The von Mises stress of overload condition

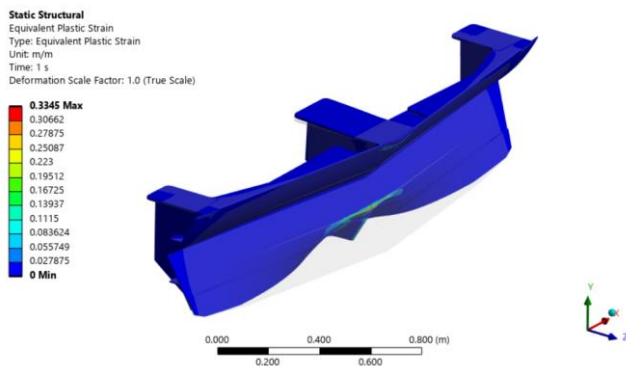


Fig. 15. The equivalent plastic strain of overload condition

## Fastener analysis

The fastening system has been analyzed using a finite element model, as shown in Fig. 6. This analysis focuses on the fastening system's capability. Fig. 17. shows that the bolt (M20) at the center fastener zone of the obstacle deflector experiences maximum stress at the bolts in the front row, exceeding the allowable limit of 940 MPa. However, the bolts in the rear row remain below the allowable limit, with a minimum safety factor of approximately 1.39. Similarly, Fig. 18. shows that the stress of the bolt at the right fastener zone (symmetric to the left side) reaches a maximum of 556 MPa, with a minimum safety factor of about 1.69. The results indicate that, under the analyzed overload conditions, the bolt in the front row at the middle fastener zone fails. However, the obstacle deflector will remain attached to the vehicle, as it is secured by the other 14 bolts as shown in Fig. 16.

According to the EN 15227 standard, in the case of overload, the obstacle deflector should not deform in a way that causes detachment from the vehicle. This indicates that, under the given analysis conditions, the obstacle deflector meets the overload requirements.

Note that the front-row bolts in the middle fastener zone exhibit stress levels exceeding the material yield limit under overload conditions. Although further design refinement is not necessary to meet the standard requirements, it could improve the strength of the attachment between the obstacle deflector and the chassis. Potential improvements include upgrading the bolt grade, increasing the number of fasteners in critical areas, or introducing load-distribution elements to alleviate peak stress concentrations. Moreover, fastener loosening due to service conditions may pose a long-term risk and should be taken into account in future design considerations.

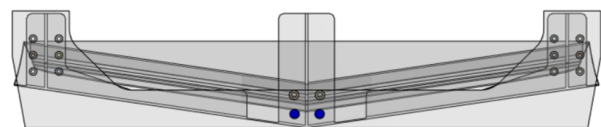


Fig. 16. Two bolts at the front row of the center fastener zone fails

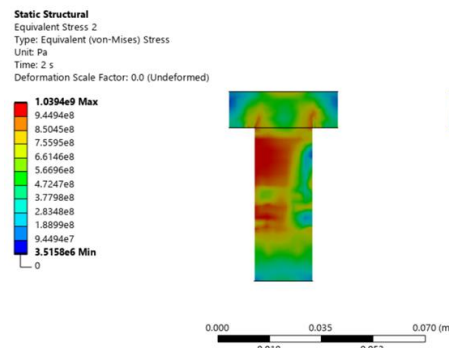


Fig. 17. The von Mises stress of bolts at the center fastener zone (section view)

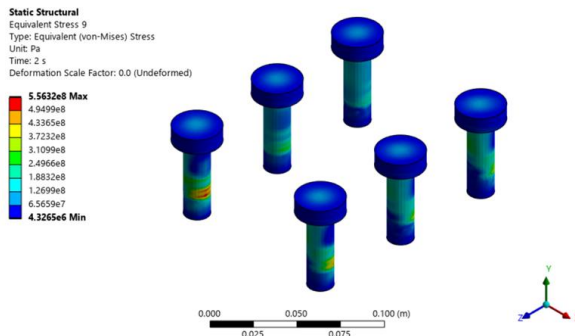


Fig. 18. The von Mises stress of side bolts at the right fastener zone

## V. CONCLUSION

This study analyzes the new design of the obstacle deflector requirements for the Aachen Rail Shuttle based on the EN 15227 standard. The study includes static load assessments at the center and side positions of the obstacle deflector, as well as static overload requirements. The analysis is divided into two parts: the structural response of the obstacle deflector under static load and the performance of the fastening system under overload conditions. The study begins by developing a finite element model and performing simulations using ANSYS to evaluate whether the obstacle deflector meets the standard requirements by maximum stress, strain energy, and minimum safety factors. The results indicate that the obstacle deflector fulfills all EN 15227 requirements. Furthermore, it can withstand a critical overload case of 600 kN. Although some fastening system components may fail, other components continue to support the obstacle deflector, preventing detachment from the ARS. This confirms that the obstacle deflector meets the intended design objectives. Additionally, the new design successfully relocates the obstacle deflector beneath the chassis, eliminating interference with the buffer operation.

As the present study is based entirely on numerical simulation, experimental validation was not conducted. Future experimental testing is recommended to further validate the findings of this study.

## ACKNOWLEDGMENT

The authors would like to express my sincere gratitude to the Institute for Rail Vehicles, RWTH Aachen University, for providing valuable data of the Aachen rail shuttle. I also extend my appreciation to all the Academic supervisors and professors who generously offered their guidance and expertise in reviewing this research. Your contributions have been instrumental in enhancing the development of rail vehicles.

## REFERENCES

[1] C. Schindler, "The Aachen Rail Shuttle ARS - Autonomous and energy self-sufficient feeder transport," *Journal of Rail Transport Planning & Management*, vol. 21, 100299, Feb. 2022.

- [2] EN 15227:2020 – Railway applications – Crashworthiness requirements for railway vehicle bodies, European Committee for Standardization (CEN), Brussels, Belgium, 2020.
- [3] N. Prasomsuk, S. Winkelheide, and C. Schindler, "Crashworthiness Design of a Light Commuter Rail Vehicle Operating on Secondary Lines," in *Proceedings of the 4th International Railway Symposium Aachen*, Aachen, Germany, 2023.
- [4] M. Boos and S. Brendel, "Obstacle deflector for a rail vehicle," European Patent EP3575178A1, Dec. 4, 2019.
- [5] M. Taguchi, A. Sano, T. Yamada, H. Kumamoto, S. Yagi, and M. Tomizawa, "Obstacle deflector of railcar," U.S. Patent 9,027,485 B2, May 12, 2015.
- [6] R. Duella, "Obstacle deflector for a front carriage of a train," European Patent EP1930227A1, Jun. 11, 2008.
- [7] S. Li, Z. Zheng, and J. Yu, "Mechanical analysis of a cowcatcher for a high-speed train in crashing," *Appl. Mech. Mater.*, vol. 437, pp. 18–23, 2013.
- [8] Y. Guo, L. Zhang, W. Dou, Y. Zhu, and H. Zhang, "Static strength and crashworthiness analysis of a train cowcatcher at a running speed of 160 km/h," *High-speed Railway*, vol. 1, no. 4, pp. 258–264, 2023.
- [9] EN 12663-1:2021 – Railway applications – Structural requirements of railway vehicle bodies – Part 1: Locomotives and passenger rolling stock (and alternative method for freight wagons), European Committee for Standardization (CEN), Brussels, Belgium, 2021.
- [10] V. Milovanović, D. Arsić, M. Milutinović, M. Živković, and M. Topalović, "A comparison study of fatigue behavior of S355J2+N, S690QL and X37CrMoV5-1 steel," *Metals*, vol. 12, no. 7, p. 1199, 2022. DOI: 10.3390/met12071199.
- [11] R. Redondo and A. Mehmanparast, "Numerical analysis of stress distribution in offshore wind turbine M72 bolted connections," *Metals*, vol. 10, no. 5, p. 689, 2020.
- [12] U. Fischer, A. Kötter, *Mechanical and Metal Trades Handbook*, 3rd ed. Haan-Gruiten, Germany: Verlag Europa-Lehrmittel, 2015, p. 216.



# A Review on Blue Economy's Dual Role in Reducing CO<sub>2</sub> Pollution and Achieving SDGs

JAYDEEP A. KARMUR<sup>1,a)</sup>, MAHIPALSINH B. PARMAR<sup>1,b)</sup>, KEVAL H. JODHANI<sup>1,c)</sup>  
AND NITESH GUPTA<sup>1,d)</sup>

## Author Affiliations

<sup>1</sup>Department of Civil Engineering, Institute of Technology, Nirma University, Ahmedabad, 382481, Gujarat, India(+91).

## Author Emails

<sup>a)</sup>jaydeepkarmur9@gmail.com , 22BCL040@nirmauni.ac.in

<sup>b)</sup>mahipalsinhbparmar1910@gmail.com, 22BCL050@nirmauni.ac.in

<sup>c)</sup>jodhanikeval@gmail.com, keval.jodhani@nirmauni.ac.in

<sup>d)</sup>niteshrasz@gmail.com , nitesh.gupta@nirmauni.ac.in

**Abstract.** The Blue Economy has emerged as a fundamental framework for promoting sustainable development, particularly focusing on the reduction of ocean pollution and the mitigation of carbon dioxide (CO<sub>2</sub>) emissions linked to the exploitation of marine resources. Human activities, including industrial discharges, agricultural runoff, and unregulated coastal development, are significant contributors to ocean pollution, with estimates suggesting they account for around 80% of the total. Research demonstrates that the sustainable exploitation of ocean resources, as envisaged by the Blue Economy, can drive economic growth and enhance livelihoods while preserving the health of marine ecosystems. Furthermore, the application of artificial intelligence in managing marine ecosystems has shown potential in tackling climate-related threats and boosting the resilience of coastal communities. In addition, the Blue Economy emphasizes social equity and environmental sustainability, which aligns with global initiatives to address climate change. It underscores the importance of innovative financing mechanisms and effective institutional arrangements. Nevertheless, implementing Blue Economy initiatives presents challenges, particularly regarding social equity and the risks of overfishing and pollution. The competing interests of economic development and environmental conservation pose substantial barriers to achieving the objectives of the Blue Economy. Consequently, a holistic approach that integrates stakeholder perspectives and long-term impact assessments is crucial for effectively converging climate change mitigation strategies with the Blue Economy framework. Ultimately, the Blue Economy offers a transformative pathway towards sustainable management of ocean resources, addressing pollution and CO<sub>2</sub> emissions while contributing to Global Sustainability Goals.

**Index Terms:** Blue economy, CO<sub>2</sub> Pollution, SDG, Ocean Pollution, Blue Carbon Ecosystems

## I. INTRODUCTION

The Earth's surface is predominantly covered by water, with approximately 71% of the planet's area consisting of oceans and seas. This vast expanse of marine resources presents significant opportunities for sustainable utilization, which can serve as a powerful strategy for nations to combat unemployment, poverty, and food insecurity. The concept of the blue economy emerges as a viable framework for harnessing these resources in a systematic and sustainable manner, thereby contributing to national development and enhancing economic resilience. The Blue Economy, often referred to as the "ocean economy" or "Marine economy," encompasses a wide range of activities that leverage ocean resources to generate wealth while ensuring environmental sustainability. This multifaceted approach not only addresses basic human necessities such as food, transportation, and livelihoods but also provides access to essential minerals and metals found in marine environments. By focusing on sustainable practices, the blue economy can lay a strong

foundation for nation-building activities, fostering economic soundness and resilience in the face of global challenges. The significance of ocean-based economic development was underscored during the Rio+20 United Nations Conference, where the need for sustainable management of marine resources was emphasized as a critical component of global economic strategies. The Blue Economy aligns with the United Nations Sustainable Development Goals (SDGs), particularly Goal 14, which aims to conserve and sustainably use the oceans, seas, and marine resources for sustainable development. This alignment highlights the potential of the blue economy to contribute to broader global objectives while addressing local socio-economic issues.

Research indicates that the Blue Economy can play a pivotal role in generating wealth and promoting national development. By investing in sustainable marine industries, countries can create job opportunities, enhance food security, and stimulate economic growth. According to the United Nations Environment Programme (UNEP), the annual economic value of the Blue economy is estimated at \$2.5 trillion, positioning it as the world's seventh-largest economy



(Santos, 2023). Moreover, the Blue Economy offers a pathway to mitigate environmental challenges, such as carbon emissions and air pollution. By promoting sustainable practices in marine industries, countries can reduce their carbon footprint and contribute to global efforts to combat climate change. The integration of renewable energy sources, such as offshore wind and tidal energy, into the Blue Economy can further enhance its environmental benefits. These initiatives not only support the transition to a low-carbon economy but also create new economic opportunities in emerging sectors.

This research aims to explore the Blue Economy from various perspectives, focusing on its potential to generate wealth, foster national development, and address environmental challenges. By examining the interconnectedness of economic activities and environmental sustainability, this study seeks to provide insights into the mechanisms through which the Blue Economy can contribute to a more resilient and equitable future. The findings will highlight the importance of collaborative efforts among stakeholders, including governments, private sector actors, and local communities, in realizing the full potential of the Blue Economy.

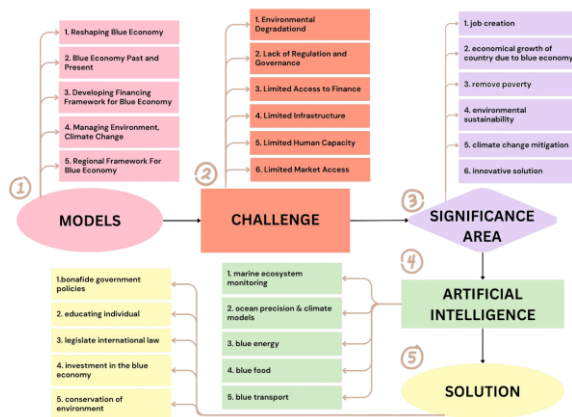


Fig. 1. This image represents a systematic framework addressing challenges, models, significance areas, and solutions within the context of the Blue Economy. It employs a structured flowchart approach, categorizing different aspects of the Blue Economy into five distinct domains.

Fig. 1. presents a structured framework analyzing the Blue Economy through interconnected aspects, including models, challenges, significance, artificial intelligence, and solutions. It identifies key models such as Marine ecosystem monitoring, Blue energy, Blue food, and Transport, which serve as foundational elements for sustainable economic activities. The primary challenges include environmental degradation, lack of regulation, limited access to finance, and infrastructure deficiencies, which hinder the effective implementation of Blue Economy initiatives. The significance of the Blue Economy is highlighted through its potential to drive job creation, economic growth, poverty alleviation, environmental sustainability, and Climate Change Mitigation. Artificial Intelligence is proposed as a

critical tool for addressing these challenges, with solutions emphasizing policy development, education, international legal frameworks, investment, and environmental conservation.

The Blue Economy faces significant challenges from CO<sub>2</sub> and air pollution as shown in Fig. 2. First, higher CO<sub>2</sub> levels cause ocean acidification, degrading marine ecosystems and affecting coral reefs and shellfish, crucial for biodiversity and fisheries (Doney et al., 2012). Second, fish stock deterioration is worsened by nutrient runoff-induced hypoxia, threatening fishing communities' livelihoods. Third, polluted coastal areas diminish tourism appeal, leading to economic losses in local economies reliant on marine tourism. Fourth, air pollution generates health issues for coastal populations, increasing healthcare costs and reducing productivity, further straining the Blue Economy. Lastly, inadequate enforcement of environmental regulations hinders progress toward a sustainable blue economy (DEB et al., 2023).

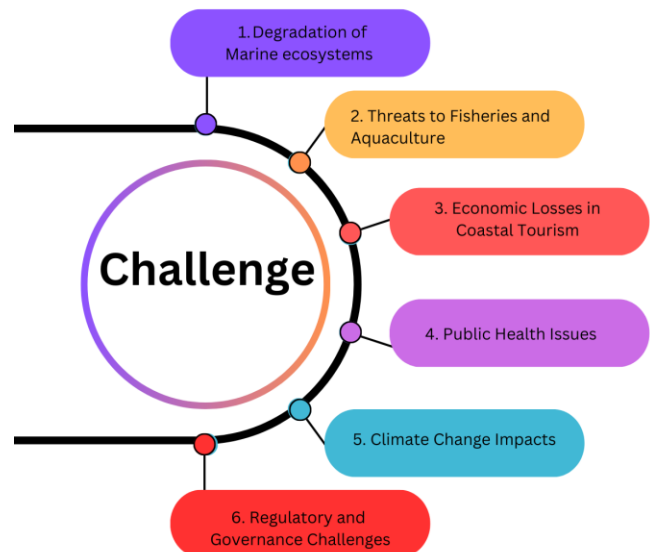


Fig. 2. Some challenges for blue economy due co2 and pollution.

## II. METHODOLOGY

### 1: THE ROLE OF BLUE CARBON ECOSYSTEMS IN MITIGATING CO<sub>2</sub> EMISSIONS.

Blue Carbon Ecosystems, which include mangroves, salt marshes, and seagrasses, play a critical role in mitigating CO<sub>2</sub> emissions through their capacity to sequester carbon. These ecosystems are highly efficient at capturing atmospheric carbon dioxide and storing it in both plant biomass and sediments, making them vital components of the global carbon cycle. Research indicates that Blue Carbon Ecosystems can sequester carbon at rates significantly higher than terrestrial forests, thus providing a potent natural solution to climate change (Alongi, 2012). The preservation and restoration of Blue Carbon habitats not only enhance carbon storage but also contribute to biodiversity conservation and the resilience of coastal communities

symbiosis models underscores the economic potential of reusing CO2 emissions(Lakshminarayana et al., 2022). In conclusion, the Bibliometric Network Visualization illustrates CO2's crucial role in linking environmental and economic factors vital for global sustainability.

Fig.4. presents The bubble graph depicting CO2 research papers published over the years illustrates a significant upward trend in scholarly activity. Beginning with just 1 publication in 1946, output remained modest, with peaks of 36 publications in 1981 and 1982. A notable shift occurs in the early 2000s, initiating accelerated research output. From 2000 to 2010, publications increased from 48 to 570, a growth of approximately 1,187.5% (Lindawati&Meiryani, 2024). This trend continued, peaking at 8,822 publications in 2024. Notably, from 2017 to 2018, publications rose from 3,094 to 5,068, reflecting a 63.7% increase. Between 2020 and 2021, numbers climbed from 4,417 to 5,315, representing about 20.3% growth. However, the data projects a sharp decline in expected publications for 2025, with a forecast of 2,266, a decrease of approximately 74.2% from 2024. This graph illustrates not only the rise in CO2 research but also fluctuations that indicate periods of intense academic focus and potential future decline, underscoring the growing significance of CO2 research amid climate change and sustainability concerns (Abeydeera et al., 2019).

Fig. 4. Bubble chart representation of CO<sub>2</sub> data.

The world map graph of CO2 research papers published by country offers a visual overview of global contributions to discussions on carbon dioxide and climate change. As shown in Fig.5, Each country's size or shading reflects the volume of publications, highlighting geographic disparities in

research output. China leads with 10,318 publications, driven by urgent air quality and climate change concerns. The United States follows with 1,752 publications, indicating strong academic activity supported by established research institutions. India ranks third with 871 publications, reflecting increasing engagement in emerging economies. Significant contributors like Germany, South Korea, and Japan have publications ranging from 540 to 468. Countries like the United Kingdom (463), Italy (423), and Spain (380) show meaningful contributions, underscoring a European research concentration. Others, including Iran (336) and France (309), participate actively, while nations like Brazil (215), Canada (254), Saudi Arabia (201), and Australia (195) reflect diverse global interest. Many countries, such as South Africa (49) and Finland (41), published fewer than 100 papers, indicating disparities in research focus.

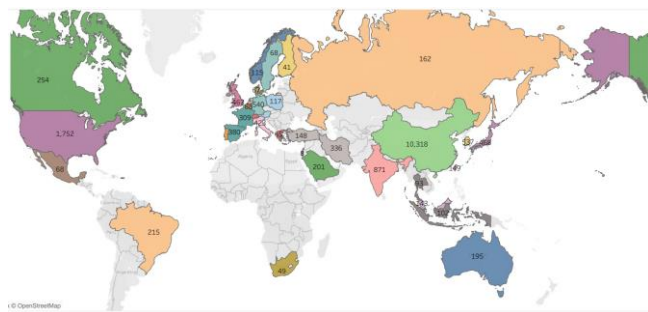


Fig. 5. Graph of Country wise Research paper published of CO<sub>2</sub>

## 2. The Impact of Marine Resource Management on Air Quality.

The relationship between Marine Resource Management and Air Quality is multifaceted, influenced by various ecological, economic, and social factors. Effective marine resource management, particularly through community-based approaches, can significantly enhance environmental quality, including air quality. For instance, the integration of Traditional Marine Management practices with modern conservation strategies has shown promise in improving coral reef conditions, which indirectly contributes to better air quality by maintaining marine biodiversity and ecosystem services. The health of marine ecosystems is crucial as they play a vital role in carbon sequestration, thus influencing atmospheric carbon levels and air quality (Beaumont et al., 2014). Additionally, the socio-economic benefits derived from well-managed marine resources can lead to reduced reliance on polluting industries, thereby improving air quality (Hsiao et al., 2021).

## 3. Economic Implications of Transitioning to a Blue Hydrogen Economy.

The transition to a Blue Hydrogen economy presents significant economic implications, particularly in the context of Carbon Capture and Storage (CCS) technologies. Blue hydrogen, produced primarily through Steam Methane Reforming (SMR) combined with CCS, offers a transitional

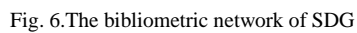
pathway towards a more sustainable hydrogen economy. This approach allows for the utilization of existing natural gas infrastructure while mitigating greenhouse gas emissions, thus providing a cost-effective solution during the transition to Green Hydrogen, which relies on renewable energy sources (Wu et al., 2024). Furthermore, the integration of CCS with Blue Hydrogen production can significantly reduce the carbon footprint, making it a competitive option as countries strive to meet climate targets (Fazioli & Pantaleone, 2021). However, the economic feasibility of Blue Hydrogen is heavily influenced by methane leakage rates during production and transportation, which can undermine its climate benefits and economic attractiveness. Moreover, the development of a Blue Hydrogen economy necessitates substantial investments in infrastructure and technology, which could lead to stranded assets if the transition to Green Hydrogen accelerates faster than anticipated (Hauglustaine et al., 2022). The potential for Blue Hydrogen to decarbonize heavy industries, such as oil sands operations in Canada, further underscores its role as a bridge in the energy transition (Sadeq et al., 2024).

## 4. Governance and Policy Frameworks for Sustainable Blue Economy Practices.

Governance and Policy Frameworks are essential for the effective implementation of sustainable Blue Economy practices, which aim to balance economic growth with environmental stewardship in marine and coastal areas. A critical aspect of these frameworks is the need for coherence and integration across various policies that govern marine resources. For instance, Voyer et al. emphasize the importance of developing a common understanding of the Blue Economy while allowing flexibility for countries to adapt frameworks to their specific circumstances and objectives (Luna, n.d.-a). Transboundary Cooperation is another critical element in establishing effective governance frameworks. Guerreiro notes that initiatives at the Large Marine Ecosystem (LME) level in the Atlantic and Indian Oceans are fostering collaborative approaches to Marine Spatial Planning, which can enhance the sustainability of marine resources (Frazão Santos et al., 2018). Such collaborative frameworks not only promote sustainable practices but also facilitate the sharing of best practices among nations.

Fig. 6. Presents The bibliometric network visualization graph illustrates interconnections among research concepts such as potable water, performance, innovation, energy, education, psychology, communication, corporate social responsibility (CSR), industry, rivers, biomass, and public health. It reveals relationships among these keywords, showing their relevance across disciplines. Education and psychology reflect socio-behavioral aspects vital for public awareness, while communication facilitates knowledge dissemination and collaborative efforts to address global challenges.





The bubble chart illustrates the exponential growth of research output over time. The x-axis represents the year, ranging from 1990 to 2020. The y-axis represents the count of publications, ranging from 0 to 1750. The bubbles are labeled with their respective counts, showing a sharp increase starting around 2005.

Year	Count
1990	1
1991	1
1992	1
1993	1
1994	1
1995	1
1996	1
1997	1
1998	1
1999	1
2000	1
2001	1
2002	1
2003	1
2004	1
2005	1
2006	1
2007	1
2008	1
2009	1
2010	1
2011	1
2012	1
2013	1
2014	1
2015	1
2016	1
2017	1
2018	1
2019	1
2020	1
2021	1
2022	1
2023	1
2024	1
2025	1
2026	1
2027	1
2028	1
2029	1
2030	1
2031	1
2032	1
2033	1
2034	1
2035	1
2036	1
2037	1
2038	1
2039	1
2040	1
2041	1
2042	1
2043	1
2044	1
2045	1
2046	1
2047	1
2048	1
2049	1
2050	1
2051	1
2052	1
2053	1
2054	1
2055	1
2056	1
2057	1
2058	1
2059	1
2060	1
2061	1
2062	1
2063	1
2064	1
2065	1
2066	1
2067	1
2068	1
2069	1
2070	1
2071	1
2072	1
2073	1
2074	1
2075	1
2076	1
2077	1
2078	1
2079	1
2080	1
2081	1
2082	1
2083	1
2084	1
2085	1
2086	1
2087	1
2088	1
2089	1
2090	1
2091	1
2092	1
2093	1
2094	1
2095	1
2096	1
2097	1
2098	1
2099	1
2100	1
2101	1
2102	1
2103	1
2104	1
2105	1
2106	1
2107	1
2108	1
2109	1
2110	1
2111	1
2112	1
2113	1
2114	1
2115	1
2116	1
2117	1
2118	1
2119	1
2120	1
2121	1
2122	1
2123	1
2124	1
2125	1
2126	1
2127	1
2128	1
2129	1
2130	1
2131	1
2132	1
2133	1
2134	1
2135	1
2136	1
2137	1
2138	1
2139	1
2140	1
2141	1
2142	1
2143	1
2144	1
2145	1
2146	1
2147	1
2148	1
2149	1
2150	1
2151	1
2152	1
2153	1
2154	1
2155	1
2156	1
2157	1
2158	1
2159	1
2160	1
2161	1
2162	1
2163	1
2164	1
2165	1
2166	1
2167	1
2168	1
2169	1
2170	1
2171	1
2172	1
2173	1
2174	1
2175	1
2176	1
2177	1
2178	1
2179	1
2180	1
2181	1
2182	1
2183	1
2184	1
2185	1</

Presents The world map graph displays the number of research papers on Sustainable Development Goals (SDGs) by country, illustrating scholarly activity related to sustainability. Each country is highlighted, with shading or size reflecting publication volume, allowing for an assessment of global engagement in SDG research. India leads with 653 publications, reflecting its commitment to sustainability. The United Kingdom (338) and United States (334) also show significant output, showcasing strengths in sustainability research. Spain (267), Italy(223), and

A world map illustrating the distribution of 1000 languages across various countries. Each country is colored and labeled with a number representing the count of languages spoken there. The map shows a high density of languages in Europe, Africa, and Asia, with lower counts in North and South America and Australia.

Continent	Country	Language Count
North America	USA	334
	Canada	134
South America	Brazil	181
	Argentina	22
Europe	Germany	1
	France	1
Africa	Nigeria	20
	Ethiopia	10
Asia	China	507
	India	858
Oceania	Australia	179
	New Zealand	1

The interplay between maritime security and environmental sustainability is increasingly recognized as a critical area of focus in maritime governance. Maritime security encompasses a wide range of issues, including illegal fishing, piracy, and environmental degradation, all of which can significantly impact the sustainability of marine ecosystems (Li, 2023). As maritime activities expand, the need for a comprehensive approach that integrates security measures with environmental stewardship becomes paramount. The case of Indonesia illustrates this point, where a comprehensive maritime security agenda has begun to incorporate elements of sustainable development, acknowledging the interconnectedness of security and environmental health (Purba & Simanjuntak, 2024). Integrating environmental science into maritime education can cultivate a workforce that understands the ecological implications of their actions and is equipped to implement sustainable practices (Simanjuntak et al., 2024a). This holistic approach to maritime education not only prepares individuals for their professional roles but also empowers them to advocate for environmental sustainability within the maritime sector (Simanjuntak et al., 2024b).

Future research on the Blue Economy should adopt a comprehensive and integrative approach that combines technological innovation, economic analysis, interdisciplinary insights, and long-term ecological evaluation to ensure sustainable marine resource management. Enhancing data and monitoring capabilities remains a critical priority; advanced remote sensing



technologies and artificial intelligence must be utilized to build robust data collection systems that accurately assess the health of marine ecosystems and dynamically track the impact of Blue Economy initiatives (Ajeigbe & Ganda, 2024). Concurrently, evaluating economic impact models is essential; studies must quantify how the adoption of sustainable marine practices influences local economies and job creation while also elucidating the interactions between marine resource management and other economic sectors, thereby paving the way for integrated and informed policy-making. In parallel, adopting interdisciplinary approaches that incorporate perspectives from economics, marine biology, and environmental science is imperative for comprehensively understanding the complex relationships between economic growth and ecological integrity. Such integration fosters the development of holistic frameworks that are capable of addressing the multifaceted challenges associated with sustainable marine management (Zhong, 2019).

Effective implementation of the Blue Economy calls for a holistic framework that integrates robust regulatory structures, innovative financing models, vigorous research and development, active community engagement, and an unwavering commitment to social equity. Governments must craft comprehensive, flexible regulatory frameworks that enforce stringent environmental standards targeting pollution from industrial discharges and agricultural runoff, while fiscal measures such as environmental taxes compel businesses to adopt sustainable practices (Michael et al., n.d.). Simultaneously, the development of innovative financing mechanisms through public-private partnerships and targeted investments in sectors such as eco-tourism and blue energy is essential to mobilize resources, facilitate technology adoption, and ensure adherence to international environmental protocols. Continuous investment in research and development, particularly in areas like artificial intelligence for marine ecosystem monitoring, can drive adaptive management strategies, improve operational efficiencies, and enhance resilience against climate change. Equally important is the active engagement of local communities; policies that integrate community-based resource management ensure that local knowledge and needs are respected, thereby fostering stakeholder buy-in and promoting marine conservation through education and public awareness initiatives.

#### IV. RESULTS AND DISCUSSION

The Blue Economy framework demonstrates significant potential to address global challenges related to ocean pollution and CO<sub>2</sub> emissions while promoting sustainable development. Our analysis indicates that Blue Carbon ecosystems—Mangroves, salt marshes, and seagrasses—are vital in sequestering Carbon at rates surpassing terrestrial forests (Zarate-Barrera & Maldonado, 2015). Integrating traditional and modern management practices has shown promise in maintaining coral reefs, which in turn supports marine biodiversity and enhances ecosystem services vital

for air quality improvement (Rayfuse, 2015). Moreover, community-based resource management systems can minimize pollutants and further promote sustainable tourism, creating economic benefits while mitigating environmental harm (Aini, 2024). Transitioning to a Blue Hydrogen Economy is economically viable and can significantly reduce greenhouse gas emissions by utilizing carbon capture and storage technologies. (Bauer et al., 2022).

Our findings also highlight the need for comprehensive governance frameworks that integrate economic growth with environmental stewardship. Collaborative approaches, such as transboundary management at Large Marine Ecosystem levels, can enhance Marine Resource Sustainability (Elliott et al., 2023). Implementing holistic strategies that encompass diverse stakeholder perspectives will be vital in overcoming existing challenges and maximizing the benefits of ocean resources for current and future generations as shown in Fig.9.

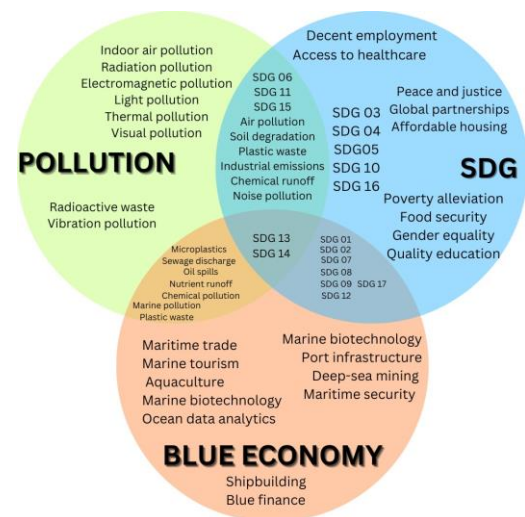


Fig. 9. Relations between Blue economy, SDG, CO<sub>2</sub>

The diagram illustrates the complex relationships among Pollution, the Blue Economy, and the Sustainable Development Goals (SDGs), highlighting the importance of environmental sustainability, economic resilience, and social equity.

The Sustainable Development Goals (SDGs), depicted in the blue domain, focus on environmental remediation, socioeconomic upliftment, and governance frameworks. The intersections of these domains reveal critical issues like industrial emissions, chemical runoff, and noise pollution, which impact marine industries and societal well-being. This necessitates comprehensive policy interventions that align economic development with ecological integrity.

#### V. CONCLUSION

In summary, the Blue Economy emerges as a

transformative framework that effectively intertwines Sustainable Development with Marine Resource Management, emphasizing the reduction of ocean pollution and the mitigation of carbon dioxide (CO<sub>2</sub>) emissions, promoting SDG 14 (Life Below Water) for Sustainable Marine Ecosystems. With an estimated 80% of Ocean Pollution stemming from human activities such as industrial discharges and agricultural runoff, the need for a holistic approach has never been more critical. By focusing on the sustainable exploitation of ocean resources, the Blue Economy not only fosters economic growth and livelihood enhancement but also prioritizes the health of marine ecosystems, ensuring resilience and biodiversity vital for achieving SDG 15 (Life on Land).

Blue Carbon Ecosystems and Blue Hydrogen are pivotal components of the Blue Economy, addressing climate change mitigation while posing limitations and policy challenges. Blue Carbon ecosystems—mangroves, salt marshes, and seagrass meadows—are among the most efficient natural carbon sinks, sequestering CO<sub>2</sub> through biomass creation and by storing carbon in waterlogged sediments. This process not only contributes to climate regulation but also enhances coastal protection and supports biodiversity. uncertainties regarding their long-term stability persist due to impacts from land-use changes, coastal development, and natural disturbances, which can lead to carbon leakage and complicate the valuation of carbon credits. Consequently, robust regulatory frameworks and active international cooperation are imperative to integrate blue carbon strategies into broader climate policies.

Despite its potential, the Blue Economy faces significant hurdles, including social equity concerns and the risks of overfishing. Implementation requires integrating diverse stakeholder perspectives and ensuring that initiatives align with environmentally sustainable practices. Addressing these obstacles is essential for meeting Global Sustainability targets and enhancing the resilience of Marine Ecosystems. Ultimately, adopting the Blue Economy framework can facilitate the transition toward a Sustainable Future, harmonizing Economic Development with Ecological Health.

The provided Fig. 10. illustrates a Conceptual Framework for the Blue Economy, emphasizing its core principles, objectives, mechanisms, outcomes, and associated global challenges. At the center of the framework lies the Sustainable use of ocean resources, which fosters Economic growth, environmental sustainability, and social equity (Luna, n.d.-b). These goals are supported by mechanisms such as sustainable practices (e.g., eco-tourism and renewable energy), innovative technologies (for instance, AI in marine management), and robust institutional frameworks (including collaboration and financing), which facilitate effective implementation.

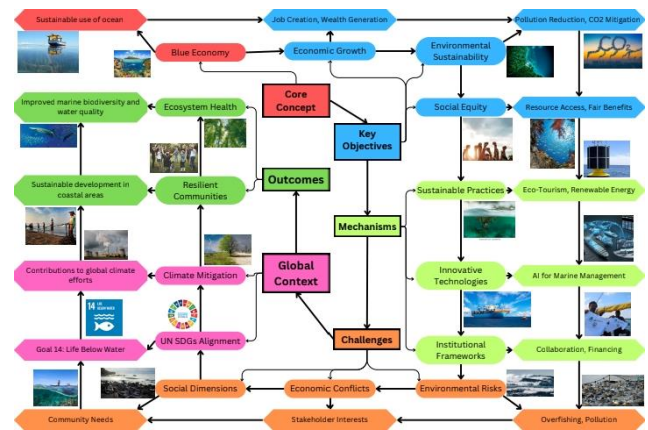


Fig. 10. Sustainable Ocean and Coastal Development Framework.

Nevertheless, multiple challenges hinder the successful implementation of Blue Economy initiatives, which can be grouped into social issues (addressing community needs), Economic conflicts (balancing stakeholder interests), and environmental threats (reducing overfishing and pollution) (Ahmed, 2024). These factors exist within a Global context, reinforcing the necessity for policies that harmonize ecological conservation with Economic Growth. Ultimately, the framework demonstrates the relationship between Sustainable Ocean Use and pollution reduction, ensuring that wealth generation does not harm marine ecosystems. By integrating scientific research, economic strategies, and policy-driven actions, the Blue Economy presents a multidimensional approach that seeks to reconcile industrial development with Marine conservation, thereby ensuring long-term socioeconomic resilience and Environmental protection.

Blue Carbon Ecosystems and Blue Hydrogen are emerging as two pivotal components within the Blue Economy framework, each offering unique benefits for climate change mitigation while presenting notable limitations and policy challenges. Blue Carbon Ecosystems—encompassing mangroves, salt marshes, and seagrass meadows—are among the most efficient natural carbon sinks. They sequester significant amounts of atmospheric CO<sub>2</sub> primarily through biomass investment and store carbon in waterlogged sediments, which reduces the risks of sudden carbon loss compared to terrestrial ecosystems. These ecosystems also contribute to coastal protection and biodiversity support, thereby enhancing local community resilience to extreme weather events. However, despite their high sequestration potential, uncertainties remain regarding their long-term stability and capacity variability. Factors such as land-use change, coastal development, and natural disturbances can undermine the permanence of stored carbon, raising concerns about carbon leakage and overestimation of carbon credits. Additionally, the fragmented institutional arrangements and the complex biophysical dynamics underlying these habitats pose

significant policy challenges. Robust regulatory frameworks and international cooperation are needed to ensure sustainable conservation, restoration, and management practices that can integrate blue carbon strategies into broader climate mitigation policies.

In parallel, Blue Hydrogen has gained recognition as a transitional pathway toward a more sustainable energy mix, particularly under frameworks seeking rapid decarbonization. Produced primarily via steam methane reforming (SMR) combined with carbon capture and storage (CCS), blue hydrogen leverages existing natural gas infrastructure, making it a potentially cost-effective alternative to green hydrogen in the short term. This production method can effectively reduce greenhouse gas emissions if key parameters—such as methane leakage during extraction, processing, and transportation—are rigorously controlled. However, the benefits of blue hydrogen are highly contingent on the efficiency of CCS technologies and the robustness of upstream emission control. Methane is a potent greenhouse gas; any leakage in the production process can offset the emission reductions achieved through CO<sub>2</sub> capture, thus undermining the overall climate benefits. Furthermore, substantial capital investments and technological advancements are required to scale blue hydrogen production, making the economic feasibility uncertain. Policy interventions, including economic incentives, stringent emission monitoring, and an aligned international regulatory framework, are essential to manage risks and foster the development of a blue hydrogen economy.

Integrating these two approaches within the Blue Economy necessitates a holistic strategy that addresses both environmental and socio-economic dimensions. While blue carbon ecosystems provide critical ecosystem services and natural climate solutions, their vulnerability to anthropogenic pressures requires continuous monitoring, adaptive management, and coordinated policy action. Similarly, blue hydrogen has the potential to bridge the gap toward a low-carbon economy, yet its full benefits can only be realized if regulatory frameworks effectively mitigate methane leakage and ensure investment in advanced CCS technologies. In summary, both blue carbon and blue hydrogen are promising pathways; however, scientific uncertainties, technical risks, and policy challenges underscore the need for integrated governance models that balance economic development with stringent environmental stewardship.

## REFERENCES

- Abeydeera, L. H. U. W., Mesthrige, J. W., & Samarasinghalage, T. I. (2019). Global research on carbon emissions: A scientometric review. In *Sustainability (Switzerland)* (Vol. 11, Issue 14). MDPI. <https://doi.org/10.3390/su11143972>
- Ahmed, R. (2024). *Fostering Sustainable Growth through the Blue Economy: Balancing Prosperity and Marine Conservation*. <https://doi.org/10.20944/preprints202407.2584.v1>
- Aini, Y. N. (2024). Sustainable Tourism in Southeast Asia: Balancing Economic Growth, Employment, and Carbon Emissions Through Evidence-Based Strategies. *Jurnal Kepariwisata Indonesia: Jurnal Penelitian Dan Pengembangan Kepariwisata Indonesia*, 18(1), 157–174. <https://doi.org/10.47608/jki.v18i12024.157-174>
- Ajeigbe, K. B., & Ganda, F. (2024). The Impact of Pollution and Carbon Emission Control on Financial Development, Environmental Quality, and Economic Growth: A Global Analysis. *Sustainability*, 16(20), 8748. <https://doi.org/10.3390/su16208748>
- Al Shammre, A. S., Benhamed, A., Ben-Salha, O., & Jaidi, Z. (2023). Do Environmental Taxes Affect Carbon Dioxide Emissions in OECD Countries? Evidence from the Dynamic Panel Threshold Model. *Systems*, 11(6). <https://doi.org/10.3390/systems11060307>
- Alongi, D. M. (2012). Carbon sequestration in mangrove forests. In *Carbon Management* (Vol. 3, Issue 3, pp. 313–322). <https://doi.org/10.4155/cmt.12.20>
- Bauer, C., Treyer, K., Antonini, C., Bergerson, J., Gazzani, M., Gencer, E., Gibbins, J., Mazzotti, M., McCoy, S. T., McKenna, R., Pietzcker, R., Ravikumar, A. P., Romano, M. C., Ueckerdt, F., Vente, J., & van der Spek, M. (2022). On the climate impacts of blue hydrogen production. *Sustainable Energy and Fuels*, 6(1), 66–75. <https://doi.org/10.1039/d1se01508g>
- Beaumont, N., Pendleton, L., Boyle Virginia Tech, K., Börger, T., Beaumont, N. J., Boyle, K. J., Cooper, P., Fletcher, S., Haab, T., Hanemann, M., Hooper, T. L., Salman Hussain, S., Portela, R., Stithou, M., Stockill, J., Taylor, T., & Austen, M. C. (2014). *Incorporating Ecosystem Services in Marine Planning: The Role of Valuation*. <https://www.researchgate.net/publication/259570105>
- DEB, S. K., DAS, M. K., VOUMIK, L. C., NAFI, S. Md., RASHID, M., & ESQUIVIAS, M. A. (2023). THE ENVIRONMENTAL EFFECTS OF TOURISM: ANALYZING THE IMPACT OF TOURISM, GLOBAL TRADE, CONSUMPTION EXPENDITURE, ELECTRICITY, AND POPULATION ON ENVIRONMENT IN LEADING GLOBAL TOURIST DESTINATIONS. *GeoJournal of Tourism and Geosites*, 51(4 supplement), 1703–1716. <https://doi.org/10.30892/gtg.514spl11-1166>
- Doney, S. C., Ruckelshaus, M., Emmett Duffy, J., Barry, J. P., Chan, F., English, C. A., Galindo, H. M., Grebmeier, J. M., Hollowed, A. B., Knowlton, N., Polovina, J., Rabalais, N. N., Sydeman, W. J., & Talley, L. D. (2012). Climate change impacts on marine ecosystems. *Annual Review of Marine Science*, 4, 11–37. <https://doi.org/10.1146/annurev-marine-041911-111611>
- Elliott, M., Borja, Á., & Cormier, R. (2023). Managing marine resources sustainably – Ecological, societal



- and governance connectivity, coherence and equivalence in complex marine transboundary regions. *Ocean and Coastal Management*, 245. <https://doi.org/10.1016/j.ocecoaman.2023.106875>
- Fazioli, R., & Pantaleone, F. (2021). Macroeconomic factors influencing public policy strategies for blue and green hydrogen. *Energies*, 14(23). <https://doi.org/10.3390/en14237938>
- Frazão Santos, C., Agardy, T., Andrade, F., Crowder, L. B., & Ehler, C. N. (2018). *Major challenges in developing marine spatial planning 1 2*. <https://www.sciencedirect.com/science/article/pii/S0308597X18306213>
- Hauglustaine, D., Paulot, F., Collins, W., Derwent, R., Sand, M., & Boucher, O. (2022). Climate benefit of a future hydrogen economy. *Communications Earth and Environment*, 3(1). <https://doi.org/10.1038/s43247-022-00626-z>
- Hsiao, C. Y., Kuo, C. M., & Tuan, C. L. (2021). Island Ecological Tourism: Constructing Indicators of the Tourist Service System in the Penghu National Scenic Area. *Frontiers in Ecology and Evolution*, 9. <https://doi.org/10.3389/fevo.2021.708344>
- Lakshminarayana, R., Vijay, K., Ambedkar, R., Rao, A. R., & Ravishankar, G. A. (2022). Biological activities and health benefits of seaweed carotenoids with special reference to fucoxanthin. In *Sustainable Global Resources of Seaweeds Volume 2: Food, Pharmaceutical and Health Applications* (pp. 539–558). Springer International Publishing. [https://doi.org/10.1007/978-3-030-92174-3\\_29](https://doi.org/10.1007/978-3-030-92174-3_29)
- Li, L. (2023). Building Up a Sustainable Path to Maritime Security: An Analytical Framework and Its Policy Applications. *Sustainability (Switzerland)*, 15(8). <https://doi.org/10.3390/su15086757>
- Lindawati, A. S. L., & Meiryani. (2024). A bibliometric analysis on the research trends of global climate change and future directions. In *Cogent Business and Management* (Vol. 11, Issue 1). Cogent OA. <https://doi.org/10.1080/23311975.2024.2325112>
- Luna, F. (n.d.-a). *Harnessing Blue Economy Potential for Sustainable Development: Navigating Opportunities and Challenges*.
- Luna, F. (n.d.-b). *Harnessing Blue Economy Potential for Sustainable Development: Navigating Opportunities and Challenges*.
- Michael, E., Simangunsong, H., Hamdi, M. F., Latifah, A., Lubis, R., Febrian, F., & Sumardiana, B. (n.d.). *Legal Implications of Deep Seabed Mining on the Sustainability of the Blue Economy in Indonesia*.
- Purba, D., & Simanjuntak, M. B. (2024). Sustainable maritime education: Integrating environmental science for global competence. *JPBI (Jurnal Pendidikan Biologi Indonesia)*, 10(1), 310–319. <https://doi.org/10.22219/jpbi.v10i1.32588>
- Rayfuse, R. (2015). Research handbook on international marine environmental law. In *Research Handbook on International Marine Environmental Law*. Edward Elgar Publishing Ltd. <https://doi.org/10.4337/9781781004777>
- Sadeq, A. M., Homod, R. Z., Hussein, A. K., Togun, H., Mahmoodi, A., Isleem, H. F., Patil, A. R., & Moghaddam, A. H. (2024). Hydrogen energy systems: Technologies, trends, and future prospects. In *Science of the Total Environment* (Vol. 939). Elsevier B.V. <https://doi.org/10.1016/j.scitotenv.2024.173622>
- Santos, T. (2023). Blue Economy and Sustainable Development Beyond Boxes. In *Sustainable Development Goals Series: Vol. Part F2766* (pp. 199–211). Springer. [https://doi.org/10.1007/978-3-031-24888-7\\_16](https://doi.org/10.1007/978-3-031-24888-7_16)
- Simanjuntak, M. B., Rafli, Z., & Utami, S. R. (2024a). Enhancing maritime education for ocean sustainability: a multidisciplinary approach. *BIO Web of Conferences*, 106. <https://doi.org/10.1051/bioconf/202410602006>
- Simanjuntak, M. B., Rafli, Z., & Utami, S. R. (2024b). Enhancing maritime education for ocean sustainability: a multidisciplinary approach. *BIO Web of Conferences*, 106. <https://doi.org/10.1051/bioconf/202410602006>
- Uddin, M. J., Rahman, A., Kibria, A. M. E., & Ali, A. Z. (2023). Soil organic carbon stocks in the blue carbon habitats of Bangladesh. *Dhaka University Journal of Biological Sciences*, 32(2), 179–188. <https://doi.org/10.3329/dujbs.v32i2.67677>
- Wu, W., Zhai, H., & Holubnyak, E. (2024). Technological evolution of large-scale blue hydrogen production toward the U.S. Hydrogen Energy Earthshot. *Nature Communications*, 15(1). <https://doi.org/10.1038/s41467-024-50090-w>
- Zarate-Barrera, T. G., & Maldonado, J. H. (2015). Valuing blue carbon: Carbon sequestration benefits provided by the marine protected areas in Colombia. *PLoS ONE*, 10(5). <https://doi.org/10.1371/journal.pone.0126627>
- Zhong, H. (2019). Exploitation and utilization of marine resources and protection of marine ecology. *IOP Conference Series: Earth and Environmental Science*, 369(1). <https://doi.org/10.1088/1755-1315/369/1/012009>



# Sugarcane Leaf Disease Classification Using a Hybrid ReXNet-Based Model and SVMs

Krankamon Phukhronghin<sup>1, a)</sup> Kanit Manatura<sup>1</sup> Natthapong Prapakarn<sup>1</sup>  
Nuttapong Wongbubpa<sup>1</sup> and Kritsada Tasuntia<sup>1</sup>

<sup>1</sup> Faculty of Engineering and Technology,  
Rajamangala University of Technology Isan, 744 Suranarai Road, Nai Mueang Subdistrict,  
Mueang District, Nakhon Ratchasima, 30000, Thailand.

<sup>a)</sup> Corresponding author: Krankamon.ph@rmuti.ac.th

**Abstract.** This study proposes a hybrid model integrating ReXNet, a lightweight convolutional neural network (CNN), with support vector machines (SVMs) for sugarcane leaf disease classification. The hybrid model leverages ReXNet's depthwise separable convolutions and channel scaling to extract hierarchical features, while SVM kernels (linear, polynomial, and RBF) optimize decision boundaries for efficient classification. Evaluated on a dataset of sugarcane leaf images across five classes (Healthy, Mosaic, Red Rot, Rust, Yellow Leaf), the model demonstrates strong performance metrics. Notably, ReXNet150 + Linear-SVM achieves an accuracy of 90.50%, precision of 90.53%, F1-score of 90.38%, and recall of 90.37%, with a training time of just 96.62 seconds, significantly faster than standalone ReXNet models (e.g., 17,145.68 seconds for ReXNet150). Additionally, ReXNet300 + Linear-SVM achieves the highest accuracy among hybrid configurations (92.48%) with minimal training time (96.46 seconds). Non-linear kernels like RBF and Polynomial achieve high AUC values ( $\geq 0.98$  across most classes), underscoring their effectiveness in handling complex decision boundaries, albeit at higher computational costs. This trade-off highlights the adaptability of the hybrid model, enabling users to prioritize accuracy, speed, or resource usage based on specific needs. By addressing the limitations of standalone CNNs and SVMs, this approach provides a scalable solution for real-time agricultural diagnostics, supporting sustainable sugarcane farming in Thailand. Future work could explore semi-supervised learning techniques to optimize labeling efforts and enhance generalizability across diverse datasets.

**Index Terms—** Convolutional Neural Networks, ReXNet, Support Vector Machine, Sugarcane Disease Classification.

## I. INTRODUCTION

Thailand, the world's second-largest sugar exporter, depends significantly on sugarcane cultivation, which contributes substantially to its agricultural gross domestic product (GDP) and supports over 1.5 million farming households [1]. The industry plays a critical role in global sugar trade, yet sugarcane productivity is threatened by leaf diseases such as mosaic disease, red rot disease, rust disease, and yellow leaf disease. These diseases collectively reduce annual yields by 30–40% [2], compromising sucrose content and stalk integrity, thereby diminishing crop suitability for industrial processing [3]. Traditional diagnostic methods, reliant on manual inspection by agricultural experts, are labor-intensive, prone to human error, and ineffective in differentiating diseases with overlapping symptoms, particularly during early infection stages [4]. For example, yellow leaf disease and nutrient deficiencies often exhibit similar chlorotic patterns, leading to delayed or incorrect interventions [5].

Artificial intelligence (AI) has emerged as a transformative solution for precision agriculture [8]. Convolutional neural networks (CNNs), including architectures like ResNet [8], VGG [9], and Inception [9], have demonstrated efficacy in plant disease detection by

autonomously extracting hierarchical features from leaf imagery. However, CNNs face challenges such as computational inefficiency due to fully connected layers, susceptibility to overfitting with limited training data [10], and limited adaptability to environmental variations in lighting and leaf orientation [11]. Support vector machines (SVMs), with kernel functions like linear, polynomial, and radial basis function (RBF), offer robust performance in high-dimensional classification tasks [12]. Yet, standalone SVMs require manual feature engineering, which is impractical for large-scale agricultural applications [13].

Hybrid CNN-SVM models have been proposed to integrate the strengths of both approaches. Previous studies have shown that combining lightweight CNNs with SVM classifiers reduces training time while maintaining accuracy in tomato disease detection [14]. Similarly, MobileNet integrated with RBF-SVM kernels has achieved high F1-scores in rice leaf disease classification. However, these studies rarely address the unique morphological characteristics of sugarcane leaves, such as elongated shapes and dense venation, or systematically evaluate the trade-offs between SVM kernel performance and computational efficiency.

This study proposes a hybrid model that integrates ReXNet [15]—a CNN architecture with channel attention mechanisms and depthwise separable convolutions—with SVM classifiers using linear, polynomial, and RBF kernels. ReXNet’s efficient feature extraction capabilities enable the capture of fine-grained disease patterns, while the SVM layer reduces model complexity and overfitting compared to traditional fully connected layers. The evaluation on a comprehensive dataset of sugarcane leaf images, comprising healthy leaves and four types of diseases (mosaic disease, red rot disease, rust disease, and yellow disease), demonstrated that the hybrid model achieved a peak F1-score of 92.5% with the RBF kernel when paired with ReXNet 300. The RBF kernel also exhibited faster convergence and more stable learning curves compared to the linear and polynomial kernels, reinforcing its effectiveness in handling complex data patterns. Notably, the hybrid approach significantly reduced training time compared to conventional CNN architectures, highlighting its efficiency and suitability for real-time disease diagnostics. By addressing the limitations of existing approaches, this research provides a scalable and efficient tool for improving agricultural sustainability and economic resilience in Thailand.

## II. METHODOLOGY

### Dataset Description and Preprocessing Rationale

The experimental dataset comprises 2,521 sugarcane leaf images systematically categorized into five classes: healthy leaves, mosaic disease (yellow-green mottling from Sugarcane mosaic virus), red rot disease (red necrotic lesions caused by *Colletotrichum falcatum*), rust disease (reddish-brown pustules from *Puccinia kuehnii*), and yellow leaf disease (chlorosis induced by *Candidatus Phytoplasma* spp.). Fig. 1 illustrates representative samples of each class, highlighting the distinct visual characteristics of healthy leaves and disease manifestations.

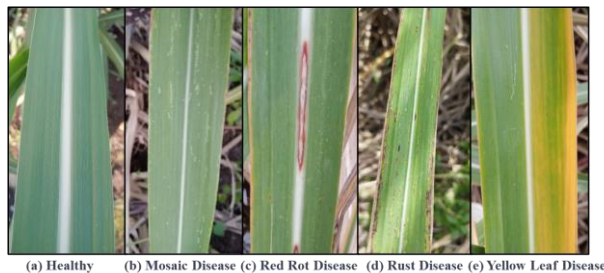


Fig. 1. Example images of the dataset classes.

All images were preprocessed to  $224 \times 224$  pixels (RGB format) to ensure input consistency for the ReXNet model, which requires fixed-size tensors for convolutional operations. Normalization (mean = [0.485, 0.456, 0.406], std = [0.229, 0.224, 0.225]) was applied to align pixel values with the ImageNet distribution, enhancing model convergence by reducing illumination variance. Horizontal flipping (random left-right inversion) was employed during training to artificially augment data, mitigating overfitting by

introducing spatial variability. The dataset was partitioned into 80% training data (2,017 images) and 20% testing data (504 images) via stratified sampling to preserve class distribution, ensuring robust evaluation of the ReXNet model’s diagnostic performance as depicted in Fig. 2.

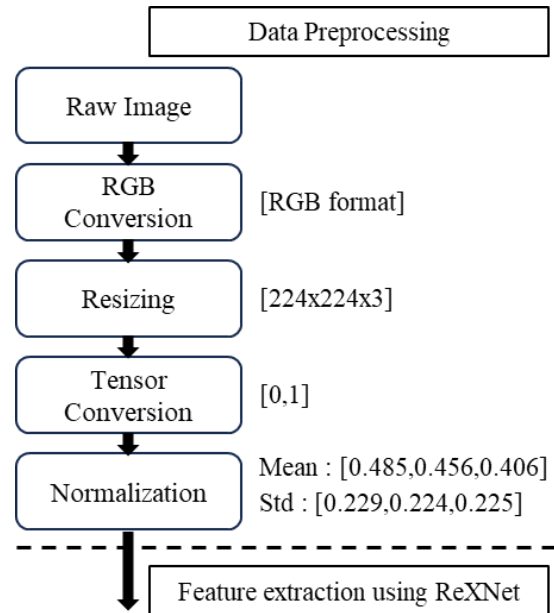


Fig. 2. Data preprocessing workflow before feature extraction.

### Hybrid Model Architecture

The proposed hybrid model integrates ReXNetV1, a lightweight convolutional neural network (CNN), with Support Vector Machines (SVMs) to classify sugarcane leaf diseases. ReXNetV1, configured with varying width multipliers (1.0, 1.3, 1.5, 2.0, 3.0), extracts hierarchical features from preprocessed leaf images (resized to  $224 \times 224$  pixels and normalized with ImageNet statistics) through depthwise separable convolutions and channel-wise scaling. Wider variants capture finer disease patterns at the cost of increased computational overhead. These features are flattened into 1D vectors and fed into SVM classifiers with linear, polynomial (poly), or radial basis function (RBF) kernels. SVMs are trained incrementally on growing subsets of data to evaluate their suitability for non-linear disease pattern classification. The architecture’s workflow begins with preprocessing, followed by ReXNetV1-based feature extraction, and culminates in SVM-based decision boundaries optimized for accuracy and efficiency. The model dynamically selects pre-trained ReXNet variants, processes stratified datasets, and logs convergence behavior during SVM training, ensuring adaptability to diverse sugarcane disease datasets as depicted in Fig. 3.

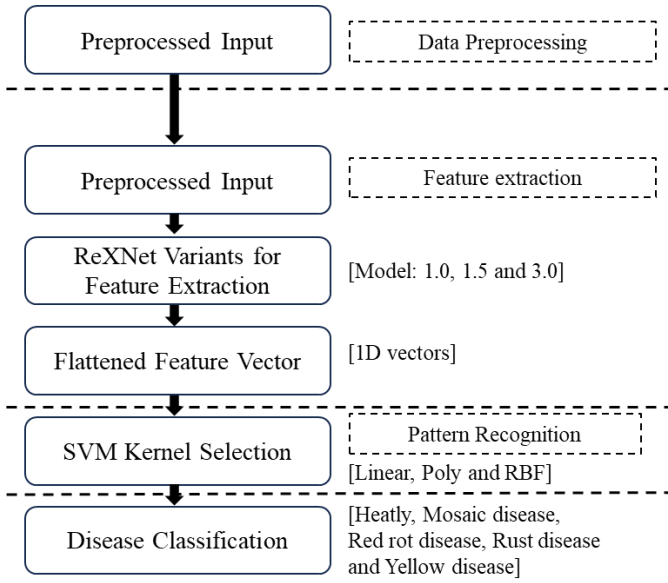


Fig. 3. Workflow for disease classification with hybrid model.

### Model Training and Evaluation

The training and evaluation process begins with preprocessing sugarcane leaf images followed by feature extraction using ReXNetV1 variants (ReXNet\_100, ReXNet\_150, ReXNet\_300) with width multipliers 1.0, 1.5, and 3.0, respectively. These models employ depth wise separable convolutions and channel scaling to extract hierarchical features, where wider variants (e.g., ReXNet\_300) capture finer disease patterns at higher computational cost. Extracted features are fed into SVM classifiers with three kernels as follows:

$$\text{Linear kernel: } K(x, y) = x^T y \quad (1)$$

$$\text{Polynomial kernel: } K(x, y) = (\gamma x^T y + r)^d \quad (2)$$

$$\text{Rbf kernel: } K(x, y) = \exp(-\gamma \|x - y\|^2) \quad (3)$$

SVM classifiers were trained incrementally on stratified subsets of the dataset (80% training, 20% testing) to analyze convergence behavior. The performance of the hybrid model was rigorously evaluated using a comprehensive suite of metrics, including accuracy, precision, recall, F1-score, and training time, alongside visualization tools such as confusion matrices, ROC-AUC curves, and convergence plots to assess classification robustness and stability. Accuracy, defined as

$$\text{Accuracy} = \frac{TP + TN}{FP + FN + TP + TN} \quad (4)$$

where TP (true positives), TN (true negatives), FP (false positives), and FN (false negatives) denote correctly and incorrectly classified instances. Precision, defined as

$$\text{Precision} = \frac{TP}{TP + FP} \quad (5)$$

Evaluates the model's ability to avoid false positives, while Recall quantifies its sensitivity to true positives, defined as

$$\text{Recall} = \frac{TP}{TP + FN} \quad (6)$$

The F1-score harmonizes precision and recall into a single metric can be written as follows:

$$\text{F1-score} = 2 \cdot \frac{\text{Precision} + \text{Recall}}{\text{Precision} \cdot \text{Recall}} \quad (7)$$

The confusion matrix provides a visual representation of true positives (TP), true negatives (TN), false positives (FP), and false negatives (FN) across all classes. The receiver operating characteristic (ROC) curve plots the true positive rate (TPR) against the false positive rate (FPR), with the area under the curve (AUC) quantifying classifier robustness. Computational efficiency was assessed by measuring training time (Training Time=End Time–Start Time) and performing convergence analysis through monitoring accuracy across incrementally increasing training subsets.

### III. RESULTS AND DISCUSSION

The experimental results, summarized in Table 1, provide a comprehensive comparison of the performance metrics for the hybrid model configurations. The evaluation focused on accuracy, precision, F1-score, recall and training time, with additional visualizations including the confusion matrix, ROC curve, and convergence graph to validate the robustness and efficiency of the models.

#### Performance Metrics

Among the standalone ReXNet models, ReXNet150 achieved the highest accuracy (97.22%) and F1-score (97.18%), albeit at a significantly higher computational cost (17,145.68 seconds, or ~285.76 minutes). In contrast, ReXNet100 demonstrated a balanced trade-off between performance (96.23% accuracy) and training time (1,477.93 seconds, or ~24.63 minutes). However, ReXNet300, despite its wider architecture and richer feature extraction capabilities, did not outperform ReXNet150, achieving similar accuracy (96.23%) but requiring an extensive training time (48,483.04 seconds, or ~808.05 minutes).

When combined with SVM kernels, the hybrid models exhibited notable improvements in efficiency while maintaining competitive performance. For instance, ReXNet150 + RBF-SVM achieved 90.69% accuracy with a significantly reduced training time (199.47 seconds, or ~3.32 minutes), making it a practical choice for real-time deployment. Similarly, ReXNet300 + Linear-SVM achieved 92.48% accuracy with a training time of 96.46 seconds, highlighting the potential of linear kernels for faster

inference. However, non-linear kernels (e.g., RBF) generally outperformed linear and polynomial kernels in terms of accuracy, likely due to their ability to capture complex decision boundaries in the dataset.

TABLE I  
Performance Metrics of Hybrid Models for Sugarcane  
Leaf Disease Classification

Model	Accuracy	Precision	F1-score	Recall	Training Time (sec.)
ReXNet 100	0.9623	0.9642	0.9623	0.9626	1477.93
ReXNet 150	0.9722	0.9727	0.9718	0.9723	17145.68
ReXNet 300	0.9623	0.9658	0.9625	0.9615	48483.04
Kernel: linear	0.8811	0.8811	0.8794	0.8798	107.73
ReXNet 100 Kernel: Polynomial	0.8752	0.8779	0.8745	0.8748	183.42
Kernel: Rbf	0.8574	0.8600	0.8560	0.8562	219.30
Kernel: linear	0.9050	0.9053	0.9038	0.9037	96.62
ReXNet 150 Kernel: Polynomial	0.9109	0.9124	0.9099	0.9094	158.33
Kernel: Rbf	0.9069	0.9091	0.9058	0.9053	199.47
Kernel: linear	0.9248	0.9249	0.9245	0.9250	96.46
ReXNet 300 Kernel: Polynomial	0.8713	0.8759	0.8720	0.8706	153.31
Kernel: Rbf	0.8752	0.8785	0.8756	0.8744	199.73

### Convergence Analysis

The convergence graph shown in Fig. 4 illustrates the training behavior of hybrid models combining ReXNet variants (100, 150, and 300) with different SVM kernels (Linear, Polynomial, and RBF). The models exhibited consistent convergence patterns, stabilizing after approximately 2,017 training samples. Among the SVM kernels, the RBF kernel demonstrated faster convergence and more stable learning curves compared to the linear and polynomial kernels, suggesting its capacity to handle complex data patterns more effectively. Larger ReXNet models (e.g., ReXNet 300) exhibited smoother and more consistent convergence, indicating enhanced feature extraction capability and improved generalization. The overall results suggest that combining ReXNet with RBF-SVM provides a more effective approach for complex classification tasks while balancing convergence speed and classification accuracy.

The confusion matrix shown in Fig. 5 provided insights into class-wise performance. The classes with the highest recall rates, in descending order, were Red Rot, Healthy, Rust, Yellow Leaf, and Mosaic. This ranking reflects the model's effectiveness in distinguishing critical disease classes with distinct visual patterns. However, misclassifications were observed between visually similar classes, such as Healthy and Yellow Leaf, likely due to overlapping features in color and texture. These findings highlight both the strengths and areas for improvement in the model's classification capabilities.

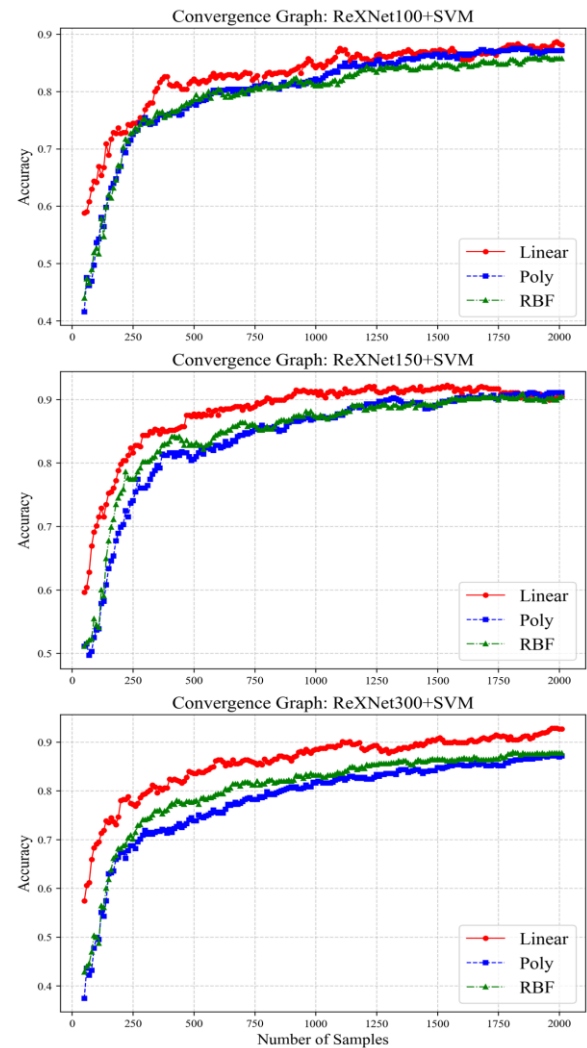


Fig. 4. Training Convergence of ReXNet with Different SVM Kernels.

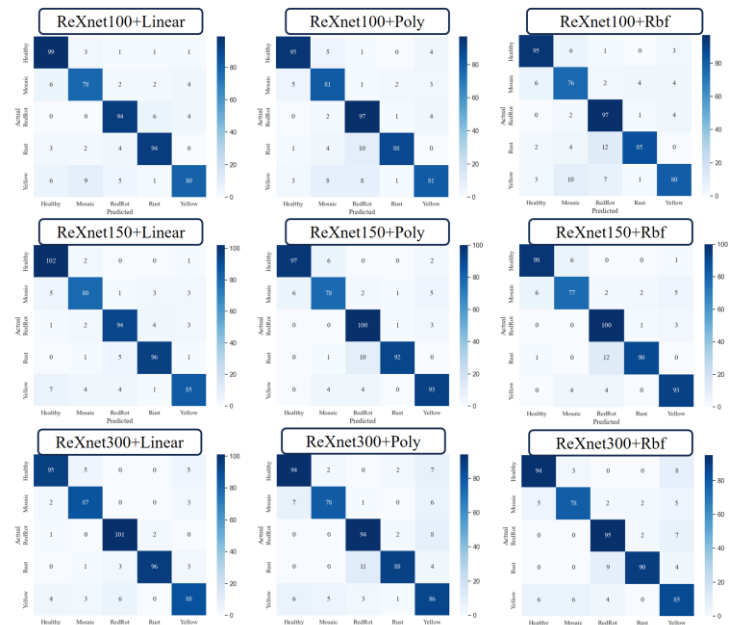


Fig. 5. Confusion Matrices of ReXNet with Different SVM Kernels.



The ROC curves compare Hybrid ReXNet-SVM models (ReXNet100, ReXNet150, ReXNet300) with Linear, Polynomial, and RBF kernels. All models achieve high AUC values, indicating strong performance as shown in Table 2. Notably, the Linear kernel outperforms RBF and Polynomial kernels, especially in deeper architectures (ReXNet150, ReXNet300), suggesting linear decision boundaries suffice when using ReXNet's deep features. The RBF kernel, while effective, does not consistently excel, likely due to the discriminative power of extracted features. Increasing ReXNet depth improves performance, as ReXNet300 shows higher AUC scores than ReXNet100. In conclusion, the Linear kernel performs best, highlighting the separability of ReXNet features in a linear space and challenging the assumption that non-linear kernels are always superior as depicted in Fig. 6.

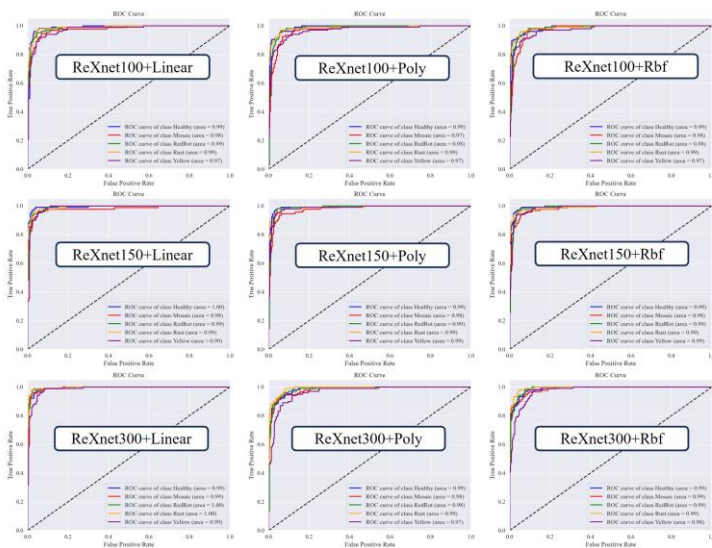


Fig. 6. ROC Curves of Hybrid ReXNet-SVM Models.

TABLE 2

The Area Under the Curve (AUC) of Hybrid ReXNet-SVM Models Across Different Kernel Functions

Model		Area under the curve (AUC)				
		Healthy	Mosaic	RedRot	Rust	Yellow
ReXNet100	Kernel: linear	0.99	0.98	0.99	0.99	0.97
	Kernel: Polynomial	0.99	0.97	0.98	0.99	0.97
	Kernel: Rbf	0.99	0.98	0.98	0.99	0.97
ReXNet150	Kernel: linear	1.00	0.98	0.99	0.99	0.99
	Kernel: Polynomial	0.99	0.98	0.99	0.99	0.99
	Kernel: Rbf	0.99	0.98	0.99	0.99	0.99
ReXNet300	Kernel: linear	0.99	0.99	1.00	1.00	0.99
	Kernel: Polynomial	0.99	0.98	0.98	0.99	0.97
	Kernel: Rbf	0.99	0.99	0.99	0.99	0.98

#### IV. CONCLUSION

The hybrid model combining ReXNet and SVM demonstrates strong potential for sugarcane leaf disease classification, balancing accuracy and computational efficiency. By leveraging ReXNet's depthwise separable convolutions and channel scaling, the model extracts fine-

grained disease patterns with fewer parameters than traditional CNNs. Integrating SVM classifiers reduces complexity, particularly with linear kernels, which achieve competitive performance in significantly shorter training times (e.g., 96.46 seconds for ReXNet300 + Linear-SVM vs. 48,483.04 seconds for standalone ReXNet300). Although linear kernels show slightly lower accuracy than non-linear kernels like RBF, their speed and simplicity make them ideal for resource-constrained environments. Non-linear kernels (RBF and Polynomial) excel in handling complex decision boundaries, achieving high AUC values ( $\geq 0.98$  across most classes) but at higher computational costs. This trade-off highlights the model's adaptability, enabling users to prioritize accuracy, speed, or resource usage based on specific needs. Overall, this approach addresses the limitations of standalone CNNs and SVMs, offering a scalable solution for real-time agricultural diagnostics and supporting sustainable sugarcane farming in Thailand. Future work could explore semi-supervised learning to optimize labeling efforts and enhance generalizability across diverse datasets.

#### ACKNOWLEDGMENT

The authors gratefully acknowledge the Sustainable Development and Intelligent Systems Research Unit at Rajamangala University of Technology Isan for their support and resources during this research. Their dedication to advancing sustainable development and intelligent systems has been pivotal to this study. Special thanks are extended to all collaborators and team members whose contributions have greatly improved the quality and outcomes of this work.

#### REFERENCES

- [1] Office of Agricultural Economics (Thailand), Sugarcane Production Report in Thailand, Tech. Rep. 2023.
- [2] P. Thongpae, S. Lertworapreecha, and W. Saksirirat, "Economic impact of sugarcane diseases in Northeast Thailand," *Agric. Econ. Res. J.*, vol. 37, no. 2, pp. 45–58, 2021.
- [3] R. Viswanathan, R. Selvaraj, and M. Premkumar, "Pathogen-induced stalk lodging in sugarcane: A review," *Plant Pathol. J.*, vol. 18, no. 3, pp. 178–186, 2019.
- [4] S. K. Singh, R. K. Singh, and A. K. Mishra, "Human error in manual disease diagnosis: A case study in Indian agriculture," *IEEE Trans. Agric. Syst.*, vol. 15, no. 4, pp. 112–120, 2020.
- [5] T. H. Thai, N. T. Nguyen, and H. V. Le, "Misdiagnosis of yellow leaf disease in Vietnamese sugarcane farms," *Trop. Plant Pathol.*, vol. 47, no. 5, pp. 301–310, 2022.
- [6] K. He, X. Zhang, S. Ren, and J. Sun, "Deep residual learning for image recognition," in *Proc. IEEE Conf. Comput. Vis. Pattern Recognit. (CVPR)*, pp. 770–778, 2016.
- [7] K. Simonyan and A. Zisserman, "Very deep convolutional networks for large-scale image recognition," *arXiv preprint arXiv:1409.1556*, 2014.
- [8] C. Szegedy et al., "Going deeper with convolutions," in *Proc. IEEE Conf. Comput. Vis. Pattern Recognit. (CVPR)*, pp. 1–9, 2015.
- [9] A. Krizhevsky, I. Sutskever, and G. E. Hinton, "ImageNet

classification with deep convolutional neural networks,” in Advances in Neural Information Processing Systems, vol. 25, pp. 1097–1105, 2012.

[10] M. H. Rahman, M. A. Razzaque, and T. Islam, “Environmental robustness in plant disease detection using CNNs,” IEEE Trans. Pattern Anal. Mach. Intell., vol. 43, no. 11, pp. 3801–3815, 2021.

[11] C. Cortes and V. Vapnik, “Support-vector networks,” Mach. Learn., vol. 20, no. 3, pp. 273–297, 1995.

[12] Y. LeCun, Y. Bengio, and G. Hinton, “Deep learning,” Nature, vol. 521, no. 7553, pp. 436–444, 2015.

[13] J. Zhang, Y. Wang, and L. Zhao, “Lightweight CNN-SVM model for tomato disease detection,” IEEE Trans. Cybern., vol. 52, no. 3, pp. 1234–1245, 2022.

[14] L. Wang, H. Chen, and Q. Zhang, “MobileNet-RBF-SVM for rice leaf disease classification,” IEEE Access, vol. 8, pp. 12345–12356, 2020.

[15] D. Han et al., “ReXNet: Channel Attention - Enhanced Network for Efficient Image Classification,” Proc. IEEE ICCV, pp. 1–10, 2021.

# Taguchi-Based Optimization of Torrefaction Conditions for Enhancing Corncob Biomass Properties

Kanit Manatura<sup>1, 2, a)</sup>, Kunthakorn Khaothong<sup>3</sup>, Kitipong Jaojaruek<sup>3</sup>, Kankamon Phookronghin<sup>1</sup>, Den Kogphimai<sup>1</sup>, Preecha Somwang<sup>1</sup> and Namfon Samsalee<sup>4</sup>

<sup>1</sup>Department of Mechatronics Engineering, Faculty of Engineering and Technology, Rajamangala University of Technology Isan, Nakhon Ratchasima, Thailand, 30000

<sup>2</sup>Sustainable Development and Intelligent Systems Research Unit, Faculty of Engineering and Technology, Rajamangala University of Technology Isan, Nakhon Ratchasima, Thailand, 30000

<sup>3</sup>Department of Mechanical Engineering, Faculty of Engineering at Kamphaeng Saen, Kasetsart University, Nakhon Pathom, Thailand, 73140

<sup>4</sup>Department of Applied Biology, Faculty of Sciences and Liberal Arts, Rajamangala University of Technology Isan, Nakhon Ratchasima, 30000 Thailand

<sup>a)</sup> Corresponding author: kanit.ma@rmuti.ac.th

**Abstract.** This study investigates the optimization of the torrefaction process for corncob biomass using the Taguchi method, aiming to enhance fuel quality and energy efficiency. The effects of temperature (T), residence time (t), heating rate (HR), and nitrogen flow rate (N<sub>2</sub>) on key performance indicators, including mass yield (MY), energy yield (EY), higher heating value (HHV), and specific energy consumption (SEC), were analyzed using an L9 (4<sup>3</sup>) orthogonal array. The S/N ratio analysis revealed that temperature was the most influential parameter, significantly impacting all performance metrics. The optimal conditions for minimizing MY, EY, and SEC were identified as 200°C, 15 min, 10°C/min, and 0.1 l/min, ensuring efficient energy consumption with maximum biomass retention. Conversely, HHV was maximized at 300°C, 35 min, 20°C/min, and 0.2 l/min, indicating improved energy densification. The findings highlight a trade-off between fuel quality and process efficiency, where lower temperatures favor mass retention, while higher temperatures enhance HHV. These results contribute to the sustainable utilization of agricultural residues, optimizing corncob torrefaction for biofuel applications.

**Index Terms**— Taguchi method, Corncob, Torrefaction, Specific Energy Consumption, Heating value

## I. INTRODUCTION

Biomass has gained significant attention as a renewable and sustainable energy source due to its ability to mitigate greenhouse gas emissions and reduce reliance on fossil fuels. Among various biomass feedstocks, agricultural residues such as corncobs offer a low-cost and widely available bioenergy resource. However, raw biomass typically faces limitations such as high moisture content, low calorific value, and poor grindability, making direct combustion or co-firing inefficient [1]. These limitations necessitate pre-treatment techniques such as torrefaction, a mild thermal process that improves biomass energy density, hydrophobicity, and thermal stability [2]. By optimizing torrefaction conditions, the efficiency and applicability of biomass as an alternative fuel source can be significantly enhanced.

Torrefaction is a thermochemical process that modifies the structural and chemical properties of biomass by removing some volatile compounds and increasing fixed carbon content. This process, typically conducted at temperatures ranging from 200°C to 300°C, enhances the higher heating value (HHV), carbonization efficiency, and combustion

properties of the biomass [3]. However, the effectiveness of torrefaction is influenced by multiple process variables, including temperature, residence time, heating rate, and nitrogen flow rate, all of which play a crucial role in determining the final fuel quality [4]. Understanding the relationship between these parameters and biomass properties is essential for improving the torrefaction process.

Despite the advantages of torrefaction, identifying optimal process conditions is a challenge due to the complex interactions between process variables. Studies have shown that higher temperatures generally lead to increased HHV, but they also result in greater mass loss, reducing the overall energy yield [5]. Similarly, longer residence times and higher heating rates contribute to enhanced carbon retention, but excessive treatment can lead to undesirable decomposition and energy inefficiencies [6]. These trade-offs necessitate a systematic approach to determine the best combination of torrefaction parameters to balance fuel quality and energy efficiency.

To address this challenge, researchers have adopted the Taguchi method, a widely used statistical optimization technique that minimizes experimental complexity, reducing cost while maximizing accuracy. The Taguchi experimental design utilizes an L9 (4<sup>3</sup>) orthogonal array, allowing for the

efficient study of multiple variables with fewer experimental trials [7]. This method not only helps identify the most influential factors but also reduces process variability, ensuring consistency in biofuel quality. Additionally, signal-to-noise (S/N) ratio analysis provides a quantitative measure to optimize the response variables, enhancing the overall torrefaction efficiency [8].

This study employs the Taguchi method to systematically optimize the torrefaction process of corncob biomass, focusing on critical performance indicators such as mass yield (MY), higher heating value (HHV), energy yield (EY), and specific energy consumption (SEC). The optimization is conducted by analyzing the influence of key torrefaction parameters, including temperature, residence time, heating rate, and nitrogen flow rate, to determine the most effective operating conditions. By identifying the optimal torrefaction settings, this research enhances the utilization of agricultural residues as a viable feedstock for sustainable bioenergy production.

## II. METHODOLOGY

### A. Materials preparation

Corn cob biomass used in this study was sourced from a corn cob farm in Chiang Mai, Thailand, where it was collected as an agricultural by-product. The corncobs were manually sorted to remove unwanted impurities and then washed with distilled water to eliminate dust and dirt. Afterward, the cleaned corncobs were air-dried under ambient conditions for 48 hours to reduce surface moisture before further processing. To ensure uniformity in the torrefaction, the dried corncobs were mechanically milled using a rotary beater mill and sieved to obtain a particle size range of 2 mm by manual sieve shaker. The sieved corn cob biomass was then stored in an airtight container at room temperature ( $25^{\circ}\text{C} \pm 2^{\circ}\text{C}$ ) to prevent moisture reabsorption before the torrefaction experiments.

### B. Torrefaction

Torrefaction was conducted using a fixed-bed furnace, designed to operate under precisely controlled thermal conditions. The 2 kW - reactor was equipped with a programmable temperature controller and a nitrogen gas purging system to ensure an inert environment, thereby preventing oxidative reactions during the process. The experimental setup also included a thermocouple sensor to monitor and regulate the temperature within the reactor chamber. Prior to run each experiment, the reactor was preheated to the designated torrefaction temperature before introducing the prepared corn cob samples. A sample of 10 g was placed in a stainless steel crucible and positioned at the center of the reactor to ensure uniform heat distribution. Throughout the process, high-purity nitrogen (99.9%) was continuously supplied at a controlled flow rate of 0.1 – 0.3 l/min to maintain an oxygen-free environment and facilitate thermal degradation.

### C. Taguchi analysis for experimental design

To optimize the torrefaction for corncob, the Taguchi method was utilized as a structured statistical approach for

experimental design. This method enables the efficient evaluation of multiple process parameters while minimizing the number of experimental trials required for optimization [4]. In this study, an L9 ( $4^3$ ) orthogonal array was employed, facilitating a systematic analysis of the impact of four critical torrefaction parameters including temperature, residence time, heating rate and nitrogen flow rate, each at three distinct levels as shown in Table 1. The experimental design is presented in Table 2. This approach ensures a balanced distribution of experimental runs, allowing for the identification of optimal conditions with reduced variability and improved reproducibility.

TABLE I  
TORREFACTION PARAMETER FOR TAGUCHI ANALYSIS

Parameter	Level 1	Level 2	Level 3
Temperature ( $^{\circ}\text{C}$ ), T	200	250	300
Residence time (min), t	15	35	55
Heating rate ( $^{\circ}\text{C}/\text{min}$ ), HR	10	20	30
Nitrogen flow rate (l/min), $\text{N}_2$	0.1	0.2	0.3

By systematically varying these parameters according to the Taguchi orthogonal array, the design of experiments (DOE) was structured to efficiently assess their influence on key torrefaction performance indicators, including mass yield (MY), energy yield (EY), higher heating value (HHV), energy-mass co-benefit index (EMCI), and specific energy consumption (SEC). To further validate the experimental results, signal-to-noise (S/N) ratio analysis was conducted to quantify the robustness of the process parameters, minimizing the influence of external variability.

To effectively evaluate torrefaction performance, Signal-to-Noise (S/N) ratio analysis was employed to identify the optimal levels of temperature, residence time, heating rate, and nitrogen flow rate, ensuring maximum efficiency while minimizing process variability. The S/N was determined using two primary approaches: Larger-the-Better (LB) and Smaller-the-Better (SB). The LB was applied to maximize key performance indicators, including higher heating value (HHV) and energy yield (EY), as higher values enhance fuel quality and energy content. Conversely, the SB was used for specific energy consumption (SEC), where lower values indicate greater energy efficiency by reducing the energy input required for torrefaction. The S/N for LB and SB are presented by Eqs (1) and (2) as

$$\text{LB: } \text{S/N} = -10 \times \log(1/y^2) \quad (1)$$

$$\text{SB: } \text{S/N} = -10 \times \log(y^2) \quad (2)$$

where y is the desired value.

TABLE II  
TAGUCHI L9 ( $4^3$ ) ORTHOGONAL ARRAY

No.	T ( $^{\circ}\text{C}$ )	t (min)	HR ( $^{\circ}\text{C}/\text{min}$ )	$\text{N}_2$ (l/m)
1	200	15	10	0.1
2	200	35	20	0.2
3	200	55	30	0.3



4	250	15	20	0.3
5	250	35	30	0.1
6	250	55	10	0.2
7	300	15	30	0.2
8	300	35	10	0.3
9	300	55	20	0.1

#### D. Torrefaction Performance

The performance of the torrefaction process was assessed using key indicators, including mass yield (MY), energy yield (EY), higher heating value (HHV), energy-mass co-benefit index (EMCI), and specific energy consumption (SEC). These parameters were calculated to evaluate the effectiveness of the process in enhancing the energy properties of corncob biomass.

##### 1) Mass yield

Mass yield (MY) measures the percentage of biomass retained after torrefaction and is an indicator of thermal degradation. A lower mass yield indicates a higher degree of decomposition, leading to increased energy densification. It was calculated using the following equation:

$$MY (\%) = M_{tor}/M_0 \times 100\% \quad (3)$$

##### 2) Energy yield

Energy yield (EY) evaluates the retention of energy in the torrefied biomass relative to the raw biomass. It represents that the energy retained per unit mass is optimized while accounting for material loss during torrefaction. It is determined as:

$$EY (\%) = MY \times HHV_0/HHV_{tor} \quad (4)$$

##### 3) Specific Energy Consumption

Specific Energy Consumption, SEC, represents the energy required for torrefaction per unit mass of biomass. A lower SEC value indicates a more energy-efficient process, as less energy is consumed per unit mass of biomass converted:

$$SEC (kWh/kg) = E_{process}/M_{tor} \quad (5)$$

where M and HHV are weight (g) and higher heating value (MJ/kg) of corncob sample. Subscript 0 and tor are raw and torrefaction, respectively.  $E_{process}$  is total energy input to the torrefaction system (kWh).

### III. RESULTS AND DISCUSSION

The analysis of torrefaction performance based on the L9 (4<sup>3</sup>) orthogonal array experiments and the subsequent optimization using Taguchi analysis was presented in this section. Three key aspects: (1) the effect of experimental runs on torrefaction performance, (2) the relationship between parameter levels and S/N ratios, and (3) the identification of the optimal torrefaction conditions were presented.

#### A. Effect of process parameters on torrefaction performances

The torrefaction performance of corncob biomass is significantly influenced by the key parameters: temperature (T), residence time (t), heating rate (HR), and nitrogen flow rate (N<sub>2</sub>), as shown in Fig. 1. Among these, temperature plays the most dominant role. As the temperature increases from 200°C to 300°C, a pronounced decline in MY and EY is observed, primarily due to enhanced devolatilization and the breakdown of biomass structure. While this leads to greater mass loss, it simultaneously promotes an increase in HHV, indicating improved energy density of the torrefied product. Residence time further amplifies these effects. Longer durations (up to 55 mins) allow for more complete decomposition, thereby reducing MY and EY but enhancing HHV through the progressive removal of volatiles and the concentration of carbon content. However, this improvement in fuel quality comes at the cost of higher energy consumption, as reflected in the SEC trend. Heating rate also plays a crucial role in influencing reaction kinetics. A moderate heating rate (20°C/min) provides a balanced enhancement of HHV without causing rapid decomposition, while higher rates (30°C/min) lead to elevated SEC, indicating lower energy efficiency. Although nitrogen flow rate has a comparatively minor effect, it helps maintain an inert atmosphere, suppressing oxidation and stabilizing thermal conditions during torrefaction. Notably, early experimental runs at 200°C (Runs 1–3) recorded the lowest SEC values due to minimal thermal degradation and reduced energy requirements. In contrast, Run 9 at 300°C exhibited the highest SEC, highlighting the trade-off between maximizing HHV and maintaining energy efficiency.

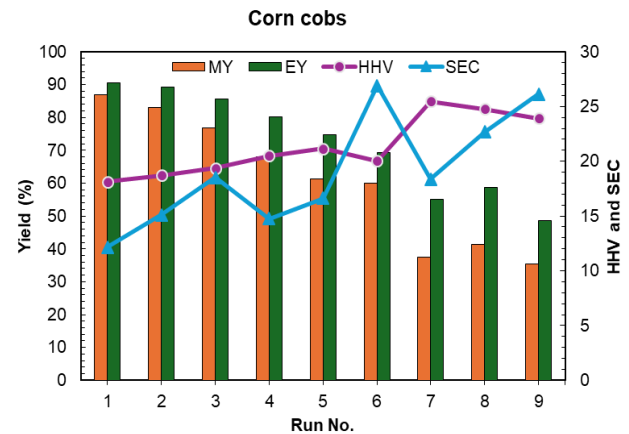


Fig. 1. Sensitivity analysis

#### B. S/N ratio analysis

The S/N ratio analysis provides critical insights into the influence of four torrefaction parameters T, t, HR, and N<sub>2</sub> on the performance indicators of corncob torrefaction (MY, EY, HHV, and SEC). As shown in Fig. 2, the analysis employed both Larger-the-Better (LB) and Smaller-the-Better (SB) criteria depending on the desired performance output: LB for HHV and EY, and SB for MY and SEC. The plots clearly demonstrate that temperature exerts the strongest influence

on all performance metrics. For MY and EY, increasing temperature from Level 1 (200°C) to Level 3 (300°C) causes a steep decline in S/N values, indicating that higher temperatures accelerate biomass decomposition, resulting in reduced mass and energy retention. In contrast, the HHV plot shows a continuous increase in S/N ratio with temperature, highlighting enhanced carbonization and energy densification at higher thermal settings. For SEC, the S/N ratio declines sharply with increasing temperature and residence time, confirming that higher thermal intensity and prolonged exposure lead to elevated energy consumption. Meanwhile, the HR and N<sub>2</sub> flow rate show more moderate and stable trends across all indicators, suggesting their secondary impact relative to temperature and residence time. Overall, the S/N ratio analysis underscores the critical need to optimize temperature and residence time. High temperature enhances HHV, but compromises MY, EY, and SEC. Thus, achieving an optimal balance between fuel quality and process sustainability requires a careful trade-off between these interdependent variables.

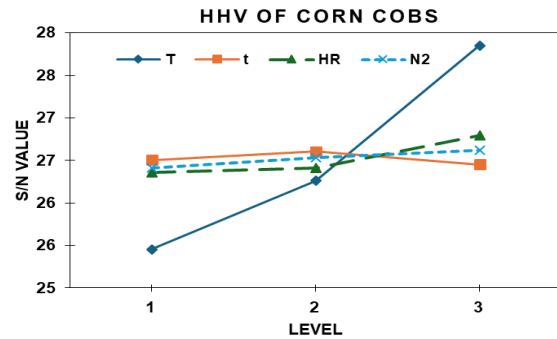
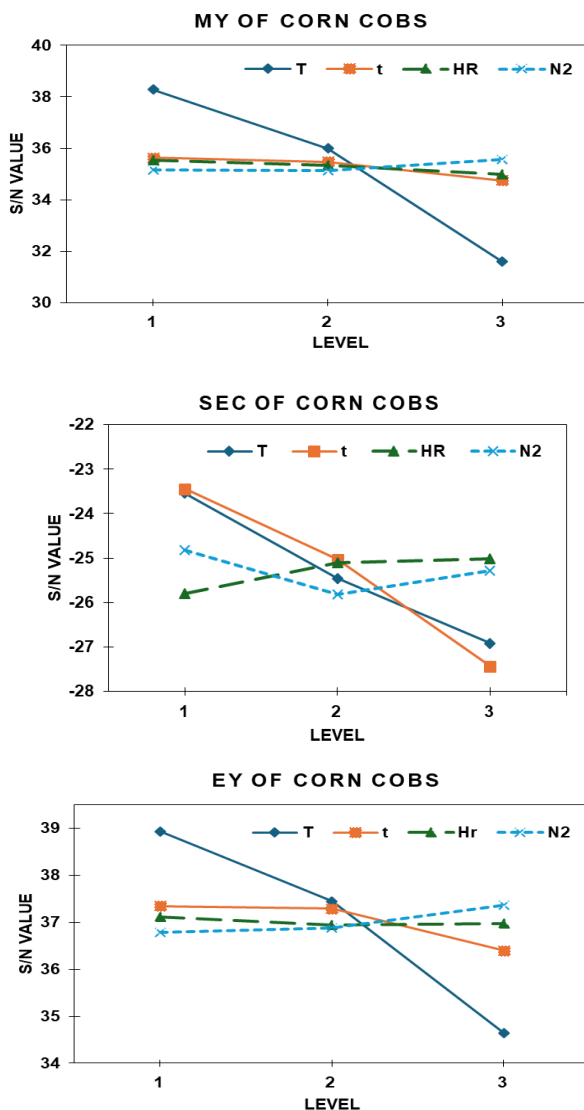


Fig. 2. S/N results on the performances

### C. Optimal torrefaction conditions

Based on the S/N ratio analysis, the optimal torrefaction conditions were identified to achieve the most favorable outcomes for MY, EY, HHV, and SEC. The highest MY was observed at lower torrefaction temperatures (200°C), where minimal decomposition retained more biomass. A short residence time (15 min) and low heating rate (10°C/min) helped prevent excessive mass loss, while the lowest nitrogen flow rate (0.1 l/min) minimized oxidative effects and gas usage. EY followed a similar trend, with 200°C, 15 min, and 10°C/min offering the best energy retention with minimal degradation. In contrast, the best HHV was achieved at 300°C, where enhanced carbonization increased fuel quality. A moderate residence time (35 min) and controlled heating rate (20°C/min) facilitated efficient lignocellulosic breakdown, while a nitrogen flow rate of 0.2 l/min maintained an inert environment. The lowest SEC was recorded at 200°C, reflecting minimal energy input due to milder conditions, shorter processing time, and reduced heating intensity. From an economic perspective, these conditions help reduce energy consumption and operational costs, especially under lower-temperature settings. Environmentally, lower SEC and optimized N<sub>2</sub> use contribute to lower carbon emissions, while maximizing MY and EY under mild torrefaction supports resource-efficient biofuel production. The findings confirm that temperature is the most dominant factor, with 200°C ideal for energy and material efficiency, and 300°C optimal for HHV improvement. Overall, the selected operating range offers a balanced, sustainable, and cost-effective approach to biomass valorization.

## IV. CONCLUSION

This study successfully optimized the torrefaction process of corncob biomass using the Taguchi method, evaluating the influence of temperature (T), residence time (t), heating rate (HR), and nitrogen flow rate (N<sub>2</sub>) on key performance indicators: mass yield (MY), energy yield (EY), higher heating value (HHV), and specific energy consumption (SEC). The results demonstrated that temperature is the most dominant factor, significantly impacting all performance indicators.

The optimal conditions varied depending on the desired outcome. For minimizing MY, EY, and SEC, the best parameters were 200°C, 15 min, 10°C/min, and 0.1 l/min, ensuring higher mass retention and lower energy consumption. However, for maximizing HHV, the optimal settings were 300°C, 35 min, 20°C/min, and 0.2 l/min, enhancing energy densification and improving fuel quality.

These findings highlight the trade-off between fuel quality and process efficiency. Lower torrefaction temperatures retain more biomass and energy with reduced SEC, while higher temperatures improve HHV but require higher energy input. By selecting appropriate operating conditions, corncob biochar can be optimized as a sustainable biofuel, enhancing its energy efficiency and economic feasibility for renewable energy applications.

#### ACKNOWLEDGMENT

The authors would like to acknowledge department of Mechanical Engineering, Kasetsart University Kamphaeng Saen campus for providing necessary resource and experimental facilities for this research.

#### REFERENCES

- [1] Huang, C. W., Li, Y. H., Xiao, K. L., & Lasek, J. (2019). Cofiring characteristics of coal blended with torrefied Miscanthus biochar optimized with three Taguchi indexes. *Energy*, 172, 566–579.
- [2] Chen, W. H., Lin, B. J., Lin, Y. Y., & Liu, H. (2021). Progress in biomass torrefaction: Principles, applications and challenges. *Progress in Energy and Combustion Science*, 82, 100887.
- [3] Manatura, K. (2020). Inert torrefaction of sugarcane bagasse to improve its fuel properties. *Case Studies in Thermal Engineering*, 19, 100623.
- [4] Manatura, K., Samsalee, N., & Kaewtrakulchai, N. (2025). Optimization of torrefaction parameters for coconut shell using the Taguchi method: Impact on torrefaction performances, combustion characteristics, and thermal stability. *Thermal Science and Engineering*, 57, 103137.
- [5] Chen, W. H., Biswas, P. P., Kwon, E. E., & Lin, K. Y. A. (2024). Optimizing bone and biomass co-torrefaction parameters: High-performance arsenic removal from wastewater via co-torrefied bone char. *Environmental Research*, 252, 118990.
- [6] Saidur, R., Islam, M. R., & Rahim, N. A. (2023). Recent developments in torrefaction of biomass for energy applications: A comprehensive review. *Journal of Cleaner Production*, 412, 136045.
- [7] Ganesan, S. R., Joseph, P. S., & Patel, M. (2022). The application of the Taguchi method for optimizing biomass torrefaction process. *Journal of Renewable and Sustainable Energy*, 14(5), 1–12.
- [8] Nguyen, T. A., Lee, D. Y., & Kim, J. W. (2023). Process optimization and kinetic analysis of biomass torrefaction using the Taguchi method. *Applied Energy*, 322, 119693.

# Investigation into Acoustic Pressure Distribution Across Various Liquids within an Ultrasonic Tank

Nongnapat Phadungjiraphanthatip<sup>1, a)</sup> and Karuna Tuchinda<sup>1, b)</sup>

## Author Affiliations

<sup>1</sup> Mechanical Engineering Simulation and Design Mechanical and Automotive Engineering, The Sirindhorn International Thai-German Graduate School of Engineering, King Mongkut's University of Technology North Bangkok (KMUTNB), Bangkok 10800, Thailand.

## Author Emails

<sup>a)</sup> s6409092860021@email.kmutnb.ac.th

<sup>b)</sup> karuna.t@tggs.kmutnb.ac.th

**Abstract.** Ultrasonic cleaning is a widely utilized technology in manufacturing for removing surface contaminants from objects. Its efficiency depends on several factors, including temperature, solvent type, transducer distance, solvent level, frequency, and power, all of which influence acoustic pressure and cavitation zones. While much research has focused on the parameters of ultrasonic cleaning components, limited studies explore the impact of solvent properties on acoustic pressure distribution. This study investigates the effect of different solvents—acetone, oil, isopropyl alcohol, and water—on acoustic pressure distribution at 298 K, as suggested by an industry partner. The research utilizes COMSOL Multiphysics simulation software and validates the model experimentally using a foil corrosion test in water at 298 K for 2 minutes. Results show strong agreement between the simulated and experimental pressure distributions. Computational results of the acoustic pressure distribution revealed that oil exhibits the highest peak acoustic pressure during the transient period due to its higher density and viscosity. The findings further indicate that acoustic pressure distribution is more effective in bubbly liquids than in non-bubbly ones. Water and ethanol demonstrate clearer wave propagation and precisely defined regions of maximum and minimum acoustic pressure. This study underscores the importance of solvent properties, particularly density and viscosity, in determining acoustic pressure behavior, providing valuable insights into optimizing ultrasonic cleaning processes.

**Index Terms**—COMSOL Multiphysics, ultrasonic cleaner, transducer, acoustic pressure distribution

## I. INTRODUCTION

Ultrasonic cleaning, a technology that emerged in the 1950s, finds widespread applications across various industries such as electronics, food, medical instruments, clothing and textiles, and petroleum, among others [1]–[3]. It generates the frequency 20 – 400 kHz for cleaning contaminants, oil, dust, etc., and suitable to clean the small component [1], [4], [5]. Piezoelectric transducer that is attached the bottom of the ultrasonic cleaner generates acoustic pressure to create large quantities of bubble called cavitation for clean the object [4], [5]. The cleaning efficiency of ultrasonic cleaning depends on temperature, type of solvent, distance from transducer, solvent level, frequency, power, and others that effect to acoustic pressure and cavitation zone [1], [3], [6], [7].

As part of the preliminary literature review, this study examines the use of ultrasonic cleaning to remove contaminants from various objects. It involves a range of solvents typically used in manufacturing environments, including isopropyl alcohol, water, acetone, and crude oil. W. Tangsopa et al. [3] studied the impact of transducer placement on the distribution of acoustic pressure using harmonic response analysis (HRA) in ANSYS. To validate the model, a foil corrosion test was conducted by submerging the foil in water for three minutes, which demonstrated a similar pattern in acoustic pressure distribution. The test

allowed for the identification of the cavitation zones necessary for effectively cleaning objects. Additionally, the position of the transducer significantly influences the characteristic pattern of acoustic pressure distribution within the ultrasonic tank. W. Tangsopa et al.[8] studied the acoustic pressure distribution at various positions within the ultrasonic tank by varying the power of the piezoelectric transducers. The results indicate that while increasing the power of the piezoelectric transducers does not alter the acoustic pressure distribution, the frequency does have an effect. The middle section of the tank demonstrated the highest cleaning efficiency. V. Rokad et al [5] studied the material made ultrasonic tank from structural steel effect to acoustic pressure by using COMSOL. Niazi et al. [9] used CFD simulations to predict the cavitation zone in a sonoreactor filled with water and oil at 20 kHz and 2 kW, the results from the simulation were validated by comparing them with experimental data from Hielscher Ultrasound Technology. The findings indicated that the acoustic pressure distribution in both oil and water is similar, although the acoustic pressure in oil is higher than that in water. All mention research focus effect to acoustic pressure distribution with the component of ultrasonic tank such as placement of transducer, power, frequency, and ultrasonic tank by using simulation.

The objective of this research is to investigate how solvents, including isopropyl alcohol, water, ethanol, and crude oil influence acoustic pressure distribution within



ultrasonic cleaning tanks, to identify the suitable positioning for effective cleaning. The solvents being analyzed will be maintained at a temperature of 298 K. Additionally, COMSOL Multiphysics will be employed to simulate the impact of these solvents on acoustic pressure distribution. To validate the simulation results, aluminum foil will be placed in the ultrasonic tank at a height of over 2 cm from the bottom. The study will compare the acoustic pressure distribution based on the observed corrosion of the foil. Additionally, study the behavior of acoustic pressure from transient to steady state for each solvent. This is useful for manufacturers aiming to enhance the performance of ultrasonic cleaning processes.

## II. METHODOLOGY

This study investigates the pressure distribution of various liquids, i.e. isopropyl alcohol, water, ethanol, and crude oil, on cleaned surfaces. The research will be conducted through two primary sections: experimental methods and numerical simulations. The experimental component will involve practical testing in water to observe the behavior of pressure distribution when the water interacts with selected cleaned objects to validate the simulation model. In parallel, numerical methods will be employed to examine the pressure distribution, allowing for a more comprehensive understanding of the fluid dynamics at play. By combining these two approaches, the study aims to achieve a thorough and accurate assessment of how each liquid behaves under the same conditions.

### EXPERIMENT SETUP

GT SONIC-D6 which is the ultrasonic tank made from stainless steel used for investigation. The rectangular ultrasonic tank is 300 mm x 155 mm x 150 mm (L x W x H), has a volume of 6 L. Refer Fig. 3 for geometry CAD of ultrasonic tank. Under ultrasonic tank is PZT-4 piezoelectric transducer with 3 horns for source of generate the acoustic waves at 40kHz with 230 V. The tank is constructed from stainless steel detailed in Tables 1. To validate the simulation results using the foil corrosion test, which is a typical way to assess the model for ultrasonic cleaning. Aluminum foil is chosen due to its low weight, consistent properties, high moisture resistance, and thinness, among other factors[10]. Add water to the ultrasonic tank with the full tank and place aluminum foil above 2 cm from the bottom tank. The size of rectangular aluminum foil is 280 mm x 120 mm. As suggested by the industrial partner, ultrasonic cleaning will operate at 150 W, 40 kHz, with 2 min of sonication time at a temperature of 298 K. The results of foil corrosion test would be compared with acoustic pressure distribution predicted from computational model. Using ImageJ software to calculate the diameter of the high acoustic pressure area and position of acoustic pressure both of simulation result and experimental results. Calculating the accuracy of model with 3 samples of experiment by using below equation:

$$\% \text{ error} = \frac{A_2 - A_1}{A_1} \times 100\%$$

Where,  $A_2$  are diameter and position of simulation result, and  $A_1$  are diameter and position of experiment result

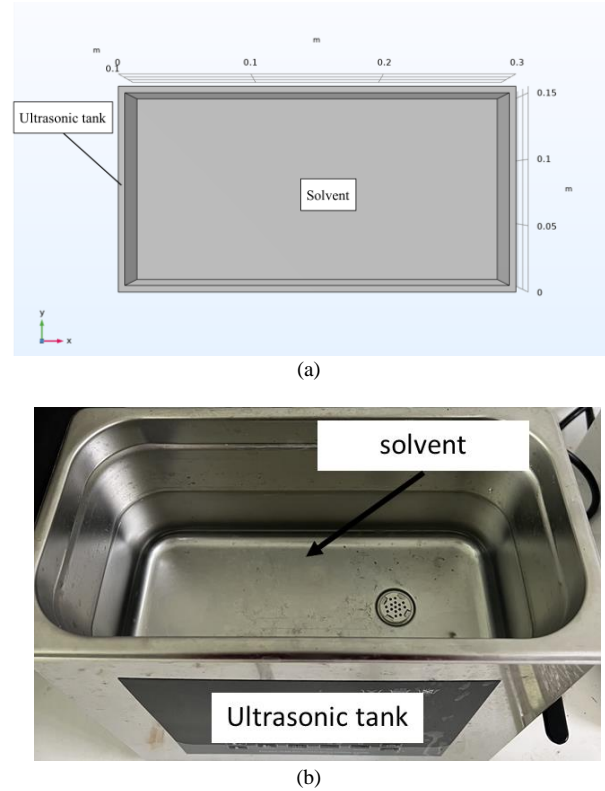


Fig. 3. The geometry of ultrasonic tank: (a) CAD model (b) The actual ultrasonic tank

TABLE I  
Material properties of stainless steel [11]

Type	Value
Density	7750 kg/m <sup>3</sup>
Young's modulus	193 GPa
Poisson's ratio	0.31
Bulk modulus	16.93 GPa
Shear modulus	73.66 GPa

### NUMERICAL METHODS

The GT SONIC-D6 is an advanced ultrasonic tank model designed to simulate pressure distribution accurately, utilizing the powerful capabilities of COMSOL Multiphysics software. For the simulations, a variety of solvents are employed, including crude oil, isopropyl alcohol, acetone, and water, each selected for their distinct properties that are meticulously detailed in Table 2. The simulation was set to operate at a controlled temperature of 293 Kelvin, providing a standard environment for analysis. The primary focus of this study is to meticulously examine the pressure distribution dynamics as they evolve from the initial conditions through to the steady state for each of the selected solvents

TABLE II

Property of solvent at temperature of 298 K [9][12]

Solvent	Density (kg/m <sup>3</sup> )	Sound speed (m/s)
Crude oil	864	1406
Isopropyl	785	1614
Ethanol	789	1706
Water	997	1499

Using COMSOL Multiphysics that suitable to simulate the ultrasonic cleaning with acoustic module [5]. Specific physics includes acoustic pressure, solid mechanics, and electrostatics.

Pressure acoustic module is assigned to fluid domain. Setting pressure acoustic module in linear elastic behavior and exhibit the speed of sound and density from material that assign to fluid domain [13]. It uses the following equation to calculate acoustic pressure [14], [15]:

$$\nabla \cdot \left( \frac{-1}{\rho_c} (\nabla \cdot p_t - q_d) \right) - \frac{K_{eq}^2 \cdot p_t}{\rho_c} = Q_m \quad (1)$$

where,

$$K_{eq}^2 = \left( \frac{\omega}{C_c} \right)^2 \quad (2)$$

$$C_c = c, \quad (3)$$

$$\rho_c = \rho \quad (4)$$

where,  $K_{eq}$  is muck number,  $\omega$  is angular velocity,  $C_c$  and  $c$  are sound speed,  $\rho_c$  and  $\rho$  is density,  $p_t$  is total acoustic pressure,  $Q_m$  is monopole source.

Solid mechanics module is assigned to solid domain including ultrasonic tank and piezoelectric transducer. Set piezoelectric material to piezoelectric transducer. Define solid material in linear elastic material and the physics is calculated by equation [15], [16]:

$$-\rho \omega^2 u = \nabla \cdot s + F_v e^{i\phi} \quad (6)$$

where,  $u$  is fluid velocity,  $F_v$  – body force  $S$  is second Piola-Kirchhoff stress tensor.

Electrostatics are assigned to piezoelectric which is an important component in ultrasonic cleaning. Applied voltage and ground are 230 V and 0 V, respectively, to operating transducer [5]. Using following formula [15]:

$$\nabla \cdot D = \rho_v \quad (7)$$

$$E = -\nabla V \quad (8)$$

where,  $D$  is electric charge density,  $\rho_v$  is electric charge concentration,  $E$  is electric field,  $V$  is electric potential.

In simulation, meshing size is the most important to calculate the accurate result. It was suggested that element size of at least 5 element per wavelength should be employed [17]. Wavelength of fluid can be calculated by following equation:

$$\text{wavelength}(m) = \frac{\text{sound speed (m/s)}}{\text{frequency (Hz)}} \quad (9)$$

Meshing study was carried out and the size selected to ensure the accurate result is shown in Fig.4, the maximum element are 3.7 mm and 1.2 mm, respectively. The maximum element growth rate is 1.2 Also, curvature factor is 0.4 and resolution of narrow regions is 0.7.

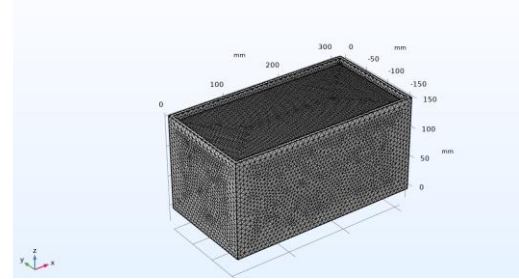
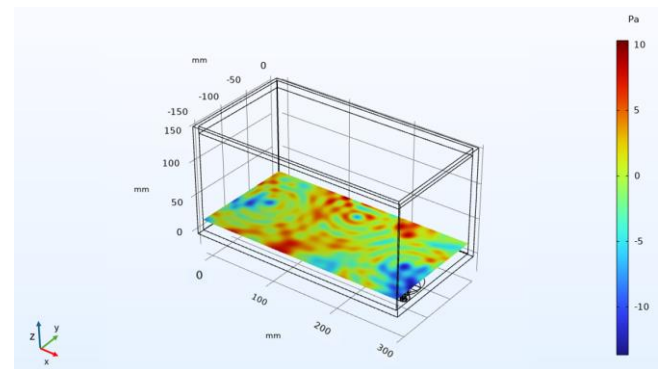


Fig. 4. Meshing Parts

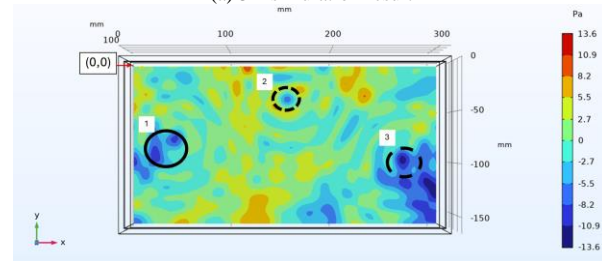
### III. RESULTS AND DISCUSSION

#### VALIDATION

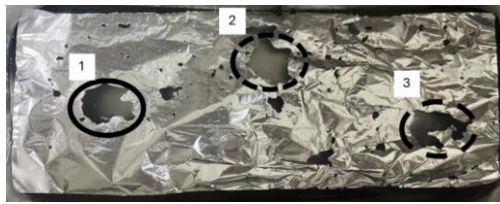
The validation process will involve a detailed comparison with the simulation results concerning the distribution of acoustic pressure in the water, specifically at a depth of 2 cm from the bottom of the ultrasonic tank, measured within 2 minutes at a temperature of 298 K. To assess the accuracy of the acoustic pressure generated within the ultrasonic tank, Figure 5 presents a comparison between the acoustic pressure distribution observed in aluminum foil tests and the corresponding simulation results. Previous study [3], [8], [18], [19] have indicated that the tiny hole in aluminum foil illustrates acoustic pressure distribution. The corrosion test conducted on the aluminum foil revealed several small holes, which correspond to areas where acoustic pressure is concentrated. Notably, the locations of these corrosion-induced tiny holes align closely with the predicted areas of acoustic pressure distribution as shown in the simulation results.



(a) 3D simulation result



(b) 2D simulation result



c) Foil corrosion test

Fig. 5. Comparison of acoustic pressure distribution between foil corrosion test and simulation result for case with water solvent

The circle best fit for the hole is identify as position 1, position 2, and position 3. The hole in the aluminum foil during the experiment presents high negative acoustic pressure, as shown in the simulation results. The negative pressure moments are associated with rarefactions in the liquid, where cavitation bubbles are formed, while the positive pressure moments correspond to the compression points at which the bubbles implode[20]. Some experimental results differ from the simulation results due to slight variations in operating temperature, and some parts of the aluminum foil float in water. Additionally, the diameter area of acoustic pressure simulation result and experimental results in the table demonstrate that the % errors between the simulation and experimental data are consistently low, ranging from 1.47% to 2.84% as shown Table 3. The position of the hole in the simulation and experiment results is shown in Table 4. The percentage errors for both x and y directions are relatively low, ranging from 0.7% to 3.9%. At Position 1, the simulation slightly underestimates the x-direction displacement and slightly overestimates the y-direction, with percentage errors of 3.9% and 1.2%, respectively. Position 2 shows the smallest discrepancy, with percentage errors of 0.7% in the x-direction and 3.9% in the y-direction. For Position 3, the simulation predicts the displacement with 2.5% error in the x-direction and 1.1% in the y-direction. This variability can be attributed to factors such as measurement uncertainty and external influences. Despite this, the overall agreement between the simulation and experimental results supports the reliability of the simulation in predicting acoustic pressure distribution.

Once the model validation is complete, we plan to utilize the simulation results to predict the acoustic pressure distribution when varying different solvents, including crude oil, isopropyl alcohol, water, and ethanol.

TABLE III

Diameter of high acoustic pressure area of simulation result and experiment result.

	position 1	position 2	position 3
Simulation(mm)	31.3	29.8	32.2
Experiment(mm)	30.4	29.3	31.6
% error	2.8	1.5	1.9

TABLE IV

Position of high acoustic pressure area of simulation result and experiment result.

	position1		position2		position3	
	x	y	x	y	x	y
Simulation (mm)	36.1	-72.3	138.6	-35.8	249.0	-81.7
Experiment(mm)	37.6	-71.4	139.6	-37.3	243	-82.6
% error	3.9	1.2	0.7	3.9	2.5	1.1

## EFFECT OF SOLVENT ON ACOUSTIC PRESSURE DISTRIBUTION

To simulate the steady state of acoustic pressure distribution in crude oil, isopropyl, water, and ethanol at 298 K, the relationship between maximum acoustic pressure and time was investigated. Figure 6 shows the relationship of the graph between maximum acoustic pressure and time. For each case, the results for the first 2000  $\mu$ s covering the initial state to steady. The graph represents the variation in acoustic pressure (Pa) over time ( $\mu$ s) for four liquids: water, ethanol, isopropyl alcohol (IPA), and oil. The x-axis shows the time in microseconds, ranging from 0 to 2000  $\mu$ s, while the y-axis represents the acoustic pressure in pascals. Each liquid's behavior is depicted by a distinct curve, allowing for a comparative analysis of their acoustic responses. Initially, all four liquids exhibit sharp increases in acoustic pressure, reaching their respective peaks within the first 200  $\mu$ s. Oil demonstrates the highest peak acoustic pressure, approximately 1730 Pa, occurring at around 150  $\mu$ s. This value is significantly higher than the peaks observed for water, ethanol, and IPA, which all reach around 1200 Pa. The differences in peak pressures highlight the influence of physical properties such as density, viscosity, and compressibility on the propagation of acoustic waves. Oil's distinct behavior suggests its higher density and viscosity compared to the other liquids, allowing it to sustain larger pressure amplitudes[9]. Water, ethanol, and IPA show similar trends, with peak pressures occurring within a close time range. Their peaks are slightly lower than that of oil and decay more rapidly. Among these three liquids, the curves for ethanol and IPA are nearly identical, suggesting that their solvent properties are closely aligned. As time progresses, the acoustic pressure in all liquids decreases significantly. By 800  $\mu$ s, the pressure levels for all four liquids have substantially decayed and reached to steady state. While the decay is relatively fast in water, ethanol, and IPA, oil shows a slightly slower decline in acoustic pressure, which may be attributed to its higher viscosity[21], [22]. In summary, the graph underscores the impact of liquid properties such as density, viscosity, and compressibility on acoustic wave propagation. Oil, with its high peak pressure and slower decay, behaves differently from water, ethanol, and IPA, which exhibit lower peaks and faster dissipation. These findings have implications for various applications, including ultrasonic imaging, fluid characterization, and acoustic wave propagation studies, where the acoustic



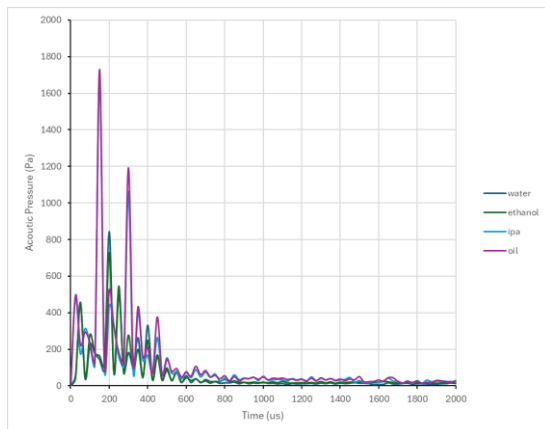
behavior of different liquids plays a critical role. This relationship can be described by the following equation [9]:

$$c = \sqrt{\frac{dp}{d\rho}}$$

Crude oil possesses a lower density than water, which has significant implications for its behavior in various operational contexts. Variations in operating pressure can enhance these effects, leading to noticeable alterations in acoustic pressure and the behavior of sound waves in the medium. Additionally, when considering a solvent that is a bubbly liquid, it becomes evident that the acoustic pressure distribution is much more distinct and well-defined compared to that observed in a non-bubbly liquid [9]. The presence of bubbles creates a more complex acoustic environment, allowing for clearer differentiation in pressure levels and wave propagation patterns, which can be critical for applications involving fluid dynamics and acoustics.

Figure 7 illustrates the acoustic pressure distribution at a height of 2 cm above the bottom of the tank during steady state at 800  $\mu$ s. The areas highlighted in blue and red represent what is known as the cavitation zone, a critical region where cavitation bubbles experience a phenomenon of implosion and collapse. Within this zone, these bubbles undergo cyclical oscillations that lead to varying acoustic pressures in the surrounding environment. The phases of acoustic pressure alternate between periods of positive pressure, illustrated in blue, and periods of negative pressure, represented in red.

The research results suggested that water and ethanol could serve as effective indicators for identifying the areas of maximum and minimum acoustic pressure, thus making them ideal for the cleaning of various objects. This phenomenon could illustrates the behavior and movement of acoustic waves through these mediums. On the other hand, oil and isopropyl alcohol fail to clearly display distinct acoustic wave propagation patterns, resulting in difficulty in defining cavitation zone. Consequently, their efficacy in cleaning applications is considerably diminished compared to that of water and ethanol. The effectiveness of cleaning can vary based on the type of item being cleaned and the cleaning solution employed.



Fi g. 6. The maximum of acoustic pressure for water, ethanol, isopropyl, and crude oil from initial phase to steady state

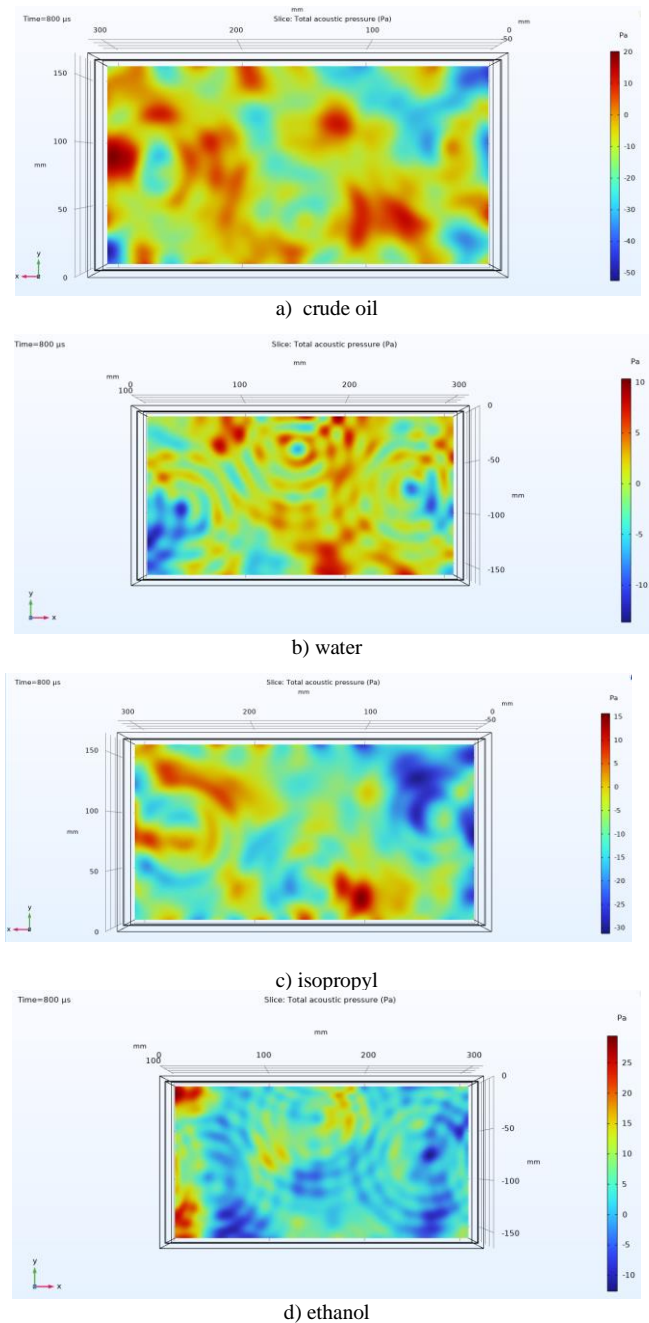


Fig. 7 Acoustic pressure distribution at 800 us above 2 cm from the bottom tank of a) crude oil, b) water, c) isopropyl, and d) ethanol

#### IV. CONCLUSION

The results indicate that acoustic pressure distribution is more effective in bubbly liquids compared to those without bubbles. Notably, ethanol and water exhibit a clearly defined cavitation zone compared to crude oil and isopropyl alcohol. Density and viscosity are important properties of solvent to affect the acoustic pressure and acoustic pressure distribution

#### ACKNOWLEDGMENT

I would like to express my sincere gratitude to my advisor, Asst. Prof. Dr. Karuna Tuchinda, for their invaluable guidance and support throughout this research.



## REFERENCES

- [1] T. J. Mason, "Ultrasonic cleaning: An historical perspective," *Ultrason. Sonochem.*, vol. 29, pp. 519–523, 2016, doi: 10.1016/j.ultsonch.2015.05.004.
- [2] S. B. Awad and R. Nagarajan, "Chapter 6 - Ultrasonic Cleaning A2 - Kohli, Rajiv," pp. 225–280, 2010, Accessed: May 06, 2022. [Online]. Available: <http://www.sciencedirect.com/science/article/pii/B9781437778304100064>
- [3] W. Tangsopa and J. Thongsri, "Development of an industrial ultrasonic cleaning tank based on harmonic response analysis," *Ultrasonics*, vol. 91, no. July 2018, pp. 68–76, 2019, doi: 10.1016/j.ultras.2018.07.013.
- [4] F. J. Fuchs, "Ultrasonic cleaning and washing of surfaces," in *Power Ultrasonics: Applications of High-Intensity Ultrasound*, Elsevier Inc., 2015, pp. 577–609. doi: 10.1016/B978-1-78242-028-6.00019-3.
- [5] V. Rokad and D. H. Pandya, "Development of 3D improved acoustic transient model for vibro cleaner using COMSOL multiphysics," *Mater. Today Proc.*, vol. 44, pp. 776–781, 2021, doi: 10.1016/j.matpr.2020.10.635.
- [6] Z. Wei and L. K. Weavers, "Combining COMSOL modeling with acoustic pressure maps to design sono-reactors," *Ultrason. Sonochem.*, vol. 31, no. January, pp. 490–498, 2016, doi: 10.1016/j.ultsonch.2016.01.036.
- [7] T. Tao, J. Zhao, and W. Wang, "Study on the Characterization Method of Ultrasonic Cavitation Field based on the Numerical Simulation of the Amplitude of Sound Pressure," *MATEC Web Conf.*, vol. 319, p. 02003, 2020, doi: 10.1051/mateconf/202031902003.
- [8] W. Tangsopha, J. Thongsri, and W. Busayaporn, "Simulation of ultrasonic cleaning and ways to improve the efficiency," *2017 Int. Electr. Eng. Congr. IEEECON 2017*, no. March, 2017, doi: 10.1109/IEEECON.2017.8075747.
- [9] S. Niazi, S. H. Hashemabadi, and M. M. Razi, "CFD simulation of acoustic cavitation in a crude oil upgrading sonoreactor and prediction of collapse temperature and pressure of a cavitation bubble," *Chem. Eng. Res. Des.*, vol. 92, no. 1, pp. 166–173, 2014, doi: 10.1016/j.cherd.2013.07.002.
- [10] "Aluminum foil test method for performance of ultrasonic cleaner," Oct. 2010.
- [11] W. Tangsopa and J. Thongsri, "A dual frequency ultrasonic cleaning tank developed by transient dynamic analysis," *Appl. Sci.*, vol. 11, no. 2, pp. 1–20, 2021, doi: 10.3390/app11020699.
- [12] S. Lago and P. A. Giuliano Albo, "Thermodynamic properties of acetone calculated from accurate experimental speed of sound measurements at low temperatures and high pressures," *J. Chem. Thermodyn.*, vol. 41, no. 4, pp. 506–512, 2009, doi: 10.1016/j.jct.2008.11.005.
- [13] J. A. Morton *et al.*, "Effect of Temperature and Acoustic Pressure During Ultrasound Liquid-Phase Processing of Graphite in Water," *Jom*, vol. 73, no. 12, pp. 3745–3752, 2021, doi: 10.1007/s11837-021-04910-9.
- [14] COMSOL Multiphysics User Guide, "Acoustics Module," *Interfaces (Providence)*, p. 214, 2010.
- [15] COMSOL Multiphysics, "The COMSOL Multiphysics Reference Manual," *Manual*, pp. 1–1336, 2015, [Online]. Available: [www.comsol.com/blogs](http://www.comsol.com/blogs)
- [16] COMSOL Multiphysics and COMSOL, "Structural Mechanics Module," *Manual*, p. 454, 2008, [Online]. Available: [www.comsol.de](http://www.comsol.de)
- [17] M. Definition, "Piezoelectric Tonpilz Transducer," pp. 1–48.
- [18] W. Tangsopa and J. Thongsri, "A novel ultrasonic cleaning tank developed by harmonic response analysis and computational fluid dynamics," *Metals (Basel)*, vol. 10, no. 3, 2020, doi: 10.3390/met10030335.
- [19] N. Bretz, J. Strobel, M. Kaltenbacher, and R. Lerch, "Numerical simulation of ultrasonic waves in cavitating fluids with special consideration of ultrasonic cleaning," *Proc. - IEEE Ultrason. Symp.*, vol. 1, no. c, pp. 703–706, 2005, doi: 10.1109/ULTSYM.2005.1602948.
- [20] H. Lais, P. S. Lowe, T. H. Gan, and L. C. Wrobel, "Numerical modelling of acoustic pressure fields to optimize the ultrasonic cleaning technique for cylinders," *Ultrason. Sonochem.*, vol. 45, no. October 2017, pp. 7–16, 2018, doi: 10.1016/j.ultsonch.2018.02.045.
- [21] D. Qin *et al.*, "Influence of interactions between bubbles on physico-chemical effects of acoustic cavitation," *Ultrason. Sonochem.*, vol. 104, no. 2, p. 106808, 2024, doi: 10.1016/j.ultsonch.2024.106808.
- [22] K. Yasui, A. Towata, T. Tuziuti, T. Kozuka, and K. Kato, "Effect of static pressure on acoustic energy radiated by cavitation bubbles in viscous liquids under ultrasound," vol. 130, no. November, pp. 3233–3242, 2011, doi: 10.1121/1.3626130.

# Dynamic Responses of Prestressed Concrete Sleeper due to Flat-Spot on Railway Wheels using Finite Element Method

Supapol Rahannok<sup>1, a)</sup>, Kittichai Sojiphan<sup>1, b)</sup>, Chayut Ngamkhanong<sup>2, c)</sup>

## Author Affiliations

<sup>1</sup> Railway Vehicles and Infrastructure Engineering Program, The Sirindhorn International Thai-German Graduate School of Engineering (TGGS), King Mongkut's University of Technology North Bangkok, 1518 Pracharat 1 Road, Wongsawang, Bangsue, Bangkok, 10800, Thailand.

<sup>2</sup> Advanced Railway Infrastructure, Innovation and Systems Engineering (ARIISE) Research Unit, Department of Civil Engineering, Chulalongkorn University, Phayathai Road, Pathumwan, Bangkok, 10330, Thailand

## Author Emails

<sup>a)</sup> s6409096860077@kmutnb.ac.th

<sup>b)</sup> kittichai.s@tggs.kmutnb.ac.th

<sup>c)</sup> Corresponding author: chayut.ng@chula.ac.th

**Abstract.** This study conducts a detailed simulation analysis to understand the dynamic responses of monoblock prestressed concrete sleeper for metre-gauge track on ballast bed under the impact forces generated wheel flat-spots. This study uses DTrack to generate force-time histories due to wheel flats, and ANSYS for creating Finite Element (FE) models and simulating structural behavior. The model is the first validated against negative bending test. It thoroughly evaluates how forces from wheel flat-spots affect sleeper performance, focusing on sleeper displacement and stress and stresses on ballast. This study considers several scenarios considering flat-spot depths varying from 1 mm to 3 mm with train velocities between 60 km/h and 150 km/h, revealing a clear link between increased flat-spot depths and velocities on the structural responses of prestressed concrete sleeper.

**Index Terms**— Prestressed Concrete Sleeper, Finite Element Method, Wheel Flat-Spot, Railway Vehicle, Impact Load

## I. INTRODUCTION

In railway engineering, flat spots on train wheels significantly impact wheel-rail contact dynamics, leading to the deterioration of both rails and wheels. Flat spots form when a wheel slides, creating a flattened segment on its circumference [1, 2]. This results in high-impact forces that can potentially increase stress on the rail and its support structures, accelerating degradation. In general, wheel forces can be divided into two main types [3]:

- Quasi-static and dynamic ride forces, which occur at lower frequencies and relate to gradual loading during regular operations.
- Dynamic wheel-rail or impact forces, occurring at higher frequencies from either wheel or rail anomalies that can significantly increase dynamic factor [4].

Finite Element Analysis (FEA) is extensively used to study the relationship between wheel flats and impact forces, model the effects of wheel flat dimensions and train velocity on track dynamics. FEA accurately estimates impact forces, aiding engineers in assessing how vehicle speed, wheel diameter, and flat spot size influence these forces [5]. However, this requires extensive computational time. Concrete sleepers play a crucial role in distributing loads

from rails to ballast, ensuring track stability and alignment. Due to their embedded position on the ballast bed, sleepers can sometimes be difficult to inspect. The sleepers are generally susceptible to damage from impact forces that may create stress exceeding their tensile strength, emphasizing the need for timely crack detection [5, 6].

Recent advancements in Deep Convolutional Neural Networks (DCNN) and Finite Element Analysis (FEA) have improved the precision of real-time crack detection in sleepers. Integrating advanced crack detection with FEA simulations allows engineers to understand and mitigate risks from wheel flat-induced forces, enhancing infrastructure resilience and safety [7].

Stress concentration zones like the sleeper's midspan and rail seat are crucial for crack initiation detection. These areas undergo significant stresses that can cause fractures, impairing sleeper integrity and accelerating track deterioration [8, 9]. Advanced simulation tools such as Finite Element Modeling (FEM) and regular maintenance are essential for monitoring and addressing these issues, ensuring the reliability and longevity of railway tracks [10]. To reduce computational time, two methods are utilized: first, a dynamic analysis is performed on DTrack to obtain the applied loads; then, these loads are used as input in the Finite Element Model (FEM) for further analysis. This study employs a developed sleeper model that can be used to

further enhance track stability and sleeper durability.

## II. METHODOLOGY

The methodological framework of this investigation is succinctly encapsulated and depicted in the flowchart presented in Fig. 1.

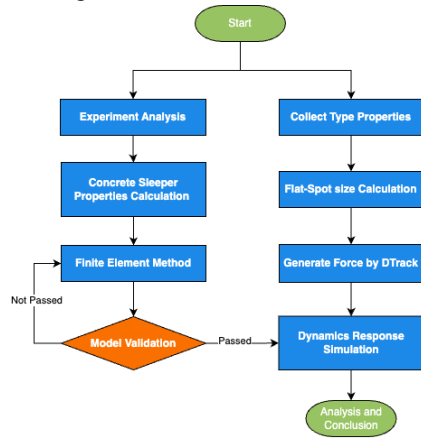


Fig. 1 Methodology adopted in the study

## Experiment and structural details of prestressed concrete sleeper

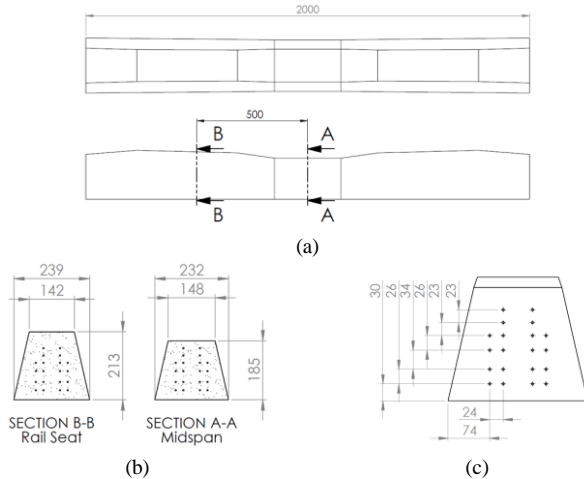


Fig. 2 SRT prestressed concrete sleeper [11] (a) overall, (b) cross-section, and (c) reinforcement wire position

A Monoblock sleeper prototype used in Thailand (shown in Fig. 2), underwent a three-point negative bending test. The modulus of elasticity for the prestressed concrete sleeper was calculated to be 32,657 N/mm<sup>2</sup>, based on the proportional limits from the load-displacement curve [12]. The slope of the curve's linear portion measured 123.4 kN/mm. Per SRT specifications, a total prestressing force of 335 kN was applied to 20 wires, with each wire experiencing 16.75 kN [11]. The estimated ultimate tensile and compressive strengths of the concrete were 6 N/mm<sup>2</sup> and 60 N/mm<sup>2</sup>, respectively [13, 14, 15]. Material properties for the concrete and wire are detailed in Table 1.

## MATERIAL PROPERTIES OF CONCRETE AND PRESTRESSWIRE

Material	Variable	Value	Unit
Concrete	Modulus of Elasticity	32657	N/mm <sup>2</sup>
	Poisson Ratio	0.2	-
	Tensile Ultimate Strength	6	N/mm <sup>2</sup>
	Compressive Ultimate Strength	60	N/mm <sup>2</sup>
Prestressed Wire	Young's Modulus	200	M10 <sup>3</sup> N/mm <sup>2</sup>
	Poisson Ratio	0.3	-
	Tensile Yield Strength	1724	N/mm <sup>2</sup>
	Tensile Ultimate Strength	1860	N/mm <sup>2</sup>
	Prestress Force	16.75	kN

## Modelling of prestressed concrete sleeper in ANSYS

The 3D modeling of the sleeper was conducted using ANSYS, leveraging the SOLID65 element to simulate crack initiation and propagation [16, 17, 18, 19]. SMART crack growth techniques [13] enhanced the accuracy of these simulations by effectively mapping crack evolution. The combination of SOLID65 and LINK180 elements in prestressed concrete sleepers accurately models the concrete and reinforcement under dynamic loads [16, 20, 21], representing high-strength concrete and high-tension steel wires, respectively. Command codes were used to specify element types. To refine mesh quality, the highly curved ends of the SRT sleeper were simplified. The CEINTF command created inter-element connectivity with constraint equations between the nodes of SOLID65 and LINK180, ensuring effective load transfer. This configuration allows the rebar (LINK180) to withstand both tensile and compressive stresses, while the concrete (SOLID65) manages overall structural responses, including potential cracking or crushing. An initial prestressing force of 1333 N/mm<sup>2</sup> was applied to the LINK180 elements. The material properties are detailed in Table 1.

## Concrete sleeper with track bed modeling

The numerical model of the sleeper rests on a detailed foundation composed of ballast, sub-ballast, and subgrade layers, as shown in Fig. 3. This setup accurately mimics the sleeper's interaction with the track bed under dynamic loads, enhancing simulations of load transfer and track stability. The ballast layer extends at least 300 mm beyond the sleeper's edges to ensure adequate support and load distribution, with material properties detailed in Table 2. Rail seats, modeled as 140 mm x 140 mm steel plates with a 7 mm thickness and placed 538 mm from the sleeper's center [11], emulate real force distribution.

TABLE I

TABLE II  
PROPERTIES OF TRACK BED [9]

Component	Density [kg/m <sup>3</sup> ]	Young's Modulus [N/mm <sup>2</sup> ]	Poisson's Ratio
Ballast	1,590	97	0.12
Sub-Ballast	1,910	212	0.2
Subgrade	2,300	200	0.25

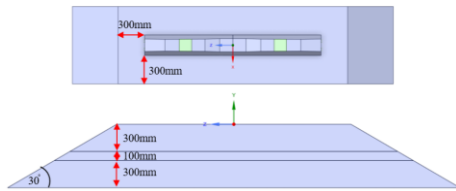


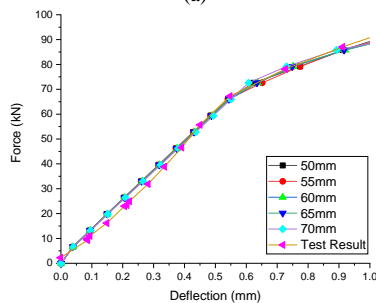
Fig. 3 Dimension of substructure model

### Model validation

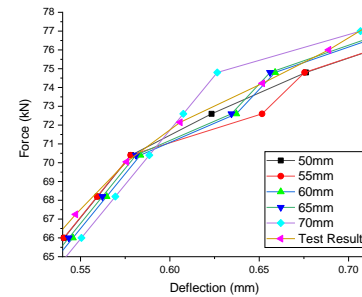
The sleeper model was validated by applying a 110 kN load, consistent with real-world conditions and experimental setups. The load was applied at the bottom middle of a small section as a pusher beneath the sleeper, as shown in Fig. 4(a), using steel elements. The upper two pieces on the sleeper served as fixed support, made of the same material as the pusher. SOLID65 was used for concrete material, while LINK180 was assigned to 20 reinforcement steel bars. The load was applied as a linear curve from zero to 110 kN. Initial crack observations, particularly at midspan, aligned with experimental results, confirming the model's accuracy. Mesh convergence analysis identified 50 mm as the optimal mesh size, balancing precision and computational efficiency, while 70 mm meshes failed to converge in load capacity. The validated 50 mm mesh was applied to the sleeper-ballast model, enabling a detailed analysis of dynamic responses, including the effects of wheel flat-spots. The simulations successfully captured key aspects such as crack initiation and stress distribution. The results showed a stiffness slope of 119 kN/mm and crack initiation at 71 kN, closely matching experimental data and demonstrating the model's reliability for both static and dynamic load predictions. Fig. 4(b and c) illustrates the load-displacement curves comparing numerical and experimental results.



(a)



(b)



(c)

Fig. 4 (a) Mesh pattern for model validation (b) Comparison of load displacement curves (c) Load displacement curve at first crack zone zoomed

### Influence of wheel flat-spot

The Dynamics Analysis of Rail Track Structures Program (DTrack) is specialized software designed to simulate and analyze railway track dynamics under various loads. It models the interaction between train loads, track components, and infrastructure, helping engineers assess track performance, safety, and maintenance [4]. DTrack generates force data for conditions like wheel flat spots to study their impact on sleeper stress and longevity [22]. Simulation variables, including wheel dimensions and operational parameters, with flat-spot depths of 1 mm, 2 mm, and 3 mm and corresponding flat lengths of 86 mm, 121 mm, and 148 mm on a 915 mm diameter wheel.

The State Railway of Thailand (SRT) infrastructure accommodates up to a 20-ton axle load. For dynamic analysis, a coal wagon with a 26.5-ton axle load was modeled to replicate heavy-haul coal transportation scenarios. This higher load model helps in understanding track performance and durability under extreme conditions. Evaluating these conditions is vital for determining the resilience of the sleeper and ballast system against significant dynamic loads.

The variation of force on the sleeper from a train with a normal wheel at speeds of 60 km/h, 100 km/h, and 150 km/h is shown in Fig. 5. Fig. 6 illustrates the peak force variations on the sleeper for flat-spot depths. The force generated by lower speed has a longer force occur than the higher speed according to figure 5. For each speed, the larger wheel flat generates the higher maximum amplitude of impact force by the figure 6.

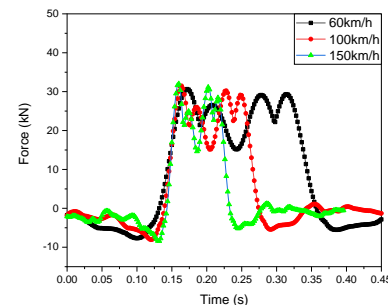


Fig. 5 Force acting on the rail seat of the sleeper for a train with normal wheel at varying train velocities



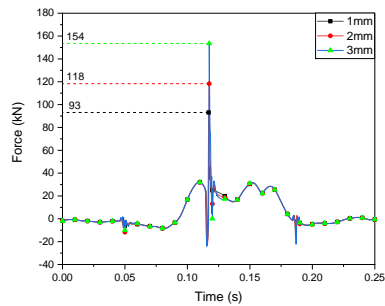


Fig. 6 Force acting on the rail seat of the sleeper for different wheel-flat depths 150 km/h

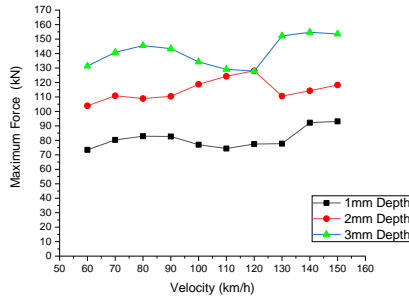


Fig. 7 Maximum force on sleeper for the different flat-spot depths

Fig. 7 displays the maximum forces generated by varying wheel flat-spot depths and vehicle speeds (60–150 km/h), showing a clear trend of increasing force with higher speeds and larger flat spots. These results indicate that both factors significantly amplify the impact on the sleeper. Each set of force data was subsequently applied to the complete model, as shown in Fig. 8. The mesh size of the substructure is larger than that of the sleeper mesh to reduce unnecessary simulation time.

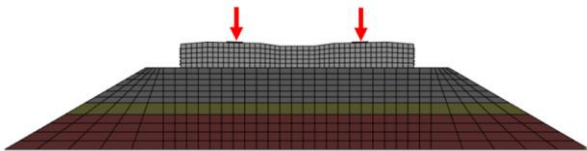


Fig. 8 Application of force data on the full model

The bottom of the subgrade, represented by the brown part, is fixed. Each substructure (Ballast, Sub-ballast, and Subgrade) is bonded through contact modeling in this study. The contact between the sleeper and ballast includes two types: no-separation, which prevents the sleeper from lifting out of the ballast due to positive force, and frictional contact with a coefficient of 0.7, assuming the highest friction between rock surfaces.

### III. RESULTS AND DISCUSSION

#### Sleeper Displacement

The sleeper's displacement response was assessed at the rail seat and midspan to determine how varying wheel flat-spot depths and train velocities affect sleeper displacement. Results confirm that displacement increases with both higher speeds and larger flat-spot depths, highlighting a direct correlation between dynamic loads and sleeper deformation.

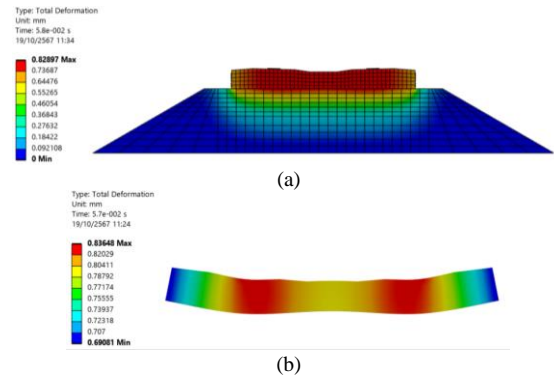


Fig. 9 Results of (a) sleeper deformation at true scale and (b) sleeper deformation with 100-time scale

Fig. 9 shows the sleeper's deformation at actual scale under maximum load conditions (3 mm flat-spot depth and 150 km/h speed).

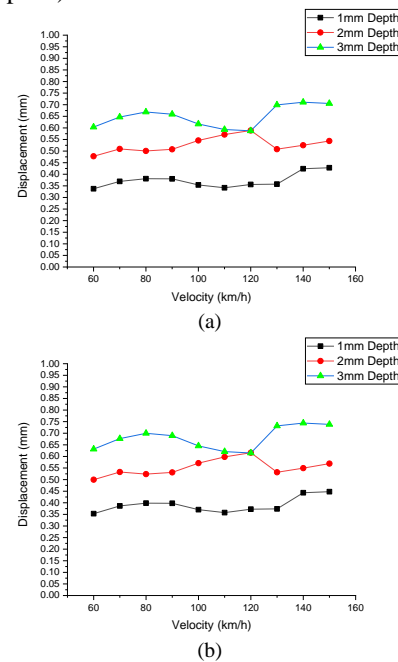


Fig. 10 Displacement at (a) midspan and (b) rail seat of a sleeper

Fig. 10 shows that for flat-spot depths of 1 mm, 2 mm, and 3 mm, maximum displacements at the midspan are 0.428 mm, 0.589 mm, and 0.711 mm respectively, and at the rail seat, they are 0.448 mm, 0.616 mm, and 0.744 mm respectively. This aligns with the peak force trends in Fig. 7, confirming that larger flat-spot depths and higher speeds significantly increase sleeper displacement.

#### Stress on Ballast

The compressive stress on the ballast was analyzed to understand load transfer and potential ballast degradation over time. The distribution of stress between the sleeper and ballast affects track stability and durability. Variations in flat-spot depth and speed notably affect the compressive stress exerted on the ballast, particularly at the midspan and rail seat locations.

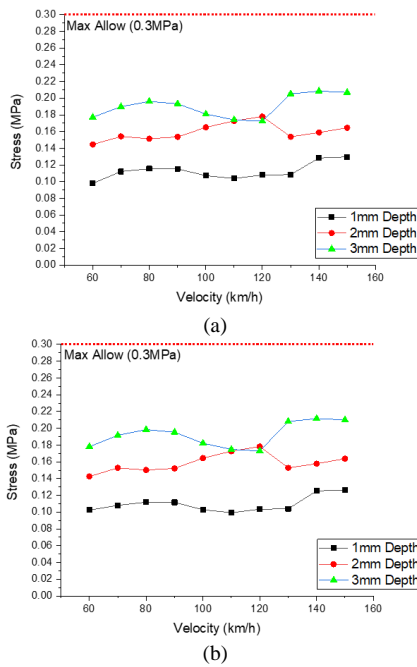


Fig. 11 Compressive stress at (a) midspan and (b) rail seat of a ballast

Fig. 11 illustrate compressive stress at the midspan and rail seat for varying depths. Maximum compressive stresses at midspan are 0.147 N/mm<sup>2</sup>, 0.202 N/mm<sup>2</sup>, and 0.244 N/mm<sup>2</sup>, while at the rail seat, they reach 0.157 N/mm<sup>2</sup>, 0.215 N/mm<sup>2</sup>, and 0.258 N/mm<sup>2</sup>. All results are lower than the maximum stress allowable as 0.3 N/mm<sup>2</sup> [9]. These elevated stress levels suggest that prolonged exposure to severe conditions could contribute to ballast settlement or degradation over time. This highlights the importance of maintaining adequate ballast conditions to ensure long-term track stability and reduce maintenance demands. Thus, monitoring these parameters becomes crucial to prevent potential ballast damage and track instability due to excessive stress.

#### IV. CONCLUSION

A comprehensive numerical and experimental study was conducted to assess the dynamic response of a Monoblock prestressed concrete sleeper on a ballast bed subjected to impact load due to wheel flat-spot. This study utilized prestressed concrete sleepers and employed DTrack and ANSYS software, adhered to Thai railway specifications. It examined how varying flat-spot depths (1-3 mm), and train velocities (60-150 km/h) affect key sleeper response parameters like rail seat and midspan displacement, stress distribution, and ballast stress.

Results showed that sleeper displacement increases with both flat-spot depth and train velocity. Maximum displacements at midspan were 0.428 mm, 0.589 mm, and 0.711 mm, while at the rail seat they were 0.448 mm, 0.616 mm, and 0.744 mm for flat-spot depths of 1 mm, 2 mm, and 3 mm, respectively. Under the most extreme loading conditions (3 mm flat-spot depth at 150 km/h), ballast stress levels peaked at 0.208 N/mm<sup>2</sup> and 0.212 N/mm<sup>2</sup>, respectively indicating the need for regular monitoring and maintenance of ballast structure. Note that there was no crack

observed in the model by a single impact load. In fact, the repeated impact load can be considered to further enhance the understanding on fatigue behavior.

Effective monitoring of wheel conditions and managing train velocities are crucial to reducing structural damage and enhancing railway safety. Future research should explore a wider range of flat-spot depths and velocities, incorporating more complex real-world scenarios. This will enhance predictive models and support the development of advanced safety and maintenance protocols, promoting a more sustainable and resilient railway infrastructure.

Maintaining optimal railway conditions is essential for the durability of prestressed concrete sleepers under dynamic loads from wheel flat-spots. Regular track maintenance and real-time wheel monitoring help prevent excessive stress. Proper ballast compaction and sleeper support reduce localized stress, while high-performance concrete enhances crack resistance. Rail pads and damp materials further mitigate impact forces, improving sleeper longevity and railway reliability.

#### ACKNOWLEDGMENT

The first author immensely grateful to the DAAD scholarship for funding his studies at RWTH Aachen University in Germany. This study would not have progressed without the experimental results of the prestressed bending test provided by Mr. Ratabhat Wangtawesap. His practical insights were invaluable for this research.

#### REFERENCES

- [1] U. Olofsson, Y. Zhu, S. Abbasi and S. Lewis, "Tribology of the Wheel–Rail Contact – Aspects of Wear, Particle Emission and Adhesion," 2013.
- [2] M. Sysyn, M. Przybylowicz, O. Nabochenko and J. Liu, "Mechanism of Sleeper–Ballast Dynamic Impact and Residual Settlements Accumulation in Zones with Unsupported Sleepers," 2021.
- [3] C. Esveld, *Modern Railway Track* (2nd edn), Netherlands: MRT-Productions, 2001.
- [4] A. M. Remennikov, M. Murray and S. Kaewunruen, "Conversion of AS1085.14 for prestressed concrete sleepers to limit states design format," 2008.
- [5] M. Mohammadi, A. Mosleh, C. Vale and D. Ribeiro, "An Unsupervised Learning Approach for Wayside Train Wheel Flat Detection," 2023.
- [6] R. U. A. Uzzal, "Dynamic Analysis of Railway Vehicle-Track Interactions Due to Wheel Flat with a Pitch-Plane Vehicle Model," 2008.
- [7] D. Li, R. You and S. Kaewunruen, "Crack Propagation Assessment of Time-Dependent Concrete Degradation of Prestressed Concrete Sleepers," 2022.

- [8] S. Kaewunruen, A. Freimanis and K. Goto, "Impact responses of railway concrete sleepers with surface abrasions," 2018.
- [9] A. Raj, C. Ngamkhanong, L. Prasittisopin and S. Kaewunruen, "Nonlinear Dynamic Responses of Ballasted Railway Tracks using Concrete Sleepers Incorporated with Reinforced Fibres and Pre-Treated Crumb Rubber," 2023.
- [10] C. Ngamkhanong and S. Kaewunruen, "Effects of under sleeper pads on dynamic responses of railway prestressed concrete sleepers subjected to high intensity impact loads," 2020.
- [11] State Railway of Thailand (SRT), Prestressed Concrete Sleeper Drawing.
- [12] R. Wangtawesap, "Impact of Drainage Problem on Dynamic Behavior of Ballasted Trackbridge," 2024.
- [13] R. Youa, K. Goto, C. Ngamkhanong and S. Kaewunruenb, "Nonlinear finite element analysis for structural capacity of railway prestressed concrete sleepers with rail seat abrasion," 2018.
- [14] Department of Rail Transport Thailand, Track Component "มขร. – C - 005 – 2566", Bangkok, 2023.
- [15] สำนักงานมาตรฐานผลิตภัณฑ์อุตสาหกรรม, Prestress Concrete Sleeper (มอก.2528 เล่ม3-2553), Bangkok, 2010.
- [16] D. Tjitradi and S. Taufik, "3D ANSYS Numerical Modeling of Reinforced Concrete Beam Behavior under Different Collapsed Mechanisms," 2017.
- [17] J. Sadeghi and A. Babaee, "Structural Optimization of B70 Railway Prestressed Concrete Sleepers," 2006.
- [18] J. Nairn and N. Stevens, "Rational Design Method for Prestressed Concrete Sleeper," 2010.
- [19] L. Dahmani, A. Khennane and S. Kaci, "Crack identification in reinforced concrete beams using ANSYS software," 2010.
- [20] D. Fisseha, M. Mulugeta and E. Gebreyouhannes, "Optimal Design and Analysis OF Pre-Stressed Concrete Sleepers," 2016.
- [21] P. Mani and P. M. Raju, "Finite-element modeling of partially prestressed concrete beams with unbonded tendon under monotonic loadings Finite-element modeling," 2022.
- [22] A. Favorskaya and N. Khokhlov, "Modeling the impact of wheelsets with flat spots on a railway track," 2018.

# Enhancing Road Traffic Accident Data Collection and Reconstruction Process in Thailand

Anyamanee Suksing<sup>1, a)</sup> and Julaluk Carmai<sup>1,2, b)</sup>

## Author Affiliations

<sup>1</sup>The Sirindhorn International Thai-German Graduate School of Engineering (TGGS), Thailand

<sup>2</sup>Automotive Safety and Assessment Engineering Research Centre, Bangkok, Thailand

## Author Emails

<sup>a)</sup> s6309093860069@email.kmutnb.ac.th

<sup>b)</sup> julaluk.c@tggs.kmutnb.ac.th

**Abstract.** Road traffic accidents represent a major global challenge, with Thailand having one of the highest fatality rates, particularly in motorcycle-related crashes. This paper addresses the issue of fragmented and inconsistent accident data collection in Thailand, which hinders effective policy-making and the development of safety interventions. Through a comprehensive analysis of global accident databases, including FARS from the USA and GIDAS from Germany, this study proposes a structured framework to improve accident data collection and enhance computational accident reconstruction processes in Thailand. By standardizing the collection of critical data, including vehicle details, crash scenarios, and victim information, the proposed digital platform aims to support better accident reconstructions and provide insights into common crash characteristics. This platform will streamline data collection, improve collaboration among stakeholders, and ultimately contribute to reducing road traffic injuries and fatalities in Thailand.

**Index Terms**—Accident data collection, Accident investigation, Accident database, Accident reconstruction

## I. INTRODUCTION

ROAD traffic accidents are a significant global issue, with the United Nations aiming to reduce injuries and fatalities by 50% by 2030[1] through the Safe System approach. Thailand has one of the highest road traffic fatality rates, ranking 9th globally and 1st in motorcycle-related deaths[2]. On average, Thailand witnesses approximately 61 deaths daily due to road traffic injuries (RTIs), with a staggering 74.4% involving motorcycle riders and passengers [3]. The lack of a standardized accident investigation process contributes to data inconsistencies, limiting effective policy-making. Traffic-related injuries and fatalities are influenced by various factors, such as impact speed, angle, vehicle mass, motorcycle design, sitting position, and road and environmental conditions. Understanding the events before and during a crash is crucial to identifying the factors that contribute to accidents and injuries. The reconstruction of accidents and injuries helps identify how crashes occur and what causes both accidents and injuries. However, in Thailand, macro-level accident data are insufficient to accurately reconstruct accidents or investigate the influence of specific accident parameters on motorcyclist injuries.

In Thailand, various organizations collect traffic accident data for their purposes, leading to differences in the level of

detail based on each organization's focus. As a result, some critical information is often missing. For example, the Ministry of Public Health's Injury Surveillance System provides detailed data on victims' injuries but lacks information on accident scenes and scenarios. Similarly, accident data collected by insurance companies (E-Claim) is primarily intended for claim processing, often omitting other necessary details. The traffic police focus on recording the number of victims and general accident information, while the Ministry of Transportation emphasizes road and environmental conditions. Each dataset reflects the responsibilities and priorities of the respective organization, creating inconsistencies and gaps in essential data. These gaps make it challenging to conduct comprehensive analyses that identify the true factors and nature of accidents across different areas.

Computational accident reconstruction is essential for understanding accident dynamics, aiding forensic analysis, and developing preventive measures by identifying root causes and improving safety. It provides insights into the nature, severity, and contributing factors of road accidents that result in injuries or fatalities. However, effective reconstruction relies on detailed crash scenarios, vehicle deformation data, and victim injuries—information often lacking in Thailand due to fragmented and inconsistent data collection methods. The essential data fields should be collected. This study proposes improving Thailand's



accident investigation and data collection process through a structured framework based on international best practices while also addressing sustainability concerns. A key benefit of the proposed data collection approach is the enhancement of data analysis and its suitability for computational accident reconstruction, which requires highly accurate, well-structured datasets for simulations and forensic analysis.

## II. METHODOLOGY

The study adopted a structured approach to enhance accident data collection and reconstruction processes. Fig. 1 presents a flow diagram outlining the key tasks involved in this study. Existing accident databases from both developed countries and Thailand were analyzed to identify key data fields and structures. Essential data elements were refined to align with Thailand's environmental and cultural constraints, addressing gaps in local accident reporting. A government or institutional department responsible for accident investigations was selected based on its data collection capabilities, accessibility, and readiness for improvement. This selection aimed to establish a scalable and sustainable model for accident data enhancement. Based on insights from the database review and existing workflows, a structured framework was developed to enhance accident data collection. The framework addresses challenges in data accuracy, completeness, and standardization. To ensure efficiency, the framework was implemented in a digital format, improving systematic accident investigations and reconstructions. The enhanced data collection process also supports deeper analysis for developing targeted preventive measures. Accident Reconstruction and Crash Analysis Finally, the collected data were utilized in accident reconstructions to determine impact velocity and position, enabling the identification of common crash characteristics. These insights contribute to a better understanding of accident dynamics and support the development of effective safety interventions.



Fig. 1. Overall Methodology

## III. RESULTS AND DISCUSSION

High-quality accident databases in Germany (German in-depth accident study cooperation-GIDAS), the UK (STATS19), and the USA (Fatal Accident Report System-FARS)[4] serve as benchmarks for road safety research and policymaking. These databases provide structured, in-depth data on accident causes, vehicle details, environmental factors, and injury outcomes. Table 1 summarizes the key features, strengths, and limitations of these databases.

TABLE I

SUMMARY OF ACCIDENT DATABASE

Database	Organization	Key Features and Strengths	Limitations
GIDAS	BASt-Germany	In-depth investigations with medical and vehicle data for detailed research	2 city-specific data, separate from national stats, with fewer cases.
STATS 19	DFT-UK	Systematic collection of detailed road accident data on injury and fatal crashes reported to the police.	Focuses on accident circumstances, lacking biomechanical, causation.
FARS	NHTSA-USA	Systematic data collection with detailed, publicly accessible information for research and policy.	Limited to fatal crashes, with accuracy varying by state reporting.

In Thailand, multiple organizations manage accident databases, each focusing on specific aspects of crash reporting. These organizations include, the Ministry of Public Health (MOPH) with Health Data Center -HDC, Injury Surveillance System-IS, the Road Traffic Injury collecting system for Situation Awareness Team -RTI SAT, the Royal Thai Police (RTP) with the CRIME and Police report System-PRS, the Road Accident Victims Protection Company Limited (RVP) with the E-Claim, the Ministry of Transport (MOT) with the Highway Accident Information Management System -HAIMS, Accident Report Management System -ARMS and the Ministry of Interior (MOI). Additionally, the Central Institute of Forensic Science (CIFS) under the Ministry of Justice (MOJ) provides intensive accident investigation reports. The key features, strengths, and limitations of each database are summarized in Table 2.

Since the NHTSA accident databases are the only ones offering public access, this study focuses on reviewing the data fields of the FARS database. The investigation and reporting of road traffic accidents in Thailand involve numerous organizations, each playing a role in collecting and managing data related to various factors. Each organization employs an individual template and platform, which are not shared with others due to security and data governance concerns. The MOPH focuses on gathering injury and personal factors. MOT focuses on the vehicle, road condition, and environment, while the CIFS and police also include the crash scenario in detail and injury but less on vehicle-related data. Insurance company focuses on claims. However, the existing Thailand data lacks details related to the causes of the accidents and safety equipment usage, which are crucial for implementing measures to prevent accidents or reduce their severity.

TABLE II  
SUMMARY OF THAI ACCIDENT DATABASE

Database	Organization	Key Features and Strengths	Limitations
CRIMES	RTP	Covers all crimes, including traffic accidents.	Internal use; focused on legal aspects.
PRS	RTP	Reliable data from officers, covering all accident types.	Legal-focused; limited accident details.
E-Claim	RVP	Large dataset on personal injury claims.	Lacks road/accident details, no vehicle damage.
RTI SAT	MOPH	Collects accident scenarios, risk factors, human, vehicle, and road data.	Small sample, limited injury data, quality varies.
IS	MOPH	Focuses on human injuries from patients.	Lacks event, road, and vehicle details.
Investigation Report	MOPH-public health office	Collects accident scenarios and risk factors.	Limited to fatal accidents, small sample.
HDC	MOPH	Injury data from hospital patients.	Focused on injuries, lacks accident details.
HAIMS, ARMS	MOT	Focuses on fatal accidents on department-owned roads.	Limited to department roads; environment focus.
E-Report	MOI	Nationwide data from hospitals and police on various incidents.	Limited to New Year and Songkran.
Investigation report	MOJ (CIFS)	Forensic investigation with detailed accident scenarios.	Limited to fatal accidents, small sample.

The data fields in FARS serve as a benchmark for comparison. The FARS database categorizes variables into six levels: Crash level, Vehicle level, Driver level, Pre-crash level (vehicle/driver), Person level (motor vehicle occupant) and Person level (non-motor vehicle occupant). Each level consists of various field variables (data elements). The comparison of the field variables was conducted for each category of data elements. They are summarized in table 3.

The necessary variables were identified as described in Table 4. They must be sufficient for accident reconstruction. Considering completeness, expandability, sustainability, and data accessibility, the public health office, which documented essential information, plays a key role. This office is under the MOPH and includes units at a comprehensive level, spanning all areas and districts with a similar structure. Finally, the public health offices in Khon-Kaen and Udon-Thani provinces were willing to provide information and collaborate.

TABLE III  
DATA COMPARISON BETWEEN FARS AND THAI DATABASE

Database	Element group						
	Crash level	Vehicle level	Driver level	Precrash level	Person level (MVO)	Person level (non-MVO)	All data element
FARS	5	48	26	25	33	53	190
PRS	24	13	5	10	18	22	92
E-claim	10	3	1	1	9	7	31
RTI SAT	26	15	3	11	19	29	103
IS	8	1	1	1	14	12	37
Public health office report	22	16	5	10	20	32	105
HDC	6	0	0	0	8	8	22
HAIMS, ARMS	19	3	1	10	8	4	45
E-report	18	1	2	2	11	7	41
CIFS report	20	25	2	9	18	9	83

TABLE IV  
SUMMARY OF DATA FIELDS IN PILOT TOOL

Factors	Data fields
General information (9 fields)	General information about the incident Detailed information of the location
Crash Event and Direction (7 fields)	Number of vehicles involved Characteristic of crash Collision diagram and direction of the crash
Road and environment (13 fields)	Type of the road Environment condition Roadside furniture
Vehicle information (13 fields)	Type of vehicle and Information about the vehicle Information about safety equipment Vehicle damage information including picture
Injured person's information (16 fields)	General information about the injured person Information about the use of safety equipment Injury information

The existing data collection process of the local public health office was assessed and the issues and root causes for each issue within the process was identified. Accident investigations at local public health offices involve multiple stakeholders, including rescuers, police, paramedics, nurses, and public health officers. Each maintains separate records, making data integration and analysis difficult, especially for road accidents. Limited cooperation further complicates the process. At accident scenes, responders face time pressure to assist victims and manage traffic but often lack training in capturing detailed photos, leading to incomplete documentation. Data collection is inefficient due to fragmented systems, errors, and reliance on inaccurate

witness accounts. Limited expertise in vehicle and road data among nurses and public health officials, along with delays in police evidence collection, further weakens investigations.

A digital platform for data import and storage was proposed to streamline information collection, including images and audio reports from rescue teams. This system allows secure access for public health officials and verification teams, supporting cross-agency collaboration. Data can be exported in various formats to meet different needs. Training accident investigators—including rescuers, doctors, nurses, public health officials, and police—on photography, data collection, and program use is essential. Tailored training adapted to the Thai context will enhance analysis, particularly in vehicle and road safety. Clear photography guidelines and standardized documentation methods will improve accuracy and efficiency. These improvements will streamline workflows, reduce redundancy, and enhance the accuracy and usability of accident data.

A structured digital platform is designed to enhance accident data collection and management. The system gathers information in a standardized format with designated data fields, ensuring easy linking, sorting, and extraction for analysis. The system is adaptable for use across different districts. It incorporates picture symbols and diagrams to illustrate accident scenarios and impact directions, as shown in figure 4, similar to established frameworks like FARS,

The platform is user-friendly, accessible via both mobile and PC, and enables data export in usable report formats. Interconnectivity is a key feature, allowing integration with other database platforms. Additionally, the system supports multimedia data collection, including images and audio recordings, ensuring comprehensive documentation. It also facilitates retroactive verification, enabling authorities to review and validate records efficiently. Finally, the platform accommodates multi-agency collaboration, allowing various stakeholders—such as emergency responders, law enforcement, and public health officials—to access and contribute to a shared database.

The implementation of a digital data entry system has significantly enhanced the efficiency and accuracy of road traffic accident data collection. By categorizing essential variables into five key sections—reporter information, event details, road and environmental factors, vehicle specifics, and injury data—the system streamlines data management and analysis. The verification and pilot processes ensured the system's usability, with iterative refinements based on stakeholder feedback. The transition to a new platform further improved data handling capabilities, reducing redundancy and enhancing usability for field personnel. These advancements contribute to a more structured and reliable approach to accident data collection and analysis.

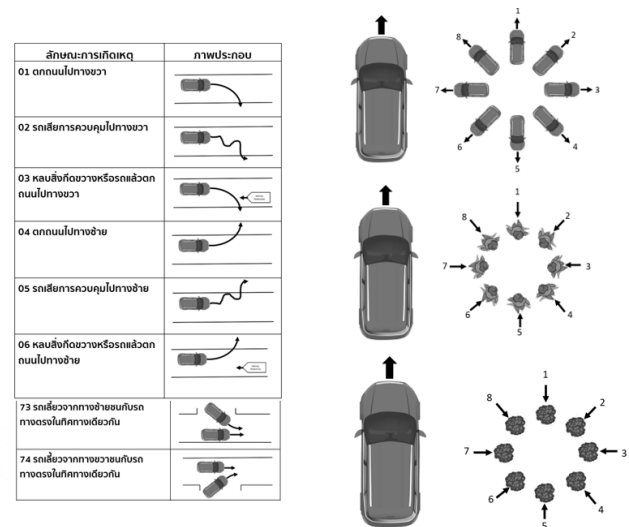


Fig. 2. Collision Diagram(a) And Direction Of Crash(b) In Pilot Tool

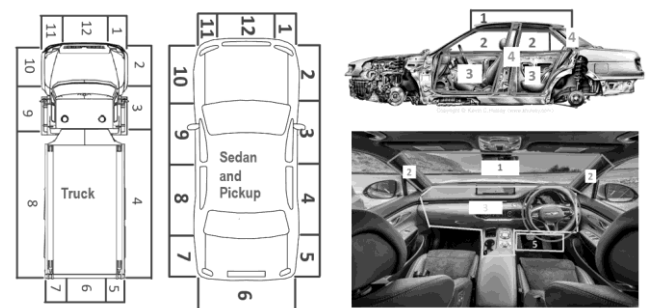


Fig. 3. Damaged Area Outside(a) And Inside(b) The Car In Pilot Tool

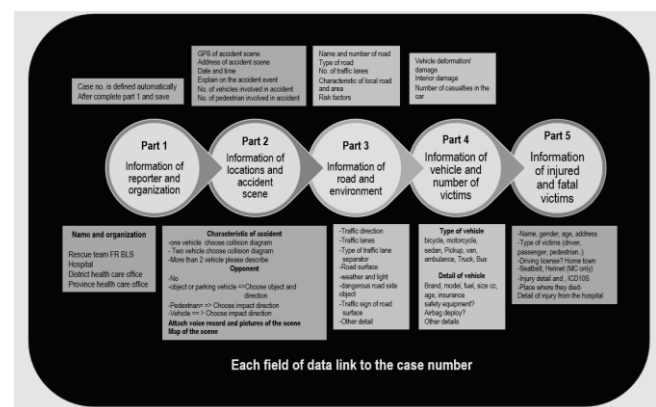


Fig. 4. Structure Of Pilot Tool

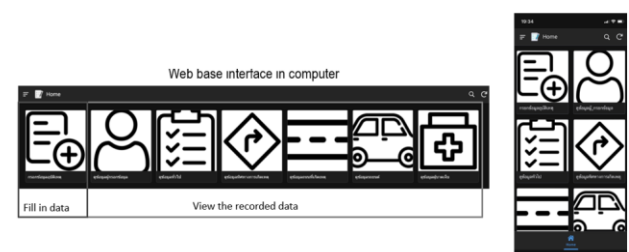


Fig. 5. Interface Of Pilot Tool

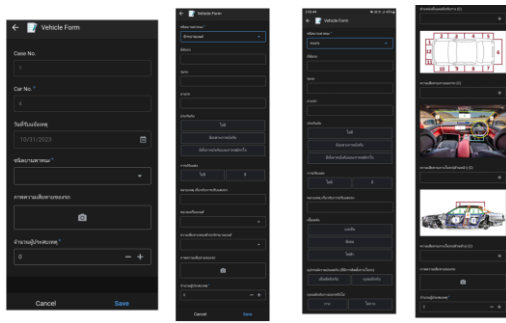


Fig. 6. Interface Of Pilot Tool



Fig. 7. The Linkage Between Each Section Through Variables

The application was used to collect and store accident data within a defined field, organized in a format that allows easy extraction and analysis. The data collected, including collision type, direction, and position of impact, can be directly used to analyze common crash characteristics. The analysis of car-motorcycle collisions revealed that head-on collisions (33.33%) were the most common, followed by side impacts (25%) and rear-end collisions (16.67%), as shown in Figure 8 a. As illustrated in Figure 8 b, most crashes occurred at the front of the vehicle (75.01%), particularly on the driver's side (41.67%). The mid and passenger sides each accounted for 16.67%, while rear-end collisions were less common (8.3%).

An analysis of incidents between cars and motorcycles

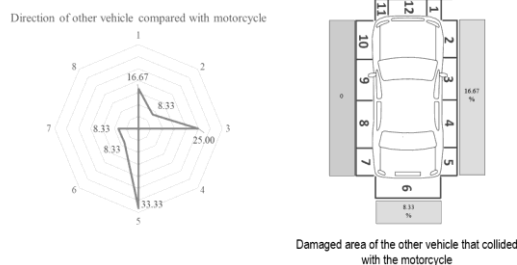


Fig. 8. An Analysis Of Incidents Between Cars And Motorcycle, (a)Direction Of Other Vehicle Compared With Motorcycle, (b) Damaged Area Of Other Vehicle That Collided With The Motorcycle

The reconstruction process requires detailed vehicle information, including type, brand, and stiffness estimates, as well as the point of impact (POI), point of rest (POR) for both the vehicle and motorcyclist, impact direction, damage profiles, and occupant details such as weight, height, and injuries. This data is gathered from physical evidence, including accident scene photographs and vehicle damage records. The crash scenario is simulated using impact direction, angle, and crash area information. The simulation results are then compared with recorded scene evidence to ensure accuracy. PC-crash program was employed to reconstruct the accidents using the accident data collected using the new recording system.

For the sample reconstruction case, a motorcycle turned right at an intersection and collided with a pickup truck traveling straight. As a result, the motorcyclist and the motorcycle slid approximately 5 meters from the point of impact, while the pickup truck continued moving forward. The deceased's head hit the sidewalk curb. This data was then used to create a scene sketch, as shown in Figure 9a, and was input into a simulation program. The comparison of the collision point, collision characteristics, and the final positions of the motorcyclist and motorcycle is shown in Figures 9b and 9c. From the reconstruction, the motorcycle's speed was determined to be 40 km/h, and the pickup truck's speed was 60 km/h. The relative heading angle was 20.74 degrees.



Fig. 9. Sample Reconstruction Case, (a) Scene Sketch, (b)Evidence, (c)Reconstruction

Twelve cases were reconstructed to obtain impact speed, vehicle angulation, and damaged areas. The calculated relative speeds ranged from 30 km/h to 140 km/h, as shown in Table 5. Speed is a critical issue that the Road Safety Center of Thailand places great importance on[5]. If accident data from motorcycles, which are the vehicles most involved in accidents (over 80%)[6], can be collected and used to calculate the speed retrospectively, it would be extremely beneficial for setting measures and policies related to road safety in Thailand.



TABLE V  
RESULT FROM ACCIDENT RECONSTRUCTION

	Direction	Damaged area of another vehicle	Relative speed (kph)
Case 1	3	1	62
Case 2	3	3	30
Case 3	5	1	99
Case 4	1	1	88
Case 5	6	12	49
Case 6	2	12	100
Case 7	3	4	58
Case 8	7	11	62
Case 9	5	1	140
Case 10	1	6	80
Case 11	5	1	99
Case 12	5	11	117

According to the 2024 road traffic accident situation in Thailand reported by the Injury Prevention Division, Department of Disease Control, the economic loss from road traffic accidents in 2022 was approximately 116.4 billion baht for fatalities. For medical expenses, the cost for severe injuries was approximately 6.7 billion baht, and for minor injuries, the medical cost was 1.1 billion baht. However, inconsistent data collection limits accurate loss estimation. This study's structured data approach enhances accident analysis, supporting policies that could reduce accident severity and associated costs.

This study primarily focuses on car-motorcycle collisions, a major contributor to Thailand's road traffic fatalities. According to the Department of Land Transport and the Ministry of Public Health, motorcycle-related accidents account for 74.4% [3] of all road traffic deaths in Thailand. Within this category, the study examines common crash characteristics such as collision type, impact direction, and injury outcomes. Although the research does not cover all types of accidents, it addresses a significant portion of Thailand's traffic incidents by focusing on one of the most vulnerable road user groups—motorcyclists. Expanding this methodology to include other accident types and injured cases could provide a more comprehensive analysis of accident causes nationwide.

#### IV. CONCLUSION

This study highlights the significant gaps in Thailand's current road traffic accident data collection processes, which impede accurate accident reconstructions and the identification of key factors contributing to injuries and fatalities. By analyzing international best practices and adapting them to local contexts, a structured and digital platform for data collection has been proposed. The new system addresses critical issues such as data fragmentation, inefficiency, and inconsistency, enabling more comprehensive analysis of road traffic accidents.

The collection of detailed information, including vehicle types, crash characteristics, environmental conditions, and injury outcomes, will facilitate more accurate computational accident reconstruction. This approach will not only improve accident investigation accuracy but also aid in the development of targeted safety interventions, ultimately supporting Thailand's efforts to reduce road traffic fatalities and improve public safety. Benefits of the structured accident data system include lower medical costs, reduced vehicle damage, and improved legal processes. This makes the approach a valuable investment for policymakers and supports its integration into national accident data strategies.

#### ACKNOWLEDGMENT

We sincerely thank the Nong Ruea and Udon Thani health officers and nurses for their cooperation in the pilot project. Their contributions were instrumental in refining the study. Lastly, we extend our gratitude to all who supported this research.

#### REFERENCES

- [1] World Health Organization, "WHO kicks off a Decade of Action for Road Safety." Accessed: Oct. 28, 2021. [Online]. Available: <https://www.who.int/news/item/28-10-2021-who-kicks-off-a-decade-of-action-for-road-safety>
- [2] *Global Status Report on Road Safety 2023*, 1st ed. Geneva: World Health Organization, 2023.
- [3] S. Suerungruang, N. Chaiyaratana, and J. Carmai, "Associations between the Accident Parameters and Motorcyclist Injuries using Multibody Simulation and Decision Tree Analysis," 2024.
- [4] "Fatality Analysis Reporting System Analytical User's Manual, 1975-2020," p. 661.
- [5] Road Safety Operations Center, "Road Traffic Accident Fatality Rate Target for the Years 2020-2027," Department of Disaster Prevention and Mitigation, Ministry of Interior, Thailand. Accessed: May 08, 2023. [Online]. Available: [http://roadsafety.disaster.go.th/inner.road-safety-1.196/download/menu\\_8581/](http://roadsafety.disaster.go.th/inner.road-safety-1.196/download/menu_8581/)
- [6] Division of Injury Prevention, Department of Disease Control, "Road Traffic Death Data Integration, RTDDI ( 3 Databases Integrated )." Accessed: Oct. 28, 2021. [Online]. Available: <https://dip.ddc.moph.go.th/new/%E0%B8%9A%E0%B8%A3%E0%B8%B4%E0%B8%81%E0%B8%B2%E0%B8%A3/%E0%B8%9A%E0%B8%A3%E0%B8%B4%E0%B8%81%E0%B8%B2%E0%B8%A3%E0%B8%94%E0%B9%89%E0%B8%B2%E0%B8%99%E0%B8%82%E0%B9%89%E0%B8%AD%E0%B8%A1%E0%B8%B9%E0%B8%A5>

# Biomimetic Kinetic Facade Design for Enhanced Daylighting: A LEED v 4 Based Approach for a Reading Room of a Dormitory in Chittagong, Bangladesh

Gourav Dey<sup>1,a)</sup> and Vorapat Inkarojrit<sup>2,b)</sup>

## Author Affiliations

<sup>1</sup>Graduate student, Department of Architecture, Faculty of Architecture, Chulalongkorn University

<sup>2</sup>Assistant Professor, Department of Architecture, Faculty of Architecture, Chulalongkorn University

## Author Emails

<sup>a)</sup> Corresponding author: 6678503125@student.chula.ac.th

<sup>b)</sup> vorapat.i@chula.ac.th

**Abstract.** This study investigates the role of biomimetic kinetic façades in improving the daylighting performance of a reading room in Chittagong, Bangladesh. This design is inspired by the thigmonastic behavior of *Mimosa pudica* plants which adapts to environmental changes. The design focuses on a kinetic façade that adjusts based on sunlight and environmental conditions, maximizing daylight access, while decreasing glare and heat gain to enhance occupant comfort. As the space performance addressed with relative standard, the study explores critical aspects including Spatial Daylight Autonomy (sDA) and Annual Sunlight Exposure (ASE) aligned with other vital parameters via LEED v4 rating system, confirms the kinetic façade design advances not merely the visual comfort but also aligns with the energy-efficiency and sustainability standards in developing habitations. The proposed facade model demonstrated a better distribution of daylight and independence from artificial lighting in comparison with static shading systems by conducting parametric simulations. Results show that the kinetic facade fulfilled the LEED v4 requirements for daylighting performance, and provided a cost-effective, energy-efficient, green sustainable solution for tropical climates. This research could spotlight how biomimetic architecture can be a vehicle towards the UN Sustainable Development Goals for buildings that behave like adaptive ecosystems.

**Index Terms—** Biomimetic architecture, Daylighting performance, Kinetic façade, LEED v4, Sustainability, Sustainable design.

**Abbreviation:** AF; Adaptive façade; ASE, Annual Sunlight Exposure; KF, Kinetic Façade; sDA, Spatial Daylight Autonomy; sDG, Spatial Distributing Glare; LEED, Leadership in Energy and Environmental Design; KSS, Kinetic Shading System; CIBSE, Chartered Institution of Building Services Engineers; IES, Illuminating Engineering Society; SDG, Sustainable Development Goal;

## I. INTRODUCTION

The design of a sustainable building envelop plays a vital role to regulate the indoor climate, energy consumption, and overall comfort of occupants as well as it has great impact on user experience[1]. Traditionally, facades were static elements, designed to protect the interior from external elements, providing minimal flexibility in responding to the changing daylight conditions[2]. However, as urbanization increases and the impact of climate change intensifies, the need for more adaptive, efficient, and sustainable architectural solutions has become evident[3]. In this context, the integrated biomimicry architectural design, particularly through the use of kinetic facades[4], puts a novel approach that addresses both environmental performance throughout different climatic condition and time and occupant well-being.

Biomimicry has increasingly changed architectural innovations, especially in the development of adaptive

building envelopes as a design philosophy[5, 6]. By studying biological systems and processes, architects can derive natural strategies to address different challenges from energy efficiency, daylighting to environmental control[7, 8]. The dynamic behavior of natural organisms such as plants' responses to touch sensitivity offers valuable insights into the design of facades that can evolve and adapt to environmental stimuli[9]. One such example is the thigmonastic leaf movement of plants, where touch stimulation leads to rapid folding of the stimulated leaflet[10]. These adaptive mechanisms can be rendered into KF, which move or alter their form in response to different climatic condition to cut down heat and improve daylight condition[11].

The shift from static to dynamic facades is important as the need for sustainable architecture grows[12]. Static facades with fixed shading elements often cannot adapt to the changing angles of sunlight. Even though they can block heat from the sun in certain conditions, they find it hard to make the best use of natural light throughout the day or during different seasons [13]. On the other hand, KFs use moving

parts that respond immediately to outdoor conditions, providing clear benefits over static designs. KFs enhance a building's energy efficiency and provide greater comfort for its occupants from the inspiration of natural adaptability [14]. Furthermore, AFs can help reduce emissions, increase interior comfort, improve comfort outside the building, and provide aesthetic benefits[15].

Several bio-inspired facade designs exemplify the potential of biomimicry to optimize daylighting in green buildings. The Al Bahr Towers in Abu Dhabi, inspired by the traditional Mashrabiya, employ 2,000 PTFE fabric units that dynamically adjust to solar angles [16]. The Gherkin in London, drawing from the porous structure of sea sponges (*Euplectella aspergillum*), features a diagrid glass facade with spiraling atria that channel daylight, illuminating 85% of the floor area and reducing lighting energy by 40% [2]. Similarly, the Q1 ThyssenKrupp Headquarters in Essen, Germany, emulates sunflower heliotropism with rotating stainless steel fins, ensuring 70% of the interior receives adequate daylight ( $\geq 300$  lux) for 60% of occupied hours [8]. Lastly, the Eden Project in Cornwall, UK, inspired by the hexagonal lattice of dragonfly wings and soap bubbles, utilizes ETFE panels to achieve 90% light transmission, reducing energy use for lighting and heating [2].

LEED is a globally recognized green building rating system that promotes sustainable design and construction practices[17, 18]. According to the LEED v4 standards, which guide green building practices, designs that improve daylight and reduce energy use, like these facades, help buildings earn points for being eco-friendly[19].

In the context of tropical Chittagong, where sunlight exposure is strong and inconsistent throughout the year, KFs present a promising solution to the challenges posed by static facades. By adjusting to changing solar angles using environmental feedback, KFs successfully manage daylight while reducing the negative impacts of glare and excessive heat [20]. To support the United Nations' 17 Sustainable Development Goals, especially the 11<sup>th</sup> goal, which aims to create sustainable cities and communities, we must adopt strategies that reduce energy use and lower carbon emissions[21]. Studies show that in hot places, KFs can reduce energy use by 20-30% compared to fixed designs[22].

## II. CONCEPT THEORY FRAMEWORK

Daylighting plays a vital role in shaping indoor environments, particularly in spaces like reading rooms where visual comfort is essential. Natural light enhances concentration, reduces eye strain, and promotes mental well-being. However, overexposure to sunlight can lead to glare and heat build-up, making it crucial to find a balance between daylight access and thermal comfort[23].

This paper is grounded in three core theories: biomimicry in architecture, kinetic architecture, and sustainability through LEED v4. Biomimicry involves outlining

inspiration from natural systems to solve human challenges[24]. Biomimicry draws inspiration from natural systems, such as the thigmonastic behavior of *Mimosa pudica*, to design facades that dynamically respond to environmental stimuli, optimizing daylighting and energy efficiency while enhancing occupant comfort[2, 25]. A KF is a structure placed on the exterior of a building as a protective layer, featuring movable shading elements that can adjust their shape to respond to the surrounding environment[26-28]. Kinetic architecture introduces movable shading elements that adapt to changing conditions, offering greater flexibility and energy savings [12, 29].

For evaluating daylight performance of the case study, sDA and ASE are used as critical metrics as per LEED v4 standards[30]. sDA measures the percentage of floor area receiving at least 300 lux for 50% of annual occupied hours (8:00 AM to 6:00 PM), indicating daylight sufficiency for reading tasks. Also consider, the daylighting standards for a reading room, as outlined by the Chartered Institution of Building Services Engineers (CIBSE) and the Illuminating Engineering Society (IES), specify a minimum illuminance level of 500 lux to ensure adequate lighting for reading tasks[31, 32].

The glare standard for visual comfort categorizes glare levels as Imperceptible (<35%), Perceptible (35%–40%), Disturbing (40%–45%), and Intolerable (>45%), based on the percentage of floor area experiencing excessive illuminance[33]. These standards aim to provide sufficient daylight on the work plane (typically 0.8 m above the floor) to support visual comfort and reduce reliance on artificial lighting, aligning with energy efficiency goals in sustainable building design.

## III. METHODOLOGY

This research follows a structured methodology (Fig 1) to design and evaluate a biomimetic KF system aimed at enhancing daylighting performance for a reading room. The methodology begins with an in-depth literature review, which critically examines existing studies on biomimetic architecture, KFs, and sustainable design principles. The review focuses on biomimetic inspiration drawn from natural phenomena such as thigmonastic and how these strategies have been applied in architectural fields.

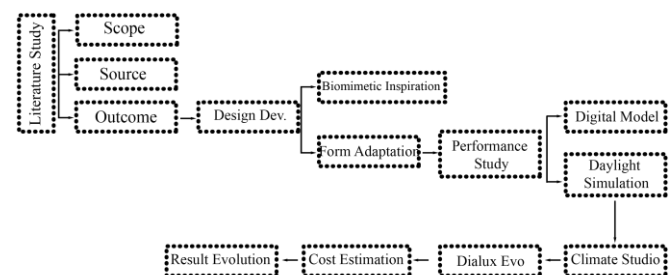


Fig 1: Flowchart of Methodology

Building on insights from the literature study, the research then progresses to façade design development, where the core objective is to integrate adaptive biomimetic principles, particularly sensitivity movement mechanisms inspired by the thigmonastic behavior of plants. This design phase emphasizes dynamic responsiveness of the façade, addressing both daylight optimization and cost effectiveness. By utilizing advanced computational tools such as Rhinoceros and Grasshopper, the geometry and movement patterns of the façade is tailored to Chittagong's unique solar conditions, ensuring an effective response to changing sunlight throughout the day and across seasons.

Following the development of the digital façade model, daylight performance simulations are conducted using Climate Studio[34], a plugin for Rhinoceros and Grasshopper, to evaluate key metrics such as sDA and ASE. These simulations critically assess the performance of the KF system in optimizing daylight and minimizing glare and heat gain. Moreover, Dialux Evo simulations is focus on seasonal variations, particularly during peak solar periods like the summer and winter solstices, to understand how well the façade adapts to the different intensity of sunlight of Chittagong throughout the year.

DIALux Evo was employed to assess daylight uniformity in the reading room, across façade states. Chittagong's weather data, including solar radiation, is modeled under a clear sky condition (CIE clear sky model), emphasizing direct sunlight with minimal diffuse light, as specified in the base case. Simulations are conducted at key times (8:00, 12:00, 16:00) on significant dates (March 21, June 21, September 21, December 21) to capture seasonal variations, with solar angles.

The evaluation of simulation results is critically comparing the performance of the biomimetic KF façade with that of conventional static façade systems. This step is determined whether the kinetic design significantly improves energy efficiency and occupant well-being, while reducing reliance on artificial lighting. Additionally, cost estimation is conducted to assess the feasibility of implementing the KF system, considering both initial investment and long-term energy savings.

#### IV. SITE AND SETTING

The five storied Sheikh Rasel Hall (student's dormitory) in Chittagong University of Engineering and Technology was selected for examination and simulation study. This University is situated in Chittagong, which is the Bangladesh's second-largest city and principal seaport, located in the southeastern region of the country along the Bay of Bengal.

The south east facing reading room (22°27'48.8"N 91°58'11.5"E) in the second floor of the building was chosen for the simulation study (Fig. 2).

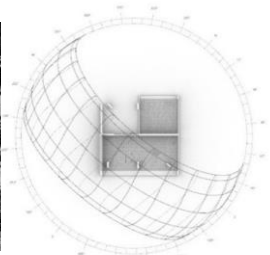


**Fig 2:** (Left) Exterior view of the Site (Right) Sun path Diagram

#### V. BASE CASE

The reading room chosen for the study, experiences significant morning sunlight. Chittagong's tropical monsoon climate brings high solar radiation, peaking in summer (March–June), alongside elevated humidity year-round, intensified during the monsoon season (July–September), and a cooler, drier winter (December–February). With solar angles reaching up to 90° in summer and 67° at noon on the equinox, the climate demands adaptive shading to manage glare, heat gain, and uneven daylight, making this site ideal for testing the biomimetic KF's performance in balancing light and comfort in a reading space. The following assumptions are applied to the daylight performance simulation:

The simulation involves dividing the room into a 0.5 m x 0.5 m sensor grid, using Climate Studio with Chittagong's weather data, and determining the percentage of sensors achieving  $\geq 300$  lux for at least 1,825 hours (50% of occupied hours). Clear sky with sun, minimum of 500 Lux on the work plane in height of 0.85 m from the floor, occupancy schedule (8–16), no shading and no artificial light (Fig 3).

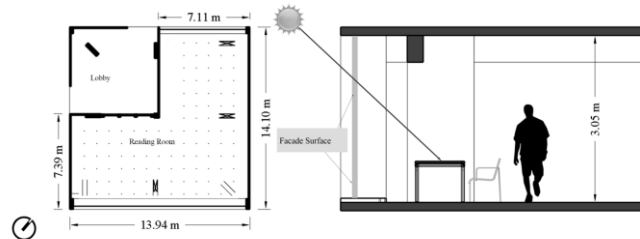


**Fig 3:** (Left) Plan of the case stud (Right) Elevation

The evaluation of daylight performance of plain window (base case) through climate-based daylight metrics show that not enough useful daylight is provided to satisfy occupants' requirements. Although enough daylight is admitted into the room (Table 1), the chart shows that most of the admitted light is higher than expected 500 Lux, resulting in visual discomfort.

Simulation and calculation of the base case scenario of the proposed variables, it is examined that the ASE<sub>1000,250</sub> 24.2%, sDA<sub>300/50%</sub> 99%, avg UDI 67.1% and avg lux is 1684.

From the Table 1, it is also calculated that the daylight condition is not constant throughout the year. The floor area, adjacent to the opening, receives maximum amount of illuminance in the winter solstice (December 21) and Spring Equinox (March 21). From 8am to 12am the space remains over illuminated comparing to the other time of the day or year.



TABLE 1: EXISTING DAYLIGHT CONDITION

Sky Condition	Date	21-Mar			21-Jun			21-Sep			21-Dec		
	Time	8:00	12:00	16:00	8:00	12:00	16:00	8:00	12:00	16:00	8:00	12:00	16:00
Clear sky	$E_{min}$	923	579	397	683	422	460	947	525	388	997	829	250
	$E_{max}$	25419	2749	25583	4477	2218	33177	28833	2569	21997	12194	4748	2893
	$E_{avg}$	5103	1089	1974	1604	867	2998	4964	1035	1805	5805	1858	598
Overcast Sky	$E_{min}$	178	350	178	225	376	213	197	350	160	118	264	96.2
	$E_{max}$	1314	2579	1311	1660	2773	1566	1451	2577	1176	866	1947	709
	$E_{avg}$	439	861	438	554	926	523	484	860	393	289	650	237

TABLE 2: DAYLIGHT CONDITION WITH STATIC SHADING

Date	21-Mar			21-Jun			21-Sep			21-Dec		
Time	8:00	12:00	16:00	8:00	12:00	16:00	8:00	12:00	16:00	8:00	12:00	16:00
$E_{min}$	693	395	307	480	326	348	685	386	299	778	532	194
$E_{max}$	21905	2143	4015	2426	1613	22528	8996	2071	9253	14503	3411	1509
$E_{avg}$	3890	716	870	901	615	2108	2285	701	1084	4674	974	430

It creates an uneven uniformity of the reading space. It is mentioned that there is no existing static shading placed outside the opening.

## VI. BASE CASE WITH STATIC SHADING

To compare our base case, a static shading before the opening is provided. The depth of the shading is calculated based on the solar altitude angle and window height. In tropical climates like Chittagong, the sun is high year-round (e.g.,  $67^\circ$  at noon on equinox,  $90^\circ$  in summer). ASHRAE 90.1[35] suggests a projection factor (depth/height ratio) of 0.5-1.0 for south-facing windows. A 1-1.5 m deep overhang fixed shading is calculated for tropical regions, blocking direct sun while allowing indirect light (Fig 4).

From Table 2, it is shown that even providing a shading did not comply with our expected outcome throughout the year. The problem with the over illuminated space seems to be resolve in some extent for a specific amount of the time.



Fig 4: (Left) Light Penetration on March 21 at 8am on existing condition  
(Right) Light Penetration on March 21 at 8am with static shading

## VII. BIO-INSPIRED KINETIC FAÇADE

The literature review process for selecting reports on kinetic shading systems (KSS) used three clear criteria[12]. First, the systems must have mechanical movement, meaning they physically move to be considered kinetic. This includes sliding (translation), rotating, or changing shape (deformation) to manage light and heat. Second, the systems must have different states, like fully open, partially open, or closed, allowing them to adapt to changing weather or light conditions

for better building performance. Third, the systems must be inspired by nature, copying mechanisms from plants or other living things, such as leaves opening and closing with sunlight, using materials that adapt like natural organisms, or showing efficient and sustainable designs[12]. Again, according to Mahmoud, Rotation movement performs better than translation, improve daylight by 50% in summer and 30% in winter[29].

Mimosa pudica, commonly known as the sensitive plant, was chosen for its unique ability to respond to environmental stimuli, particularly its rapid movement in response to touch (Fig 5). The Mimosa pudica was chosen over other plants, such as sunflowers (which track light) or lotus (which repel water), because its rapid, protective folding response directly addresses the need to manage sudden changes in sunlight and rain, common in Chittagong's climate. It's simple, repeatable leaf structure also translates easily into façade-effective, locally adaptable facade using recycle wood and glass or bamboo, aligning with sustainable design principles for tropical environments.

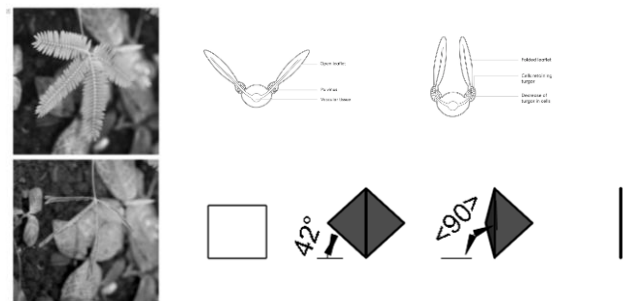
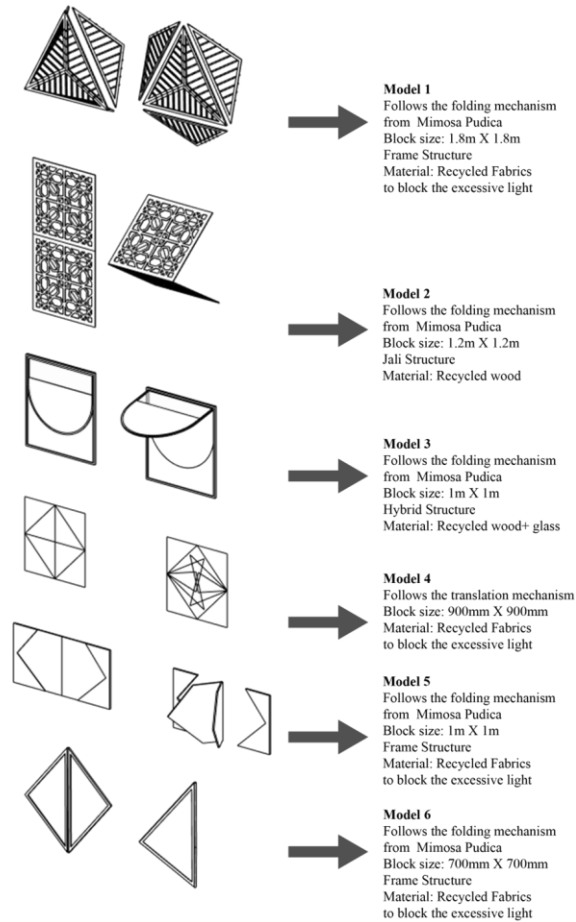


Fig 5: Leaf Movement Mechanism of Mimosa Pudica[36]

The design development of the biomimetic KF begins with a deep understanding of fundamental geometric forms like circles, equilateral triangles, squares, pentagons, and spirals and their proportional relationships (e.g., 3:4, 5:8, Golden Section). The approach moves beyond mere aesthetic mimicry, embracing the “dinergetic” principles of balanced oppositional forces[37], focusing on optimizing daylight, reducing glare,

rather than adhering strictly to idealized geometric perfection. Instead, it incorporates subtle imperfections found in nature, selecting a harmonious yet practical geometric pattern to ensure appeal and efficiency.



**Fig 6:** Iteration of different models

Different forms and patterns are explored (Fig. 6) that resonates with the mimosa plant mechanism. The folding mechanism is visually represented through geometric shapes, such as triangles and diamonds, which can pivot or slide to adjust the building's exposure to sunlight (Fig. 6). The movement mechanism is incorporated into modular panels, allowing for independent adjustments of each section of the façade based on the amount of sunlight changes (Fig. 7). Exploring different forms gives the opportunity to find the exact simple yet effective functional design that is more suitable for manual operation (Fig. 8).

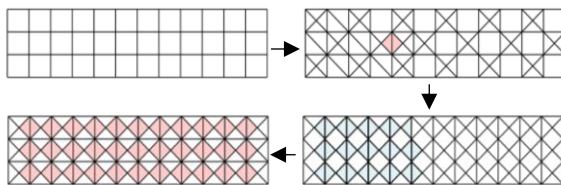


**Fig 7:** Grid Division

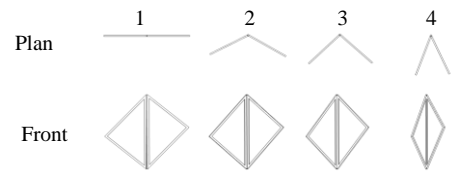


**Fig 8:** Inspired mechanism from Mimosa Pudica

1. Fully closed 2.30° open 3. 45° open 4. 75° open

After modeling the forms, a simulation study is done to verify its possibility to reduce the excessive heat gain on our expected times with different shading angles from full open to closed varying from 25°, 35°, 45°, 75° etc. (Fig. 9).

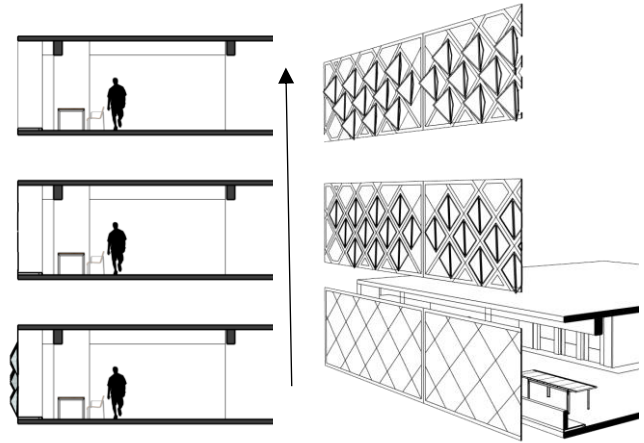


**Fig 9:** (Left) Proposed Model on the site condition

(Right) Phases of the proposed model

The daylight analysis for the KF is detailed across Tables 3 to 5, evaluating performance metrics like Annual Sunlight Exposure (ASE), Spatial Daylight Autonomy (sDA), and illuminance levels ( $E_{min}$ ,  $E_{max}$ ,  $E_{avg}$ ) to assess its effectiveness in optimizing daylight while minimizing glare and heat gain.

## VIII. DAYLIGHT & GLARE ANALYSIS

Table 3 compares six proposed models of the KF. Model 6 emerges as the best performer, achieving an ASE of 8.9% (below the LEED v4 threshold of  $\leq 10\%$ ) and an sDA of 70.2% (well above the LEED v4 requirement of  $\geq 55\%$ ), with an average lux of 510 (maintaining the standard for a reading room by CIBSE), indicating good daylight sufficiency for reading (target 300-500 lux). Other models show higher ASE values ranging from 10.5% (Model 5) to 24.20% (Model 1) indicating excessive direct sunlight, while sDA values range from 69.90% (Model 4) to 94.8% (Model 3), suggesting varying daylight availability.

Table 4 examines Model 6's performance across key dates (March 21, June 21, September 21, December 21) and times (8:00, 12:00, 16:00). Illuminance levels fluctuate significantly, with  $E_{avg}$  peaking at 874 lux on March 21 at 16:00 and dropping to 267 lux on December 21 at 8:00 (likely closed).  $E_{min}$  and  $E_{max}$  values show uneven light distribution, such as 94.9 lux ( $e_{min}$ ) and 1888 lux ( $e_{max}$ ) on March 21 at 8:00, indicating over-illumination near the window and under-

TABLE 3: VARIABLES ON DIFFERENT PROPOSED MODELS CONDITION

Variables	Propoed Design 1	Propoed Design 2	Propoed Design 3	Propoed Design 4	Propoed Design 5	Propoed Design 6
ASE	24.20%	3.20%	12.50%	11.40%	10.50%	10.00%
sDA	72.60%	72.60%	71.90%	69.90%	72.30%	82.30%
avg lx	1560	720	948	1068	1175	510

TABLE 4: DAYLIGHT CONDITION WITH THE PROPOSED MODEL

Date	21-Mar			21-Jun			21-Sep			21-Dec		
Time	8:00	12:00	16:00	8:00	12:00	16:00	8:00	12:00	16:00	8:00	12:00	16:00
E <sub>min</sub>	94.9	55.3	36.9	76.1	38.4	41.4	97.8	49.9	36.3	80.4	83.2	23.6
E <sub>max</sub>	1888	427	17504	677	350	17691	3055	397	13472	2892	824	390
E <sub>avg</sub>	360	126	380	219	97.1	422	368	118	323	297	243	72.9

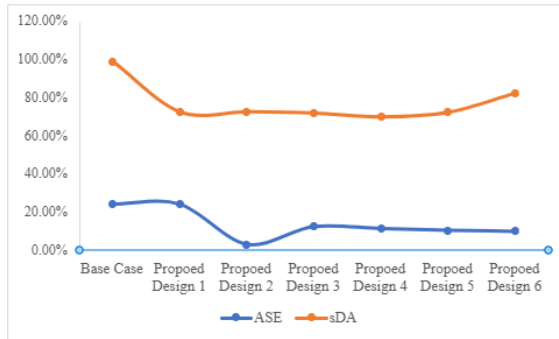


Fig 10: ASE and sDA % of Different Proposed Model

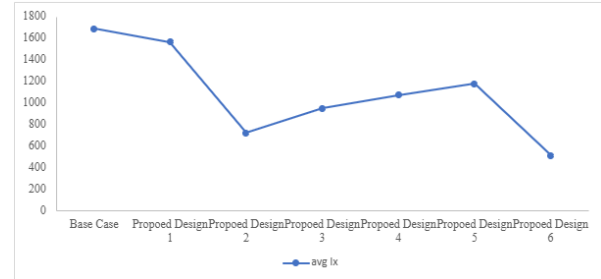


Fig 11: Avg Lux of Different Proposed Model

illumination deeper in the room, a challenge the KF aims to address through adjustable states.

Fig 10 and Fig 11 shows the graphical representation of the above data from 6 proposed model for ASE, sDA and avg lux. This figure shows that even the two proposed model (2 and 6) gives almost similar result for two variables (sDA and ASE), model 2 does not reach the acceptable standard lux level suggested by CIBSE.

Table 5 summarizes Model 6's annual performance: sDA of 70.2%, ASE of 8.9%, and an average lux of 480, meeting LEED v4 standards (sDA  $\geq 55\%$ , ASE  $\leq 10\%$ ) and providing comfortable reading conditions (target 300-500 lux). The visualizations likely illustrate light distribution, confirming uniform daylight penetration when the facade adjusts to optimal angles.

TABLE 5: VARIABLES VISUALIZATION

	<b>70.2% sDA<sub>300/50%</sub></b>
	<b>8.9% ASE<sub>1000.250</sub></b>
	<b>avg lux 510</b>

To do a visibility analysis, a annual glare simulation is conducted using Climate studio of the proposed model 6 with

different variation of openness of the façade from full open to full close.

In Fig 12, at 0% openness, the facade is fully closed, yielding an sDG of 8.2%, indicating imperceptible glare but insufficient daylight for reading (target 300 lux), well below the LEED v4 threshold ( $\geq 55\%$ ), compromising visual comfort. At 100% openness, sDG reaches 83.4%, exceeding the intolerable glare threshold ( $>45\%$ ), as high illuminance near the window (likely  $>1,000$  lux) causes significant visual discomfort, akin to the base case (ASE 24.2%). The 50% openness achieves an sDG of 56.4%, falling into the intolerable range ( $>45\%$ ) but meeting LEED v4 requirements ( $\geq 55\%$ ), offering adequate daylight though still posing glare risks. The Middle 100% (sDG 40.8%) and Half (sDG 43.5%) configurations result in disturbing glare (40%–45%), providing moderate daylight but potential discomfort.

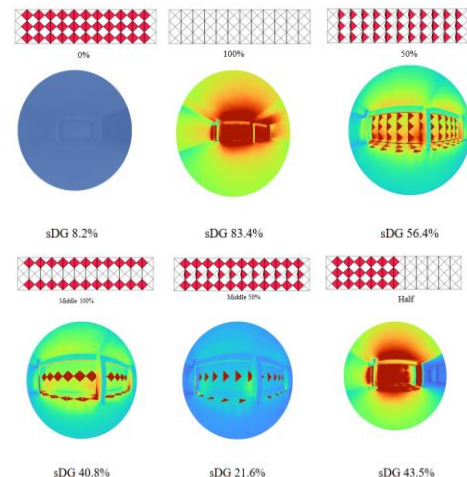


Fig 12: Glare Analysis of Different Openness of Proposed Design 6

The Middle 50% (sDG 21.6%) offers imperceptible glare (<35%) but insufficient light for reading tasks. Compared to Model 6 (sDA 70.2%, ASE 8.9%), which likely falls into the intolerable range based on sDA, the 50% openness provides a better balance of daylight and glare control.

## IX. CONTROL MECHANISM AND COST CALCULATION

The facade features a grid of lightweight rectangular panels (e.g., 30 cm wide x 50 cm tall), each hinged at the top to a simple wooden frame. These panels mimic the plant's leaf-folding action, adjusting to sunlight changes. Made from recycled wood, abundant and affordable at around \$0.5 per square meter in local markets.

The mechanism uses a manual pull-cord system for cost-effective operation. A rope (\$0.1 per meter), attached to the bottom of each panel row, runs through small wooden pulleys (\$0.2 each) mounted above the frame and connects to a single handle inside the room. Pulling the handle lifts the panels to a vertical closed position, blocking harsh sunlight or monsoon rain, much like the plant's leaves folding shut for protection. Releasing the handle allows the panels to drop to a near-horizontal open position, letting in maximum daylight during overcast conditions or early mornings, similar to the plant's open state in softer light. For midday, the panels can be adjusted to a 45-degree tilt using a notched cleat on the handle, diffusing sunlight to reduce glare while maintaining illumination, reflecting the plant's adaptive response.

This simple design avoids complex materials or mechanisms, using locally sourced recycled wood and jute, with minimal labor (estimated \$5/hour for 10-15 hours per 3 m<sup>2</sup> window). The wood is treated with a borax-boric acid solution (\$0.5-\$1 per panel) and lime wash (\$0.2 per application) to resist humidity, ensuring durability without added expense.

## X. RESULTS AND DISCUSSION

This study aimed to evaluate the effectiveness of a biomimetic kinetic façade, inspired by *Mimosa pudica*, in improving daylighting performance in a reading room. Simulation result based on daylight metrics, including sDA, ASE, sDG and average lux, were used to assess the proposed kinetic façade's performance in meeting LEED v4 standards.

The results demonstrated that the kinetic façade significantly improved daylighting conditions when compared to a static façade. In particular, the proposed models (Model 1, Model 3, and Model 4) showed higher ASE and sDA values than the base case with static shading. Model 6, the most reliable design, achieved 70.2% sDA and 8.9% ASE, meeting the LEED v4 requirements for daylight performance. Additionally, the kinetic façade demonstrated a better ability to adapt to varying solar conditions, reducing glare and excessive heat while maintaining adequate lighting levels.

The dynamic adjustment of the façade based on the sun's position provided a more uniform distribution of daylight

throughout the day, which addressed the problem of over-illumination observed in the base case. The folding mechanism, inspired by *Mimosa pudica*, effectively minimized sunlight during the peak hours and optimized light levels during the early morning and cloudy days. The simple mechanism also made it a feasible solution for both operational and cost considerations in tropical climates like Chittagong.

The KF's jute hinges may degrade in humidity, increasing maintenance costs (\$0.5-\$1/panel for treatment), and the manual system's effectiveness relies on consistent student use, which may vary (70% are comfortable, per pilot study). The cost (\$81.5 for 3 m<sup>2</sup>) is affordable, but uneven light and potential glare require further optimization.

## XI. CONCLUSION

The kinetic facade, inspired by the thigmonastic leaf-folding of *Mimosa pudica*, presents a promising yet imperfect solution for enhancing daylighting in a reading room. Achieving a sDA of 70.2% and an ASE of 8.9%, it satisfies LEED v4 standards, outperforming unshaded (sDA 99%, ASE 24.2%) and static shading alternatives. Constructed with lightweight recycled wood panels, a jute pull-cord system, wooden pulleys, the design is cost-effective. It delivers an average illuminance of 480 lux, peaking at 510 lux at a 45° tilt (March 21, 8:00 AM), sufficient for reading, though slightly below the CIBSE and IES standard of 500 lux. By leveraging locally sourced, eco-friendly materials, it aligns with UN SDG 11, claiming a 20-30% energy reduction in Chittagong's tropical climate, marking a commendable step toward affordable, sustainable architecture in resource-constrained regions like Bangladesh.

This biomimetic facade is an innovative concept, blending sustainability and local adaptation, yet it remains a prototype requiring refinement. To bridge the gap to practical viability, a full-scale prototype must be tested in Chittagong's real-world conditions to validate daylighting, energy efficiency, and material resilience. Glare control demands design adjustments, and manual operation should be reconsidered for reliability. Enhanced material durability and thermal performance data are critical to substantiate its environmental and economic benefits. Yet, its real-world success hinges on further investigation into user behavior, maintenance demands, and broader applicability to ensure it delivers on its sustainable promise over time. If refined and widely adopted, it could significantly advance energy-efficient architecture in regions like Bangladesh.

## Use of Generative Artificial Intelligence (AI) and AI-Assisted Technologies

During the preparation of this manuscript AI is used to improve readability and language of some passages. After using this tool/service, the author(s) reviewed and edited the content as needed and take(s) full responsibility for the content of the publication.



## REFERENCES

- [1] A. K. D. Tom Lawrence, Janice K. Means. "ASHRAE GreenGuide : Design, Construction, and Operation of Sustainable Buildings": W. Stephen Comstock; 2018.
- [2] M. López, Rubio R., Martín S., Ben C. "How plants inspire façades. From plants to architecture: Biomimetic principles for the development of adaptive architectural envelopes". *Renewable and Sustainable Energy Reviews*. 2017;67:692-703.
- [3] M. López, Rubio R., Martín S., Croxford B., Jackson R. "Active materials for adaptive architectural envelopes based on plant adaptation principles". *Journal of Facade Design and Engineering*. 2015;3(1):27-38.
- [4] H. S. M. Shahin. "Adaptive building envelopes of multistory buildings as an example of high performance building skins". *Alexandria Engineering Journal*. 2019;58(1):345-52.
- [5] Z. Han, Mu Z., Yin W., Li W., Niu S., Zhang J., et al. "Biomimetic multifunctional surfaces inspired from animals". *Adv Colloid Interface Sci*. 2016;234:27-50.
- [6] A. N. E. Houda. "Advanced Building Skins Inspired From Plants Adaptation Strategies to Environmental Stimuli: A Review". 2018.
- [7] L. B. KADRI. "Towards the LIVING envelope: biomimetics for building envelope adaptation"2012.
- [8] S. M. Hosseini, Fadli F., Mohammadi M. "Biomimetic Kinetic Shading Facade Inspired by Tree Morphology for Improving Occupant's Daylight Performance". *Journal of Daylighting*. 2021;8(1):65-85.
- [9] S. Gilroy. "Plant Tropisms"2008.
- [10] P. J. Simons. "The Role of Electricity in Plant Movements". *New Phytologist*. 2006;87(1):11-37.
- [11] R. Armstrong. "Living Architecture\_ How Synthetic Biology Can Remake Our Cities and Reshap"2012.
- [12] M. Brzezicki. "A Systematic Review of the Most Recent Concepts in Kinetic Shading Systems with a Focus on Biomimetics: A Motion/Deformation Analysis". *Sustainability*. 2024;16(13).
- [13] S. Attia, Lioure R., Declaude Q. "Future trends and main concepts of adaptive facade systems". *Energy Science & Engineering*. 2020;8(9):3255-72.
- [14] S. Fattahi Tabasi, Banihashemi S. "Design and mechanism of building responsive skins: State-of-the-art and systematic analysis". *Frontiers of Architectural Research*. 2022;11(6):1151-76.
- [15] D. Borschewski, Voigt M. P., Albrecht S., Roth D., Kreimeyer M., Leistner P. "Why are adaptive facades not widely used in practice? Identifying ecological and economical benefits with life cycle assessment". *Building and Environment*. 2023;232.
- [16] S. Attia. "Evaluation of adaptive facades: The case study of Al Bahr Towers in the UAE". *QScience Connect*. 2018;2017(2).
- [17] R. A. Mangkuto, Kurnia K. A., Azizah D. N., Atmodipoero R. T., Soelami F. X. N. "Determination of discomfort glare criteria for daylit space in Indonesia". *Solar Energy*. 2017;149:151-63.
- [18] B. Dabaj, Rahbar M., Fakhr B. V. "Impact of Different Shading Devices on Daylight Performance and Visual Comfort of A Four Opening Sides' Reading Room In Rasht". *Journal of Daylighting*. 2022;9(1):97-116.
- [19] I. U.S. Green Building Council. "LEED v4 for Building Design And Construction". 2019.
- [20] F. F. Roel C.G.M. Loonen, Jose Miguel Rico-Martinez, Brzezicki Marcin. "Design for façade adaptability – Towards a unified and systematic characterization". 2015.
- [21] U. Nation. "SDG Resource Document". 2015.
- [22] K. M. Al-Obaidi, Azzam Ismail M., Hussein H., Abdul Rahman A. M. "Biomimetic building skins: An adaptive approach". *Renewable and Sustainable Energy Reviews*. 2017;79:1472-91.
- [23] K. Kalaimathy, Shanthi Priya R., Rajagopal P., Pradeepa C., Senthil R. "Daylight performance analysis of a residential building in a tropical climate". *Energy Nexus*. 2023;11.
- [24] Janine\_Benyus. "A\_Biomimicry\_Primer".
- [25] J. M. Benyus. "Biomimicry innovation inspired by nature "1997.
- [26] H. Z. A. Jaafar Ahmad Ibrahim. "Kinetic Façade As A Tool For Energy Efficiency". 2019.
- [27] S.-J. Choi, Lee D.-S., Jo J.-H. "Method of Deriving Shaded Fraction According to Shading Movements of Kinetic Façade". *Sustainability*. 2017;9(8).
- [28] J. Moloney. "Designing Kinetics for Architectural Facades State Change". 2011.
- [29] A. H. A. Mahmoud, Elghazi Y. "Parametric-based designs for kinetic facades to optimize daylight performance: Comparing rotation and translation kinetic motion for hexagonal facade patterns". *Solar Energy*. 2016;126:111-27.
- [30] U. S. G. B. Council. LEED Certification Overview: Comprehensive Guide to Sustainable Building Practices 2023 [
- [31] I. E. Society. "The Lighting Handbook Reference and Application". 2011.
- [32] S. o. L. a. Lighting. "Code for Lighting". 2002.
- [33] A. Yunitsyna, Sulaj E. "Daylight Optimization of the South-Faced Architecture Classrooms Using Biomimicry-Based Kinetic Facade Shading System". *Journal of Daylighting*. 2025;12(1):1-20.
- [34] E. Kızılörenli, Maden F. "Modular responsive facade proposals based on semi-regular and demi-regular tessellation: daylighting and visual comfort". *Frontiers of Architectural Research*. 2023;12(4):601-12.
- [35] R. American Society of Heating, and Air-Conditioning Engineers I. "Energy Standard for Buildings Except Low-Rise Residential Buildings". 2008.
- [36] A. Bakshi, Swanson S. J., Gilroy S. "A touchy subject: Ca(2+) signaling during leaf movements in Mimosa". *Cell Calcium*. 2023;110:102695.
- [37] S. Colman. "Harmonic Proportion and Form in Nature, Art and Architecture"2003.

# Design Drying Control System from LPG by Proportional Integral Derivative (PID) Controller for Charcoal Briquettes

Chanon Bunmephiphit<sup>1</sup>, Kittikorn Sasujit<sup>1</sup>, Churat Thararux<sup>1</sup> and Nigran Homdoun<sup>1,a)</sup>

<sup>1</sup>Renewable Energy Engineering, School of Renewable Energy, Maejo university, Chiang Mai Province 50290

Author Emails

<sup>a)</sup>Corresponding author: nigran@mju.ac.th

**Abstract.** In this study, the drying oven for fuel briquette was designed using Liquefied Petroleum Gas (LPG) infrared heating and controlled with a Proportional Integral Derivative (PID) Controller system to adjust the temperature working from heating infrared ignition 3 set to regulate temperature inside oven. It was tested in comparison with the number of LPG infrared heating. The testing results showed that developing a high-temperature oven for charcoal briquette production using LPG infrared heating heads can provide fast-drying heat. The speed-up of temperature is proportional to the number of heating heads. The PID Controller control system can maintain a constant temperature throughout the drying process in the desired temperature range.

**Keyword:** Charcoal, Briquettes, Drying, Controller, PID

## I. INTRODUCTION

Biomass energy is energy from organic substances that can store energy from nature and produce energy. Organic substances can be obtained from various plants and animals, such as wood chips, garbage, agricultural waste, and animal waste [1, 2]. Biomass energy can be burned to convert into heat energy or produce electricity [2]. It can replace fossil energy that the country imports. Biomass energy is an interesting alternative energy because it helps preserve the environment. It is also a cheap fuel source found anywhere in Thailand. Currently, the process of producing compressed charcoal is popular and produced for sale to create sustainable careers [3, 4]. However, when considering the limitations in the process of producing compressed charcoal, it can be divided into 3 main groups: raw material preparation, compression, and drying. When considering the factors related to all 3 steps, it was found that the drying process still cannot determine or control the production time. It is still a factor that affects the production volume of the entire system [1, 5].

Drying technology aims to reduce the moisture content of moist materials by using heat to evaporate water from the material into the surrounding air. In the case of biological materials such as vegetables and fruits, drying or sun-drying helps extend the material's shelf life because drying or sun-drying reduces the moisture content of the material, thus slowing down or inhibiting the growth of microorganisms and preventing the material from spoiling or molding [6, 7].

## II. METHODOLOGY

### Design requirements

- 2.1 Develop an oven using gas LPG to generate a temperature inside the oven between 100-200 °C.
- 2.2 The design for drying charcoal is 50 kg/time.
- 2.3 The charcoal has an initial moisture content that does not exceed 20% (wet standard).

This case study uses a cubic-shaped dryer with a hole for compressing air at the bottom using a fan to create air pressure into the oven and a ventilation hole on the top that can be opened or closed. The cabinet walls use metal as a structural material with heat insulation to prevent heat loss. The heat is provided by a cooking gas burner at the bottom of the oven. The heating system can control the temperature from a cooking gas fuel for a temperature control system with a temperature measurement system installed at the center of the oven. The charcoal compressed in other level will be arranged in layers inside the oven that can be moved in and out. One side of the oven wall can be opened and closed like a door with a locking latch to prevent heat loss, as shown in Fig 1 and Fig 2.

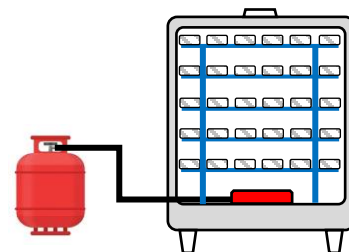


Fig 1 Characteristics of the designed dryer

## III. RESULTS AND DISCUSSION

### Operation of the dryer

The working characteristics of the dryer consist of 3 important parts:

- Part 1 Temperature control system by PID Controller
- Part 2 Gas LPG On-Off system and gas ignition
- Part 3 Temperature maintenance system



Fig 2 Electrical control cabinet

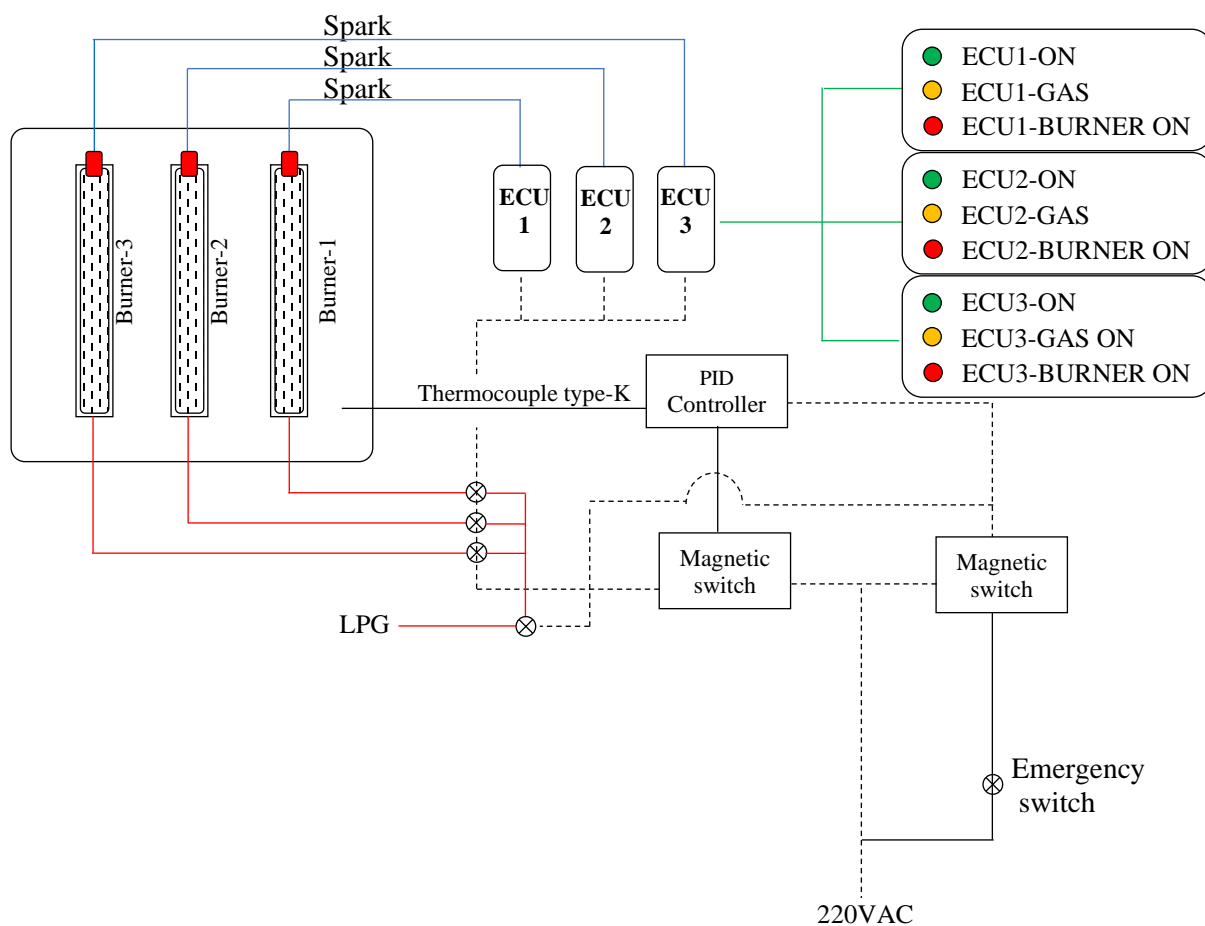


Fig 3 Control System Diagram

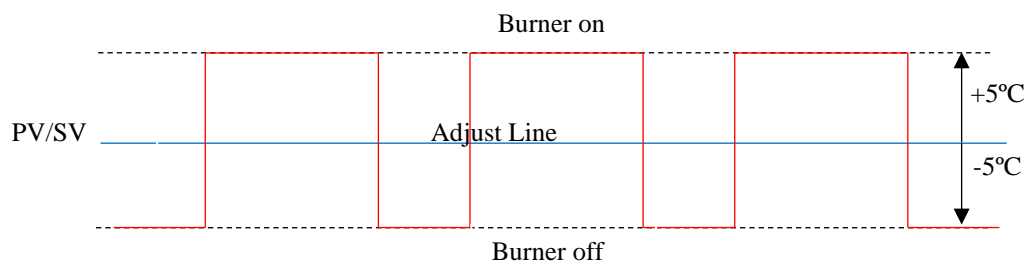


Fig 4 System operation model PID Controller Type On/Off

Part 1: The temperature control system through the PID Controller system is shown in Fig 2 and Fig 3, in the form of the on-off and electrical system. This system relies on measuring the temperature inside the drying room (PV) and showing it on the display screen with Thermocouple type K in the form of an Analog signal, and the desired actual temperature can be set as desired. The desired temperature will be shown in the signal channel (SV) in Fig 4.

The operation of the system (case study) is used together with the heating system from LPG combustion with an infrared burner. While working or increasing the temperature, the system will measure the temperature in the drying room and display it on the PV channel. If the temperature difference does not exceed  $\pm 5^{\circ}\text{C}$  (the appropriate temperature for LPG), the system will not order the other system (LPG Burner) to work. However, if the temperature difference is greater than the appropriate value (lower), the system will order the LPG Burner to start working to create the temperature in the drying room.

Part 3 Temperature control system is shown in Fig 5 A. The selected PID Controller system can work in a temperature difference range of up to  $\pm 0.5^{\circ}\text{C}$ , which can maintain the desired temperature at its best. However, this type of temperature control is suitable for heating through a heating coil that supplies a constant electric current, but it is not suitable for maintaining the temperature with LPG gas, which has an ignition time of 5-10 seconds. Therefore, the temperature control for LPG should have a temperature difference range of not less than  $\pm 5^{\circ}\text{C}$ .

Temperature control with PID Controller system for LPG fuel with electronic ignition should have a time gap of 30-60 seconds or a temperature difference of  $\pm 5^{\circ}\text{C}$  to allow safe ignition and reduce the frequency of ignition to an appropriate time.

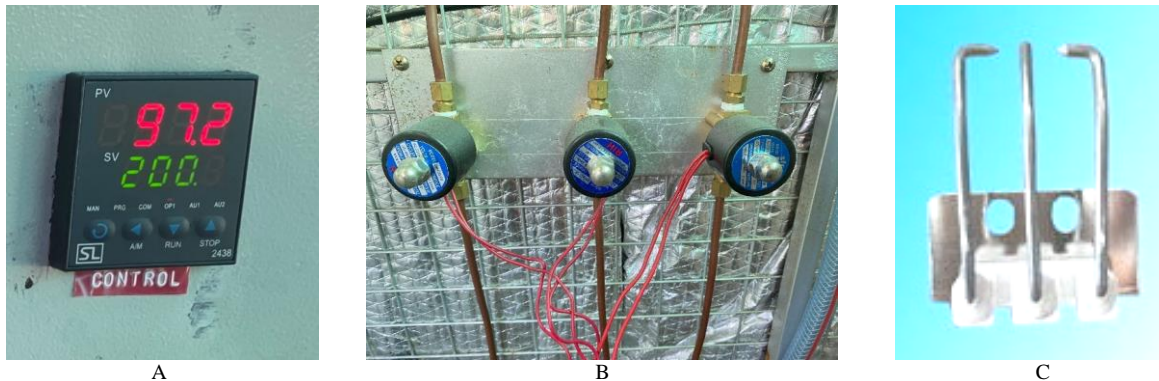


Fig 5 A-PID Temperature Controller Model SL2438, B-Solenoid-valves and C-Spark Electronic

Part 2: The gas on-off system and gas ignition are operated automatically through the PID Controller system according to the specified temperature values, as shown in Fig 5-B. The LPG gas on-off system will start working when the temperature control system commands the Electronic Control Unit (ECU) of each system (ECU GAS) for all 3 sets to work simultaneously. Electricity (220VAC) will be released into all 3 systems simultaneously, and solenoid valves will open to operate LPG gas to supply each burner. At the same time, the system will command Spark Electronic to spark at the tip of each claw to create sparks (spark duration 5-10 seconds). Each burner will ignite and can continue to heat the system. Each burner will clearly report the working status of each burner, including (green light) the system is ready to work (yellow light) Solenoid-valves open and release gas to the burner ready to ignite, and (red light) indicates the status of the burner working or heating. During operation, if there is a problem or the light cannot be ignited, the status indicator will be turned off to check and maintain the safety of the system and users.

#### System evaluation from the model

Testing the drying characteristics of the drying of the number of charcoal briquettes in each drying, not less than 50 kg/time (weight when the briquettes are finished) with a power source system from cooking gas between the temperature of  $100^{\circ}\text{C}$  - $200^{\circ}\text{C}$  with the size of the dryer as shown in Fig 6 with the initial moisture content of the charcoal briquettes not exceeding 20% to consider the air movement characteristics.

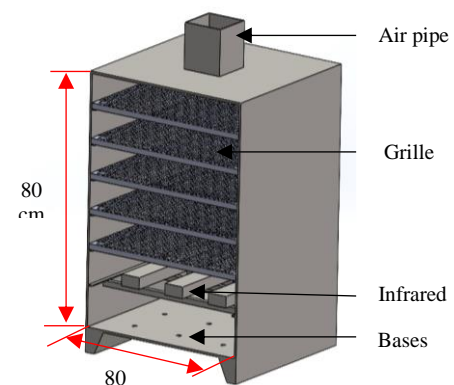


Fig 6 Characteristics of the dryer used in the case study





Fig 7 Dryer inside

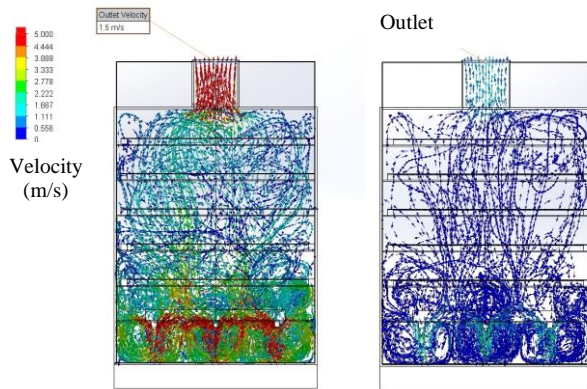


Fig 8 Solidworks simulated airflow characteristics

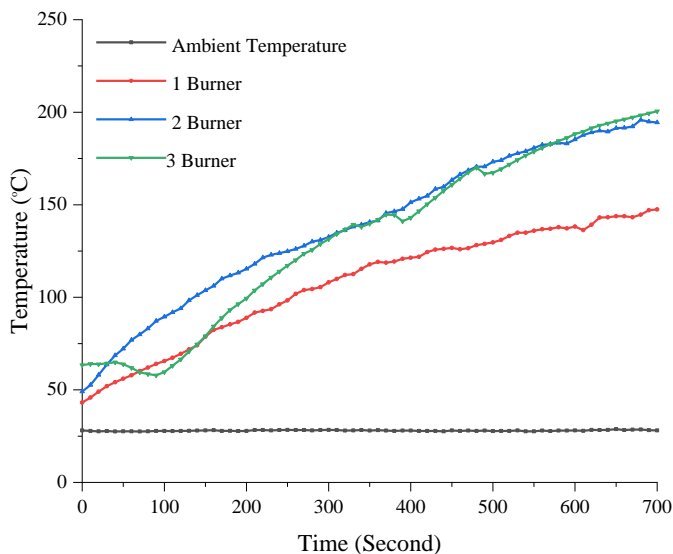


Fig 9 characteristics of step up of temperature 100-200°C

Figure 8-9 shows the result of the seed of the highest temperature of 200°C/time. It was found that at the ambient

temperature of  $28 \pm 3^\circ\text{C}$ , the fastest heating from the temperature of 3 infrared burners at the same time took about 675 seconds, 2 burners took 680 seconds, and the heating from 1 burner could not heat the oven up  $200^\circ\text{C}$  and had a low ability to increase the temperature, which was different from 2 and 3 burners, which could heat up to  $200^\circ\text{C}$  and had a steeper or faster temperature increase than 1 burner, which was the result of the amount of baking chamber. For 2 burners, the temperature variation in the first 0-200 seconds might be the result of the difference in the distance of the burners.

The heating characteristics of all burners are shown in Fig 10. The speed test results are the result of the distance between burners a:b, c:d and e:f. 1 burner (middle, No. 2) will generate the least heat and the slowest. Due to the distance between the two walls of the burner (a+b+c):(d+e+f). Therefore, the heat distribution from both the left and right sides of the burner cannot reach all the way. Therefore, the temperature distribution is not evenly distributed throughout the burner (depending on the volume of the burner). Therefore, the temperature cannot be raised to the set point ( $200^\circ\text{C}$ ) or may be able to be raised to the desired temperature but it will take longer than if there are many burners and may affect the amount of fuel (LPG) that is more than normal.

2 burners (left and right, No. 1 and 3) will be able to heat up to the set point ( $200^\circ\text{C}$ ) within 680 seconds, but there will be a fluctuation in the temperature range in the beginning. This may be due to the distance between the furnace walls a: b+c+d+e : f, which makes the distance in the middle between the two burners unable to spread heat to the gap between the two burners. Therefore, it directly affects the temperature variation in the beginning. However, both burners must work all the time or use the heating period all the time. The three burners (numbers 1, 2 and 3) can provide constant heat and are the most stable in this study. The working period (ignition) is not constant, which affects the longevity and ignition during temperature maintenance.

3 burner heating system in this study can provide more consistent heat than other types because the ratio of a: b, c: d and e: f is the appropriate distance for heat distribution from the burner to the drying layer throughout the furnace. And from the burner that provides heat throughout, the heat maintenance does not have to be lit all the time but will work or ignite in a short loop or have a short ignition period.

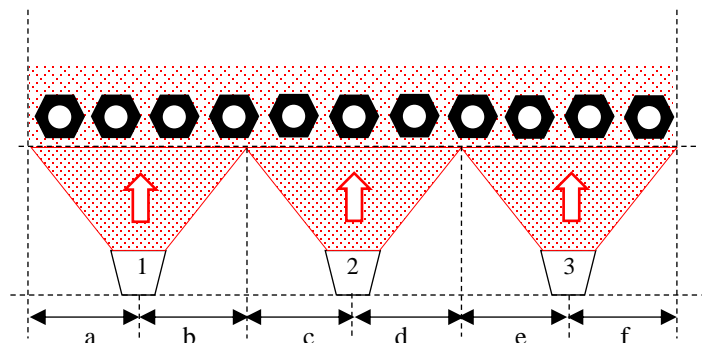


Fig 10 The heating characteristics of all burners (a, b, c, d, e, f = 13:13 cm)

#### IV. CONCLUSION

The development of a high-temperature oven for charcoal briquette production using an infrared heating head from LPG fuel can provide heat for drying quickly. The speed of temperature is varied according to the number of heating heads. The control system with PID Controller can maintain a constant temperature throughout the drying process in the desired temperature range.

#### ACKNOWLEDGMENT

Thank you for Renewable Energy Engineering, School of Renewable Energy, Maejo university for the Scholarship.

#### REFERENCES

- [1] Kritsada Boonchom and Nirubol Chaisompan., Study of charcoal briquette from longan wood., Naresuan Phayao Journal, Vol. 13 No. 2, May-August 2020, Page 51-56
- [2] Pongsak Yuman., Development of a Cold Production Biomass Charcoal Briquette Machine to use Waste from Coffee Bean Processing., Industrial Technology Lampang Rajabhat University Journal, Vol 9. No.1 Jan-June 2016, Page 34-48.
- [3] Pakorn Auntaisong and Rachata Maneechot., The Constructure and Efficiency Evaluate of Charcoal Briquette Machine from Cassia Pods., Udon Thani Rajabhat University Journal of Science and Technology, Vol 7, Issue 2, 2019, Page 147-157
- [4] Natthaphon Vichan, Kanyaphorn Chaiwong, Phornpimon Promraksa and Apinum Kanoi. The Production of Charcoal Briquette with Charcoal Residue from Banana Chip Production. Journal of Innivative Technology Research, Vol 3, No 2, July-December, 2019, Page 11-22.
- [5] Sirichai Jirawongnusun and Changwat Charoensuk. The Study on the Production of Charcoal Briquettes from Pomelo Peels., Kasem Bundit Engineering Journal, Vol. 12, No.1, January-April, 2022, Page 55-74.
- [6] Arkom Palamanit, Pisit Throngleart, Pakinee Thongshi, Ravisuda Deangpea and Sumate Chaiprapat. Effects of Binder Types and Ratios on Quality of Palmyra Palm Shell Charcoal Briquettes by Using Solar Greenhouse Dryer., Thai Science and Technology Journal (TSTJ), Vol. 28, No 6, June 2020, Page 117-1125.
- [7] Pomgpun Rerkkumsup, Panurut Yaruan and Jaratsri Soeatuptim. The Development of an Automatic Control System for Charcoal Briquettes Drying. Pathumwan Academic Journal, Vol. 10, Issue 27, 2020, Page 70-83.

# Improvement on the Cooling Efficiency of a Split-Type A/C Using Waste Heat Recovery

Chanwit Wittavirote<sup>1</sup> and Chanon Bunmephiphit<sup>1,a)</sup>

<sup>1</sup>Rattanakosin College for Sustainable Energy and Environment, Rajamangala University of Technology Rattanakosin, Nakhonpathom, 73170, Thailand.

Author Emails

<sup>a)</sup>Corresponding author: chanon.bun@rmutr.ac.th

**Abstract.** This research therefore has a concept to improve the air conditioning system by exchanging heat with the outside air by condensate water and ventilation air which have low temperature to lower the temperature of the air before entering the condenser to reduce the energy consumption of the air conditioning system. This will result in higher efficiency of the air conditioning system leading to reduced energy consumption. Therefore, the equipment has been designed, installed and tested. Design of air conditioning system in the laboratory room size 2.4×2.9×2.2 m. A small office room size 2.4×2.9×2.2 m. was used for the experiment. Split-type air conditioner with a cooling capacity of 12,000 Btu/hr was used, which was already in use. For this experiment, a 1 set of condensate-air heat exchange panels and a 1 set of ventilation fan were installed. The experimental steps are as follows: Before starting the experiment, measure and record the temperature and relative humidity of the atmosphere. Install an electrical energy meter to record the energy value. Experimental results Case I The air conditioning system uses 1.298 kW of electrical energy, the COP coefficient of performance of air conditioning system is 3.742 and the energy efficiency ratio EER is 11.345. Case II The air conditioning system uses 1.242 kW of electrical energy, the COP coefficient of performance of air conditioning system is 3.881 and the energy efficiency ratio EER is 11.856.

From the experimental results, it can be concluded that in Case II, the air conditioning system uses 0.056 kW less electrical energy than Case 1, or 4.31% less, the COP coefficient of performance of air conditioning system is increased by 0.157 or 4.22%, and the energy efficiency ratio EER is increased by 0.511 or 4.5%. This shows that the use of the ventilation system in this research can increase efficiency and help reduce energy.

**Index Terms**—Air conditioning, Air ventilation, Condensate water, Energy saving, West heat recovery.

## I. INTRODUCTION

Energy is currently very important to humans for their lives, transportation, and driving the economy in both the agricultural and industrial sectors. This causes the raw materials for energy production to decrease rapidly. Due to the energy crisis, energy conservation is very important to save and reduce energy consumption in order to have longer-lasting energy. According to the energy conservation results of the Ministry of Energy in 2022, Thailand used up to 91,210 ktoe of electricity. However, when there were energy conservation measures, Thailand saved 7,032 ktoe of accumulated energy and had a ratio of energy consumption to the results of activities (Energy Intensity, EI) that decreased by 7.73%. According to the Energy Efficiency Plan (EEP 2018), Thailand has a goal to reduce the accumulated EI by 30% and save 49,064 ktoe of energy. Thailand is a country located in the tropics almost all year round. Therefore, air conditioners are used to cool down and create a comfortable feeling. Air conditioners are therefore very popular electrical appliances. However, air conditioners are electrical appliances that use quite a lot of electricity. In the past, there have been people who have invented ways to reduce the energy usage of air conditioning systems by various methods to reduce energy usage.

## II. METHODOLOGY

Design of air conditioning system in the laboratory room size 2.4×2.9×2.2 m. A small office room size 2.4×2.9×2.2 m. was used for the experiment. Split-type air conditioner with a cooling capacity of 12,000 Btu/hr, and a constant speed was used, which was already in use. For this experiment, a 1 set of condensate-air heat exchange panels and a 1 set of ventilation fan were installed. See Fig.1

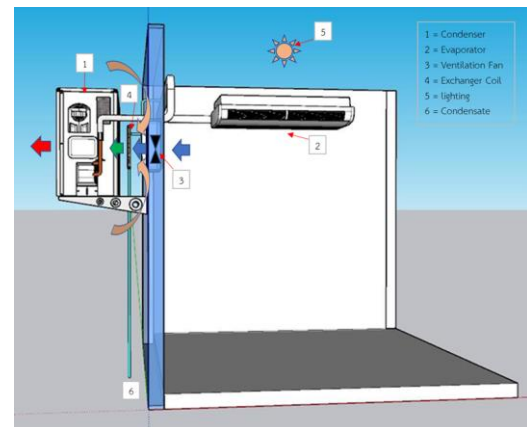


Fig. 1. Image showing air cooling.

After designing and installing the air conditioning system and equipment, various measuring instruments are installed, such as air temperature meter, air humidity meter, air conditioner refrigerant temperature meter, electrical energy meter, anemometer, and condensate water volume meter, etc. According to the standard system model and this research model, as shown in Fig. 2 and Fig. 3, This experiment is not to find the standard test value of air conditioners, but to compare the energy consumption of the same air conditioner between the standard system and the research system. Therefore, the indoor and outdoor air temperature was controlled at 25°C DB/23.2°C WB and 36.5°C DB/32.9°C WB according to the actual weather conditions of the climate in the experimental area.

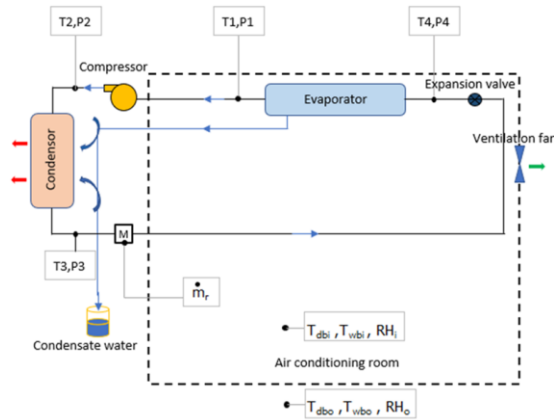


Fig. 2. Installation of equipment and installation location of measuring instruments of the standard s

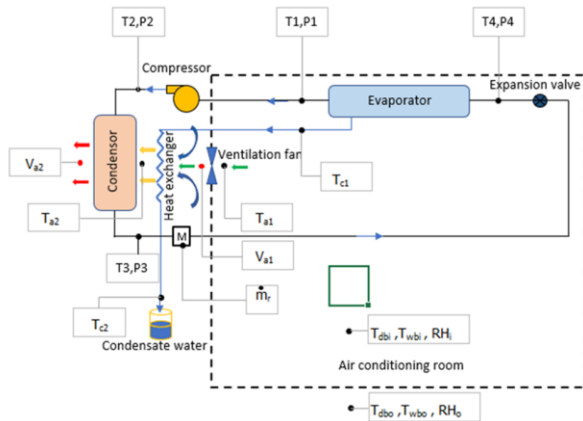


Fig. 3. Installation of equipment and installation location of measuring instruments of the research system.

Coefficient of performance of air conditioning system (COP)

$$COP = \frac{Q_t}{W_t} = \frac{\dot{m}_r(h_1 - h_4)}{\dot{m}_r(h_2 - h_1)} = \frac{(h_1 - h_4)}{(h_2 - h_1)} \quad (1)$$

- COP = Theoretical coefficient of performance of air conditioning system  
 $Q_t$  = Total cooling capacity (kW)  
 $W_t$  = Total power consumption of air conditioning system (kW)  
 $\dot{m}_r$  = Mass flow rate of refrigerant (kg/s)  
 $h_1$  = Enthalpy of refrigerant before entering compressor (kJ/kg)  
 $h_2$  = Enthalpy of refrigerant after passing through compressor (kJ/kg)  
 $h_4$  = Enthalpy of refrigerant before entering evaporator (kJ/kg)

Energy efficiency ratio EER. is the ratio of cooling capacity to total energy of the air conditioner, expressed in Btu/hr.Watt. In cooling capacity is expressed in Btu/hr, energy supplied to the system is expressed in Watt.

$$EER = \frac{Q_E}{W_{input}} \times 3.412 \quad (2)$$

- $Q_E$  = Cooling capacity (Btu/hr)  
 $Q_t$  =  $Q_E \times 3.412$  (Btu/hr)  
 $W_{input}$  =  $W_t$  = Total work in put to system (Watt)

This condensate water is used in a copper tube heat exchanger to pre-cool the air before it mixes with outside air and then cools the condenser. The heat transfers can be calculated using below fomula.

$$Q_w = \dot{m}_w \times C_p \times \Delta T \quad (3)$$

- $Q_w$  = Energy of condensate water (Watt)  
 $\dot{m}_w$  = Mass flow rate of condensate water (kg/s)  
 $C_p$  = Specific heat capacity of water (kJ/kg.°C)  
 $\Delta T$  = Temperature difference of condensate water (°C)

### III. RESULTS AND DISCUSSION

Calculation of the Coefficient of performance of air conditioning system (COP) and the Energy efficiency ratio (EER) from the experiment according to equations 1 and 2 in case 1, the standard system and case 2, the system of this research, which the values of the experimental results are according to Tables 1 and 2.



Case I, the standard system

Weather conditions

$$T_{\text{room}} : T_{\text{db}} = 25.0 \text{ }^{\circ}\text{C}, : T_{\text{wb}} = 23.2 \text{ }^{\circ}\text{C}$$

$$T_{\text{outdoor}} : T_{\text{db}} = 36.5 \text{ }^{\circ}\text{C}, : T_{\text{wb}} = 32.9 \text{ }^{\circ}\text{C}$$

Refrigerant R-32

$$\dot{m}_r = 0.025 \text{ (kg/s)}$$

Table 1. Results of EER, COP and  $W_t$  of case I.

EER	COP	$W_t$
11.345	3.742	1,298

Case II, the research system

Weather conditions

$$T_{\text{room}} : T_{\text{db}} = 25.1 \text{ }^{\circ}\text{C}, : T_{\text{wb}} = 23.3 \text{ }^{\circ}\text{C}$$

$$T_{\text{outdoor}} : T_{\text{db}} = 36.4 \text{ }^{\circ}\text{C}, : T_{\text{wb}} = 32.9 \text{ }^{\circ}\text{C}$$

Refrigerant R-32

$$\dot{m}_r = 0.025 \text{ (kg/s)}$$

Table 2. Results of EER, COP and  $W_t$  of case II.

EER	COP	$W_t$
11.856	3.881	1,242

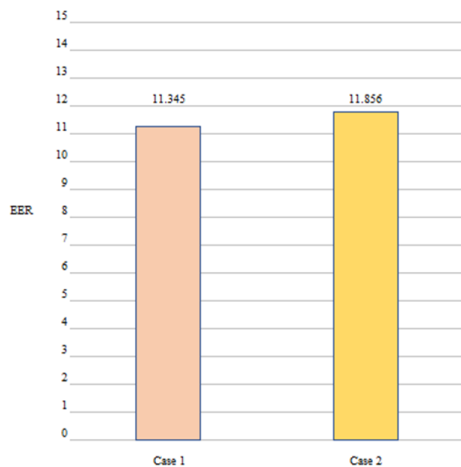


Fig. 4 Compare EER values in case 1 and 2.

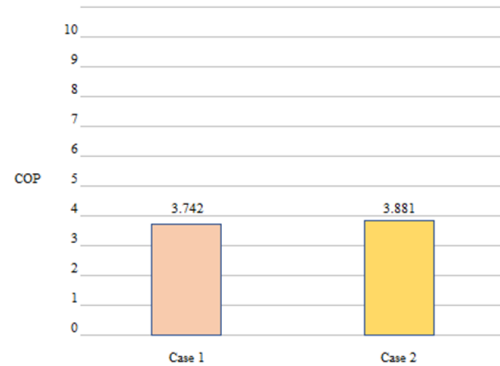


Fig. 5 Compare COP values in case 1 and 2.

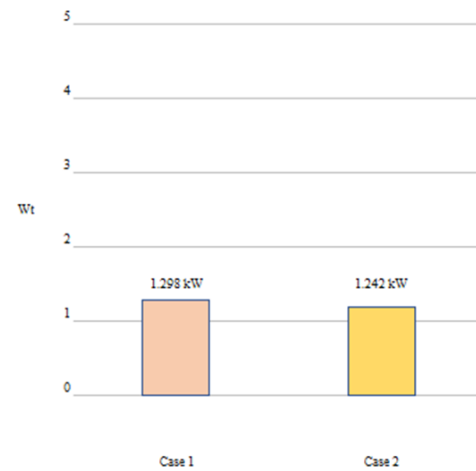


Fig. 6 Compare  $W_t$  values in case 1 and 2.

#### IV. CONCLUSION

This research aims to reduce energy consumption of the air conditioning system of the air-conditioned room in Case II by using air from the ventilation system and condensate water with a lower temperature than the outside air to reduce the temperature of the outside air before cooling the condenser and comparing the energy consumption of this research with the energy consumption of the air-conditioned room in Case I which uses an air conditioning system that cools only outside air. Case I and Case II were studied, measured and recorded the total energy consumption, the state of the refrigerant, the temperature inside the room, the temperature outside the room, the ventilation rate and compared the total energy consumption of both systems. The experimental steps are as follows: Before starting the experiment, measure and record the temperature and relative humidity of the atmosphere. Install an electrical energy meter to record the energy value. Experimental results Case 1 The air conditioning system uses 1.298 kW of electrical energy, the COP coefficient of performance of air conditioning system is 3.742 and the energy efficiency ratio EER is 11.345. Case 2 The air conditioning system uses 1.242 kW of electrical energy,

the COP coefficient of performance of air conditioning system is 3.881 and the energy efficiency ratio EER is 11.856.

From the experimental results, it can be concluded that in Case II, the air conditioning system uses 0.056 kW less electrical energy than Case I, or 4.31% less, the COP coefficient of performance of air conditioning system is increased by 0.157 or 4.22%, and the energy efficiency ratio EER is increased by 0.511 or 4.5%. This shows that the use of the ventilation system in this research can increase efficiency and help reduce energy.

#### ACKNOWLEDGMENT

Rajamangala University of Technology Rattanakosin

#### REFERENCES

- [1] Ardita N. and Subagia W.A. (2018). The application of condensate water as an additional cooling media intermittently in condenser of a split air conditioning, *Journal of Physics: Conference Series*, 953, 012059
- [2] Azridjal A., Muhammad R., Afdhal K.M. and Rahmat I.M. (2021) Experimental Investigation of a Split Air Conditioning Using Condensate as Direct Evaporative Cooling, *Journal of Advanced Research in Fluid Mechanics and Thermal Sciences*, 86(1), 140-153
- [3] Hua Y., Na P., Liansheng L., Man F. and Yue Q. (2021). Experimental study on the effect of condensate water on the performance of split air conditioning system, *Energy Reports*, 7, 840-851
- [4] İbrahim A., Ali Ş. and Ahmet Ç. (2022). Performance testing and optimization of a split-type air conditioner with evaporatively-cooled condenser, *Engineering Science and Technology, an International Journal*, 32, 101064
- [5] Surasit T., Tuan A. D., Pana S. and Yuttana M. (2022) Energy reduction of split-type air conditioners using a pre-cooling system for the condenser, *Energy Reports*, 7(3), 1-6
- [6] R.F. Boehm, H. Yang, J. Yan, *Handbook of clean energy systems*, n.d.
- [7] B. Fankam Tchance, G. Papadakis, G. Lambrinos, A. Frangoudakis, Fluid selection for a low-temperature solar organic Rankine cycle, *Appl. Therm. Eng.* (2008), <https://doi.org/10.1016/j.applthermaleng.2008.12.025>.
- [8] F. Vélez, J.J. Segovia, M.C. Martín, G. Antolín, F. Chejne, A. Quijano, A technical, Economical and market review of organic Rankine cycles for the conversion of low-grade heat for power generation, *Renew. Sustain. Energy Rev.* 16 (2012) 4175–4189, <https://doi.org/10.1016/J.RSER.2012.03.022>.
- [9] J. Larjola, Electricity from industrial waste heat using high-speed organic Rankine cycle (ORC), *Int. J. Prod. Econ.* 41 (1995) 227–235, [https://doi.org/10.1016/0925-5273\(94\)00098-0](https://doi.org/10.1016/0925-5273(94)00098-0).
- [10] D. Wei, X. Lu, Z. Lu, J. Gu, Performance analysis and optimization of organic Rankine cycle (ORC) for waste heat recovery, *Energy Convers. Manag.* (2006), <https://doi.org/10.1016/j.enconman.2006.10.020>.
- [11] Y. Dai, J. Wang, L. Gao, Parametric optimization and comparative study of organic Rankine cycle (ORC) for low grade waste heat recovery, *Energy Convers. Manag.* 50 (2008) 576–582, <https://doi.org/10.1016/j.enconman.2008.10.018>
- [11] Surasit T., Tuan A. D., Pana S. and Yuttana M. (2022) Energy reduction of split-type air conditioners using a pre-cooling system for the condenser, *Energy Reports*, 7(3), 1-6

# Experimental Fretting Wear Resistance Study of Chromizing Treatment on AAR M101 Railway Axle Steel

Manassanun Nitiruksakul<sup>1, a)</sup>, Karuna Tuchinda<sup>2, b)</sup>, Anchalee Manonukul<sup>3, c)</sup>  
and Nuksit Noomwongs<sup>4, d)</sup>

## Author Affiliations

<sup>1</sup>Department of Railway Vehicle and Infrastructure Engineering, The Sirindhorn International Thai-German Graduate School of Engineering, King Mongkut's University of Technology North Bangkok, Bangkok, Thailand

<sup>2</sup>Material Manufacturing and Surface Engineering Research Center, The Sirindhorn International Thai-German Graduate School of Engineering, King Mongkut's University of Technology North Bangkok, Bangkok, Thailand

<sup>3</sup>National Metal and Materials Technology Center (MTEC), National Sciences and Technology Development Agency (NSTDA), Pathumtani, Thailand

<sup>4</sup>Department of Mechanical Engineering, Faculty of Engineering, Chulalongkorn University, Bangkok, Thailand

## Author Emails

<sup>a)</sup>Corresponding author: ntr.manas@gmail.com

<sup>b)</sup>karuna.t@tggs.kmutnb.ac.th

<sup>c)</sup>anchalm@mtect.com

<sup>d)</sup>Nuksit.N@chula.ac.th

**Abstract** Chromizing treatment is recommended to mitigate unavoidable damage caused by wear for metallic components under contact. The work presented a fretting wear resistance study of railway axle steel, AAR M101 after chromizing treatment. The flat specimen of AAR M101 was treated by pack cementation chromizing treatment at 1,075 °C in 24 hours. The fretting experiment of a commercial SUJ2 ball-on-flat contact system under an applied normal load of 10 N with an oscillatory sliding frequency of 2 Hz was carried out for 10,000 cycles. The displacement amplitude was varied in this study. Once comparing the wear profile of ball and flat specimens after the tests, the surface morphology of the counter bodies was smoother on untreated contact systems. In contrast, the asperity wear was observed on the treated contact system. In both untreated and treated systems, severe wear was found at the higher displacement amplitude due to gross slip conditions. The treated contact system experienced a change in contact behavior due to the instantaneous friction coefficient gradually increasing after the first rise at the early cycles and the stabilized friction coefficient was reportedly higher. The contact system's wear volume and energy wear coefficient were also experimentally quantified using the energy accumulated dissipation model. Even though the wear volume and energy wear coefficient of the flat specimens between the untreated and treated contact system were considerably similar, the wear process in the treated contact system was deferred. The energy wear coefficient of the counter ball decreased subsequently, the wear volume of the ball in the treated flat system was reduced by 30%.

**Index Terms**— Chromizing, Dissipated energy, Fretting wear, Friction coefficient, Railway axle

## I. INTRODUCTION

Once two bodies are in contact, surface degradation is unavoidable. Fretting wear is a type of surface degradation occurring when the surfaces of two bodies contact under oscillatory movement with small amplitude displacement [1]. Fretting wear plays a significant role in the railway axle fracture due to it could initiate the crack [2, 3]. Besides, other mechanical applications under the press-fit condition tend to experience a fretting process, for instance, the contact systems of blade-disc in an aircraft engine, stem-cement in a hip implant, and automotive electric connectors [4]. By the fitting design, the wear debris is easily trapped at the contacting surface and the feature make it different to the classical sliding wear [5].

Many studies of fretting wear revealed that the oscillatory displacement amplitude and applied normal force are strongly influential on fretting wear owing to the factors that affect the fretting regime [2, 6]. The fretting condition can be categorized into 3 main regimes: stick regime, partial slip regime (or mixed stick-slip regime), and gross slip. The regimes can be explained by the fretting loop. The fretting loop is a hysteresis plot between displacement amplitude and tangential force along the contacting surface at each cycle. Fig. 1 (a) illustrated the normal contact with contact radius,  $a$ . In the partial slip regime, the part of the contact body sticks at the contact center while the other part experiences the slip as shown in Fig. 1(b) and (c). In gross slip condition, the contacting surface experiences the slip along the displacement amplitude as shown in Fig. 1(d) and (e). Gross slip regime induces severe wear at the center of contact while

partial slip condition encounters less wear but is associated with crack [7, 8].

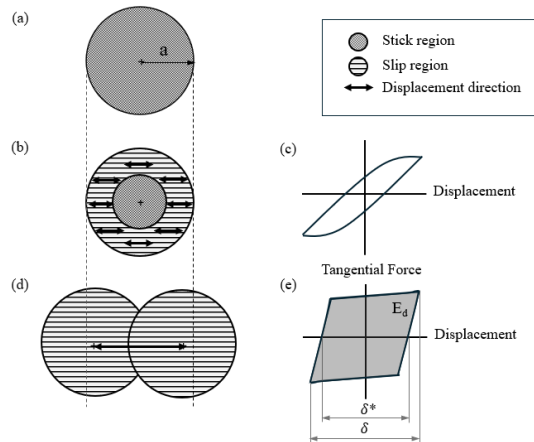


Fig. 1 Characteristic of contact and fretting loop

- (a) Contact without fretting  
(b) and (c) contact and fretting loop in a partial slip condition  
(d) and (e) contact and fretting loop in a gross slip condition

$$\text{Slip ratio} = \frac{\delta^*}{\delta} \quad (1)$$

$$V = \alpha \sum E_d \quad (2)$$

The fretting regimes can be quantitatively distinguished by using the criteria of slip ratio [9] as in Eq. (1) where  $\delta^*$  is slip amplitude and  $\delta$  is applied displacement amplitude. The criteria of the slip ratio of partial slip-to-gross slip delimitation is 0.26.

The material degradation process was attributed to the accumulative energy at the surface. The energy-based approach (Eq. (2)) was developed and widely used, recently [10] where  $V$  denotes the worn volume,  $\alpha$  denotes energy wear coefficient and  $E_d$  denotes the total dissipated energy. The energy wear coefficient indicates a materials resistance to wear. The total dissipated energy can be determined by the enclosure area in the fretting loop.

Since fretting wear has a direct influence on the axle service life, surface treatments is one of the promising approaches to mitigate the fretting wear [11], for instance, by the coating of ZrN [12], TiN, CrN and DLC [13]. The chromizing treatment is recommended for temperature surface protection, corrosion reduction, and wear mitigation [14, 15], particularly, for the application in extreme conditions, i.e., cyclic loading, corrosive environment, or high temperature since Chromium has a high melting temperature (1857°C), corrosion resistance and hardness [16]. The chromizing process is a surface treatment process in which chromium is enriched into the steel by diffusion to form a chromized coating layer [17]. The pack-cementation chromizing is considered a simple, effective, macroscopic, and low-cost method to generate a chromium carbide coating [16]. By the pack cementation method, a sealed retort contains a pack of feedstock alloy, activator, and inert filler for burying components to be coated. The temperature in the

retort is raised to the desired value under

either a hydrogen atmosphere or an inert gas to avoid oxidation during the process. Pack-cementation chromizing is considered a simple, effective, macroscopic, and low-cost method to generate a chromium carbide coating [16, 18]. The formed coating layer results in higher hardness when compared to untreated components with chromizing [19]. The studies of chromized coating steel under the application of sliding wear conditions showed a positive result on wear resistance improvement [19, 20, 21]. However, no recent data on fretting wear resistance of chromized coating on railway axle steel is available. This work aims to study the effect of fretting wear resistance of chromized coating on AAR M101, railway axle steel, over different displacement amplitudes. The fretting test with ball-on-flat configuration was carried out. The wear result between contact systems with untreated and treated AAR M101 was compared and investigated. The energy wear coefficients of both counter bodies in the contact system were quantified. The frictional behavior during the fretting cycles was also studied.

## II. METHODOLOGY

Commercial SUJ2 ball with hardness of 772 HV and young's modulus of 210.00 GPa [22] was selected. AAR M101 with hardness of 265 HV and young's modulus is of 186.77 GPa [23] was prepared as flat specimen. The ball specimen was 6.35 mm in diameter and the flat specimen was 24 mm in diameter with 8 mm in thickness. Three flat specimens were treated by pack cementation chromizing treatment. The chromizing condition is under the temperature of 1,075 °C in 24 hours which is domestically commercially available. After the chromizing treatment, the surface hardness of the flat was also measured by a Vicker Hardness tester. Nanoindentation was also performed, and the young's modulus was determined by nanoindentation curve. Prior to the fretting test, the surface topography was measured by OM-Confocal microscope 3 times for all specimens, i.e. ball, untreated flat and treated flat.

Fretting wear tests were performed on a fretting tester with an electromagnetic actuated motion control. In this paper, the contact system using untreated flat specimen was denoted as the untreated contact system while the other using treated flat specimen was denoted as the treated contact system. For all fretting tests, the normal force was vertically applied on the top of the ball at 10 N and the reciprocating frequency was set at 2 Hz. The fretting tests were carried out in dry conditions at an ambient temperature of 25 °C until 10,000 cycles. The displacement amplitude was the only experimental operating condition to be varied in this work. To experimentally simulate the fretting condition, the required displacement amplitude must be less than the contact width. The displacement amplitude was varied at 0.04 and 0.08 mm. The tests were repeatedly conducted 3 times for each fretting test condition. The test condition was summarized in Table 1. Throughout each test, the displacement amplitude, the normal force and the tangential force were measured and logged for every cycle. Also, the



friction coefficient was determined from the relation of the normal force and the tangential force.

Prior to the fretting tests, the specimens were cleaned with acetone and alcohol. After testing, the morphology of the wear scar of flat specimens was observed by OM-Confocal Microscope and Scanning Electron Microscope (SEM) and the wear profile was measured by OM-Confocal microscope. The results of both counter bodies, ball and flat specimens, were investigated. Apart from that, in the severe wear cases of both untreated and treated contact systems, the wear volume of the ball and flat specimens and energy wear coefficient were determined.

TABLE 1: THE SUMMARY OF FRETTING TEST CONDITIONS

Flat specimen treatment condition	Untreated and treated
Applied normal force [N]	10
Displacement amplitude [mm]	0.04 and 0.08
Frequency [Hz]	2
Temperature [°C]	25 at dry condition
Test duration [cycles]	10,000

### III. RESULTS AND DISCUSSION

#### 1. Surface roughness and material characterization

After the chromizing treatment, the surface roughness,  $R_a$  increased to 1.24  $\mu\text{m}$ . The increased roughness of surface may be attributed to protuberances and observed pores which could be expected. In other works [16, 19, 24], the imperfection of surface were observed from the adherent Cr and may be uneven saturated Cr due to the chromizing is a thermo-chemical process. The hardness and young's modulus were increased to 1,689 HV and 306.35 GPa. This is expected to be due to the chromium carbides formation at the chromized coating layer [16].

#### 2. Fretting wear morphology

Figure 2 and Figure 3 illustrated fretting wear scars of all test conditions. The wear trace was observed on the ball's moving directions. The dark strain on the left of the wear scar was greatly detected on untreated flat specimens (Figure 2(a) and (b)) when compared to the treated flat specimens (Figure 3(a) and (b)). Under high amplitude, the area of dark strain was found greater than that under small amplitude. And Figure 4(a) shows the wear scar of the untreated flat specimen at high amplitude. In Figure 4(b), the silver reflected areas were expected to be the area of high oxidative material accumulation. This was also observed in other works [6, 25]. The oxidative layers observed are expected to be formed by entrapped wear debris. And the material pull-off flow by plastic deformation can be seen. The material flow can be mainly detected as shown in Figure 4(c). The

accumulation of material over the wear

scar, particularly, at the left edge was the material pulled off by plastic deformation.

Once the counter bodies in fretting contact have different hardness levels, the formation of oxide layers was facilitated, especially on the softer material due to it being rather prone to abrasion. This also explained the phenomenon of high material accumulation around wear scar on the flat specimen of untreated contact system yet on the ball specimen of treated contact system.

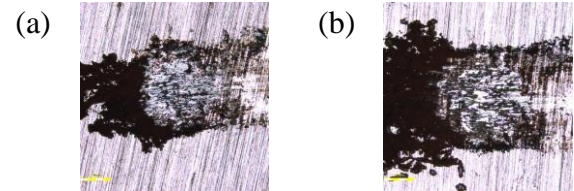


Fig.2 Wear morphology of untreated flat specimens with the amplitude at (a) 0.04 mm (b) 0.08 mm

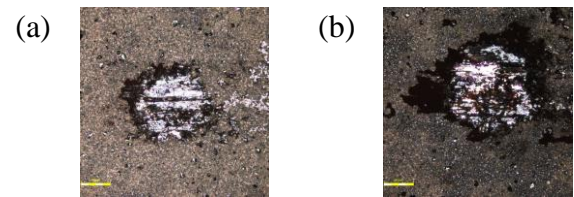


Fig.3 Wear morphology of treated flat specimens with the amplitude at (a) 0.04 mm (b) 0.08 mm

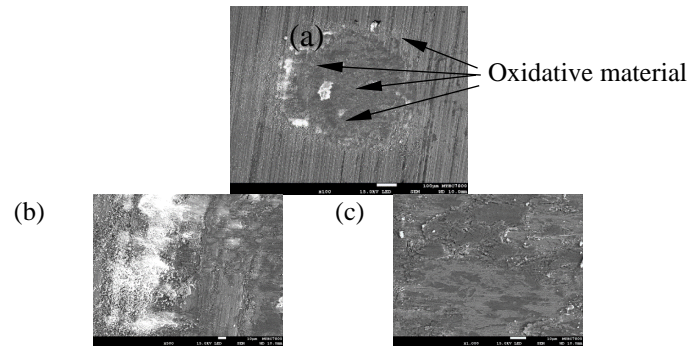


Fig. 4 Wear morphology of untreated flat specimens at 0.08mm amplitude (a) wear scar (b) left side (c) contact center

#### 3. Wear profile

The flat wear profile of the flat specimen was illustrated in Figure 5. In the lower displacement amplitude condition, the contact center lied between the distance of -20 mm and 20 mm while at the higher displacement amplitude, the contact center was along the distance between -40 mm and 40 mm. The higher topography was found outmost contact center. At the same amplitude, the maximum wear depths were almost the same for both untreated and treated flat specimens and found at the contact center except on the treated specimens from the lower amplitude condition where the greatest wear depth was detected beside the contact

center. The specimens encountered severe wear at 0.08 mm of displacement amplitude. However, the peak of surface morphology was found still sharper in treated specimens and the result became more obvious when severe wear occurred. The dissipated cumulative energy of the untreated contact pair was 20 J, while that of the treated contact system was 16 J.

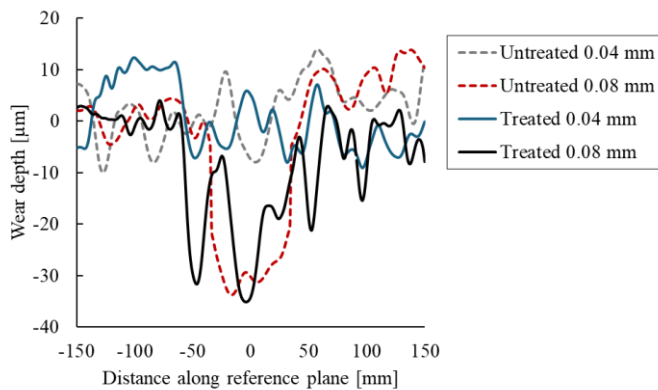


Fig.5 Wear profile of flat specimen at different displacement amplitudes

The wear depth on the treated AAR M101 flat specimen was considerably the same level as the untreated flat specimen. The wear process in the treated specimen was deferred by the observation of asperities wear at both low and high displacement amplitude, 0.04 and 0.08 mm, respectively. By the investigation of the size of wear scar by the surface morphology and wear profile, the more severe wear was noticeable at the high amplitude. The contacting surface experiences more slip when the amplitude is higher. Subsequently, the shear stress at the interface increases and the wear depth increases. This is expected as it was reported that the displacement amplitude has a strong effect on the wear behavior [2, 6].

The wear profile in Fig.5. show a slight change in wear depth when comparing untreated and treated flat specimens at both displacement amplitudes. Nevertheless, as a result of asperities wear, the spikes on the surface were rather found on the treated specimens than on the untreated specimen.

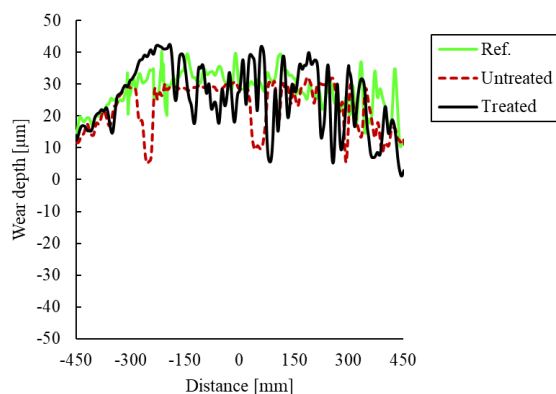


Fig.6 Wear profile of ball specimen at displacement amplitude of 0.08 mm

The wear profile of ball specimens at the displacement amplitude of 0.08 mm was assessed (in Figure 6). The surface topology of the commercial ball was overlayed for reference (ref.). Still, the maximum depth of the ball specimens was similar in both treated and untreated contact systems. However, the spikes on the surface, higher than the reference profile, at the surface were rather found in the treated contact system.

Once investigating the commercial SUJ2 ball, with no additional treatment process applied in this study, a greater amount of material loss by wear was observed on the untreated contact system. Similar to the flat specimen profile after testing, the surface profile of the ball in the treated contact system showed spikes on the surface which was attributed to asperities wear. The retention of the wear debris under fretting contact became more beneficial in wear mitigation [21, 26].

#### 4. Friction coefficient

Fig. 7 illustrated the frictional behavior throughout the fretting cycles. On the contact system with the untreated flat specimen, the friction coefficient aggressively increased in 2 steps. The first rise of the friction coefficient below the 100th cycle due to the wear process occurred and remained constant due to the accumulation of an oxide layer formed with wear debris. Once the cyclic loading continues, the accumulative layers eventually fail, surface fracture was induced again leading to the second rise of the friction coefficient. The friction coefficient on the untreated contact system was stabilized at nearly the 1,000th cycle. For the treated contact system, the friction coefficient at the early fretting cycle aggressively rose up only one step as a result of its initial surface roughness increase. Since the contact area between surfaces increased with the increase in surface roughness, the contact between the surfaces becomes more incomplete, resulting in an increase in the coefficient of friction. After that, the friction coefficient gradually increased until stable at nearly the 3,000th cycle. The friction coefficient observed in the treated system is higher than the untreated system. The surface condition (e.g., roughness) has a significant effect on frictional behavior in relation to wear behavior of a contact system. However, the increase of friction coefficient has less effect on fretting wear, particularly, under gross slip conditions [27]. Note that, although the result of the fretting loop is not shown here, it was confirmed by the estimation of slip ratio of 0.9 that for all conditions studied in this work, the contact was found to be under gross slip conditions. Therefore, even with the slightly higher friction coefficient, the adverse effect of the wear on flat specimens was not noticeably seen in this study.

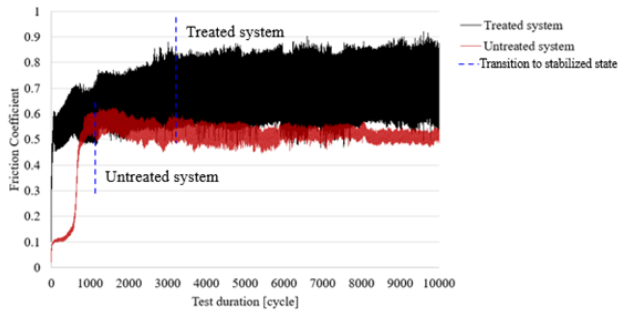


Fig.7 Friction coefficient at 0.08 mm displacement amplitude

##### 5. Wear volume and energy wear coefficient

Material loss in the severe wear of this study was quantified into wear volume for ball and flat specimens (in the cases of 0.08mm displacement amplitude). The wear volume of both untreated and treated flat specimens was insignificantly different (see Fig.8). Nevertheless, in the treated contact system, ball specimens experienced less wear volumes than in the untreated contact system by approximately 30% as illustrated in Figure 8. Subsequently, the energy wear coefficient of the ball in the treated contact system was less than that in the untreated contact system as shown in Table 4.

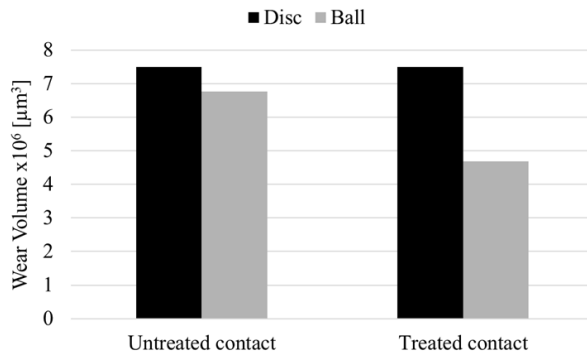


Fig.8 Wear volume of ball and flat at 0.08 mm displacement amplitude

TABLE 4: FLAT SPECIMEN WEAR COEFFICIENT  
[UNIT:  $\times 10^3 \mu\text{m}^3/\text{J}$ ]

Flat-Untreated system	37.48
Ball-Untreated system	33.80
Flat-Treated system	46.88
Ball-Treated system	29.25

The wear volume of the flat specimen in both contact systems was considerably similar, while the positive result on wear resistance was found in the ball specimen from treated contact systems. The hardness of treated specimen was increased near the top surface. The level of hardness in

this study could be ordered from the highest to the lowest: treated flat, ball and untreated flat specimens. The adhesive wear was identified a major part of fretting damage. The wear debris easily adheres to the softer body and is formed the oxide layers. The oxide layers acted as the surface protection leading to fretting wear mitigation. The positive result in wear resistance can be seen in the softer bodies of the contacting systems which, in this work, are the flat specimen on the untreated system and the ball specimen in the treated system. It could be seen that, considering the high amplitude case in this work, chromizing treatment showed the potential to improve wear resistance of the contact system by reducing visible wear, especially on the ball and which could be uniquely quantified by the reduction in energy wear coefficient.

#### IV. CONCLUSION

This work presented the effect of chromizing treatment on fretting wear behavior of SUJ2 and AAR M101 contact system using ball on flat testing arrangement. The followings could be observed.

- Severe wear was found at the higher displacement amplitude because of the higher shear stress on the surface.
- When considering the contact systems between AAR M101 and SUJ2, the fretting wear could be mitigated by applying the chromizing treatment on the AAR M101. With the observation of surface topography after the experiment, the wear process can be deferred by the change of friction coefficient behavior.
- The wear loss comparison between the treated and untreated AAR M101 specimen showed similar levels. However, the severe wear was found on the untreated contact system while the asperities wear was observed on the treated contact system. Once comparing the counter ball specimens, the wear loss was reduced in treated contact systems by 30% and energy wear coefficient was reduced due to the oxide layers formation at the ball, softer surface, gave the positive impact on the fretting wear resistance.
- By the positive result on the fretting wear resistance, the surface degradation can be delayed after applying chromizing treatment and subsequently, may delay the fretting induced crack initiation on the railway axle component.

#### ACKNOWLEDGMENT

This project was financially supported by the National Science and Technology Development Agency (NSTDA), Thailand under TGIST scholarship no. SCA-CO- 2563-12144-TH. The AAR M101 material was provided by the State of Railway Thailand (SRT).

#### REFERENCES

- [1] M. Varenberg, I. Etsion, G. Halperin, "Slip Index: A New Unified Approach to Fretting," *Tribology Letters*, vol. 17, no. 3, pp. 569-573, 2004.

- [2] J. F. Zheng, J. Luo, J. L. Mo, J. F. Peng, X. S. Jin, M. H. Zhu, "Fretting wear behaviors of a railway axle steel," *Tribology International*, vol. 43, no. 5-6, pp. 906-911, 2010.
- [3] C. Zhu, J. He, J. Peng, Y. Ren, X. Lin, M. Zhu, "Failure mechanism analysis on railway wheel shaft of power locomotive," *Engineering Failure Analysis*, vol. 104, pp. 25-38, 2019.
- [4] L. Ma, K. Eom, J. Geringer, T. S. Jun, K. Kim, "Literature review on fretting wear and contact mechanics of tribological coatings," *Coatings*, vol. 9, no. 8.
- [5] L. O. A. Affonso, "Machinery Failure Analysis Handbook: Sustain Your Operations and Maximize Uptime," in *Wear*, L.O.A. Affonso, Ed. Gulf Publishing Company, 2013, pp. 55-82.
- [6] A. Ben Cheikh Larbi, B. Tlili, "Fretting wear of multilayered PVD TiAlCN/TiAlN/TiAl on AISI 4140 steel," *Surface and Coatings Technology*, vol. 201, no. 3-4, pp. 1511-1518, 2006.
- [7] O. Vingsbo, S. Staffan Söderberg, "On Fretting Maps," *Wear*, vol. 126, no. 2, pp. 131-147, 1988.
- [8] J. J. Madge, S. B. Leen, I. R. McColl, P. H. Shipway, "Contact-evolution based prediction of fretting fatigue life: Effect of slip amplitude," *Wear*, vol. 262, no. 9-10, 2007.
- [9] S. Fouvry, Ph. Kapsa, L. Vincent, "Analysis of sliding behaviour for fretting loadings: determination of transition criteria," *Wear*, vol. 185, no. 1, pp. 35-46, 1995.
- [10] S. Fouvry, Ph. Kapsa, L. Vincent, "Quantification of fretting damage," *Wear*, vol. 200, pp. 186-205, 1996.
- [11] S. Fouvry, K. Kubiak, "Development of a fretting-fatigue mapping concept: The effect of material properties and surface treatments," *Wear*, vol. 267, no. 12, pp. 2186-2199, 2009.
- [12] S. Kowalski, M. Cygnar, B. Cieřlikowski. "Analysis of the application of ZrN coatings for the mitigation of the development of fretting wear processes at the surfaces of push fit joint elements," *Proceedings of the Institution of Mechanical Engineers, Part J: Journal of Engineering Tribology*, vol. 234, no. 8, 2019.
- [13] Y. Okamura, D. Suzuki, K. Takahashi, T. Nagatomo, H. Utsunomiya, "Suppression Effect of Fretting Wear in Railway Axle Journal Bearings by Means of Hard-film Coatings," *Tetsu-to-Hagane*, vol. 104, no.6, pp. 303-311, 2018.
- [14] J. W. Lee, J. G. Duh, S. Y. Tsai, "Corrosion resistance and microstructural evaluation of the chromized coating process in a dual phase Fe Mn Al Cr alloy," *Surface and Coatings Technology*, vol. 153, no. 1, pp. 59-66, 2002.
- [15] F. A. P. Fernandes, S. C. Heck, C. A. Picon, G. E. Totten, L. C. Casteletti, "Wear and corrosion resistance of pack chromised carbon steel," *Surface engineering*, vol. 28, no. 5, 2012.
- [16] J. Hu, Y. Zhanga, X. Yanga, H. Lia, H. Xub, C. Maa, Q. Dong, N. Guo, Z. Yao, "Effect of pack-chromizing temperature on microstructure and performance of AISI 5140 steel with Cr-coatings," *Surface and Coatings Technology*, vol. 344, pp. 656-663, 2018.
- [17] S. R. J. Saunders, J. R. Nicholls, "Oxidation, Hot Corrosion and Protection of Metallic Materials," in *Physical Metallurgy*, R.W. Cahn and P. Haasent, Eds. Elsevier Science BV, 1996.
- [18] R. Yang, A. Lan, H. Yang, X. Jin, J. Qiao, "The chromization on hot-rolled Fe40Mn20Cr20Ni20 high-entropy alloys by pack cementation," *Journal of Alloys and Compounds*, vol. 947, 2023.
- [19] S. Li, Z. Yang, Q. Wan, J. Hou, Y. Xiao, X. Zhang, R. Gao, L. Meng, "Increase in wear resistance of traction wheel via chromizing: a study combining experiments and simulations," *Coatings*, vol. 12, 2022.
- [20] N. Lin, X. Faqin, H. Yang, W. Tian, H. Wang, B. Tang, "Assessments on friction and wear behaviors of P110 steel and chromizing coating sliding against two counterparts under dry and wet conditions," *Applied Surface Science*, vol. 258, no. 11, pp. 4960-4970, 2012.
- [21] F. Mukhtar, F. Qayyum, Z. Anjum, M. Shah, "Effect of chrome plating and varying hardness on the fretting fatigue life of AISI D2 components," *Wear*, vol. 419-418, pp. 215-225, 2019.
- [22] Misumi, n.d.
- [23] M. Anchalee, et al., "Improving the Reliability of Wheelset", October 14, 2021.
- [24] Z. Donga, T. Zhoua, J. Liua, X. Zhanga, B. Shena, W. Hub, L. Liu, "Effects of pack chromizing on the microstructure and anticorrosion properties of 316L stainless steel," *Surface & Coatings Technology*, vol. 366, no. 86 – 96, 2019.
- [25] J. Wang, H. Li, Z. Li, Y. Lei, Q. Ren, Y. Jiao, Z. Cai1, "Fretting Wear Characteristics of Nuclear Fuel Cladding in High-Temperature Pressurized Water," *Chinese Journal of Mechanical Engineering*, vol. 36, 2023.
- [26] J. D. Lemma, A. R. Warmuthb, S. R. Pearsonb, P. H. Shipway, "The influence of surface hardness on the fretting wear of steel pairs—Its role in debris retention in the contact," *Tribology International*, vol. 81, no. 258 – 266, 2015.
- [27] T. Yue, M. Abdel Wahab, "Finite Element Analysis of Fretting Wear Under Variable Coefficient of Friction and Different Contact Regimes," *Tribology International*, vol. 107, pp. 274–282, 2017.



# Economic Evaluation of Conversation Energy in Oil Palm Mill Industrial

Kanitpong Chitsopon<sup>1</sup> and Chanon Bunmephiphit<sup>1,a)</sup>

<sup>1</sup> Energy and Environmental, Rattanakosin College for Sustainable Energy and Environment, Rajamangala University of Technology Rattanakosin, Nakhonpathom, Thailand 73170

<sup>a)</sup>Corresponding: Chanon.bun@rmutr.ac.th

**Abstract.** This research evaluates conversation energy in oil palm mill industries through motor inverter installation to serve as an energy conservation guideline and reduce electricity costs for the industry. The study is about the palm oil mill industry of Thongmongkol Palm Oil Industry Co., Ltd in October 2024 compared with 2021-2023. An economic evaluation of conversation energy in the oil palm mill industrial includes payback period, NPV and IRR. Thong Mongkol Palm Oil Industry Co., Ltd.'s electricity consumption was found that from 2021-2023, electricity consumption was 3,557.91-4,599.65 MWh, an average of 3,937.14 MWh. Improving energy usage in palm oil production involves installing equipment to adjust motor speeds appropriately, using inverters to adjust the speed of high-efficiency motors to reduce motor operation, and using SCADA. That resulted in a reduction in electricity expenses to only 93,918.70 baht/month, which could reduce electricity expenses for Thong Mongkol Palm Oil Industry Co., Ltd. by 56.44%, 57.96% and 41.79% compared to 2021, 2022 and 2023, respectively. That reduces its electricity expenses to only 20,772,516.94, 18,538,912.97 and 14,071,705.03 baht/year. The NPV was 822,461.41 baht, with a project duration of 5 years and a discount rate of 7%. When analyzing the internal rate of return of the project, it was high at 96.59%, indicating a high return on the project and a short payback period of 1 month and 13 days.

**Index Terms**—Oil Palm, Economic, Conversation energy, Motor inverters

## I. INTRODUCTION

Oil Palm is an important and productive vegetable oil in the world. The most efficient oil crop, palm oil production from major producing countries, constituted about 31.6% of global total oil and fats production. The efficient oil crop and palm oil production from major producing countries constituted about 31.6% of global total oil and fats production. This massive oil production comes from a meagre 6% of global agricultural land devoted to oil crops, further strengthening palm oil's sustainability in land usage [1]. Energy use is an important factor in production costs and the value of investing in entrepreneurs. The recent energy crisis has greatly affected industrial progress. Industrial factories and various businesses must have energy conservation measures or find alternative energy sources to reduce their limitations. In 2022, Thailand had a total final energy consumption of 84,178 thousand tons of crude oil equivalent, an increase of 16.7% from 2021, representing a total energy consumption value of more than 2,089,316 million baht, with the industrial sector having the highest final energy consumption at 32,985 thousand tons of crude oil equivalent. The proportion is 39.2%, an increase of 7% from 2021 [2].

The palm oil mill industry uses motors as the main electrical equipment in the production process, which is high-power electrical equipment, resulting in energy waste. Normally, various controls have been employed to enhance the flexibility and consistency of manufacturing processes, such as controlling the speed of the equipment, changing gear ratios or pulleys, and using hydraulic drives. A variable speed drive (VSD) is a device that regulates the speed and rotational force, or output torque of mechanical

equipment. Some examples of mechanical equipment incorporate pumps, fans, compressors, conveyors, and motor inverters. That reduces motor electricity consumption by 24–60%. The potential for electrical motor energy savings is enormous since motor systems use more than 60% of the electrical power consumed by industry [3, 4]. Thus, this research evaluates conversation energy in oil palm mill industries through motor inverter installation to serve as an energy conservation guideline and reduce electricity costs for the industry.

## II. METHODOLOGY

The study is about the palm oil mill industry of Thongmongkol Palm Oil Industry Co., Ltd in October 2024 compared with 2021-2023. Economic evaluation of conversation energy in oil palm mill industrial includes the following:

Payback Period (PB) is a period of investment in which the net cash inflows from the project are equal to the net cash outflows, or the investment has no profits and no losses. The payback period is a tool for evaluating the feasibility of an investment. The payback is a quick assessment suitable for investment [5], as calculated in equation (1)

$$PB = \frac{IC}{CF} \quad (1)$$

Where IC is the value of the invested capital, CF is cash flow, achieved as the result of the implementation of energy-saving measures and savings in operating costs or expected to be achieved at the stage of project development after the end of the calendar year.

NPV is net present value; this is a method for future cash flow; it calculates the time value of cash flow and turns it into a current value with a given discount rate. In Gallo's business review, Knight defines NPV as Net present value is the present value of the cash flows at the required rate of return of your project compared to your initial investment [6], as calculated in equation (2)

$$NPV = CF_0 + \frac{CF_1}{(1+r)^1} + \frac{CF_2}{(1+r)^2} + \dots \frac{CF_t}{(1+r)^t} \quad (2)$$

Where  $r$  is the discount rate,  $C$  is cash flow, and  $t$  is the time of the project.

IRR is the internal rate of return; it works on discount cash flow methodology, the same as NPV. However, unlike NPV, IRR results in a meaningless return rate. IRR works by comparing itself with a hurdle rate or base rate in the capital market. In Gallo's business review, Knight defines IRR as "The rate at which the project breaks even [6]. The calculation of IRR is to find the discount rate that will cause NPV equal to zero, as calculated in equation (3)

$$0 = CF_0 + \frac{CF_1}{(1+IRR_1)} + \frac{CF_2}{(1+IRR_2)} + \dots \frac{CF_t}{(1+IRR_t)} \quad (3)$$

### III. RESULTS AND DISCUSSION

The palm oil production process of Thong Mongkol Palm Oil Industry Co., Ltd. consists of 9 stations, as mentioned in the chapter above. The Loading ramp station and Sterilizer station are adjacent stations and share the same machinery. Therefore, the energy use is measured together, and the energy use is evaluated together. In addition, there are other energy use parts such as office buildings and Boiler stations. Boiler is the station that produces energy for the palm oil production process. Therefore, the energy use evaluation will be explained using the following abbreviations:

- S1 is Loading ramp station and Sterilizer station
- S2 is Threshing station
- S3 is Pressing station

- S4 is Empty bunch station
- S5 is Kernel recovery station
- S6 is Clarification station
- S7 is CPO Loading station
- S8 is Water Treatment station
- ETC is Office and Boiler station

The measurement of Thong Mongkol Palm Oil Industry Co., Ltd.'s electricity consumption was found that from 2021-2023, electricity consumption was 3,557.91-4,599.65 MWh, an average of 3,937.14 MWh. From Figures 4.1 and 4.2, it can be observed that ECT has the highest electricity consumption because electricity is used from office buildings and Boiler stations, with electricity consumption of 1,365.17-1,764.89 MWh, an average of 1,510.68, followed by S4, Empty bunch station, with electricity consumption of 899.94-1,163.44 MWh, an average of 995.86 MWh, and S5, Kernel recovery station, with electricity consumption of 813.29-1,051.42 MWh, an average of 899.98 MWh, both of which are waste separation and disposal stations. Thong Mongkol Palm Oil Industry Co., Ltd. has 177 motors, a total motor power of 2,574.14 kW and an average of 92.36 kW. The S3 has 14 motors with the highest motor power, an average of 25.31 kW and a combined motor power of 540.50 kW. The amount of electricity used depends on the amount of palm used to produce palm oil, which is consistent with the electricity usage of S1, which is the Loading ramp station and the Sterilizer station, which are the stations for transporting raw materials into the palm oil pressing process, so it uses only slightly less electricity. When considering the electricity usage of S3, which is the process of pressing to obtain oil, which is the most important process and the main process in the palm oil production process, it was found that the electricity usage was 513.48-663.82 MWh, an average of 568.21 MWh, and the Threshing station, which is the process of massaging palm oil before entering the oil pressing process, used an energy of 158.03-204.30 MWh, an average of 174.87 MWh. When the electricity usage of both stations is combined, the electricity usage will be 671.51-868.12 MWh, an average of 743.08 MWh, which is close to S5. In general, from past research, it was found that the palm oil pressing process used the highest electricity at 71%, the massaging process at 22.32%, the sterilization process at 3.75%, and the raw material reception at 2.93% [7].

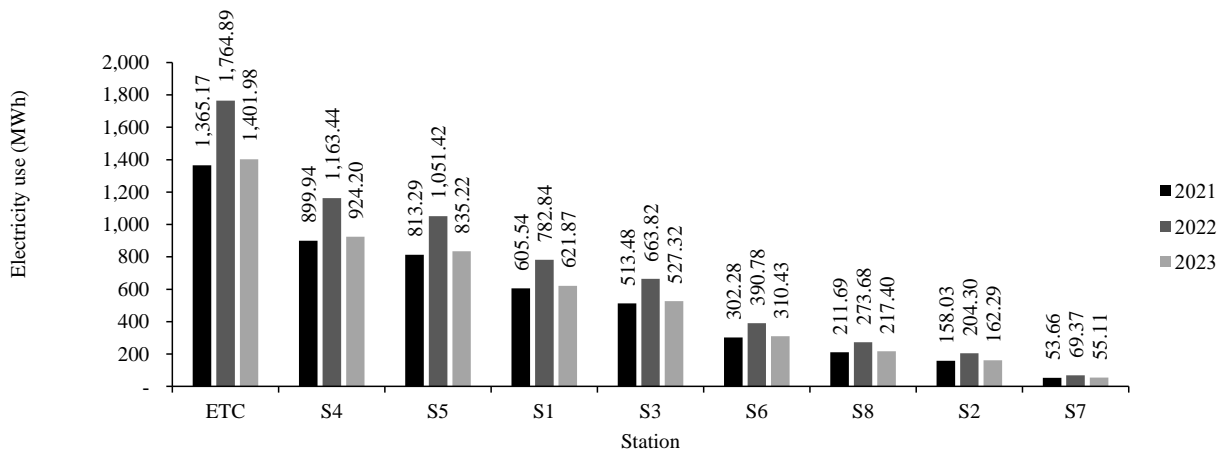


Fig. 1. Electricity consumption of palm oil factories in 2021-2023

Improving energy usage in palm oil production involves installing equipment to adjust motor speeds appropriately, using inverters to adjust the speed of high-efficiency motors to reduce motor operation, and using SCADA programs to adjust motor speeds to operate when needed and stop operating when not in use. In October 2021-2023, Thong Mongkol Palm Oil Industry Co., Ltd. had 161,344.80-223,403.32 baht/month in electricity expenses. When Thong Mongkol Palm Oil Industry Co., Ltd. installed the inverter motor, it resulted in a reduction in electricity expenses to only 93,918.70 baht/month, which could reduce electricity expenses for Thong Mongkol Palm Oil Industry Co., Ltd. by 56.44%, 57.96% and 41.79% compared to 2021, 2022 and 2023, respectively, as shown in Fig. 1. In 2023, Thong Mongkol Palm Oil Industry Co., Ltd. had 22,336,039.72 baht/year in electricity expenses. Suppose the electricity savings are calculated based on the 7%, 17% and 37% reduction in electricity usage. In that case, Thong Mongkol Palm Oil Industry Co., Ltd. will be able to reduce its electricity expenses to only 20,772,516.94, 18,538,912.97 and 14,071,705.03 baht/year, respectively, as shown in Fig. 2.

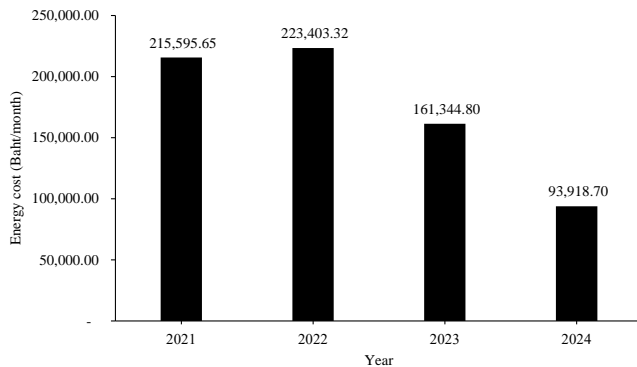


Fig. 1. Comparison of monthly electricity bills before and after installing the inverter motor.

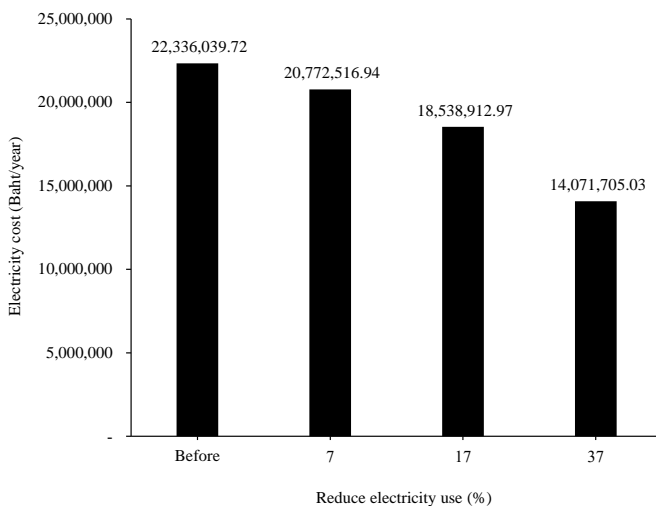


Fig. 2. Comparison of electricity costs before and after installing the inverter motor based on reduced electricity consumption.

The economic analysis of the installation of the inverter motor found that the investment value of the equipment was 161,260.70 baht. After installation, the electricity saving was 106,195.89 baht/month, resulting in an annual energy saving of 1,274,350.68 baht/year. The NPV was

822,461.41 baht, with a project duration of 5 years and a discount rate of 7%. When analyzing the internal rate of return of the project, it was high at 96.59%, indicating a high return on the project and a short payback period of 1 month and 13 days, as shown in Table 1.

TABLE I ECONOMIC OF CONVERSATION ENERGY IN OIL PALM MILL INDUSTRIAL

Detail	Amount
Saving cost of energy (Baht/month)	106,195.89
Saving cost of energy (Baht/year)	1,274,350.68
Investment (Baht)	161,260.70
Discount rate (%)	7.00
Time of project (year)	5
PB (year)	0.13
NPV (Baht)	822,461.41
IRR (%)	96.594821

## I. CONCLUSION

Thong Mongkol Palm Oil Industry Co., Ltd.'s electricity consumption was found that from 2021-2023, electricity consumption was 3,557.91-4,599.65 MWh, an average of 3,937.14 MWh. Improving energy usage in palm oil production involves installing equipment to adjust motor speeds appropriately, using inverters to adjust the speed of high-efficiency motors to reduce motor operation, and using SCADA. That resulted in a reduction in electricity expenses to only 93,918.70 baht/month, which could reduce electricity expenses for Thong Mongkol Palm Oil Industry Co., Ltd. by 56.44%, 57.96% and 41.79% compared to 2021, 2022 and 2023, respectively. That reduces its electricity expenses to only 20,772,516.94, 18,538,912.97 and 14,071,705.03 baht/year. The NPV was 822,461.41 baht, with a project duration of 5 years and a discount rate of 7%. When analyzing the internal rate of return of the project, it was high at 96.59%, indicating a high return on the project and a short payback period of 1 month and 13 days. If electricity costs are reduced, the company will maintain the same increase in production to support consumer needs.

## ACKNOWLEDGMENT

The authors would like to thank Rattanakosin College for Sustainable Energy and Environment and Palm Oil Industry Co., Ltd. for supporting the equipment and facilities for this research.

## REFERENCES

- [1] G.K. Parveez, N.N. Kamil, N.Z. Zawawi, M.ong-abdullah, R. Rasuddin, S.K. Loh, K.R. Selvadura, S.S. Hoong, Z. Idris, "Oil Palm Economic Performance in Malaysia and R&D Progress in 2021", Journal of Oil Palm Research. 34(2):185-218, 2021.
- [2] Department of Alternative Energy Development and Efficiency. 2022. Energy Situation of Thailand January - Desember 2022, Retrieved January 7 2024, from <https://kc.dede.go.th/knowledge-view.aspx?p=409>

- [3] R. Saidur, S. Mekhilef, M.B. Ali, A. Safari, H.A. Mohammed, “Applications of Variable Speed Drive (VSD) in Electrical Motors Energy Savings”, *Renewable and Sustainable Energy Reviews*. 16(1):543-550, 2012.
- [4] Hi. Sakai, “Effect of Energy Saving of Electric Motor Driven Line Hauler Using Inverter”, *Fisheries Science*. 61(6): 931-936, 1995.
- [5] A. Gorshkov, N.I. VatinNikolai, P.P. Rymkevich, O.O. Kydrevich, “Payback Period of Investments in Energy Saving”, *Magazine of Civil Engineering*. 2: 65-75, 2018.
- [6] M. Lai, “Analyze and Improvement of NPV and IRR Methods”, *Highlights in Business, Economics and Management*. 42: 204-208, 2024.
- [7] A. Kushairi, “The Oil Palm Industry in Malaysia: Thriving with Transformative Technologies”, *Journal of Oil Palm Research*, 29(4), 431–439, 2018.



# Development of alternative UV-protective cotton fabrics using natural dyes from ethanolic extract of carrot and black glutinous rice

Apiwitch Kraykome <sup>1</sup>, Benyapa Wasasiri <sup>1</sup>, Thanaporn Maswanna <sup>2, a)</sup>  
and Tussanee Chantiwas <sup>1, b)</sup>

## Author Affiliations

<sup>1</sup> Princess Chulabhorn Science High School, Pathum Thani, Thailand, 12140

<sup>2</sup> Scientific Instruments Center, School of Science, King Mongkut's Institute of Technology Ladkrabang, Bangkok, Thailand 10520

## Author Emails

<sup>a)</sup> Corresponding author: thanaporn.ma@kmitl.ac.th

<sup>b)</sup> tussanee@pccp.ac.th

**Abstract.** Long-term exposure to ultraviolet radiation (UV-R) can lead to skin cancer and degenerative alterations in blood vessels, fibrous tissues, and cells. This study aims to develop UV-protective cotton fabrics by dyeing the black glutinous rice and carrot extracts with banana sap as a mordant. The black glutinous rice and carrots were extracted with 70% and 95% ethanol, respectively. The cotton samples were dyed using various combinations of dyeing ethanolic extracts. The effective UV-R was measured using UV-Vis DRS and by the UV-R Protection category as well as UV protection efficiency, according to standard AS/NZS 4399:1996. The result indicated that black glutinous rice and carrot extracts could enhance the UV protection of cotton fabrics by up to 18.27% ( $P < 0.05$ ). The cotton fabrics dyed with 70% and 95% ethanolic black glutinous rice and the combination with 70% and 95% ethanolic carrot extract have an efficiency of up to 100% UV protection and were categorized in the excellent UV protection category according to the standard. Therefore, this study could be applied as an alternative natural dyeing agent in the cotton industry to increase the value of agricultural outcomes for local growers in the future.

**Index Terms**— Banana sap, Black glutinous rice, Carrot, Cotton, UV protection.

## I. INTRODUCTION

The atmosphere on Earth is depleting ozone, resulting in a progressive increase in ultraviolet (UV) radiation on human skin in recent years. Chronic exposure to UV rays can lead to a variety of adverse health effects, including photo dermatoses, erythema, and skin cancer [1]. Accessible sunblock with UV protection provides a solution that may be applied directly to the human skin. It must be washed or rubbed off and reapplied multiple times to provide long-term protection [2]. It has specific adverse effects such as acne, burning, itching, and skin stinging [3]. To address this issue, UV protection fabric has been created, and dermatologists advocate wearing clothing that covers the body as UV protection [4, 5].

Natural colorants were humanity's sole source of color in ancient times. However, the Industrial Revolution introduced synthetic dyes, significantly transforming the textile industry. For over a century, natural dyes saw limited use due to the rise of synthetic alternatives [6]. Since synthetic dyes release contaminants into the environment, developed countries have prohibited the majority of artificial dyes in the age group and anthraquinone dyes. Natural dyes are in high demand due to growing ecological consciousness, and more scientific advancements and discoveries are being made worldwide. Plants and vegetables could be used as natural

colorants, namely black glutinous rice (*Oryza sativa* Linn), and carrots (*Daucus carota* Linn), along with their bioactive ingredients to protect the skin against UV radiation. Several pigmented rice varieties, mainly red and black rice, have been cultivated in Thailand, especially black glutinous rice. It is a plant with hereditary protection against ultraviolet radiation and contains antioxidant properties [7]. and arrests high amounts of phenolic compounds, especially anthocyanins, in the pericarp [8] Carrots contain antioxidant compound, including  $\beta$ -carotene and vitamin E [9].  $\beta$ -carotene shows functional activities, such as free radical scavenging, anti-mutagenicity, chemoprevention, photoprotection, and immune enhancement [10]. This suggests that  $\beta$ -carotene can act as a sunscreen. Therefore, carrots are present as natural sunscreen.

*Musa sapientum* Linn sap collected from the harvested banana plant's pseudostem has been used as a mordant for natural dyeing silk fabric [11]. Banana pseudo stems have been used to fix the color of natural dye extracts (such as palash flower) [12] because they have tannin. Tannin has excellent dye-fixation characteristics due to its chemical composition. Tannin establishes hydrogen bonds between tannins' phenolic hydroxyl groups and protein's free amino and amido groups. Tannins are amorphous chemicals that cannot be crystallized, and their aqueous solution exhibits an acidic response. Therefore, tannin in banana sap is

responsible for color fixing [12].

Cotton is the fine seed hair of plants in the Mallow family. These natural hollow fibers are soft, cool, breathable, and absorbent. Cotton fibers can store water 24–27 times their weight. They are durable, dye absorbent, and withstand abrasion wear and high temperatures [13]. Cotton serves more than simply being wearable; it is also used in various protective applications. Culminate consumers value not just textile utility and cost-effectiveness but also safety, environmental friendliness, and health impact [14]. However, the cotton fabric must be bleached to remove any naturally occurring substances or those introduced during the weaving process, which reduces the UV protection of cotton.

This study aims to improve the UV protection ability of cotton fabric by using black glutinous rice and carrot extracts, with raw banana sap as a natural mordant in the dyeing process. The findings offer valuable applications for cotton manufacturers and related industries, enabling the production of eco-friendly, UV-protective fabrics without synthetic chemicals. This approach benefits fashion, outdoor clothing, and healthcare textiles while promoting sustainability through the use of agricultural byproducts.

## II. METHODOLOGY

### Materials and Chemicals

Black glutinous rice (*Oryza sativa* Linn) and Carrots (*Daucus carota* Linn) used in this study were bought from local markets in Pathum Thani province, Thailand, in June 2024. Hand-woven cotton fabric was bought from local shop in Pathum Thani province, Thailand. Analytical grade of Ethanol was purchased from QR&C (New Zealand).

### Preparation of crude extract

Black glutinous rice and carrots were extracted and used as the colorant in the dyeing process. The black glutinous rice was ground into powder using a kitchen milling machine. The carrots were rinsed with clean water, grated into strips, and dried under the sun for 16 hours or until dry at 50-60 °C. Then, finely grind the dried carrots to obtain powder with a kitchen milling machine. 250 g of black glutinous rice and carrot powder were extracted with 1 L of 70% v/v and 95% v/v ethanol, soaked for 3 days at 30 °C, then filtered with Whatman filter paper no. 42. The ethanol solution was evaporated to achieve the concentrated extract by a Rotary evaporator. The final volume is 25 mL. The natural dye extract was stored in brown glass bottles at 4 °C until use. The extraction was done in triplicate and combined.

### Preparation of banana sap

The sharp end of the knife was pushed tangentially into the stem. The incision was left to bleed for 2 hours and stored in a wide-mouth plastic bottle in the refrigerator at 4 °C until use.

### Dyeing process

Dyeing was done in the following manner. Hand-woven cotton fabric was cut to a size of 2\*2 cm<sup>2</sup> and was washed with a solution consisting of detergent and distilled water

with a ratio of 1:2 for one time. The cotton was then washed with distilled water and dried. The dye was varied, as the condition shown in Table 1. The dye combination was prepared at a ratio of 1:1. The cotton fabrics were introduced into 3 mL of dye in a beaker at 50 °C. After 30-minute of dyeing, the fabrics were removed and oxidized by drying in air. The fabrics were introduced into 3 mL of banana sap at 30 °C for 30 minutes and then dried in the air overnight. A schematic representation of the dyeing process is shown on Fig. 1.

### Analysis of Ultraviolet Radiation (UV-R) value UV-R protection category and UV Light blocked Calculation by Ultraviolet-Visible Diffuse Reflectance Spectrophotometer (UV-Vis DRS)

Direct and diffuse Ultraviolet-Visible transmittance through a textile is the critical factor determining the UV protection of fabrics. The basic concept of UV-Vis DRS (ISR-2600Plus for UV-2600, Shimadzu, Japan) is relatively straightforward: a light source under standard testing conditions, a device that splits light into its constituent wavelengths, a sample that the light crosses through, and a detector that measures the light. Effective UVR transmission wavelengths range 290 to 400 nm were analyzed to determine the UV-R value and UV-R protection category according to standard AS/NZS 4399:1996 [15], as shown in Table 2. The UV light blocked was calculated as (1)

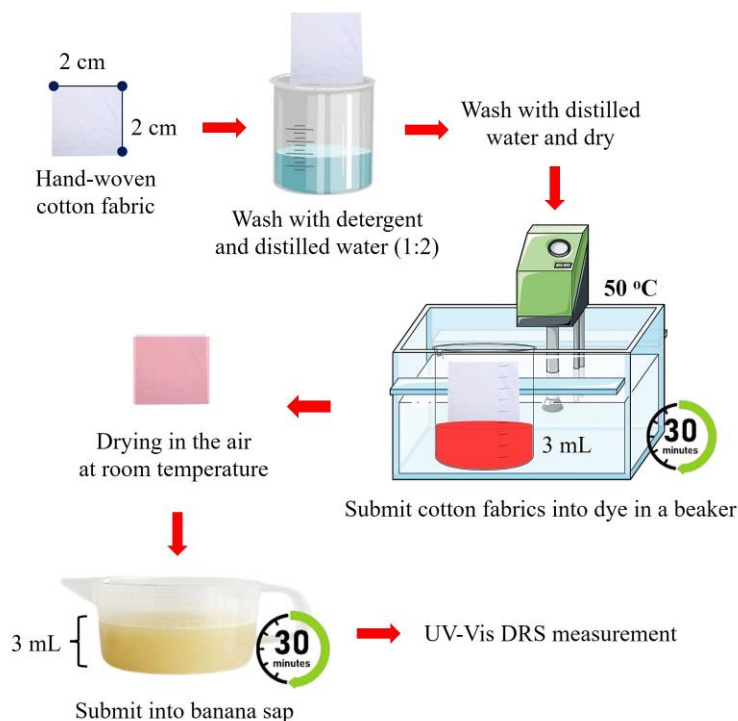


Fig 1. A schematic representation of the dyeing process of hand-woven cotton fabric with black glutinous rice and carrot ethanolic extracts.

TABLE I  
THE CONDITION OF DYE EXTRACTS AND SAMPLE  
IDENTIFICATION

Sample no.	Dye extract condition			
	Carrot (70% EtOH)	Carrot (95% EtOH)	Rice <sup>a</sup> (70% EtOH)	Rice <sup>a</sup> (95% EtOH)
Control <sup>b</sup>	-	-	-	-
1	✓	-	-	-
2	-	-	✓	-
3	-	✓	-	-
4	-	-	-	✓
5	✓	-	+	-
6	-	✓	-	✓
7	✓	-	-	✓
8	-	✓	✓	-

<sup>a</sup> Black glutinous rice.

<sup>b</sup> Control is hand-woven cotton fabric without dyeing.

✓ indicated the dye was used in dye combination conditions with a ratio of 1:1.

$$\text{UV Light blocked (\%)} = 100 - \text{UV Transmittance (\%)} \dots (1)$$

Here, UV Light blocked is UV protection efficiency (%) and UV Transmittance is the UV transmittance of fabric (%).

TABLE II  
UV-R CLASSIFICATION SYSTEM [15]

UV-R Protection category	Effective UV-R transmission (%)	Ultraviolet Protection Factor (UPF) range
Good	4.2-6.7	15-24
Very good	2.6-4.1	25-39
Excellent	<2.5	40 -50, >50

### Statistical testing

All determinations were done in triplicate and all were averaged. The data was expressed as a mean  $\pm$  standard deviation (SD). The confidence limits used in this study were based on 95% ( $P < 0.05$ ).

### III. RESULTS AND DISCUSSION

Table 3 shows the effective UV-R transmission percentage of cotton and sample no. 1-8. The average UV-R transmission from 290 to 400 nm of cotton before dyeing was  $18.2688 \pm 2.53$  %, which was out of the categories according to the Protection category (Table II). Effective UV-R transmission of sample no. 1 to 8 was 0.0000% to 0.1610% indicating an excellent UV-R protection according to the Protection (<2.5%) Based on the UV-R protection category, the UPF of samples 1-8 was in range of 40 to 50 or 50+. This result shows that cotton dyed with black glutinous rice and carrot extract could protect against UV better than without dyeing, which was consistent with other research on the dyeing of plain weave fabric with madder (*Rubia tinctorum*)

and indigo (*Indigofera tinctoria*) and the natural colorant of insect origin was cochineal (*Dactylopius coccus*) [16].

TABLE III  
EFFECTIVE UV-R TRANSMISSION MEASUREMENT

Sample no.	Effective UV-R transmission (%)	UV-R Protection category
Control <sup>a</sup>	$18.2688 \pm 2.53$	Uncategorized
1	$0.0875 \pm 0.03$	Excellent
2	$0.0012 \pm 0.00$	Excellent
3	$0.0120 \pm 0.01$	Excellent
4	$0.0004 \pm 0.00$	Excellent
5	$0.1610 \pm 0.02$	Excellent
6	$0.0005 \pm 0.00$	Excellent
7	$0.0110 \pm 0.00$	Excellent
8	$0.0000 \pm 0.00$	Excellent

<sup>a</sup> Control is hand-woven cotton fabric without dyeing.

After using the efficiency of light transmission in the UV range to calculate the UV protection efficiency of cotton dyed with black glutinous rice and carrot extracts, the results are shown in Fig. 2. The samples no. 2, 4, 6, and 8 could potentially block the UV light up to 100% suggesting this result shows the dye condition extracts of 95% carrot, 95% black glutinous rice, 95% carrot mixed with black glutinous rice, and 95% carrot mixed with 70% black glutinous rice ethanolic extracts., was the most suitable for enhancing the UV protection efficiency with significantly different values ( $P < 0.05$ ). It also shows that the concentration of 95% ethanol was more effective than 70% ethanol. However, regarding the development of a larger scale, 70% ethanol to extract and dye cotton could be considered as sufficient dyeing condition. When considering standards, cotton fabric dyed with 70% ethanolic extract had a standard UV protection category of "excellent," which was the same level as cotton dyed with 95% ethanolic extract. Moreover, 70% ethanol tends to extraction than 95% ethanol because a smaller amount of ethanol was used for extraction.

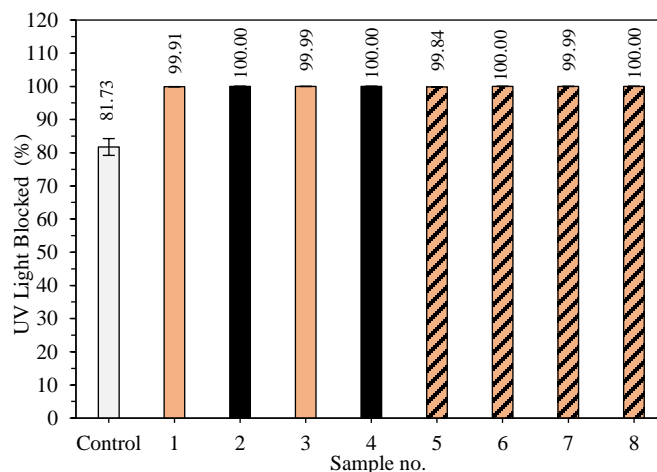


Fig. 2. The UV light blocked of cotton with black glutinous rice and carrot extracts

Furthermore, Fig. 2 reveals the cotton dyed with extract of 95% carrot, 95% black glutinous rice, 95% carrot mixed with black glutinous rice, and 95% carrot mixed with 70% black glutinous rice can enhance the UV light blocked of 18.27% when compared with control. This was because the extracts showed absorption properties in the UV range of 290 to 400 nm, as shown in Fig. 3. Carrot contains a bioactive compound such as  $\beta$ -carotene, which has a conjugated double bond in its structure [10]. Moreover, carrots contain vitamin E in form of tocopherol, which can protect the active components from UV exposure. Carrot extract has also been proven to suppress tyrosinase, an enzyme synthesizing melanin pigment [9]. The bioactive compound is not only in carrots but also in black glutinous rice, such as  $\gamma$ -oryzanol, which can absorb UV in the range of 190 to 370 nm [17]. Also, it contains high amounts of phenolic compounds, especially anthocyanins in pericarp [8]. Many studies have demonstrated antioxidant activity and radical scavenging ability of the pigmented rice and/or its extract in both *in vitro* and *in vivo* models [18-21]. These can be defined as extracts; they are essential properties for dyed fabrics to protect against UV rays.

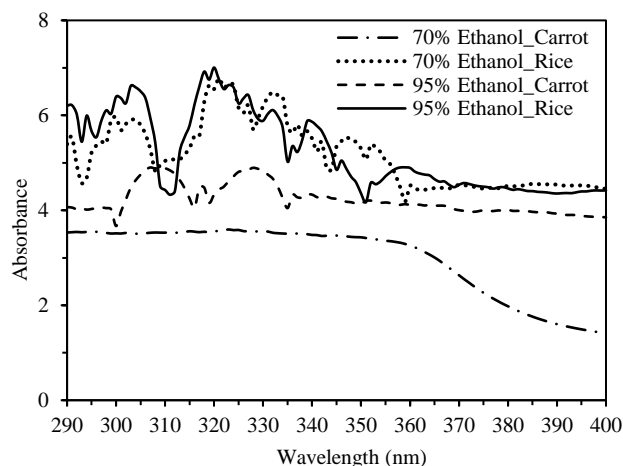


Fig. 3. The UV protection absorption of black glutinous rice and carrot extracts. 70% ethanol and 95% ethanol were used as blank.

#### IV. CONCLUSION

This study represents the efficacy of UV-protective cotton fabrics dyed with black glutinous rice and carrot extracts with a mordant of banana sap. The black glutinous rice and carrot extracts can enhance the UV protection of cotton fabrics up to 18.27%. The cotton fabrics dyed with 70% and 95% ethanolic black glutinous rice and the combination with 70% and 95% ethanolic carrot extract have an efficiency of up to 100% UV protection and were level in the excellent UV protection category according to the standard AS/NZS 4399:1996. To complete this research, further studies should be conducted to test the effectiveness of UV protection after washing and for cytotoxicity to be developed for use in making clothing for wear in the future. Test the biological activity of the extract, such as antibacterial and the antioxidant effect, and test the efficiency of dye adhesion of banana rubber.

#### ACKNOWLEDGMENT

The authors would like to acknowledge the Scientific Instruments Center, School of Science, King Mongkut's Institute of Technology Ladkrabang for the UV-Vis DRS measurement.

#### REFERENCES

- [1] Y. Matsumura and H. N. Ananthaswamy, "Toxic effects of ultraviolet radiation on the skin," *Toxicol Appl Pharmacol*, vol. 195, pp. 298-308, Mar 15 2004.
- [2] B. Petersen and H. C. Wulf, "Application of sunscreen--theory and reality," *Photodermatol Photoimmunol Photomed*, vol. 30, pp. 96-101, Apr-Jun 2014.
- [3] M. R. Repon, B. Dev, M. A. Rahman, S. Jurkonienė, A. Haji, M. A. Alim, *et al.*, "Textile dyeing using natural mordants and dyes: a review," *Environmental Chemistry Letters*, vol. 22, pp. 1473-1520, 2024/06/01 2024.
- [4] F. R. de Grujil, "Skin cancer and solar UV radiation," *Eur J Cancer*, vol. 35, pp. 2003-9, Dec 1999.
- [5] S. Davis, L. Capjack, N. Kerr, and R. Fedosejevs, "Clothing as protection from ultraviolet radiation: which fabric is most effective?," *Int J Dermatol*, vol. 36, pp. 374-9, May 1997.
- [6] M. Bouchard, M.-O. Hubert, and B. Gandini, "Dyes and Pigments," in *Conservation Science: Heritage Materials*, P. Garside and E. Richardson, Eds., ed: The Royal Society of Chemistry, 2021, p. 0.
- [7] F. F. Anggun H. Kusumawati, Maulana Y. Alkandhari, Asman Sadino, Lilis S. Agustina, Sukma D. Apriana, "Antioxidant Activity and Sun Protection Factor of Black Glutinous Rice (*Oryza sativavar. glutinosa*)," *Trop J Nat Prod Res.*, vol. 5, pp. 1958-1961, 2021.
- [8] S. M. Abdel-Aal el, J. C. Young, and I. Rabalski, "Anthocyanin composition in black, blue, pink, purple, and red cereal grains," *J Agric Food Chem*, vol. 54, pp. 4696-704, Jun 28 2006.
- [9] S. Bagus Komang, I. G. A. Widiandi, and I. B. G. F. Manuaba, "The potential of carrot extract as a sunscreen to prevent apoptosis in white mice (*Mus musculus*) fibroblast cell cultures exposed to UVB light," *Bali Medical Journal*, vol. 11, pp. 527-530, 06/28 2022.
- [10] C. Bayerl, "Beta-carotene in dermatology: Does it help?," *Acta Dermatovenereol Alp Pannonica Adriat*, vol. 17, pp. 160-2, 164-6, Dec 2008.
- [11] L. A. K. Krishnan, "A study on fastness properties of a natural dye extracted from pseudo-stem of *Musa Paradisiaca* on silk fabric," *Man-Made Textiles in India*, vol. 47, pp. 218-220, 2004.
- [12] A. K. Shyam Barhanpurkar, Roli Purwar, "Characterisation of Banana Pseudostem Sap Used As a Mordant for Dyeing," *International Journal of Polymer and Textile Engineering*, vol. 2, pp. 1-7, 2015.
- [13] K. E. Perepelkin, "Physicochemical Nature and Structural Dependence of the Unique Properties of Polyester Fibres," *Fibre Chemistry*, vol. 33, pp. 340-352, 2001/09/01 2001.
- [14] J. Ghosh and N. S. Rupanty, "Study on a cationic agent-based salt-free reactive dyeing process for cotton knit fabric and comparison with a traditional dyeing process," *Heliyon*, vol. 9, p. e19457, Sep 2023.
- [15] *Sun protective clothing—Evaluation and classification*, Standards Australia/Standards New Zealand: AS/NZS 4399, 1996.
- [16] A. K. Sarkar, "An evaluation of UV protection imparted by cotton fabrics dyed with natural colorants," *BMC Dermatol*, vol. 4, p. 15, Oct 27 2004.
- [17] A. Sakunpak, J. Suksaeree, C. Monton, P. Pathompak, and K. Kraisintu, "Quantitative analysis of gamma-oryzanol content in cold pressed rice bran oil by TLC-image analysis method," *Asian Pac J Trop Biomed*, vol. 4, pp. 119-23, Feb 2014.
- [18] C. Hu, J. Zawistowski, W. Ling, and D. D. Kitts, "Black rice (*Oryza sativa* L. indica) pigmented fraction suppresses both reactive oxygen species and nitric oxide in chemical and



- biological model systems," J Agric Food Chem, vol. 51, pp. 5271-7, Aug 27 2003.
- [19] S. H. Nam, S. P. Choi, M. Y. Kang, H. J. Koh, N. Kozukue, and M. Friedman, "Antioxidative activities of bran extracts from twenty one pigmented rice cultivars," Food Chemistry, vol. 94, pp. 613-620, 2006/03/01/ 2006.
- [20] K. Tananuwong and W. Tewaruth, "Extraction and application of antioxidants from black glutinous rice," LWT - Food Science and Technology, vol. 43, pp. 476-481, 2010/04/01/ 2010.
- [21] H. Ichikawa, T. Ichiyanagi, B. Xu, Y. Yoshii, M. Nakajima, and T. Konishi, "Antioxidant Activity of Anthocyanin Extract from Purple Black Rice," J Med Food, vol. 4, pp. 211-218, Winter 2001.

# The Effect of Insulin Pen Instructions Video on Patient with Diabetes by Line Application at HRH Princess Mahachakri Sirindhorn Medical Center

Nara Kaewkwan<sup>1</sup>, Marisa Mayusoh<sup>1</sup>, Sumet Klinhom<sup>2</sup> Pattarawit Rukthong<sup>1,3</sup>  
and Tulaya Potaros<sup>1,3,a)</sup>

## Author Affiliation

<sup>1</sup>Faculty of Pharmacy, Srinakharinwirot University, Nakhon Nayok, 26120, Thailand <sup>2</sup>Division of audiovisual education, Srinakharinwirot University, Bangkok, 10110, Thailand

<sup>2</sup>Division of audiovisual education, Srinakharinwirot University, Bangkok, 10110, Thailand

<sup>3</sup>Center for Excellence in Plant and Herbal Innovation Research, Strategic Wisdom and Research Institute, Srinakharinwirot University, Nakorn Nayok, 26120, Thailand

## Author Emails

<sup>a)</sup> Corresponding author: tulaya@gs.wu.ac.th

**Abstract.** Improper insulin administration usually leads to ineffectiveness or side effects in diabetic patients therefore alternative education such as VDO is necessary to improve knowledge and skill for insulin injection technique. This study aimed to develop an insulin pen instructions video and an educational model using LINE official account application, to evaluate the knowledge and skill of insulin injection techniques before and after watching the video and evaluate satisfaction with giving knowledge through the LINE application. A quasi-experimental, one group pretest-posttest design was performed in diabetic patients or caregivers using an insulin pen at HRH Princess Maha Chakri Sirindhorn Medical Center during January 2022 to January 2023. Three instruction VDO for NovoPen® 4, Lantus® SoloStar® and Toujeo® SoloStar® were created with duration of 8.16, 6.47 and 6.44 minutes, respectively. Their contents included methods of insulin device usage, storage, etc. Among 15 enrolled participants, the knowledge scores after watching the video increased significantly compared to before watching the video ( $8.93 \pm 2.87$  vs  $13.40 \pm 0.74$ , respectively;  $P < 0.05$ ). The skill scores after watching the video increased significantly compared to before watching the video in patients using Lantus®/Toujeo® ( $11.33 \pm 2.24$  vs.  $13.11 \pm 1.62$ , respectively;  $P = 0.024$ ) and has potential to increase in patients using Novopen®4 ( $12.83 \pm 6.77$  vs.  $18.33 \pm 0.52$ , respectively;  $P = 0.091$ ). The satisfaction scores for the LINE application were in a very satisfactory range. In conclusion, insulin pen instructions video available on Line application platform has potential to improve the knowledge and skill of insulin injection techniques in diabetic patients or caregivers.

**Index Terms—** Diabetic patients, Insulin pen instructions, Knowledge, LINE, VDO

## I. INTRODUCTION

Diabetes mellitus has been a common metabolic disease. Insulin therapy has been important for treatment of diabetes mellitus. It promotes good blood sugar control leading to decrease diabetic complications. However, there are some limitations such as side effects, pain, difficulty in injection. Nowadays, insulin pens such as NovoPen® 4, Lantus® SoloStar® and Toujeo® SoloStar® are available to replace insulin syringe. Although they are designed for easier usage, there are some complex steps which probably lead to wrong use<sup>1, 2</sup>. Therefore, it is necessary to educate patients as well as caregivers who inject insulin for patients correct knowledge and skill about insulin therapy. Multimedia is an effective tool for educating patients<sup>3</sup>. It helps to promote proper knowledge and skills to patients. For this reason, our research objectives to develop an insulin pen instructions video and an educational model using LINE official account application, to evaluate the knowledge and practice of insulin injection techniques before and after watching the video and evaluate satisfaction with giving knowledge through the LINE application.

## II. METHODOLOGY

The study protocol was approved by Srinakharinwirot ethics committee, SWUEC/E-413/2564. A quasi-experimental, one group pretest posttest design was performed in diabetic patients or caregivers using an insulin pen at HRH Princess Maha Chakri Sirindhorn Medical Center between January 2022 to January 2023. Using convenient sampling techniques, participants were eligible recruited if they were patients with type1 or type2 diabetes mellitus who used insulin pens or caregiver who injected insulin for diabetic patients. All were aged  $\geq 18$  years, used insulin pen less than 2 years, able to access on internet or VDO calling and well Thai language communicate (reading and writing). They were excluded if they had been unable to complete throughout procedures. Participants voluntarily consented to participate in this research via a written informed consent form.

Sample sizes ( $n=34$ ) were calculated using G\*Power 3.1 program with significant level = 0.05, Level of power = 0.8 and effect size=0.5

We developed three instruction VDO for insulin pens as NovoPen® 4, Lantus® SoloStar® and Toujeo® SoloStar® with contents involving to 7 parts as components of insulin pen, preparing insulin pen for injection, site of injection, how to check amount of insulin left, how to inject if insulin left less than needed amount, Insulin pen storage, and how to discard needle. The accuracy and validity of contents were assessed by 4 experts, whereas quality of VDO were assessed by 3 media-experts. Then, three instruction VDO were upload to YouTube.

We created platform Line official account and rich menu including link for general information questionnaire, link for satisfactory questionnaire, YouTube

Link for Video Demonstrating How to Use the Insulin Injection Pen Developed by the Researcher.

Participants attend to this research by scanning QR code or Line id. They completed their general information in google form available on rich menu. Researchers assessed participant's knowledge and skill before and after watching VDO. Participants were permitted only one time to watch VDO. After finishing, participants completed their opinion in satisfactory questionnaire link.

The demographic characteristics of participants were presented as mean  $\pm$  standard deviation (SD.). The differences scores prior compared to after watching VDO of knowledge and practices were tested using paired-sample t-test with statistical significance defined at the alpha level of 0.05.

### III. RESULTS AND DISCUSSION

Line application platform was created rich menu. Using program Canva and Final cut pro, three instruction VDO for insulin pens as NovoPen® 4, Lantus® SoloStar® and Toujeo® SoloStar® were created with duration of 8.16, 6.47 and 6.44 minutes, respectively and upload to YouTube. Our 6-10 minutes length of VDO appeared to be appropriated duration for concentration in contents with correlation to study by Lagerstrom L4

Among fifteen participants, they were male (53.33%) with average aged of 51.60 $\pm$ 17.29 years. Most of them (93.93%) used insulin pens less than 1year. They used different type of insulin pens as Toujeo® Solostar (53.33%), NovoPen®4 (40.00%) and Lantus Solostar® (6.67%). In addition, most of them (86.67%) were diabetic patients whereas the rest (13.33%) were caregivers.

As shown in Table 1, to evaluate participant's knowledge involving insulin pens usage, 14-points pretest and posttest were performed. The pretest total averaged scores appeared to be 8.93 $\pm$ 2.87 points. The most corrected steps with score of 0.93 $\pm$ 0.26 points included steps of "Wash your hands with soap, water and wipe to dry", and steps of "Choose appropriate injection sites". On the other hands, the least corrected steps appeared as steps of "Do not wipe a tip of needle with alcohol", and steps of "Always rotate injection sites to avoid lipo-hypertrophy, lipo-atrophy" with score of 0.40 $\pm$ 0.51, and 0.47 $\pm$ 0.52 points, respectively. After finishing VDO watch, the posttest total averaged scores significantly increased to 13.40 $\pm$ 0.74 points ( $P < 0.05$ ). In

consideration of each step, most of the knowledge scores significantly increased compared with before watching VDO. These steps represented as steps of "Always rotate injection sites to avoid lipo-hypertrophy, lipo-atrophy.", and "Do not wipe a tip of needle with alcohol." ( $P = 0.004$  and  $0.001$ , respectively). In addition, other steps significantly ( $P = 0.004$ ) improved such as steps of "Check needle and air bubble until drop of insulin at needle tip." and "If you don't have enough insulin for the rest of your dose, use new insulin."

TABLE 1  
KNOWLEDGE SCORES OF THREE INSULIN PENS  
USAGE BEFORE AND AFTER WATCHING VDO  
(N=15)

Topics	Score ( $\bar{x} \pm SD$ )		P - value
	Before	After	
Total Score (14 points)	8.93 $\pm$ 2.87	13.40 $\pm$ 0.74	<0.05
1. Wash your hands with soap, water and wipe to dry.	0.93 $\pm$ 0.26	1.00 $\pm$ 0.00	0.334
2. Choose appropriate injection sites (thighs, stomach, buttocks or backs of the upper arms) In case of choosing stomach site, more than two-inch circled around the navel.	0.93 $\pm$ 0.26	1.00 $\pm$ 0.00	0.334
3. Always rotate injection sites to avoid lipo-hypertrophy, lipo-atrophy.	0.47 $\pm$ 0.52	0.93 $\pm$ 0.26	0.004
4. Do not wipe a tip of needle with alcohol.	0.40 $\pm$ 0.51	0.93 $\pm$ 0.26	0.001
5. Repeat using needle until feel pain or more than 5 times.	0.73 $\pm$ 0.46	1.00 $\pm$ 0.00	0.041
6. Before discard, put the outer needle cap back on the needle.	0.80 $\pm$ 0.41	1.00 $\pm$ 0.00	0.082
7. Throw needles away in a closed container for infectious waste.	0.53 $\pm$ 0.52	0.93 $\pm$ 0.26	0.009
8. Store unopened insulin pens in refrigerator. Do not place pens in lid, freezer or vegetable compartment.	0.53 $\pm$ 0.52	0.93 $\pm$ 0.26	0.009
9. Store opened insulin pens at room temperature.	0.67 $\pm$ 0.49	1.00 $\pm$ 0.00	0.019
10. Do not use opened insulin pens after 28 days.	0.53 $\pm$ 0.52		0.041
11. Check needle and air bubble until drop of insulin at needle tip.	0.53 $\pm$ 0.52	0.80 $\pm$ 0.41	0.004
12. Dial back up or down if you dialed the wrong amount.	0.67 $\pm$ 0.49	1.00 $\pm$ 0.00	
13. Check if you cannot dial the dose you want, it may be because you don't have enough insulin left.	0.67 $\pm$ 0.49	1.00 $\pm$ 0.41	0.019
14. If you don't have enough insulin for the rest of your dose, use new insulin.	0.52 $\pm$ 0.13	0.87 $\pm$ 0.35	0.189
		1.00 $\pm$ 0.00	0.004

Note: Data represented as mean $\pm$ SD. Paired-samples t-test was used to test statistically significant differences.

Regarding to evaluation of participant's skill involving insulin pens usage, 14-points pretest and posttest were performed for Lantus®/Toujeo®, whereas 19-points pretest and posttest were performed for NovoPen® 4. As shown in table 2, the pretest total averaged scores appeared to be 11.33±2.24 and 12.83±6.77 points for Lantus®/Toujeo® and NovoPen® 4, respectively. The most corrected steps with score of 0.93±0.26 points included steps of "Remove the protective seal from a new needle.", "Make sure the needle is firmly attached." and "Slowly press injection button until number of doses return to zero." The least corrected steps included steps of "Wipe the rubber seal on the pen body with an alcohol swab." with scores of 0.40±0.51points. The posttest total averaged scores appeared to be 13.11±1.62 and 18.33±0.52points for Lantus®/Toujeo® and NovoPen® 4, respectively. Only the posttest total score for Lantus®/Toujeo® significantly increased compared with the pretest score (13.11±1.62 vs 11.33±2.24 points,  $P = 0.024$ ). Consideration in details, watching instruction VDO could promote significantly increased skill score in some steps such as steps of "Wipe the rubber seal on the pen body with an alcohol swab.", "all three step to test insulin flow and remove air bubbles before usage.", "Press injection button for 10 second before removing needle from skin.", "Do not massage or rub injection site." and "If insulin is suspension, resuspend insulin before usage by gently roll in hand or swing 10 times. Do not shake"( $P < 0.05$ ).

Our results indicated that the improvement of participant knowledge and skill after watching instruction VDO with in correlated to study by Ratri DMN et.al.<sup>5</sup> Their study was conducted on one hundred T2DM patients who were received subcutaneous insulin therapy at Universitas Airlangga Teaching Hospital. They found that after watching the 6-minute VDO on insulin therapy education, patient's knowledge and attitude were significantly improved compared to before watching VDO. Moreover, our results showed that the least corrected steps in pretest of skill appeared as steps of "Wipe the rubber seal on the pen body with an alcohol swab.", similarly to the study by Apichart Jittsue et.al.<sup>6</sup> They found that some eighty-six diabetic patients lack skill of "wiping the front rubber stopper with an alcohol swab".

TABLE 2  
SKILL SCORES OF THREE INSULIN PENS USAGE  
BEFORE AND AFTER WATCHING VDO (N=15)

Topics	Scores ( $\bar{x} \pm SD$ )		P - value
	Before	After	
Total Score NovoPen® 4 (19 points)*	12.83±6.77	18.33±0.52	0.091
Total Score Lantus®/Toujeo® (14 points)**	11.33±2.24	13.11±1.62	0.024
<b>For all NovoPen® 4, Lantus® SoloStar® and Toujeo® SoloStar®</b>			
<b>Attachment of Needle</b>			
1. Wipe the rubber seal on the pen body with an alcohol swab.	0.40±0.51	0.87±0.35	0.004
2. Remove the protective seal from a new needle. Then, line up the needle	0.93±0.26	1.00±0.00	0.334

with the pen. Keep the needle straight as you screw it on.

3. Make sure the needle is firmly attached. 0.93±0.26 1.00±0.00 0.334

**Test insulin flow and remove air bubbles before usage**

1. Select a dose of 2 units by turning the dosage knob. 0.67±0.49 0.93±0.26 0.041

2. Take off the outer and inner needle cap. 0.67±0.49 0.93±0.26 0.041

3. Hold the pen with the needle pointing upward. Press the injection button. Check whether insulin comes out to needle tip. If not, repeat this step until insulin comes out. 0.67±0.49 0.93±0.26 0.041

**Injection of insulin**

1. Select dose as doctor recommended by turning the dosage knob. 0.87±0.35 0.93±0.26 0.582

2. Wipe injection site with an alcohol swab. 0.87±0.35 1.00±0.00 0.164

3. Insert needle straight into injection site. 0.73±0.46 0.87±0.35 0.164

4. Slowly press injection button until number of doses return to zero. 0.93±0.26 1.00±0.00 0.334

5. Press injection button for 10 second before removing needle from skin. 0.60±0.51 0.93±0.26 0.019

6. Do not massage or rub injection site. 0.67±0.49 0.93±0.26 0.041

7. Put inner needle cap on needle and put pen cap. 0.87±0.35 0.93±0.26 0.334

8. Rotate injection site by a 3 cm. width from the last injection point. 0.87±0.35 1.00±0.00 0.164

**Insertion of insulin cartridge (For NovoPen® 4)\***

1. Pull off the pen cap and Twist off the cartridge holder. 1.00±0.00 1.00±0.00 -

2. The piston rod may stick out of your pen. If so, push it in until it stops. 0.67±0.52 1.00±0.00 0.175

3. Slide the cartridge into the cartridge holder with the threaded end first. 0.67±0.52 1.00±0.00 0.175

4. Twist the cartridge holder back on. 0.83±0.41 1.00±0.00 0.363

5. If insulin is suspension, resuspend insulin before usage by gently roll in hand or swing 10 times. Do not shake 0.17±0.41 0.83±0.41 0.025

Note: Data represented as mean±SD. Paired-samples t-test was used to test statistically significant differences.

\* data obtained from six participants using NovoPen® 4

\*\* data obtained from nine participants using Lantus®/Toujeo®

In the aspect of evaluation participant's satisfaction with giving knowledge through the LINE application All fifteen participants fulfilled in satisfactory form available on LINE application. Based on total satisfactory scores was 5 points, our results revealed that the average score for consideration of Designing LINE OA, Usability and contents appeared as 4.60 ± 0.58, 4.87 ± 0.28 and 4.87 ± 0.28 points, respectively. All the aspects were considered as in level of very satisfactory (Table 3). Line application platform has rich menu which is able to easily connect to link instruction VDO on YouTube. These characteristics of rich menu help participants feel easy to use. In addition, participants are able to directly communicate with researchers by typing in conversation chat.



TABLE 3  
SATISFACTORY SCORES WITH GIVING KNOWLEDGE THROUGH  
THE LINE APPLICATION (N=15)

Topics	Scores ( $\bar{x} \pm$ SD) (Total score=5.00 points)	Level of satisfactory
<b>Designing LINE OA (LINE Official Account)</b>	4.60 $\pm$ 0.58	Very satisfactory
Beautiful	4.53 $\pm$ 0.74	Very satisfactory
Easy to use	4.60 $\pm$ 0.62	Very satisfactory
Easy-to-read font size	4.60 $\pm$ 0.63	Very satisfactory
<b>Usability</b>	4.87 $\pm$ 0.28	Very satisfactory
Get more knowledge of insulin pens usage.	4.80 $\pm$ 0.41	Very satisfactory
Get more knowledge of insulin pens storage.	4.87 $\pm$ 0.35	Very satisfactory
Increase confidence for usage of insulin pens.	4.87 $\pm$ 0.35	Very satisfactory
More easily for using insulin pens	4.93 $\pm$ 0.28	Very satisfactory
<b>Contents</b>	4.87 $\pm$ 0.28	Very satisfactory
Point to contents	4.80 $\pm$ 0.41	Very satisfactory
Easily understanding	4.87 $\pm$ 0.35	Very satisfactory
Interesting	4.93 $\pm$ 0.26	Very satisfactory

Note Data represented as mean  $\pm$  SD.

This study limitations included small sample size. Some diabetic patients or caregivers were unable to access on internet, VDO calling or Line application as well as do not have equipment. We suggest adding some important topics on Line platform such as topics involved with side effects and treatment. It is better to determine clinical laboratory parameters as patient's fasting plasma glucose or Hemoglobin A1c (HbA1c) in parallel to pretest/posttest evaluation in order to confirm the effectiveness of Instruction VDO.

#### IV. CONCLUSION

We confirmed that three insulin pens instruction video available in Line application platform has highly potential to improve the knowledge and practice of insulin injection techniques in diabetic patients or caregivers.

#### ACKNOWLEDGMENT

(USE THE MICROSOFT WORD TEMPLATE STYLE: HEADING 1)  
OR (USE TIMES NEW ROMAN FONT: 10 PT, BOLD, ALL CAPS,  
CENTERED)

#### REFERENCES

- [1] Aazami S, Mozafari M, Poorabdollah H. Insulin-related outcomes (satisfaction, pain, and adherence) among type II diabetes patients switched from syringe to insulin pen. *Bali Med J*. 2018; 7: 678–81.
- [2] Trief PM, Cibula D, Rodriguez E, Akel B, Weinstock RS. Incorrect Insulin Administration: A Problem That Warrants Attention. *Clin Diabetes*. 2016 Jan; 34(1): 25-33.

- [3] Huang MC, Hung CH, Yu CY, Berry DC, Faan A-BC, Shin SJ, et al. The effectiveness of multimedia education for patients with type 2 diabetes mellitus. *J Adv Nurs*. 2017; 73(4): 943-954.
- [4] Lagerstrom L. The myth of the six minute rule: student engagement with online videos. *Proceedings of the American Society for Engineering Education*. 2015;14-17.
- [5] Ratri DMN, Hamidah KF, Puspitasari AD, Farid M. Video-based health education to support insulin therapy in diabetes mellitus patients. *J Public Health Res*. 2020; 9(2): 1849.
- [6] Apichat J, Panarat S, Charoen T, Titiya H. Assessment of Knowledge and Practice of Patients Before and After Counseling in the Use of the Reusable Insulin Pen at Vachiraphuket Hospital. *Songkla Med J* 2016; 34(1): 27-37.

# Poster Presentation

# New Insights into the Status and Distribution of Durian Seed Borers (*Mudaria* spp.) (Lepidoptera: Noctuidae) in Thailand

Pornthap Chamsuk<sup>1</sup>, Arthit Rukkasikorn<sup>2</sup>, Sunudda Chaovalit<sup>2</sup>, Paradorn Dokchan<sup>3</sup>,  
Supakorn Tangsuan<sup>2</sup>, Korakot Ratanamahamaneekorn<sup>2</sup> and Pisit Poolprasert<sup>1, a)</sup>

<sup>1</sup>Department of Entomology, Faculty of Agriculture, Kasetsart University, Bangkok, 10900

<sup>2</sup>Plant Protection Research and Development Office, Department of Agriculture, Bangkok, 10900

<sup>3</sup>Environmental Entomology Research and Development center, Faculty of Agriculture at Kampaeng Saen, Kasetsart University, Nakhon Pathom 73140

<sup>a)</sup> Corresponding author: [fagrpspo@ku.ac.th](mailto:fagrpspo@ku.ac.th)

**Abstract.** The durian seed borer (*Mudaria* spp.) is a significant pest threatening durian production in Thailand, yet its species diversity and distribution remain unclear. This study examined their geographic range and genetic diversity through field surveys and molecular techniques. Specimens were collected from affected durian plantations in Uttaradit, Songkhla, Yala, Pattani, and Narathiwat provinces between March 2024 and February 2025 using light traps and hand collection. Some samples from insect collections and species recorded from previous public reports were also included. Morphological identification was performed by comparing specimens with reference collections and literature, followed by DNA barcoding of cytochrome oxidase I (COI) sequences for species confirmation and phylogenetic analysis. A total of 11 *Mudaria* species were recorded across Thailand, with *Mudaria major*, *M. minor*, *M. stahlgretschae*, and *M. szalkayjosefi* being the most prevalent species affecting durian production. Phylogenetic analysis of a 553-bp COI fragment revealed that all *Mudaria* species were reciprocally monophyletic, with genetic distances (including both transitions and transversions) among all *Mudaria* species analyzed averaging 0.0569. Intraspecific variation ranged from as low as 0.0018 between *Mudaria major* populations from Chiang Mai and Yala provinces to as high as 0.1300 between *M. major* and *M. stahlgretschae*. These findings clarify *Mudaria* species distribution and genetic relationships, providing essential data for targeted pest management strategies. The damage caused by *Mudaria* spp. to durian crops significantly impacts both the quality and yield of durian, resulting in economic losses due to reduced export quality. As Thailand is a leading global exporter of durian, particularly to China, pest contamination in exported produce poses a major economic threat. Effective pest control strategies, informed by this study's findings, are crucial to minimizing these impacts and sustaining durian cultivation in Thailand.

**Index Terms**—Distribution, DNA barcoding, Durian Seed Borers, *Mudaria* species, Thailand

## I. INTRODUCTION

THE durian seed borer, the larval stage of moths from the genus *Mudaria* (family Noctuidae, order Lepidoptera), is a significant pest affecting durian crops. The genus *Mudaria* consists of 28 species found across Asia [1-5]. Currently, Hungarian taxonomists are revising the classification of *Mudaria* and identifying new species, as past misidentifications may have led to inaccurate reports of species infesting durian worldwide, including in Thailand. Five species, namely *Mudaria luteileprosa*, *M. magniplaga*, *M. minor*, *M. stahlgretschae*, and *M. szalkayjosefi*, have been identified as durian pests, with all five feeding exclusively on *Durio zibethinus* [1,5].

As one of the world's leading producers and exporters of durian, Thailand supplies over 90% of its durian exports to China. Durian exports have seen significant growth from 2018 to 2023, reaching 1,480,382 tons valued at 139,539 million baht in 2023 [6,7]. However, durian seed borers represent a substantial threat to the industry. In June 2024, the Nong Khai Customs Office detected seed borers in five containers of durians destined for export to China. These

durians, sourced from Uttaradit Province, were returned for corrective action, and the exporter was instructed to reapply for a new phytosanitary certificate. The issue is especially prevalent in southern Thailand during the durian harvest season, prompting Chinese customs authorities to issue warnings [8]. The presence of seed borers in exported durians threatens both international trade and the national economy.

Previous reports of insect outbreaks in Thailand, particularly those impacting durian crops, have been inconsistent and unsystematic. This lack of standardized reporting has hindered accurate assessments of pest threats, as many reports are missing critical geographic and temporal data, making it difficult to track the spread and impact of pest species. Additionally, limited use of molecular techniques has led to misidentifications, preventing a comprehensive understanding of pest diversity. The absence of standardized monitoring and reporting methods further complicates the development of effective pest management strategies. This study aims to address these gaps by providing a more structured approach to identifying *Mudaria* species, assessing their distribution and genetic diversity, and

offering essential data to enhance pest control efforts.

With the agricultural sector in Thailand reducing its reliance on chemical pesticides to ensure the safety of farmers, consumers, and the quality of agricultural products, alternative pest control methods—such as biological control, natural enemies, antagonistic microorganisms, and pest-specific pheromones—are becoming more widely used. Accurate taxonomic classification, species identification, and distribution data for *Mudaria* species are essential for developing effective control measures and addressing durian seed borer contamination in export products.

## Methodology

### Sample Collection

Specimens were collected from affected durian plantations in Specimens were collected from affected durian plantations in Uttaradit, Songkhla, Yala, Pattani, and Narathiwat provinces between March 2024 and February 2025. These provinces were selected based on known infestations of durian seed borers, ensuring a broad geographic range for the study. To capture the full range of *Mudaria* species, a combination of light traps and hand collection methods was employed. Light traps were set up from 18:00 to 06:00 to attract adult moths, while larvae were hand-collected directly from infested durian fruits during the day. For each species, a minimum of 15 samples from both larval and adult stages were obtained from each province to ensure sufficient genetic diversity for molecular analysis.

Collected specimens were preserved in 95% ethanol for further molecular and morphological analysis. In addition to the newly collected specimens, samples deposited in the main museum and those reported in previous studies were also included to create the distribution map for *Mudaria* species. All moths were morphologically identified to the genus and species levels based on key taxonomic references, including Holloway [1], Kononenko and Pinratana [2], Pellinen et al. [3], Ronkay et al. [4], and Ronkay et al. [5]. DNA barcoding using cytochrome oxidase I (*COI*) sequences was then conducted to confirm species identification and facilitate phylogenetic analysis.

### DNA Extraction, Amplification and Sequencing

Total genomic DNA was extracted from a single leg of *Mudaria* moth specimens using the DNeasy® Blood & Tissue Kit (Qiagen, Germantown, MD, USA, catalog #69504). The mitochondrial *COI* gene, a protein-coding gene commonly used in molecular analysis, was targeted for amplification in this study. PCR amplification was performed using the primers LCO1490 (5'-GGT CAA CAA ATC ATA AAG ATA TTG G-3') and HCO2198 (5'-TAA ACT TCA GGG TGA CCA AAA AAT CA-3') [9].

Each PCR reaction was set up in a final volume of 20 µl, consisting of 4 µl of 5x PCR Enhancer, 2 µl of 10x HF Reaction Buffer, 0.4 µl of 10 mM dNTP Mix, 0.3 µl of each primer (10 µmol/L), 0.3 µl of Long and High Fidelity DNA Polymerase (0.75 U) (biotechrabbit, Germany), 10.7 µl of

nuclease-free water, and at least 2 ng of genomic DNA template. The PCR program included an initial activation step of 3 minutes at 94 °C, followed by 35 cycles of denaturation at 94 °C for 1 minute, annealing at 48 °C for 1 minute, extension at 72 °C for 1 minute, and a final extension step at 72 °C for 5 minutes.

The PCR products were visualized under UV light following electrophoresis on a 1% agarose gel stained with ethidium bromide in 1x TAE buffer. The desired amplicon was purified using the GenUP PCR/Gel Cleanup Kit (biotechrabbit, Germany) following the manufacturer's instructions and then sent for sequencing at MacroGen Inc. (<http://www.macrogen.com>).

### Alignment of sequences and Phylogenetic analysis

Phylogenetic analysis was carried out using the Maximum Likelihood (ML) method to construct the phylogenetic tree. Genetic distances were computed using the Kimura 2-parameter (K2P) model using [10]. The reliability of the clades was evaluated through a bootstrap analysis with 1,000 replications. Additionally, the overall AT bias and nucleotide diversity ( $\pi$ ) were determined using the DNAsp v5.10.01 software [11].

Sequences were aligned and analyzed for phylogenetic relationships.

## II. RESULTS AND DISCUSSION

### Geographic Distribution of *Mudaria* spp.

Of all 11 species, four main species were recorded from this survey, including *Mudaria stahlgretschae*, *M. szalkayjosefi*, *M. major*, and *M. minor*, as depicted in the Thailand map (Fig. 1).

*Mudaria stahlgretschae* was recorded in Thailand, with specimens collected from Uttaradit, Rayong, Chanthaburi, Trat, and Surat Thani provinces [5], as well as from Songkhla, Pattani, Narathiwat, and Yala.

*Mudaria szalkayjosefi* was found in Thailand, specifically in Lampang, Uttaradit, Chonburi, and Prachuap Khiri Khan provinces [5], along with Songkhla, Yala, and Narathiwat. This species was observed at elevations between 90 and 480 meters above sea level.

*Mudaria major* was distributed in Thailand, occurring in Chiang Mai, Lampang, Phayao, and Nan provinces [2,3], as well as in Uttaradit, Loei, Kanchanaburi, Prachuap Khiri Khan, and Yala. The species was typically encountered at altitudes ranging from 250 to 2,050 meters above sea level.

*Mudaria minor* was recorded in Thailand, with sightings in Surat Thani, Songkhla, Yala, Pattani, and Narathiwat provinces. This species was commonly found at elevations between 90 and 850 meters above sea level.



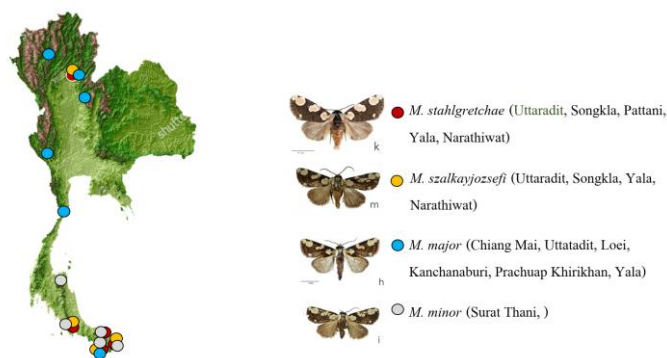


Fig. 1 Geographical distribution of *Mudaria* spp. in Thailand, based on collections using light traps and rearing of larvae and pupae to adulthood (March 2024–February 2025).

### Pattern of Nucleotide Substitution

The DNA sequence of the mitochondrial 5'COI gene region was isolated to infer phylogenetic correlation of *Mudaria* species (family Noctuidae). DNA fragments containing 553 base pairs of COI gene were successfully obtained from five *Mudaria* species including *M. major* (Warren, 1914); *M. minor* (Holloway, 1982); *M. stahlgretschae* Ronkay, Ronkay, Pekarsky & Landry, 2023, *M. szalkayjosefi* Ronkay, Ronkay, Pekarsky & Landry, 2023 and *M. sp.* together with *M. cornifrons* Moore, 1893; *M. luteileprosa* Holloway, 1982, *M. rudolfi* Kobes, 1983 and *M. variabilis* Roepke, 1916. Consequently, the transition/transversion rate ratios are  $k_1 = 8.561$  (purines) and  $k_2 = 17.342$  (pyrimidines). The overall transition/transversion bias is  $R = 5.751$ , where  $R = [A \cdot G \cdot k_1 + T \cdot C \cdot k_2] / [(A+G) \cdot (T+C)]$ . The average nucleotide composition proportions for all coccinellid sequences were detected to be A = 30.93%, T = 40.04%, G = 13.38% and C = 15.20%. These findings conformed to the results of the COI gene region of other insect groups exhibiting a bias towards adenine and thymine which was consistent with the base composition of the corresponding COI region. Generally, the base composition of the COI fragment varied among the species, but it was commonly demonstrated with an overall AT bias of 66.70% and 33.3% [12]. Correspondingly, the AT and GC contents for these results were 70.10% and 29.90%, respectively. The average nucleotide composition proportions for the *Mudaria* spp. sequences were: G, 13.28; A, 30.93; T, 40.04; and C, 15.20, implying that AT content (71.86%) was at a higher level [13]. Identifying *Mudaria* species is crucial for effective pest management. In this study, DNA barcoding of cytochrome oxidase I (COI) sequences successfully confirmed the identity of several *Mudaria* species, contributing to a more accurate understanding of their distribution. However, the genetic distribution differences among the surveyed areas warrant further discussion. The genetic distances (including both transitions and transversions) among all *Mudaria* species analyzed averaged 0.0569, suggesting a clear divergence between species. Intraspecific variation ranged

from as low as 0.0018 between *Mudaria major* populations from Chiang Mai and Yala provinces to as high as 0.1300 between *M. major* and *M. stahlgretschae*, indicating substantial genetic differentiation.

Based on the Maximum Likelihood Estimate of Transition/Transversion Bias, the estimated transition/transversion bias (R) was 2.28, indicating that transitions occurred approximately 2.28 times more frequently than transversions among the analyzed sequences. Transitions are nucleotide substitutions between purines (A ↔ G) or between pyrimidines (C ↔ T), while transversions involve substitutions between purines and pyrimidines (e.g., A ↔ T, G ↔ C). This transition bias is commonly observed in mitochondrial genes such as COI, where transitions are generally more frequent. The substitution patterns and rates were estimated using the Kimura 2-parameter (K2P) model, which accounts for the varying rates of transitions and transversions, allowing for a more accurate estimation of genetic distances and evolutionary relationships compared to simpler models. The use of the K2P model enhances the reliability of the phylogenetic inferences made in this study.

Furthermore, while the overall genetic distances among *Mudaria* species indicate divergence, additional analyses could explore whether genetic differentiation correlates with geographic distribution. The variation observed within species, such as between *M. major* populations from different provinces, suggests potential local adaptation or isolated populations, which could inform future pest control strategies tailored to specific regions. These genetic differences, especially when combined with geographic and ecological data, will help improve the understanding of *Mudaria* species distribution, facilitating more targeted and effective pest management practices.

### Phylogenetic status

DNA was extracted from larvae (abdomen) and adults (legs) moth samples and amplified via PCR using mitochondrial COI gene markers (658 bps). Universal primers LCO1490 and HCO2198 [9] were applied. The nucleotide sequences obtained were compared with those of the *Mudaria* genus of durian seed-borer moths in GenBank using BLAST, showing identity percentages between 95.00–99.00%. Sequences were aligned using ClustalW and analyzed with [9]. Phylogenetic relationships were assessed using the Maximum Likelihood (ML) method, with the *Conogethes* genus of durian fruit-borer moths as the outgroup. The phylogenetic tree clearly grouped the *Mudaria* genus samples by their sampling locations into distinct clades: Clade A (*Mudaria szalkayjosefi*), B (*M. luteileprosa*), C (*M. major*), D (*M. cornifrons* + *M. variabilis*), E (*M. minor*), F (*M. stahlgretschae*), G (*Mudaria* sp.), and the outgroup (*Conogethes punctiferalis*) as depicted in Fig. 2.

### III. CONCLUSION

In conclusion, this study provides the first molecular phylogenetic analysis of *Mudaria* species based on Thai specimens, offering valuable insights into their genetic relationships and diversity. The results reveal distinct phylogenetic clustering among the *Mudaria* species, confirming their taxonomic status and supporting the use of COI mtDNA sequencing for rapid and reliable species identification. The study also highlights significant genetic variation within and between species, with intraspecific genetic distances as low as 0.0018 and interspecific variation reaching 0.1300. This genetic divergence underscores the complex evolutionary relationships within the genus and suggests that geographic isolation may play a role in shaping species distribution.

The findings are critical for pest control strategies, as understanding the genetic relationships among *Mudaria* species can help identify potential local populations and guide the development of targeted pest management approaches. The clear genetic differentiation observed between *M. major* populations in different provinces, for example, may inform regional pest control measures. Future studies incorporating additional molecular markers and broader sampling will further enhance the resolution of phylogenetic relationships and provide a more comprehensive framework for managing *Mudaria* infestations in durian orchards.

By improving our understanding of the genetic structure and distribution of *Mudaria* species, this research contributes to more effective and sustainable pest control strategies, ultimately supporting the durability of durian production in Thailand.

### ACKNOWLEDGMENTS

The authors sincerely appreciate the Agricultural Research Development Agency (Public Organization) (ARDA) for funding this research (grant number: PRP6705030700) and extend their gratitude to those who provided support and guidance, ensuring the successful completion of this study.

### REFERENCES

- [1] J. D. Holloway, "The moths of Borneo. Part 12. Family Noctuidae, triline subfamilies: Noctuidae, Heliethinae, Hadeninae, Acronictinae, Amphipyridae, Agaristinae," The Malayan Nature Society, Kuala Lumpur, 226 p., 1989.
- [2] V. Kononenko and A. Pinratana, "Moths of Thailand. Vol. 3. Part 2. Noctuoidea," Brothers of St. Gabriel in Thailand, Bangkok, 624 p., 2013.
- [3] M. Pellinen, M. Mutanen and P. Sihvonen, "New species of genus *Mudaria* Moore, 1893 and the first record of *Mudaria cornifrons* Moore, 1893 from Thailand (Lepidoptera, Noctuidae, Noctuinae)," *Zootaxa*, vol. 4500, no.2, 292-300, 2018.
- [4] G. Ronkay, L. Ronkay, and O. Pekarsky, "New *Mudaria* and *Chodapsaphida* (Lepidoptera, Noctuidae, Psaphidinae)

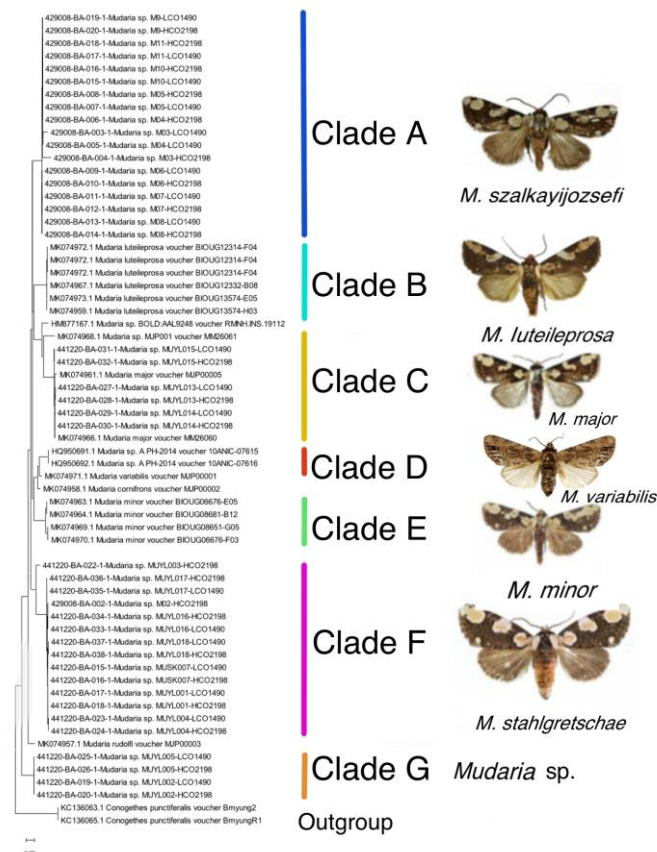


Fig. 2. Shows the evolutionary relationships of the durian seed-borer moths of the genus *Mudaria* based on the nucleotide sequences of the COI gene using the Maximum Likelihood (ML) method.

In this study, we explored the phylogenetic relationships within the *Mudaria* genus of durian seed-borer moths for the first time, utilizing DNA barcoding as a powerful and reliable method for identifying both genus and species levels. Our findings demonstrate the effectiveness of DNA barcoding in lepidopteran species, aligning with previous research on various arthropod groups, including Hymenoptera (bees and wasps), Neuropterida (lacewings and antlions), Heteroptera (true bugs), Myriapoda (millipedes, centipedes, pauropods, and symphylans), and Orthoptera (grasshoppers and crickets) [14-16]. These studies provide strong evidence supporting DNA barcoding as an effective tool for identifying arthropods. In the case of the Thai durian seed borer, however, further research is needed to investigate the phylogenetic status of these species through tree topology analysis using both mitochondrial and nuclear genes. This will contribute to more effective agricultural management strategies, particularly in controlling durian seed-borer pests in Thailand. Our work sets the foundation for future studies aimed at improving pest control techniques and understanding the genetic diversity of key agricultural pests.

species from the Himalayan region and Indochina,” in: G. Ronkay, ed., *Fibigeriana Supplement*, Book series of Taxonomy and Faunistics, Vol. 3, Heterocera Press, Budapest, pp. 143–152, 2022.

[5] G. Ronkay, L. Ronkay and B. Landry, “The Plante Noctuidae Collection. Part 2. Descriptions of new taxa,” in: Landry, B., ed., *Mém. Soc. phys.-hist. nat. Genève*, vol. 49, no. 2, pp. 1–445, 2023.

[6] Plant Protection Research and Development Office, “Academic document on insects and mites, pests of durian,” Dept. of Agriculture, Bangkok, 88 p., 2019.

[7] Office of Agricultural Economics Research, “Situation of major agricultural products and trends for 2023,” Office of Agricultural Economics, Bangkok, 241 p., 2022.

[8] Office of Provincial Commercial Affairs Trang. 2025 <https://trang.moc.go.th/th/content/category/detail/id/112/iid/56357>

[9] O. Folmer, M. Black, W. Hoeh, R. Lutz, R. Vrijenhoek, “DNA primers for amplification of mitochondrial cytochrome c oxidase subunit I from diverse metazoan invertebrates”. *Molecular marine biology and biotechnology*, vol. 3, no. 5, pp. 294-299, 1994.

[10] K. Tamura, G. Stecher, and S. Kumar “MEGA11: Molecular Evolutionary Genetics Analysis version 11”. *Molecular, Biology and Evolution*, vol. 38, pp. 3022-3027, 2021.

[11] P. Librado and J. Rozas “DnaSP v5: a software for comprehensive analysis of DNA polymorphism data.” *Bioinformatics*, vol. 25, no. 11, pp. 1451-1452, 2009.

[12] F. Jing and Z. YingChun “Sequence analysis of mtDNA-COI gene and molecular phylogeny on twenty-seven species of coccinellids (Coleoptera: Coccinellidae).”, pp.179-186, 2006.

[13] A. G. B. Aruggoda, R. Shunxiang and Q. Baoli “Molecular phylogeny of ladybird beetles (Coccinellidae: Coleoptera) inferred from mitochondrial 16S rDNA sequences.” *Tropical Agricultural Research*, vol. 21, no. 2, 2010.

[14] P. D. N. Hebert, S. Ratnasingham and JR. deWaard. “Barcoding animal life: cytochrome c oxidase subunit 1 divergences among closely related species.” *Proceedings of the Royal Society of London. Series B: Biological Sciences*, vol. 270., suppl\_1, S96-S99(2003b).

[15] P. D. N. Hebert, J. R. deWaard, J. F. Landry. “DNA barcodes for 1/1000 of the animal kingdom.” *Biology letters*, vol. 6, no. 3, pp. 359-362, 2010.

[16] P. Karthika, N. Krishnaveni, C. Vadivalagan, K. Murugan, M. Nicoletti and G. Benelli. “DNA barcoding and evolutionary lineage of 15 insect pests of horticultural crops in South India.” *Karbala International Journal of Modern Science*, vol. 2, no.3,156-168, 2016.

# Effect of Chitosan and Silicon on Growth and Strength of *Dendrobium* sp. Plantlets

Tuansobariyah Lateh<sup>1, a)</sup>, Alisa Kongjaiman Yoshida<sup>1</sup>, Yupa Pootaeng-on<sup>1</sup>,  
Chaowanee Laosutthipong<sup>1, a)</sup>

<sup>1</sup>Faculty of Animal Sciences and Agricultural Technology, Silpakorn University,  
Phetchaburi Information Technology Campus, Phetchaburi, Thailand.

<sup>a)</sup> Corresponding author: teamhuahin.1234@gmail.com

<sup>a)</sup> laosutthipong\_c@su.ac.th

**Abstract.** *Dendrobium* sp. orchid is one of the most popular cut flowers, widely produced and exported Thailand. The main problem for orchid plants during transportation for in vitro culture is the damage of young plant since the ex vivo condition and strength of plant structure. Therefore, this study aimed to enhance the strength of young orchid plants through culture media supplementation. Chitosan and silicon, both known as plant growth promoters, were added to the orchid tissue culture medium. The results revealed that supplementing VW medium with chitosan at 10 ml/L and silicon at 1.5 ml/L had a positive effect on the number of roots, number of leaves, plant height, and plant weight at the fourth collection. The results of the study found that the use of silicon had an effect on the growth of orchids. Silicon promoted the development of roots and height. The number of roots, it was found that the use of silicon at a level of 1.5 ml/L (T3) gave the best results, with an average number of roots of  $9.31 \pm 1.47$ , while the average of plant height was  $6.13 \pm 0.66$  cm. (T3). However, there were no statistically significant differences in lignin, protein, or chlorophyll content among the experimental groups supplemented with either chitosan or silicon. This study may benefit orchid farmers seeking to improve plant tissue culture techniques to enhance plant strength during transportation.

**Keywords:** *Dendrobium* sp. orchid, chitosan, silicon

## I. INTRODUCTION

Among all ornamental flowers exported to the world market, Thailand is one country that has a significant market share of this agricultural product. That is because of the long standing support for both the public and private sectors in country, thus, Thailand has played a role in being the world exporting country of cut flowers. The worldwide floriculture trades, especially cut flower is rapid development in trading caused by the improvements in logistics that make long haul transportation more feasible. Cut flowers in the floriculture trade of Thailand have been expected to rise further (Rijswick, 2015).

In preparing young plant received by tissue culture technique for transplanting in greenhouses, an important step is hardening technique. Hardening technique is preparing stage for micro-propagated plants before plant them in outside environment. Because, micro propagated plants have been cultured under controlled conditions, thus, is less effective (assessment from the mortality and survival rate) when growing them directly in the greenhouse or in field; under the uncontrolled condition (Bhalsing et al., 2001). So, the artificial setting in a greenhouse in hardening such as

shade houses, less humidity for slowly acclimation; is imitate the field condition (Hudson et al., 1990).

However, damage in micro-propagation plants have been observed at the step of transportation, it is a major criterion for barrier healthy plants before hardening process and growing in the true environment (Chen & Chien, 2012; Grimmer et al., 2012). For this circumstance, both cost and time are used until getting healthy plants enough for transplanting to the field. Moreover, during the restoration of the young plant damaged from transportation or logistic processes, damaged roots and leaves can also be a cause of disease and infestation as well (Freeman, 2008).

The purpose of this research is to enhance the plants' ability to withstand stress and reduce damage during the transportation of orchid products.

## II. METHODOLOGY

The study consisted of two independent experiments designed to evaluate the effects of chitosan and silicon on the growth and development of *Dendrobium* sp. orchids. Each experimental replicate consisted of two plants cultured in 8 oz (240 ml) glass jars containing VW medium. The culture period for orchid plants lasted 180 days.



#### Experiment A: Chitosan Treatments

Chitosan was tested at different concentrations to assess its influence on plant growth.

Treatment	Composition
T1	VW medium without chitosan (control)
T2	VW + 10 mg/L chitosan
T3	VW + 20 mg/L chitosan
T4	VW + 30 mg/L chitosan

#### Experiment B: Silicon Treatments

Silicon was added using potassium silicate at various concentrations to determine its effect on plant growth.

**Table 2.** The composition the treatment of silicon.

Treatment	Composition
T1	VW medium without silicon (control)
T2	VW + 1.0 mg/L silicon
T3	VW + 1.5 mg/L silicon
T4	VW + 2.0 mg/L silicon

#### VW culture (Vacin and Went, 1949)

Potassium silicate was added to the medium after adjusting the pH to 4.8–4.9. Activated carbon was then added at a concentration of 2 g/L. The medium was subsequently sterilized by autoclaving at 121°C for 15 minutes.

The culture process was carried out in a tissue culture laboratory under artificial light. Young orchids were cultivated on the prepared medium containing experimental substances for 180 days.

#### Dehydration and Embedding

The intracellular water was replaced with butanol for 24 h. The samples were embedded in molten paraplast, which was maintained at 58°C in an oven for 30 min, the paraplast was then changed three times, each time for 4 h in the oven, the paraplast was then poured into the mold, and the samples were aligned in the desired orientation, the paraplast blocks were prepared and thin sections were cut using a microtome.

#### Anatomical analysis

Washing was performed on the roots using a blade, 5–8 mm. Samples were cut and fixed in FAA solution with a volume ratio of 90:5:5 (ethanol 90%, formalin 5%, acetic acid 5%) for 18 hours and then stored in 70% ethanol.

#### Sectioning and staining

Thin sections were mounted onto slides and dried in an oven at 56–60°C. The tissue sections were then coated with xylene to dissolve, followed by immersion in ethanol before staining with 1% Safranin. The slides were rinsed twice with water before staining with 0.2% Fast Green. Excess stains were removed by washing the slides in ethanol. Finally, the slides were mounted using DPX and allowed to dry.

#### Lignin analysis

A glass crucible was baked at 105°C for 4 hours, and plant samples were dried in an oven overnight at 105°C. The dried samples were treated with acid, followed by 72% sulfuric acid for 1 hour, and then left in the acid solution for

another hour. The samples were subsequently washed and filtered, and the precipitate was washed with 10–20 mL of acetone. The washed precipitate was dried, weighed, and then baked at 105°C for 12–24 hours. After baking, the samples were weighed to determine the dry mass. The samples were then burned at 600°C for 3–4 hours, allowed to cool for 30 minutes to absorb atmospheric moisture, and weighed again to calculate the percentage of lignin.

Protein content was determined using nitrogen combustion analysis.

#### Chlorophyll extraction process.

Orchid samples were collected and weighed (2 g). The samples were ground in a mortar with 80% acetone and 95% ethanol, then filtered for analysis.

#### Chlorophyll Analysis

The extract's absorbance was measured using a spectrophotometer at wavelengths of 660, 642, and 643 nm. The chlorophyll content was then calculated.

#### Measurement of number of roots, leaves, height and weight

The appropriate ratio of chitosan extract used as a replacement for growth were measured the number of roots, number of leaves, plant heights, and weight at four time points. The first measurement was when the orchids were removed from the bottle. The number of roots, leaves, height and weight were measured. After 60 days, the second measurement was made. After 60 days, the third and fourth measurements were made, respectively.

#### Post-Transplant Growth

After transferring the plants to a greenhouse, growth data was recorded for one month. By measuring the number of roots, leaves, height and weight.

#### Statistical Analysis

Data were analyzed using analysis of variance (ANOVA) in the R program (version 4.0.3). Differences among means were tested using Duncan's multiple range test ( $p \leq 0.05$ ).

### III. RESULTS AND DISCUSSION

The application of chitosan resulted in a higher number of roots compared to the control. The results showed that at the 4th collection, treatments T2, T3, and T4 promoted root production, with root numbers of  $6.75 \pm 0.77$ ,  $6.68 \pm 0.94$ ,  $6.53 \pm 0.67$ , respectively (Table 3). In vitro culture of VW formula seedlings supplemented with 60 mg/L chitosan exhibited a root induction percentage of 97.5% and a maximum root number of 1.98 roots/plant. Moreover, chitosan at concentrations of 100 and 60 mg/L were considered as the best treatments for promoting shoot and root formation, respectively (Ritti et al., 2018).

The root numbers at 4<sup>th</sup> collection a statistically significant difference at the  $p < 0.05$  level. Treatment T2 with 10 ml/L chitosan shown the best results that had the root number  $6.75 \pm 0.77$ . Similarly, T3, T4 and T1 promoted root production by  $6.68 \pm 0.94$ ,  $6.53 \pm 0.67$ ,  $5.87 \pm 0.78$  (Table3).

The leaf numbers at 4<sup>th</sup> collection a statistically significant difference at the  $p < 0.05$  level. Treatments T2 and T3 showed the best results, with leaf numbers of  $7.42 \pm 0.43$  and  $7.42 \pm 0.38$ , Similarly T4 had the leaf number  $7.40 \pm 0.73$ . In control T1 has a minimum value of  $6.64 \pm 0.66$ . (Table3).

In 2010, Dendrobium ‘Queen Pink’ seedlings with 2-3 leaves and 0.5 cm in height were cultured in modified VW medium supplemented with chitosan at concentrations of 0, 10, 20, 40 and 60 mg/L. The results showed that chitosan at 20 mg/L gave the highest height, fresh weight, dry weight and leaf area with statistically significant differences, while chitosan at 60 mg/l gave the highest number of new shoots (Obsuwan and Sawangri, 2010).

The height numbers at 4<sup>th</sup> of collection a statistically significant difference at the  $p < 0.05$  level. Treatment (T2) with 10 mL/L chitosan showed the best results, with a height number  $6.06 \pm 0.66$ . Chitosan helps supplement the nutrients necessary for plant growth, while treatments T3, T1 and T4 had values of  $5.47 \pm 0.80$ ,  $5.41 \pm 0.76$  and  $5.31 \pm 0.73$  respectively (Table 3).

The weight numbers at 4<sup>th</sup> collection a statistically significant difference at the  $p < 0.05$  level. Treatment T2 with 10 mg/L chitosan also showed the best results in terms of weight, with a value of  $1.72 \pm 0.77$ g. Similarly, T4, T3 and T1 promoted weight production by  $1.59 \pm 0.17$ ,  $1.55 \pm 0.09$ ,  $1.47 \pm 0.18$  respectively (Table 3). The values of lignin, protein and chlorophyll in each treatment were slightly different, but there was no statistically significant difference between the experimental groups.

**Table 3.** Plant root number, leaf number, height (cm), and weight (g) (Mean  $\pm$  SD) of orchids grown using different ratios of chitosan.

Treatment <sup>2</sup>	Root 1 <sup>st</sup>	Root 2 <sup>nd</sup>	Root 3 <sup>rd</sup>	Root 4 <sup>th</sup>
T1	$3.93 \pm 0.79$	$4.71 \pm 0.94$	$5.15 \pm 0.81$	$5.87^b \pm 0.78$
T2	$3.90 \pm 0.86$	$5.21 \pm 0.89$	$5.87 \pm 0.86$	$6.75^a \pm 0.77$
T3	$3.71 \pm 0.99$	$4.90 \pm 0.86$	$5.87 \pm 0.89$	$6.68^a \pm 0.94$
T4	$3.75 \pm 0.81$	$5.06 \pm 0.87$	$5.87 \pm 0.82$	$6.53^a \pm 0.67$
F	ns	ns	ns	*
CV	22.75	18.88	15.80	12.46
Treatment <sup>2</sup>	Leaf 1 <sup>st</sup>	Leaf 2 <sup>nd</sup>	Leaf 3 <sup>rd</sup>	Leaf 4 <sup>th</sup>
T1	$3.21 \pm 0.50$	$4.14 \pm 0.63$	$4.71 \pm 0.73$	$6.64^b \pm 0.66$
T2	$3.14 \pm 0.62$	$4.53 \pm 0.72$	$5.21 \pm 0.83$	$7.42^a \pm 0.43$
T3	$3.18 \pm 0.71$	$4.25 \pm 0.58$	$5.03 \pm 0.74$	$7.42^a \pm 0.38$
T4	$3.53 \pm 0.63$	$4.35 \pm 0.66$	$5.18 \pm 0.73$	$7.40^a \pm 0.73$
F	ns	ns	ns	*
CV	20.94	20.14	16.68	13.31
Treatment <sup>2</sup>	Height 1 <sup>st</sup>	Height 2 <sup>nd</sup>	Height 3 <sup>rd</sup>	Height 4 <sup>th</sup>
T1	$2.87 \pm 0.75$	$3.61 \pm 0.74$	$4.33 \pm 0.73$	$5.41^b \pm 0.76$
T2	$2.85 \pm 0.81$	$3.98 \pm 0.95$	$4.96 \pm 0.80$	$6.06^a \pm 0.66$
T3	$2.76 \pm 0.82$	$3.86 \pm 0.70$	$4.53 \pm 0.74$	$5.47^b \pm 0.80$
T4	$2.86 \pm 0.78$	$3.78 \pm 0.66$	$4.43 \pm 0.73$	$5.31^b \pm 0.73$
F	ns	ns	ns	*
CV	20.94	20.14	16.68	13.31
Treatment <sup>2</sup>	Weight 1 <sup>st</sup>	Weight 2 <sup>nd</sup>	Weight 3 <sup>rd</sup>	Weight 4 <sup>th</sup>
T1	$1.36 \pm 0.17$	$1.34 \pm 0.18$	$1.40 \pm 0.19$	$1.47^b \pm 0.18$
T2	$1.35 \pm 0.21$	$1.37 \pm 0.23$	$1.49 \pm 0.13$	$1.72^a \pm 0.04$
T3	$1.36 \pm 0.12$	$1.41 \pm 0.12$	$1.47 \pm 0.10$	$1.55^{ab} \pm 0.09$
T4	$1.28 \pm 0.15$	$1.33 \pm 0.14$	$1.43 \pm 0.13$	$1.59^{ab} \pm 0.17$
F	ns	ns	ns	*
CV	12.80	12.79	14.53	13.98

**Note:** <sup>1</sup>Means in each column with different superscripts letters were significantly different by Duncan’s Multiple Range Test ( $p \leq 0.05$ ).

<sup>2</sup>The treatments were control (T1), 10mg/L chitosan supplementation (T2), 20 mg/L chitosan supplementation (T3), and 30 mg/L chitosan supplementation (T4), respectively.

<sup>3</sup>F The F-value which is the value obtained from the F-test is used to compare the variance between groups of data especially in analysis of variance. ns is not significant, \* significant ( $p < 0.05$ ).

**Table 4.** Plant root number and height (cm) (Mean  $\pm$  SD) of orchids grown using different ratios of silicon.

Treatment <sup>2</sup>	Root 1 <sup>st</sup>	Root2 <sup>nd</sup>	Root3 <sup>rd</sup>	Root4 <sup>th</sup>
T1	3.21 $\pm$ 0.77	4.19 $\pm$ 0.99	5.81 $\pm$ 1.20	7.81 <sup>b</sup> $\pm$ 1.78
T2	3.21 $\pm$ 0.75	4.50 $\pm$ 0.87	6.56 $\pm$ 1.40	7.90 <sup>b</sup> $\pm$ 0.99
T3	3.22 $\pm$ 0.73	5.06 $\pm$ 0.83	5.93 $\pm$ 1.06	9.31 <sup>a</sup> $\pm$ 1.47
T4	3.25 $\pm$ 0.78	4.58 $\pm$ 0.75	6.25 $\pm$ 1.18	8.50 <sup>ab</sup> $\pm$ 1.29
F	ns	ns	ns	*
CV	29.70	22.96	19.87	16.83
Treatment <sup>2</sup>	Height 1 <sup>st</sup>	Height 2 <sup>nd</sup>	Height 3 <sup>rd</sup>	Height 4 <sup>th</sup>
T1	2.16 $\pm$ 0.36	3.24 $\pm$ 0.74	4.29 $\pm$ 0.65	5.32 <sup>b</sup> $\pm$ 0.63
T2	2.13 $\pm$ 0.27	3.63 $\pm$ 0.95	4.71 $\pm$ 0.69	6.09 <sup>a</sup> $\pm$ 0.67
T3	2.12 $\pm$ 0.47	3.72 $\pm$ 0.45	4.85 $\pm$ 0.70	6.13 <sup>a</sup> $\pm$ 0.66
T4	2.16 $\pm$ 0.26	3.17 $\pm$ 0.70	4.32 $\pm$ 0.78	5.39 <sup>b</sup> $\pm$ 0.76
F	ns	ns	ns	*
CV	20.94	20.14	16.68	13.31

**Note:** <sup>1</sup>Means in each column with different superscripts letters were significantly different by Duncan's Multiple Range Test ( $p \leq 0.05$ ).

<sup>2</sup>The treatments were control (T1), 1 mg/L silicon supplementation (T2), 1.5 mg/L silicon supplementation (T3), and 2 mg/L silicon supplementation (T4), respectively.

<sup>3</sup>F The F-value which is the value obtained from the F-test is used to compare the variance between groups of data especially in analysis of variance. ns is not significant, \*significant ( $p < 0.05$ ).

However, silicon (Si) in the form of SiO<sub>2</sub> at different concentrations (0, 0.5, 1.0, 1.5, and 2.0 g/L) showed a negative effect on the growth of, *Cattaya forbesii* (Orchidaceae) when applied in MS medium and cultured for 200 days. Growth variables, including the number of roots, root length, leaf area, number of shoots, number of leaves, shoot height, fresh and dry weight of roots and shoots, and water content in both shoots and roots, decreased as the Si concentration increased. As the concentration of Si in the culture medium increased, reductions in the number of roots and root length were observed. At a concentration of 2 g/L root fresh and dry matter decreased by approximately 50% compared to the treatment without Si (Colombo et al., 2016). This result has been explained caused by the source and concentration of Si in medium, and Si form that plant prefer to absorb may be mono-silicic acid (H<sub>4</sub>SiO<sub>4</sub>), and SiO<sub>2</sub> is the form to deposit to leaf (Epstein, 1999).

The experiment (T3) using 1.5 mL/L of silicon gave the best result, with a root number of 9.31 $\pm$ 1.47. Similarly, treatment T4, T2 and T1 root production by 8.50  $\pm$  1.29, 7.90  $\pm$  0.99, 7.81  $\pm$  1.78, respectively. The leaf values in each experiment varied slightly, there was

no statistically significant difference between the experimental groups ( $p > 0.05$ ).

In experiment T3, using 1.5 mL/L of silicon showed the best result, with the height value of 6.13 $\pm$ 0.66 cm, as silicon helps supplement essential nutrients for plant growth. Similarly, T2, T4 and T1 having values of 6.09 $\pm$ 0.67, 5.39 $\pm$ 0.76, 5.32 $\pm$ 0.63 respectively (Table 4). The weight values in each experiment varied slightly, there was no statistically significant difference between the experimental groups ( $p > 0.05$ ).

Orchid tissue is located at the center of the root, particularly in aerial roots of some orchid species. Its primary function is to store water and nutrients. The tissue cells contain large spaces that enable water and nutrient storage, allowing the plant to sustain during periods of scarcity. Additionally, this tissue provides structural support and flexibility to the roots, helping maintain their stability and resilience (Figure 1). Anatomical characteristics of *Dendrobium* sp. orchid roots. The appropriate ratio of chitosan extract was used as a substitute for growth in four treatments.

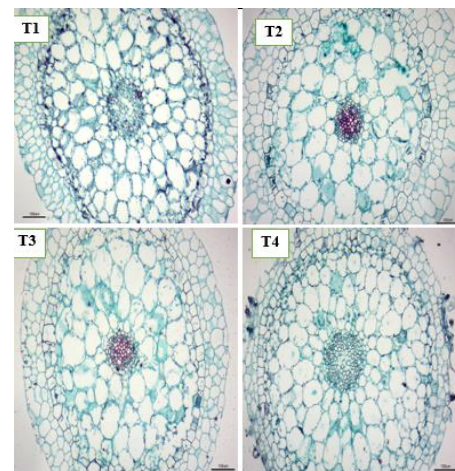


**Figure 1.** Anatomical characteristics of *Dendrobium* sp. orchid roots. The treatments included a control (T1), 10 mg/L chitosan supplementation (T2), 20 mg/L chitosan supplementation (T3), and 30 mg/L chitosan supplementation (T4). The appropriate ratio of chitosan extract was used as a substitute for growth in four treatments. C= Cortex, EX=Exodermis. (At 10x)



(Figure 2) Anatomical characteristics of *Dendrobium* sp. orchid roots. The appropriate ratio of silicon extract was used as a substitute for growth 4-in four treatments.

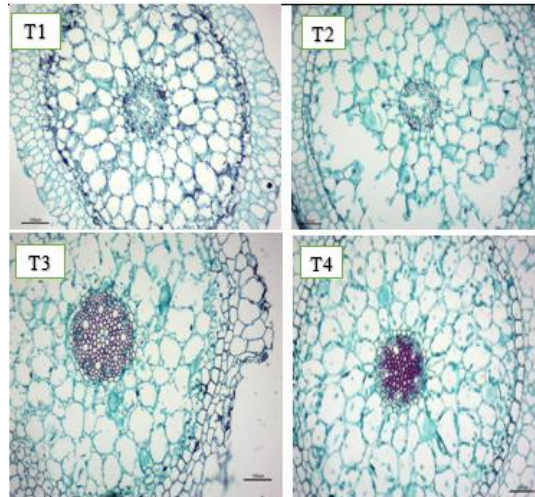


**Figure 2.** Anatomical characteristics of *Dendrobium* sp. orchid roots. The treatments included a control (T1), 1 mg/L silicon supplementation (T2), 1.5 mg/L silicon supplementation (T3), and 2 mg/L silicon supplementation (T4). The appropriate ratio of silicon extract was used as a substitute for growth in four 4 treatments. C= Cortex EX=Exodermis. (At 10x)

#### IV. CONCLUSION

In conclusion, both chitosan and silicon can be used to stimulate the growth of orchids, particularly in terms of root number, leaf number, height, and weight. In this study, the application of chitosan at 10 mL/L had the most significant effect on the growth of *Dendrobium* sp. orchids. The results also showed that silicon positively impacted orchid growth in several aspects, with the use of silicon at 1.5 mL/L yielding the best result. Silicon helped promote the development of roots, leaves and height, which are key factors influencing overall growth. However, the use of chitosan and silicon did not significantly affect the levels of lignin, protein, and chlorophyll in the plants.

#### ACKNOWLEDGMENT

The author would like to acknowledge the faculty of Animal Sciences and Agricultural Technology, Silpakorn University for offering the lab facility.

#### REFERENCES

[1] Bekker, T. F., Kaiser, C. and Labuschagne, N. 2006. *In vitro* inhibition of several phytopathogenic fungi

from avocado by soluble potassium silicate. South

African Avocado Growers' Association Yearbook 29, p. 64-67.

[2] Bhalsing, S. R., Teli, N. P., Pawar, P. K., Saindana, P. V., Baviskar, M. P. and Maheshwari, V. L. 2001. Tissue culture grown banana: A cost effective strategy for hardening. *Physiology and Molecular Biology of Plants* 7(2): 185-189.

[3] Chen, C. and Chien, M. 2012. The leaf growth model and influencing factors in *Phalaenopsis* orchid. *African Journal of Agricultural Research* 7(28): 4045-4055.

[4] Colombo, R., C., Eavetta, V., de Faria, R. T., de Andrade, F. A. and Melem, V. M. 2016. Response of *Cattleya forbesii* orchid to increasing silicon concentrations in vitro. *Revista Caatinga Mossoro* 29(1): 18-24.

[5] Freeman, B. and Beattie, G. A. 2008. An overview of plant defenses against pathogens and herbivores. In: *The plant health instructor*. doi:10.1094/PHI-I-2008-0226-01.

[6] Epstein, E. 1999. Silicon. *Annual Review of Plant Physiology and Plant Molecular Biology* 50: 641-664.

[7] Grimmer, M. K., Foulkes, M. J. and Paveley, N. D. 2012. Foliar pathogenesis and plant water relations: a review. *Journal of Experimental Botany* 63(2): 4321-4331.

[8] Hudson, T. H., Date, E. K., Fred, T. D. and Rho, J. R. 1990. Propagation structures, media, fertilizers, sanitation and containers. In: *Plant propagation Principles and Practice*. Prentice Hall Inc., New Jersey, USA, pp. 15-47.

[9] Obsuwan, K., Sawangsri, K., Ukong, S. and Uthairatanakij, A. (2010). Effects of chitosan concentration on in vitro growth of *Dendrobium* hybrid seedlings. *Acta hort.* 878, 289-294 doi: 10.17660/ActaHortic.2010.878.36 <https://doi.org/10.17660/ActaHortic.2010.878.36>

[10] Rijswijk, C. V. 2015. World floriculture map 2015. Retrieved from World\_ Floriculture Map 2015 vanRijswijk Jan2015.pdf [Accessed 28 February 2015].

[11] Ritti, W., Chourykaew, B. and Sreenamkhun, O. 2018. Effect of chitosan on growth of *in vitro* seedling culture of *Dendrobium lindleyi* Steud. *Burapha Science Journal* 23(2): 669-681.

[12] Vacin, E. and Went, F. W. 1949. Some pH changes in nutrient solutions. *Botanical Gazette* 110: 605-613.



# Measurement of Forearm Muscle Electromyography during Finger Movements

Dithaporn Thungsotanon<sup>1, a)</sup>, Sakapan Klaydokjan<sup>2, b)</sup>, Nathaporn Suwanpayak<sup>3</sup>  
and Chompoonud Kulketwong<sup>1</sup>

## Author Affiliations

<sup>1</sup>Department of Mechanical Engineering, King Mongkut's Institute of Technology Ladkrabang  
Prince of Chumphon Campus, Chumphon

<sup>2</sup>Department of Electrical Engineering, King Mongkut's Institute of Technology Ladkrabang  
Prince of Chumphon Campus, Chumphon

<sup>3</sup>Department of General Science, King Mongkut's Institute of Technology Ladkrabang  
Prince of Chumphon Campus, Chumphon

## Author Emails

<sup>a)</sup>dithaporn.th@kmitl.ac.th

<sup>b)</sup>Corresponding author: sakapan.kl@kmitl.ac.th

**Abstract.** Electromyography (EMG) is one of the methods to detect the signals from nerves and muscles for controlling the neuroprosthetic devices and the robotic hands by the human. This article presented a technique for measuring the electrical signals of the forearm muscle with the surface electromyography while the fingers of the volunteers were flexion and extension, and creating the multiple linear regression equation. The volunteers in the experiment were divided into 3 groups: who played computer games, who played guitar and who did not do both of them. The electrode pads were attached to the anterior and posterior of the two lower arm muscles of the volunteers then they moved the 5 fingers bending and straightening. The results found that attaching the EMG pads to the forearm muscles were proper for detecting the electrical signals from the finger movements of all groups. The electrical signals from the finger flexion and extension on the right-hand side of the specimen that played the computer games and the left-hand side of the volunteer who played guitar were higher significantly than the people who did not do anything. The values of finger movements on each hand-side of the group that did not take two activities were proximate which impacted the predicted equation for controlling devices by EMG was improper. However, the equation can be predicted the finger movements of the right and left hand and showed the coefficient of determination of 0.71 and 0.70, respectively.

**Index Terms—** electromyography (EMG), neuroprosthetic, muscles, multiple linear regression

## I. INTRODUCTION

The study of the patterns of human movement and muscle flexibility by using electromyography (EMG) is important for neuroprosthetics. The interaction between the human actions and the electric potential differences or voltage is processed to control the external devices [1-3]. EMG is a technique for directly detecting the electrical signals transmitted from the nerves and muscles during activities and has been available in biomechanics, biomedical engineering and medicine [4] for a long time. The main system of EMG consists of two electrodes: one for stimulation and another for receiving and recording the signals. The signal receiving electrode is divided into 2 types, needle and surface electrode [5].

In general, the surface electrode is applied in the human computer interaction (HCI) [6] and is called the surface electromyography (sEMG). The obtained signals are interpreted in terms of the precise algorithm and led to controlling the studied devices. The proper algorithm should not be more complex or high computational efficiency,

moreover, the system should be easy to use without training before. The sEMG was able to detect and display in the entropy parameter from the flexion of each finger and many fingers simultaneously, the outcome showed that the arm was motioned following the programmed conditions but could not move in the other posture [7].

Research on finger movements focuses on studying anatomy and biomechanical of the hand, including kinematics from muscle activation inputs, controlling robotic hand [8]. In 2019, a new method to replace conventional EMG sensor placement with array EMG system covered forearm by Bio-semi sensor and detected the signal theal finger angle motion [9]. Recently year, surface EMG game control interface for people, to estimate and translate a machine learning model of neck rotations signal. Control interfaces can be applied in several areas that involve neck activities, e.g., robot control and rehabilitation, as well as game interfaces, to enable entertainment for people with disabilities [10].

For the above-mentioned, the measuring flexibility of the anterior and posterior forearm from the flexion and extension of the volunteers' fingers with EMG sensors is proposed to

be a guide for other research such as myopathy, artificial arm and bioelectric interface.

## II. METHODOLOGY

### 1. Participants and Experimental Setup

The 9 right-handed healthy males aged 20-23 years old with the average weight of  $75 \pm 24$  kg and height of  $174 \pm 11$  cm were divided into 3 testing groups: played computer game, played guitar and did not do both activities.

Fig. 1 showed the schematics of the experiment. The 3-lead differential sensor (MyoWare Muscle Sensor model AT-04-001; Advancer Technologies, USA) was connected to the analog to digital acquisition NI-USB 6001 (National Instrument, Hungary) with the resolution of 16 bit and the aggregate maximum sampling rate of 20 kS/s that was adequate to measure the frequency response of the sEMG, and displayed and recorded data via LabVIEW software. The voltage 5 VDC from NI-USB 6001 was transferred to the two pieces of the sEMG and the resistance of the output signal was gained following the manufacturer's instruction and the A/D frequency was set at 1000 Hz.

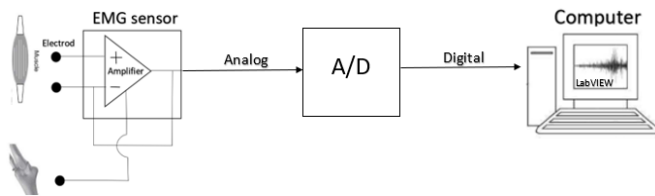


Fig. 1. Schematic diagram for sEMG sensor setup

### 2. Experiment

The priority of the specimens was randomly drawn lots to eliminate the bias before testing. After that, the forearm skins of the volunteers were cleaned with Ethyl Alcohol 70% v/v and naturally left for 5 minutes. Then mounted the ECG electrode pads by the mid muscle electrode snap and the end muscle electrode snap was adhered at Flexor Carpi Radialis when considered at the anterior of the forearm and Flexor Carpi Ulnaris while posterior forearm testing and the reference electrode was attached at the elbow bones as shown in Fig. 2. In the experiment, the flexion-extension interval was equal by using the metronome. The flexion and extension steps of all volunteers started from the thumb to the little finger, was repeated 5 times per each batch and then rested for 5 minutes to relax the muscle and tested again. The electrical potential differences in the considered positions that were recorded and found that the output signals from the back of the arm were too low, so they were not able to analyze the results. The EMG signals from the 5 fingers bending and straightening were calculated the average electromyography (aEMG) [3] as Equation (1) for discussion of the activities, left-right upper limb of the specimens and led aEMG to future development.

$$aEMG = \frac{1}{N} \sum_{i=1}^N V_i \quad (1)$$

where  $aEMG$  is the average value of electromyography (V),  $V_i$  is the voltage of N sampler from the finger flexion (V), and  $N$  is the amount of sampling data (dimensionless)



Fig.2. The ECG Electrode Pad takes the stick on the forearm muscles.

## III. RESULTS AND DISCUSSION

### 1. Data and Statistical Analysis

In the experiment, when the fingertip touched the palm, the sEMG was measured the electrical signal from the muscle the connected to the thumb, index finger, middle finger, ring finger and little finger. Fig. 3 showed the right-handed side data of the specimen who play guitar. The results found that the voltages of each finger and each side of hand of the volunteer who did activities in everyday were obviously different. The flexion signal showed the peak at the ring finger because this finger did not have the muscle for bending, but deepened on the muscle of the middle and little finger. The minimum signal occurred at the thumb since the thumb consisted of the deep muscle, whereas another showed the proximate value. After that, the sets of data in every condition were calculated to aEMG for the statistical analysis and mathematical model.

Compare the signal voltage of the finger muscles all of 3 groups volunteers: during play game, play guitar and non-activity (never play game and guitar). The data were collected using the muscles of five finger of forearm and back arm of both hands as showed Table 1. The statistics data analysis of 5 fingers within forearm muscles of non-activity group was found the least signal, the ring finger and the little finger of guitar player group were the highest. Others finger, there was non-significant difference in the left forearm muscles.

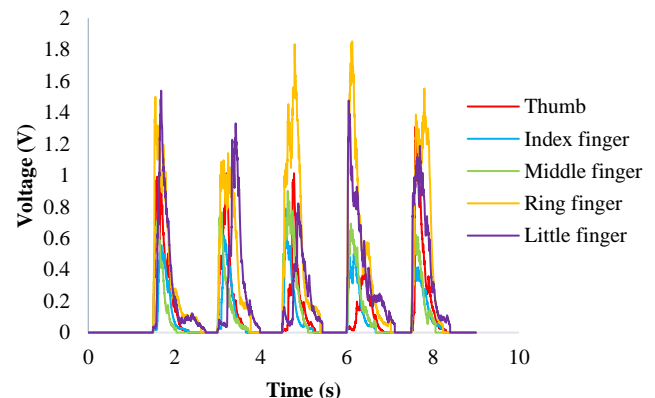


Fig. 3. Voltage of EMG sensor of right hand finger forearm muscles of guitar volunteers.

**TABLE 1** The aEMG value of each finger flexion of the all group of volunteer

Side	Arm	finger	EMG $\pm$ S.D. (V)		
			Game	Guitar	Non-activity
Left	Fore	Thumb	1.062 <sup>B</sup> $\pm$ 0.60	0.961 <sup>B</sup> $\pm$ 0.36	0.405 <sup>A</sup> $\pm$ 0.22
		Index	0.806 <sup>B</sup> $\pm$ 0.33	0.828 <sup>B</sup> $\pm$ 0.23	0.237 <sup>A</sup> $\pm$ 0.08
		Middle	1.078 <sup>B</sup> $\pm$ 0.40	1.073 <sup>B</sup> $\pm$ 0.34	0.507 <sup>A</sup> $\pm$ 0.15
		Ring	2.474 <sup>B</sup> $\pm$ 1.23	2.762 <sup>C</sup> $\pm$ 1.28	0.529 <sup>A</sup> $\pm$ 0.23
		Little	1.058 <sup>B</sup> $\pm$ 0.45	1.547 <sup>C</sup> $\pm$ 0.87	0.388 <sup>A</sup> $\pm$ 0.31
	Back	Thumb	0.747 <sup>B</sup> $\pm$ 0.22	1.202 <sup>C</sup> $\pm$ 0.43	0.332 <sup>A</sup> $\pm$ 0.09
		Index	0.659 <sup>B</sup> $\pm$ 0.29	0.899 <sup>C</sup> $\pm$ 0.32	0.505 <sup>A</sup> $\pm$ 0.30
		Middle	0.588 <sup>A</sup> $\pm$ 0.23	1.090 <sup>B</sup> $\pm$ 0.44	0.523 <sup>A</sup> $\pm$ 0.26
		Ring	0.960 <sup>B</sup> $\pm$ 0.35	1.143 <sup>B</sup> $\pm$ 0.30	0.659 <sup>A</sup> $\pm$ 0.26
		Little	0.759 <sup>B</sup> $\pm$ 0.23	0.852 <sup>B</sup> $\pm$ 0.27	0.391 <sup>A</sup> $\pm$ 0.15
Right	Fore	Thumb	0.695 <sup>C</sup> $\pm$ 0.41	0.466 <sup>B</sup> $\pm$ 0.13	0.288 <sup>A</sup> $\pm$ 0.09
		Index	0.925 <sup>C</sup> $\pm$ 0.42	0.436 <sup>B</sup> $\pm$ 0.16	0.287 <sup>A</sup> $\pm$ 0.15
		Middle	1.252 <sup>C</sup> $\pm$ 0.55	0.716 <sup>B</sup> $\pm$ 0.48	0.388 <sup>A</sup> $\pm$ 0.14
		Ring	2.736 <sup>C</sup> $\pm$ 1.09	1.598 <sup>B</sup> $\pm$ 0.90	0.458 <sup>A</sup> $\pm$ 0.12
		Little	1.264 <sup>C</sup> $\pm$ 0.60	0.568 <sup>B</sup> $\pm$ 0.15	0.358 <sup>A</sup> $\pm$ 0.21
	Back	Thumb	0.868 <sup>B</sup> $\pm$ 0.27	0.426 <sup>A</sup> $\pm$ 0.15	0.378 <sup>A</sup> $\pm$ 0.10
		Index	0.801 <sup>C</sup> $\pm$ 0.34	0.596 <sup>B</sup> $\pm$ 0.18	0.370 <sup>A</sup> $\pm$ 0.13
		Middle	0.769 <sup>B</sup> $\pm$ 0.37	0.779 <sup>B</sup> $\pm$ 0.28	0.400 <sup>A</sup> $\pm$ 0.12
		Ring	0.812 <sup>B</sup> $\pm$ 0.41	0.787 <sup>B</sup> $\pm$ 0.22	0.469 <sup>A</sup> $\pm$ 0.14
		Little	1.024 <sup>C</sup> $\pm$ 0.53	0.652 <sup>B</sup> $\pm$ 0.29	0.442 <sup>A</sup> $\pm$ 0.16

A, B, C means in the same row with difference superscript letters are different at a 95% significance level.

## 2. Mathematical Modeling

The concept of the parameter model for controlling the robot was easy and reliable. The relationship of the aEMG from data and statistical analysis section was the linearity. Therefore, the mathematical model was chosen the methods of the multiple linear regression analysis to predict the aEMG of each finger from all fingers and activities of the specimens. The regression equation of the right forearm as shown in equation (2) and was able to estimate the voltage from the flexion-extension behavior of 71%. The standard error of the forecasting was  $\pm 0.121$ . The correlation was considered and indicated that the p-value of the five fingers was 0.006 and the p-value of the activities was 0.001.

$$aEMG_{right} = 0.4245 + 0.0732x_1 - 0.1621x_2, \\ R^2 = 0.71 \quad (2)$$

where  $x_1$  = Fingers flexion of right hand (Thumb = 1, Index finger = 2, Middle finger = 3, Little finger = 4, Ring finger = 5) and  $x_2$  = Activity (Play computer games = 1, Play guitar = 2, Non activity = 3)

For the left forearm, the multiple linear regression analysis showed in equation (3), the predicted coefficient was 0.70 and the standard error was  $\pm 0.165$ . The correlation manifested the p-value  $> 0.05$  for the five fingers and activities. Therefore, the multiple linear regression equation

of the left hand did not predict the voltages because the data of the aEMG of each activity were overlap.

$$aEMG_{left} = 0.1824 - 0.0288x_3 - 0.1101x_4 \\ + 0.0059x_5 + 0.243x_6 + 0.1558x_7 + 0.3371x_8 \\ , R^2 = 0.70 \quad (3)$$

where  $x_3$  = Thumb finger flexion of left hand,  $x_4$  = Index finger flexion of left hand,  $x_5$  = Little finger flexion of left hand,  $x_6$  = Ring finger flexion of left hand,  $x_7$  = Play

Computer Games and  $x_8$  = Play Guitar

## IV. CONCLUSION

The study of the muscle flexibility during the finger flexion-extension with sEMG sensor showed that the output signals of each volunteer were different when measured with MyoWare muscle sensor; especially the side of the hand that usually did activity. The sEMG sensors were mounted on the anterior forearm had higher voltage than the posterior side. The maximum bending and straightening output values from each finger were differences and the data was led to create the equation or the algorithm for controlling the robot and arm artificial, but should be tested more conditions with the sEMG or the other types for easy to use and proper applications. The model of the multiple linear regression was able to predict the right-hand side output voltage of the

specimens in all conditions with the reliability level of 71%, on the other hand, the equation of the left-hand side should be developed to be more accurate by taking and considering the RAW data to complicated process.

#### REFERENCES

- [1] M. A. Oskoei and H. Hu, "Support Vector Machine-Based Classification Scheme for Myoelectric Control Applied to Upper Limb," in *IEEE Transactions on Biomedical Engineering*, vol. 55, no. 8, pp. 1956-1965, Aug. 2008, doi: 10.1109/TBME.2008.919734.
- [2] Tieck, J. C. V., Weber, S., Stewart, T. C., Kaiser, J., Roennau, A., & Dillmann, R. (2020). A spiking network classifies human sEMG signals and triggers finger reflexes on a robotic hand. *Robotics and Autonomous Systems*, 131, 103566.
- [3] Yang, Z., & Chen, Y. (2016). Surface EMG-based sketching recognition using two analysis windows and gene expression programming. *Frontiers in neuroscience*, 10, 445.
- [4] Reaz, M. B. I., Hussain, M. S., & Mohd-Yasin, F. (2006). Techniques of EMG signal analysis: detection, processing, classification and applications. *Biological procedures online*, 8(1), 11-35.
- [5] Norali, A., Som, M., & Kangar-Arau, J. (2009, October). Surface electromyography signal processing and application: A review. In *Proceedings of the International Conference on Man-Machine Systems (ICoMMS)* (No. 11–13).
- [6] Chen, Y., Yang, Z., & Wang, J. (2015). Eyebrow emotional expression recognition using surface EMG signals. *Neurocomputing*, 168, 871-879.
- [7] You, K. J., Rhee, K. W., & Shin, H. C. (2010). Finger motion decoding using EMG signals corresponding various arm postures. *Experimental neurobiology*, 19(1), 54.
- [8] Jimson G Ngeo., Tomoya Tamei and Tomohiro Shibata, Continuous and simultaneous estimation of finger kinematics using inputs from an EMG-to-muscle activation model, *Journal of NeuroEngineering and Rehabilitation* 2014,11:122<http://www.jneuroengrehab.com/content/11/1/122>
- [9] Sorawit Stapornchaisit, Yeongdae Kim, Atsushi Takagi, Natsue Yoshimura and Yasuharu Koike, Finger angel estimation form array EMG system using linear regression model with independent component analysis, *Frontiers in Neurorobotics*, 2019, 13, 1-12. <https://doi.org/10.3389/fnbot.2019.00075>
- [10] Joseph K. Muguro , Pringgo Widyo Laksono , Wahyu Rahmaniar, Waweru Njeri , Yuta Sasatake , Muhammad Syaiful Amri bin Suhaimi , Kojiro Matsushita, Minoru Sasaki, Maciej Sulowicz and Wahyu Caesarendra, Development of Surface EMG Game Control Interface for Persons with Upper Limb Functional Impairments, *Signal*, 2021, 2, 834-851. <https://doi.org/10.3390/signals2040048>



# Pattern of Pediatric Bacterial Infection and Antibiotic Resistance in Tertiary Care Hospitals, Southern Thailand: A 12-Year Experience

Phanvasri Saengsuwan<sup>1, a)</sup>, Narongdet Kositpantawong<sup>2, b)</sup>,  
Wacharakrit Wachirapichet<sup>3, c)</sup> and Wisanuwee Suriyaamorn<sup>4, d)</sup>

## Author Affiliations

<sup>1</sup>Department of Biomedical Sciences and Biomedical Engineering,  
Faculty of Medicine, Prince of Songkla University, Songkhla, Thailand

<sup>2</sup>Department of Internal Medicine, Faculty of Medicine, Prince of Songkla University, Songkhla, Thailand

<sup>3</sup>Department of Pathology, Faculty of Medicine, Prince of Songkla University, Songkhla, Thailand

<sup>4</sup>Division of Digital Innovation and Data Analytics, Faculty of Medicine, Prince of Songkla University, Songkhla, Thailand

## Author Emails

<sup>a)</sup> Corresponding author: sphanvas@medicine.psu.ac.th

<sup>b)</sup> knarongd@medicine.psu.ac.th

<sup>c)</sup> wacharakrit41@gmail.com

<sup>d)</sup> swisanuw@medicine.psu.ac.th

**Abstract.** Bacterial multidrug-resistant infections pose substantial global challenges through increased pediatric morbidity, mortality, and healthcare expenditures. However, there is limited scientific data available in our region that focuses on antibiotic resistance in pediatric patients. Therefore, this study aimed to evaluate antimicrobial susceptibility patterns, including multidrug-resistant *Pseudomonas aeruginosa* (MDRPA), vancomycin-resistant *Enterococci* (VRE), ESBL-producing *E. coli*, and ESBL-producing *Klebsiella pneumoniae* infections. A retrospective descriptive study was conducted on these pathogens from tertiary care hospitals in Southern Thailand over a 12-year period from 2012 to 2024. In the present study, 546 strains of these isolates were collected. Out of 61 bacterial isolates analyzed, MDRPA represented 54.1% (33), followed by *Proteus mirabilis* (27.9%, 17), VRE (8.2%, 5), and ESBL-producing *E. coli* and ESBL-producing *Klebsiella pneumoniae* (9.8%, 6), respectively. A higher incidence (62.3%, 38) was found in male infants. Most of the positive isolations were from sputum (32.8%, 20) and the genitourinary tract (16.4%, 10). The pediatric intensive care unit demonstrated the highest infection (32.8%, 20), followed by the pediatric ward (23.0%, 14), the medical ward (9.8%, 6), and the operating room (3.3%, 2), respectively. MDRPA showed the highest frequency of resistance against piperacillin/tazobactam (100%) and imipenem (90.3%), while VRE was completely resistant to vancomycin and penicillin (100%). Furthermore, *P. mirabilis* and ESBL isolates showed resistance to colistin (100%) due to natural intrinsic resistance and cefoperazone (100%). All isolates were 100% susceptible to amikacin, ceftazidime, ertapenem, and norfloxacin. All of these were multidrug-resistant isolates. Our study highlights the alarming prevalence of MDR among hospitalized pediatric patients, mainly those in the pediatric intensive care unit. Therefore, it is important to monitor the distribution of bacteria and their antibiotic resistance to revise certain empirical criteria, which may provide useful insights into disease epidemiology.

**Index Terms**—Antibiotic resistance, ESBL-producing *E. coli*, ESBL-producing *Klebsiella pneumoniae*, Pediatric patients, *Proteus mirabilis*, *Pseudomonas aeruginosa*, Vancomycin-Resistant *Enterococci*,

## I. INTRODUCTION

Multidrug-resistant infections (MDR) produced by bacteria are a major global health concern, increasing morbidity, mortality, and healthcare spending [1]. The World Health Organization (WHO) has recognized antimicrobial resistance (AMR) as one of humanity's top ten global public health challenges (WHO, 2020). The rise in MDR infections is especially worrying in pediatric patients, who are more vulnerable due to their developing immune systems and the limited range of approved antimicrobial treatments [2]. The pediatric populations demonstrate increased infection susceptibility and complication risks due to immunocompromised individuals [3]. However, National data on the susceptibility of MDR pathogens from various sources is scarce. A recent investigation in 2024 discovered 12 Enterobacteriaceae strains during a short 6-month period in 2019, including a carbapenem-resistant Enterobacteriaceae [4].

This study aims to address these gaps by providing longitudinal data on the antimicrobial susceptibilities of key pathogens, including multidrug-resistant *Pseudomonas aeruginosa* (MDRPA), vancomycin-resistant *Enterococci* (VRE), ESBL-producing *Escherichia coli*, ESBL-producing *Klebsiella pneumoniae*, and *P. mirabilis* infections among pediatric patients from 2012 to 2024 in Southern Thailand. Understanding the epidemiology and antimicrobial susceptibility patterns of key pathogens in pediatric populations is essential for improving clinical outcomes and reducing the burden of MDR infections [5, 6]. The findings from this study will provide valuable insights into the local epidemiology of antibiotic resistance, enabling the development of targeted interventions and evidence-based guidelines to improve pediatric care in Southern region.

## II. METHODOLOGY

### A. Bacterial isolation

This retrospective descriptive study was conducted between 2012 to 2024 at a 1,000-bed tertiary care hospital in Songkhla Province in Southern Thailand. A total of 546 strains were isolated from various clinical specimens collected from pediatric patients admitted to a tertiary care hospital in Songkhla Province, Thailand, of which 61 were selected for multidrug-resistant *Pseudomonas aeruginosa* (MDRPA), vancomycin-resistant *Enterococci* (VRE), ESBL-producing *Escherichia coli*, ESBL-producing *Klebsiella pneumoniae*, and *P. mirabilis* for epidemiology analysis. All bacterial strains isolates were grown on Tryptic Soy Agar plates at 37°C overnight to identify species using conventional biochemical tests. Both bacteria characterization and antibiotic susceptibility tests were conducted at Microbiology Unit, Department of Pathology, Faculty of Medicine, Prince of Songkla University and Hat Yai Hospital. Antimicrobial susceptibility tests were

performed using the disk diffusion method according to the Clinical and Laboratory Standards Institute guidelines [7].

### B. Antimicrobial susceptibility testing

Antimicrobial susceptibility testing was performed using the disk diffusion method for Enterobacteriaceae [7]. Different antibiotic disks (BD, Heidelberg, Germany) were used as follows: amikacin (AK, 30 µg), ampicillin (AMP, 10 µg), cefoperazone-sulbactam (SPZ, 75/30 µg), cefuroxime (CXM, 30 µg), cefoxitin (FOX, 30 µg), cefotaxime (CTX, 30 µg), ceftazidime (CAZ, 30 µg), ceftriaxone (CRO, 30 µg), ciprofloxacin (CIP, 5 µg), colistin (DA, 10 µg), ertapenem (ERT, 10 µg), gentamicin (GM, 10 µg), imipenem (IMP, 10 µg), meropenem (MEM, 10 µg), norfloxacin (NOR, 10 µg), piperacillin-tazobactam (TZP, 100/10 µg), and trimethoprim/sulfamethoxazole (SXT, 1.25/23.75 µg).

For Enterococci, the following antibiotic disks were used according to CLSI guidelines (CLSI 2019). Each disk (Becton Dickinson, Heidelberg, Germany) contained ampicillin (AM, 10 µg), cefoperazone-sulbactam (sulperazone) (SPZ, 75/30 µg), cefotaxime (CTX, 30 µg), ceftazidime (CAZ, 30 µg), ceftriaxone (CRO, 30 µg), ciprofloxacin (CIP, 5 µg), colistin (DA, 10 µg), ertapenem (ETP, 10 µg), gentamicin (GM, 10 µg), imipenem (IMP, 10 µg), meropenem (MEM, 10 µg), norfloxacin (NOR, 10 µg), penicillin (P, 10 µg), piperacillin-tazobactam (TZP, 100/10 µg), and vancomycin (VA, 30 µg).

Drug-resistant categories were defined as follows: multidrug-resistant (MDR) strains were defined as isolates resistant to at least one agent in ≥3 different antimicrobial categories; extensive drug-resistant (XDR) strains were defined as those resistant to at least one agent in all but two or fewer antimicrobial categories; and pan drug-resistant (PDR) strains were defined as those resistant to all classes except colistin [8].

### C. Ethical statement

This study was approved by the institutional ethics committee of Faculty of Medicine (REC58-1830-04-8, REC60-234-07-7, REC63-557-4-7, and REC66-381-38-7) and was performed in accordance with the principles of the Helsinki Declaration. The requirement for informed consent was waived as this study was an observational retrospective analysis, and all patient data were anonymized.

### D. Statistical analyses

Demographic data are reported as counts with percentages. SPSS Statistics, version 23 (SPSS Inc., Chicago, IL, USA), was utilized to analyze all statistical data.

## III. RESULTS AND DISCUSSION

Out of the 61 bacterial isolates analyzed, the predominant isolate was multidrug-resistant *Pseudomonas aeruginosa* (MDRPA), accounting for 54.1% (33 isolates) followed by *P. mirabilis*, which constituted 27.9% (17 isolates), VRE at

8.2% (5 isolates), and ESBL-producing *E. coli* and *K. pneumoniae*, which together made up 9.8% (6 isolates). The incidence of these bacterial isolates was notably higher in male infants, representing 62.3% (38 isolates) of the total. The most common sources of positive isolates were sputum samples, accounting for 32.8% (20 isolates), and genitourinary tract samples, which constituted 16.4% (10 isolates). In terms of infection rates across different hospital units, the highest rates were observed in the pediatric intensive care unit (PICU), with 32.8% (20 isolates), followed by the pediatric ward at 23.0% (14 isolates), the medical ward at 9.8% (6 isolates), and the operating room at 3.3% (2 isolates) as depicted in Table 1.

This study highlights the critical issue of MDR bacterial infections in pediatric patients, particularly in Southern Thailand. The high prevalence of MDRPA, VRE, and ESBL-producing bacteria aligns with global trends, where antibiotic resistance is increasingly recognized as a major public health threat [9]. The PICU emerged as a hotspot for MDR infections, consistent with previous studies indicating that intensive care units are high-risk environments for MDR pathogens [10].

The high prevalence of MDRPA (54.1%) as depicted in Fig. 1 is comparable to findings from other regions. For instance, a study conducted in India reported a similar prevalence of MDRPA in pediatric patients as 32-38% [11]. Another study in China found that MDRPA was the most common MDR pathogen in pediatric ICUs [12]. These findings suggest that MDRPA is a global concern, particularly in intensive care settings.

The prevalence of VRE (8.2%) in our study is lower than that reported in some Western countries but higher than in some Asian countries [13]. A study in the United States reported a VRE prevalence of 15% in pediatric patients [14], while a study in Japan reported a prevalence of 5% [15].

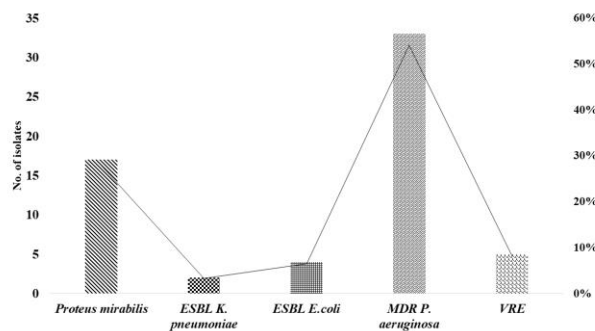


Fig. 1. Prevalence of bacterial pathogens in pediatric infections from tertiary care hospitals, Southern Thailand, 2012–2024 given as numbers and percentages of isolates.

The variation in VRE prevalence could be attributed to differences in antibiotic usage patterns and infection control practices across regions.

The prevalence of ESBL-producing *E. coli* and *K. pneumoniae* (9.8%) in our study is consistent with global trends. A study in Europe reported a similar prevalence of

ESBL-producing bacteria in pediatric patients [16], while a study in the maternity ward of Mulago hospital, Uganda that 36% of the isolates were ESBL-producing [17]. These findings highlight the global spread of ESBL-producing bacteria and the need for enhanced surveillance and control measures. Additionally, *P. mirabilis* infection was detected most frequently in early adolescence (12–17 years, 58.8%). This is related to an updated report indicating the presence of MDR in 36.4% of isolates, with the majority of these cases occurring in individuals under 18 years of age [18].

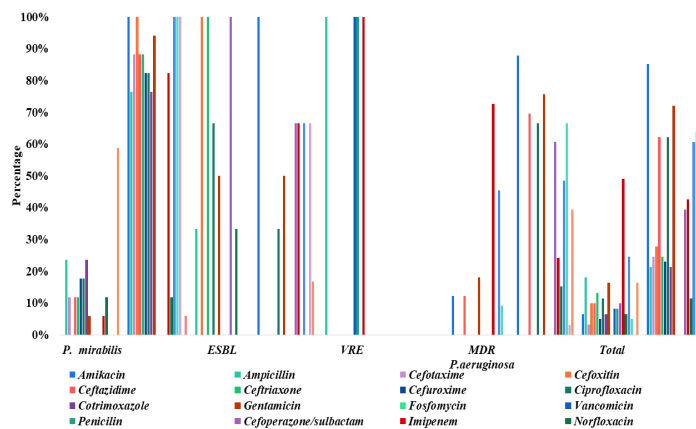


Fig. 2. Antimicrobial susceptibility profile of multidrug resistant bacteremia in pediatric patients from tertiary care hospitals, Southern Thailand, 2012–2024 given as numbers and percentages of isolates.

The high resistance rates of MDRPA to piperacillin/tazobactam (100%) and imipenem (90.3%) are alarming as shown in Fig. 2. Similar resistance patterns have been reported in other studies. A study in China found that MDRPA isolates were highly resistant to piperacillin/tazobactam and imipenem [19]. Another study in the Middle East reported similar resistance patterns [20]. These findings underscore the need for alternative treatment options for MDRPA infections.

The complete resistance of VRE to vancomycin and penicillin (100%) is consistent with previous studies. A study in the United States reported that VRE isolates were completely resistant to vancomycin and penicillin [21]. Another study in Europe found similar resistance patterns with resistance rates above 20% in clinical isolates of *Enterococcus faecium* in Netherlands and Germany [22]. These findings highlight the limited treatment options for VRE infections and the need for new antibiotics.

The resistance of ESBL-producing isolates to colistin (100%) and cefoperazone (100%) is concerning with relate from a patient with UTIs in Jordan and Ecuador [23, 24].

The current study also demonstrated *P. mirabilis* isolates exhibited resistance (58.8%) to colistin due to naturally resistant as also previously detected in Germany [25], while carbapenem, cefoxitin and Amikacin are susceptible to *P. mirabilis* infection with 100%, suggesting that these antibiotics can be used in the treatment of *P.*

*mirabilis* infections which relates with report from Taiwan in 99.8% [25].

The high prevalence of MDR bacteria in pediatric patients highlights the need for continuous monitoring and surveillance of antibiotic resistance patterns. Effective infection control measures, such as hand hygiene, environmental cleaning, and isolation of infected patients, are crucial for preventing the spread of MDR bacteria [26, 27]. Additionally, the revision of empirical treatment guidelines based on local resistance patterns is essential for improving patient outcomes [28].

#### IV. CONCLUSION

The study underscores a significant prevalence of multidrug-resistant (MDR) bacteria among hospitalized pediatric patients in Southern Thailand. The high resistance rates observed, particularly within the pediatric intensive care unit, necessitate continuous monitoring and surveillance of antibiotic resistance patterns to inform effective treatment strategies and robust infection control measures. These findings provide valuable insights into the epidemiology of MDR bacteria in the region, which can guide future research, revise empirical treatment guidelines, enhance and implications for clinical practice to combat the spread of antimicrobial resistance in Southern Thailand.

#### ACKNOWLEDGMENT

This study was supported by the Faculty of Medicine, Prince of Songkla University, with a Grant number of REC58-1830-04-8, REC60-234-07-7, REC63-557-4-7, and REC66-381-38-7, respectively.

#### References

- [1] R. Laxminarayan, A. Duse, C. Wattal, A. K. Zaidi, H. F. Wertheim, N. Sumpradit, E. Vlieghe, G. L. Hara, I. M. Gould, H. Goossens et al., "Antibiotic resistance-the need for global solutions," *Lancet Infect Dis*, vol. 13, no. 12, pp. 1057-1098, 2013.
- [2] C. L. Ventola, "The antibiotic resistance crisis: part 1: causes and threats," *P & T: a peer-reviewed journal for formulary management*, vol. 40, no. 4, pp. 277-283, 2015.
- [3] A. Y. Peleg, D. C. Hooper, "Hospital-acquired infections due to gram-negative bacteria," *The New England journal of medicine*, vol. 362, no. 19, pp. 1804-1813, 2010.
- [4] T. Yaikhan, S. Suwannasin, K. Singkhamanan, S. Chusri, R. Pomwiset, M. Wonglaphsuwan, and K. Surachat, "Genomic Characterization of Multidrug-Resistant *Enterobacteriaceae* Clinical Isolates from Southern Thailand Hospitals: Unraveling Antimicrobial Resistance and Virulence Mechanisms," *Antibiotics*, vol. 13, no. 6, pp. 531, 2024.
- [5] E. Tacconelli, E. Carrara, A. Savoldi, S. Harbarth, M. Mendelson, D. L. Monnet, C. Pulcini, G. Kahlmeter, J. Kluytmans, Y. Carmeli et al., "Discovery, research, and development of new antibiotics: the WHO priority list of antibiotic-resistant bacteria and tuberculosis," *The Lancet Infectious Diseases*, vol. 18, no. 3, pp. 318-327, 2018.
- [6] A. Parmanik, S. Das, B. Kar, A. Bose, G. R. Dwivedi, M. M. Pandey, "Current Treatment Strategies Against Multidrug-Resistant Bacteria: A Review," *Current microbiology*, vol. 79, no. 12, pp. 388, 2022.
- [7] Clinical and Laboratory Standards Institute (CLSI), "Performance Standards for Antimicrobial Susceptibility Testing. 34th ed. CLSI supplement M100. Clinical and Laboratory Standards Institute; 2024," 2024.
- [8] A. P. Magiorakos, A. Srinivasan, R. B. Carey, Y. Carmeli, M. E. Falagas, C. G. Giske, S. Harbarth, J. F. Hindler, G. Kahlmeter, B. Olsson-Liljequist et al., "Multidrug-resistant, extensively drug-resistant and pandrug-resistant bacteria: an international expert proposal for interim standard definitions for acquired resistance," *Clinical Microbiology and Infection*, vol. 18, no. 3, pp. 268-281, 2012.
- [9] S. Khafaja, Y. Salameh, C. F. Boutros, C. Awad, K. Faour, N. Tfaily, S. Merhi, Z. E. Zein, S. B. Karroum, D. Oweini et al., "Increased rate of multidrug-resistant gram-negative bacterial infections in hospitalized immunocompromised pediatric patients," *Frontiers in cellular and infection microbiology*, vol. 14, pp. 1382500, 2024.
- [10] C. González-Anleo, M. Girona-Alarcón, A. Casaldàliga, S. Bobillo-Perez, E. Fresán, A. Solé-Ribalta, E. Velasco-Arnaiz, M. Monsonís, M. Urrea, I. Jordan, "Risk factors for multidrug-resistant bacteria in critically ill children and MDR score development," *European journal of pediatrics*, vol. 183, no. 12, pp. 5255-5265, 2024.
- [11] S. Patel, H. Prabhakar, I. Kapoor, "Rate of Multidrug-resistance to Antimicrobial Drugs in Patients in Pediatric Neurointensive Care," *Indian journal of critical care medicine: peer-reviewed, official publication of Indian Society of Critical Care Medicine*, vol. 27, no. 1, pp. 67-72, 2023.
- [12] W. Huang, X. Wei, G. Xu, X. Zhang, X. Wang, "Carbapenem-resistant *Pseudomonas aeruginosa* infections in critically ill children: Prevalence, risk factors, and impact on outcome in a large tertiary pediatric hospital of China," *Frontiers in public health*, vol. 11, 2023.
- [13] S. Shrestha, S. Kharel, S. Homagain, R. Aryal, S. K. Mishra, "Prevalence of vancomycin-resistant *Enterococci* in Asia-A systematic review and meta-analysis," *J Clin Pharm Ther*, vol. 46, no. 5, pp. 1226-1237, 2021.
- [14] V. M. Eichel, K. Last, C. Brühwasser, H. von Baum, M. Dettenkofer, T. Götting, H. Grundmann, H. Guldénhöven, J. Liese, M. Martin et al., "Epidemiology and outcomes of Vancomycin-resistant *Enterococcus* infections: a systematic review and meta-analysis," *Journal of Hospital Infection*, vol. 141, pp. 119-128, 2023.
- [15] M. Tokano, N. Tarumoto, J. Sakai, K. Imai, M. Kodana, T. Kawamura, T. Maeda, S. Maesaki, "Vancomycin-resistant *Enterococcus faecium* in Japan, 2007-2015: a



molecular epidemiology analysis focused on examining strain characteristics over time," *Microbiol Spectr*, vol. 12, no. 1, pp. e0244423, 2024.

[16] N. A. El Aila, N. A. Al Laham, B. M. Ayesh, "Prevalence of extended spectrum beta lactamase and molecular detection of *blaTEM*, *blaSHV* and *blaCTX-M* genotypes among Gram negative bacilli isolates from pediatric patient population in Gaza strip," *BMC Infect Dis*, vol. 23, no. 1, pp. 99, 2023.

[17] R. Mayanja, A. Muwonge, D. Aruhomukama, F. A. Katabazi, M. Bbuye, E. Kigozi, A. Nakimuli, M. Sekikubo, C. F. Najjuka, D. P. Kateete, "Source-tracking ESBL-producing bacteria at the maternity ward of Mulago hospital, Uganda," *PLoS One*, vol. 18, no. 6, pp. e0286955, 2023.

[18] L. A. Salama, H. H. Saleh, S. H. Abdel-Rhman, R. Barwa, R. Hassan, "Assessment of typing methods, virulence genes profile and antimicrobial susceptibility for clinical isolates of *Proteus mirabilis*," *Ann Clin Microbiol Antimicrob*, vol. 24, no. 1, pp. 4, 2025.

[19] L. He, A. He, Y. Qian, "Imipenem-resistant *Pseudomonas aeruginosa* treated with piperacillin/tazobactam in a patient with severe pneumonia: a case report and related literature review," *Annals of Palliative Medicine*, vol. 10, no. 1, pp. 810-817, 2021.

[20] C. Truppa, M. N. Abo-Shehadeh, "Antimicrobial resistance among GLASS pathogens in conflict and non-conflict affected settings in the Middle East: a systematic review," *BMC Infect Dis*, vol. 20, no. 1, pp. 936, 2020.

[21] Y. Cetinkaya, P. Falk, C. G. Mayhall, "Vancomycin-Resistant *Enterococci*," *Clin Microbiol Rev*, vol. 13, no. 4, pp. 686-707, 2000.

[22] C. Cimen, M. S. Berends, E. Bathoorn, M. Lokate, A. Voss, A. W. Friedrich, C. Glasner, A. Hamprecht, "Vancomycin-resistant enterococci (VRE) in hospital

settings across European borders: a scoping review comparing the epidemiology in the Netherlands and Germany," *Antimicrobial Resistance & Infection Control*, vol. 12, no. 1, pp. 78, 2023.

[23] C. K. Dhanush, M. Lekshmi, S. K. Girisha, B. B. Nayak, S. H. Kumar, "Quinolone and Colistin Resistance Genes in Extended-Spectrum Beta-Lactamase (ESBL)-Producing *Escherichia coli* of Diverse Phylogenetic Groups Isolated from Seafood in Mumbai, India," *Applied Microbiology*, vol. 5, no. 1, pp. 3, 2025.

[24] W. M. Al Momani, N. Ata, A. O. Maslat, "Colistin-resistance genes in *Escherichia coli* isolated from patients with urinary tract infections," *PLoS One*, vol. 19, no. 6, pp. e0305431, 2024.

[25] J-T. Wang, P-C. Chen, S-C. Chang, Y-R. Shiau, H-Y. Wang, J-F. Lai, I. W. Huang, M-C. Tan, T-L. Y. Lauderdale, T. Hospitals, "Antimicrobial susceptibilities of *Proteus mirabilis*: a longitudinal nationwide study from the Taiwan surveillance of antimicrobial resistance (TSAR) program," *BMC Infect Dis*, vol. 14, no. 1, pp. 486, 2014.

[26] M. Elghanam, M. Emara, M. Abdelhalim, W. Moustafa, "Prevalence and Antibiotic Resistance Patterns of Multidrug-Resistant (MDR) Bacteria Isolated from Pediatric Intensive Care Units". *Egyptian Journal of Medical Microbiology*. 33(1):119-128, 2024.

[27] A.R. Rezk, S.A. Bawady, N.N. Omar, "Incidence of emerging multidrug-resistant organisms and its impact on the outcome in the pediatric intensive care". *Egyptian Pediatric Association Gazette*. 69(1):25, 2021.

[28] C. Elias, L. Moja, D. Mertz, M. Loeb, G. Forte, N. Magrini, "Guideline recommendations and antimicrobial resistance: the need for a change". *BMJ Open*. 7(7): e016264, 2017.

TABLE I  
THE DEMOGRAPHIC AND CLINICAL CHARACTERISTICS OF MULTIDRUG RESISTANT BACTEREMIA IN PEDIATRIC PATIENTS FROM  
TERTIARY CARE HOSPITALS, SOUTHERN THAILAND, 2012–2024.

Variables	No. of infection				Total (n=61, %)
	ESBL, n (%)	MDR <i>P. aeruginosa</i> , n (%)	<i>P. mirabilis</i> , n (%)	VRE, n (%)	
<b>Gender</b>					
Female	2 (33.3)	10 (30.3)	7 (41.2)	4 (80)	23 (37.7)
Male	4 (66.7)	23 (69.7)	10 (58.8)	1 (20)	38 (62.3)
<b>Group</b>					
infancy (28 days-12 months)	4 (66.7)	11 (33.3)	2 (11.8)	3 (60.0)	20 (32.8)
toddler (13 months-2 years)	1 (16.7)	11 (33.3)	0	0	12 (19.7)
early childhood (2-5 years)	0	5 (15.2)	2 (11.8)	0	7 (11.5)
middle childhood (6-11 years)	0	3 (9.1)	3 (17.6)	0	6 (9.8)
early adolescence (12-17 years)	1 (16.7)	3 (9.1)	10 (58.8)	2 (40.0)	16 (26.2)
<b>Infection sites</b>					
sputum	0	20 (60.6)	3 (17.6)	0	23 (37.7)
urine	5 (83.3)	4 (12.1)	4 (23.5)	1 (20.0)	14 (23.0)
blood	0	2 (6.1)	0	2 (40.0)	4 (6.6)
tissues	1 (16.7)	2 (6.1)	5 (29.4)	0	8 (13.1)
pus	0	2 (6.1)	2 (11.8)	0	4 (6.6)
rectal	0	0	0	1 (20.0)	1 (1.6)
plural	0	1 (3.0)	0	0	1 (1.6)
body fluid (abdominal fluid, bronchial wash, percutaneous nephrostomy, corneal ulcer, bile, and pleural fluid)	0	2 (6.1)	2 (11.8)	1 (20.0)	5 (8.2)
nasopharyngeal swab	0	0	1 (5.9)	0	1 (1.6)
<b>Source of infections</b>					
Pediatric Intensive Care Units (PICU)	2 (33.3)	15 (45.5)	4 (23.5)	3 (60)	24 (39.3)
Surgical ward	1 (16.7)	0	1 (5.9)	0	2 (3.3)
Pediatric ward	2 (33.3)	10 (30.3)	2 (11.8)	2 (40)	16 (26.2)
Operating room	0	2 (6.1)	6 (35.3)	0	8 (13.1)
Medical wards	1 (16.7)	5 (15.2)	1 (5.9)	0	7 (11.5)
Emergency room	0	1 (3.0)	0	0	1 (1.6)
Orthopedic ward	0	0	3 (17.6)	0	3 (4.9)

# Comprehensive protein analysis of blackchin tilapia for surimi production potential

Theeraphol Senphan<sup>1,a)</sup>, Natthapong Mungmueang<sup>1,b)</sup> and Chodsana Sriket<sup>2, c)</sup>

<sup>1</sup>Program in Food Science and Technology, Faculty of Engineering and Agro-Industry, Maejo University, Sansai, Chiangmai 50290, Thailand

<sup>2</sup>Food Innovation and Management Program, Department of General Science and Liberal Arts, King Mongkut's Institute of Technology Ladkrabang, Prince of Chumphon Campus, Pathiu, Chumphon 86160, Thailand

<sup>a)</sup> theeraphol\_s@mju.ac.th

<sup>b)</sup> maxnatthaphong\_2541@hotmail.com

Corresponding author: <sup>c)</sup> chodsana.sr@kmitl.ac.th

**Abstract.** Blackchin tilapia (*Sarotherodon melanotheron*), an invasive species in Thailand's waterways, presents potential for surimi production as an alternative to declining marine fish resources. This study investigated the chemical composition, protein fractionation, thermal properties, and secondary structure of blackchin tilapia muscle proteins. Fresh specimens were obtained from Chumphon Province and analyzed. Results showed that blackchin tilapia muscle contained 73.05±0.30% moisture, 21.13±0.17% protein, 2.22±0.13% lipid, 1.22±0.02% ash, and 2.38±0.08% carbohydrate. Protein fractionation revealed that myofibrillar protein was the predominant fraction (55.08±1.03%), followed by sarcoplasmic protein (23.42±1.23%), alkali-soluble protein (15.80±0.97%), non-protein nitrogen compounds (5.41±0.10%), and stromal protein (4.75±0.39%). Differential scanning calorimetry analysis showed distinct thermal transitions for each protein fraction, with myofibrillar proteins exhibiting a denaturation temperature of 64.14°C and enthalpy change of 28.65 J/g. FTIR spectroscopy revealed characteristic secondary structural features of the protein fractions, with distinctive amide I, II, and III bands. The high myofibrillar protein content, favorable thermal properties, and structural characteristics suggest that blackchin tilapia has promising potential as a raw material for surimi production, offering a strategy to control this invasive species while providing an alternative protein source for the food industry.

**Index Terms:** Blackchin tilapia, Surimi production, Protein fractionation, Thermal properties, FTIR spectroscopy

## I. INTRODUCTION

Surimi is a refined fish protein product obtained by washing minced fish flesh to remove fat and water-soluble components, leaving primarily myofibrillar proteins with excellent gel-forming properties [1]. As a key ingredient in the processed food industry, surimi is widely used to produce imitation seafood products such as crab sticks, fish balls, and various other value-added items. The global surimi market continues to grow steadily, with projections reaching US\$4,404.4 million by 2027 at a compound annual growth rate of 5.6% [2].

Currently, surimi production relies heavily on marine fish species, particularly Alaska pollock, which is preferred for its white flesh and high gel strength. However, with declining marine fish catches worldwide, there is an urgent need to identify alternative raw materials for surimi production. Freshwater fish represents an interesting alternative, and although surimi from freshwater species typically yields lower production rates (less than 15% of fresh fish weight), it offers advantages in terms of production control compared to marine fish [3].

Blackchin tilapia (*Sarotherodon melanotheron*), a fish species native to Ghana [4], has become an invasive species in Thailand's waterways, threatening native aquatic species and impacting biodiversity [5]. Utilizing this invasive fish for surimi production represents a strategic approach to

controlling its population while simultaneously creating economic value [6]. However, producing high-quality surimi from blackchin tilapia requires understanding its fundamental biochemical properties, particularly protein characteristics, as these directly influence the functionality and quality of the final product.

The properties of fish muscle proteins, especially myofibrillar proteins, are crucial determinants of gel-forming ability in surimi [7]. These proteins are responsible for important functional attributes such as water-holding capacity, gel strength, and textural properties [8]. While extensive research has been conducted on the protein characteristics of various marine fish species used for surimi production [9], limited information exists regarding the protein composition and properties of blackchin tilapia.

This research aims to investigate the chemical composition and protein fractionation of blackchin tilapia muscle as the first research phase toward its utilization in surimi production. The findings will provide essential baseline information for understanding the potential of this species as an alternative raw material for surimi processing and contribute to the development of appropriate processing technologies in subsequent research phases.

TABLE I  
PROXIMATE COMPOSITION OF BLACKCHIN  
TILAPIA MUSCLE

Compositions	Content (%)
Moisture	73.05±0.30 <sup>a</sup>
Protein	21.13±0.17 <sup>b</sup>
Lipid	2.22±0.13 <sup>c</sup>
Ash	1.22±0.02 <sup>c</sup>
Carbohydrate	2.38±0.08 <sup>c</sup>

NOTE: VALUES ARE MEAN ± STANDARD DEVIATION (N=3).  
DIFFERENT SUPERScript LETTERS IN THE SAME COLUMN  
INDICATE SIGNIFICANT DIFFERENCES (P < 0.05).

## II. METHODOLOGY

### Fish Sample Preparation

Fresh blackchin tilapia (*S. melanotheron*) were purchased from local fishermen in Chumphon Province, Thailand. After harvesting, the fish were immediately stored in ice at a fish:ice ratio of 1:2 (w/w) and transported to the Food Innovation and Management Laboratory within 3 hours. Upon arrival, the fish were washed thoroughly to remove mucus and impurities, and excess water was drained before further analysis.

### Proximate Composition Analysis

The proximate composition of blackchin tilapia muscle was determined according to AOAC methods [10]. Moisture content was determined by oven drying at 105°C until constant weight (AOAC method 950.46). Crude protein content was analyzed using the Kjeldahl method with a conversion factor of 6.25 (AOAC method 981.10). Lipid content was determined by the Soxhlet extraction method using petroleum ether (AOAC method 960.39). Ash content was determined by incineration in a muffle furnace at 550°C (AOAC method 920.153). Carbohydrate content was calculated by difference. All analyses were performed in triplicate, and results were expressed as a percentage wet weight basis.

### Protein Fractionation

Protein fractionation was performed according to the method of Hashimoto et al. [11] with slight modifications. Four protein fractions were sequentially extracted: non-protein nitrogen compounds, sarcoplasmic proteins, myofibrillar proteins, and alkali-soluble proteins. The insoluble residue was considered stromal proteins. Briefly, minced fish muscle (10 g) was homogenized with 40 mL of cold deionized water and centrifuged at 5,000 × g for 15 min at 4°C. The supernatant containing non-protein nitrogen compounds and sarcoplasmic proteins was collected. The

precipitate was then extracted with 40 mL of cold 0.5 M NaCl solution (pH 7.5) to obtain myofibrillar proteins. The residue was further extracted with 40 mL of cold 0.1 M NaOH to obtain alkali-soluble proteins. The remaining residue represented stromal proteins. The nitrogen content of each fraction was determined using the Kjeldahl method [10], and the protein content was calculated using a conversion factor of 6.25.

### Differential Scanning Calorimetry (DSC)

Thermal properties of blackchin tilapia muscle and different protein fractions were analyzed using differential scanning calorimetry (DSC) based on the method of Benjakul and Visessanguan [17] with slight modifications. Approximately 10 mg of sample was placed in an aluminum pan and sealed. The sample was heated from 20°C to 150°C at a rate of 10°C/minute using a differential scanning calorimetry device (X-DSC7000, SII Nano Technology Inc., Japan). An empty aluminum pan was used as a reference. The denaturation temperature ( $T_{max}$ ) and enthalpy change ( $\Delta H$ ) were calculated from the thermograms.

### Fourier Transform Infrared Spectroscopy (FTIR)

The secondary structure of blackchin tilapia muscle proteins and different protein fractions was analyzed using Fourier transform infrared spectroscopy (FTIR) according to the method of Sae-Leaw and Benjakul [18] with modifications. Freeze-dried samples were analyzed using an FT-IR spectrometer (EQUINOX 55, Bruker, Ettlingen, Germany) in the wavenumber range of 4000-400 cm<sup>-1</sup>. The spectra were recorded with 32 scans at a resolution of 4 cm<sup>-1</sup>. The secondary structure components, including  $\alpha$ -helix and  $\beta$ -sheet, were determined by analyzing the amide I region (1700-1600 cm<sup>-1</sup>).

### Statistical Analysis

All experiments were performed in triplicate. Data were expressed as mean ± standard deviation. Statistical analysis was performed using one-way analysis of variance (ANOVA) followed by Duncan's multiple range test. Differences were considered significant at p < 0.05.

## III. RESULTS AND DISCUSSION

### Proximate Composition

The proximate composition of blackchin tilapia muscle is presented in Table I. The moisture content was 73.05±0.30%, which is within the typical range (70-80%) reported for freshwater fish species [12]. Moisture content is an important parameter affecting the shelf life and processing characteristics of fish, including its suitability for surimi production, as excessive moisture can adversely affect gel strength [13].

The protein content of blackchin tilapia muscle was 21.13±0.17%, which is comparable to other tilapia species such as Nile tilapia (*Oreochromis niloticus*) with reported protein content ranging from 18.5% to 22.5% [14]. This relatively high protein content is favorable for surimi production, as protein content directly influences gel-forming ability and final product quality [15].



The lipid content was  $2.22 \pm 0.13\%$ , classifying blackchin tilapia as a low-fat fish ( $< 5\%$  fat) according to the classification proposed by Ackman [16]. The low-fat content is advantageous for surimi production, as lipids can interfere with protein gelation and contribute to off-flavors and reduced shelf-life due to oxidation. Low-fat fish typically yield surimi with better gel-forming properties and stability during frozen storage [17].

Ash content, representing the mineral content, was  $1.22 \pm 0.02\%$ . Low ash content is generally preferred for surimi production, as minerals can affect protein functionality. Carbohydrate content, calculated by difference, was  $2.38 \pm 0.08\%$ . Carbohydrates have a minimal direct impact on surimi quality, though they can contribute to Maillard reactions during processing and storage.

The proximate composition of blackchin tilapia appears favorable for surimi production, particularly its high protein and low fat content. These characteristics suggest potential for good gel-forming properties, which is a primary determinant of surimi quality [18].

### Protein Fractionation

The protein fractionation results of blackchin tilapia muscle are shown in Table II. Myofibrillar protein was the predominant fraction, accounting for  $55.08 \pm 1.03\%$  of the total protein. This proportion is particularly significant for surimi production, as myofibrillar proteins are primarily responsible for the gel-forming properties of surimi [19]. The myofibrillar protein content in blackchin tilapia is comparable to that of Alaska pollock (50-70%), which is the most widely used species for commercial surimi production.

TABLE II  
PROTEIN FRACTIONATION OF BLACKCHIN  
TILAPIA MUSCLE

Protein Fractions	Content (%)
Non-protein nitrogen	$5.41 \pm 0.10^d$
Sarcoplasmic proteins	$23.42 \pm 1.23^b$
Myofibrillar proteins	$55.08 \pm 1.03^a$
Alkali-soluble proteins	$15.80 \pm 0.97^c$
Stromal proteins	$4.75 \pm 0.39^d$

Note: Values are mean  $\pm$  standard deviation ( $n=3$ ). Different superscript letters in the same column indicate significant differences ( $p < 0.05$ ).

Sarcoplasmic proteins constituted  $23.42 \pm 1.23\%$  of the total protein, which is within the typical range (20-30%) for fish muscle. These water-soluble proteins include enzymes, myoglobin, and other globular proteins that are largely removed during the washing process in surimi production. The washing process is crucial for improving the gel-forming properties of surimi by concentrating myofibrillar proteins and removing components that can interfere with gelation.

Alkali-soluble proteins accounted for  $15.80 \pm 0.97\%$  of the total protein. These proteins are soluble in alkaline solutions

and may contribute to the functional properties of fish muscle during processing. The role of alkali-soluble proteins in surimi quality is less well understood compared to myofibrillar and sarcoplasmic proteins.

Non-protein nitrogen compounds represented  $5.41 \pm 0.10\%$  of the total protein. These include free amino acids, peptides, nucleotides, and other nitrogenous compounds that contribute to the flavor characteristics of fish. Most of these compounds are removed during washing in surimi production, which can help reduce fishy odors in the final product.

Stromal proteins, primarily consisting of collagen and elastin, constituted the smallest fraction at  $4.75 \pm 0.39\%$  of the total protein. The low content of stromal proteins is favorable for surimi production, as these proteins have limited gel-forming ability and can interfere with the gelation of myofibrillar proteins.

The protein distribution in blackchin tilapia muscle, particularly the high proportion of myofibrillar proteins, suggests good potential for surimi production. The ratio of myofibrillar to sarcoplasmic proteins (approximately 2.35:1) is comparable to that of many commercial surimi species, indicating that blackchin tilapia could be a suitable alternative raw material for surimi production.

### Thermal Properties of Muscle Proteins

The DSC thermograms of blackchin tilapia muscle and its protein fractions are shown in Fig. 1. The whole blackchin tilapia muscle showed a major endothermic transition with a denaturation temperature of  $76.60^\circ\text{C}$  and peak maximum temperature ( $T_{\max}$ ) of  $91.42^\circ\text{C}$ , with an enthalpy change ( $\Delta H$ ) of  $14.75 \text{ J/g}$ . This thermal transition primarily reflects the denaturation of myofibrillar proteins, particularly myosin and actin, which are the major contractile proteins in muscle tissue.

Among the protein fractions, myofibrillar proteins exhibited a distinctive thermal transition with  $64.14^\circ\text{C}$  and  $T_{\max}$  of  $68.54^\circ\text{C}$  ( $\Delta H = 28.65 \text{ J/g}$ ). The lower denaturation temperature of the isolated myofibrillar proteins compared to the whole muscle suggests that these proteins may be stabilized by interactions with other components in the intact muscle system. The relatively high enthalpy value indicates the considerable energy required to unfold these highly ordered protein structures, which is consistent with their important structural role in muscle.

Sarcoplasmic proteins showed a thermal transition at  $76.60^\circ\text{C}$  with  $T_{\max}$  of  $91.42^\circ\text{C}$  ( $\Delta H = 14.75 \text{ J/g}$ ), which is characteristic of globular proteins. The stromal protein fraction exhibited a transition at  $61.51^\circ\text{C}$  with  $T_{\max}$  of  $72.14^\circ\text{C}$  ( $\Delta H = 13.25 \text{ J/g}$ ), reflecting the thermal behavior of collagen and other connective tissue proteins. Alkali-soluble proteins displayed a transition at  $71.06^\circ\text{C}$  with  $T_{\max}$  of  $85.55^\circ\text{C}$  ( $\Delta H = 28.35 \text{ J/g}$ ), while non-protein nitrogen compounds showed multiple transitions, including one at  $44.41^\circ\text{C}$  with  $T_{\max}$  of  $57.36^\circ\text{C}$  ( $\Delta H = 3.99 \text{ J/g}$ ) and another at  $79.54^\circ\text{C}$  with  $T_{\max}$  of  $83.25^\circ\text{C}$  ( $\Delta H = 12.04 \text{ J/g}$ ).

The thermal stability of the protein fractions generally follows the order: non-protein nitrogen compounds  $<$

myofibrillar proteins < stromal proteins < alkali-soluble proteins < sarcoplasmic proteins. This information on thermal transitions is valuable for understanding the behavior of blackchin tilapia proteins during heat processing, which is particularly relevant for surimi production where heat-induced gelation is a critical functional property.

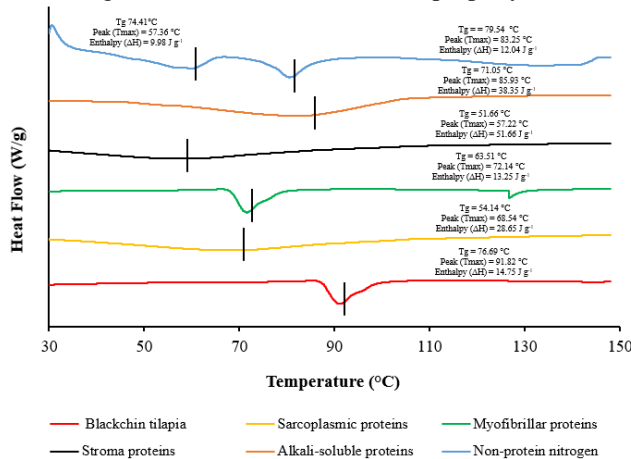


Fig. 1. Thermal properties of blackchin tilapia muscle and its protein fractions analyzed by differential scanning calorimetry. The thermograms show distinct denaturation patterns for whole muscle tissue (red), sarcoplasmic proteins (yellow), myofibrillar proteins (green), stromal proteins (black), alkali-soluble proteins (orange), and non-protein nitrogen (blue).

### FTIR Spectroscopic Analysis

The FTIR spectra of blackchin tilapia muscle and its protein fractions are presented in Fig. 2. The spectra exhibited characteristic absorption bands associated with protein structures. The amide I band (1700-1600 cm<sup>-1</sup>), primarily arising from C=O stretching vibrations, is particularly sensitive to protein secondary structure. The amide II band (approximately 1550 cm<sup>-1</sup>) results from N-H bending and C-N stretching vibrations, while the amide III band (approximately 1300 cm<sup>-1</sup>) is associated with a combination of C-N stretching and N-H bending.

All samples showed prominent absorption bands at approximately 3281 cm<sup>-1</sup> (N-H stretching) and 2925 cm<sup>-1</sup> (C-H stretching). The blackchin tilapia muscle and the various protein fractions exhibited distinctive patterns in the fingerprint region (1800-400 cm<sup>-1</sup>). Particularly notable were the absorption bands at 1640-1650 cm<sup>-1</sup> (amide I), 1536-1550 cm<sup>-1</sup> (amide II), and 1230-1250 cm<sup>-1</sup> (amide III), which provide information about protein conformation.

The non-protein nitrogen compounds fraction showed the most distinctive spectrum, with strong absorption bands at 1740 cm<sup>-1</sup> (characteristic of ester C=O stretching), 1650 cm<sup>-1</sup>, 1542 cm<sup>-1</sup>, 1239 cm<sup>-1</sup>, and in the fingerprint region between 1000-400 cm<sup>-1</sup>.

The myofibrillar protein fraction exhibited characteristic bands indicating a predominance of α-helical structures, which is consistent with the structural features of myosin. The differences in absorption patterns among the protein fractions reflect their distinct structural characteristics, which in turn influence their functional properties in food

systems, particularly their gelation behavior during surimi processing. These spectroscopic data provide valuable insights into the molecular structure of blackchin tilapia proteins that complement the thermal analysis and protein fractionation results.

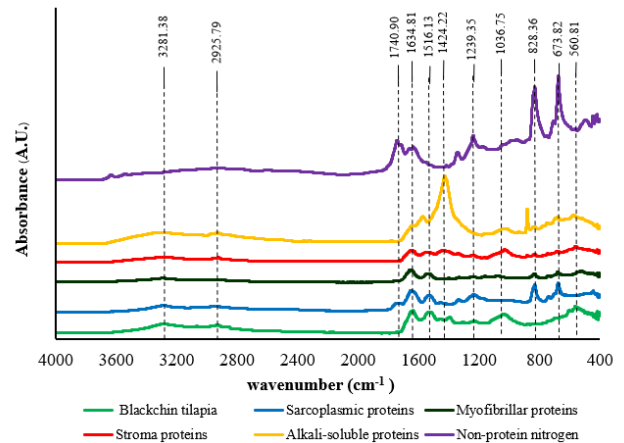


Fig. 2. FTIR spectra of blackchin tilapia muscle and its protein fractions. The spectra demonstrate characteristic absorption patterns of whole muscle tissue (green), sarcoplasmic proteins (blue), myofibrillar proteins (black), stromal proteins (red), alkali-soluble proteins (yellow), and non-protein nitrogen (purple) in the wavenumber range of 4000-400 cm<sup>-1</sup>.

### IV. CONCLUSION

A complete investigation of blackchin tilapia muscle proteins for surimi production is presented here. The proximate composition was high in protein (21.13%) and low in fat (2.22%). Myofibrillar proteins (55.08%) dominated protein fractionation, similar to commercial surimi species. Thermal study revealed unique denaturation patterns for each protein fraction, with myofibrillar proteins having adequate thermal characteristics (T<sub>g</sub> = 64.14°C, ΔH = 28.65 J/g) for heat-induced gelation. FTIR spectroscopy verified protein fraction structural characteristics that affect function. The high myofibrillar-to-sarcoplasmic protein ratio (2.35:1) and low stromal protein concentration (4.75%) improve blackchin tilapia's surimi production capability. These discoveries provide the metabolic basis for using this invasive species in surimi production, providing ecological benefits and a food industry protein supply.

### ACKNOWLEDGMENT

This research was financially supported by King Mongkut's Institute of Technology Ladkrabang Research Fund under Grant No 2568-02-08-002, given to Asst. Prof. Dr. Chodsana Sriket.

### REFERENCES

- [1] S. Benjakul, "Surimi: Science and Technology of Minced Fish Products," Food Science and Technology (in Thai), Kasetsart University, Bangkok, Thailand, 2017.
- [2] Grand View Research, "Surimi Market Size, Share & Trends Analysis Report By Source (Alaska Pollock,

- Itoyori, Croaker), By Application (Crab Sticks, Fish Sausage, Fish Balls), By Region, And Segment Forecasts, 2020 - 2027," Market Research Report, 2023.
- [3] B.B. Dağtekin, "Comparison of shear stress and chemical quality parameters of surimi from marine and freshwater fish species," *Journal of Aquatic Food Product Technology*, vol. 31, no. 5, pp. 482-498, 2022.
- [4] E.K. Abban, K. Agyakwa, and P. Falk, "Field guide to the freshwater fishes of Ghana," World Fish Center, 2004.
- [5] A. Suvarnaksha, S. Lek, S. Lek-Ang, and T. Jutagate, "Life history of the riverine cyprinid *Henicorhynchus siamensis* (Sauvage, 1881) in a small reservoir," *Journal of Applied Ichthyology*, vol. 27, no. 4, pp. 995-1000, 2011.
- [6] Y. Bettarel, M. Bouvier, C. Bouvier, C. Carre, A. Desnues, I. Domaizon, S. Jacquet, A. Robin, and H. Sime-Ngando, "Ecological traits of phytoplankton and planktonic viruses in Lake Geneva," *Freshwater Biology*, vol. 63, no. 10, pp. 1169-1184, 2018.
- [7] S. Benjakul, W. Visessanguan, and C. Tueksuban, "Heat-activated proteolysis in lizardfish (*Saurida tumbil*) muscle," *Food Research International*, vol. 35, no. 1, pp. 48-55, 2002.
- [8] W. Wuthipatpong, "Processing technology for quality improvement of surimi products" (in Thai), *Journal of Applied Science*, vol. 9, no. 2, pp. 19-30, 2010.
- [9] X.D. Sun and R.A. Holley, "Factors influencing gel formation by myofibrillar proteins in muscle foods," *Comprehensive Reviews in Food Science and Food Safety*, vol. 10, no. 1, pp. 33-51, 2011.
- [10] AOAC, "Official methods of analysis," Association of Official Analytical Chemists, 16th ed., Washington DC, 1999.
- [11] K. Hashimoto, S. Watabe, M. Kono, and K. Shiro, "Muscle protein composition of sardine and mackerel," *Bulletin of the Japanese Society for the Science of Fish*, vol. 45, no. 11, pp. 1435-1441, 1979.
- [12] M.N. Lund, M. Heinonen, C.P. Baron, and M. Estévez, "Protein oxidation in muscle foods: A review," *Molecular Nutrition & Food Research*, vol. 55, no. 1, pp. 83-95, 2011.
- [13] T. Chaijan, W. Panpipat, J. Panya, and M. Cheong, "Gel properties of surimi from yellow stripe trevally (*Selaroides leptolepis*) as affected by washing treatment and frozen storage," *Journal of Aquatic Food Product Technology*, vol. 29, no. 7, pp. 677-690, 2020.
- [14] L.S. Liu, Y.F. Guo, J.J. Li, D.D. Hao, and Z.Q. Zhuang, "Comparative study on protein composition and functional properties of tilapia surimi: Effects of washing cycles," *Journal of Texture Studies*, vol. 51, no. 1, pp. 93-103, 2020.
- [15] S. Rawdkuen, S. Benjakul, W. Visessanguan, and T.C. Lanier, "Rheological and textural properties of Pacific whiting surimi gels as influenced by chicken plasma," *International Journal of Food Properties*, vol. 10, no. 4, pp. 757-772, 2007.
- [16] R.G. Ackman, "Nutritional composition of fats in seafoods," *Progress in Food & Nutrition Science*, vol. 13, no. 3-4, pp. 161-289, 1989.
- [17] X. Jin, B. Chen, Y. Li, X. Yang, M. Chen, Y. Cai, and W. Wang, "Removal of lipid and fish bloodstain of freshwater carp surimi by modified washing processes," *Journal of Food Processing and Preservation*, vol. 44, no. 4, e14381, 2020.
- [18] J.W. Park, "Surimi and surimi seafood," 3rd ed., CRC Press, Boca Raton, FL, 2013.
- [19] N. Özogul, Y. Özogul, and E. Kuley, "The function and importance of trace elements on marine fish quality," in *Improving Seafood Products for the Consumer*, T. Børresen (Ed.), Woodhead Publishing, Cambridge, UK, 2008, pp. 348-366.
- [20] H. Ochiai, H. Hamada, M. Tamura, H. Kinoshita, and T. Ohnishi, "Effect of calcium chloride addition on gel formation of unwashed and washed meat from marine fish," *Journal of the Science of Food and Agriculture*, vol. 92, no. 12, pp. 2410-2415, 2012.
- [21] K. Martinsen and R. Offstad, "Post-mortem degradation of glycogen to lactic acid in muscle of stressed Atlantic cod (*Gadus morhua*)," *ICES Journal of Marine Science*, vol. 46, no. 1, pp. 1-7, 1989.
- [22] J.W. Park and T.M. Lin, "Surimi: Manufacturing and evaluation," in *Surimi and Surimi Seafood*, J.W. Park (Ed.), CRC Press, Boca Raton, FL, 2005, pp. 33-106.
- [23] T.C. Lanier, P. Carvajal, and J. Yongsawatdigul, "Surimi gelation chemistry," in *Surimi and Surimi Seafood*, J.W. Park (Ed.), CRC Press, Boca Raton, FL, 2005, pp. 435-489.
- [24] N.K. Howell, P. Arteaga, S. Nakai, and E.C.Y. Li-Chan, "Raman spectral analysis in the C-H stretching region of proteins and amino acids for investigation of hydrophobic interactions," *Journal of Agricultural and Food Chemistry*, vol. 47, no. 3, pp. 924-933, 1999.
- [25] S. Tadpitchayangkoon, J.W. Park, and J. Yongsawatdigul, "Conformational changes and dynamic rheological properties of fish sarcoplasmic proteins treated at various pHs," *Food Chemistry*, vol. 121, no. 4, pp. 1046-1052, 2010.
- [26] K.A. Beaulieu, S.S. Saffat, J. Yongsawatdigul, and J.W. Park, "Protein-protein interactions and transglutaminase catalyzed cross-linking in surimi gels," in *Seafood Enzymes: Utilization and Influence on Postharvest Seafood Quality*, N.F. Haard and B.K. Simpson (Eds.), Marcel Dekker, New York, 2000, pp. 335-354.
- [27] A.M. Herrero, P. Carmona, and M. Careche, "Raman spectroscopic study of structural changes in hake (*Merluccius merluccius* L.) muscle proteins during frozen storage," *Journal of Agricultural and Food Chemistry*, vol. 52, no. 8, pp. 2147-2153, 2004.
- [28] S. Sriket, P. Sriket, and S. Benjakul, "Effect of alkaline salt washing on gel-forming ability and protein pattern of surimi from some tropical fish," *Songklanakarin Journal of Science and Technology*, vol. 39, no. 3, pp. 373-381, 2017.
- [29] Y. Thawornchinsombut and J.W. Park, "Role of pH in solubility and conformational changes of Pacific

- whiting muscle proteins," *Journal of Food Biochemistry*, vol. 28, no. 2, pp. 135-154, 2004.
- [30] S. Benjakul and W. Visessanguan, "Transglutaminase-mediated setting in bigeye snapper surimi," *Food Research International*, vol. 36, no. 3, pp. 253-266, 2003.
- [31] D.D. Pietrowski, G.C. Tahergorabi, K.E. Matak, J.C. Tou, and J. Jaczynski, "Chemical properties of surimi seafood nutrified with  $\omega$ -3 rich oils," *Food Chemistry*, vol. 129, no. 3, pp. 912-919, 2011.



# Targeted Metabolomics Analysis of Plant Pathogen *Ralstonia solanacearum* Towards *Bacillus amyloliquefaciens*

James Danga<sup>1,2</sup>, Alisa S. Vangnai<sup>2,3</sup>, Pimsiri Tiayon<sup>2,4</sup> and Nawaporn Vinayavekhin<sup>1,2,a)</sup>

<sup>1</sup>Center of Excellence in Natural Products Chemistry, Department of Chemistry, Faculty of Science, Chulalongkorn University, Bangkok 10330, Thailand

<sup>2</sup>Center of Excellence in Biocatalyst and Sustainable Biotechnology, Faculty of Science, Chulalongkorn University, Bangkok 10330, Thailand

<sup>3</sup>Department of Biochemistry, Faculty of Science, Chulalongkorn University, Bangkok 10330, Thailand

<sup>4</sup>School of Agricultural Resources, Chulalongkorn University, Bangkok 10330, Thailand

<sup>a)</sup>Corresponding author, Email: nawaporn.v@chula.ac.th

**Abstract.** *Ralstonia solanacearum*, a soil-borne Gram-negative bacterial pathogen, causes crop wilt, posing a serious threat to global food security through significant agricultural losses. While *Bacillus amyloliquefaciens* has emerged as a promising biocontrol agent, its effectiveness in rescuing or fully protecting crops from this pathogen remains limited, and the mechanisms underlying their interactions are poorly understood. This study investigated how *R. solanacearum* responds to substances released by *B. amyloliquefaciens* BNC5 by analyzing changes in intracellular lipid metabolites using targeted metabolomics. Culturing *R. solanacearum* in casamino acid-peptone-glucose medium supplemented with 15% *B. amyloliquefaciens* supernatant for 24 h significantly increased the levels of fatty acids and phosphatidylethanolamines compared to control cultures without the supernatant. Other lipid metabolites, including monoacylglycerols, diacylglycerols, triacylglycerols, and phosphatidylglycerols showed minimal or no statistically significant changes. These substantial changes in *R. solanacearum*'s signaling and membrane lipid composition in response to *B. amyloliquefaciens* substances suggest that alterations in these pathways may influence the pathogen's sensitivity and defensive mechanism to biocontrol agents, presenting new opportunities for developing effective management strategies.

**Index Terms**— *Bacillus amyloliquefaciens*, lipids, metabolomics, *Ralstonia solanacearum*.

## I. INTRODUCTION

### 1.1 Background

*Ralstonia solanacearum* is an aerobic, Gram-negative, non-spore-forming bacterium that infects plants through wounds, root tips, or fissures at lateral root emergence sites [1]. After entry, *R. solanacearum* colonizes the root cortex and penetrates the xylem vessels, where it produces extracellular polysaccharides (EPS) that accumulate and block water flow, ultimately causing bacterial wilt [2]. This plant pathogen is a significant concern due to its broad host range, infecting over 200 plant species across more than 50 families, including tomato, tobacco, pepper, ginger, potato, and eggplant [1], [3].

Previous research has identified *Bacillus amyloliquefaciens*, a Gram-positive, aerobic rhizobacterium, as one of the most effective biocontrol agents [4]. It is known to produce secondary metabolites, including lipopeptides (iturins, surfactins, fengycins) and bacillomycin, which exhibit strong antagonistic activity against *R. solanacearum* [5], [6]. However, several challenges hinder its application as a biocontrol agent, such as the potential development of pathogen resistance [7], reduced efficacy under extreme environmental conditions [8], and limited understanding of its long-term impact on *R. solanacearum*. These limitations

underscore the need for further research to optimize its use and develop sustainable, effective disease management strategies.

It has been reported that alterations in membrane lipid composition and associated proteins play a crucial role in protecting bacterial cells from antimicrobial peptides and other compounds that disrupt membrane integrity [9], [10]. Building on these findings, this study investigates the metabolic response of *R. solanacearum* to substances released by *B. amyloliquefaciens* using liquid chromatography (LC)–mass spectrometry (MS)-based targeted metabolomics analysis. Specifically, it focuses on quantifying changes in key lipid classes, including free fatty acids (FFA), monoacylglycerols (MAG), diacylglycerols (DAG), triacylglycerols (TAG), phosphatidylethanolamines (PE), and phosphatidylglycerols (PG), to gain insight into the pathogen's adaptive strategies.

### 1.2 Objectives

This study aims to investigate the metabolic response of the plant pathogen *R. solanacearum* to secret metabolites from the biocontrol agent *B. amyloliquefaciens* using targeted metabolomics, providing insights to enhance biocontrol strategies and mitigate its agricultural impact.

## II. METHODOLOGY

### 2.1 Materials and growth conditions

The *R. solanacearum* race 1 used in this study was obtained from the Plant Protection Research and Development Office, Department of Agriculture, Ministry of Agriculture and Cooperatives, Thailand, while the *B. amyloliquefaciens* BNC5 was previously isolated from Nan province, Thailand. The bacteria were cultured in casamino acid-peptone-glucose (CPG) medium, which consisted of 1 g/L casamino acid sourced from Bio Basic (Toronto, Canada), 10 g/L peptone (CAS 91079-38-8) from HiMedia (Maharashtra, India), and 5 g/L D-glucose from Kemaus (Cheerybrook, NSW, Australia). The cultures were incubated aerobically at 30°C with agitation at 200 rpm.

### 2.2 Preparation of *B. amyloliquefaciens* BNC5 supernatant (BNC5sup)

*B. amyloliquefaciens* BNC5 was cultured for 24 h and centrifuged at 9000g, 10°C for 30 min to obtain the supernatant. The supernatant was then sterilized by filtering through a 0.2 µm membrane filter.

### 2.3 Metabolite extraction for metabolomics analysis

*R. solanacearum* was cultured in CPG medium containing 0% (control) or 15% BNC5sup for 24 h. Bacterial pellets were harvested by centrifugation at 9000g, 10°C for 30 min, and metabolites were extracted as previously described, with minor modifications [11]. Briefly, the pellets were resuspended in 3 mL of cold CPG medium and extracted with 6 mL of chloroform and 3 mL of methanol. The mixtures were centrifuged at 1500 g for 30 min to separate the organic and aqueous layers. The organic layer was carefully transferred into separate vials, and the solvent was evaporated under a stream of nitrogen.

### 2.4 LC-MS and LC-MS/MS analysis of metabolites

Each sample was analyzed using an Ultimate DGP-3600SD LC system coupled to a Bruker MicroTOF Q-II mass spectrometer in both positive and negative ion modes, as previously described [11].

### 2.5 Targeted metabolomics data analysis

Targeted metabolomics was employed to analyze changes in known lipids of *R. solanacearum*. Metabolite ions were identified, aligned, and quantified across samples using the XCMS program [12]. To account for differences in cell density, metabolite intensities were normalized to each sample's optical density at 600 nm (OD<sub>600</sub>). The normalized intensities of samples in the corresponding BNC5-treated and untreated groups were averaged and compared by calculating their ratios. Statistical significance was determined by Student's *t*-test. Specific metabolites—including FFA, MAG, DAG, TAG, PE, and PG—with even-numbered side chains ranging from 10 to 20 carbons [13],

[14] were identified based on accurate masses, tandem mass spectra, and retention times, which were compared to previously described values in the literature [9], [15].

## III. RESULTS AND DISCUSSION

To investigate the metabolic response of *R. solanacearum* to secreted substances from *B. amyloliquefaciens*, *R. solanacearum* was cultured in CPG medium with (RSBNC5m) or without (RSm; control) 15% BNC5sup for 24 h. Hydrophobic metabolites were then extracted from the cell pellets using a chloroform-methanol mixture and analyzed by LC-MS. Metabolites, including FFA, MAG, DAG, TAG, PE, and PG, were identified. The selected side chains—14:0, 16:0, 16:1, 18:0, 18:1, and 18:2, as well as their combinations—were chosen based on their predominance in *R. solanacearum* lipid profiles [16], [17].

Among the targeted lipids, only two metabolite classes, FFA and PE, contained side chains that exhibited at least a 2-fold, statistically significant increase ( $p < 0.05$ ) in RSBNC5m compared to the RSm control (Table 1 and Figure 1). Specifically, these intracellular metabolites—FFA (16:1), PE (16:0/16:0), PE (16:1/18:1), and PE (16:0/18:1)—showed 2.4-, 3.6-, 2.1-, and 2.1-fold increases, respectively, in the presence of BNC5sup. Additionally, PE (14:0/14:0) exhibited a 3.0-fold increase, though this change was not statistically significant. These findings suggest that *R. solanacearum* may modify its fatty acid and phospholipid biosynthesis pathways as part of an adaptive response to stress induced by *B. amyloliquefaciens* secreted metabolites.

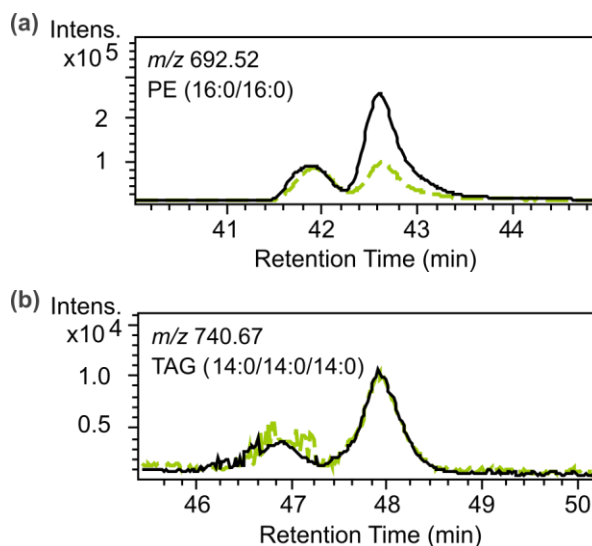


Fig. 1. Examples of extracted ion chromatograms of (a) PE (16:0/16:0) and (b) TAG (14:0/14:0/14:0) in *R. solanacearum*. The green dashed line represents the level of each of the respective metabolites in *R. solanacearum* grown alone (RSm; control), while the black line represents *R. solanacearum* supplemented with 15% *B. amyloliquefaciens* supernatant (RSBNC5m).

TABLE I  
RELATIVE LEVELS OF TARGETED LIPIDS IN *R. solanacearum* CULTURED WITH 15% *B. amyloliquefaciens* BNC5 SUPERNATANT COMPARED TO UNTREATED CONTROLS

Lipid class and acyl chain	Ion	<i>m/z</i>	Retention time (min)	RSBNC5m/RSm <sup>a,b</sup>
Free fatty acid (FFA)				
14:0	[M - H] <sup>-</sup>	227.20	19.6	1.7*
16:1	[M - H] <sup>-</sup>	253.22	19.9	2.4*
16:0	[M - H] <sup>-</sup>	255.23	20.4	1.2
18:2	[M - H] <sup>-</sup>	279.23	20.4	1.7
18:1	[M - H] <sup>-</sup>	281.25	20.7	1.5
18:0	[M - H] <sup>-</sup>	283.26	21.1	1.4
Monoacylglycerol (MAG)				
14:0	[M + Na] <sup>+</sup>	325.24	32.1	1.8***
16:0	[M + Na] <sup>+</sup>	353.37	34.4	1.3
Diacylglycerol (DAG)				
16:0/18:2	[M + Na] <sup>+</sup>	615.49	44.6	0.8
16:0/18:1	[M + Na] <sup>+</sup>	617.51	45.2	0.9
18:0/18:2	[M + Na] <sup>+</sup>	643.52	45.4	1.0
Triacylglycerol (TAG)				
14:0/14:0/14:0	[M + NH <sub>4</sub> ] <sup>+</sup>	740.67	47.9	1.1
18:2/18:2/18:2	[M + NH <sub>4</sub> ] <sup>+</sup>	896.76	48.6	1.1
18:1/18:1/18:1	[M + NH <sub>4</sub> ] <sup>+</sup>	902.81	49.2	1.5
Phosphatidylethanolamine (PE)				
14:0/14:0	[M + H] <sup>+</sup>	636.46	40.3	3.0
16:0/16:0	[M + H] <sup>+</sup>	692.52	42.6	3.6*
16:1/18:1	[M + H] <sup>+</sup>	716.52	42.3	2.1****
16:0/18:1	[M + H] <sup>+</sup>	718.53	43.0	2.1***
16:0/18:0	[M + H] <sup>+</sup>	720.54	43.7	2.4
18:1/18:1	[M + H] <sup>+</sup>	744.55	43.3	1.7
18:0/18:1	[M + H] <sup>+</sup>	746.56	44.0	1.0
Phosphatidylglycerol (PG)				
16:0/16:0	[M - H] <sup>-</sup>	721.50	38.3	1.7
16:0/18:2	[M - H] <sup>-</sup>	745.50	37.4	1.8
16:0/18:0	[M - H] <sup>-</sup>	749.53	40.3	1.2
18:1/18:1	[M - H] <sup>-</sup>	773.53	39.1	1.3
18:0/18:1	[M - H] <sup>-</sup>	775.54	40.6	1.3

Abbreviations: *m/z*, mass-to-charge ratio; RSBNC5m, *R. solanacearum* grown in CPG medium containing 15% *B. amyloliquefaciens* supernatant; RSm, *R. solanacearum* grown in CPG medium without *B. amyloliquefaciens* supernatant

<sup>a</sup>RSBNC5m/RSm value represents the ratio of the normalized mass ion intensity of *B. amyloliquefaciens* supernatant (BNC5sup)-exposed sample compared to the unexposed control

<sup>b</sup>Student's *t* test: \*, *p* < 0.05; \*\*, *p* < 0.01; \*\*\*, *p* < 0.005; \*\*\*\*, *p* < 0.001; *N* = 3

Bacteria are constantly adapting to environmental pressures, and one of the most effective ways they do this is by modifying their membrane lipid composition [18]. These changes help them maintain cellular integrity and survive under stressful conditions, such as exposure to antimicrobial compounds or competing microorganisms [9]. In this study, we explored how *R. solanacearum* responds to the biocontrol bacterium *B. amyloliquefaciens* by analyzing changes in its lipid profile. The results showed a significant increase in FFA and PE levels, while other lipid classes, including DAG and TAG, remained largely unchanged.

The observed increase in FFA levels in *R. solanacearum* upon exposure to *B. amyloliquefaciens* supernatant suggests a potential stress response mechanism. FFA plays a critical role in bacterial membrane homeostasis, serving as precursors for phospholipid biosynthesis and energy reservoirs during environmental stress [19]. In particular, the increased levels of FFA (16:1) observed in this study may facilitate the enhanced synthesis of PE (16:1/18:1),

supporting membrane adaptation under stress conditions.

PE is a crucial phospholipid in bacterial membranes, playing a key role in maintaining cellular integrity and enabling adaptive responses to environmental stressors [20]. PE also helps maintain membrane fluidity, allowing bacteria to adjust to changes in temperature, osmotic pressure, and pH, which is critical for survival in fluctuating environments [21]. In *R. solanacearum*, the upregulation of specific PE species, such as PE (16:0/16:0) and PE (16:1/18:1), highlights its importance in the bacterium's defensive mechanisms. This type of lipid remodeling has been observed in other bacteria when faced with antimicrobial stress, reinforcing the idea that *R. solanacearum* may be modifying its membrane to resist disruption by *B. amyloliquefaciens* metabolites, such as surfactins, fengycins, and iturins [13], [14]. Unlike energy-storage lipids such as DAG and TAG, which remain unchanged, PE's increase indicates that *R. solanacearum* is prioritizing membrane stability over metabolic storage, a common strategy among

bacteria facing environmental stress [9].

The ability of *R. solanacearum* to alter its lipid composition has significant implications for its virulence and survival. Membrane lipids are not just structural components; they also influence essential processes like biofilm formation and EPS production, which help the bacterium establish infections in host plants [1], [2]. The upregulation of PE could enhance the pathogen's ability to maintain its EPS production and biofilm stability, making it more resilient against *B. amyloliquefaciens*. This aligns with findings from quorum sensing studies, which highlight the role of membrane composition in regulating bacterial communication and virulence [15].

#### IV. CONCLUSION

In conclusion, this study reveals a key metabolic adaptation in *Ralstonia solanacearum* when exposed to *Bacillus amyloliquefaciens* supernatant, highlighting increased free fatty acid (FFA) and phosphatidylethanol (PE) levels as a potential defense mechanism. These findings underscore the role of lipid-mediated membrane remodeling in bacterial survival under biocontrol-induced stress and demonstrate the value of targeted metabolomics in elucidating pathogen adaptation. However, further validation through comprehensive untargeted metabolomics studies is needed to fully characterize the specific metabolite changes and provide deeper insights into the adaptive mechanisms employed by *R. solanacearum* during interactions with *B. amyloliquefaciens*. Understanding these responses opens new avenues for optimizing *B. amyloliquefaciens* as a biocontrol agent and developing targeted interventions to disrupt *R. solanacearum* survival strategies, ultimately enhancing the efficacy and sustainability of agricultural disease management.

#### REFERENCES

- [1] J. Mansfield *et al.*, "Top 10 plant pathogenic bacteria in molecular plant pathology," *Mol Plant Pathol*, vol. 13, no. 6, pp. 614-29, 2012.
- [2] A. C. Hayward, "Biology and epidemiology of bacterial wilt caused by *Pseudomonas solanacearum*," *Annu Rev Phytopathol*, vol. 29, pp. 65-87, 1991.
- [3] G. Orgambide, H. Montrozier, P. Servin, J. Roussel, D. Trigalet-Demery, and A. Trigalet, "High heterogeneity of the exopolysaccharides of *Pseudomonas solanacearum* strain GMI 1000 and the complete structure of the major polysaccharide," *Journal of Biological Chemistry*, vol. 266, no. 13, pp. 8312-8321, 1991.
- [4] L. Luo, C. Zhao, E. Wang, A. Raza, and C. Yin, "Bacillus amyloliquefaciens as an excellent agent for biofertilizer and biocontrol in agriculture: An overview for its mechanisms," *Microbiological Research*, vol. 259, p. 127016, 2022.
- [5] W. Raza, N. Ling, L. Yang, Q. Huang, and Q. Shen, "Response of tomato wilt pathogen *Ralstonia solanacearum* to the volatile organic compounds produced by a biocontrol strain *Bacillus amyloliquefaciens* SQR-9," *Sci Rep*, vol. 6, p. 24856, 2016.
- [6] A. Koumoutsis *et al.*, "Structural and functional characterization of gene clusters directing nonribosomal synthesis of bioactive cyclic lipopeptides in *Bacillus amyloliquefaciens* strain FZB42," *J Bacteriol*, vol. 186, no. 4, pp. 1084-96, 2004.
- [7] J. M. Raaijmakers and M. Mazzola, "Diversity and natural functions of antibiotics produced by beneficial and plant pathogenic bacteria," *Annu Rev Phytopathol*, vol. 50, pp. 403-24, 2012.
- [8] Y. Cao *et al.*, "Antagonism of Two Plant-Growth Promoting *Bacillus velezensis* Isolates Against *Ralstonia solanacearum* and *Fusarium oxysporum*," *Sci Rep*, vol. 8, no. 1, p. 4360, 2018.
- [9] J. R. Willdigg and J. D. Helmann, "Mini Review: Bacterial Membrane Composition and Its Modulation in Response to Stress," *Front Mol Biosci*, vol. 8, p. 634438, 2021.
- [10] A. H. Nguyen, K. S. Hood, E. Mileyskaya, W. R. Miller, and T. T. Tran, "Bacterial cell membranes and their role in daptomycin resistance: A review," *Front Mol Biosci*, vol. 9, p. 1035574, 2022.
- [11] N. Vinayavekhin, T. Wattanophas, M. F. Murphy, A. S. Vangnai, and G. Hobbs, "Metabolomics responses and tolerance of *Pseudomonas aeruginosa* under acoustic vibration stress," *PLoS One*, vol. 19, no. 1, p. e0297030, 2024.
- [12] C. A. Smith, E. J. Want, G. O'Maille, R. Abagyan, and G. Siuzdak, "XCMS: processing mass spectrometry data for metabolite profiling using nonlinear peak alignment, matching, and identification," *Anal Chem*, vol. 78, no. 3, pp. 779-87, 2006.
- [13] A. W. Kingston, C. Subramanian, C. O. Rock, and J. D. Helmann, "A  $\sigma$ W-dependent stress response in *Bacillus subtilis* that reduces membrane fluidity," *Mol Microbiol*, vol. 81, no. 1, pp. 69-79, 2011.
- [14] N. Vinayavekhin, G. Mahipant, A. S. Vangnai, and P. Sangvanich, "Untargeted metabolomics analysis revealed changes in the composition of glycerolipids and phospholipids in *Bacillus subtilis* under 1-butanol stress," *Applied Microbiology and Biotechnology*, vol. 99, no. 14, pp. 5971-5983, 2015.
- [15] C. M. Waters and B. L. Bassler, "Quorum sensing: cell-to-cell communication in bacteria," *Annu Rev Cell Dev Biol*, vol. 21, pp. 319-46, 2005.
- [16] J. Y. Liu *et al.*, "Proposal to classify *Ralstonia solanacearum* phylotype I strains as *Ralstonia nicotianae* sp. nov., and a genomic comparison between members of the genus *Ralstonia*," *Front Microbiol*, vol. 14, p. 1135872, 2023.
- [17] D. R. Zeiss *et al.*, "Lipopolysaccharides from *Ralstonia solanacearum* induce a broad metabolomic response in *Solanum lycopersicum*," *Front Mol Biosci*, vol. 10, p. 1232233, 2023.
- [18] T.-H. Lee, P. Charchar, F. Separovic, G. E. Reid, I. Yarovsky, and M.-I. Aguilar, "The intricate link between membrane lipid structure and composition and membrane structural properties in bacterial membranes," *Chemical Science*, vol. 15, no. 10, pp. 3408-3427, 2024.
- [19] Y. M. Zhang and C. O. Rock, "Membrane lipid homeostasis in bacteria," *Nat Rev Microbiol*, vol. 6, no. 3, pp. 222-33, 2008.
- [20] V. W. Rowlett *et al.*, "Impact of Membrane Phospholipid Alterations in *Escherichia coli* on Cellular Function and Bacterial Stress Adaptation," *J Bacteriol*, vol. 199, no. 13, 2017.
- [21] Q. Guo, L. Liu, and B. J. Barkla, "Membrane Lipid Remodeling in Response to Salinity," *Int J Mol Sci*, vol. 20, no. 17, 2019.



# Water-assisted Extraction Of Asiatic Acid from *Centella asiatica*

Zue Zue Win Myat<sup>1,a)</sup> and Surachai Pornpakakul<sup>2,b)</sup>

<sup>1</sup>Green Chemistry and Sustainability Program, Department of Chemistry, Faculty of Science, Chulalongkorn University

<sup>2</sup>Research Center for Bioorganic Chemistry, Department of Chemistry, Faculty of Science, Chulalongkorn University

<sup>a)</sup> zuezuewinmyat.mdy@gmail.com

<sup>b)</sup> Surachai.p@chula.ac.th

**Abstract.** *Centella asiatica* is widely recognized for its therapeutic properties, attributed to its bioactive triterpenoids—asiaticoside (AS), madecassoside (MS), asiatic acid (AA), and madecassic acid (MA). Among them, asiatic acid (AA), an ursane-type pentacyclic triterpene, plays a key role in wound healing and exhibits anti-proliferative properties. Efficient extraction of these compounds is crucial for their bioactivity studies and chemical characterization. This study explores water-assisted extraction as a green and efficient method for enhancing the yield and purity of AA, minimizing solvent use while maintaining bioactive integrity. Conventional methods often face limitations such as lengthy extraction times, low yields, and high energy consumption. Ultrasound-assisted extraction (UAE) presents a green and effective alternative, increasing solid particle permeability, accelerating diffusion of bioactives, and reducing both time and environmental impact. This study investigates the extraction of major triterpenoids, particularly asiatic acid, using a solvent system of water, ethyl acetate (EtOAc), and hexane (hex). Water, a polar protic solvent, enhances matrix permeability by disrupting hydrogen bonds and increasing cellulose fiber spacing. Two bioactive compounds, AA and MA, were identified and quantified using Thin Layer Chromatography (TLC) and Quantitative Nuclear Magnetic Resonance (qNMR). qNMR analysis revealed that 10 mg of water-based EtOAc extract (after hexane defatting) contained 19.83% AA and 16.48% MA (w/w), highlighting the efficiency of this solvent system. These findings suggest that the EtOAc:water mixture, following defatting with hexane, enhances the extraction and possibly the solubility or stability of asiatic acid more effectively than EtOAc alone.

**Keywords**—bioactive compounds, *Centella asiatica*, triterpenoids, water-assisted extraction

## I. INTRODUCTION

*Centella asiatica*, commonly known as gotu kola, bua-bok in Thai is a herbaceous plant natively in the tropical and subtropical regions including South Asia, Southeast Asia, South Africa, South Pacific and Eastern Europe.<sup>1</sup> Because of the vast array of therapeutic properties of *C. asiatica*, it has been consumed in some regions as a culinary vegetable. Historically, *C. asiatica* has been employed to boost memory, accelerate wound healing, address skin conditions, mitigate stress and anxiety, reduce cancer, prevent ulcers, and exhibit antibacterial and anti-inflammatory properties.<sup>2</sup> The therapeutic properties of *C. asiatica* are attributed to its rich phytochemical composition, which includes triterpenoids, flavonoids, phenolic acids, and other bioactive compounds. Among these, triterpenoids, such as asiaticoside (AS), madecassoside (MS), asiatic acid (AA), and madecassic acid (MA) have gained significant attention for their pharmacological activities, including antioxidant and anti-inflammatory effects. Asiatic acid (AA), an aglycone ursane-type pentacyclic triterpene saponin (C<sub>30</sub>H<sub>48</sub>O<sub>5</sub>), is a key chemical constituent of *C. asiatica*. It plays a crucial role in the plant's wound healing properties. Pharmacokinetic studies have demonstrated the significant contribution of asiatic acid to the therapeutic effects of *C. asiatica*.<sup>3</sup> Asiatic acid (AA), which contains a methyl substituent at C-19, has hydroxyl groups in its molecular structure that allow it to form hydrogen bonds. These interactions influence its biological activity and enhance its anti-proliferative

properties.<sup>4-6</sup> Some studies also suggest that it plays a crucial role in cancer treatment.<sup>7</sup>

Extraction is a crucial initial step for bioactivity studies and chemical analysis. The primary goal of the extraction process is to obtain the maximum amount of biologically active metabolites in the final extract while preserving its highest antioxidative properties.<sup>3</sup> The right choice of extraction method and solvent system can improve the quality of the extract and prevent loss of the target compounds. To obtain the desired compounds, isolation is indeed an important step in the process of identifying and characterizing the nature and composition of various bioactive compounds present in *C. asiatica*.<sup>8</sup> Many research works have been conducted to extract bioactive compounds of *C. asiatica* by conventional methods. Traditional extraction methods often suffer from drawbacks such as prolonged extraction times, low yields, and inefficient energy usage.<sup>9</sup> Among them, ultrasound-assisted extraction (UAE) is the most suitable choice to extract major compounds of plants with high antioxidant activities.<sup>2</sup> UAE efficiently extracts bioactive compounds from natural sources in a shorter time with minimal environmental impact, making it a green and effective technology. The attractiveness of UAE is due to its increasing the permeability of solid particles to the solvent, facilitating efficient polyphenol release through accelerated diffusion.<sup>5,9</sup> Acoustic cavitation is the primary driving force in ultrasound-assisted extraction. The collapse of cavitation bubbles, along with the action of ultrasonic waves, triggers various physical effects such as cell wall disruption, surface erosion, pore formation, shear forces, and enhanced swelling

and solvent uptake within the plant matrix. The resulting shockwaves and intensified particle collisions cause cellular fragmentation, which significantly reduces particle size, increases surface area, and enhances mass transfer efficiency. These changes collectively facilitate the rapid release and dissolution of bioactive compounds into the solvent.<sup>10, 11</sup> Plant cell walls are complex three-dimensional networks primarily composed of polysaccharides such as cellulose, hemicellulose, and pectin.<sup>12</sup> Plant matrices typically exhibit limited permeability to solvents due to their dense structural organization. However, this rigidity can be alleviated through a swelling process. Swelling arises from the interaction of polar solvents with the hydroxyl and carboxyl functionalities of cellulose fibers, leading to their adsorption onto these sites.<sup>13</sup> This molecular interaction increases the intermolecular spacing within the fibrous network, resulting in tissue expansion and subsequently enhancing solvent diffusion into the plant matrix.<sup>12, 13</sup> This study investigates the extraction of major bioactive triterpenoids, with a particular focus on asiatic acid, which has significant applications in the pharmaceutical and skincare industries. The extraction employs a solvent system consisting of water, and ethyl acetate (EtOAc) and hexane (hex). This step is critical in allowing efficient partitioning into the EtOAc phase. Protic solvents such as water predominantly induce swelling within the amorphous domains of cellulose, where they effectively disrupt the extensive hydrogen-bonded framework.<sup>12, 14</sup> Water-assisted approach not only enhances the extraction efficiency but also minimizes the use of excessive organic solvents, aligning with green extraction principles. The synergy between water pretreatment and EtOAc extraction ensures an efficient and selective recovery of asiatic acid and other major triterpenoids, making it a promising strategy for natural product isolation.

## II. METHODOLOGY

### 2.1 Materials

*C. asiatica* powder was purchased from Tha Prachan Herbs company. Thin layer chromatography (TLC) silica coated with 0.2 mm silica gel 60 F<sub>254</sub> 25 aluminium sheets 20 x 20 cm<sup>2</sup> purchased from Merck, Germany was used for monitoring the target compounds. Commercial *n*-hexane, and ethyl acetate (98.0%), were purchased from QREC, New Zealand and Lab Scan, Supelo. Standard compounds including asiatic acid, madecassic acid, asiaticoside and madecassoside were purchased from MySkinRecipes.

### 2.2 Defatting of *C. asiatica* plant powder

For defatting, *n*-hexane was warm on hot plate at 40°C and *Centella asiatica* plant powder: warm *n*-hexane (1:30, w/v) was used. The mixture was shaken frequently and left for 30 min and 1 hour to facilitate the removal of non-polar lipophilic compounds.<sup>15</sup> The hexane extracts (HE) were collected after filtration, while the remaining residue was air-dried and set aside for subsequent extraction using ultrasound-assisted extraction (UAE). The same procedure was done by optimizing the defatting time (x2 times defatting with hexane) and defatting temperature (40±5°C).

### 2.3 Ultrasound-assisted extraction

#### 2.3.1 Ultrasound-assisted extraction

(UAE) was performed successively using defatted *C. asiatica* residue : solvent mixture (1:40, w/v). Solvent systems were the mixture of EtOAc:water in a 2:1 ratio, and EtOAc:water in a 3:1 ratio at a temperature range of 45±5°C for 20 min. The extraction was carried out using an Shenzhen ultrasonic bath (PS-30A with 40 KHz frequency, 180W ultrasonic power and AC220-240V) to facilitate the efficient release of bioactive compounds from the plant matrix. The extracts were filtered through Whatman No.1 filter paper to separate any solid particles. The filtrate was then transferred to a separation funnel, where the organic (ethyl acetate) and aqueous layers were carefully separated. The organic layer containing the ethyl acetate extract (EE) and the water layer containing the water extract (WE) were collected separately. To remove residual solvents, both the ethyl acetate extract (EE) and the water extract (WE) were evaporated using a rotary evaporator (Rotavapor R-300, Büchi Labortechnik AG, Switzerland). The EtOAc extract and WE were evaporated at under reduced pressure. After solvent removal, both extracts were stored in a desiccator for 24 hour to ensure complete dryness and prevent any moisture absorption before further analysis.

**2.3.2** Individual UAE was carried out using *C. asiatica* powder:EtOAc:water (solvent mixture) in a 3:1 ratio (1:40, w/v) at the same temperature range of 45±5°C for 20 min without defatting with hexane initially. The extracts were first filtered using Whatman No.1 filter paper to remove solid residues. The resulting filtrate was then transferred into a separation funnel to allow phase separation. The immiscible layers: ethyl acetate (organic) and water (aqueous) were separated. The ethyl acetate layer, containing the ethyl acetate extract (EE-0), and the aqueous layer, containing the water extract (WE-0), were collected individually for further analysis.

**2.3.3** For comparative study, individual UAE was done using *C. asiatica* powder:*n*-hexane (1:30, w/v), and *C. asiatica* powder:EtOAc (1:30, w/v) at a temperature range of 45±5°C for 20 min. The extracts were filtered and evaporated at under reduced pressure. Individual hexane extract (hex-E) and EtOAc extract (EtOAc-E) were kept in a desiccator for 24 hour for further analysis.

#### 2.3.3 2.4 Thin Layer Chromatographic (TLC) Analysis

The extracts were spotted on normal-phase TLC Silica gel 60 F<sub>254</sub> and allowed them to dry. The TLC was developed using mobile phase which is the combination chloroform: methanol (9:1)<sup>16</sup> and visualized under UV and staining with *p*-anisaldehyde/H<sub>2</sub>SO<sub>4</sub>. Comparison of the R<sub>f</sub> (retention factor) values of the extracts to the standards was done to identify the presence of major compounds mainly asiatic acid (AA).<sup>17</sup>

#### 2.5 Nuclear Magnetic Resonance (NMR)

<sup>1</sup>H NMR spectroscopy was performed using a JEOL JNM-ECZ500R/SI spectrometer ((JEOL Ltd., Tokyo, Japan) operating at 500 MHz. The acquired spectra were analyzed with MestReNova v2.2.1.5206 software. Structural elucidation was carried out by interpreting chemical shifts, signal multiplicities, and comparison with AA and MA standard.

## 2.6 Quantitative NMR (qNMR)

For quantitative analysis, qNMR was performed to calculate the percentage of the target compound present in the sample.<sup>18</sup> The acquired spectra were analyzed with MestReNova v2.2.1.5206 software. 10 mg of sample (crude extract) was dissolved in CD<sub>3</sub>OD and 20  $\mu$ L of pyridine (10  $\mu$ L /mL, v/v), pyridine was added to the prepared solution. Quantification was calculated by using the following formula :

$$P\% = \frac{I_x}{I_i} \times \frac{N_i}{N_x} \times \frac{M_x}{M_i} \times \frac{m_i}{m_x} \times 100\% \quad (1)$$

Where P% is the percentage of compound present in sample,  $I_x$  is the integral of analyte,  $I_i$  is integral of internal standard peak,  $N_i$  is number of protons of the internal standard at specific signal (at  $\delta$ H 8.50 ppm for H-2 & H-6),  $N_x$  is number of protons of the analyte at specific signal (at  $\delta$ H 3.48 ppm for H-3 of AA,  $\delta$ H 3.56 ppm for H-3 of MA),  $M_x$  (g/mol) is the molecular weight of the target compound,  $M_i$  (g/mol) is the molecular weight of the internal standard,  $m_i$  (mg) is the mass of the internal standard, and  $m_x$  (mg) is the mass of the analyte.

## III. RESULTS AND DISCUSSION

TLC profiles of *C. asiatica* extracts obtained by different extraction parameters such as amount of defatting times and temperature, the ratios of EtOAc:Water were shown in Figure 1.

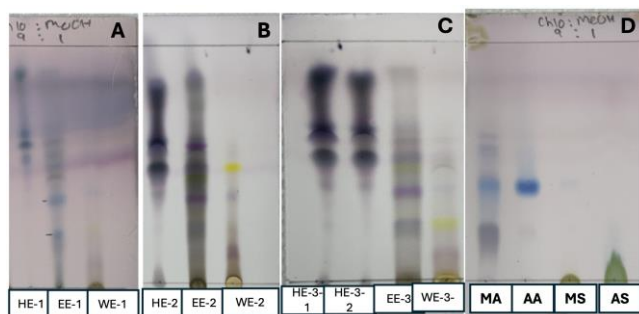


**Fig. 1.** TLC analysis of *Centella asiatica* extracts using Chloroform:Methanol (9:1) as the mobile phase. (A) HE-1, EE-1, WE-1: defatting for 30 min, EtOAc:Water (2:1), (B) HE-2, EE-2, WE-2: defatting for 1 hour, EtOAc:Water (3:1), (C) HE-3, EE-3, WE-3: defatting with hexane twice. (D) Standards: MA (madecassic acid), AA (asiatic acid), MS (madecassoside), AS (asiaticoside).

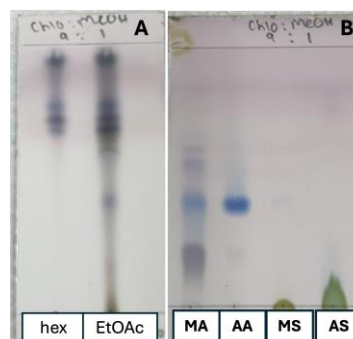


**Fig. 2.** TLC analysis of *Centella asiatica* extracts using Chloroform:Methanol (9:1) as the mobile phase. (A) hexane and ethyl acetate extracts, (B) standards : MA (madecassic acid), AA (asiatic acid), MS (madecassoside), AS (asiaticoside).

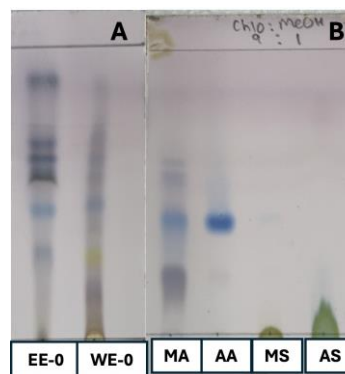


**Fig. 3.** TLC analysis of *Centella asiatica* extracts using Chloroform:Methanol (9:1) as the mobile phase. (A) ethyl acetate extract (EE-0) and water extract (WE-0) without defatting with hexane, (B) standards : MA (madecassic acid), AA (asiatic acid), MS (madecassoside), AS (asiaticoside).

TLC analysis of ethyl acetate (EtOAc) extracts in Figure 1 (A), (B), (C) revealed the presence of bioactive triterpenoids, primarily asiatic acid (AA) with an  $R_f$  values of 0.40 and madecassic acid (MA) at 0.30 in comparison to  $R_f$  values of standards in Figure 1 (D). As we can see in Figure 2 (A), only EtOAc can extract AA but it contains fats or waxes, however the hexane extract (hex) showed no visible triterpenoid spots. The role of hexane in defatting enhances the purity of polar bioactive compounds in *C. asiatica*. While EtOAc alone can extract AA, defatting the plant material with hexane followed by extraction using a water-based EtOAc system facilitates the partitioning of triterpenoids, thereby increasing the yield of asiatic acid in the EtOAc layer—a moderately polar solvent. This effect is evident in samples EE-1, EE-2, and EE-3 (Figure 1), where water played a crucial role by softening the plant matrix. These findings suggest that EtOAc, when combined with water, serves as the most effective solvent system for extracting bioactive triterpenoids—particularly asiatic acid from *C. asiatica*. The <sup>1</sup>H-NMR spectra of hexane crude extract, ethyl acetate (EtOAc) crude extract obtained from individual extractions, and water-based EtOAc extract after defatting with hexane were analyzed to evaluate the composition of each extract and the role of the solvent system in extraction.



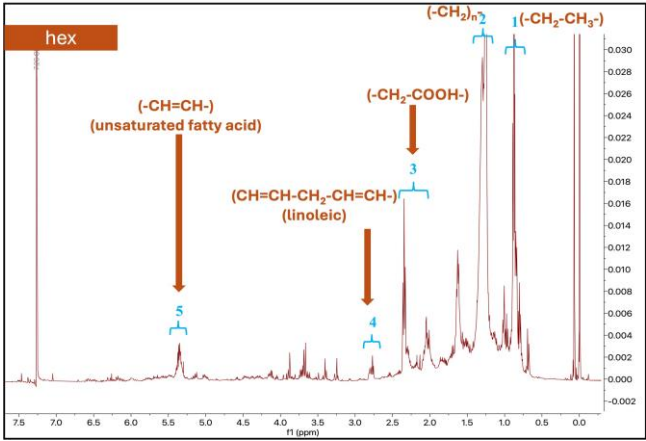


Fig. 3. 1H NMR spectrum of hexane extract (hex)

According to Siudem.et.al<sup>19</sup>, the hexane extract (hex) from *C. asiatica* was predominantly composed of fatty acids, as indicated in Figure 3.

TABLE I

1H-NMR DATA OF AA AND MA

Chemical shift $\delta$ (ppm)	Multiplicity	Integration	Functional group
5.23	t	1H	H-12 (olefinic proton)
3.50	d	1H	H-3 (hydroxyl-bearing methine)
3.36	s	1H	OH/methylene
3.27	s	1H	OH/methylene
3.25	s	—	OH/methylene
2.20	d	1H	Methylene protons
2.06	d (J = 6.7 Hz)	2H	—
2.01	d (J = 2.6 Hz)	1H	—
1.52–1.48	m	2H	—
1.14–1.13	s/d	3H	Methyl groups (C-27, C-28, etc.)
1.06	s	3H	Methyl group
0.84	s	3H	Methyl group
0.88–0.92	m	3H	Methyl groups
0.69	s	4H	Methyl group
4.36	d	1H	H-6 CH <sub>2</sub> -OH (indicative of MA)

The comparison of proton 1H NMR spectra of EtOAc only extract and water-based EtOAc extract after defatting with hexane twice to the standards 1H NMR of asiatic acid and madecassic acid in Figure 4 reveals identical chemical shifts of AA and MA in EE-3 at  $\delta$  5.23 (t, 1H) for H-12 which represents same functional groups such as olefinic group, 3.50 (d, 1H) for H-3 proton attached to hydroxyl group, 3.36 (s, 1H), 3.27 (s, 1H), 3.25 (s)-protons to other hydroxyl or methylene groups, 2.20 (d, 1H), 0.84 (s, 3H), 0.88-0.92 (m, 3H)-methyl groups attached to pentacyclic triterpenoid skeleton respectively. The peak at  $\delta$  4.36 (d, 1H) for H-6-CH<sub>2</sub> group attached to hydroxyl group indicated that EE-3 extract contains madecassic acid as well. According to these results, using EtOAc:water solvent system after defatting with hexane twice is more effective for extraction of our

target bioactive compounds especially asiatic acid. These findings highlight the crucial role of water in enhancing asiatic acid extraction, making it an essential component of the solvent system.

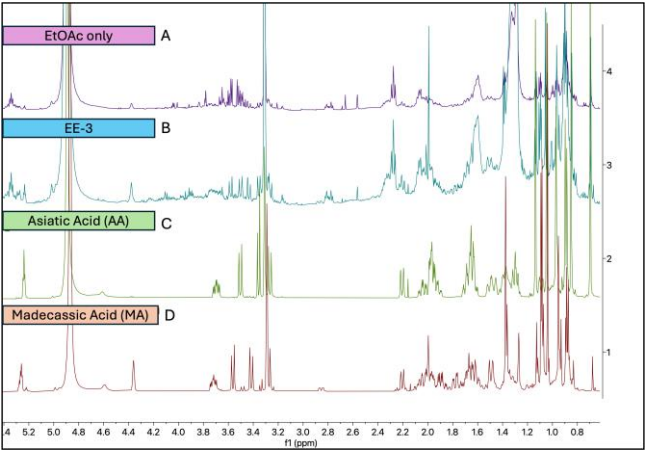


Fig. 4. 1H NMR spectra of (A) only EtOAc extract, (B) water-based EtOAc extract after defatting with hexane twice (C) standard Asiatic Acid, (D) standard Madecassic Acid

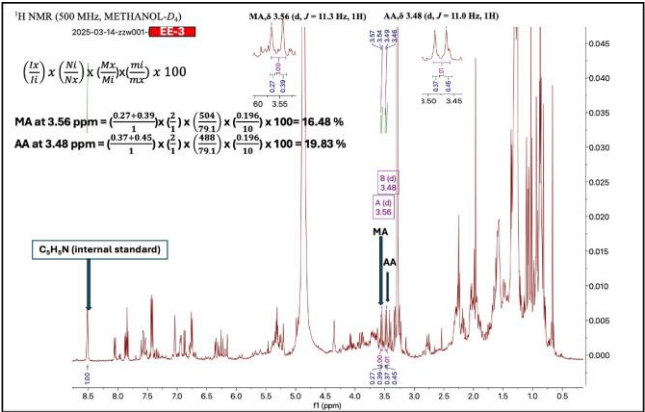


Fig. 5. 1H qNMR spectrum of water-based EtOAc extract after defatting with hexane twice

TABLE II

1H-qNMR DATAS OF WATER-BASED EtOAc EXTRACTS

Sample	Compound	Crude (m <sub>x</sub> ) (mg)	Percentage %
EtOAc only	MA	10	15.23
	AA	10	10.16
EE - 0	MA	10	1.62
	AA	10	5.32
EE - 1	MA	10	7.99
	AA	10	9.99
EE - 2	MA	10	2.49
	AA	10	3.39
EE - 3	MA	10	16.48
	AA	10	19.83

Quantification of the target compounds in the crude extract using EtOAc:water after defatting with hexane was



performed using qNMR and calculated by the equation (1), a straightforward yet precise method for determining the amount of target compound present in crude extract. As shown in Figure 5, 10 mg of water-based EtOAc extract contained 19.83% (w/w) asiatic acid and 16.48% (w/w) madecassic acid. These results indicated that employing an EtOAc:water solvent system after defatting with hexane twice is the most suitable choice to achieve our objective of obtaining a higher percentage of asiatic acid compared to other extracts mentioned in Table II. Furthermore, the detection of a higher percentage of asiatic acid compared to madecassic acid in water-based EtOAc extracts after suggests that AA might be more soluble in the chosen solvent system or more stable under the applied extraction conditions than when using EtOAc alone.

#### IV. CONCLUSION

This study highlights the critical role of water in enhancing the extraction of asiatic acid from *Centella asiatica*. The water-assisted extraction using an ethyl acetate (EtOAc) solvent system after defatting with hexane significantly improved the yield and purity of asiatic acid, demonstrating the synergistic effect of water in the extraction process. Water facilitated the partitioning of triterpenoids, thereby increasing asiatic acid recovery compared to other solvent systems. NMR and qNMR analyses confirmed that asiatic acid was the predominant bioactive compound in the water-based EtOAc extracts, most notably 19.83% (w/w) in EE-3, with a higher concentration than madecassic acid. These findings underscore the importance of water in optimizing the extraction process for bioactive compounds, particularly asiatic acid, which holds great promise for pharmaceutical and skincare applications.

#### ACKNOWLEDGMENT

The financial support, provision of chemicals and instruments, as well as the assistance provided by the Surachai Pornpakakul (SP) Lab group of Chulalongkorn University, and the Graduate Scholarship for ASEAN and Non-ASEAN Students were gratefully acknowledged.

#### REFERENCES

[1] Kamol, P.; Nukool, W.; Pumjaroen, S.; Inthima, P.; Kongbangkerd, A.; Suphrom, N.; Buddhachat, K. Assessing the genetic diversity of *Centella asiatica* (L.) Urb. and seasonal influence on chemotypes and morphotypes in Thailand. *Industrial Crops and Products* 2024, 218, 118976.  
[2] Brinkhaus, B.; Lindner, M.; Schuppan, D.; Hahn, E. G. Chemical, pharmacological and clinical profile of the East Asian medical plant *Centella asiatica*. *Phytomedicine* 2000, 7 (5), 427-448.  
[3] Khursheed, T.; Khalil, A. A.; Akhtar, M. N.; Khalid, A.; Tariq, M. R.; Alsulami, T.; Mugabi, R.; Nayik, G. A. Ultrasound-assisted solvent extraction of phenolics, flavonoids, and major triterpenoids from *Centella asiatica* leaves: A comparative study. *Ultrason Sonochem* 2024, 111, 107091.

[4] Li, Y.; Wang, J.; Li, L.; Song, W.; Li, M.; Hua, X.; Wang, Y.; Yuan, J.; Xue, Z. Natural products of pentacyclic triterpenoids: from discovery to heterologous biosynthesis. *Natural Product Reports* 2023, 40 (8), 1303-1353.  
[5] Sabaragamuwa, R.; Perera, C. O. Total Triterpenes, Polyphenols, Flavonoids, and Antioxidant Activity of Bioactive Phytochemicals of *Centella asiatica* by Different Extraction Techniques. *Foods* 2023, 12 (21), 3972.  
[6] Zulkiply, N. N.; Zakaria, R.; Long, I.; Abdullah, S. F.; Muhammad, E. F.; Wahab, H. A.; Sasongko, T. H. In Silico Analyses and Cytotoxicity Study of Asiaticoside and Asiatic Acid from Malaysian Plant as Potential mTOR Inhibitors. *Molecules* 2020, 25 (17), 3991.  
[7] Wicinski, M.; Fajkiel-Madajczyk, A.; Kurant, Z.; Gajewska, S.; Kurant, D.; Kurant, M.; Sousak, M. Can Asiatic Acid from *Centella asiatica* Be a Potential Remedy in Cancer Therapy?-A Review. *Cancers (Basel)* 2024, 16 (7), 1317.  
[8] Kandasamy, A.; Aruchamy, K.; Rangasamy, P.; Varadhaiyan, D.; Gowri, C.; Oh, T. H.; Ramasundaram, S.; Athinarayanan, B. Phytochemical Analysis and Antioxidant Activity of *Centella Asiatica* Extracts: An Experimental and Theoretical Investigation of Flavonoids. *Plants (Basel)* 2023, 12 (20), 3547.  
[9] Mohapatra, P.; Ray, A.; Jena, S.; Nayak, S.; Mohanty, S. Influence of extraction methods and solvent system on the chemical composition and antioxidant activity of *Centella asiatica* L. leaves. *Biocatalysis and Agricultural Biotechnology* 2021, 33(1), 101971.  
[10] Kumar, K.; Srivastav, S.; Sharanagat, V. S. Ultrasound assisted extraction (UAE) of bioactive compounds from fruit and vegetable processing by-products: A review. *Ultrasonics Sonochemistry* 2021, 70, 105325.  
[11] Wang, Z.; Mei, X.; Chen, X.; Rao, S.; Ju, T.; Li, J.; Yang, Z. Extraction and recovery of bioactive soluble phenolic compounds from brocade orange (*Citrus sinensis*) peels: Effect of different extraction methods thereon. *Lwt* 2023, 173, 114337.  
[12] Zuorro, A.; Iannone, A.; Lavecchia, R. Water–Organic Solvent Extraction of Phenolic Antioxidants from Brewers’ Spent Grain. *Processes* 2019, 7 (3), 126.  
[13] Zuorro. Influence of Extraction Conditions on the Recovery of Phenolic Antioxidants from Spent Coffee Grounds. *American Journal of Applied Sciences* 2013, 10 (5), 478-486.  
[14] El Seoud, O. A. Understanding solvation. *Pure and Applied Chemistry* 2009, 81 (4), 697-707.  
[15] Surma, M.; Sadowska-Rociek, A. Sample preparation techniques for the determination of fats in food. In *Reference Module in Chemistry, Molecular Sciences and Chemical Engineering*, 2024, 203-211.  
[16] Biradar, S. R. Extraction of Some Secondary Metabolites & Thin Layer Chromatography from Different Parts of *Centella Asiatica* L. (URB). *American Journal of Life Sciences* 2013, 1 (6), 243.  
[17] Lian, Y.; Jin, L.; Wang, F.; Zhang, J.; Ren, Y. Biosynthesis of plant-derived triterpenoid asiatic acid in

*Saccharomyces cerevisiae* cell factories. *Bio-organic Chemistry* 2024, 153, 107861.

[18] Bharti, S. K.; Roy, R. Quantitative <sup>1</sup>H NMR spectroscopy. *TrAC Trends in Analytical Chemistry* 2012, 35, 5-26.

[19] Siudem, P.; Zielinska, A.; Paradowska, K. Application of (<sup>1</sup>H) NMR in the study of fatty acids composition of vegetable oils. *Journal of Pharmaceutical and Biomedical Analysis* 2022, 212, 114658.

# Characterization of acid-soluble collagen isolated from Spotted Sickfish (*Drepane punctata*) skin

Yannawut Meuykamnerd<sup>1</sup>, Saofa Chaloeisamai<sup>1</sup>, Supaporn Maknamnit<sup>1</sup>  
and Sitthipong Nalinanon<sup>1,a)</sup>

<sup>1</sup>School of Food Industry, King Mongkut's Institute of Technology Ladkrabang, Ladkrabang, Bangkok 10520, Thailand

<sup>a)</sup> Corresponding author: sitthipong.na@kmitl.ac.th

**Abstract.** The objective of this research was to prepare and characterize acid-soluble collagen (ASC) from the skin of spotted sickfish (*Drepane punctata*). The yield of the resultant ASC from spotted sickfish skin was 25.44% (on a dry weight basis). ASC had a hydroxyproline content of  $91.60 \pm 0.26$  mg/g sample. Protein patterns revealed that ASC consisted of two  $\alpha$  chains ( $\alpha 1$  and  $\alpha 2$ ),  $\beta$  and  $\gamma$  chains as the major components. ASC had  $\alpha 1$  and  $\alpha 2$  intensity ratios of approximately 2:1 and was characterized as type I collagen. Fourier transform infrared (FTIR) spectroscopy revealed that ASC showed an FTIR spectrum consisting of major peaks similar to collagen type I, representing the existence of a triple helical structure. ASC was soluble at concentrations of NaCl below 2% (w/v), and its solubility decreased markedly at higher NaCl concentrations. ASC could dissolve well in acidic solutions (pH 1-4), but its solubility decreased with increasing pH.

**Index Terms**—Spotted sickfish, Characterization, Collagen, Fish, Acid-soluble collagen, FTIR, Solubility

## I. INTRODUCTION

Collagen is a vital fibrous protein that consists primarily of three key amino acids: glycine, proline, and hydroxyproline. These amino acids intertwine to create a unique triple-helix structure, which is essential for the protein's stability and function [1]. As a major component of connective tissues, collagen makes up approximately 30% of the total protein content found in animals, illustrating its significant role in bodily structure [2]. This remarkable protein is abundantly present throughout various parts of the body, including tendons, skin, bones, blood vessels, and other connective tissues, providing them with strength and elasticity [3]. Given its diverse functional properties—such as promoting skin elasticity, aiding in joint health, and supporting overall structural integrity. Collagen has found extensive applications across a myriad of industries. It is widely utilized in food products, medical therapies, pharmaceuticals, dietary supplements, and cosmetics, highlighting its versatility and importance in both the health and beauty sectors [1, 4].

According to Global Market Estimates [5], the global collagen market is anticipated to grow at an annual rate of 10.2% from 2023 to 2028. In the Asia-Pacific region, this growth rate is expected to reach 10.6%, with the most significant expansion projected in Asia, particularly in Thailand. Bovine and porcine skins serve as the primary raw materials in the collagen production industry [6]. As of 2023, the market share of bovine-derived collagen was 32% larger than that of fish-derived collagen, largely due to its more straightforward extraction process, which consumes less energy [5]. However, bovine collagen can trigger allergic reactions [1], and there are concerns regarding bovine

spongiform encephalopathy (BSE), which introduces additional risks [7]. Furthermore, religious restrictions prevent individuals following Islam, Hinduism, and Judaism from using bovine and porcine collagen [8]. Consequently, fish-derived collagen has become an increasingly popular alternative. Research has investigated the extraction and characterization of collagen from various fish species, including snakehead fish [9] and gourami fish [10].

The spotted sickfish (*Drepane punctata*) is a marine species notable for its thick skin [11], which is a suitable raw material for collagen extraction. Furthermore, its low market value makes it an economical resource, thereby enhancing the economic potential of this fish species. Considering these advantages, this study explores the feasibility of extracting collagen from the skin of the spotted sickfish using acid-based methods. The research aims to characterize various properties of the extracted collagen, including hydroxyproline content, protein pattern analysis, secondary structural properties, the effect of sodium on collagen solubility, and the influence of pH on collagen solubility. The findings of this study could contribute to the valorization of underutilized fish species and provide an alternative source of collagen that may serve as a substitute for bovine and porcine collagen. Thus, the primary objective of this study was to investigate the preparation of collagen from spotted sickfish skin through acid extraction methods and to characterize the properties of the resulting acid-soluble collagen.

## II. METHODOLOGY

### 1. Preparation of Spotted Sickfish Skin Samples

The spotted sickfish (*Drepane punctata*) was purchased from Ying Charoen Market in Bangkok District, Bangkok, Thailand. The fish were transported in polystyrene boxes

with ice at a 1:2 fish-to-ice ratio to the School of Food Industry, King Mongkut's Institute of Technology Ladkrabang. Upon arrival, the fish were cleaned with chilled tap water, eviscerated, and de-scaled. The skin was separated from the flesh and cut into  $2.0 \times 2.0$  cm<sup>2</sup> pieces. These were packed in polyethylene bags and stored at -20°C for up to three months, with all steps conducted at 0–4°C.

## 2. Preparation of Collagen from Spotted Sickfish Skin

### 2.1 Removal of Non-Collagenous Proteins and Fat

Non-collagenous proteins and fat were removed from fish skins following Sukkon et al. [10]. All procedures were performed at temperatures below 4°C. Fish skins were soaked in 0.1 M NaOH (1:15 w/v) for 6 h, with the solution stirred continuously and replaced every 2 h. The skins were then rinsed with cold distilled water until neutral pH. For fat removal, the skins were treated with 10% butyl alcohol (1:10 w/v) for 18 h, stirred continuously, and the solution was replaced every 6 h, followed by washing with cold water.

### 2.2 Extraction of Acid-soluble Collagen

The defatted skins were extracted using 0.5 M acetic acid at a skin-to-solution ratio of 1:15 (w/v). The mixture was continuously stirred for 48 h. Afterward, it was filtered through two layers of cheesecloth to separate the supernatant from the residue. The residue underwent a second extraction with 0.5 M acetic acid under the same conditions. The two supernatants were then combined for further processing.

### 2.3 Collagen Recovery

Collagen recovery was conducted using the method described by Truong et al. [9]. The combined supernatants from section 2.2 were salted out by adding NaCl to achieve a final concentration of 2.6 M. The mixture was then centrifuged at 9,000 g for 20 min at 4°C. Following centrifugation, the precipitate was dissolved in a minimal volume of 0.5 M acetic acid and dialyzed against distilled water for 12 h. Finally, the collagen solution was freeze-dried and referred to as “acid-soluble collagen; ASC”.

## 3. Extraction Yield and Hydroxyproline Content

The extraction yield on a dry weight basis was calculated using the following equation:

$$\% \text{ Yield (dry basis)} = (\text{Weight of freeze-dried ASC (g)} \times 100) / \text{Dry weight of fish skin sample (g)}$$

The hydroxyproline content was analyzed using the method by Bergman and Loxley [12]. The samples included fresh fish skin, fish skin after the removal of non-collagenous proteins, and the extracted collagen.

## 4 Characterization of ASC

### 4.1 Protein Pattern Analysis

The protein pattern of the collagen sample was analyzed using the Laemmli method [13]. Three grams of sample were homogenized with 27 ml of 5% SDS for 60 s, incubated at 85°C for 60 min, and centrifuged at 8,500 g for 5 min. The supernatant was evaluated for protein concentration via the

Biuret method, adjusted to 15 µg/µl, and mixed with SDS-PAGE sample buffer (1:1 v/v), then heated at 95°C for 3 min. The sample solution (15 µg protein) was loaded onto a polyacrylamide gel (7.5% running gel and 4% stacking gel) and electrophoresed at 15 mA/gel. Gels were stained with 0.25% Coomassie Brilliant Blue R-250 in 15% methanol and 5% acetic acid, then destained in 30% methanol and 10% acetic acid.

### 4.2 Secondary Structure Analysis

The secondary structure of collagen was analyzed using Fourier Transform Infrared Spectroscopy (FTIR), following the method described by Sukkon et al. [10]. Collagen samples were scanned with an FTIR spectrometer at a spectral resolution of 4 cm<sup>-1</sup> within the range of 4000–800 cm<sup>-1</sup>. Measurements were conducted at room temperature (25°C), and each spectrum averaged over 32 scans.

### 4.3 Effect of NaCl on Collagen Solubility

The solubility of collagen in NaCl was evaluated following the method of Sukkon et al. [11]. Collagen was dissolved in 0.5 M acetic acid at 6 mg/ml and stirred at 4°C for 24 hours. Aliquots of 5 ml of this solution were mixed with NaCl solutions at 0%, 1%, 2%, 3%, 4%, 5%, and 6% (w/v) in 0.5 M acetic acid, stirred for 30 minutes, and then centrifuged at 20,000 g for 30 min at 4°C. Protein content in the supernatant was measured using the Lowry method [14], and relative solubility was calculated based on the maximum solubility found.

### 4.4 Effect of pH on Collagen Solubility

The effect of pH on collagen solubility was studied following Nalinanon et al. [15]. A sample of 0.24 g of collagen was dissolved in 80 ml of 0.5 M acetic acid at 4°C for 12 h. Eight milliliters of this solution were distributed into ten 50-ml centrifuge tubes, where the pH was adjusted from 1 to 10 using 6 M sodium hydroxide or hydrochloric acid, and the final volume was made to 10 ml with distilled water. The solutions were centrifuged at 10,000 g for 30 minutes at 4°C. Protein content in the supernatant was measured using the method of Lowry et al. [14], and relative solubility was calculated based on the highest solubility pH.

## 5. Statistical Analysis

All data were analyzed using analysis of variance (ANOVA), and differences between means were evaluated using Duncan's multiple range test [16]. Data analysis was conducted with the IBM SPSS Statistic Program (Version 29).

## III. RESULTS AND DISCUSSION

### 1. Yield and Hydroxyproline Content

The extraction of ASC collagen from the skin of the spotted sicklefish (*Drepane punctata*) yielded 25.44% on a dry weight basis. However, this yield is lower compared to the collagen extracted from the skin of striped catfish (73.40%) [17], red snapper (41.19%) [18], and snakeskin gourami (34.65%) [10]. The variations in collagen yield among different fish species may be influenced by factors



such as species differences, environmental conditions, and the body temperature of the fish [19].

The hydroxyproline (Hyp) content in the skin of spotted sicklefish, along with non-collagenous protein removed skin and extracted ASC, was measured using the method described by Bergman and Loxley [12]. The results are summarized in Table I. Fresh spotted sicklefish skin contained  $20.67 \pm 0.25$  mg/g of Hyp. After treating the skin with NaOH solution to remove non-collagenous proteins, the Hyp content increased to  $22.28 \pm 0.20$  mg/g. Following acid extraction, the Hyp content in the collagen rose further to  $91.60 \pm 0.26$  mg/g. This increase in Hyp content aligns with the findings of Kittiphattanabawon et al. [20], who reported similar trends when extracting collagen from the skin and bones of bigeye snapper. The elevated Hyp content in the extracted collagen indicates a higher purity of collagen achieved through the removal of non-collagenous proteins during the extraction process. As a result, the Hyp concentration in the final collagen product was significantly higher than in the raw fish skin.

TABLE I

HYDROXYPROLINE (HYP) CONTENT IN SPOTTED SICKLEFISH SKIN AND COLLAGEN COUNTERPART

Sample	Hyp content (mg/g sample)*
Fresh skin	$20.67 \pm 0.25$
Non-collagenous protein removed skin	$22.28 \pm 0.20$
Acid-soluble collagen (ASC)	$91.60 \pm 0.26$

\*Values are presented as mean  $\pm$  standard deviation (n = 3).

## 2. Protein Pattern of Collagen

The protein pattern of ASC extracted from the skin of spotted sicklefish (*Drepane punctata*) is displayed in Fig. 1. The electrophoretic analysis revealed two distinct  $\alpha$ -chains ( $\alpha 1$  and  $\alpha 2$ ), a  $\beta$ -component (dimer), and a  $\gamma$ -component (trimer). This pattern aligns with the findings of Giraud-Guille et al. (2000), who noted that collagen extracted from fish skin typically consists of two  $\alpha$ -chains ( $\alpha 1$  and  $\alpha 2$ ), a  $\beta$ -component, and a  $\gamma$ -component. Similar protein compositions have also been identified in collagens extracted from salmon and cod [21], as well as in striped catfish [22]. The study was conducted under both reducing and non-reducing conditions. No differences in the protein pattern were observed between these two conditions, suggesting that the ASC from spotted sicklefish skin does not contain disulfide bonds. Furthermore, the protein pattern of spotted butterflyfish skin collagen was similar to that of calfskin collagen, exhibiting an  $\alpha 1$  to  $\alpha 2$  chain ratio of 2:1. This characteristic is indicative of type I collagen, which is the primary collagen found in connective tissues [23]. Typically, type I collagen consists of two forms of protein chain composition:  $([\alpha 1]_2\alpha 2)$  and  $(\alpha 1\alpha 2\alpha 3)$ . However, the  $\alpha 3$  chain is generally not detected because its position on the electrophoretic gel overlaps with the  $\alpha 1$  chain [24].

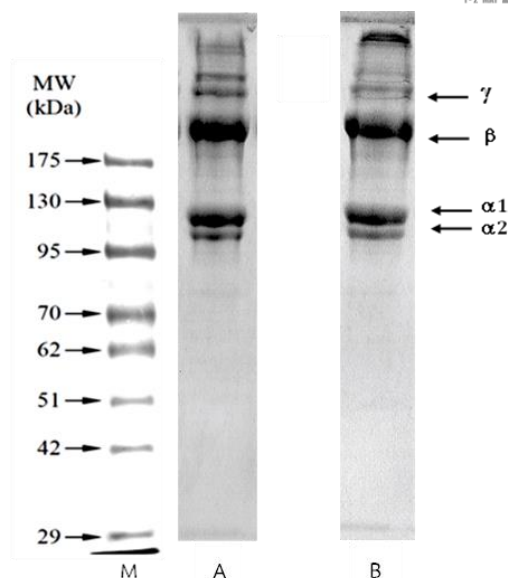


Fig. 1. Protein patterns of acid-soluble collagen (ASC) from the skin of spotted sicklefish (*Drepane punctata*) under non-reducing conditions (A) and reducing conditions (B). M denotes molecular weight marker.

## 3. Secondary Structure of ASC

The molecular structure of acid-soluble collagen (ASC) obtained from the skin of spotted sicklefish (*Drepane punctata*) was examined using Fourier Transform Infrared Spectroscopy (FTIR). The spectra were recorded from 4000 to 400  $\text{cm}^{-1}$  at ambient temperature, with the findings illustrated in Fig. 2. The FTIR spectra of the isolated collagen revealed distinct absorption bands that are consistent with collagens sourced from various fish species. The amide A band was detected at  $3283.03 \text{ cm}^{-1}$ , which is linked to the N–H stretching vibrations involved in hydrogen bonding [25]. When free N–H groups are present (not engaged in hydrogen bonding), the absorption band generally occurs between 3400 and 3440  $\text{cm}^{-1}$ . However, in the presence of hydrogen bonding at the N–H site, the absorption shifts to a lower wavenumber, usually around 3300  $\text{cm}^{-1}$ . Furthermore, the amide B band was identified at  $2922.65 \text{ cm}^{-1}$ , attributed to the asymmetrical stretching vibration of  $\text{CH}_2$  groups [23]. The amide I band was found at  $1629.74 \text{ cm}^{-1}$ , primarily associated with C=O stretching vibrations within peptide linkages [26]. This band is closely related to proteins' secondary structure [27]. The amide II band appeared at  $1541.07 \text{ cm}^{-1}$ , corresponding to N–H bending and C–N stretching vibrations [28]. The amide III band was recorded at  $1236.37 \text{ cm}^{-1}$ , related to C–N stretching and N–H bending vibrations, indicating the presence of the typical triple-helical structure of collagen molecules [23]. These findings validate that the collagen extracted from the skin of spotted sicklefish maintained its triple-helical molecular structure. Additionally, the absorption bands of amide A, amide B, amide I, amide II, and amide III found in the ASC from spotted sicklefish skin were comparable to those reported by Inthuserdh and Chiradetprapai [29], which examined collagen from Nile tilapia skin. Their research indicated absorption bands at 3331.22, 2933.10, 1651.18, 1534.83, and 1235.37  $\text{cm}^{-1}$ , respectively.

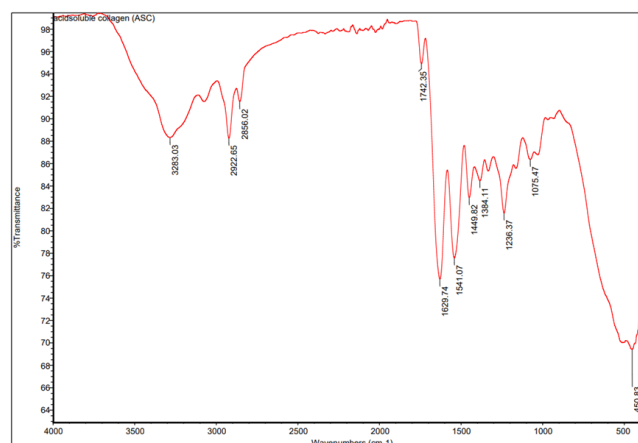


Fig. 2. Fourier Transform Infrared (FTIR) spectrum of acid-soluble collagen (ASC) extracted from the skin of spotted sicklefish (*Drepane punctata*).

#### 4. Solubility of ASC

The influence of NaCl concentration on the solubility of acid-soluble collagen (ASC) extracted from the skin of spotted sicklefish (*Drepane punctata*) is depicted in Fig. 3. The results demonstrate that ASC exhibits high solubility in sodium chloride solutions at concentrations below 2% (w/v). However, as the NaCl concentration increases, a marked decrease in solubility is observed, with a minimum solubility reached at 4% (w/v). Beyond this threshold, solubility remains consistently low. This trend can be attributed to the elevated ionic strength resulting from increased salt concentrations, which intensifies hydrophobic interactions among the collagen molecules. This phenomenon facilitates protein aggregation, leading to precipitation from the solution, commonly known as the "salting out" effect [30].

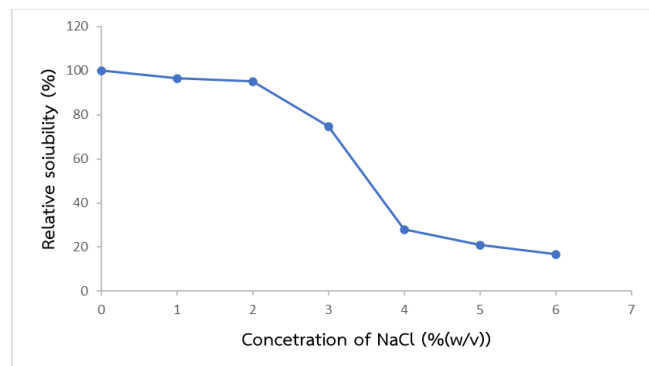


Fig. 3. Relative solubility of acid-soluble collagen (ASC) from spotted sicklefish skin in varying NaCl concentrations.

The impact of pH on the solubility of collagen extracted from the skin of spotted sicklefish is illustrated in Fig. 4. Under acidic conditions (pH 1 to 4), collagen exhibits substantial solubility, with relative solubility exceeding 90%. However, as the pH increases beyond this range, there is a progressive decline in solubility, reaching a nadir around pH 7. This reduction correlates with the isoelectric point (pI) of collagen, where the net charge of the protein molecules is neutral, thereby diminishing electrostatic repulsion. At this neutral pH, hydrophobic interactions become dominant,

prompting protein aggregation and subsequent precipitation from the solution, resulting in decreased solubility. Conversely, at pH levels below or above the pI, the net charge of the collagen molecules increases, enhancing electrostatic repulsion between the chains and thereby improving solubility [30]. Typically, the pI of collagen is reported to be within the pH range of 6 to 9 [3]. Consistent with these literature findings, our study demonstrates a marked reduction in collagen solubility between pH 7 and 10, as shown in Fig. 4.

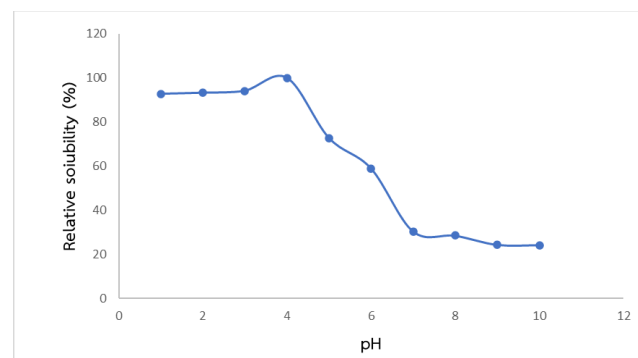


Fig. 4. Relative solubility of acid-soluble collagen (ASC) from spotted sicklefish skin at different pHs.

#### IV. CONCLUSION

This research focused on extracting acid-soluble collagen (ASC) from the skin of spotted sicklefish (*Drepane punctata*), achieving a yield of 25.44% based on dry weight. The extracted collagen was found to be of high purity, resembling type I collagen present in other fish species, as confirmed by hydroxyproline content and its protein pattern. Its solubility was influenced by pH levels and NaCl concentration, being higher in acidic conditions and low salt concentrations, while decreasing near the isoelectric point and with increased salt. The study suggests that spotted butterflyfish skin is a promising alternative for collagen extraction, suitable for use in food, cosmetics, and pharmaceuticals, and addresses concerns related to mammalian collagen sources.

#### ACKNOWLEDGMENT

The authors would like to extend their sincere appreciation to the School of Food Industry at KMITL for the generous financial support provided, which has contributed significantly to the success of this initiative.

#### REFERENCES

- [1] S. Benjakul, S. Nalinanon, and F. Shahidi, "Fish Collagen," in *Food Biochemistry and Food Processing: Second Edition*: Wiley-Blackwell, 2012, pp. 365-387.
- [2] A. J. Bailey and N. D. Light, *Connective Tissue in Meat and Meat Products*. Elsevier Applied Science, 1989.
- [3] E. Foegeding, T. Lanier, and H. Hultin, "Food Chemistry. Characteristics of Edible Muscle Tissue," ed: New York: Marcel Dekker, Inc, 1996.

- [4] P. Inthuserdh, "Collagen extraction from aquatic animal processing wastes and its applications," Department of Fisheries, Ministry of Agriculture and Cooperatives, Bangkok, Thailand, 2020.
- [5] G. M. Estimates. Global Collagen Market Size [Online] Available: <https://www.globalmarketestimates.com/market-report/collagen-market-4126>
- [6] T. Nagai, Y. Araki, and N. Suzuki, "Collagen of the skin of ocellate puffer fish (*Takifugu rubripes*)," *Food Chem.*, vol. 78, no. 2, pp. 173-177, 2002.
- [7] A. Jongjareonrak, S. Benjakul, W. Visessanguan, and M. Tanaka, "Isolation and characterization of collagen from bigeye snapper (*Priacanthus macracanthus*) skin," *Journal of the Science of Food and Agriculture*, vol. 85, no. 7, pp. 1203-1210, 2005.
- [8] S. Xuan Ri, K. Hideyuki, and T. Koretaro, "Characterization of molecular species of collagen in scallop mantle," *Food Chem.*, vol. 102, no. 4, pp. 1187-1191, 2007.
- [9] T. M. T. Truong, V. M. Nguyen, T. T. Tran, and T. M. T. Le, "Characterization of acid-soluble collagen from food processing by-products of Snakehead fish (*Channa striata*)," *Processes*, vol. 9, no. 7, p. 1188, 2021.
- [10] P. Sukkon, A. M. M. Ali, S. Nalinanon, H. Kishimura, and S. Takeungwongtrakul, "Characterization of acid soluble collagen from the skin of snakeskin gourami (*Trichogaster Pectoralis*)," *Carpathian J. Sci. Technol. Food*, Article vol. 12, no. 2, pp. 80-92, 2020.
- [11] F. Department of, *Thai Fish Species from Streams to Oceans: 95th Anniversary of the Department of Fisheries* (Department of Fisheries). Bangkok, Thailand: Ministry of Agriculture and Cooperatives, 2021.
- [12] I. Bergman and R. Loxley, "Two improved and simplified methods for the spectrophotometric determination of hydroxyproline," *Analytical Chemistry*, vol. 35, no. 12, pp. 1961-1965, 1963.
- [13] U. K. Laemmli, "Cleavage of structural proteins during the assembly of the head of bacteriophage T4," *Nature*, vol. 227, no. 5259, pp. 680-5, 1970.
- [14] O. H. Lowry, N. J. Rosebrough, A. L. Farr, and R. J. Randall, "Protein measurement with the Folin phenol reagent," (in eng), *Journal of Biological Chemistry*, vol. 193, no. 1, pp. 265-75, 1951.
- [15] S. Nalinanon, S. Benjakul, W. Visessanguan, and H. Kishimura, "Use of pepsin for collagen extraction from the skin of bigeye snapper (*Priacanthus tayenus*)," (in English), *Food Chem.*, Article vol. 104, no. 2, pp. 593-601, 2007.
- [16] R. G. D. Steel, J. H. Torrie, and D. A. Dickey, *Principles and procedures of statistics: a biometrical approach*. McGraw-Hill, 1997.
- [17] D. K. Vijayan *et al.*, "Extraction and characterization of acid soluble collagen (ASC) from airbladder of striped cat fish (*Pangasius hypophthalmus*)," *International Journal of Fisheries and Aquatic Studies*, vol. 6, no. 4, pp. 310-318, 2018.
- [18] B. F. D. Zaelani, M. Safithri, K. Tarman, I. Setyaningsih, and Meydia, "Collagen isolation with acid soluble method from the skin of Red Snapper (*lutjanus sp.*)," *IOP Conference Series: Earth and Environmental Science*, vol. 241, no. 1, p. 012033, 2019.
- [19] R. Duan, J. Zhang, X. Du, X. Yao, and K. Konno, "Properties of collagen from skin, scale and bone of carp (*Cyprinus carpio*)," *Food Chem.*, vol. 112, no. 3, pp. 702-706, 2009.
- [20] P. Kittiphattanabawon, S. Benjakul, W. Visessanguan, T. Nagai, and M. Tanaka, "Characterisation of acid-soluble collagen from skin and bone of bigeye snapper (*Priacanthus tayenus*)," *Food Chem.*, vol. 89, no. 3, pp. 363-372, 2005.
- [21] A. L. Alves, A. L. P. Marques, E. Martins, T. H. Silva, and R. L. Reis, "Cosmetic potential of marine fish skin collagen," *Cosmetics*, vol. 4, no. 4, p. 39, 2017.
- [22] P. Singh, S. Benjakul, S. Maqsood, and H. Kishimura, "Isolation and characterisation of collagen extracted from the skin of striped catfish (*Pangasianodon hypophthalmus*)," *Food Chem.*, vol. 124, no. 1, pp. 97-105, 2011.
- [23] J. H. Muyonga, C. G. B. Cole, and K. G. Duodu, "Characterisation of acid soluble collagen from skins of young and adult Nile perch (*Lates niloticus*)," *Food Chem.*, vol. 85, no. 1, pp. 81-89, 2004.
- [24] S. Kimura, "Wide distribution of the skin type I collagen  $\alpha 3$  chain in bony fish," *Comparative Biochemistry and Physiology Part B: Comparative Biochemistry*, vol. 102, no. 2, pp. 255-260, 1992.
- [25] B. B. Doyle, E. G. Bendit, and E. R. Blout, "Infrared spectroscopy of collagen and collagen-like polypeptides," *Biopolymers*, vol. 14, no. 5, pp. 937-957, 1975.
- [26] K. J. Payne and A. Veis, "Fourier transform ir spectroscopy of collagen and gelatin solutions: Deconvolution of the amide I band for conformational studies," *Biopolymers*, vol. 27, no. 11, pp. 1749-1760, 1988.
- [27] W. K. Surewicz and H. H. Mantsch, "New insight into protein secondary structure from resolution-enhanced infrared spectra," (in eng), *Biochim Biophys Acta*, vol. 952, no. 2, pp. 115-30, 1988.
- [28] S. N. Gharagheshlagh, M. R. Nourani, S. Jamili, M. J. Fatemi, and A. M. Sharifi, "Isolation and Characterization of acid-soluble Collagen from the Skin of *Scomberomorus guttatus* of Persian Gulf," *Journal of Applied Tissue Engineering*, vol. 5, no. 3, 2018.
- [29] P. Inthuserdha and N. Chiradetprapai, "Extraction of acid-soluble collagen from Nile tilapia (*Oreochromis niloticus*) skins," Fishery Technological Development Division, Department of Fisheries, Bangkok, Thailand, 2020.
- [30] F. Vojdani, "Solubility," in *Methods of Testing Protein Functionality*, G. M. Hall Ed., 1 ed. Great Britain: St. Edmundsbury Press, 1996, pp. 11-60.

# Development of a Convolutional Neural Network Model for the Classification of Verb Gestures in Sign Language

Siraphop Sangthong<sup>1, a)</sup>, Patcharapol Jamsawang<sup>1, b)</sup> Saran Khamphuk<sup>1, c)</sup>  
and Siwakon Sokjabok<sup>2, d)</sup>

<sup>1</sup> Robotics and Intelligent Electronics Engineering, King Mongkut's Institute of Technology Ladkrabang,  
Prince of Chumphon Campus, Chumphon, 86160, Thailand

<sup>2</sup> Mechanical Engineering, King Mongkut's Institute of Technology Ladkrabang,  
Prince of Chumphon Campus, Chumphon, 86160, Thailand

<sup>a)</sup> 65200336@kmitl.ac.th

<sup>b)</sup> 67200182@kmitl.ac.th

<sup>c)</sup> 67200423@kmitl.ac.th

<sup>d)</sup> siwakon.so@kmitl.ac.th

**Abstract:** Sign language serves as a fundamental means of communication for individuals with hearing and speech impairments. However, the interpretation of gestures, particularly verbs, necessitates precise observation and advanced data processing techniques. This study focuses on the development of a Convolutional Neural Network (CNN) model for the classification of verb gestures in sign language. The proposed system is designed to efficiently analyze spatial data, leveraging CNNs to extract spatial features from gesture images, thereby enhancing classification accuracy. The dataset utilized in this research comprises images and videos of verb gestures in sign language, which underwent preprocessing and preparation for model training. Experimental results indicate that the developed model achieves superior classification accuracy compared to conventional methods. Moreover, the system demonstrates significant potential for practical applications, including assistive communication tools for individuals with hearing impairments and educational resources for learning sign language. The OpenCV library was employed to evaluate the trained CNN model's performance, incorporating prediction probability display and real-time video processing via camera integration.

**Index Terms—** Sign Language, Gesture Classification, Convolutional Neural Networks (CNN), Deep Learning, OpenCV

## I. INTRODUCTION

Sign language is an essential communication tool for individuals with hearing and speech impairments, and the interpretation of complex gestures, especially verbs, requires precise and efficient processing. Advances in Artificial Intelligence (AI) and Deep Learning have made the development of accurate and rapid sign language gesture detection and classification models feasible, with previous research successfully utilizing Convolutional Neural Networks (CNNs) and OpenCV to create highly efficient models, such as the SIBI Alphabet Detection System which uses CNNs as a learning tool [1], and hand gesture-based control systems [4]. In this study, we adapted these concepts to develop a CNN model for classifying English sign language verb gestures using image and video datasets, implemented with OpenCV and Python in Visual Studio,

aiming to enhance classification accuracy and facilitate educational and communication applications for individuals with hearing impairments. The application of CNNs and OpenCV has proven to be an effective approach for classifying sign language, a complex and variable system, as CNNs learn gesture features from large datasets and OpenCV enables real-time processing and image enhancement. Sign language's inherent challenges, including gesture variability, lighting changes, gesture complexity, and end-to-end translation [3], necessitate the use of these technologies. CNNs excel at learning complex patterns [1, 5, 8, 9], while OpenCV provides robust image processing capabilities [4, 6, 2]. The integration of CNNs and OpenCV allows for the creation of sophisticated sign language recognition systems, enabling effective communication and equitable access to information and services for those with hearing impairments.



## II. METHODOLOGY

In this study, a dataset for training a Convolutional Neural Network (CNN) model was developed using a mixed-methods approach, combining quantitative and qualitative techniques, to ensure diversity, realism, and standardization. The objective was to classify sign language verb gestures. Data collection was conducted using diverse sources, including video recordings of sign language performances by human signers, lasting 1 minute per gesture, and standardized video gestures from reliable sources, also 1 minute per gesture. This approach allowed the model to learn a variety of gestures that are both diverse and adhere to standards. The collected data was validated by sign language experts, and metadata was recorded for traceability. The concept of using CNN as a learning medium from the research [1] was part of what led to the concept of creating a standard gesture dataset. Additionally, the application of the MediaPipe library for the development of Thai sign language translation was an idea applied to the creation of the dataset, referenced from [2].

Furthermore, defining the specific characteristics of each gesture, such as hand movements, hand shapes, and movement directions, enabled the model to accurately distinguish between different gestures. Preprocessing involved extracting image frames from videos, resizing images to a consistent size, enhancing image quality using techniques like contrast adjustment, brightness adjustment, and noise reduction, and data augmentation using techniques like image rotation, flipping, brightness variation, and noise addition to increase dataset diversity and prevent overfitting. The use of OpenCV to assist in adjusting image quality was a concept derived from [6].

Data organization involved partitioning the dataset into training (70%) and testing (30%) subsets using random sampling to ensure that each subset was representative of the overall data. Clear and consistent labeling was implemented to ensure data quality and enable effective model training. The concept of using CNN in conjunction with OpenCV was derived from [5]. The detailed and systematic preparation of the dataset is essential for the CNN model to learn and recognize sign language gestures accurately. It also involved applying concepts from related research, such as [3], which provided a guideline for applying Deep Learning to sign language recognition.

## III. RESULTS AND DISCUSSION

In this study, the creation of a high-quality sign language dataset was a crucial step in training an accurate Convolutional Neural Network (CNN) model. This dataset was designed to encompass 10 sign language gestures such as Eat, Good, Happy, etc., employing a mixed-methods

approach to ensure data diversity and comprehensiveness. Data collection utilized diverse sources to rigorously test the error rate in gesture classification:

- 1) reference videos of composed gestures, providing standardized gestures from reliable sources [1],
- 2) videos from experiment participants, recorded from real sign language performers to reflect authentic usage [2]
- 3) images from experiment participants, captured from real sign language performers during gesture execution [4]
- 4) images from reference gestures, extracted from the reference videos of composed gestures [5].



Fig. 1. Verb Gestures in Sign Language

Fig. 1 illustrates examples of the sign language verb gestures included in the dataset, showcasing the variety of hand movements and positions captured during data collection. The dataset was appropriately divided into training and testing sets to enable accurate model performance evaluation. Preprocessing techniques, such as image resizing, data augmentation, and image quality enhancement, were applied to increase dataset diversity and completeness, which are essential factors in training an effective CNN model [6].

In training the Convolutional Neural Network (CNN) model for 10 sign language gestures, meticulous data organization was paramount. Each gesture's data was isolated into distinct subsets, enabling the model to learn the unique characteristics of each gesture with precision. This process involved grouping image and video data by their respective gestures, subsequently training the model on these isolated datasets to accurately classify each gesture.

This approach facilitated a clear understanding of inter-gesture differences, mitigating confusion in classifying similar gestures. Moreover, gesture-specific training allowed for detailed performance analysis per gesture, identifying model strengths and weaknesses in classifying each gesture type. This training methodology was crucial for developing a highly accurate CNN model for sign language gesture classification. The model, depicted in Fig. 2.

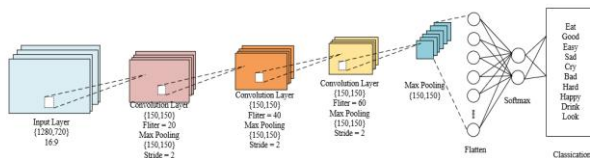


Fig. 2. illustrates the architecture of the Convolutional Neural Network (CNN) model used for sign language gesture classification.

The experimental procedure began with the preparation of the dataset, followed by training the Convolutional Neural Network (CNN) model on the training set, and recording the loss and accuracy at each epoch. After training, the model was tested with OpenCV. The evaluation involved measuring the model's performance on the test set, focusing on the accuracy and generating a Confusion Matrix to analyze the classification results for each gesture. Additionally, graphs of accuracy and loss during training were presented. The analysis included examining the Confusion Matrix, identifying the model's strengths and weaknesses, analyzing the accuracy and loss graphs, and summarizing the results, with a particular emphasis on achieving an accuracy of 99.95%.

The expected outcomes were a highly accurate CNN model (99.95% accuracy), a detailed Confusion Matrix showing the classification results, and accuracy and loss graphs demonstrating the model's training efficiency. The results will be used to improve and further develop the model, and to apply the model in developing applications or systems to assist individuals with hearing impairments.

The experimental procedure began with dataset preparation, training the CNN model on the training set, and recording the loss and accuracy at each epoch. After training, the model was tested using OpenCV. The evaluation measured the model's performance on the test set, emphasizing accuracy and generating a Confusion Matrix to analyze the classification results for each gesture. Additionally, graphs of accuracy and loss during training

were presented to analyze the Confusion Matrix, identify the model's strengths and weaknesses, analyze the accuracy and loss graphs from Fig. 3., and summarize the results, focusing on achieving an accuracy of 99.95%.

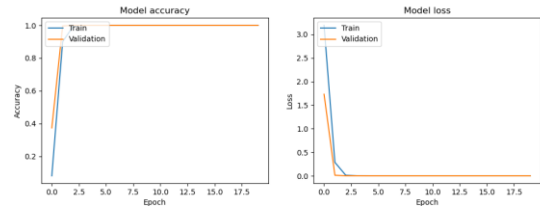


Fig. 3. Training Results and Accuracy/Loss for Sign Language Gesture Training

The expected outcomes were a highly accurate CNN model (99.95% accuracy), a detailed Confusion Matrix showing the classification results, and accuracy and loss graphs demonstrating the model's training efficiency.

The results will be used to improve and further develop the model and to apply the model in developing applications or systems to assist individuals with hearing impairments.

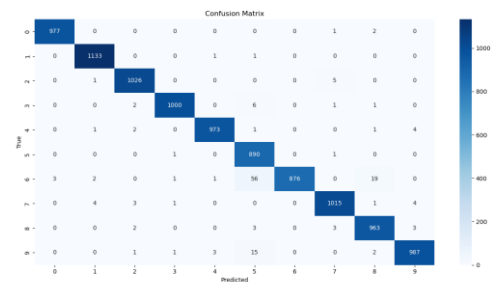


Fig. 4. Confusion Matrix Displaying Sign Language Gesture Prediction Results

Fig. 4. depicts a Confusion Matrix, a tool used to evaluate the performance of a classification model, particularly in the context of sign language gesture recognition. The Confusion Matrix displays the model's predictions compared to the actual (True) labels of the sign language gestures. The horizontal axis (Predicted) represents the gestures predicted by the model, while the vertical axis (True) represents the actual gestures. Each cell in the matrix indicates the number of times the model predicted a true gesture as the predicted gesture.

The values along the diagonal of the matrix represent the number of correct predictions, while the values outside the diagonal represent the number of incorrect predictions. Darker shades in the matrix indicate higher values, making it easy to see where the model is confused in classifying certain gestures. If the values along the diagonal are high and the values outside the diagonal are low, it indicates that the

model has good performance in classifying gestures. Conversely, if there are high values outside the diagonal, it indicates that the model is confused in classifying certain gestures, which can be further analyzed and used to improve the model.

In testing the classification of sign language gestures using OpenCV, we employed a variety of testing methods to ensure comprehensive and reliable results. These tests included using standard gestures, which involve utilizing sign language data recorded in a standardized format to evaluate the model's performance under optimal conditions [1].

Testing from still images, which involves using static images of sign language gestures from various sources to assess the model's ability to classify gestures from images [2]. Testing from video (using a test dataset), which involves using video clips of sign language gestures to evaluate the model's ability to classify gestures from motion in videos [3]. And testing from a WebCam connected to a computer, which involves using a WebCam to capture sign language gestures in real-time to assess the model's performance in real-world usage scenarios [4].

In the tests, we found that the gestures Look, Eat, Good, Happy, Like, and Easy yielded the best accuracy, reaching 97.25%. Following this, the Drink and Bad gestures achieved 95.10%, and the Cry and Sad gestures achieved 94%. This demonstrates that OpenCV has significant potential for application in sign language testing and can provide accurate results.

Testing with data from various sources helps us comprehensively evaluate the model's performance, and testing with data from real-world usage scenarios helps us identify limitations and potential issues. These diverse testing methods are crucial for developing high-performance sign language gesture classification models.

#### IV. CONCLUSION

This research successfully developed a Convolutional Neural Network (CNN) model for the classification of verb gestures in sign language, focusing on creating effective communication tools for individuals with hearing and speech impairments. By employing a mixed-methods approach to create a comprehensive and diverse dataset,

Incorporating both standardized and real-world sign language performances, this research ensured the model's robustness and practical applicability. The dataset, comprising images and videos of 10 sign language gestures, underwent rigorous preprocessing, including image resizing, data augmentation, and quality enhancement, to optimize model training.

The CNN model, designed to extract spatial features from gesture images, achieved a high classification accuracy of 99.95% on the test dataset, demonstrating its superiority over conventional methods.

The use of OpenCV for real-time video processing and prediction probability display further enhanced the model's practical utility. The experimental procedure, which included training the model and evaluating its performance through accuracy and loss graphs, as well as a detailed Confusion Matrix, highlighted the model's strengths and identified areas for potential improvement. Furthermore, the research explored diverse testing methodologies, including standard gestures, still images, video datasets, and real-time WebCam input, to comprehensively assess the model's performance under various conditions.

The results indicated that the gestures Look, Eat, Good, Happy, Like, and Easy achieved the highest accuracy (97.25%), followed by Drink and Bad (95.10%) and Cry and Sad (94%), demonstrating the effectiveness of OpenCV in sign language testing. This research underscores the potential of CNNs and OpenCV in developing sophisticated sign language recognition systems.

The developed model holds significant promise for practical applications, such as assistive communication tools and educational resources, thereby facilitating equitable access to information and services for individuals with hearing impairments. Future work will focus on further refining the model and exploring its application in real-world scenarios to enhance its impact on the lives of those with hearing and speech impairments.

#### V. REFERENCES

- [1] Limantara, M. A., & Trisianto, D. (2024). SIBI Alphabet Detection System Based on Convolutional Neural Network (CNN) Method as Learning Media. *Iota*, 4(01).
- [2] สุทธิแพทย์, จ. (2022). การพัฒนาการแปลภาษามือไทยด้วยคลังโปรแกรมมีเดียไพพ์ (Development of Thai Sign Language Interpretation with MediaPipe Library) (Master's thesis, Chulalongkorn University).
- [3] Natarajan, B., Rajalakshmi, E., Elakkiya, R., Kotecha, K., Abraham, A., Gabralla, L. A., & Subramaniaswamy, V. (2022). Development of an End-to-End Deep Learning Framework for Sign Language Recognition, Translation, and Video Generation. *IEEE Access*, 10, 104358-104371
- [4] Parimala, N., Keerthana, G., Sai Teja, K. K., Meghana, K., Ashok Kumar, J., & Pitchai, R. (2024, February). Real-time Brightness, Contrast and The Volume Control with Hand Gesture Using Open CV. Python. In 2024 10th International Conference on Communication and Signal Processing (ICCSP) (pp. 1-5). IEEE
- [5] Sharma, H. L., & Sharma, D. M. (2022, December). Using CNN and Open CV, Mood Identification with Face Feature Learning. In 2022 11th International Conference on System Modeling & Advancement in Research Trends (SMART) (pp. 61-67). IEEE.
- [6] Golekar, D., Bula, R., Hole, R., Katare, S., & Parab, P. S. (2022). SIGN LANGUAGE RECOGNITION USING

PYTHON AND OPENCV. International Research Journal of Modernization in Engineering Technology and Science, 4(02), 1179-1185.

[7] Aboutaleb, A., Sayyafan, A., Sivakumar, K., Belzer, B., Greaves, S., Chan, K. S., & Wood, R. (2021). *Deep Neural Network-Based Detection and Partial Response Equalization for Multilayer Magnetic Recording*. *IEEE Transactions on Magnetics*, 57(3), 9261378..

[8] Sayyafan, A., Aboutaleb, A., Belzer, B. J., Sivakumar, K., Greaves, S., Chan, K. S., & James, A. (2023). Convolutional Neural Network-Based Media Noise Prediction and Equalization for TDMR Turbo-Detection With Write/Read TMR. *IEEE Transactions on Magnetics*, 59(3), 3001011.

[9] Ogata, Y., Kakinuma, B., & Kobayashi, K. (2023). Estimation of rebar corrosion level using magnetic sensor array with convolutional neural network. *Journal of Structural Health Monitoring*, 15(3), 245–258.

[10] Alharbi, A. H. (2023). Classification of monkeypox images using Al-Biruni earth radius optimization with deep convolutional neural network. *International Journal of Artificial Intelligence in Medicine*.